



Towards Predictable Tuning of Spin Crossover

Luca Bondi

*A thesis submitted for the degree of
Doctor of Philosophy*

*Co-tutelled program
at the University of Otago, Dunedin, New Zealand
and the University of Florence, Florence, Italy.*



22nd April 2021

(Revised version at the 11th July 2021)

To everyone who has crossed path with me during this journey.

Dit is voor iedereen waarmee mijn wegen zijn gekruist tijdens mijn reis.

இப்பயணத்தில் என் உடன் பயணித்த அனைவருக்கும்.

Para todos aquellos con los que me he cruzado durante este camino.

جو اس سفر ميں ميرے ساتھ تھے، ان سب کو میرا سلام

Para todos que cruzaram esse caminho comigo durante essa jornada.

A tutti quelli che hanno condiviso una parte di questo viaggio con me.

The research presented in this thesis was carried out in the Department of Chemistry at the University of Otago, Dunedin, New Zealand under the supervision of Professor Sally Brooker (eight months per year, twenty-four months in total) and in the Department of Chemistry Ugo Schiff at the University of Florence, Florence, Italy under the supervision of Professor Federico Totti (four months per year, twelve months in total) in a co-tutelled program between December 2017 and January 2021. Parts of the content of this thesis have been published, submitted for peer review, or presented elsewhere as described below.

Peer reviewed papers – containing results included in this thesis:

“Quantitative Evaluation of The Nature Of M-L Bonds in Paramagnetic Compounds: Application Of EDA-NOCV Theory to Spin Crossover Complexes”, Luca Bondi, Anna L. Garden, Paul Jerabek, Federico Totti, Sally Brooker, *Chemistry A European Journal*, 2020, 26, 13677 - 13685. I carried out all the theoretical studies on the ten iron(II) azine-triazole complexes, analysed the data and drafted the entire manuscript as well as the large supporting information file.

Peer reviewed papers – containing results not included in this thesis:

“Predictable Electronic Tuning By Choice of Azine Substituent in Five Iron^{II} Triazoles: Redox Properties and DFT Calculations”, Santiago Rodríguez-Jiménez, Luca Bondi, Mingrui Yang, Dr. Anna L. Garden and Sally Brooker, *Chemistry – An Asian Journal* 14.8 (2019): 1158-1166. I carried out the *DFT* studies on the five iron(II) azine-triazole complexes, drafted the sections of the manuscript concerning these results, and provided the associated supporting information.

“Predictable Substituent Control of Co^{II/III} Redox Potential and Spin Crossover in Bis(dipyridylpyrrolide)cobalt Complexes”, James N. McPherson, Ross W. Hogue, Folaranmi Sunday Akogun, Luca Bondi, Ena T. Lui, Jason R. Price, Anna L. Garden, Sally Brooker and Stephen B. Colbran, *Inorganic Chemistry* 2019, 58, 3, 2218–2228. I carried out the *DFT* studies on the five cobalt(II) bis(dipyridylpyrrolide) complexes, drafted the sections of the manuscript concerning these results, and provided the associated supporting information.

Oral presentations at conferences

“New Approach to Improving Understanding of M-L bond in Spin Crossover Complexes” (15 min, by zoom because of the pandemic due to COVID-19). Presented at the 1st Asian Conference on Molecular Magnetism (ACMM2020), Fukuoka, Japan, 8th-10th March 2021.

“Quantitative Assessment of the Energetic Contribution on the M-L Interaction in Fe^{II} 2,6-Di(Pyrazol-1-yl)Pyridine Complexes” (20 min). Accepted for the International Chemical Congress of Pacific Basin Societies 2020 (PACIFICHEM), Hawaii, USA. Scheduled for 15th-20th December 2020, now postponed to December 2021 because of the pandemic due to COVID-19.

“New Approach to Improving Understanding of M-L bond in Spin Crossover Complexes” (20 min, by zoom because of the pandemic due to COVID-19). Presented at the 5th Bordeaux Oliver Kahn Discussions (BOOK-D), Bordeaux, France, 31st August to 4th September 2020.

“A Simple Method of Predicting Spin State in Solution” (15 min). Presented at the MacDiarmid Institute’s 9th International Conference on Advanced Materials and Nanotechnology (AMN9), Wellington, New Zealand, 10th-14th February 2019.

“Quantitative Assessment of the Energetic Contribution on the M-L Interaction in Fe^{II} 2,6-Di(Pyrazol-1-yl)Pyridine Complexes” (15 min). Presented at the Quantum and Computational Chemistry Student Conference (QUACCS) student conference at the Australian National University’s Kioloa campus, New South Wales coast, Australia, 9th-14th December 2018.

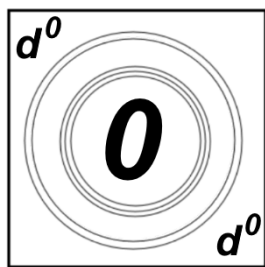
Conference poster presentations

“Testing the Generality of Correlating Ligand ¹⁵N NMR Chemical Shift With T_{1/2} of Corresponding Spin Crossover Complex”. Accepted for the 44th International Conference of Coordination Chemistry (ICCC), Rimini, Italy. Scheduled for 5th-10th July 2020; now postpone to July 2021 because of the pandemic due to COVID-19.

“Testing the generality of correlating ligand ¹⁵N NMR chemical shift with T_{1/2} of corresponding spin crossover complex”. Presented at the 9th Conference of the Asia-Pacific Association of Theoretical and Computational Chemists (APATCC 2019) Sydney, Australia, 30th Sept - 3rd Oct 2019.

“Testing the generality of correlating ligand ¹⁵N NMR chemical shift with T_{1/2} of corresponding spin crossover complex”. Presented at the 7th European Conference on Molecular Magnetism (ECMM – 2019), Florence, Italy, 15th-18th September 2019.

“Testing the generality of correlating ligand ¹⁵N NMR chemical shift with T_{1/2} of corresponding spin crossover complex”. Presented at the 1st Workshop on Otago Future Fuels (OFF) Dunedin, New Zealand, 7th – 8th Feb 2019



Abstract

Spin crossover (SCO) active metal complexes are highly versatile materials thanks to their sensitivity to tiny physical or chemical environmental changes. This property makes them very useful for a wide range of applications: employable for experimental studies as molecular switches or for theoretical studies investigating the **M-L** bonds. In both cases, these studies aim to develop strategies of predictably tuning them.

Chapter One. An introduction to the SCO phenomenon: from *gradual* to *cooperative* SCO; various methods of monitoring the SCO transition. A summary of some literature examples of SCO-active systems is given. An overview of the published achievements in predicting the SCO phenomenon, including an introduction to the computational models deployed across the years. The *EDA-NOCV* model, employed in this field for the first time in this PhD thesis, is introduced. Finally, the aims of this study are presented.

Chapter Two. The synthesis and characterisation of four new non-symmetrical ligands, 3-(2-(5-**Z**-pyridyl))-4-tolyl-5-phenyl-1,2,4-triazole (L^{pytZ} , **Z** = **CF**₃, **Br**, **F**, **Me**), and the corresponding $[Fe^{II}(L^{pytZ})_2(NCBH_3)_2]$ complexes are presented. All four of these new complexes are SCO-active in the solid state and in $CDCl_3$ solution, but $T_{1/2}$ tuning by the *meta*-**Z** substituents was very modest. Three literature families were also tested, successfully extending the generality of using the ¹⁵N NMR chemical shift δN_A of the coordinated nitrogen atom of the free ligand as measure of the $T_{1/2}$ in the resulting Fe(II) complex.

Chapter Three. Theoretical study of a family of five iron(II) *SCO*-active $[\text{Fe}(\text{L}^{\text{azine}})_2(\text{NCBH}_3)_2]$ ($\text{L}^{\text{azine}} = 3\text{-(2-aziny1)-4-toly1-5-phenyl-1,2,4-triazole}$) and of the related five *LS* $[\text{Fe}(\text{L}^{\text{azine}})_3(\text{BF}_4)_2]$. The *EDA-NOCV* model was applied to molecular fragments to provide *quantitative* assessment of the σ - and π -bonding. A new corrected $[\text{M}^{\text{n+}} + \text{L}_6]$ fragmentation was implemented which promises to enable a general approach suitable for any ML_6 system. Finally, the σ - and π -bonding character is strongly correlated with the experimental $T_{1/2}$ of the *SCO*-active $[\text{Fe}(\text{L}^{\text{azine}})_2(\text{NCBH}_3)_2]$ complexes.

Chapter Four. Theoretical study of the **M-L** bond in a family of sixteen *SCO*-active differently *para-X* substituted $[\text{Fe}(\text{bpp}^{\text{X}})_2]^{2+}$ complexes (bpp^{X} is 2,6-di(pyrazol-1-yl)-4-**X**-pyridine). Results of the *EDA-NOCV* revealed the σ -strength of the bpp^{X} ligand is correlated with $\sigma_{\text{p}^+}(\text{X})$, $\delta\text{N}_A(\text{bpp}^{\text{X}})$, experimental $T_{1/2}([\text{Fe}(\text{bpp}^{\text{X}})_2]^{2+})$ and calculated *AILFT* $\Delta_o([\text{Fe}(\text{bpp}^{\text{X}})_2]^{2+})$. Results are explained at the molecular level by investigating the orbital population of the valence orbitals of the coordinating nitrogen involved in the aromatic π -system (p_π) and in the Fe-N bond ($sp^2(\text{Fe})$). From the observed correlations, the unknown σ_{p^+} parameter for two substituents (**X** = **SOMe**, **SO₂Me**) is predicted.

Chapter Five. First theoretical study on $[\text{Co}^{\text{II}}(\text{dpzca})_2]$ *SCO* in the solid state, aiming to establish a computational protocol able to predict experimental $T_{1/2}$ in pressure-activated *SCO*. The first part of the study validated a *DFT* protocol at $p = 1$ bar. The protocol was then extended and trialled up to 4300 bar. Results revealed good reproduction of the experimental results up to 2100 bar; but beyond this pressure, the theoretical and experimental findings diverge. Theoretical data suggest a possible phase change for the crystalline structure of *HS* $[\text{Co}^{\text{II}}(\text{dpzca})_2]$ at higher pressures than 2100 bar; this would explain why the implemented computational protocol lost validity.

Acknowledgments

I would like to begin with this attempt of mine, in trying to explain you all what this PhD meant to me. Tough time, extremely tough; but also, extremely dense. Everything began almost four years ago. It was June 2017. I started this experience as a lost boy, wishing to be an explorer and craving to reach the edges of the World. But leaving was not enough, I wanted to keep my 'foot into two shoes', as a very common Italian saying recites. I wanted to be able to go back and forth, summer after summer. Therefore, the first of my acknowledgments is for prof. Brooker and prof. Totti; you two put in place this co-tutelled program; without you both, this journey would have never begun. You taught me how to live in an international framework, where I needed to be always online, responding to calls from the European or the Pacific time zone. Being away from your direct supervision was hard, but also motivating. I needed to become more responsible and self-organised; I wanted to prove you both that no time was ever lost. I've been the fulcrum of a collaboration between Italy, New Zealand and Germany (sometimes), and it was far from an easy task.

Prof. Sally Brooker – thank you for teaching me the organic and the inorganic chemistry. Thank you for trying over and over to make me appreciate the act of 'cooking' chemistry. And thank you for showing me a wider perspective on the synthetic chemistry, as it helped me to better bridge it with my theoretical background. Thank you for your trust, your understanding, your support. And overall, thank you for all the opportunities you promoted for me.

Prof. Federico Totti, thank you for everything you taught me in those years together. Beyond discussions and divergences, I am thankful for everything you gave me.

It was December 2018 when Dr. Anna Garden welcomed me as ‘plus-one’ in Garden’s gnomes and we all left for a trip to Australia, an unforgettable time together. Thank you for the times you spent in talking about science with me and, overall, for all those numerous times that you believed in me, as a person and as an asset for my research group. None of those words have fallen on deaf ears.

December 2018, again. My first paper published in the Brooker Bunch, with Dr. Santiago Rodríguez-Jiménez. Maybe the first of a collection, surely the beginning of a deep partnership that helped me to grow immensely as a scientist. You surely were the best of my colleagues, and a friend.

Next, in July 2020, the publication of my first first-name-paper in this PhD came to light. Stressful, but satisfying. I worked at this paper with all my supervisors together and Dr. Paul Jerabek, my mentor for the *EDA-NOCV* method. Whom of you will go through this thesis will see how intensely I used his teachings in these past three years, and how much I enjoyed it.

I care to acknowledge my PhD colleagues, that shared the ups-and-downs of this time with me. Among all, Sriram and Matt surely deserves a special mention.

Finally, a special thought for the ones that were always there, by my side. I am talking about my dad, that messed up with his sleep time because it wanted to sync with my time zone. Thank you to be always there for me. And thank you to Emilia, because we went through a lot during these past three years, together.

As I said, my PhD was more about the journey rather than the goal. And even if science is important, the life I experienced meant to me much more than my academic goals. This journey has opened the gates of an international life that has changed me forever. The same dawn that the slave experienced outside of Plato’s cave; whatever he knew before, it is

irreversibly behind him. The people I met in these three years taught me cultures, politics, diplomacy. I learnt to appreciate my condition of European citizen, as we are granted of the possibility of a free choice when several others don't. Not nice to say, but I could feel why I was born in the right side of the World. I talked to people that escaped their country and other that left everything they loved behind, looking for better opportunities. The internationality of the life I experienced are carving the choices I am making; and I doubt this will ever change.

Therefore, I want to express a special thank for all the people that I met out of my working life; the ones that I met by mistake or by twist of faith, who became my friends. I cannot list you all, but I hope you can hear my call as you all are an unreplaceable part of this journey and I will never be able to thank you enough for sharing a part of your walk with me. Thank you for the times we got drunk and the times we explored the World together. Thank you for the simple moments and for all the dense laughs. Thank you to hold me tight when I was falling and for showing me the bright sides when I could see only darkness. Thank you for pushing me over my limits, so I could turn in something new, something better. Thank you for the morning coffees, or night beers. Thank you for our holidays in the hot pool or the beers in St. Claire, stolen from the office hours. We confess Sally, sometimes the weather was way too good for not responding that call! Hope you can forgive us.

I want to thank you all, and it doesn't matter if we crossed our path for days, weeks or months, I want to dedicate this thesis to all of you. You all that showed me how wide is the World.

Table of Contents

0	ABSTRACT	V
	ACKNOWLEDGMENTS	VII
	TABLE OF CONTENTS	XI
	LIST OF ABBREVIATIONS	XVII
1	INTRODUCTION	1
1.1.	ABSTRACT.....	2
1.2.	INTRODUCTION TO SPIN CROSSOVER (SCO)	3
1.2.1.	<i>General Overview</i>	3
1.2.2.	<i>Thermodynamics of SCO</i>	5
1.2.3.	<i>From Solid to Solution SCO</i>	7
1.3.	METHODS TO MONITOR SCO	12
1.3.1.	<i>General Overview</i>	12
1.3.2.	<i>Solid State Magnetic Measurements</i>	13
1.3.3.	<i>¹H-NMR Evan's Method</i>	15
1.4.	REPORTED TRENDS IN SCO FAMILIES	18
1.4.1.	<i>Introduction to Hammett Parameter</i>	18
1.4.2.	<i>Solid State SCO Family Trends</i>	19
1.4.3.	<i>Solution Phase SCO Family Trends</i>	20
1.5.	TEMPERATURE AND PRESSURE INDUCED Co ^{II} SCO.....	28
1.6.	THEORETICAL APPROACHES TO SCO	34
1.6.1.	<i>General Overview</i>	34
1.6.2.	<i>Ab Initio Ligand Field Theory on SCO Systems</i>	34
1.6.3.	<i>Density Functional Theory on SCO Systems</i>	36
1.6.4.	<i>DFT+U on SCO Systems: The Hubbard U Term</i>	40
1.6.5.	<i>Monte Carlo and Molecular Dynamics (MC/MD) on SCO Systems</i>	41
1.6.6.	<i>Artificial Neural Networks (ANN) on SCO Systems</i>	43
1.6.7.	<i>Introduction to EDA-NOCV</i>	44
1.7.	AIMS OF THIS PHD	52
2	TESTING THE GENERALITY OF T _{1/2} OF SPIN CROSSOVER COMPLEX VS. LIGAND	
	¹⁵ N NMR CHEMICAL SHIFT CORRELATIONS: TOWARDS PREDICTABLE TUNING	55
2.1.	ABSTRACT.....	56
2.2.	INTRODUCTION.....	57
2.3.	RESULTS AND DISCUSSION	61
2.3.1.	<i>Synthesis of L^{pytz} Ligands</i>	61
2.3.2.	<i>Synthesis of [Fe^{II}(L^{pytz})₂(NCBH₃)₂] Complexes</i>	62

2.3.3.	Crystal Structures of $[Fe^{II}(L^{pytz})_2(NCBH_3)_2]$	63
2.3.4.	Solid State Spin Crossover of $[Fe^{II}(L^{pytz})_2(NCBH_3)_2] \cdot nH_2O$	66
2.3.5.	Solution Spin Crossover of $[Fe^{II}(L^{pytz})_2(NCBH_3)_2]$	68
2.3.6.	Experimental and Calculated $^{15}N_A$ Chemical Shift of Ligands	72
2.3.7.	^{15}N NMR vs $T_{1/2}$ Correlations in Five Different Fe^{II} SCO Families	73
2.3.8.	Hammett vs ^{15}N NMR Correlations for the Five Families	77
2.4.	CONCLUSIONS	79
2.5.	EXPERIMENTAL SECTION	80
2.5.1.	Organic Synthesis	80
2.5.2.	Inorganic Synthesis	87
3 	QUANTITATIVE EVALUATION OF THE NATURE OF M-L BONDS IN PARAMAGNETIC COMPOUNDS: APPLICATION OF EDA-NOCV THEORY TO SPIN CROSSOVER COMPLEXES	91
3.1.	ABSTRACT	92
3.2.	INTRODUCTION	93
3.2.1.	General Overview	93
3.2.2.	Choice of Test System	94
3.3.	FRAGMENTATION DILEMMA	96
3.4.	RESULTS AND DISCUSSION	101
3.4.1.	LS $[Fe^{II}(L^{azine})_2(NCBH_3)_2]$	101
3.4.2.	HS $[Fe^{II}(L^{azine})_2(NCBH_3)_2]$	103
3.4.3.	Correlation of EDA-NOCV Parameters with $T_{1/2}$	106
3.4.4.	LS $[Fe^{II}(L^{azine})_3]^{2+}$	107
3.4.5.	L^{azine} vs $2NCBH_3$: Ligand Field Strength Comparison	110
3.5.	CONCLUSIONS	111
3.6.	COMPUTATIONAL PROTOCOL	113
4 	QUANTITATIVE ASSESSMENT OF THE ENERGETIC CONTRIBUTION ON THE M-L INTERACTION IN $Fe(II)$ 2,6-DI(PYRAZOL-1-YL)PYRIDINE COMPLEXES	115
4.1.	ABSTRACT	116
4.2.	INTRODUCTION	117
4.3.	RESULTS AND DISCUSSION	120
4.3.1.	DFT optimisation of $[Fe(bpp^X)_2]^{2+}$ (LS and HS)	120
4.3.2.	AILFT Analysis Effect of X on Δ_o for LS $[Fe(bpp^X)_2]^{2+}$	121
4.3.3.	EDA Analysis of Effects of X in $[Fe(bpp^X)_2]^{2+}$ (LS and HS)	122
4.3.4.	NOCV Analysis of the effects of X vs σ - and π - Bonding Terms of $[Fe(bpp^X)_2]^{2+}$ (LS and HS)	127
4.3.5.	Correlations of NOCV Results with $T_{1/2}$, σ_p^+ , δN and Δ_o	131
4.3.6.	EDA-NOCV results explained by Mulliken charges	136
4.3.7.	Predicted σ_p^+ Parameter for X = SOMe, SO_2Me	141
4.4.	CONCLUSION	143
4.5.	COMPUTATIONAL PROTOCOL	144

5 	ACCURATE PREDICTION OF PRESSURE AND TEMPERATURE $T_{1/2}$ VARIATION IN SOLID STATE SPIN CROSSOVER BY <i>AB INITIO</i> METHODS: THE $[\text{Co}^{\text{II}}(\text{DPZCA})_2]$ CASE....	147
5.1.	ABSTRACT.....	148
5.2.	INTRODUCTION.....	149
5.3.	METHODOLOGY: MODELLING A <i>SCO</i> TRANSITION.....	155
5.4.	RESULTS AND DISCUSSION	157
5.4.1.	<i>Fine Tuning of the U_{eff} term</i>	157
5.4.2.	<i>Structural Distortions in $[\text{Co}(\text{dpzca})_2]$ Unit Cell</i>	160
5.4.1.	<i>Pressure Effects on Molecular Structure of $[\text{Co}(\text{dpzca})_2]$ Complexes</i>	162
5.4.2.	<i>Pressure Effects on $[\text{Co}(\text{dpzca})_2]$ Density of States</i>	166
5.4.3.	<i>Pressure effects on IR and Raman spectra of $[\text{Co}(\text{dpzca})_2]$</i>	169
5.4.4.	<i>Calculation of $T_{1/2}$ for SCO transition for $[\text{Co}(\text{dpzca})_2]$</i>	172
5.5.	CONCLUSIONS	176
5.6.	COMPUTATIONAL PROTOCOL	177
6 	FINAL REMARKS	179
A1 	ADDITIONAL DETAILS.....	A1
A1.1.	EXPERIMENTAL SECTION: GENERAL PROCEDURES.....	A1
A1.2.	THEORETICAL BACKGROUND	A3
A1.2.1.	<i>Schrödinger Equation</i>	A3
A1.2.2.	<i>Density Functional Theory</i>	A5
A2 	TESTING THE GENERALITY OF $T_{1/2}$ OF SPIN CROSSOVER COMPLEX VS LIGAND
	^{15}N NMR CHEMICAL SHIFT CORRELATIONS: TOWARDS PREDICTABLE TUNING
	A11
A2.1.	COMPUTATIONAL DETAILS	A11
A2.2.	NMR AND MS FIGURES FOR $L^{\text{PYT}CF3}$ LIGAND	A12
A2.3.	MS FIGURES FOR $[\text{Fe}(L^{\text{PYT}CF3})_2(\text{NCBH}_3)_2]$ COMPLEX	A19
A2.4.	NMR AND MS FIGURES FOR $L^{\text{PYT}BR}$ LIGAND.....	A22
A2.5.	MS FIGURES FOR $[\text{Fe}(L^{\text{PYT}BR})_2(\text{NCBH}_3)_2]$ COMPLEX	A29
A2.6.	NMR AND MS FIGURES FOR $L^{\text{PYT}F}$ LIGAND	A32
A2.7.	MS FIGURES FOR $[\text{Fe}(L^{\text{PYT}F})_2(\text{NCBH}_3)_2]$ COMPLEX.....	A39
A2.8.	NMR AND MS FIGURES FOR $L^{\text{PYT}ME}$ LIGAND	A42
A2.9.	MS FIGURES FOR $[\text{Fe}(L^{\text{PYT}ME})_2(\text{NCBH}_3)_2]$ COMPLEX SPECTRA	A49
A2.10.	SINGLE CRYSTAL X-RAY DATA.....	A52
A2.11.	SOLID STATE MAGNETIC MEASUREMENTS	A62
A2.12.	SOLUTION PHASE MAGNETIC MEASUREMENTS	A68
A2.12.1.	<i>Evans Method VT ^1H-NMR Spectra</i>	A69
A2.12.2.	<i>Evans Method: Error Analysis</i>	A75
A2.13.	UV-VIS SPECTRA OF $[\text{Fe}(L^{\text{PYTZ}})_2(\text{NCBH}_3)_2]$	A79
A2.14.	COMPUTATIONAL DETAILS	A80
A2.14.1.	<i>Ligand Structures</i>	A80
A2.14.2.	<i>Calculated N_A-NMR Chemical Shifts</i>	A81

A2.15.	CORRELATIONS.....	A85
A3 QUANTITATIVE EVALUATION OF THE NATURE OF M-L BONDS IN PARAMAGNETIC COMPOUNDS: APPLICATION OF EDA-NOCV THEORY TO SPIN CROSSOVER COMPLEXES		
A89		
A3.1.	GEOMETRY OPTIMISATION PROTOCOL	A90
A3.2.	EDA-NOCV OPTIMISATION PROTOCOL DEVELOPMENT	A99
A3.2.1.	First Application of EDA-NOCV to Paramagnetic Complexes	A99
A3.2.2.	Convergence Troubleshooting	A99
A3.2.3.	Symmetry Constraint in $[Fe^{II}(L^{azine})_2(NCBH_3)_2]$ Family.....	A100
A3.2.4.	Frag. 1 - LS $[Fe^{II}(Lazine)_2(NCBH_3)_2]$	A101
A3.2.5.	Frag. 2 - LS $[Fe^{II}(L^{azine})_2(NCBH_3)_2]$	A102
A3.2.6.	Frag. 3 - LS $[Fe^{II}(L^{azine})_2(NCBH_3)_2]$	A103
A3.2.7.	Frag. 4 - LS $[Fe^{II}(L^{azine})_2(NCBH_3)_2]$	A103
A3.2.8.	L^{azine} vs $2NCBH_3$ in Frag. 1 - 4	A106
A3.2.9.	Frag. 5a-5e: correct Fe^{2+} Energy Levels in LS $[Fe^{II}(L^{azine})_2(NCBH_3)_2]$ Family....	A107
A3.3.	EDA-NOCV RESULTS	A123
A3.3.1.	Frag. 1 - LS $Fe^{II}(L^{azine})_2(NCBH_3)_2$	A123
A1.2.3.	Frag. 2 - LS $Fe^{II}(L^{azine})_2(NCBH_3)_2$	A125
A3.3.2.	Frag. 3 - LS $Fe^{II}(Lazine)_2(NCBH_3)_2$	A127
A3.3.3.	Frag. 4 - LS $Fe^{II}(L^{azine})_2(NCBH_3)_2$	A129
A3.3.4.	Frag. 5b/5e - LS $Fe^{II}(L^{azine})_2(NCBH_3)_2$	A131
A3.3.5.	Frag. 5b/5e - HS $Fe^{II}(L^{azine})_2(NCBH_3)_2$	A134
A3.3.6.	Frag. 5b/5e - LS $[Fe(L^{azine})_3]^{2+}$	A142
A4 QUANTITATIVE ASSESSMENT OF THE ENERGETIC CONTRIBUTION ON THE M-L INTERACTION IN FE(II) 2,6-DI(PYRAZOL-1-YL) PYRIDINE COMPLEXES		
A147		
A4.1.	ATOMIC STRUCTURE RESULTS.....	A147
A1.1.	AILFT RESULTS.....	A149
A1.2.	EDA-NOCV RESULTS	A150
A4.1.1.	EDA: Fragmentation 5e.....	A154
A4.1.2.	NOCV: Fragmentation 5b.....	A156
A4.1.3.	NOCV Figures for LS $[Fe(bpp^X)_2]^{2+}$	A158
A4.1.4.	NOCV Figures for HS $[Fe(bpp^X)_2]^{2+}$	A167
A4.2.	CORRELATIONS OF ΔE_i IN LS $[Fe(bpp^X)_2]^{2+}$	A185
A4.2.1.	Transition Temperature $T_{1/2}$	A185
A4.2.2.	$^{15}N_A$ NMR Chemical Shift (δN_A)	A186
A4.3.	CORRELATIONS OF ΔE_i IN HS $[Fe(bpp^X)_2]^{2+}$	A187
A4.3.1.	Hammett Parameter $\sigma_p^+(X)$	A187
A4.3.2.	Transition Temperature $T_{1/2}$	A188
A4.3.3.	$^{15}N_A$ NMR Chemical Shift (δN_A)	A189
A4.4.	MULLIKEN POPULATION IN THE BPP^X LIGAND	A190
A4.5.	PUBLISHED CORRELATIONS.....	A191

A5 ACCURATE PREDICTION OF PRESSURE AND TEMPERATURE $T_{1/2}$ VARIATION IN SOLID STATE SPIN CROSSOVER BY AB INITIO METHODS: THE $[\text{Co}^{\text{II}}(\text{DPZCA})_2]$ CASE.....	A193
.....	
A5.1. COMPUTATIONAL PROTOCOL VALIDATION	A193
A5.1.1. <i>U_{eff} Tuning in Geometry Optimisation Procedure</i>	A193
A5.1.2. <i>U_{eff} Tuning for Cell Parameters in Cell Optimisation Procedure</i>	A196
A5.1.3. <i>U_{eff}(Co(d)) Tuning in Cell Optimisation Procedure</i>	A198
A5.2. ADDITIONAL STRUCTURAL DATA	A200
A5.2.1. <i>Cell Parameters of 1_{cry} vs. Pressure and Measured $T_{1/2}$</i>	A200
A5.2.1. <i>Structural Distortion of 1_{cry} vs. Pressure</i>	A214
A5.2.1. <i>Structural Distortion of 1_{cry} vs. Measured $T_{1/2}$</i>	A219
A5.2.1. <i>Structural Distortions associated with Spin State Transition</i>	A224
A5.3. ADDITIONAL ELECTRONIC DATA	A226
A5.3.1. <i>LDOS: Cobalt Atoms</i>	A236
A5.3.2. <i>LDOS: Nitrogen Atoms</i>	A244
A5.3.3. <i>LDOS: Carbon Atoms</i>	A246
A5.4. MOLECULAR ORBITALS OF $[\text{Co}(\text{DPZCA})_2]$	A248
A5.5. ADDITIONAL DATA FOR GRADUAL SCO MODELLING	A272
A5.5.1. <i>CP2K 6.1 Calculated IR Spectra</i>	A272
A5.5.1. <i>IR/Raman Spectra ORCA4.1 Code</i>	A273
A5.5.2. <i>Thermodynamic Terms</i>	A274
REFERENCES.....	I

List of Abbreviations

$\mathbf{1}_{cry}$	Co(<i>dpzca</i>) ₂
$\mathbf{1}_{cry,LS}$	crystalline <i>LS</i> Co(<i>dpzca</i>) ₂
$\mathbf{1}_{cry,HS}$	crystalline <i>HS</i> Co(<i>dpzca</i>) ₂
$\mathbf{1}_{cf,LS}$	charge-fielded <i>LS</i> Co(<i>dpzca</i>) ₂
$\mathbf{1}_{cf,HS}$	charge-fielded <i>HS</i> Co(<i>dpzca</i>) ₂
$\mathbf{1}_{iso,LS}$	isolated <i>LS</i> Co(<i>dpzca</i>) ₂
$\mathbf{1}_{iso,HS}$	isolated <i>HS</i> Co(<i>dpzca</i>) ₂
AILFT	Ab-Initio Ligand Field Theory
ANN	Artificial Neural Network
B3LYP	Becke, Three-Parameter, Lee-Yang-Parr
BP86	Becke, Perdew 1986
bpp^X	2,6-di(pyrazol-1-yl)-4- X -pyridine
bpp^Y	2,6-di((4- Y)-pyrazol-1-yl)-4-pyridine
c	Concentration
c	Light Speed Constant
calc.	Calculated
CASSCF	Complete Active Space Self-Consistent Field
CC	Coupled Cluster
CHCl₃	Chloroform
CIGARAD	Constant Time Inverse-Detected Gradient Accordion Rescaled Adiabatic
CPCM	Conductor-like Polarisable Continuum Model
CT	Charge Transfer

DCM	Dichloromethane
DOS	Density of States
DLPNO	Domain-based Local Pair Natural Orbital
DFT	Density Functional Theory
DMF	Dimethyl Formamide
EDA-NOCV	Energy Decomposition Analysis – Natural Orbital for Chemical Valence
EDG	Electron Donating Group
ETS	Extended Transition State
EtOH	Ethanol
Et₂O	Diethyl Ether
EWG	Electron Withdrawing Group
<i>f</i>	Frequency
<i>h</i>	Planck's Constant
<i>HF</i>	Hartree Fock
<i>HS</i>	High Spin
<i>HQD-NEVPT</i>	Hermitian quasi-degenerate NEVPT
IR	Infrared
<i>k_B</i>	Boltzmann constant
<i>L^{pyt}/L^{pytH}</i>	3-(2- <i>pyridyl</i>)-4-tolyl-5-phenyl-1,2,4-triazole
<i>L^{4pyrimidine}</i>	3-(2-(4- <i>pyrimidinyl</i>))-4-tolyl-5-phenyl-1,2,4-triazole
<i>L^{2pyrimidine}</i>	3-(2-(2- <i>pyrimidinyl</i>))-4-tolyl-5-phenyl-1,2,4-triazole
<i>L^{pyridazine}</i>	3-(2- <i>pyridazinyl</i>)-4-tolyl-5-phenyl-1,2,4-triazole
<i>L^{pyrazine}</i>	3-(2- <i>pyrazinyl</i>)-4-tolyl-5-phenyl-1,2,4-triazole

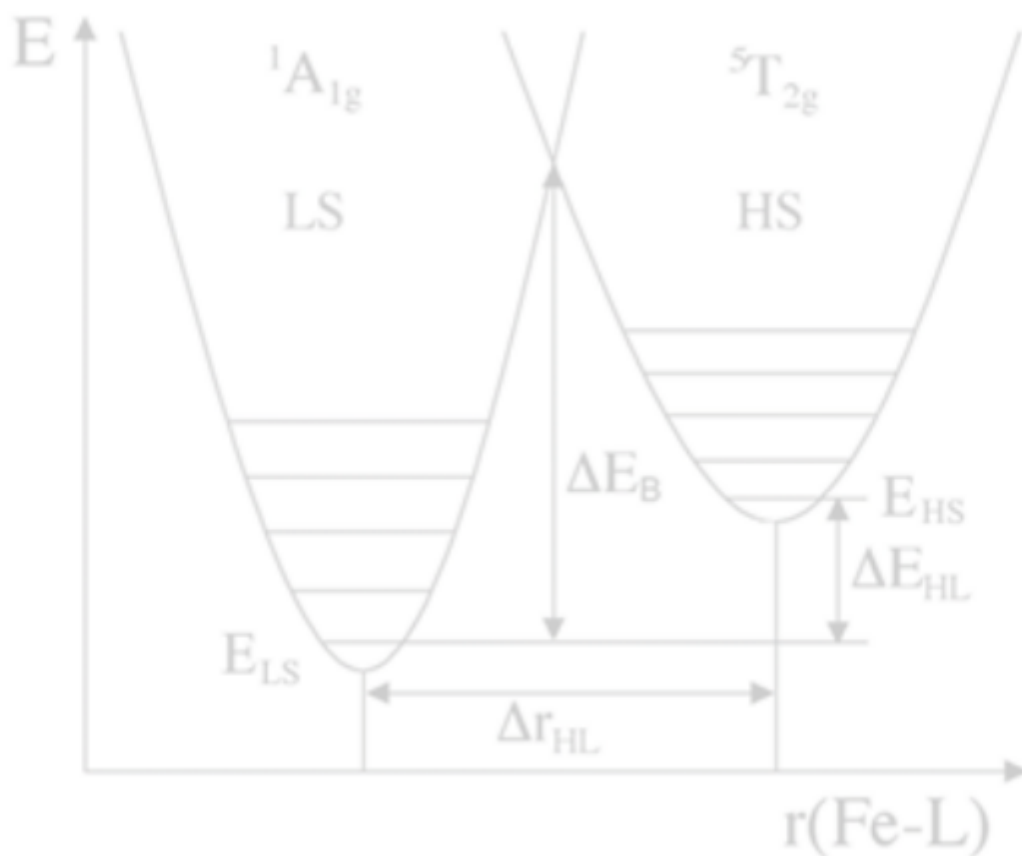
<i>L_{pytMe}</i>	3-(2-(5- <i>Methyl-pyridyl</i>)-4-tolyl-5-phenyl-1,2,4-triazole
<i>L_{pytF}</i>	3-(2-(5- <i>Fluoro-pyridyl</i>)-4-tolyl-5-phenyl-1,2,4-triazole
<i>L_{pytBr}</i>	3-(2-(5- <i>Bromo-pyridyl</i>)-4-tolyl-5-phenyl-1,2,4-triazole
<i>L_{pytCF3}</i>	3-(2-(5- <i>Trifluoromethyl-pyridyl</i>)-4-tolyl-5-phenyl-1,2,4-triazole
<i>LDA</i>	Local Density Approximation
<i>LFMM</i>	Ligand Field Molecular Mechanics
<i>LF-FF</i>	Ligand Field Force Field
<i>LFT</i>	Ligand Field Theory
<i>LF</i>	Ligand Field
<i>LS</i>	Low Spin
<i>GGA</i>	General Gradient Approximation
<i>m</i>	mass
<i>MC</i>	Montecarlo Method
<i>MD</i>	Molecular Dynamic
<i>meas.</i>	Measured
<i>MeOH</i>	Methanol
<i>MOF</i>	Metal Organic Frameworks
<i>MOs</i>	Molecular Orbitals
<i>MS</i>	Mass Spectrometry
<i>N_A</i>	Avogadro's Number
<i>NEVPT</i>	N-Electron Valence State Perturbation Theory
<i>N-BuOH</i>	N-Butanol

NMR	Nuclear Magnetic Resonance
OTf	trifluoromethanesulfonate (CF_3SO_3^-)
p	Pressure
PBE	Perdew–Burke–Ernzerhof Functional
PES	Potential Electronic Surface
phen	phenanthroline
pybox^x	2,6-di(oxazolin-2-yl)-4- X -pyridine
pytacn^x	1-(2- X -pyridylmethyl)-4,7-dimethyl-1,4,7-triazacyclononane
RT	Room Temperature
SCO	Spin Crossover
SC-XRD	Single-Crystal X-Ray Diffraction
T	Temperature
T_{1/2}	Spin Transition Temperature or Switching Temperature
TGA	Thermogravimetric Analysis
VdW	Van Der Waals
VP	Variable Pressure
VT	Variable Temperature
ΔE_{int}	Change in Interaction Energy
ΔE_{Pauli}	Change in Pauli Energy
ΔE_{elstat}	Change in Electrostatic Energy
ΔE_{orb}	Change in Orbitalic Energy
ΔE_{pol}	Change in Polarisation Energy
ΔE_{rest}	Change in Residual Energy
ΔG	Change in Gibb's Free Energy

ΔH	Change in Enthalpy
ΔS	Change in Entropy
$\Delta H_{vib,HS-LS}$	Change in Vibrational Enthalpy
$\Delta S_{vib,HS-LS}$	Change in Vibrational Entropy
$\Delta H_{el,HS-LS}$	Change in Electronic Enthalpy
$\Delta S_{el,HS-LS}$	Change in Electronic Entropy
Δ_o	Crystal Field Splitting Parameter
Δ	Average Difference between the individual M-L bonds <i>vs.</i> the mean $\langle \mathbf{M-L} \rangle$ bond length
$\Delta(\text{HOMO-LUMO})$	HOMO-LUMO Energy Gap
Θ	Trigonal Distortion
Σ	Octahedral Distortion Parameter
Π	Electron Pairing Energy
μ_{eff}	Effective Magnetic Moment
μ_o	Magnetic Permittivity of Vacuum
χ_g	Mass Magnetic Susceptibility
χ_M	Molar Magnetic Susceptibility
Δ	Variation or Change
γ_{HS}	High Spin Fraction
σ_p^+	Hammett Parameter for <i>para</i> substituents
σ_m^+	Hammett Parameter for <i>meta</i> substituents
λ	Wavelength
ϵ	Molar Extinction Coefficient



Introduction



1.1. Abstract

The aim of this thesis is the development of a general method to predict key properties in a family of iron(II) complexes in a pre-synthesis step.

In the first part of this chapter the key concepts underpinning Spin Crossover (*SCO*) are presented, with particular attention given to describing at the molecular level the *SCO* transition in the solid state and in the solution phase. Selected experimental techniques used to monitor and describe this phenomenon are discussed in detail. An overview is provided of the state of the art of the most relevant studies reported in the literature that have led to some success in predicting the *SCO* phenomenon in various Fe(II) families. Published data are reported for the [Co(*dpzca*)₂] complex and summarised; particular interest in this candidate is the *SCO* activity in the solid state, triggered by temperature and/or pressure.

The second part of this first chapter starts by describing various levels of theory that have been previously deployed in the literature for modelling and understanding key parameters in the *SCO* transition. Then, a very detailed description of the *EDA-NOCV* model is presented, as in this PhD thesis this method is employed for the first time to look at some *SCO* systems.

In the third and final part the goals of this PhD thesis are presented.

1.2. Introduction to Spin Crossover (SCO)

1.2.1. General Overview

The SCO phenomenon is mostly observed in d^4 - d^7 octahedral metal complexes.¹⁻⁵ However, less common symmetries and d -electrons configurations are also more rarely observed. The first report of SCO, was in 1931, in octahedral Fe^{III} complexes, by Cambi *et al.*^{2, 4, 6-7} Even though it was first discovered in Fe^{III} ,^{ref8-9} SCO can also be observed in Fe^{II} ,^{ref10-13} Mn^{III} ,^{ref14-15} Cr^{II} ,^{ref16} and Co^{II} .^{ref17-19}

The most common symmetry reported for SCO complexes is the octahedral coordination geometry (O_h) whereby the d -orbitals are split into a threefold set (t_{2g}) composed of d_{xy} , d_{xz} , d_{yz} and a twofold set (e_g) composed by $d_{x^2-y^2}$ and d_{z^2} (Figure 1.1). The t_{2g} - e_g gap in octahedral complexes is defined as ligand field splitting (Δ_o): the stronger the ligand field, the bigger the Δ_o ; the weaker the ligand field the smaller the Δ_o .²⁰⁻²¹ This ideal geometry is never achieved in reality: usually distorted octahedral geometries are observed, with consequent lowering of the symmetry (i.e. D_{2d} symmetry²²⁻²³ or lower²⁴) and changes in arrangement of the d -orbitals.

The spin state of the octahedral complex is closely related to the relative size of Δ_o and the Pairing Energy (Π). The Pairing Energy Π is the gain in stabilisation energy associated with arranging the electrons in spin states at higher multiplicity, which favour the *HS* over the *LS* state.

Comparison between Δ_o and Π determines whether the *LS* or the *HS* state is the most stable. If $\Pi > \Delta_o$ the *HS* state is more stable, so it is preferred; if $\Pi < \Delta_o$ the *LS* state is more stable, so preferred (Figure 1.1). The SCO phenomenon occurs when $\Pi \approx \Delta_o$, allowing external stimuli to trigger the spin state switch.¹⁻⁵ The relative rarity of the SCO-active class of metal

complexes is due to the need for a *not-too-strong* (always *LS*) and *not-too-weak* (always *HS*) ligand field strength of the coordinating ligands.^{3, 7, 25-26}

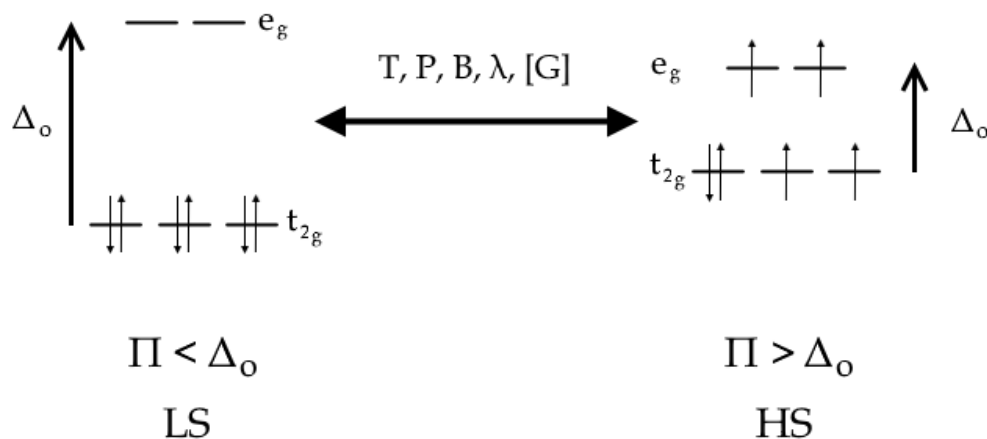


Figure 1.1. Qualitative representation of the SCO for octahedral Fe(II) complexes. Spin state switching between *LS* and *HS* happens on application of an external stimulus.

Most commonly, *SCO* is studied in Fe^{II} complexes as in this case the spin state switch has a maximal change in the magnetic response: from a *diamagnetic LS* state ($S = 0$) to a *paramagnetic HS* state ($S = 2$).¹⁰⁻¹³ The reversible conversion between *HS* and *LS* states produces profound changes in all of the properties that derive from the different distribution of the $3d^n$ valence electrons. In the case of Fe^{II} *SCO* – the main subject of this thesis research – the spin state switch affects change in the colour, molecular vibrations, metal-ligand bond lengths (av. $\Delta\text{Fe-N}_{\text{HS-LS}} \approx 0.2 \text{ \AA}$, $\sim 10\%$) and magnetic response (*HS* ($S = 2$) vs. *LS* state ($S = 0$)).^{3, 7, 25-27}

Due to being very highly sensitive to any change in environment, *SCO* complexes are extremely interesting both for technological and theoretical studies. Indeed, the main interest in this class of compounds is in the ability to switch spin state with various external stimuli such as temperature,^{3, 7, 25-26, 28-30} applied magnetic field,³¹ light irradiation,³²⁻³⁸ pressure^{19, 39-44} or guest molecule presence/absence.⁴⁵ This unique capability makes them fantastic candidates for memory storage and sensing

applications. Indeed, many applications of *SCO* have been evaluated, including molecular actuation,⁴⁶⁻⁴⁷ molecular electronics,⁴⁸⁻⁵⁰ emissive devices,⁵¹⁻⁵³ thermochromic materials,⁵⁴ data storage,⁵⁵⁻⁵⁸ and chemical sensing.^{45, 59-65} For thermal *SCO*, the spin state transition needs to occur at room temperature for most real-world applications.⁶⁶⁻⁶⁸ The vast majority of the hundreds of examples of *SCO* complexes reported in literature were studied and characterised in the solid state.^{2, 10, 69-70} For solid state *SCO* the magnetic transition profile of these compounds is very sensitive to the sample preparation (powder/crystalline sample), lattice solvents, counter ions and packing effects.⁷¹⁻⁷⁶

SCO samples are increasingly being studied in solution too, often as sensors, broadening the already large range of applications *SCO* can be used for. To date, *SCO* in solution has been monitored as a function of: concentration of a guest molecule,⁷⁷ the effect of counterion,⁷⁸⁻⁸⁰ alkyl chain length,^{29, 77, 81-82} ligand substituent,^{22, 24, 83-85} solution pH⁸⁶ or polarity of the solvent employed.^{84, 87-88} In solution state studies, where packing effects or cooperativity among molecules are not usually observed, variation in the thermal *SCO* phenomenon can be directly related to small alterations of the ligand field strength. A change in the $T_{1/2}$ reflects the changes in Δ_o ; so, *SCO* compounds are of great interest as candidates for theoretical studies that aim to understand in more depth the parameters which play a key role determining ligand field strength.^{22-23, 89-91}

1.2.2. Thermodynamics of *SCO*

Thermal *SCO* can also be discussed as a reversible second order phase transition between *LS* and *HS* as reported in Equation 1.1:

$$\Delta G = \Delta H + T\Delta S \quad (1.1)$$

where ΔG is free Gibbs Energy in *SCO* transition ($\Delta G = G_{HS} - G_{LS}$), ΔH is Enthalpy ($\Delta H = H_{HS} - H_{LS}$) and ΔS is Entropy variation ($\Delta S = S_{HS} - S_{LS}$), for a $LS \rightarrow HS$ transition.

In order to trigger a possible spin state switch, the $\Delta H \sim T\Delta S$ condition must be experienced. As the spin state switch is thermally triggered, the *LS* state is the most enthalpically stable species at the lower temperatures ($\Delta H > 0$, as $H_{HS} > H_{LS}$), meanwhile the increase in *HS* species at higher temperatures is entropically driven ($\Delta S > 0$, as $S_{HS} > S_{LS}$).^{23, 92-93} In thermal *SCO*, the most important parameter is the experimental $T_{1/2}$, the point in the spin transition when equilibrium is reached ($\Delta H = T_{1/2}\Delta S$) and, for the cases of one-step complete *SCO*, event sample composition is 50:50 *HS:LS*.

One of the most common approaches to model the *SCO* transition is through the reaction coordinate called the *breathing mode* that for the total symmetric vibration of the coordination sphere (Figure 1.2a). In *SCO* studies, whereas theoretical approaches are used for modelling this spin state switching, a large focus is pointed at the tuning of the *LS-HS* gap (ΔE_{HL} , Figure 1.2a), which approximates the real *HS-LS* barrier (ΔE_B , Figure 1.2a). In fact, ΔE_B energy is very hard to calculate because it is the molecular energy at the saddle point between the Potential Energy Surface (*PES*) of the two spin states. Molecular structure at *PES* saddle points is characterised by all real normal modes except one; this imaginary normal mode reflects the coordination of reaction; i.e., the *breathing mode* from *LS* to *HS* state (and *vice versa*). This points on the *PES* are much harder to be accurately found if compared with energy minima, as E_{LS} or E_{HS} .⁹⁴

When ΔE_{HL} increases (or decreases), the crossing point between the two *breathing modes* rises (or drops), changing the height of the energy barrier ΔE_B . In thermal *SCO* systems, ΔE_{HL} gap should be of the same order of magnitude of the k_bT thermal quantum (e.g., at 298 K is $\sim 2000 \text{ cm}^{-1}$ Figure 1.2b).⁹⁴

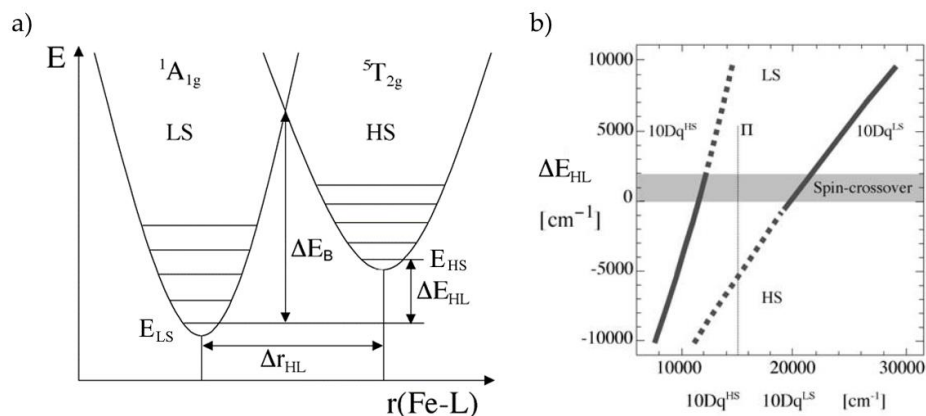


Figure 1.2. (a) Qualitative potential energy surfaces (PES) for the LS and HS state of a SCO-active octahedral Fe^{II} complex along the breathing mode reaction coordinate. (b) Regions of stability of either one or the other spin state as a function of the ligand field strength. The region of spin crossover compounds is indicated by the shaded area. Figure reproduced with modifications from ref⁹⁴.

1.2.3. From Solid to Solution SCO

Five different kinds of SCO transition are commonly seen (Figure 1.3):

- Gradual transition:* the simplest of the possible SCO transitions as it is observed for non-interacting systems; i.e., without any active cooperativity effects. In solution, whereby SCO molecules are isolated, this is the usual kind of transition seen.
- Abrupt transition:* whereby the first molecules that switch spin state catalyse the transition for the surrounding neighbours, producing a much steeper transition than observed for (a).
- Hysteresis loop:* can be seen if the molecules are strongly interacting, so it is rare in solution.⁸¹⁻⁸² It is observed as a lag of the response of the SCO material to changes in temperature.^{7, 95-96}

- (d) *Multi-step SCO*: can be observed when the metal ions are (i) equivalent but affect each other, so they undergo *SCO* at different temperatures or (ii) inherently inequivalent in the crystalline lattice, due to occupation of different sites.
- (e) *Incomplete SCO*: describes the absence of a full conversion into either the *HS* or the *LS* state of the sample, or both, even at temperatures much higher or lower than $T_{1/2}$.

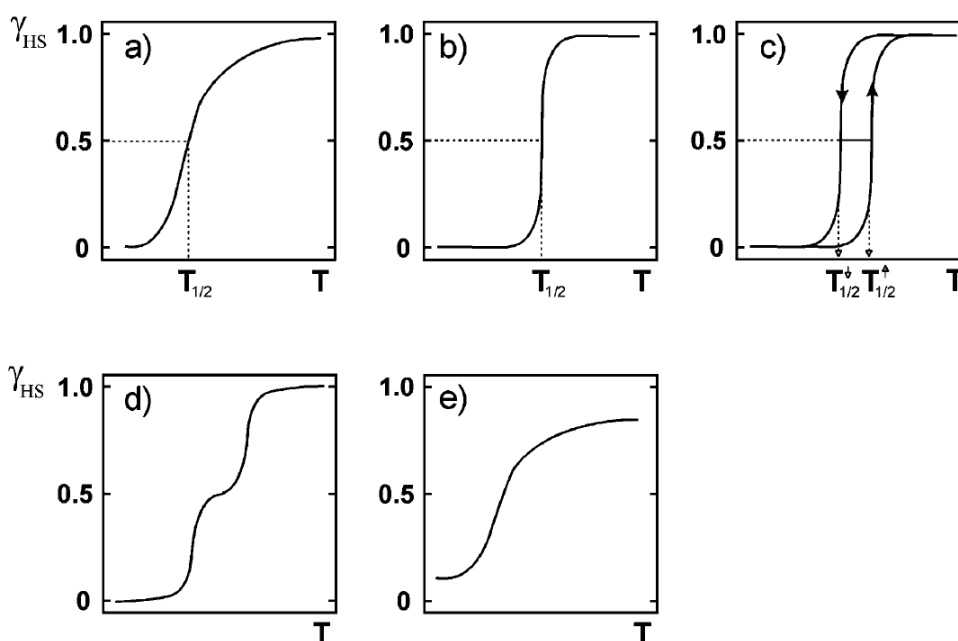


Figure 1.3. The most common types of spin transition represented as HS molar fraction (γ_{HS}) versus temperature (T) are: (a) gradual, (b) abrupt, (c) abrupt with thermal hysteresis, (d) multi-step, (e) incomplete. Figure reproduced with modifications from ref⁹⁷.

The extremely high sensitivity of the *SCO* to changes in the external environment is the reason for the great interest over the last fifty years. However, this is also the main source of issues for commercialisation of *SCO* materials as it is hard to preserve the *SCO* activity of the complex. In this regard, a key achievement for most of practical applications is the immobilisation of a layer of *SCO*-active complex on a solid support. There

is no certainty that the SCO activity in solution can be preserved in the solid state,⁹⁷ or on a surface⁹⁸⁻¹⁰¹ (e.g. Figure 1.4).

In order to produce commercially viable materials, a profound knowledge of the parameters that affect the SCO activity must be achieved. For SCO in the crystalline solid state, molecules are well packed all together in a crystalline unit cell; they are not isolated anymore and a wide range of intermolecular interactions can occur (e.g., H-bonds^{79, 102-103} or π - π stacking¹⁰⁴); this can activate or deactivate the SCO transition.

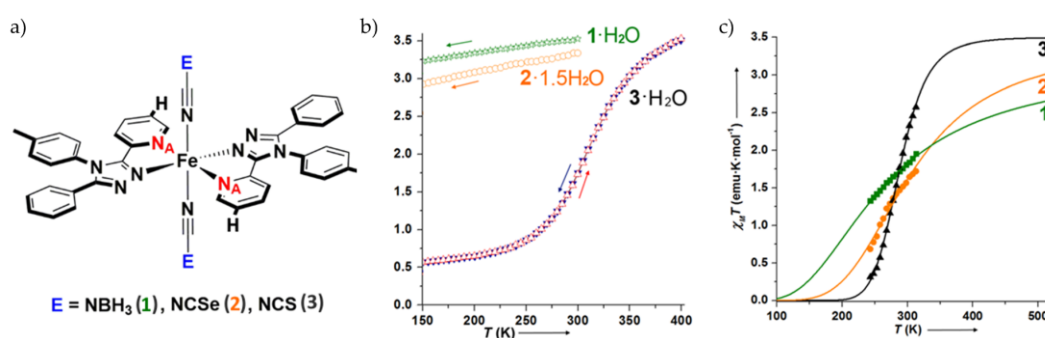


Figure 1.4. (a) Chemical structure of $[Fe^{II}(Lpyridine)_2(NCE)_2]$ complex employed in these studies of solid state and solution phase SCO. (b) χ_{MT} vs T plot for powder $[Fe^{II}(Lpyridine)_2(NCS)_2] \cdot H_2O$ (1·H₂O, green stars), crystalline $[Fe^{II}(Lpyridine)_2(NCSe)_2] \cdot 1.5H_2O$ (2·1.5H₂O, orange circles), and crystalline $[Fe^{II}(Lpyridine)_2(NCBH_3)_2] \cdot H_2O$ (3·H₂O; (blue ▼) cooling mode, (red Δ) heating mode). (c) Solution-phase magnetic data represented as χ_{MT} vs T for complexes $[Fe^{II}(Lpyridine)_2(NCS)_2]$ (1, 2.21×10^{-3} M, green ■), $[Fe^{II}(Lpyridine)_2(NCSe)_2]$ (2, 3.95×10^{-3} M, orange ●), and $[Fe^{II}(Lpyridine)_2(NCBH_3)_2]$ (3, 5.10×10^{-3} M, black ▲) in $CDCl_3$ solution from 313 to 243 K. Note that each complex solution was prepared using a Lpyridine-to-iron(II) ratio of 6:1 to ensure it is present as $[Fe^{II}(Lpyridine)_2(NCE)_2]$. Figure reproduced with modifications from ref¹⁰⁵.

The SCO phenomenon is not only affected by chemical (*intermolecular interaction*) or quantum-physical effects (*electronic coupling*) but also by the amount of *free space*. Indeed, by moving from LS to HS an expansion of the Fe(II) coordination sphere is observed; due to Fe-N bond lengths increasing by ~ 0.2 Å (+ 5-10%), with a consequent increase in the molecular volume (typically by less 5-10%). This volume expansion –

which does not suffer any constraint in the solution phase – may be restricted in the solid state. The longer Fe-N bonds in the *HS* state are consistent with a weaker and more labile bonding, that generally leads to more highly distorted complex,¹⁰⁶ which the crystalline lattice needs to be able to host.¹⁰⁷⁻¹⁰⁸

This geometrical rearrangement, and hence the *SCO* transition, can be easily prevented due to excessively large structural differences between the *LS* and *HS* states caused by, for example, the presence of satellite aromatic rings¹⁰⁹ on the ligand backbone, solvent of crystallisation or large counter ions.^{79, 110} A complete survey of this issue was written by Halcrow in 2011.¹¹¹

Solution *SCO* usually shows a much less complicated picture, so the prospect of producing successful predictive tools is considerably more realistic. Indeed, the solvent molecules usually ensure that the *SCO* molecules are isolated from one another, avoiding any cooperative behaviour.

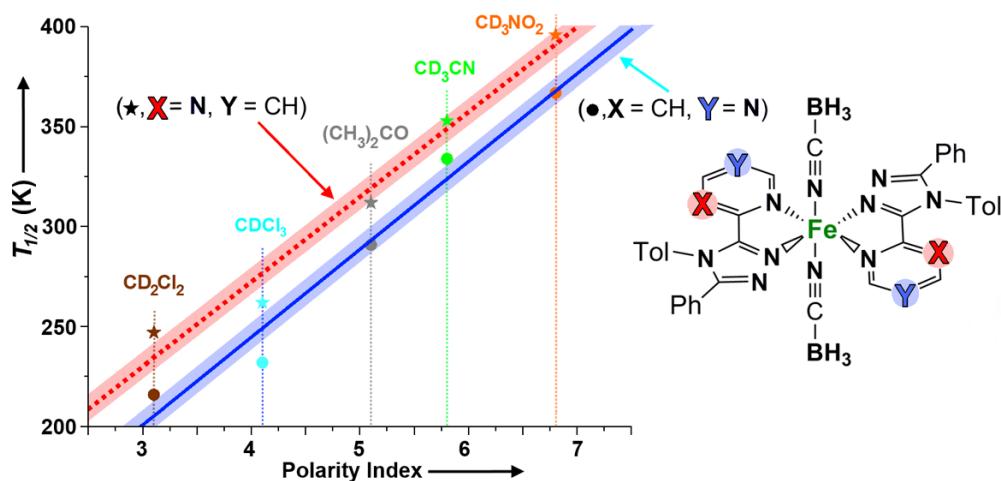


Figure 1.5. Plot showing the linear fit of $T_{1/2}$ for complexes $[Fe^{II}(L^2pyrimidine)_2(NCBH_3)_2]$ (stars and dotted lines, $R^2 = 0.96$, slope = 42.45) and $[Fe^{II}(L^4pyrimidine)_2(NCBH_3)_2]$ (circles and solid lines, $R^2 = 0.96$, slope = 44.41) vs polarity index (P') of each of the solvent used in this study: CD_2Cl_2 (pink), $CDCl_3$ (blue), $(CD_3)_2CO$ (orange), CD_3CN (green), CD_3NO_2 (red). Figure reproduced with modifications from ref⁸⁸.

This results in the simplest of the *SCO* transition profiles, with a *gradual* transition between the two spin states (Figure 1.3a). More complicated transitions, which require some level of cooperativity, such as transition (b), (c) or (d), are not usually reported in solution, unless agglomerated clusters of molecules form (e.g., micelles).^{77, 81} Hence, in solution *SCO*, it is easier to focus the impact on electronic fine-tuning of the ligand structure, as packing effects deriving from the crystal packing in solid state are absent.

Interestingly, several studies have reported an important role of the solvent chosen for this study in tuning the observed $T_{1/2}$ for an *SCO* active complex.^{84, 88, 105, 112-113} On one hand, solvent polarity itself can be used to finely tune the $T_{1/2}$ of a specific system; in some cases a shift of up to 150 K can be observed by tuning the solvent polarity (Figure 1.5 (top)).⁸⁸

But on the other hand, solvent polarity may have a very little impact on the solution *SCO*.⁸⁴ As a consequence, different systems can be compared only if measurements are performed in the same solvent, because different *SCO* equilibria may be affected by the choice of the solvent to different extents.^{84, 105, 112}

1.3. Methods to Monitor SCO

1.3.1. General Overview

Many techniques are available for monitoring the SCO phenomenon; however, some of them do not supply *quantitative* information on the HS fraction (γ_{HS}). The SCO phenomenon is generally easier to monitor in the solid state than in the solution phase: indeed, direct detection and *quantification* of the magnetic response vs. temperature can be easily obtained by using a magnetometer (see *Subsection 1.3.2*). As well, variable temperature (VT) single crystal X-ray diffraction, Mössbauer (Fe^{II/III} only) and IR/Raman spectroscopy can be used to get information on an SCO transition.^{7, 19, 29} In the case of IR/Raman spectroscopy, *quantitative* detection is possible if highly characteristic bands are present such as the strong N≡C stretch of Fe-NCE (E = Se, S), which occurs in an otherwise uncluttered part of the spectrum (for LS Fe-NCE at ~2100–2140 cm⁻¹ vs HS Fe-NCE at ~2060–2090 cm⁻¹) and the complex undergoes complete SCO in the studied temperature or pressure range.^{29, 104}

For solution SCO the transition can be monitored by VT UV-visible and ¹H-NMR spectroscopy. The key limitation of these studies is the temperature range between the freezing and the boiling point of the solvent employed, within which a significant amount of SCO transition must occur. The SCO transition can be monitored *qualitatively* using the loss in intensity of the LS *d-d* transition on heating. This can be *quantitative*, if complete SCO is observed in the studied temperature range. Sometimes the *d-d* band is obscured so, the MLCT band is monitored instead.^{24, 84, 114}

Two techniques based on VT ¹H-NMR spectroscopy are very widely used for *quantitative* investigation of the SCO phenomenon in solution: (i) monitoring the isotropic shifts of specific protons in the complexes to

evaluate the *HS* fraction of the *SCO* species;¹¹⁵ (ii) monitoring the effect that unpaired electrons of the complex has on the solvent peak, using the Evan's method (Subsection 1.3.3).¹¹⁶ Since the paramagnetism of the metal species makes the spectrum considerably broader and harder to assign compared with *diamagnetic* spectra, the Evan's method is generally preferred; however, both techniques give the same findings, as demonstrated by Walker *et al.* in 2007.¹¹⁵

1.3.2. Solid State Magnetic Measurements

SCO magnetic behaviour can be described either from the macro- or microscopic perspective. Macroscopically, the volumetric susceptibility (χ_v) can be defined as the proportionality constant which relates sample magnetisation (M) to the external field H applied (Equation 1.2)

$$M = \chi_v H \quad (1.2)$$

$$\chi_g(\text{raw}) = \chi_v / \text{mass} \quad (1.3)$$

$$\chi_g(\text{sample}) = \chi_g(\text{raw}) - \chi_g(\text{holder}) \quad (1.4)$$

$$\chi_M(\text{sample}) = M \cdot \chi_g(\text{sample}) \quad (1.5)$$

The raw mass susceptibility ($\chi_g(\text{raw})$) so measured, in $\text{cm}^3 \cdot \text{g}^{-1}$, is calculated by dividing χ_v by the mass of the sample in grams (Equation 1.3). This $\chi_g(\text{raw})$ accounts for the total gram susceptibility of the sample and sample holder; therefore, it is firstly corrected for the *diamagnetism* of the sample holder (Equation 1.4), to give $\chi_g(\text{sample})$.

The $\chi_g(\text{sample})$ is then multiplied by the molecular weight (M) of the complex to obtain the molar susceptibility $\chi_M(\text{sample})$ ($\text{emu} \cdot \text{mol}^{-1}$ or

$\text{cm}^3 \cdot \text{mol}^{-1}$ as electromagnetic units = emu = cm^3 ; Equation 1.5).¹¹⁷ In this $\chi_M(\text{sample})$ molar susceptibility, a *diamagnetic* contribution that originates from the all-paired electrons in the sample ($\chi_M(\text{diamagnetic})$) is included and must be corrected for (Equation 1.6).²⁰ This final correction leads to the real *paramagnetic* susceptibility $\chi_M(\text{paramagnetic})$ (simply called χ_M – only accounting for the number of unpaired electron in the sample):

$$\chi_M = \chi_M(\text{sample}) - \chi_M(\text{diamagnetic}) \quad (1.6)$$

This $\chi_M(\text{diamagnetic})$ term is estimated either using Pascal's constants¹¹⁸ or, as is done in this thesis, using Equation 1.7¹¹⁹ as it is dependent on the molecular mass of the studied molecule:

$$\chi_M(\text{diamagnetic}) = -0.5 \times M \times 10^{-6} \text{ cm}^3 \text{ mol}^{-1} \quad (1.7)$$

From a bottom-up perspective, in $3d^n$ metal complexes – where the spin-orbit coupling can be neglected²⁰ – the observed magnetic moment μ_{eff} can be estimated from first principles calculation of the spin-only magnetic moment μ_{so} which is easily done from the number of unpaired electrons (Equation 1.8); assuming g , a dimensionless number, is equal to -2.0023 for a free electron and S is the total spin ($1/2 \cdot \text{number of unpaired electrons}$).

$$\mu_{\text{so}} = g[S(S + 1)]^{1/2} \quad (1.8)$$

Finally, Equation 1.9 well explains how the magnetic susceptibility χ_M is linked to the observed magnetic moment μ_{eff} for $3d^n$ complexes.

$$\chi_M = \frac{N_A \mu_0 \mu_{\text{eff}}^2}{3kT} \quad (1.9)$$

Where N_A is the Avogadro number, μ_0 is the permeability of vacuum, k is the Boltzmann constant and T is the temperature.²⁰ Equation 1.9 can therefore be rearranged to give Equation 1.10 and Equation 1.11.

$$\chi_M T = 0.124 \mu_{\text{eff}}^2 \quad (1.10)$$

$$\mu_{\text{eff}} = 2.84 \cdot \sqrt{\chi_M T} \quad (1.11)$$

1.3.3. ¹H-NMR Evan's Method

In Evan's NMR method measurements, two NMR tubes are encapsulated one inside the other: in the internal tube pure solvent is placed (in the example shown in Figure 1.6 it is pure CDCl₃); in the external tube an accurately known mass of the *SCO* candidate is dissolved in an accurate known volume of the same solvent (in the example in Figure 1.6 it is pure CDCl₃). When a *LS* → *HS* spin state transition is experienced, the amount of *HS* species increases, so the number of unpaired electrons per mole increases and the solvent peak in the external tube shifts further downfield, leading to an increase in Δf . From this data, the gram susceptibility χ_g is calculated using Equation 1.12:

$$\chi_g(\text{sample}) = \frac{3\Delta f}{4\pi d f} \quad (1.12)$$

Where $\chi_g(\text{sample})$ is the gram susceptibility per mass unit; Δf is the gap between the frequency of the solvent peak into the inner tube and that in the outer one (Hz); f is the frequency of the instrument (Hz) and d is the solvent density in g/cm^3 (corrected at different temperatures).¹²⁰⁻¹²¹

The measured $\chi_g(\text{sample})$ value is then treated as above (Subsection 1.3.2, Equations 1.5-1.7) to obtain the corrected χ_M . This method enables

direct and *quantitative* monitoring of the spin state transition; however, the temperature range employed is limited to the liquid temperature range of the solvent.

The Evan's NMR method has an intrinsic error of 5-10%.¹²² The fitting of the data to the regular SCO model (Equation 1.13) also has an associated error, which is usually negligible if the SCO transition occurs in the monitored temperature range (more information about the error treatment for SCO model fitting is given in *Chapter Two, Subsection A2.12.2*).

$$\chi_M(T) = \frac{\chi_M(\text{MAX})}{1 + e^{(-\Delta H/RT + \Delta S/R)}} \quad (1.13)$$

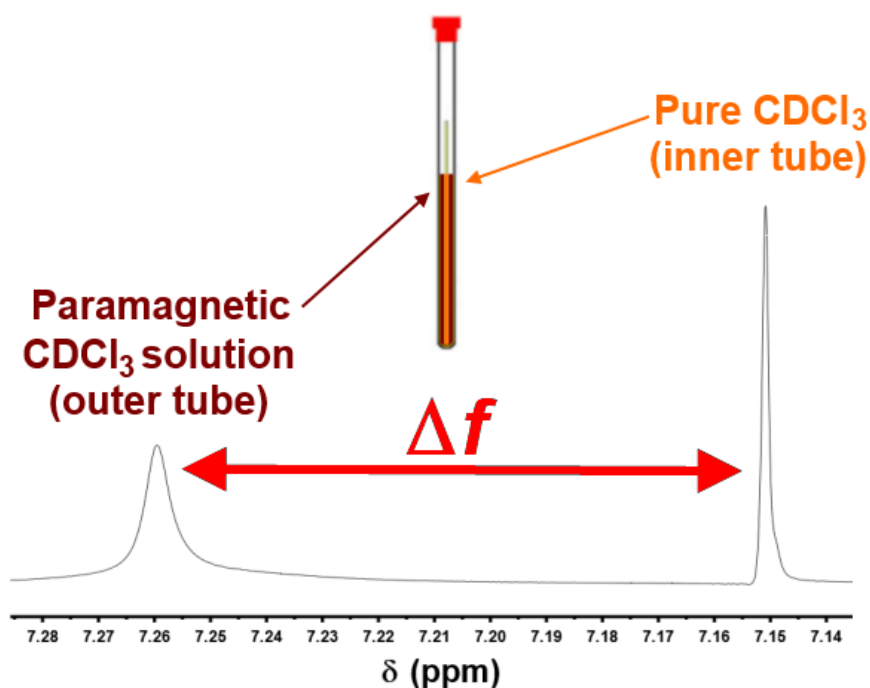


Figure 1.6. Example of the key region of the Evans' method ^1H NMR spectrum in CDCl_3 solvent, along with the type of NMR tube used to collect signals from the solvent that feels the paramagnetic sample (left peak) and that which does not (right peak). A qualitative broadening of the peak shape due to the paramagnetism is also illustrated. Figure reproduced with modifications from ref¹²³.

Where $\chi_M(T)$ is the susceptibility at different temperatures; $\chi_M(\text{MAX})$ is set to the highest theoretical value expected for the metal ion (for Fe^{II} , $\chi_M(\text{MAX}) = 4 \text{ emu} \cdot \text{K} \cdot \text{mol}^{-1}$); R is the gas constant $8.314 \text{ J} \cdot \text{mol}^{-1} \cdot \text{K}^{-1}$. ΔH is the change in enthalpy for the spin transition and ΔS is the change in entropy for the spin transition. Examples of this model fitting for solution SCO are reported in Figure 1.7.

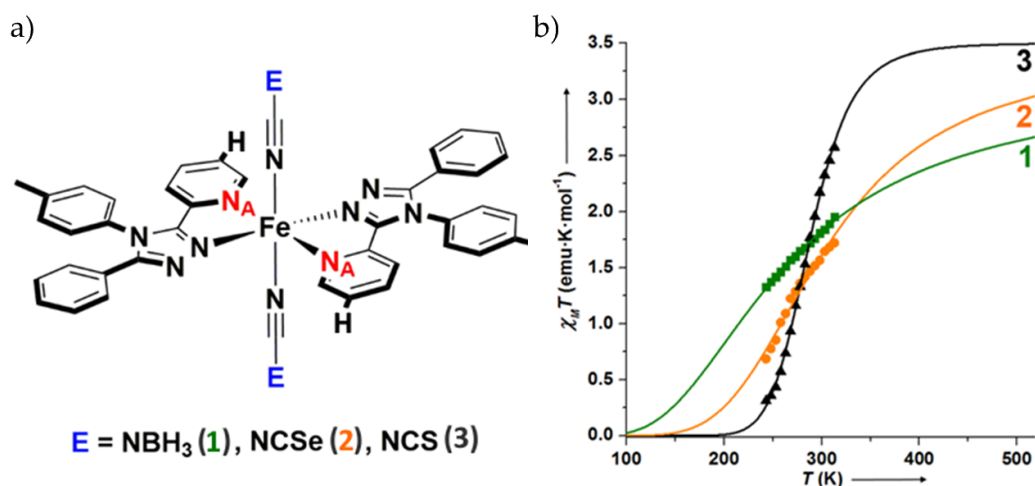


Figure 1.7. (a) Chemical structure of $[\text{Fe}^{\text{II}}(\text{Lpyridine})_2(\text{NCE})_2]$ complex employed in these studies of solid state and solution phase SCO. (b) Solution-phase magnetic data represented as χ_{MT} vs T for complexes $[\text{Fe}^{\text{II}}(\text{Lpyridine})_2(\text{NCS})_2]$ (1, $2.21 \times 10^{-3} \text{ M}$, green \blacksquare), $[\text{Fe}^{\text{II}}(\text{Lpyridine})_2(\text{NCSe})_2]$ (2, $3.95 \times 10^{-3} \text{ M}$, orange \bullet), and $[\text{Fe}^{\text{II}}(\text{Lpyridine})_2(\text{NCBH}_3)_2]$ (3, $5.10 \times 10^{-3} \text{ M}$, black \blacktriangle) in CDCl_3 solution from 313 to 243 K. Note that each complex solution was prepared using a *Lpyridine*-to-iron(II) ratio of 6:1 to ensure it is present as $[\text{Fe}^{\text{II}}(\text{Lpyridine})_2(\text{NCE})_2]$. Figure reproduced with modifications from ref¹⁰⁵.

1.4. Reported Trends in SCO Families

1.4.1. Introduction to Hammett Parameter

Electronic tuning by Electron Donating Group (EDG) and Electron Withdrawing Group (EWG), present as a *para* X (or *meta* Y) substituent on aromatic ring is historically evaluated by using the Hammett parameter¹²⁴ which was defined from equilibrium constants of benzoic substrates for acid/base reactions (σ) or nucleophilic substitution reactions at the attached carbonyl carbon (σ^+ , Figure 1.8a). Ranges of tunability are far lower in the case of the *meta* substituents ($-0.07 < \sigma_{m^+} < +0.52$)¹²⁴⁻¹²⁵ than in the case of the *para* substituents ($-1.70 < \sigma_{p^+} < +0.79$)¹²⁴⁻¹²⁵ (Figure 1.8b); due to absence of resonance effects in the former case, which are present in the latter case.

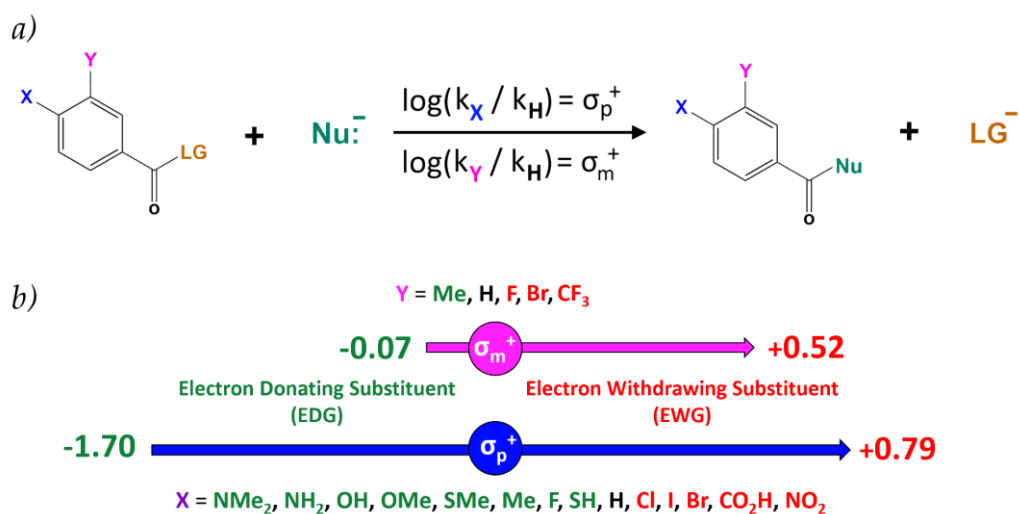


Figure 1.8. (a) Example of the nucleophilic substitution reaction at the carbonyl carbon in benzoic derivatives used to establish the Hammett parameters (σ^+) for the *para*-X and *meta*-Y substituents on the benzoic ring. (b) Range of electronic tunability for *meta*-Y substituents (σ_{m^+} , magenta) and *para*-X substituents (σ_{p^+} , blue).

1.4.2. Solid State SCO Family Trends

Over the last twenty years, electronic tuning of SCO by a *para*-X (or *meta*-Y) substituent on a pyridyl ring has revealed some excellent and generalisable results in several families, both for solid state¹²⁶⁻¹³² and solution phase^{22-24, 83} SCO. The first example of a correlation between the Hammett parameter (σ/σ^+) of a substituent and $T_{1/2}$ of the solid state of the corresponding complex SCO was obtained by Kaizaki *et al.* in 2005, for a family of binuclear Fe(II) SCO complexes (Figure 1.9, X/Y substituent reported on the left).¹³³ As σ^+ increased (increasing EWG properties), so too did the $T_{1/2}$, implying that the ligand field strength also increased with increasing EWG effects.

This achievement was further confirmed and extended thanks to interesting results reported by Harris *et al.*¹³⁰ in 2015 and by Murray *et al.*¹³¹ in 2017, for two different solid state SCO-active families of iron(II) complexes featuring ligands in which the pyridyl rings were *para* substituted with a range of halogens (X = F, Cl, Br, I).

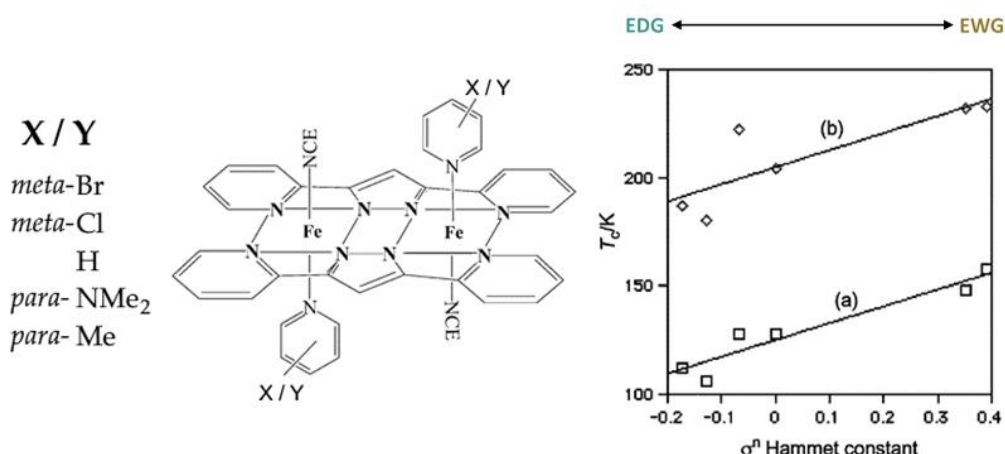


Figure 1.9. (left) Schematic of $[(\text{Fe}^{\text{II}}(\text{l-bpy})_2(\text{NCE})(\text{X/Y-py}))_2]$ ($E = \text{S}$ or BH_3); (right) Plots of T_c (i.e., $T_{1/2}$) vs. Hammett constants: (a) the NCS complexes, (b) the NCBH_3 complexes. Figure reproduced with modifications from ref¹³³.

1.4.3. Solution Phase SCO Family Trends

For solution SCO,^{22-24, 81, 83-84, 105} a range of correlations with $T_{1/2}$ have been found, using the Hammett parameter (σ/σ^+) and the chemical shift of the coordinating nitrogen N_A , among others. An introduction to these studies, in order of publication, follows.

In 2013, Costas *et al.* prepared a family of seven SCO $[\text{Fe}^{\text{II}}(\text{pytacn}^{\text{X}})_2(\text{NCCH}_3)_2](\text{OTf})_2$ complexes that were tuned by the choice of *para*-**X** substituent on the pyridyl ring in **pytacn**^X (1-(2-**X**-pyridylmethyl)-4,7-dimethyl-1,4,7-triazacyclononane, Figure 1.10). The influence of the pyridine **X** substituents on the electronic properties of the coordinated iron centre were probed by a combination of structural and spectroscopic characterisation using X-ray diffraction, ¹H NMR and UV-Vis spectroscopies, and magnetic susceptibility measurements in MeCN solution at room temperature (unfortunately, no VT studies are reported).²⁴

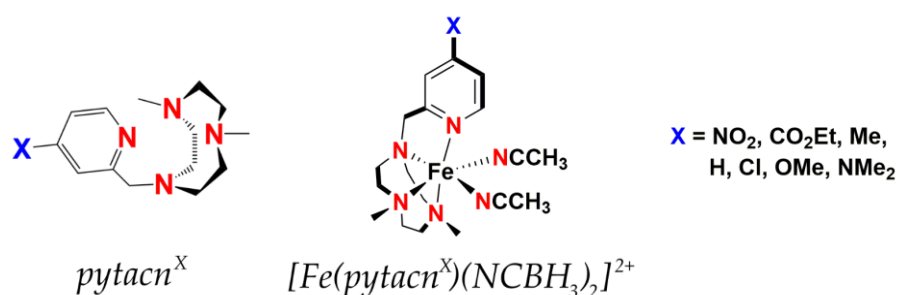


Figure 1.10. Structure of ligand (left) and Fe^{II} complex (right) for the family of seven literature²⁴ $[\text{Fe}^{\text{II}}(\text{pytacn}^{\text{X}})(\text{NCCH}_3)_2]^{2+}$ complexes, varying in *para*-**X** substituent and hence μ_{eff} at room temperature.²⁴

A range of μ_{eff} (298 K) values was observed (0.0 – 3.0 BM, Figure 1.11) as **X** varied. Indeed, this enabled the concept of the observed correlations between $T_{1/2}$ and σ_{p}^+ observed in the solid state (*Subsection 1.4.2*) to be extended to the *solution phase*: here, as σ_{p}^+ increased, the EWG properties of

the *para* substituent increases, the μ_{eff} (298 K) dropped (Figure 1.11), due to higher fraction of the Fe(II) complex being in the *LS* state (*diamagnetic*, $S = 0$) rather than the *HS* state (*paramagnetic*, $S = 2$); and consistent with increased ligand field strength. Hence, if a VT study was undertaken, then the $T_{1/2}$ would be expected to increase with increasing σ_{p}^+ (Figure 1.11).

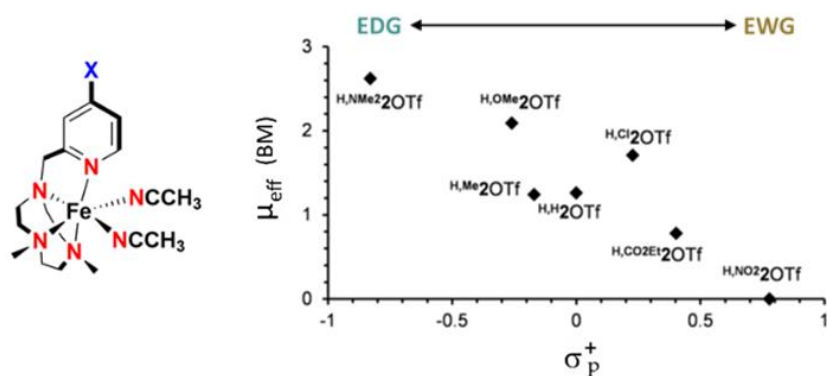


Figure 1.11. The effective magnetic moment (BM) at 298 K of the seven $[\text{Fe}(\text{pytacn}^{\text{X}})_2(\text{NCCH}_3)_2]^{2+}$ complexes in CD_3CN versus the Hammett constant of the *para*-X substituent on the pyridyl ring of the pytacn^{X} ligand used. Figure reproduced with modifications from ref²⁴.

In 2016 twenty-nine $[\text{Fe}^{\text{II}}(\text{bpp}^{\text{X,Y}})_2]^{2+}$ complexes, varying in *para*-X pyridine or *meta*-Y pyrazole substituent (where $\text{bpp}^{\text{H,H}}$ is 2,6-di(pyrazol-1-yl)-3-pyridine),^{107, 132, 134-137} were studied in depth by Deeth, Halcrow *et al.* (Figure 1.12).²³

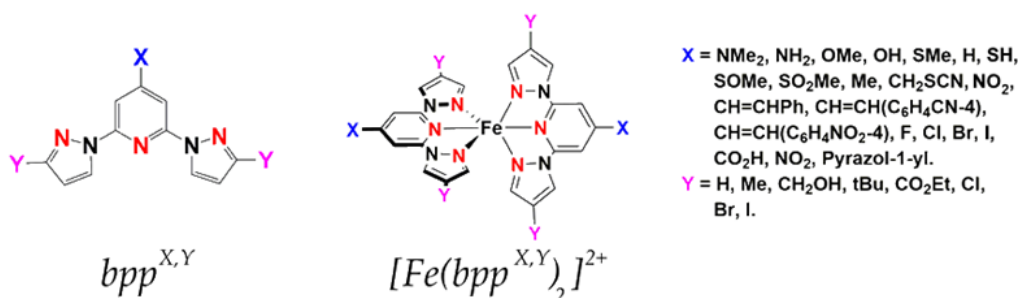


Figure 1.12. (a) Structure of the $\text{bpp}^{\text{X,Y}}$ ligands; (b) The family of twenty-nine $[\text{Fe}^{\text{II}}(\text{bpp}^{\text{X,Y}})_2]^{2+}$ complexes (right).^{23, 107, 132, 134-137}

This study set a milestone in terms of predictable tuning of the $T_{1/2}$ of the solution SCO phenomenon by modifying either a *para* **X**-substituent on the pyridyl ring or a *meta* **Y**-substituent on the pyrazolyl rings of the **bpp**^{X,Y} ligand. Firstly, they found a strong $\sigma_p^+(\mathbf{X})$ vs. $T_{1/2}$ correlation ($R^2 = 0.92$, Figure 1.13a) and a weaker $\sigma_m(\mathbf{Y})$ vs. $T_{1/2}$ correlation ($R^2 = 0.61$, Figure 1.13b), extending the *para* substituent tuning of solution phase μ_{eff} (298 K) result previously observed by Costa *et al.* in 2013.²⁴

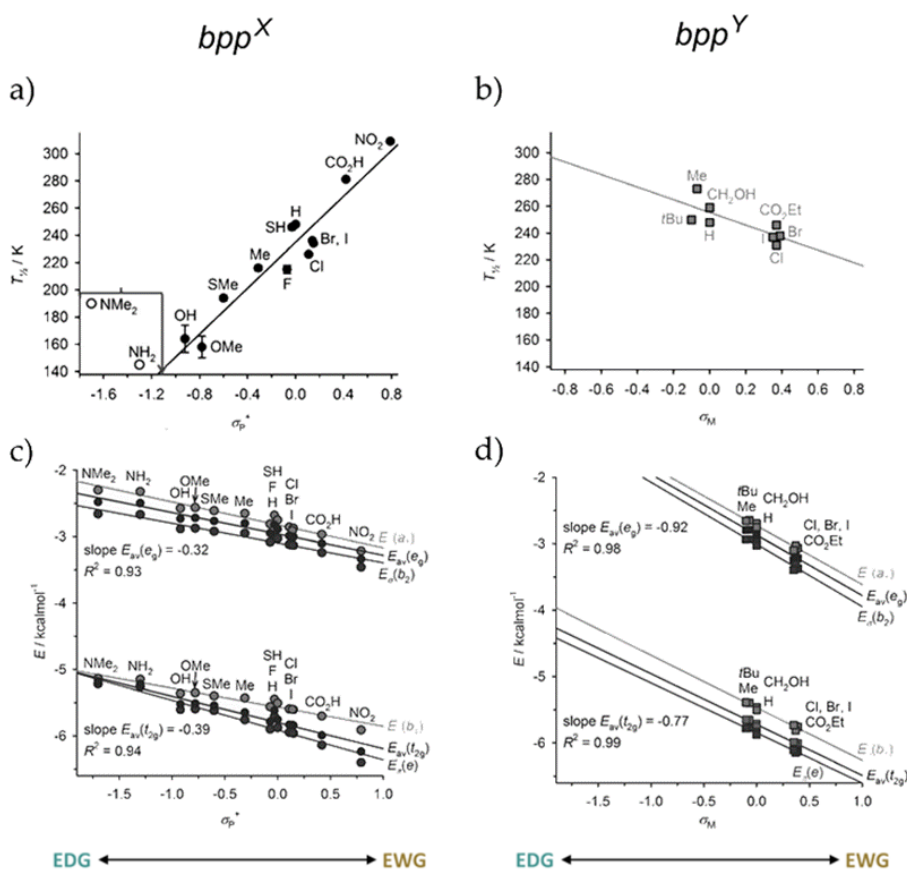


Figure 1.13. (a) Plot of $T_{1/2}$ for $[\text{Fe}^{\text{II}}(\text{bpp}^{\text{X}})_2]^{2+}$ versus the *X* substituent Hammett parameters σ_p^+ . The line shows the best fit correlation ($R^2 = 0.92$), omitting the *X* = NH_2 and NMe_2 datapoints as they are HS (b) Plot of $T_{1/2}$ for $[\text{Fe}^{\text{II}}(\text{bpp}^{\text{Y}})_2]^{2+}$ versus the *Y* substituent Hammett parameters σ_m . The line shows the best fit correlation ($R^2 = 0.61$); (c) Plot of the relevant substituent Hammett parameter versus the computed *d*-orbital energies for LS $[\text{Fe}^{\text{II}}(\text{bpp}^{\text{X}})_2]^{2+}$ ($E(t_{2g})$, $R^2 = 0.94$ and $E(e_g)$, $R^2 = 0.93$); (d) Plot of the relevant substituent Hammett parameter versus the computed *d*-orbital energies for LS $[\text{Fe}^{\text{II}}(\text{bpp}^{\text{Y}})_2]^{2+}$ ($E(t_{2g})$, $R^2 = 0.99$ and $E(e_g)$, $R^2 = 0.98$). Figure reproduced with modifications from ref²³.

Further, they found that the Hammett parameter σ_p^+/σ_m correlated with the $E(t_{2g})$ and $E(e_g)$ energy levels calculated with *DFT* for the *LS* of $[\text{Fe}^{\text{II}}(\text{bpp}^{\text{X,Y}})_2]^{2+}$ ($\sigma_p^+(\text{X})$: $E(t_{2g})$, $R^2 = 0.94$ and $E(e_g)$, $R^2 = 0.93$; $\sigma_m(\text{Y})$: $E(t_{2g})$, $R^2 = 0.99$ and $E(e_g)$, $R^2 = 0.98$; Figure 1.13(c-d)). They concluded, through close examination of the effects of **X/Y** on $E(t_{2g})$ and $E(e_g)$, that $\text{Fe} \rightarrow \text{N}$ π -back bonding effects dominate for **X** (*para*) substituents which, on **EDG** \rightarrow **EWG** strengthen the ligand field increasing $T_{1/2}$; whereas $\text{Fe} \leftarrow \text{N}$ σ -bonding effects dominate for **Y** (*meta*) substituents; with **EDG** \rightarrow **EWG** decreasing the ligand field and the $T_{1/2}$ (Figure 1.13(c-d)).^{23, 138} Also important to mention here (discussed in more detail in *Subsection 1.6.3*), is the extremely good correlation of ΔE_{HL} (Figure 1.2) with $\sigma_p^+(\text{X})$ ($R^2 = 0.89$, Figure 1.22) and a less strong correlation with $\sigma_m(\text{Y})$ ($R^2 = 0.67$, Figure 1.22).²³

Another widely reported class of *SCO* $\text{Fe}(\text{II})$ complexes in the literature is based on triazole ligands, that possess the ‘*right*’ ligand field strength to activate the *SCO* transition.^{4, 54, 67, 139} Moreover, due to the synthetic routes employed for the closure of the 1,2,4-triazole ring, a large variety of substituents can be located in the 3-, 4- and 5- positions of the triazole ring, granting design flexibility, and enabling either mono- or polytopic ligands to be constructed (Figure 1.14).^{4, 58, 123, 139-140}

In 2017 Brooker *et al.* published a study on a new family of *SCO*-active iron(II) complexes of 3-(2-*azinyl*)-4-tolyl-5-phenyl-1,2,4-triazole (*L^{azine}*) ligands (Figure 1.14).⁸³

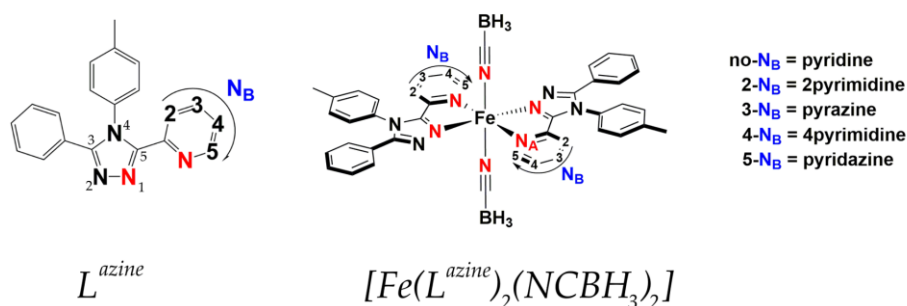


Figure 1.14. Example of some 1,2,4-triazole base ligands (left). Family of five *SCO*-active $[\text{Fe}^{\text{II}}(\text{L}^{\text{azine}})_2(\text{NCBH}_3)_2]$ complexes (right).⁸³

They reported an innovative correlation between the ^{15}N -NMR chemical shift of the coordinating nitrogen (N_A) of the free L^{azine} ligand (δN_A) with the experimental SCO $T_{1/2}$ of the $[\text{Fe}(L^{\text{azine}})_2(\text{NCBH}_3)_2]$ complex in CDCl_3 solution ($R^2 = 0.99$, Figure 1.15).⁸³

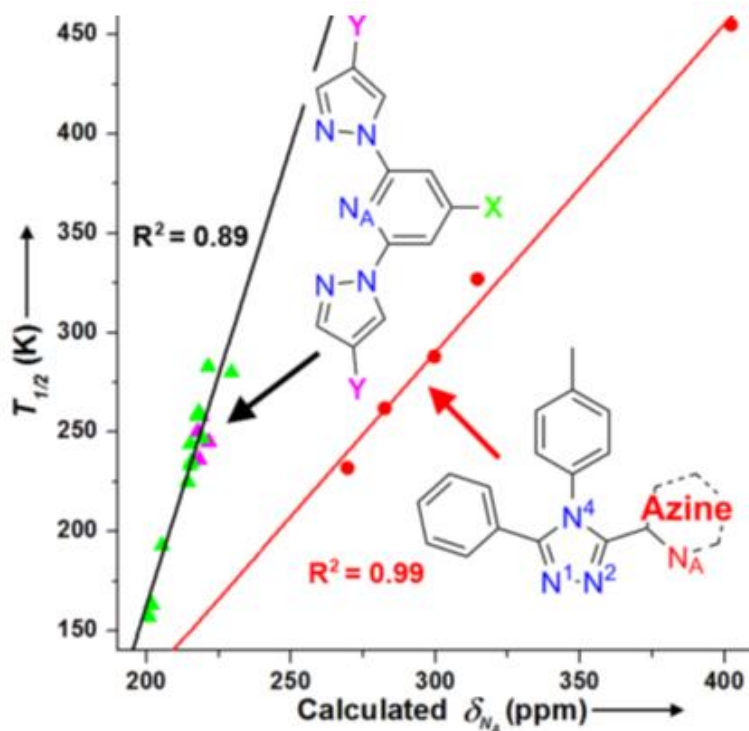


Figure 1.15. Plot of the observed $T_{1/2}$ versus our calculated ligand $^{15}\text{N}_A$ NMR peaks for the five $[\text{Fe}^{\text{II}}(L^{\text{azine}})_2(\text{NCBH}_3)_2]$ complexes (Figure 1.13; red, $R^2 = 0.99$), and the twenty-nine SCO-active $[\text{Fe}^{\text{II}}(\text{bpp}^{\text{X,Y}})_2](\text{Z})_2$ complexes (Figure 1.12; $\text{Z} = \text{BF}_4, \text{PF}_6$, black, $R^2 = 0.89$). Figure reproduced with modifications from ref⁸³.

The δN_A value was shown to be easily and quickly calculated by *DFT*, and to match closely with that determined experimentally. As a first test of how general the δN_A vs $T_{1/2}$ correlation might prove to be, twenty-nine of the literature $\text{Fe}(\text{bpp}^{\text{X,Y}})_2^{2+}$ family (Figure 1.12) were also tested, with the δN_A values calculated by *DFT*; a strong correlation δN_A vs $T_{1/2}$ was observed ($R^2 = 0.89$, Figure 1.16).⁸³ Employing δN_A instead of σ^+ has two key advantages: (a) the effects of any substituent can be evaluated even for those which σ is

not available in literature and (b) the effect of other changes in the ligand backbone (e.g., N/CH, Figure 1.13 or N/O replacements, Figure 1.16) can also be explored. In both cases no Hammett parameter is available; so, alternative approaches, such as δN_A , must be employed.

In 2018, twelve $[\text{Fe}^{\text{II}}(\text{pybox}^{\text{X}})_2]^{2+}$ complexes, varying in *para*-X pyridine (where pybox^{H} is 2,6-bis(oxazolin-2-yl)pyridine),¹⁴¹⁻¹⁴² were studied in depth by Kimura and Ishida (Figure 1.16).²²

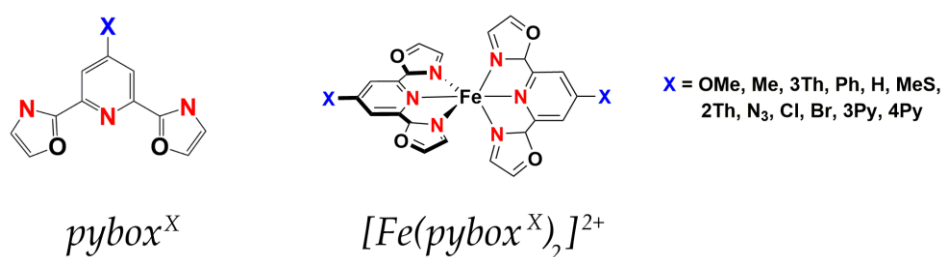


Figure 1.16. Structure of pybox^{X} ligand and the family of twelve literature $[\text{Fe}^{\text{II}}(\text{pybox}^{\text{X}})_2]^{2+}$ complexes.^{22, 141}

Kimura and Ishida found that both $\sigma_{\text{p}}(\text{X})$ ($R^2 = 0.78$) and $\sigma_{\text{p}}^+(\text{X})$ ($R^2 = 0.77$) correlated with $T_{1/2}$ for the family of twelve $[\text{Fe}^{\text{II}}(\text{pybox}^{\text{X}})_2]^{2+}$ complexes (Figure 1.17).²²

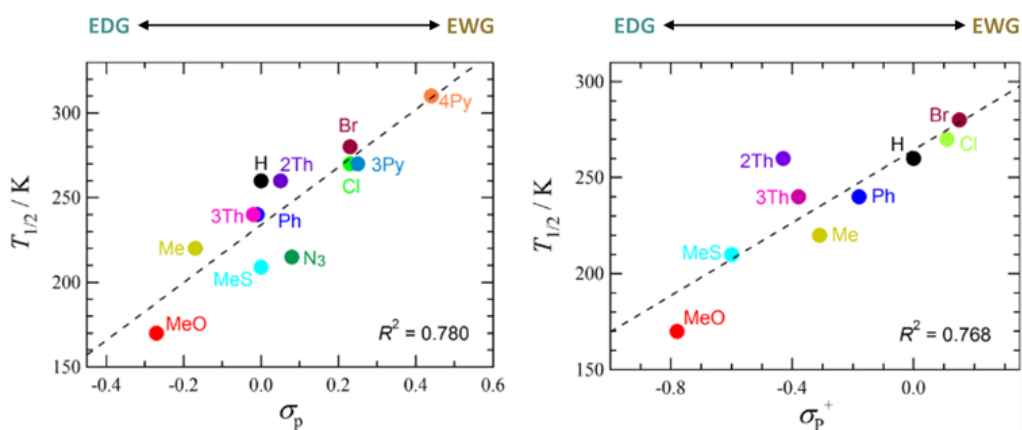


Figure 1.17. Correlation of $T_{1/2}$ with $\sigma_{\text{p}}(\text{X})$ ($R^2 = 0.78$) and $\sigma_{\text{p}}^+(\text{X})$ ($R^2 = 0.77$) for the family of twelve literature $[\text{Fe}^{\text{II}}(\text{pybox}^{\text{X}})_2]^{2+}$ complexes.^{22, 141}

Similar to Brooker *et al.*,⁸³ Kimura and Ishida ran some *DFT* calculations to assess the atomic charge on coordinating nitrogen of the pyridyl ring, but in this case not in the form of $\delta\mathbf{N}$ (easily confirmed experimentally) but, instead, directly as atomic charge ($\rho(\mathbf{N})$) of the free ligand for three solution phase SCO families: (i) $[\text{Fe}^{\text{II}}(\text{pybox}^{\text{X}})_2]^{2+}$, (ii) $[\text{Fe}^{\text{II}}(\text{bpp}^{\text{X,Y}})_2]^{2+}$, (iii) $[\text{Fe}^{\text{II}}(\text{L}^{\text{azine}})_2(\text{NCBH}_3)_2]$. Both these two parameters ($\delta\mathbf{N}$ and $\rho(\mathbf{N})$) are calculated from the electron density sitting on the coordinating nitrogen: (i) $\delta\mathbf{N}$ chemical shift accounts for the de-shielding effects of the electron density on the nuclei resonance and (ii) $\rho(\mathbf{N})$ accounts for the difference in electron charge between the examined nitrogen *vs.* native nitrogen (number of electrons equal to 7). This variation (*negative*, electron excess) is a mirror of the capability of the nitrogen to pull electrons from the surrounding carbon atoms. Among these two parameters ($\delta\mathbf{N}$ and $\rho(\mathbf{N})$), the valuable advantage of the $\delta\mathbf{N}$ is that it can be experimentally validated by simple ^{15}N NMR measurements. Not surprisingly – as the atomic charge $\rho(\mathbf{N})$ and the chemical shift $\delta\mathbf{N}$ account for the same molecular properties – good to excellent correlations were also found between $\rho(\mathbf{N})$ and $T_{1/2}$ (Figure 1.18; $R^2(\text{pybox}^{\text{X}}) = 0.73$, $R^2(\text{bpp}^{\text{X,Y}}) = 0.98$, $R^2(\text{L}^{\text{azine}}) = 0.96$).²²

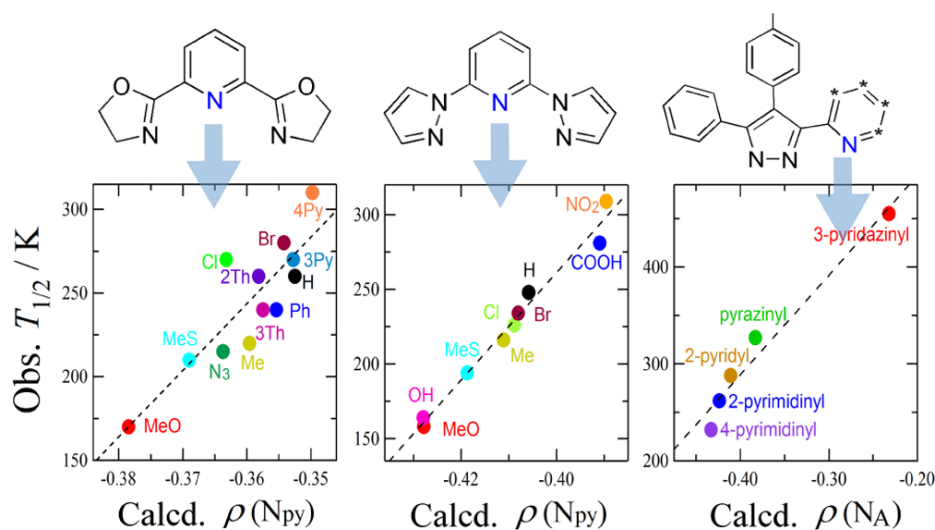


Figure 1.18. Plot of $T_{1/2}$ vs $\rho(\mathbf{N}_{\text{py}})$ from the *DFT* for three different families of SCO: $[\text{Fe}(\text{pybox}^{\text{X}})_2]^{2+}$ (left), $[\text{Fe}(\text{bpp}^{\text{X,Y}})_2]^{2+}$ (centre), $[\text{Fe}(\text{L}^{\text{azine}})_2(\text{NCBH}_3)_2]$ (right). A dashed line represents the best linear fit. Figure reproduced with modifications from ref²².

The use of the atomic charge $\rho(\text{N})$ instead of the Hammett parameter σ_{p} , provided Kimura and Ishida the chance to investigate the intimate difference between the electronic structure of $[\text{Fe}(\mathbf{bpp}^{\text{X}})_2]^{2+}$ and $[\text{Fe}(\mathbf{pybox}^{\text{X}})_2]^{2+}$. The two ligands (\mathbf{bpp}^{X} vs. $\mathbf{pybox}^{\text{X}}$) differ in the ligand backbone, by an **N/O** replacement which happens in both of the flanking five-membered rings,²² for which no σ values are available or indeed possible. This engineered modification, from **N** to **O**, increases the ligand field strength of the ligand; as at same value of **X**, $[\text{Fe}(\mathbf{bpp}^{\text{X}})_2]^{2+}$ shows a lower $T_{1/2}$ than $[\text{Fe}(\mathbf{pybox}^{\text{X}})_2]^{2+}$.

More interestingly, the **X** substituent affects the two ligands to the same extent, as the $T_{1/2}$ vs. $\rho(\text{N})$ correlations have the same slope; thanks to this discovery, Kimura and Ishida were able to establish an empirical relationship between the two systems (Equation 1.14).²²

$$\Delta T_{1/2}(\mathbf{pybox}) = 1.20 \cdot \Delta T_{1/2}(\mathbf{bpp}) + 17 \quad (1.14)$$

1.5. Temperature and Pressure induced Co^{II} SCO

In 2012, Brooker *et al.* reported the synthesis and characterisation of the robust, solvent-free crystals of [Co^{II}(*dpzca*)₂] (Figure 1.19).¹⁹

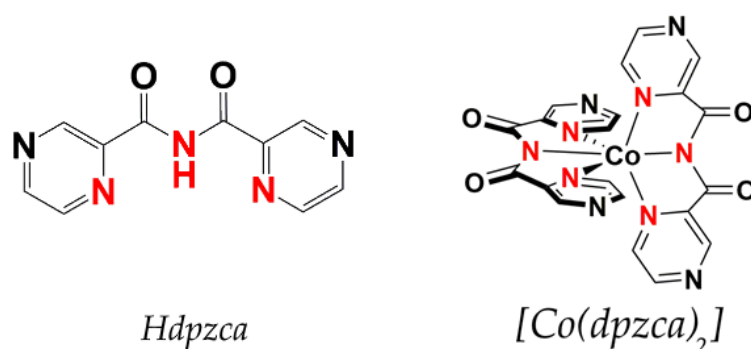


Figure 1.19. Structure of the *Hdpzca* ligand (left) and the [Co^{II}(*dpzca*)₂] (right).^{19, 104}

Particularly interesting for this Co^{II} complex is the SCO which is triggered by three different stimuli: temperature, pressure and redox. This triply switchable SCO Co^{II} complex showed (i) a thermal SCO transition ambient pressure ($p = 10^5$ Pa or 1 bar): that was *abrupt, reversible, and hysteretic* ($T_{1/2\uparrow} = 168$ K, $T_{1/2\downarrow} = 179$ K, $\Delta T_{1/2} = 11$ K) (Figure 1.20a); (ii) a *pressure-activated* SCO transition at room temperature ($T = 298$ K); which was monitored using Raman spectroscopy from 10^5 Pa to $p = 0.57$ GPa (Figure 1.20b) and (iii) reversible switching between *HS* Co^{II} ($V < 0.25$ V) and *LS* Co^{III} ($V > 0.25$ V) by reversible redox (Figure 1.20c).¹⁰⁴ Crystalline [Co(*dpzca*)₂] is a neutral complex, coordinated by two anionic ligands without solvent inclusion in the crystalline lattice. For *HS* [Co(*dpzca*)₂] at 298 K and 1 bar, the unit cell includes four equivalent molecules of [Co(*dpzca*)₂] in *I4₁/a* space group ($1/4$ of complex in asymmetric unit for general $Z = 16$ gives four complexes in unit cell, Table 1.1).¹⁹

The two tridentate *dpzca* ligand strands are each coordinated to the cobalt(II) centre meridionally, through one imide (Co–N3 = 2.049(3) Å) and two pyrazine (Co–N1 = 2.145(3) Å) nitrogen donors, at a bite angle of 77.51(7)° (Figure 1.21, Table 1.2). For LS [Co(*dpzca*)₂] at 90 K and 1 bar, the unit cell includes four equivalent molecules of [Co(*dpzca*)₂] *P2₁/c* space group (entire complex in asymmetric unit for general **Z** = 4 gives four complexes in unit cell).

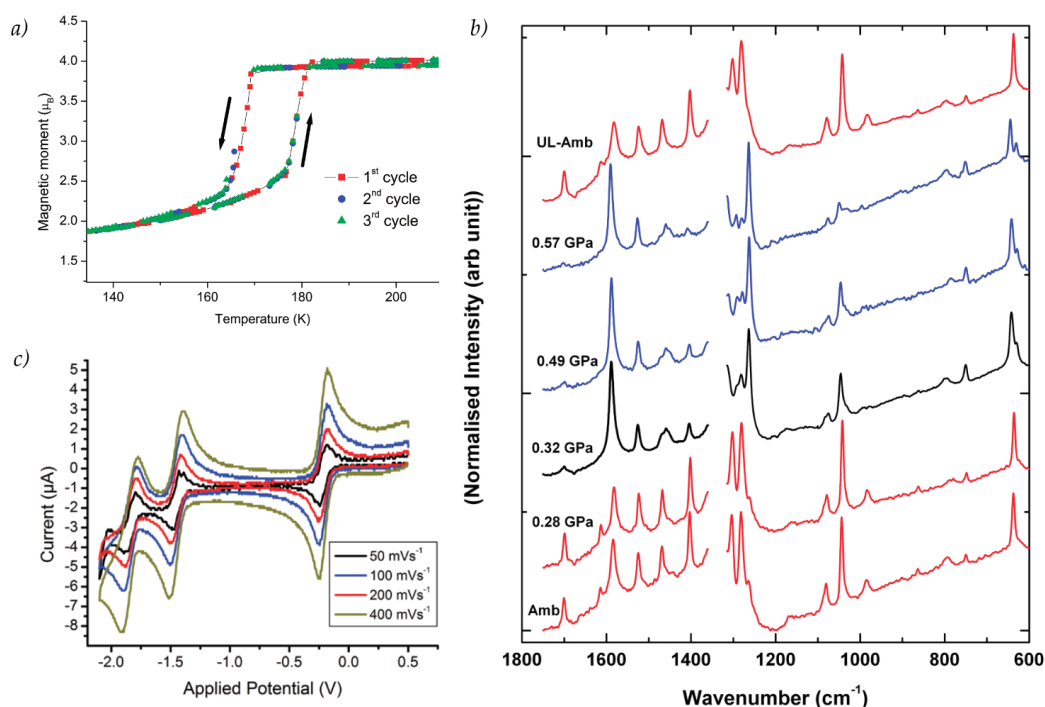


Figure 1.20. (a) Temperature dependence (at a sweep rate of 5 K min⁻¹) of the magnetic moment of a powder sample of [Co(*dpzca*)₂] over three consecutive cycles reveal the reversibility of the hysteresis loop. Note that the solid lines simply join the data points. (b) Effect of pressure on Raman spectra of [Co(*dpzca*)₂] at 298 K. Bottom to top: pressure loading spectra, from ambient (red line = HS state) to 0.28, 0.32 (black line = mixture of HS and LS states), 0.49, and 0.57 GPa (blue line = LS state), then pressure unloaded spectrum at ambient pressure. (c) CV study of an acetonitrile solution of [Co^{II}(*dpzca*)₂]/[Co^{III}(*dpzca*)₂]⁺ vs 0.01 mol L⁻¹ Ag/AgNO₃. Figure reproduced with modifications from ref.¹⁰⁴

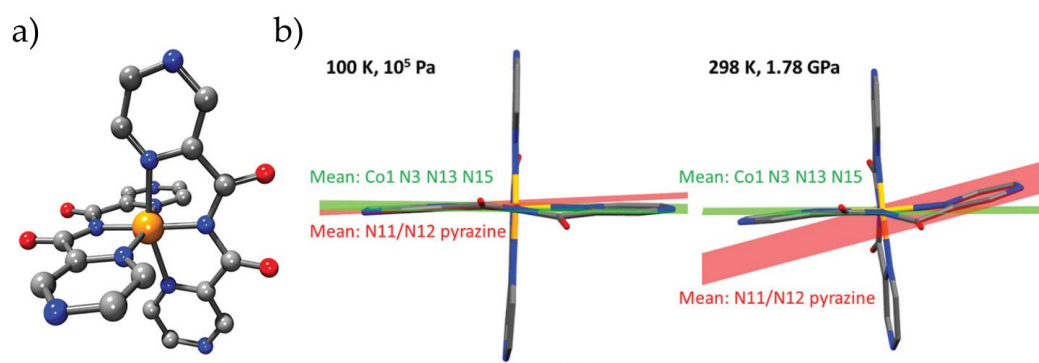


Figure 1.21. (a) $[\text{Co}^{\text{II}}(\text{dpzca})_2]$ at ambient pressure. Left: Structure at 298 K. (b) Perspective view of $[\text{Co}^{\text{II}}(\text{dpzca})_2]$ at 100 K and atmospheric pressure (left) and at 293 K and 1.78(9) GPa (right) highlighting the twisting of the N11/N12 pyrazine ring. This also distorts the octahedron significantly, which is best identified by looking at the Σ_4 , rather than the Σ_{12} where the effect is diluted by the other (relatively unchanged) cis angles, showing maximum Jahn Teller distortion. Figure reproduced with modifications from ref.¹⁹

Table 1.1. Crystal system, space group, and cell constants for $[\text{Co}(\text{dpzca})_2]$ at ambient pressure (298 and 90 K; 105 Pa \equiv 0.1 MPa \equiv 1×10^{-4} GPa \sim 1 bar) and at ambient temperature (293 K, 0.42(2) GPa and 1.78(9) GPa). [a] Note that the *b* and *c* axes in the tetragonal HS (298 K and 105 Pa) structure have been swapped to facilitate comparison with the monoclinic structures.³¹⁹

Pressure	10 ⁵ Pa 1 bar	10 ⁵ Pa 1 bar	0.42 GPa 4200 bar	1.78 GPa 178000 bar
Temperature	298 K	90 K	293 K	293 K
Spin State	HS	LS	LS	LS
Crystal system	Tetragonal	Monoclinic	Monoclinic	Monoclinic
Space group	$I 4_1/a^a$	$P2_1/c$	$P2_1/c$	$P2_1/c$
<i>a</i> axis (Å)	8.795(2)	8.668(5)	8.610(5)	8.556(5)
<i>b</i> axis (Å) ^a	27.918(9)	27.656(14)	27.630(14)	26.630(14)
<i>c</i> axis (Å) ^a	8.795(2)	8.514(5)	8.444(5)	8.130(5)
β angle (°)	90	91.52(3)	91.66(3)	90.80(3)
Volume (Å ³)	2160(1)	2040(2)	2008(2)	1852(2)

As expected for a cobalt(II) centre in the *LS* state, it is Jahn-Teller distorted: the four equatorial bonds are considerably shorter (Co-N_{Imide}: N3 = 1.91(1), N13 = 1.94(1) Å; Co-N_{Pz}: N1 = 1.99(1), N5 = 1.97(1) Å) than the apical positions (Co-N_{Pz}: N11 = 2.19(1), N15 = 2.20(1) Å), and the average bite angles for the N1 and N11 ligands, 82.6° and 79.7° respectively, are closer to 90° (Figure 1.21b and Table 1.2).

In 2015 Brooker *et al.* further studied the pressure-activated SCO behaviour of [Co(*dpzca*)₂] using a combination of Variable Pressure (VP) room temperature single crystal X-ray measurements (Table 1.2-1.3 and Figure 1.21) as well as VP and VT magnetic measurements (Figure 1.21 and Table 1.3).¹⁹ Additional X-ray structure determinations were carried out at room temperature using a diamond anvil cell, at 0.42 GPa (4200 bar) and 1.78 GPa (17800 bar).¹⁰⁴

Table 1.2. Crystal system, space group, unit cell volume (Å³), selected Co–N bond lengths (Å), N–Co–N angles (°), and octahedral distortion parameters (°) at ambient pressure for HS and LS [Co^{II}(*dpzca*)₂] (1 × 10⁻⁴ GPa; 298 and 90 K),¹⁸ and at 0.42(2) GPa and 1.78(9) GPa (293 K). [a]Σ₄ Sum of the deviation of the four *cis* pyrazine-Co-pyrazine angles from 90°.

<i>Pressure</i>	10 ⁵ Pa 1 bar	10 ⁵ Pa 1 bar	0.42 GPa 4200 bar
<i>Temperature</i>	298 K	90 K	293 K
<i>Spin State</i>	<i>HS</i>	<i>LS</i>	<i>LS</i>
Co-N _{Imide}	2.05(4)	1.94(1)	1.96(1)
	2.05(4)	1.99(1)	1.97(1)
Co-N _{Pz} 1 st L strand	2.15(2)	1.97(1)	2.00(1)
	2.15(2)	1.99(1)	2.03(1)
Co-N _{Pz} 2 nd L strand	2.15(2)	2.19(2)	2.17(2)
	2.15(2)	2.20(2)	2.18(2)
Av. Co-N	2.11	2.05	2.05
Σ ₁₂ ^b	110.8°	76.1°	89.9°
Σ ₄ <i>cis</i> -Pz)-90 ^a	10.8°	5.3°	7.3°

At these pressures [0.42, 1.78 GPa], *LS* [$\text{Co}(\text{dpzca})_2$] crystalline cell shows an intense shortening of the *c* axis that led to reduction of the whole cell volume (-7.5%, Table 1.1). The SCO transition was also investigated by VT magnetic measurements at seven different pressures ($p = 1, 1800, 2139, 2496, 2904, 3871, 4296$ bar; Table 1.3 and Figure 1.22).¹⁰⁴

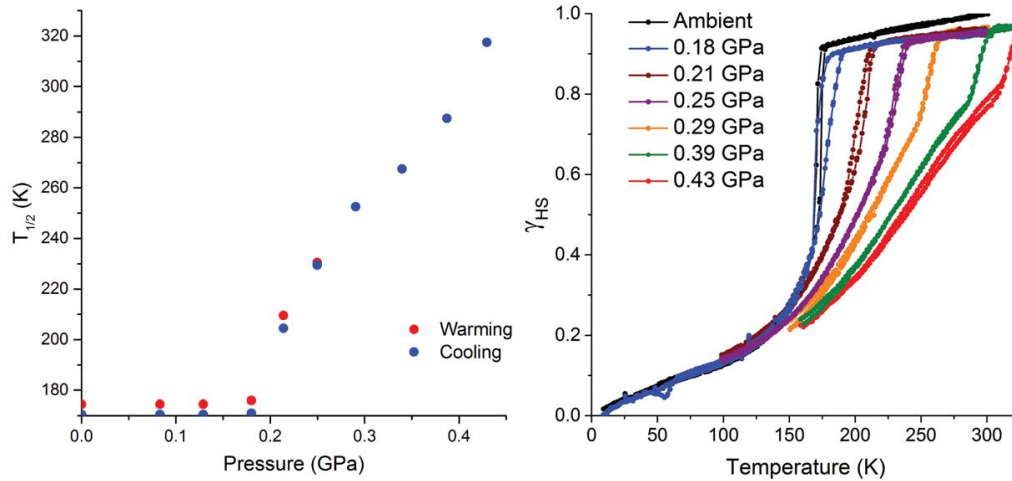


Figure 1.22. (left) The $T_{1/2}$ for the abrupt component of the SCO in $[\text{Co}(\text{dpzca})_2]$ versus applied hydrostatic pressure, obtained from the magnetic data. The four lowest pressure data points ($T_{1/2} \sim$ constant) are consistent with a threshold pressure being reached before the expected approximately linear change of $T_{1/2}$ with P is observed. Fraction HS (γ_{HS}) versus temperature for $[\text{Co}(\text{dpzca})_2]$, obtained from VT magnetic data collected at seven different pressures from ambient to 4296 bars (0.43 GPa). Figure reproduced with modifications from ref.¹⁹

Table 1.3. Reported values of $T_{1/2}$ ($\gamma_{\text{HS}} = 0.50$) for the $[\text{Co}(\text{dpzca})_2]$ overall SCO process at different pressures ($1 \text{ bar} < p < 4300 \text{ bar}$, i.e. $10^{-4} \text{ GPa} < p < 0.43 \text{ GPa}$).¹⁹

p / bar	1	1800	2139	2496	2904	3871	4296
p / GPa	10^{-4}	0.18	0.21	0.25	0.29	0.39	0.43
$T_{1/2} \downarrow$ / K	173	173	189	202	214	227	235
$T_{1/2} \uparrow$ / K	169	168	188	202	214	227	235

As the pressure increases, the $T_{1/2}$ shifted to higher temperatures (Figure 1.22(left), rising from 173 K at pressure of 1 bar up to 235 K at 4300 bar (Table 1.3, Figure 1.22).

Across this range of pressures, $[\text{Co}(\text{dpzca})_2]$ also shows a change in the nature of the SCO transition: (i) at $p \leq 2100$ bar, a highly cooperative SCO transition (*abrupt, reversible, and hysteretic*) is observed; (ii) at $p \geq 2500$ bar, a progressively higher portion of *gradual* spin transition replaces the first stages of the *abrupt* SCO (low HS fraction).

This latter condition leads to a progressively higher percentage of SCO *gradual* transition at the pressure increase (*gradual* at $p < 2100$ bar (20%, up to $\gamma_{\text{HS}} < 0.20$, mostly *abrupt* and *hysteretic* SCO transition); *gradual* at $p = 2500$ bar (60%, up to $\gamma_{\text{HS}} < 0.6$); *gradual* at $p = 4300$ bar (80%, up to $\gamma_{\text{HS}} < 0.8$)) (Figure 1.22(right)).

1.6. Theoretical Approaches to SCO

1.6.1. General Overview

The SCO phenomenon is a very complicated phenomena to theoretically reproduce with high accuracy. As mentioned in *Subsection 1.2.2*, the HS-LS gap for the SCO transition is extremely small (ΔE_{HL} , about 0-2000 cm^{-1} ; Figure 1.2). For this reason, the employment of high levels of theory is desirable, as it can provide very accurate results. Indeed, calculation involving transition metal ions, where *d*-electrons occupy degenerate and *quasi*-degenerate orbitals, usually require a multi-configurational treatment in order for them to be properly described.

Not surprisingly, more rigorous descriptions of the system wavefunction comes with heavy computational cost and also often problems with convergence. A brief overview of selected theoretical methods employed on SCO systems is provided next, followed by a detailed introduction to *EDA-NOCV* as it is employed on SCO systems for the first time in this thesis.

1.6.2. Ab Initio Ligand Field Theory on SCO Systems

A realistic reproduction of the HS-LS gap (Figure 1.2, ΔE_{HL}) for the SCO transition is only possible by using high levels of theory such as Coupled Cluster (CC)¹⁴³ or Complete Active Space Self Consistent Field (CASSCF).¹⁴⁴ The accuracy of a CC calculation is so often high that the results obtained can be used as a reference for evaluating the results obtained from 'lower' levels of theory (such as *DFT*) in which approximations are made in order to reduce computational costs.¹⁴³

On the other hand, Ab-Initio Ligand Field Theory (*AILFT*)¹⁴⁵ is a post Hartree Fock model, that enables calculation of the ligand field splitting energy (Δ_o) by employing the *CASSCF* methodology (See *Section A1.2* for general overview on Hartree Fock Theory).¹⁴⁴ The *CASSCF* approach is applied to a fixed geometry structure (previously optimised with appropriately accurate computational protocols) and it proceeds through the screening of various electron rearrangements (various spin multiplicities) in a defined set of molecular orbitals (*MOs*).¹⁴⁶⁻¹⁴⁸ In addition to *CASSCF* routine, the second order *N*-Electron Valence State Perturbation Theory (*NEVPT2*) procedure can be added to reduce the computational costs.¹⁴⁹⁻¹⁵² Some examples in literature can be easily found whereas the employment of *AILFT* calculation were run to provide a theoretical support to studies on Fe(II) *SCO* complex.¹⁵³⁻¹⁵⁶

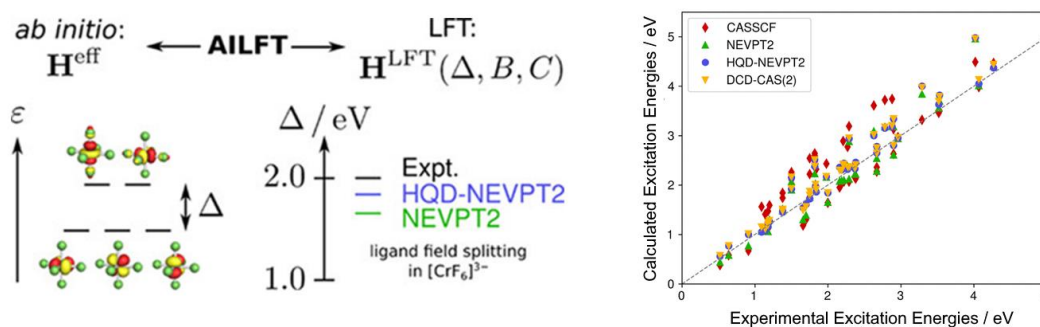


Figure 1.23. (left) Representation of the Δ_o splitting for TM complexes; besides, the level of approximation obtained in reproducing the experimental Δ_o splitting using the literature NEVPT2 level of theory and the new implemented HQD-NEVPT2. (right) Correlation between experimental excitation energies and energies of the AILFT models derived from different *ab initio* methods. The grey dashed line denotes an almost perfect agreement. Figure reproduced with modifications from ref.¹⁵⁷

Neese *et al.* published in 2020 a very interesting study where they clarify the extremely high level of accuracy in calculating Δ_o terms calculated using *AILFT-NEVPT2* (Figure 1.23(right)).¹⁵⁷ The authors implemented a new *NEVPT2* procedure called Hermitian quasi-degenerate *NEVPT2* (*HQD-NEVPT2*), which was found to be even more accurate than the *NEVPT2*

procedure (Figure 1.23(right)).¹⁵⁷ They tested this new *HQD-NEVPT2* implementation on twenty-four metal complexes (various metal complexes, first and second row transition metals), revealing an almost biunivocal matching between the calculated *vs.* the experimental excitation energies (Figure 1.23(left)); obtained results consolidate the role of *AILFT* as an irreplaceable tool in the study of Transition Metal (TM) complexes.¹⁵⁷

1.6.3. Density Functional Theory on SCO Systems

One of the first paper to employs *DFT* to study a *SCO* system was in 1998 by Toftlund *et al.*¹⁵⁸ *DFT* does not provide results at the level of theories such as *CASSCF* or *CC*; however, it is so widely used because it has much lower computational costs (*Section A1.2* for more details). This also opens up possibilities of studying much larger systems, such as surfaces or crystals. As results from *DFT* are highly dependent on the choice of the employed functional, a key step toward more common employment of *DFT* for *SCO* studies focussed on finding the ‘best’ functional for reproducing the *HS-LS* energy gap (ΔE_{HL}).¹⁵⁹⁻¹⁶³

In 2010, Neese *et al.* employed six *DFT* functionals to try to correctly reproduce ΔE_{HL} for eleven different iron(II) complexes (from the simplest Generalized Gradient Approximation (*GGA*) to the newest double-hybrid (*B2PLYP*, Figure 1.24).¹⁵⁹ The best candidate was found to be the double-hybrid density functional *B2PLYP*, in conjunction with large and flexible basis sets (def2-QZVPP).

This was observed to be able to provide *qualitatively* correct results of spin-state energetics for the investigated non-*SCO* complexes. However, in the case of the *SCO* complex, *B2PLYP* appeared to be slightly biased in favour of the *HS* state as some of the ΔE_{HL} values are negative, which cannot be correct (Figure 1.24).¹⁵⁹

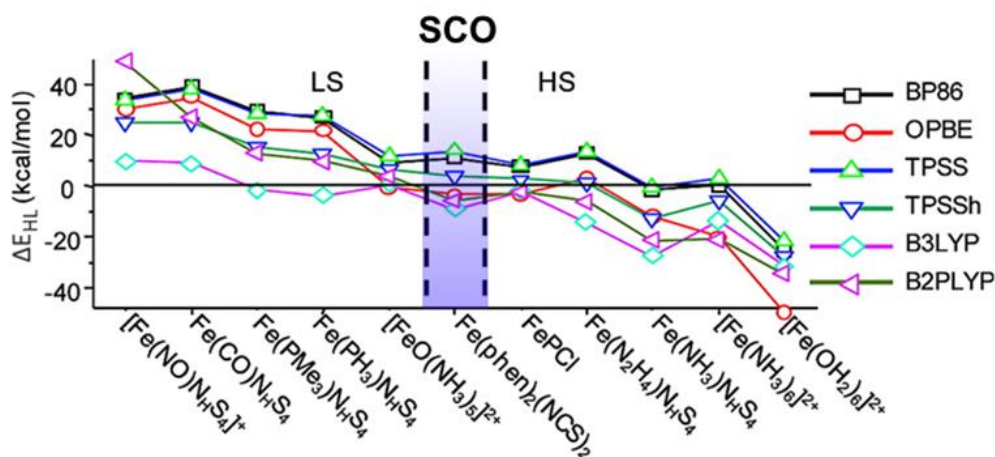


Figure 1.24. The ΔE_{HL} energies of a range of LS, SCO and HS iron(II) complexes are computed using modern density functional theory (DFT) methods with six different functionals (reported in the right side of the figure). Only the double-hybrid density functional B2PLYP, in conjunction with large and flexible basis sets (def2-QZVPP), can provide qualitatively correct results of spin-state energetics for the investigated non-spin-crossover complexes. An energy difference ΔE_{HL} of 0 to 6 kcal/mol (0 to 2100 cm^{-1}) is proposed to be indicative of SCO behaviour. Figure reproduced with modifications from ref¹⁵⁹.

As mentioned earlier (Figure 1.12, Subsection 1.4.3) in 2016, twenty-nine $[\text{Fe}^{\text{II}}(\mathbf{bpp}^{\text{X,Y}})_2]\text{A}_2$ (where $\text{A} = \text{BF}_4, \text{PF}_6$) complexes, varying in *para*-**X** pyridine or *meta*-**Y** pyrazole substituent (Figure 1.25, where $\mathbf{bpp}^{\text{H,H}}$ is 2,6-di(pyrazol-1-yl)-3-pyridine),^{107, 132, 134-137} were studied in depth by Deeth, Halcrow *et al.*²³ using DFT with a GGA functional. Along with the correlations presented in Subsection 1.4.3, the energy gap between the high spin (HS) and low spin (LS) states, ΔE_{HL} , correlated with Hammett parameter σ/σ^+ of the **X/Y** substituent in the ligand. Specifically, ΔE_{HL} correlated strongly with $\sigma_{\text{p}}^+(\mathbf{X})$ ($R^2 = 0.89$) and a less strongly with $\sigma_{\text{m}}(\mathbf{Y})$ ($R^2 = 0.67$) (Figure 1.25).²³

However, such DFT results are consistently *qualitative*, and not *quantitative*. This is in part because such *ab initio* calculations are performed at $T = 0$ K where the LS state must be more stable than the HS state. Therefore, the ΔE_{HL} term ($\Delta E_{HL} = E_{\text{HS}} - E_{\text{LS}}$) should always be positive ($\Delta E_{HL} > 0$) as the LS state is enthalpically more stable than the HS state. So, despite

the fact that the relative order of ΔE_{HL} gap across the $[\text{Fe}^{\text{II}}(\text{bpp}^{\text{X,Y}})_2]$ family is respected and the effect of the **X** substituent on ΔE_{HL} gap can be explained; the absolute magnitude of ΔE_{HL} reveals the weakness of *DFT*: it is unable to supply a *quantitative* evaluation of these energy gaps.

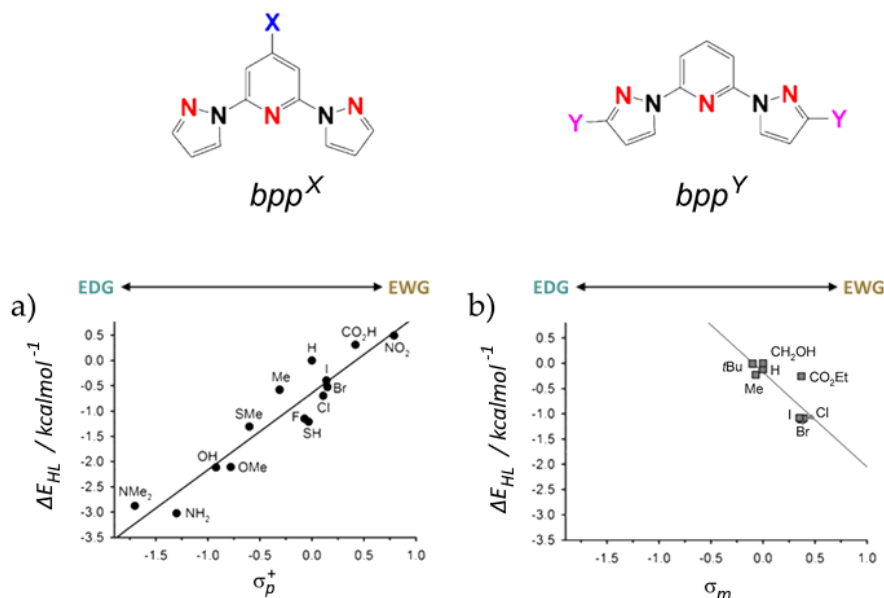


Figure 1.25. (a) Plot of the computed energy difference between the high- and low-spin states relative vs. the relevant substituent Hammett parameter (σ_p^+ , σ_m^+) (ΔE_{HL} , $R^2 = 0.89$) to $[\text{Fe}(\text{bpp}^{\text{X}})_2]^{2+}$; (b) Plot of the relevant substituent Hammett parameter vs. the computed energy difference between the high- and low-spin states relative (ΔE_{HL} , $R^2 = 0.67$) to $[\text{Fe}(\text{bpp}^{\text{Y}})_2]^{2+}$. Figure reproduced with modifications from ref²³.

Another interesting approach to study the SCO phenomenon using *DFT* is from a thermodynamic angle, that is considering enthalpy and entropy, rather than focussing on the *MO* energies. This approach was preferred in several studies.¹⁶⁴⁻¹⁶⁶ In 2012, Paesani *et al.*¹⁶⁴ attempted to reproduce the experimental trend of increasing $T_{1/2}$ of the SCO transition for the three *trans*- $[\text{Fe}(\text{styrylpyridine})_4(\text{NCX})_2]$ as **X** was varied from **S** to **Se** to **BH₃** (Figure 1.26, **styrylpyridine** in *trans* configuration). They employed a four-step procedure: (i) tuning the electronic enthalpy gap ($\Delta H_{el,HS-LS}$) employing different *DFT* functionals on isolated molecules of *trans*-

[Fe(styrylpyridine)₄(NCX)₂]; (ii) calculating normal modes of the six molecules (three different species in two different spin states); (iii) using principles of statistical thermodynamics to calculate vibrational contributions ($\Delta H_{vib,HS-LS}$ and $\Delta S_{vib,HS-LS}$) and electronic entropy ($\Delta S_{el,HS-LS}$); (iv) reproducing the *gradual* SCO transition. They succeeded in *qualitatively* reproducing the experimental data, but with a 50-100 K error in $T_{1/2}$ (Figure 1.26). This high error it is not a surprise as it comes from the strong limitation that *DFT* functionals cannot be tuned for an *ad hoc* situation.

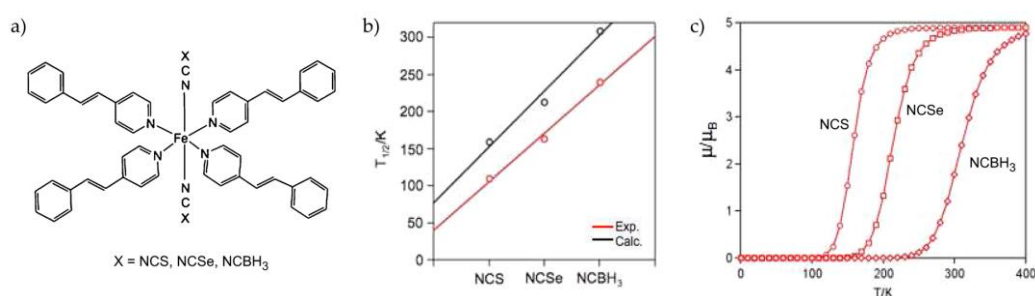


Figure 1.26. (a) Structure of *trans*-[Fe(styrylpyridine)₄(NCX)₂] ($X = S, Se, NCBH_3$, styrylpyridine in *trans* configuration). (b) Comparison of the experimental (red) and calculated (black) spin-crossover temperatures for the [Fe(stpy)₄(NCX)₂] complexes ($X = S, Se$, and BH_3). (c) Calculated magnetic moments for the [Fe(stpy)₄(NCX)₂] complexes with $X = S$ (circle), Se (square), and BH_3 (diamonds) as a function of the temperature. Figure reproduced with modifications from ref¹⁶⁴.

Finally, rationalising thermodynamic results is extremely complicated as those depend on the intrinsic properties of the system, such as the number of electrons, the charge of the systems, or the overall vibrational properties, and they can depend strongly on the number of atoms that compose the whole molecule, even if those atoms are not directly involved in any bond engagement but just belong to satellite branches of the ligand (e.g., tolyl, phenyl rings can influence the packing).

These results of these various *DFT* approaches are promising, but they are still far from supplying a reliable support for scientists in pre-synthesis phases of molecular design.

1.6.4. DFT+U on SCO Systems: The Hubbard U Term

Several functionals in DFT (as *Local Density Approximation*, LDA or *General Gradient Approximation*, GGA) do not correctly describe the strong on-site Coulomb interaction of localized electrons; in order to correct it, the strategy is to add an additional Hubbard-like term to the Hamiltonian to specific atomic orbitals, giving birth to the *DFT+U* method.

These on-site Coulomb interactions are particularly strong when atomic orbitals are localised: this always happens for *d* and *f* electrons, sometimes for *p* orbitals. The *DFT+U* correction is usually described through two different parameters accounting for the on-site *Coulomb* interaction (*U*) and on-site *Exchange* interaction (*J*). These two *U* and *J* parameters can be extracted from *ab-initio* calculations; but more often, they are obtained semi-empirically. Two main branches address different ways to introduce this *DFT+U* corrections in a *DFT* calculation: Liechtenstein *et al.*¹⁶⁷ prefer to add *U* and *J* as independent corrections; Anasimov *et al.*,¹⁶⁸ prefer to collect them in a single effective U_{eff} term ($U_{\text{eff}} = U - J$). In *Chapter Five*, the *DFT+U* approach (Anasimov version¹⁶⁸) is employed to model the solid state SCO behaviour of $\text{Co}^{\text{II}}(\text{dpzca})_2$ complex (*Section 1.5*).

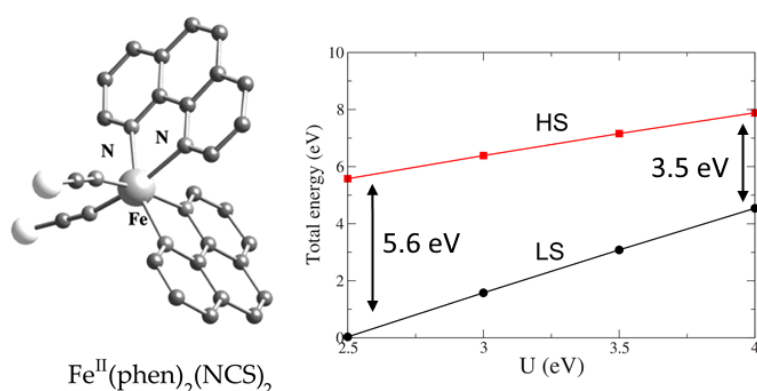


Figure 1.27. (left) Molecular structure of the solid state SCO $\text{Fe}(\text{phen})_2(\text{NCS})_2$; (right) Reported variation in the ΔE_{HL} gap (DFT+U) at the increase of the *U* potential from 2.5 eV to 4.0 eV ($J = 0.95$ eV, constant). Figure reproduced with modifications from ref¹⁶⁹.

The application of the Hubbard-U term supplies the advantage to modify ΔE_{HL} gap by unevenly affecting the absolute energy of the two different spin state; therefore, the tuning of the ΔE_{HL} gap is not connected with the employed functional (Figure 1.26, ref¹⁶⁴) but at finding the proper U_{eff} term for the right ΔE_{HL} gap to reproduce the experimental SCO.¹⁶⁹⁻¹⁷⁰

Ángyán *et al.* published in 2008 a study on solid state SCO Fe(phen)₂(NCS)₂ using periodic DFT. The DFT+U implementation (Liechtenstein version; Fe(*d*) orbitals: $U = 2.5$ eV, $J = 0.95$ eV) was used successfully tuned the ΔE_{HL} gap of Fe(**phen**)₂(NCS)₂ (where **phen** = phenanthroline) to reproduce the experimental available data (Figure 1.27).¹⁶⁹

1.6.5. Monte Carlo and Molecular Dynamics (MC/MD) on SCO Systems

Several efforts toward parametrising an *ad hoc* computational protocol to reproduce SCO phenomenon can also be found in literature. In these cases, semi-classical calculations such as *Monte Carlo/Molecular Dynamics* (MC/MD) were employed to fit molecular properties.^{89, 171-173} Most of these studies gave only partially satisfying results, as MD or MC calculations are levels of theory that are usually employed to treat larger systems in a classical or *quasi*-classical approach, when *ab initio* calculations cannot be employed.^{89, 171-172}

An interesting example from 2014, Cirera *et al.* succeeded in implementing an *ad hoc* Ligand Field Force Field (LF-FF) able to reproduce the SCO transition for a Metal Organic Frameworks (MOF) of [Fe(pz)₂Pt(CN)₄] previously modelled using DFT calculations (Figure 1.28).^{164, 173} The [Fe(pz)₂Pt(CN)₄] MOF was firstly characterised experimentally revealing a SCO behaviour at $T_{1/2} = 300$ K with *abrupt* and *hysteretic* SCO transition.¹⁷³

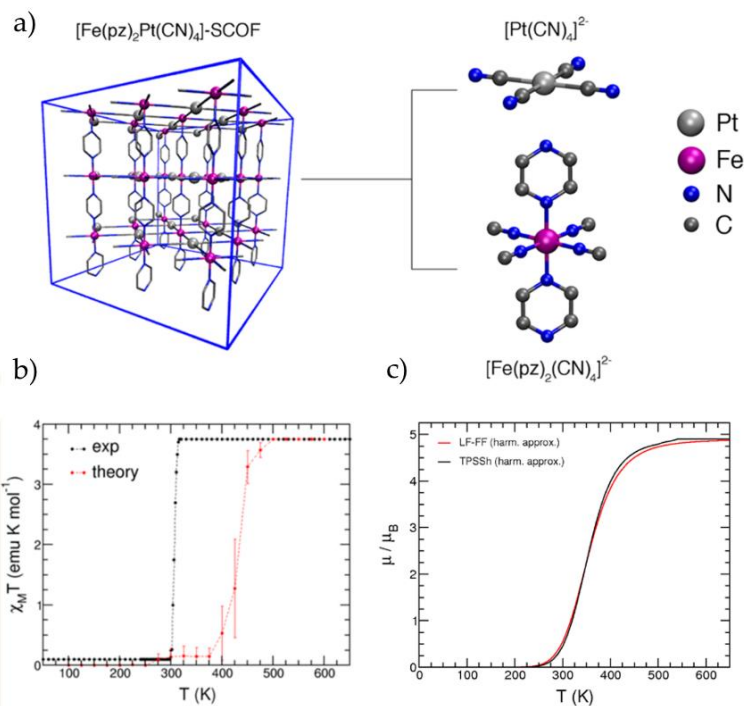


Figure 1.28. (a) Three-dimensional representation of the $[\text{Fe}(\text{pz})_2\text{Pt}(\text{CN})_4]$ MOF and secondary building units $[\text{Pt}(\text{CN})_4]^{2-}$ (upper) and $[\text{Fe}(\text{pz})_2(\text{CN})_4]^{2-}$ (lower) used as model systems in the TPSSh/triple- ζ calculations required for the parametrisation of the Fe(II) and Pt(II) Ligand Field Force Fields. All hydrogen atoms are omitted for clarity. (b) Magnetisation curves for the $[\text{Fe}(\text{pz})_2(\text{CN})_4]^{2-}$ experimental vs calculated (c) Comparison between theoretical models obtained with the harmonic approximation using DFT-TPSSh (solid black line) and MD-LFFF (solid red line). Figure reproduced with modifications from ref⁷³.

Subsequently, Cirera *et al.* proceeded in employing periodic DFT (TPSSh functional/triple- ζ basis set) to model the SCO switching as a gradual second order phase transition. The attempt led to reproduce the switching $T_{1/2}$ at 400 K ($\Delta T_{1/2} = 100$ K).

However, Cirera *et al.* did not stop at reproducing the SCO transition, they aimed to define a hybrid MC/MD method based on results obtained in the first phase of their study using DFT. MC/MD methods are lower levels of theory than DFT (calculations not from first principles, more approximated, employed for large systems) but they have the important advantage to trigger a further scale-up in the size of the systems that can

be studied. They succeeded in implementing this *MC/MD* method, and were able to reproduce *SCO* transition for the *MOF* of $[\text{Fe}(\text{pz})_2\text{Pt}(\text{CN})_4]$ as accurately as *DFT* did, but at a lower computational cost, with the potential to be scaled-up to larger systems as crystals or surfaces (Figure 1.28a). Despite the success to implement a Ligand Field Force Field (*LF-FF*) able to accurately reproduce the *DFT* results, the error from the experimental findings is still extremely high.

1.6.6. Artificial Neural Networks (ANN) on SCO Systems

In 2020, Kulik *et al.*¹⁷⁴ showed that an Artificial Neural Network (*ANN*) was able to correctly predict the actual ground spin states in over 95% of a batch of 46 Fe^{II} *SCO* complexes. This was achieved after training the *ANN* on over 2000 mononuclear Fe^{II} and Fe^{III} complexes, optimised with *DFT* (*B3LYP* functional). Training was targeted on the Fe-X ($\text{X} = \text{C}, \text{N}, \text{O}, \text{S}$) bond lengths in order to learn the specific range of bond distances corresponding to the Fe^{II} different spin states (Figure 1.29).

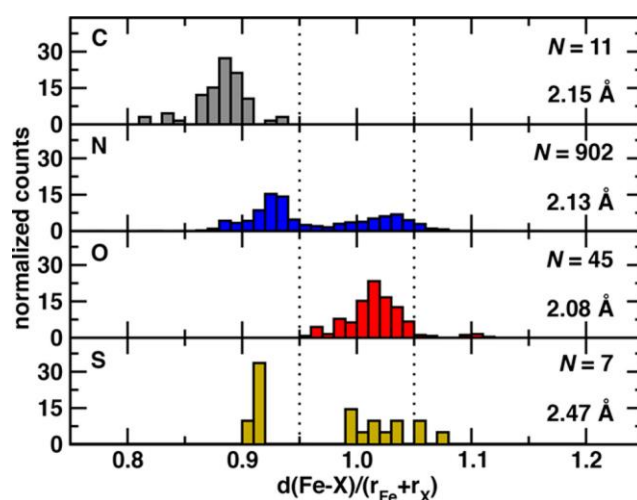


Figure 1.29. Normalised histograms of relative iron-ligand-atom bond lengths for 965 mononuclear octahedral $\text{Fe}(\text{II})$ complexes in the training set, with the coordinating element indicated in the upper left corner of each panel. Vertical dotted lines indicate 0.95 and 1.05 relative bond length thresholds which nominally indicate LS or HS character, respectively. Figure reproduced with modifications from ref¹⁷⁴.

1.6.7. Introduction to EDA-NOCV

A key limit of the above theoretical approaches, even when successful, is the absence of any *quantitative* evaluation of the M-L bond energies and hence of the detailed electronic structure. Indeed, *DFT* can provide $\Delta H_{el,HS-LS}$ or ΔG_{HS-LS} but to date has not enabled any generalisable outcome that could be extended and used in further studies on different systems.

An introduction to the recently developed Energy Decomposition Analysis through Natural Orbitals for Chemical Valence (*EDA-NOCV*) method is now presented, as it is applied for the first time to the field of *SCO* later in this thesis. This model is promising as it can supply a *quantitative* assessment of the energies in bond engagement between different molecular fragments.

An extensively employed model used in the past to investigate the chemical bond from an energetic perspective is the Extended Transition State (*ETS*) theory. *ETS* is able to provide a powerful insight of the energies taking part in bond formation between two fragments (e.g., *ionic vs covalent bonding*);¹⁷⁵⁻¹⁸⁰ however, it is not possible to extract any further information about the nature of the bonds engaged between fragments (σ -bond, π -bond or δ -bond), nonetheless the energetic breakdown.

Alternatively, Natural Orbitals for Chemical Valence (*NOCV*) theory offers a perspective of the electron flowing between pieces of the overall molecule, to form a chemical bond. Specifically, new set of orbitals (*NOCV*) are obtained through a localisation scheme and used to diagonalise the deformation density matrix (ΔP) in order to find a set of eigenvalues (v_i) for pairing each 'donor orbital' with each 'acceptor orbital' from the two different parts of the molecule whereby bond analysis is monitoring.

Interestingly, *ETS* and *NOCV* theories show an interesting complementarity in the data they can uncover; eventually, the electron flowing analysis from *NOCV* can be used to breakdown the part of the *ETS* analysis accounting for covalent bonding and supply information about the

nature of such engaged bonds, as it will be discussed shortly. *ETS* theory was consequently renamed *EDA*, maintaining the same structure of the theoretical model; therefore, *ETS*, from now on, is recalled as *EDA* (Energy Decomposition Analysis). This new implemented theory was named Energy Decomposition Analysis using Natural Orbitals for Chemical Valence (*EDA-NOCV*).¹⁸¹⁻¹⁸² The *EDA-NOCV*¹⁸³⁻¹⁸⁴ method combines the classical *EDA*, developed by Ziegler and Rauk,^{175, 185} with the *NOCV* extension (Natural Orbitals for Chemical Valence), developed by Mitoraj and Michalak.¹⁸⁶⁻¹⁸⁷

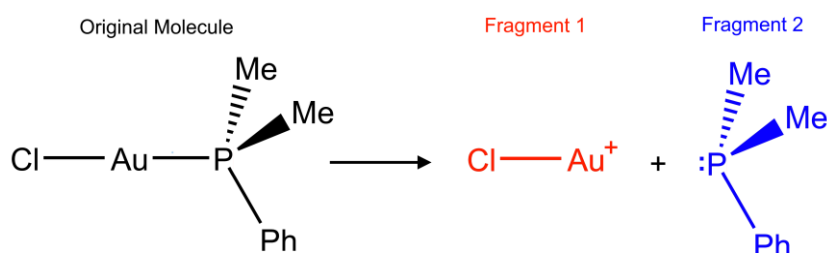


Figure 1.30. Fragmentation scheme for the *EDA-NOCV* analysis (B3LYP-D3/TZVP) for $[AuCl(PMe_2Ph)]$ into fragment 1: $ClAu^+$ and fragment 2: PMe_2Ph . Figure reproduced with modifications from ref¹⁸⁸.

Table 1.4. *EDA-NOCV* results from exemplative case¹⁸⁸ for $[AuCl(PMe_2Ph)]$ complex. The total change in energy ΔE_{int} (left) is decomposed into several contributions, ΔE_{elstat} , ΔE_{Pauli} , ΔE_{orb} and ΔE_{disp} . The ΔE_{orb} term is split into $\Delta E_{orb,\sigma}$, $\Delta E_{orb,\pi}$, $\Delta E_{orb,pol}$, $\Delta E_{orb,rest}$.¹⁸⁸ All energies are reported in kcal/mol.

ΔE_{int}	ΔE_{elstat}	ΔE_{Pauli}	ΔE_{disp}	ΔE_{orb}	$\Delta E_{orb,\sigma}$	$\Delta E_{orb,\pi}$	$\Delta E_{orb,pol}$	$\Delta E_{orb,rest}$
-67.7	-174.9	173.3	-5.4	-60.6	-37.0	-14.6	-6.7	-2.3

In the most complete description of the molecular system the result of the *EDA-NOCV* approach supplies a *quantitative* assessment of the dissociation energy (ΔE_{int} , Equation 1.14) between the considered molecular fragments (e.g. fragment 1: $ClAu^+$ vs. fragment 2 PMe_2Ph , Figure 1.30).¹⁸⁸

The total energy interaction ΔE_{int} is defined as the difference between the energy of the final molecule (ΔE_0) minus the energy of the two split molecular fragments extrapolated from the molecular structure of the studied molecule (ΔE_1 and ΔE_2) (Equation 1.15, exemplary results from ref¹⁸⁸ are reported in Table 1.4):

$$\Delta E_{int} = E_0 - E_1 - E_2 \quad (1.15)$$

An alternative, and more useful description of ΔE_{int} is given in Equation 1.16; whereas each term will be shortly described through the various steps that characterise the *EDA-NOCV* method:

$$\Delta E_{int} = \Delta E_{elstat} + \Delta E_{Pauli} + \Delta E_{orb} \quad (1.16)$$

By adding the preparation energy term (ΔE_{prep}) to ΔE_{int} the experimentally measurable dissociation energy (*DE*) is obtained (Equation 1.17).¹⁸³⁻¹⁸⁴ ΔE_{prep} term accounts for the loss in energy due to the system having to rearrange in order to be ready to interact to produce the final molecule.

$$DE = \Delta E_{int} + \Delta E_{prep} \quad (1.17)$$

The *EDA-NOCV* calculation is performed through a series of single point calculations whereby the different ΔE_i ($i = elstat, Pauli, orb$) terms are calculated stepwise.

First, the bonds of interest are identified and the molecule is split according to these into two (or more) pieces, called fragments (e.g., Figure 1.30). Then, in this preliminary step, the energies of the respective fragments are calculated individually with the same geometry they exhibit in the final molecule. At the end of this step the electron densities ρ_A and ρ_B are obtained. Once the electron densities of the fragments are calculated at infinite separation, they are replaced at the distance they hold in the

molecule and the components of the occurring interactions for each ΔE_i term are calculated (Equation 1.16). The electrostatic term ΔE_{elstat} is obtained in a quasi-classical way via interaction of Coulomb charges as reported in Equation 1.18 (exemplative results from ref¹⁸⁸ are reported in Table 1.4).

$$\Delta E_{elstat} = \sum_{\substack{\nu \in A \\ \mu \in B}} \frac{Z_\nu Z_\mu}{R_{\nu\mu}} + \sum_{\substack{\nu \in A \\ \mu \in B}} \frac{\rho_B(r) Z_\mu}{|R_\mu - r|} + \sum_{\substack{\nu \in A \\ \mu \in B}} \frac{Z_\nu \rho_A(r)}{|R_\nu - r|} + \int \frac{\rho_A(r) \rho_B(r)}{r_{12}} dr_1 dr_2 + \Delta E_{xc} \quad (1.18)$$

The error in the approximation of this ΔE_{elstat} term as being a quasi-classical interaction is partially corrected for the variation in the Exchange and Correlation term (ΔE_{xc}) is calculated (more details in *Subsection A1.2.2*). The ΔE_{xc} term is evaluated in this same step and included into the ΔE_{elstat} term. In the next step of the *EDA-NOCV* routine the Pauli energy change ΔE_{Pauli} is calculated. This term arises when the two fragments are placed at the distance they hold in the final molecule. When the wavefunctions ψ_A and ψ_B of the two fragments are allowed to overlap, energy for antisymmetrisation needs to be paid to obtain the final wavefunction ψ_0 (Equation 1.19). Indeed, in order to respect principles of antisymmetry and normalisation of the final wavefunction ψ_0 the system needs to step out from its ground state. ΔE_{Pauli} is always associated with an energy increase, resulting in destabilisation of the system (exemplative results from ref¹⁸⁸ are reported in Table 1.4).

$$\psi_0 = N\hat{A}\{\psi_1\psi_2\} \quad (1.19)$$

Hence the final form of ψ_0 is calculated as a Slater determinant of the matrix composed by a new basis $[\lambda_i; i=1, n]$ (Equation 1.18 and 1.19) obtained applying a Löwdin transformation to the original set of $[\chi_i; i=1, n]$ as reported in Equation 1.20. S_{ij} is the overlap matrix.

$$\Psi_0 = |\lambda_1\lambda_2 \cdot \lambda_i\lambda_j \cdot \lambda_n| \quad (1.20)$$

$$\lambda_j = \sum_j S_{ij}^{1/2} \chi_j \quad (1.21)$$

The related density ρ_0 is subsequently calculated as reported in Equation 1.22, where ΔE_{ij}^{Pauli} is the deformation density matrix in the basis $[\chi_i; i=1, n]$ representing the deformation density $\Delta\rho^{Pauli}$ obtained by the difference between ρ_0 and ($\rho_{12} = \rho_1 + \rho_2$).

$$\rho_0 = \sum_i^n \chi_i^* \chi_i = \sum_{i,j} S_{ij} \chi_i \chi_j = \sum_{i,j} \Delta P_{ij}^{Pauli} \chi_i \chi_j + \rho_1 + \rho_2 \quad (1.22)$$

It follows from Equation 1.22 that $[\Delta P_{ij}^{Pauli} = (S_{ij} - \delta_{ij})]$. In this final step, the ΔE_{orb} term is calculated from the deformation density $\Delta\rho^{orb}$ (Equation 1.23) which is defined as the difference between the electron density of final system ρ_0 and the value of ρ_{12} (Equation 1.23).

$$\Delta\rho^{orb} = \rho_0 - \rho_{12} = \sum_{\mu,\nu}^n \Delta P_{\mu\nu}^{orb} \lambda_\mu \lambda_\nu \quad (1.23)$$

In this step the *NOCV* method is utilised; firstly, a new set of natural orbitals is obtained by diagonalisation of ΔP^{orb} (Equation 1.24).

$$\Delta P^{orb} C_i = v_i C_i \quad (1.24)$$

Specifically, when the following equation is solved, a new set of vectors C_i that expand the new function ψ_i in the basis of the orthogonalised fragment orbitals λ_j with the following relation (Equation 1.25).

$$\psi_i = \sum_j^n C_{ij} \lambda_j \quad (1.25)$$

Through definition of the new basis set, the deformation density $\Delta\rho^{orb}$ can be also defined as a sum of complementary orbitals ($\Psi_{+k}; \Psi_{-k}$) in the *NOCV* representation. This set of complementary orbitals has corresponding eigenvalues with equal absolute value but opposite sign (Δv values in Figure 1.31, Equation 1.26).

$$\Delta\rho^{orb}(r) = \sum_k^{N/2} \Delta\rho_k^{orb}(r) \sum_j^{N/2} \Delta v_k [-\psi_{-k}^2(r) + \psi_{+k}^2(r)] \quad (1.26)$$

The value of ΔE_{orb} is then described by the change in energy between the final and initial wavefunctions, Ψ and Ψ_0 , as follows (Equation 1.27, exemplative results from ref¹⁸⁸ are reported in Table 1.4):

$$\Delta E_{orb} = E[\rho_0] - E[\rho_{12}] \quad (1.27)$$

The ΔE_{orb} term can also be defined using the new *NOCV* description, as the sum of pairs of orbitals ($\Psi_{+k}; \Psi_{-k}$) which describe the electron flowing of each ΔE_k^{orb} contribution related to each k value (ΔE values in Figure 1.31, Equation 1.28).

$$\Delta E_{orb} = \sum_k^{N/2} \Delta E_k^{orb} \quad (1.28)$$

Finally, as a result of this final step, obtained through the application of *NOCV* visual inspection, the ΔE_{orb} can be further split into different, classic, types of bonding contributions (Equation 1.29), even in systems with C_1 symmetry (exemplative results from ref¹⁸⁸ are reported in Table 1.4).

$$\Delta E_{orb} = \Delta E_{orb,\sigma} + \Delta E_{orb,\pi} + \Delta E_{orb,pol} + \Delta E_{orb,rest} \quad (1.29)$$

The inclusion of the *NOCV* orbitals gives information on the number of electrons transferred from one fragment to another. The assignment is performed by visual inspection of the deformation density $\Delta\rho^{orb}$: if the electron flow occurs between the two fragments along the internuclear axis of the nuclei involved in forming the bond between fragments, it can be defined as a sigma bond (σ), and the relative orbital energy variation is denoted as $\Delta E_{orb,\sigma}$.

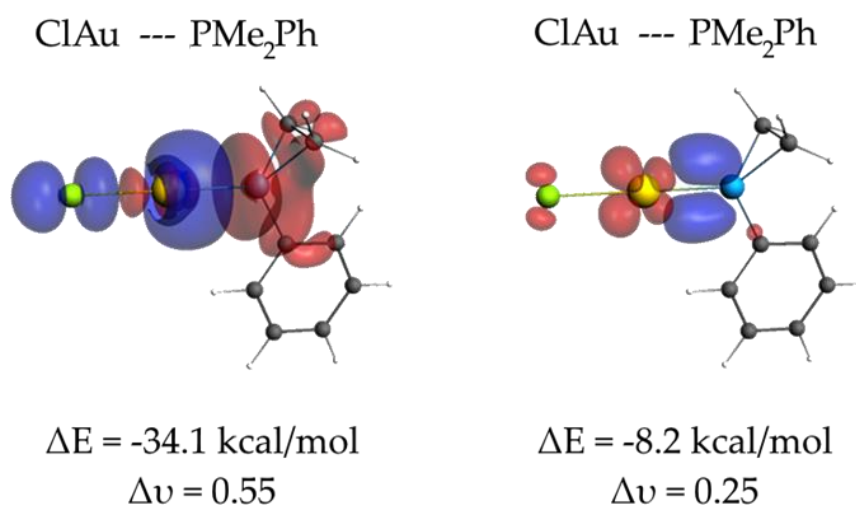


Figure 1.31. Natural orbitals for chemical valence (*NOCV*) contributions (*B3LYP-D3/TZVP*) to E_{orb} (σ -bond, left and π -bond, right) for $[AuCl(PMe_2Ph)]$ (see also Table 1.4). In deformation density plots depicted here the sense of electron “flow” is from red to blue regions. Colour code: Au (yellow), Cl (green), P (blue), C (black), H (white). Figure reproduced with modifications from ref¹⁸⁸.

If the charge flow between the two fragments shows a nodal plane which includes the nuclei, it can be classified as a pi bond (π) and the relative orbital energy variation is denoted as $\Delta E_{orb,\pi}$. If the electron flow is occurring between orbitals of the *same fragment*, then the contribution is called a ‘polarisation term’ (ΔE_{pol}) and is far less relevant for describing the inter-fragment bonding interaction.

Finally, any small energy contributions from *NOCV* flows that are below a chosen threshold are collected into the ΔE_{rest} term.¹⁸¹⁻¹⁸² They usually result from the fact that not all electron density relevant for the bonding interaction can be captured via the applied orbital localisation scheme. However, close attention must be paid if ΔE_{rest} term gets too large as this can indicate a problem in the fragmentation scheme.

1.7. Aims of this PhD

This PhD is divided into contributions for two different research fields:

1. *Solution Phase SCO (Chapters Two, Three & Four)*: An in-depth analysis of the effects of ligand electronic structure on the resulting metal complex, by surgical alterations applied through variation of substituents (*para/meta* positions) or by atom replacements in the ligand backbone (**CH/N** or **N/O**). In order to properly study these effects – without possible side effects due to crystal packing – all of these studies were performed on *solution-active* SCO complexes (*Chapters Two to Four*).
2. *Solid state SCO (Chapters Five)*: An attempt is made to develop a computational protocol that can reproduce the solid state SCO transition observed for $[\text{Co}^{\text{II}}(\text{dpzca})_2]$ at a range of different pressure conditions.^{19, 104}

A total of six different *SCO-active* families were studied (Figure 1.32): one of them was synthesised during this PhD (L^{pyZ} , Figure 1.32a); whilst the other five families examined in this thesis were available from literature (Figure 1.32(b-f)).^{19, 22-24, 83, 104}

The first research field is articulated in two distinct projects: (a) Testing the generality of the δN_{A} vs. $T_{1/2}$ correlations for pre-synthesis prediction of effects of change to L^{pyZ} or **pybox^x** or **pytacn^x** ligand on $T_{1/2}$ (*Chapter One*); (b) assessment of the energetics in place in engaging **M-L** bond in two different SCO families (L^{azine} and **bpp^x**) through the application of *EDA-NOCV* to SCO systems for the first time (*Chapters Two, Three & Four*).

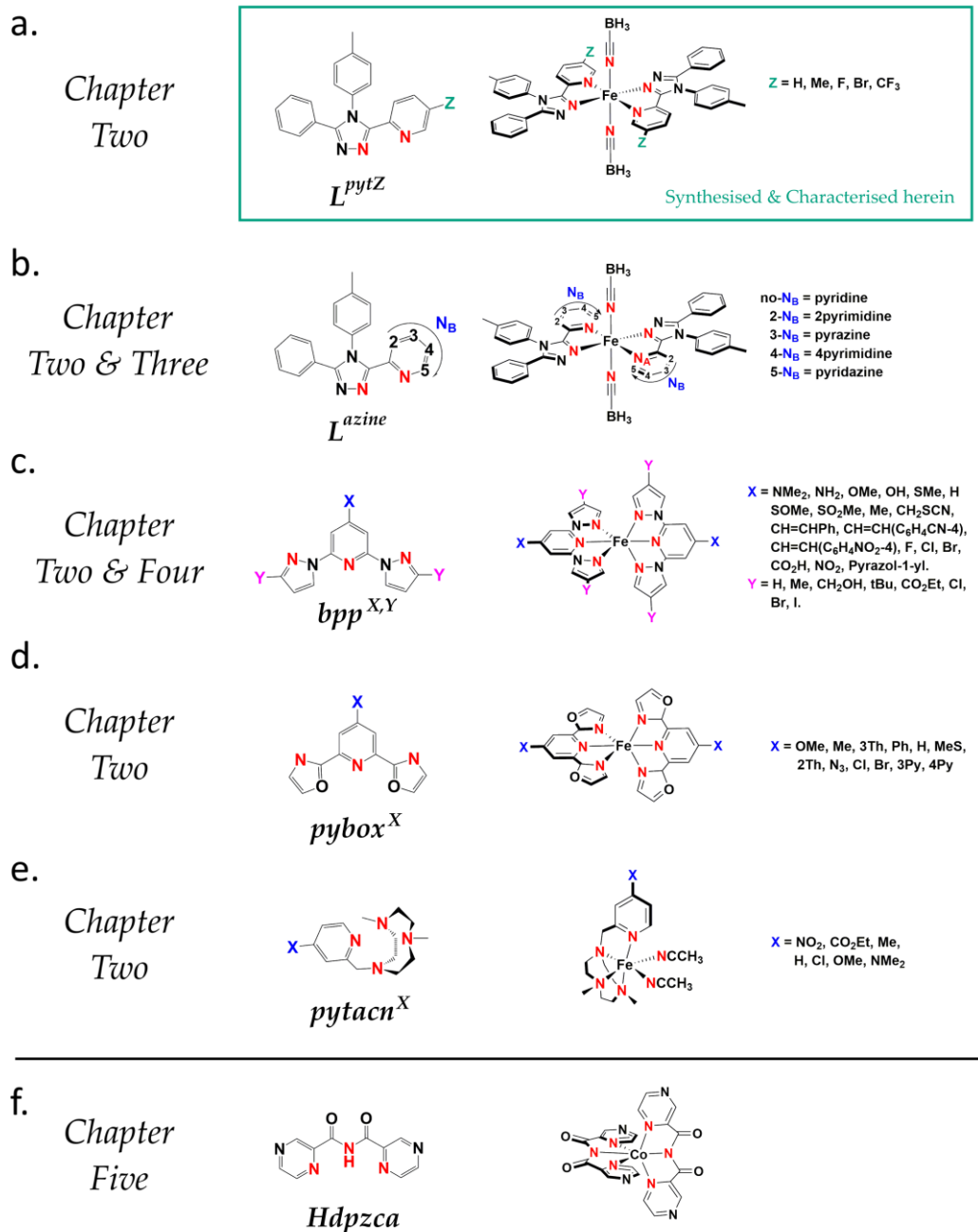


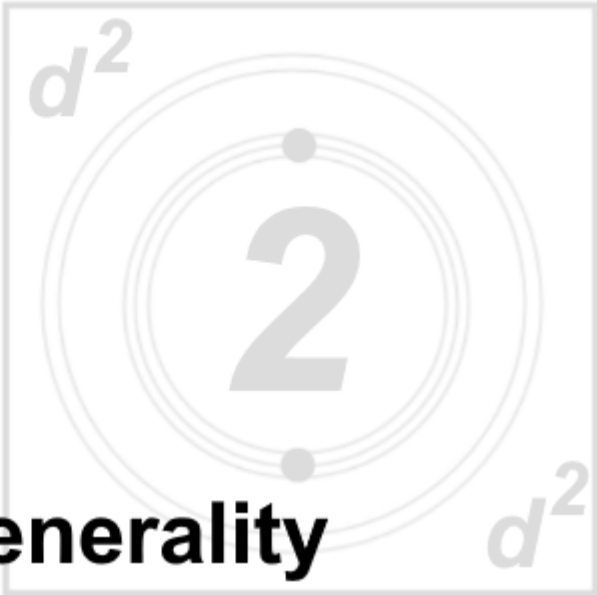
Figure 1.32. (a) Family of five $[Fe^{II}(L^{pytZ})_2(NCBH_3)_2]$, four of which are new, prepared and characterised in Chapter Two (box). (b-f) Literature families employed for theoretical studies: (b) five $[Fe^{II}(L^{azine})_2(NCBH_3)_2]$,⁸³ Chapters Two & Three; (c) fourteen $[Fe^{II}(bpp^{X,Y})_2]^{2+}$,^{ref23, 134, 136, 189-190} Chapters Two & Four; (d) twelve $[Fe^{II}(pybox^X)_2]^{2+}$,^{ref22, 141} Chapter Two (e) seven $[Fe^{II}(pytacn^X)(NCCH_3)_2]^{2+}$,^{ref24} Chapter Two; (f) $[Co^{II}(dpzca)_2]$, Chapter Five.¹⁰⁴

In the first project (*Chapter Two*), a new family of four 3-(2-(5-*Z*-pyridyl))-4-tolyl-5-phenyl-1,2,4-triazole (L^{pytZ}) and four new solution *SCO-active* $[\text{Fe}^{\text{II}}(L^{pytZ})_2(\text{NCBH}_3)_2]$ were synthesised and characterised (L^{pyZ} , Figure 1.30a). The four $[\text{Fe}^{\text{II}}(L^{pytZ})_2(\text{NCBH}_3)_2]$ plus the literature $[\text{Fe}^{\text{II}}(L^{pytH})_2(\text{NCBH}_3)_2]$,¹⁰⁵ as well as the $[\text{Fe}^{\text{II}}(\text{pybox}^X)_2]^{2+}$ and $[\text{Fe}^{\text{II}}(\text{pytacn}^X)(\text{NCCH}_3)_2]^{2+}$ families (both available from literature,^{22, 24, 141-142} Figure 1.32d and 1.32e) were then used to further test the generality of using the ¹⁵N-NMR chemical shift (δN_A) of the coordinating nitrogen in the metal-free ligand as probe of the electronic tuning by the ligand substituent on the $T_{1/2}$ of the corresponding complex.^{22-24, 83}

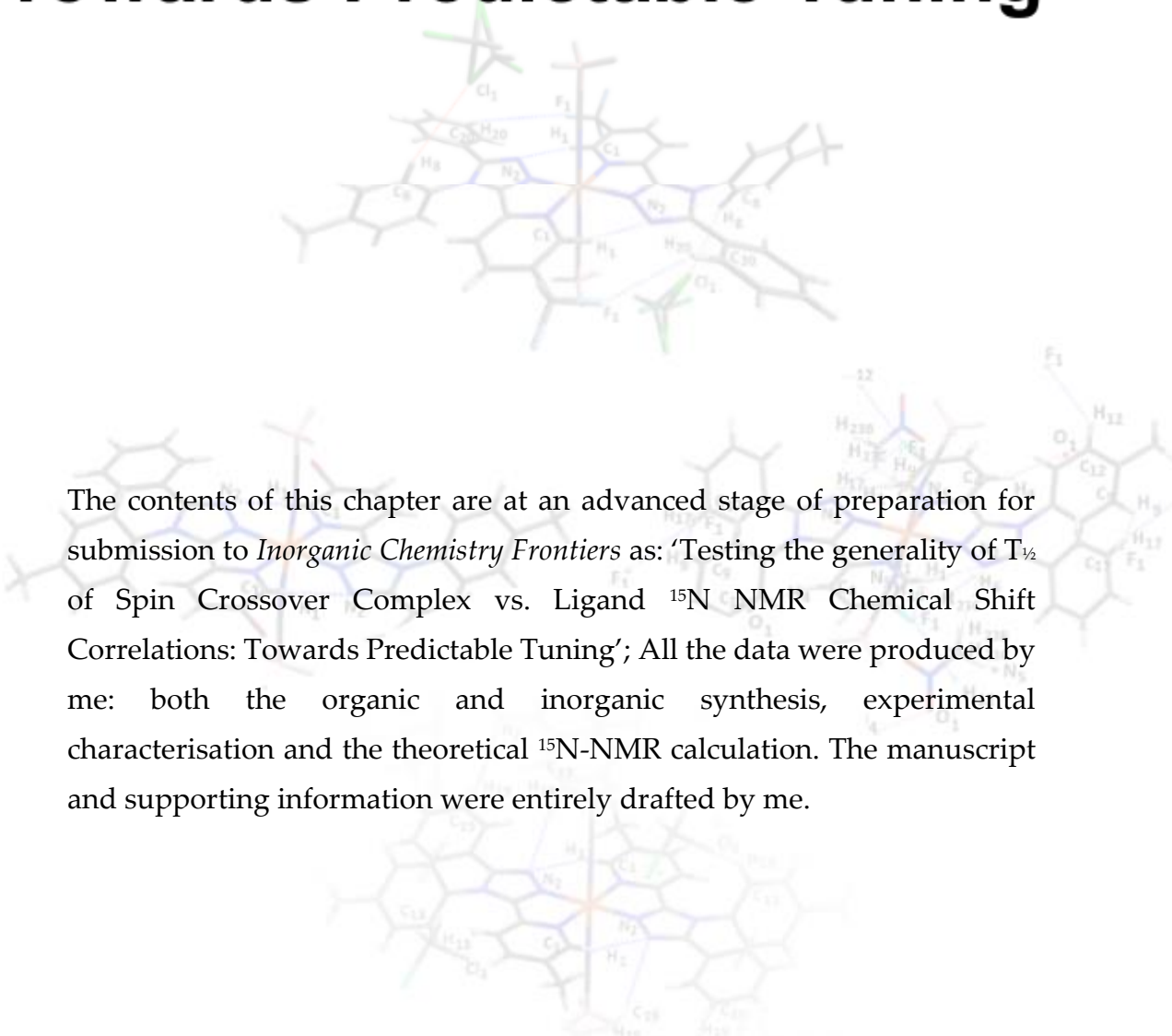
In the second project, the literature families of *solution SCO-active* $[\text{Fe}^{\text{II}}(L^{azine})_2(\text{NCBH}_3)_2]$ ⁸³ and $[\text{Fe}^{\text{II}}(\text{bpp}^X)_2]^{2+}$ ^{ref23} (Figure 1.32b and 1.32c, *Chapters Three & Four*) were employed for the first ever application of the *EDA-NOCV* theoretical model to *SCO* system through a two-step study: (i) method development and validation and (ii) analysis of the **M-L** bonds in these two, very different, iron(II) *SCO* families.

The ambitious aim of the second research field (third project) was to develop a computational protocol capable of predicting the observed solid state *SCO* of the Co(II) bis-imide complex $[\text{Co}^{\text{II}}(\text{dpzca})_2]$ at different pressures, after establishing a computational protocol at $p = 1$ bar (Figure 1.32f, *Chapter Five*).¹⁰⁴ Discussion of the steps taken to start to develop a suitable computational procedure to achieve this are reported and discussed in detail in *Chapter Five*.

The thesis concludes with a summary of the key achievements in *Chapter Six*.



Testing the Generality of $T_{1/2}$ of Spin Crossover Complex vs. Ligand ^{15}N NMR Chemical Shift Correlations: Towards Predictable Tuning



The contents of this chapter are at an advanced stage of preparation for submission to *Inorganic Chemistry Frontiers* as: 'Testing the generality of $T_{1/2}$ of Spin Crossover Complex vs. Ligand ^{15}N NMR Chemical Shift Correlations: Towards Predictable Tuning'; All the data were produced by me: both the organic and inorganic synthesis, experimental characterisation and the theoretical ^{15}N -NMR calculation. The manuscript and supporting information were entirely drafted by me.

2.1. Abstract

Four new bidentate 3-(2-(5-*Z*-pyridyl)-4-tolyl-5-phenyl-1,2,4-triazole) ligands L^{pytZ} ($Z = CF_3, Br, F, Me$) and the corresponding family of $[Fe^{II}(L^{pytZ})_2(NCBH_3)_2]$ complexes, in addition to the literature unsubstituted analogue $[Fe^{II}(L^{pytH})_2(NCBH_3)_2]$, are prepared and studied herein. Single crystal structure determinations on all four new complexes confirmed the expected octahedral coordination, with *trans*-NCBH₃ co-ligands. Solid-state variable temperature magnetic studies of air-dried crystals showed that $[Fe^{II}(L^{pytCF_3})_2(NCBH_3)_2]$ is SCO active with a *hysteresis loop* at 208 K ($T_{1/2\downarrow} = 203$ K, $T_{1/2\uparrow} = 213$ K; $\Delta T_{1/2} = 10$ K); $[Fe^{II}(L^{pytBr})_2(NCBH_3)_2]$ is not SCO active until heated above RT, while $[Fe^{II}(L^{pytF})_2(NCBH_3)_2]$ and $[Fe^{II}(L^{pytMe})_2(NCBH_3)_2]$ are SCO active close to RT ($T_{1/2} = 290$ and 300 K respectively). Solution phase variable temperature Evans NMR method studies showed that four of the complexes were SCO active close to RT ($T_{1/2} = 279$ -294 K) whilst $[Fe^{II}(L^{pytCF_3})_2(NCBH_3)_2]$ was mostly LS at RT ($T_{1/2} = 374$ K). These solution phase $T_{1/2}$ values, and those for four literature families of bi- (five *Lazine*), tri- (fourteen **bpp**^{X,Y}, twelve **pybox**^X) or tetradentate (seven **pytacn**^X) ligands, which feature *para* (**X**) pyridine or *meta* (**Y**) pyrazole ring substituents, are used, along with the calculated ¹⁵N NMR chemical shift of the coordinating azine nitrogen (**N_A**) in the ligand (for all forty-two ligands; using a refined protocol), to test the generality of the previously reported correlation of δN_A chemical shift in the free ligand with the solution $T_{1/2}$ for the respective iron(II) complex. Moderately good to excellent correlations of δN_A with $T_{1/2}$ were observed for each of the ligand families with a *para* substituent ($R^2 = 0.69$ -0.96), whereas there is no correlation when *meta* substituents are modified ($R^2 = 0.15$ -0.37), probably because the electronic impact of this is too small. Finally, δN_A also shows promise as an easily calculated measure of the electronic effect of any substituent or substitution, in contrast to the Hammett constant (σ_p^+) which is not available for all possible substituents.

2.2. Introduction

Fine tuning of ligand field strength is critical to many potential applications of coordination complexes,¹⁹¹⁻¹⁹⁶ and would greatly benefit from the development of pre-synthesis tools that could screen the proposed ligand modifications and identify the one that would provide the required properties. One existing, albeit rather approximate, method of predicting the effect of a ligand substituent on the ligand field strength is to use the Hammett parameter (σ or σ^+ , see also *Subsection 1.4.1*),^{124, 197-198} which classifies substituents as Electron Donating Substituents (**EDGs**, $\sigma/\sigma^+ < 0$) or Electron Withdrawing Substituent (**EWGs**, $\sigma/\sigma^+ > 0$) relative to an H substituent ($\sigma/\sigma^+ = 0$).¹⁹⁸

The position of the substituent relative to the donor atom affects the nature (*inductive vs mesomeric/resonance*) and hence the size of the substituent impact, with *para* (σ_{p^+}) > *meta* (σ_{m^+}), and *ortho* being problematic due to the likelihood of steric effects. But better would be the development of more general and widely applicable *in silico* methods: to do so, the considerable additional challenge that must often be met is that many such complexes are open shell (*paramagnetic*), something which is increasingly well handled.¹⁹⁹⁻²⁰¹

A family of spin crossover (*SCO*) active complexes can be arranged in order of increasing switching temperature, $T_{1/2}$ (corresponding to the midpoint of the *SCO* transition), which enables the associated ligand family to be ranked in order of increasing ligand field strength. *SCO* behaviour arises in octahedral d^4 to d^7 first row transition metal complexes where the electron pairing energy and the ligand field strength are comparable, so spin state switching can be triggered when an external stimulus is applied, most commonly temperature.^{3-4, 7, 26, 139, 202-203} The extremely high sensitivity of the $T_{1/2}$ of the complex to any change in the ligand skeleton or substituents,^{23, 83, 126, 204-206} and/or the solvato-/poly-morph,²⁰⁷ makes *SCO* compounds extremely good probes of ligand field strength. This is

especially evident when the *SCO* is monitored in solution, as this removes the crystal packing interactions which can be confounding in solid state studies, enabling the effect of the ligand modifications to be readily observed.¹¹⁹

In a few cases, the Hammett parameter (σ or σ^+) has been shown to correlate with the experimental $T_{1/2}$ in the solid state *SCO* (Subsection 1.4.2),¹²⁶⁻¹³² despite the potentially confounding issue of crystal packing. More recently it has been also employed in this way in solution *SCO* (Subsection 1.4.3): (i) in 2013 Company, Costas *et al.* found a *qualitative* correlation of $\sigma_p(\mathbf{X})$ with μ_{eff} (298 K) for seven $[\text{Fe}^{\text{II}}(\text{pytacn}^{\mathbf{X}})(\text{NCCH}_3)]^{2+}$ complexes varying in *para*- \mathbf{X} pyridine substituents (Figure 2.1e, where **pytacn**^H is 1-[(6-pyridyl)methyl]-4,7-dimethyl-1,4,7-triazacyclononane);²⁴ (ii) in 2016 twenty-nine $[\text{Fe}^{\text{II}}(\text{bpp}^{\mathbf{X},\mathbf{Y}})_2]^{2+}$ complexes, varying in *para*- \mathbf{X} pyridine or *meta*- \mathbf{Y} pyrazole substituent (Figure 2.1a, where **bpp**^{H,H} is 2,6-di(pyrazol-1-yl)-3-pyridine),^{107, 132, 134-137} were studied in depth by Deeth, Halcrow *et al.*,²³ and they found a $\sigma_p^+(\mathbf{X})$ vs. $T_{1/2}$ correlation ($R^2 = 0.92$) and a weaker $\sigma_m(\mathbf{Y})$ vs. $T_{1/2}$ correlation ($R^2 = 0.61$);²³ (iii) in 2018 Kimura and Ishida found that both $\sigma_p(\mathbf{X})$ ($R^2 = 0.78$) and $\sigma_p^+(\mathbf{X})$ ($R^2 = 0.77$) correlated with $T_{1/2}$ for a family of twelve $[\text{Fe}^{\text{II}}(\text{pybox}^{\mathbf{X}})_2]^{2+}$ complexes varying in *para*- \mathbf{X} pyridine substituent (Figure 2.1c, where **pybox**^H is 2,6-bis(oxazolin-2-yl)pyridine).²²

Deeth, Halcrow *et al.* went further, also showing that σ_p^+/σ_m correlated with: (i) the energy gap between the high spin (*HS*) and low spin (*LS*) states, $\Delta E_{\text{HL}}(\sigma_p^+(\mathbf{X}), R^2 = 0.89; \sigma_m(\mathbf{Y}) R^2 = 0.67)$, and with (ii) the $E(t_{2g})$ and $E(e_g)$ for *LS* $[\text{Fe}^{\text{II}}(\text{bpp}^{\mathbf{X},\mathbf{Y}})_2]^{2+}$ ($\sigma_p^+(\mathbf{X}): E(t_{2g}), R^2 = 0.94$ and $E(e_g), R^2 = 0.93; \sigma_m(\mathbf{Y}): E(t_{2g}), R^2 = 0.99$ and $E(e_g), R^2 = 0.98$) (details in Subsection 1.4.3).

They concluded, through close examination of the effects of *EDG*→*EWG* on $E(t_{2g})$ and $E(e_g)$, that **Fe**→**N** π -back bonding effects dominate for \mathbf{X} (*para*) substituents which strengthens the ligand field increasing $T_{1/2}$, whereas \mathbf{Y} (*meta*) substituents mostly affect the **Fe**←**N** σ -bonding, causing the opposite, decreasing $T_{1/2}$.^{23, 138}

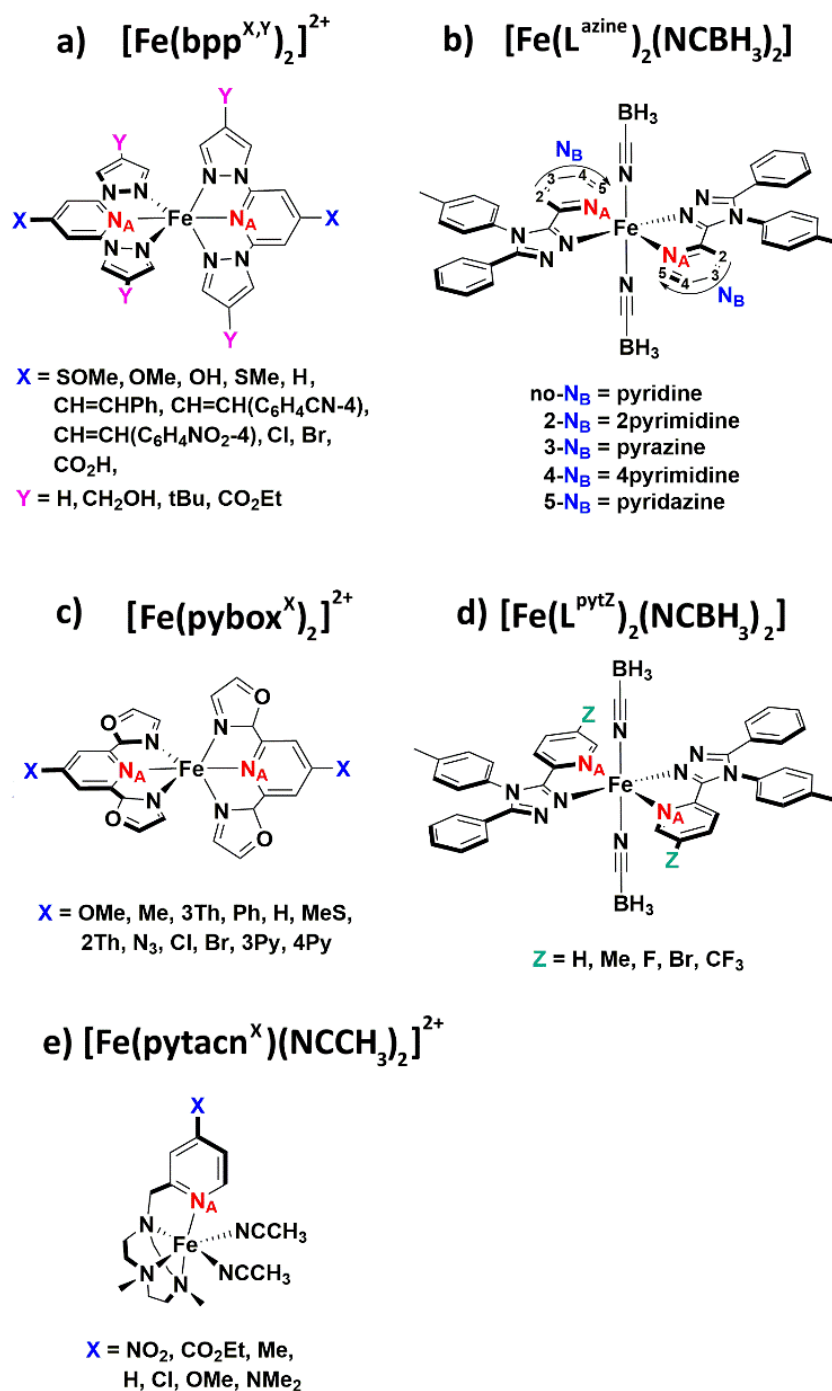


Figure 2.1. (a) Family of the fourteen^{23, 134, 136, 189-190} $[\text{Fe}^{\text{II}}(\text{bpp}^{\text{X,Y}})_2]^{2+}$ studied in acetone and (b) family of five $[\text{Fe}^{\text{II}}(\text{L}^{\text{azine}})_2(\text{NCBH}_3)_2]$,⁸³ both previously shown to exhibit a linear correlation of ligand **NA** chemical shift with complex solution $T_{1/2}$.⁸³ (c) Family of twelve literature^{22, 141} $[\text{Fe}^{\text{II}}(\text{pybox}^{\text{X}})_2]^{2+}$, (d) family of five $[\text{Fe}^{\text{II}}(\text{L}^{\text{pytZ}})_2(\text{NCBH}_3)_2]$ reported herein (the four with **Z** ≠ **H** are new) and (e) family of seven literature²⁴ $[\text{Fe}^{\text{II}}(\text{pytacn}^{\text{X}})(\text{NCCH}_3)_2]^{2+}$, used herein to further test the generality of the **NA** vs $T_{1/2}$ correlation method.

In 2017, some of us identified a promising correlation between the ¹⁵N NMR chemical shift, δN_A , of the coordinating nitrogen atom N_A of the free ligand^{83, 208} and the $T_{1/2}$ of the respective iron(II) complex: the higher δN_A (higher de-shielding of N_A nucleus²⁰⁹) the higher the $T_{1/2}$ (stronger ligand field; more recently we have also shown this corresponds to a more negative $\Delta E_{orb, \sigma+\pi}$ ⁹¹).

Using *DFT*, δN_A can be easily and quickly calculated for any ligand – and subsequently verified, if desired, by carrying out direct or indirect ¹⁵N NMR measurements. Hence δN_A is also a convenient measure of the electronic effect of any substituent, in contrast to the Hammett constant (σ^+) which is not available for all substituents. An observed δN_A vs $T_{1/2}$ correlation is potentially powerful, as for a proposed new member of the family, calculation of the δN_A (proposed new free ligand) would enable prediction of the $T_{1/2}$ (related iron(II) complex) in advance of synthesis.⁸³ Herein the generality of this simplistic, but potentially powerful, approach is tested. Specifically, we report the synthesis of four new bidentate ligands, 3-(2-(5-*Z*)pyridyl)-4-tolyl-5-phenyl-1,2,4-triazole (L^{pytZ}) ligands (*meta* substituents $Z = CF_3, Br, F, Me$), along with the solid state and solution *SCO* properties of the corresponding family of $[Fe(L^{pytZ})_2(NCBH_3)_2]$ complexes (Figure 2.1d) - which are analogues of the previously reported $[Fe(L^{azine})_2(NCBH_3)_2]$ family (Figure 1b)⁸³ of which the unsubstituted pyridine complex $[Fe(L^{pytH})_2(NCBH_3)_2]$ is common to both families. The resulting new family of five $[Fe(L^{pytZ})_2(NCBH_3)_2]$, as well as two literature families, twelve *SCO*-active $[Fe^{II}(\text{pybox}^X)_2]^{2+}$ (Figure 2.1c)^{22, 141} and seven $[Fe^{II}(\text{pytacn}^X)(CH_3CN)_2]^{2+}$ (Figure 2.1e)²⁴ are used to further test the generality of the δN_A vs $T_{1/2}$ correlation approach. Hence the N_A chemical shifts for the ligands used in these three families are calculated for the first time, using a refined protocol. The ability of the easily calculated N_A chemical shifts *versus* the Hammett parameters (not always available) to account for the observed trend in $T_{1/2}$ values of the complexes is also evaluated.

2.3. Results and Discussion

2.3.1. Synthesis of L^{pytZ} Ligands

The multi-step synthetic procedure used to access all four of the new monotopic bidentate L^{pytZ} ligands, varying in *meta* substituent **Z** on the pyridine ring (Figure 2.2), is built on that reported in 2004 by Klingele and Brooker.²¹⁰ Indeed, the key step of this route, cyclisation of a carbohydrazide and alkylated thioamide to form the 1,2,4-triazole ring of the **Rat** (R-substituted azine/azole-triazole) ligand, is proving to be very general, and offers a convenient modular approach, enabling the construction of large families of such ligands.^{64, 84, 204, 211}

The synthesis of the required alkylated thioamide was carried out as reported earlier (Figure 2.2, blue component, steps **III** and **IV**).⁸⁸ The synthesis of the required *meta*-substituted-pyridine carbohydrazides (Figure 2.2, red component) started with conversion of the appropriate **Z**-pyridine-2-carboxylic acid into the corresponding methyl ester (Figure 2.2, step **I**) by reaction with SOCl_2 in dry methanol.

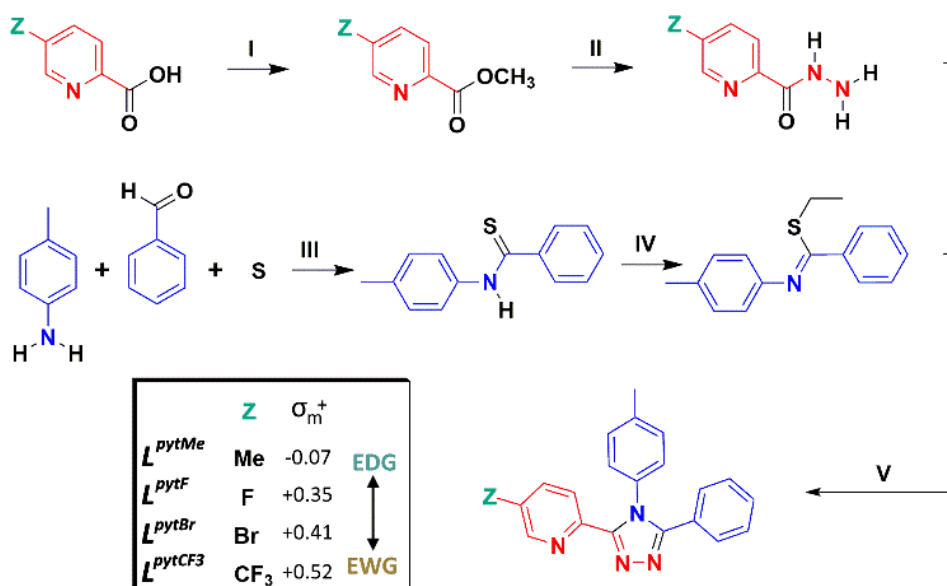


Figure 2.2. Multistep synthesis, based on the general literature method,²¹⁰ of the family of four new pyridyl-ring substituted L^{pytZ} ligands used herein; the unsubstituted ligand, L^{pytH} , was reported previously (and called L^{pytH}).⁸³

The $\text{Z} = \text{CF}_3$ ester had been previously reported, by a different method in a lower yield, by Warren *et al.* in 2019,²¹² whilst the $\text{Z} = \text{Br}$ ester was made in the same way, and in a similar yield, as was previously reported by Krauss *et al.* in 2013.²¹³ Next, the methyl esters were reacted with hydrazine hydrate to afford the desired Z -pyridine-2-carbohydrazides (Figure 2.2, step II). The $\text{Z} = \text{Br}$ and Me carbohydrazides were previously reported by Noel *et al.* in 2015 in a similar procedure with similar yields.²¹⁴

Finally, step V, by refluxing the alkylated thioamide with the appropriate carbohydrazide for 3 to 5 days at 145 °C, to give the four new L^{pytZ} ligands as analytically pure white powders in 11-61 % yields after recrystallisation. Details of the experimental procedures employed for reaction step I-V are reported in Subsection 2.5.1.

2.3.2. Synthesis of $[\text{Fe}^{\text{II}}(\text{L}^{\text{pytZ}})_2(\text{NCBH}_3)_2]$ Complexes

Solid $[\text{Fe}^{\text{II}}(\text{pyridine})_4(\text{NCBH}_3)_2]$ was added to a colourless solution of two equivalents of the appropriate L^{pytZ} in a halogenated solvent (CHCl_3 for $\text{Z} = \text{CF}_3$, Me ; DCM for $\text{Z} = \text{Br}$, F) under a nitrogen atmosphere, causing an immediate colour change ($\text{Z} = \text{CF}_3$ purple, Br dark red, F bright red, Me bright red). Subsequent vapour diffusion of diethyl ether into the reaction solution, in air, resulted in the formation of a polycrystalline precipitate in all cases ($\text{Z} = \text{CF}_3$ purple, Br dark red, F bright red, Me bright red).

The polycrystalline precipitate was filtered off, washed with diethyl ether, and air dried to give the hydrates, $[\text{Fe}^{\text{II}}(\text{L}^{\text{pytZ}})_2(\text{NCBH}_3)_2] \cdot n\text{H}_2\text{O}$ (where $n = 0.5$ or 1) in 45-59 % yield. The samples were shown to be analytically pure, with the water content confirmed by elemental analysis and thermogravimetric analysis. In all four cases, the expected major peak corresponding to $[\text{Fe}^{\text{II}}(\text{L}^{\text{pytZ}})_2(\text{NCBH}_3)]^+$ was observed in the HR-ESI-MS (Sections A2.3-A2.5-A2.7-A2.9).

2.3.3. Crystal Structures of [Fe^{II}(L^{pytZ})₂(NCBH₃)₂]

Single crystals of [Fe(L^{pytCF₃})₂(NCBH₃)₂] \cdot 2CHCl₃ (purple, Figures 2.1 and A2.58-A2.59), solvent-free [Fe(L^{pytBr})₂(NCBH₃)₂] (dark red, Figures A2.60-A2.61), [Fe(L^{pytF})₂(NCBH₃)₂] \cdot 2CH₃NO₂ (orange, Figures A.1 and A2.62-A2.63), and [Fe(L^{pytMe})₂(NCBH₃)₂] \cdot 2CHCl₃ (red, Figures A2.64-A2.65), suitable for SCXRD (Tables A2.1-A2.6), were obtained by diethyl vapor diffusion into a solution containing the re-dissolved polycrystalline material (CHCl₃ for **Z** = **CF₃**, **Me**; CH₃CN for **Z** = **Br**; CH₃NO₂ for **Z** = **F**).

All SCXRD data were collected at 100 K only, because loss of crystallinity was observed when data was collected at higher temperature. In all four of the isomorphous (all P-1) [Fe(L^{pytZ})₂(NCBH₃)₂] \cdot solvents structures, the iron(II) centre is on a centre of inversion, in an octahedral N₆-donor environment composed of two equatorially coordinated bidentate L^{pytZ} ligands (two triazole and two pyridine nitrogen donors), and completed by two *trans*-coordinated NCBH₃ anions (Tables A.1 and A2.1, *Subsection A2.1.10*). In all four cases, the average Fe–N bond length at 100 K is 1.96-1.98 Å (Table 2.1) as seen for related *LS* complexes of **Rat/Rdpt** ligands (1.93-2.02 Å).^{4, 139} The *LS* state is further confirmed for all four complexes by consideration of all of the other usual parameters (Table A.1, detailed description in *Subsection A2.1.10*),^{4, 139} albeit that for [Fe(L^{pytF})₂(NCBH₃)₂] \cdot 2CH₃NO₂, not all of these parameters fall in the usual range for *LS* iron(II) **Rat/Rdpt** complexes (Table A.1, detailed description in *Subsection A2.1.10*). In this **Z** = **F** case, this is probably due to a particularly rich array of non-classical hydrogen bonds (Figure A.3 and Table A2.5, detailed description in *Subsection A2.1.10*) involving the *meta*-F-substituents (C9-H9 \cdots F1R 3.42 Å, C12-H12 \cdots F1Q 3.31 Å, C17-H17 \cdots F1T 3.61 Å) and ordered CH₃NO₂ solvent (C23-H23B \cdots N2S 3.46 Å, C23-H23C \cdots N5S 3.60 Å, C4-H4 \cdots O1R 3.31 Å, Figure A.3, Figures A2.62- A2.63 and Table A2.5) which leads to closely packed lattice (smallest unit cell, by about 10%,

than those of the other two solvates) and higher than usual Σ and ring twist angles (Table A.1).

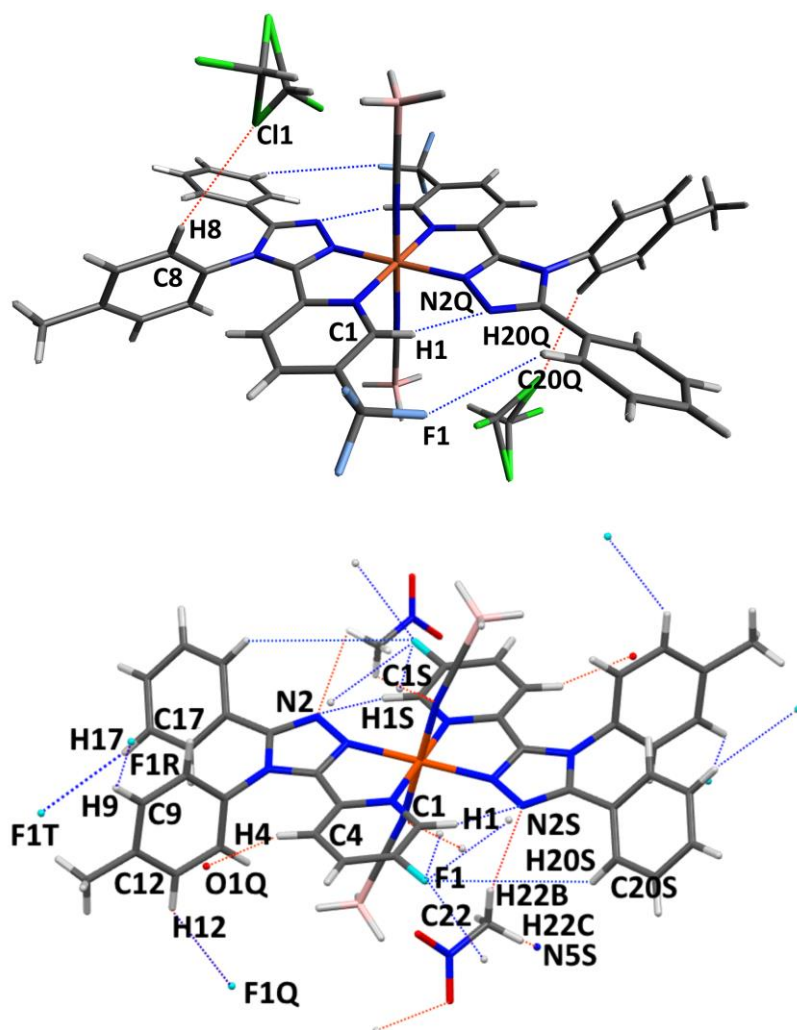


Figure 2.3. Crystal structures of: (top) $[\text{Fe}(\text{L}^{\text{pytCF}_3})_2(\text{NCBH}_3)_2] \cdot 2\text{CHCl}_3$, with H-bonds shown: (blue dotted lines) between the pair of coordinated $\text{L}^{\text{pytCF}_3}$ ligands (intramolecular H-bonds, $\text{C}20\text{Q}-\text{H}20\text{Q} \cdots \text{F}1$, $\text{C}1-\text{H}1 \cdots \text{N}2\text{Q}$ and $\text{C}20\text{S}-\text{H}20\text{S} \cdots \text{F}1$) and (red dotted lines) between the $\text{L}^{\text{pytCF}_3}$ ligands and solvent CHCl_3 (intermolecular H-bonds, $\text{C}8-\text{H}8 \cdots \text{Cl}1$), note both components of the CHCl_3 disorder are shown. (bottom) $[\text{Fe}(\text{L}^{\text{pytF}})_2(\text{NCBH}_3)_2] \cdot 2\text{CH}_3\text{NO}_2$, with H-bonds shown: (blue dotted lines) between the pair of coordinated L^{pytF} ligands (intramolecular H-bonds, $\text{C}1-\text{H}1 \cdots \text{N}2\text{S}$; intermolecular H-bonds via the F substituent $\text{C}9-\text{H}9 \cdots \text{F}1\text{R}$, $\text{C}12-\text{H}12 \cdots \text{F}1\text{Q}$, $\text{C}17-\text{H}17 \cdots \text{F}1\text{T}$) and (red dotted lines) between the L^{pytF} ligands and solvent CH_3NO_2 (intermolecular H-bonds, $\text{C}4-\text{H}4 \cdots \text{O}1\text{Q}$; $\text{C}22-\text{H}22\text{B} \cdots \text{N}2\text{S}$ and $\text{C}22-\text{H}22\text{C} \cdots \text{N}5\text{S}$). Colour code: Fe orange, N blue, O red, C black, Cl green, F light blue, B pink, H white. In both cases the iron(II) ion lies on an inversion centre. Q = $-x, -y, -z$. R = $1-x, -y, -z$. S = $-x, 1-y, -z$. T = $-x, -y, 1-z$.

In addition to the *intramolecular* H-bond (C1-H1...N2) observed for each $[\text{Fe}(\text{L}^{\text{pytZ}})_2(\text{NCBH}_3)_2] \cdot \text{solvent}$ complex, $[\text{Fe}(\text{L}^{\text{pytCF}_3})_2(\text{NCBH}_3)_2] \cdot 2\text{CHCl}_3$ shows an *additional intramolecular* H-bond occurring between the *meta*-CF₃ substituent and the facing ligand (C20Q-H20Q...F1 3.78 Å, Figures 2.3 and A2.59 and Table A2.3); interestingly this complex has by far the highest $T_{1/2}$ in solution (see below).

$[\text{Fe}(\text{L}^{\text{pytBr}})_2(\text{NCBH}_3)_2]$ is the only member of the family that crystallises without solvent. This led to the smallest unit cell (Table 2.1, Subsection A2.1.10) of the four compounds; this may be important with regard to understanding the observed much higher $T_{1/2}$ for this complex than the others, albeit all of them as hydrates, in the solid state (see below).

Table 2.1. Summary of selected structural parameters for the four $[\text{Fe}(\text{L}^{\text{pytZ}})_2(\text{NCBH}_3)_2] \cdot \text{solvents}$ complexes at 100 K. For full details see Tables A2.1 and A2.2.

Z	CF ₃	Br	F	Me	LS Fe ^{II} ref ^{4, 139}
Cryst. solvent	2CHCl ₃	-	2CH ₃ NO ₂	2CHCl ₃	
av. Fe-N (Å)	1.96 Å	1.96 Å	1.98 Å	1.97 Å	1.93-2.02 Å
distortion angle (Σ°)	44.9°	44.9°	70.8°	43.0°	42.5°-65.7°
Fe-N-C (°)	178.3°	174.7°	166.4°	178.6°	162°-178°
pyridyl twist (°)	3.1°	0.2°	6.2°	0.9°	≈0°
phenyl twist (°)	24.2°	3.6°	41.5°	21.6°	0°-25°
tolyl twist (°)	78.7°	76.0°	75.2°	73.0°	60°-90°

2.3.4. Solid State Spin Crossover of [Fe^{II}(L^{pytZ})₂(NCBH₃)₂] \cdot nH₂O

The temperature dependence of the magnetic susceptibility (χ_{MT}) of the air-dried crystalline samples of the four [Fe^{II}(L^{pytZ})₂(NCBH₃)₂] \cdot nH₂O complexes, all hydrates, was measured in settle mode from 50-400-50 K (Figure 2.4 and Figures A2.66– A2.74). Three successive cycles of 50–400–50 K (*Subsection A2.1.11*), confirmed a reproducible response for all four complexes (Figures A2.66, A2.70, A2.71 and A2.73).

All four complexes are SCO active in the solid state: **Z** = **CF₃** ($T_{1/2\downarrow}$ = 203 K, $T_{1/2\uparrow}$ = 213 K; $\Delta T_{1/2}$ = 10 K) < **F** ($T_{1/2}$ = 290 K) < **Me** ($T_{1/2}$ = 300 K) while for **Z** = **Br** the beginning of a *LS* \rightarrow *HS* transition is observed above RT, and remains far from complete at the upper limit of the instrument (400 K). For the three complexes with $T_{1/2}$ values under 400 K, these values were determined by locating the temperature at which the maximum change occurs in the first derivative of the χ_{MT} versus T plot (Figures A2.67, A2.72, A2.74).^{119, 215} [Fe^{II}(L^{pytCF₃})₂(NCBH₃)₂] \cdot 0.5H₂O (Figure 2.4, purple) undergoes a full and complete SCO, with χ_{MT} rising from 0.40 cm³ \cdot K \cdot mol⁻¹ at 50 K to 3.99 at 400 K (*HS* fraction, γ_{HS} , rises from 0.10 to 0.99), in an *abrupt* transition with a small thermal *hysteresis* ($T_{1/2\downarrow}$ = 203 K, $T_{1/2\uparrow}$ = 213 K; $\Delta T_{1/2}$ = 10 K, Figure A2.68-A2.69). As thermal *hysteresis* is a kinetic effect, the width of the *hysteresis loop* was probed, as reported by some of us in 2014,⁹⁵⁻⁹⁶ by monitoring a 150-250-150 K cycle as a function of scan rate (20, 10, 5, 2, 0.2 K/min; Figure A2.68). This reveals the expected decrease in thermal *hysteresis loop* width ($\Delta T_{1/2}$) with decreasing scan rate from 20 to 0.2 K min⁻¹, from 23 to 10 K.

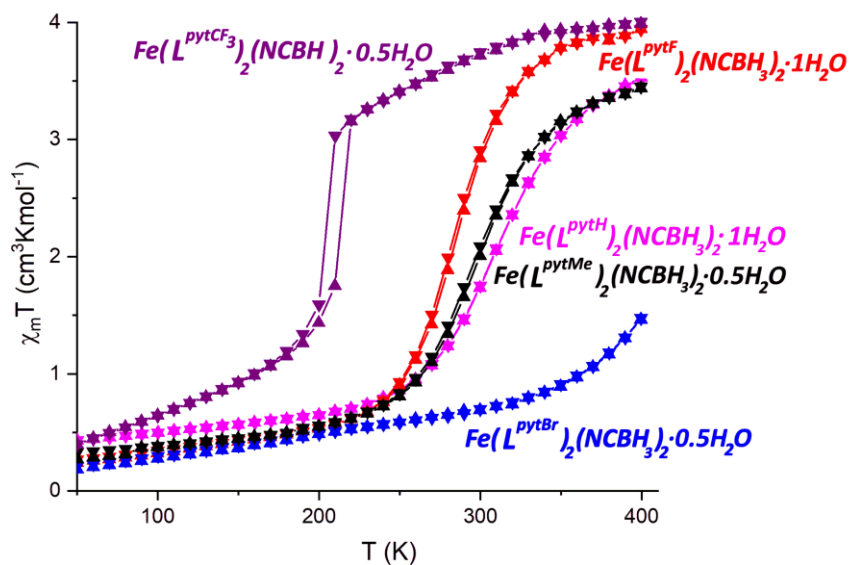


Figure 2.4. Solid state measurements of magnetic susceptibility ($\chi_{\text{M}}T$) versus temperature (T) for all four new $[\text{Fe}(\text{L}^{\text{pytZ}})_2(\text{NCBH}_3)_2] \cdot n\text{H}_2\text{O}$ complexes and the literature data for the $[\text{Fe}(\text{L}^{\text{pytH}})_2(\text{NCBH}_3)_2]$ complex,¹⁰⁵ over one cycle, 50–400–50 (cooling, down triangles; heating, up triangles), in settle mode in 10 K steps (see experimental section for more details). Lines simply join the dots to aid the eye.

Extrapolation of that trend to the imaginary case of 0 K min^{-1} , results in a non-zero predicted $\Delta T_{1/2}$, of 10 K ($T_{1/2\downarrow} = 203 \text{ K}$, $T_{1/2\uparrow} = 213 \text{ K}$, Figure A2.69), consistent with a reasonably long-life metastable state; of course, if one truly could scan infinitely slowly, then the loop is expected to close.

Both $[\text{Fe}^{\text{II}}(\text{L}^{\text{pytF}})_2(\text{NCBH}_3)_2] \cdot 1\text{H}_2\text{O}$ (Figure 2.4, red) and $[\text{Fe}^{\text{II}}(\text{L}^{\text{pytMe}})_2(\text{NCBH}_3)_2] \cdot 0.5\text{H}_2\text{O}$ (Figure 2.4, black) also undergo almost complete SCO. In the case of $[\text{Fe}^{\text{II}}(\text{L}^{\text{pytF}})_2(\text{NCBH}_3)_2] \cdot \text{H}_2\text{O}$ there is a *gradual* increase in $\chi_{\text{M}}T$ from $0.21 \text{ cm}^3 \cdot \text{K} \cdot \text{mol}^{-1}$ at 50 K to 3.93 at 400 K (γ_{HS} 0.05 to 0.98) with $T_{1/2} = 290 \text{ K}$ (Figure A2.71 - A2.72).

For $[\text{Fe}^{\text{II}}(\text{L}^{\text{pytMe}})_2(\text{NCBH}_3)_2] \cdot 0.5\text{H}_2\text{O}$ there is a *gradual* increase in $\chi_{\text{M}}T$ from $0.27 \text{ cm}^3 \cdot \text{K} \cdot \text{mol}^{-1}$ at 50 K to 3.46 at 400 K (γ_{HS} 0.68 to 0.87), with $T_{1/2} = 300 \text{ K}$ (Figure A2.73- A2.74).

Finally, in the case of $[\text{Fe}^{\text{II}}(\text{L}^{\text{pytBr}})_2(\text{NCBH}_3)_2] \cdot 0.5\text{H}_2\text{O}$, even at 300 K $\chi_{\text{M}}T$ is only $0.14 \text{ cm}^3 \cdot \text{K} \cdot \text{mol}^{-1}$ at 50 K, consistent with a fully LS state ($\gamma_{\text{HS}} = 0.04$), but the start of an SCO transition occurs at higher temperatures, with

γ_{HS} rising to 0.35 at 400 K (the limit of our instrument) (Figure 2.4, blue). If we assume that the two solvatomorphs of $[\text{Fe}^{\text{II}}(\text{L}^{\text{pytBr}})_2(\text{NCBH}_3)_2]$ crystallise with similar packing, as despite coming from CHCl_3 and CH_3CN neither of these solvents is included, then the resulting closely packed structure (see structure descriptions above) may prevent the increase in volume required for $LS \rightarrow HS$ until high temperatures are applied.

At room temperature (300 K) the χ_{MT} values ($\text{cm}^3 \cdot \text{K} \cdot \text{mol}^{-1}$) for the four hydrates differ substantially (listed by ligand):

$$\text{L}^{\text{pytCF}_3} (3.75) > \text{L}^{\text{pytF}} (2.70) > \text{L}^{\text{pytMe}} (1.92) > \text{L}^{\text{pytBr}} (0.65)$$

These can be compared with the very different order of σ_{m^+} :

$$\text{L}^{\text{pytCF}_3} (+0.52) > \text{L}^{\text{pytBr}} (+0.41) > \text{L}^{\text{pytF}} (+0.35) > \text{L}^{\text{pytMe}} (-0.07)$$

In summary, it is clear that packing effects are, as is often the case, confounding the electronic effects of the substituents on the SCO behaviour in the solid state. Hence the SCO behaviour of these complexes is also studied in solution, where packing effects are absent.

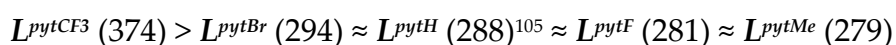
2.3.5. Solution Spin Crossover of $[\text{Fe}^{\text{II}}(\text{L}^{\text{pytZ}})_2(\text{NCBH}_3)_2]$

Variable temperature solution magnetic susceptibility data were obtained by the Evans ¹H NMR method on CDCl_3 solutions prepared, following a previous report,⁸³ by adding six equivalents of L^{pytZ} to a precisely known mass of $[\text{Fe}^{\text{II}}(\text{pyridine})_4(\text{NCBH}_3)_2]$.

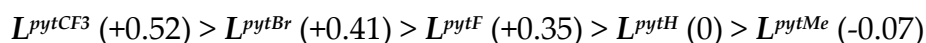
All four complexes show evidence of being SCO active within the monitored temperature range, 243 to 313 K (Table A2.8, Figure 2.5 and Figures A2.79-A2.82). The studied temperature range was limited by the freezing and boiling points of chloroform. Each data set was modelled as a

gradual and complete SCO using the regular solution model, with the maximum χ_{MT} value, $\chi_{MT}(\max)$, set to 4 cm³ K mol⁻¹.^{119, 216-217} Confidence interval associated with employment of regular SCO fitting is reported in *Subsubsection A2.1.12.2* (Figures A2.79-A2.82 and Table A2.10-A2.13). Intrinsic errors due to Evans method measurements (5-10%), and to model fitting, associated errors are reported in Table 2.2 (third column from left) and discussed in detail in *Appendix (Subsubsection A2.1.12.2; Figures A2.79-A2.82 and Table A2.10-A2.13)*.

The values of enthalpy ($\Delta H = 10-30$ kJ·mol⁻¹, Table A2.8) and entropy ($\Delta S = 39-95$ J mol⁻¹K⁻¹, Table A2.8) obtained from fitting the data for the four complexes fall within the literature ranges for solution-phase studies of SCO-active iron(II) complexes ($\Delta H = 4-41$ kJ mol⁻¹ and $\Delta S = 22-146$ J mol⁻¹ K⁻¹).^{23, 92-93} The iron(II) complexes in order of increasing $T_{1/2}$ value in K (at which the *HS* molar fraction, γ_{HS} , is 0.5; Tables 2.2 and A2.8)^{93, 116, 218} are (by ligand):



Compared with the similar order of the Hammett parameter σ_m^+ :



There is a modest correlation (Figure A2.87) between $T_{1/2}$ and σ_m^+ ($R^2 = 0.65$) or σ_m ($R^2 = 0.56$) for this new *meta-Z* substituted family, which is in agreement with results obtained by Deeth, Halcrow *et al.* for the *meta-Y* substituted **bpp**^Y family (σ_m , $R^2 = 0.61$).²³

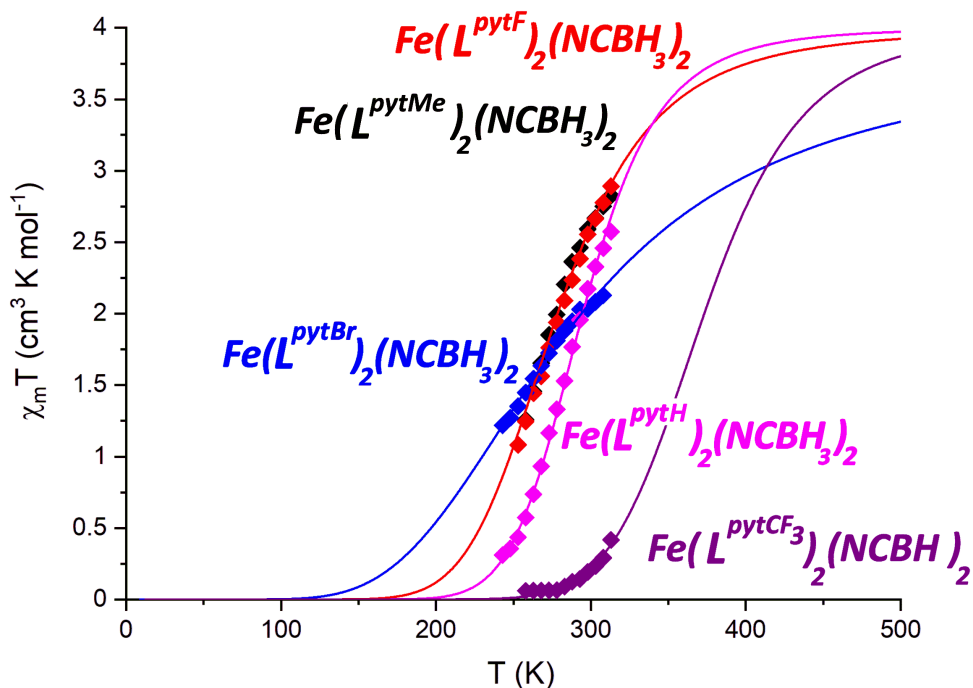


Figure 2.5. Solution phase measurements of magnetic susceptibility ($\chi_{\text{M}}T$) versus temperature (T) for all four new $[\text{Fe}(\text{L}^{\text{pytZ}})_2(\text{NCBH}_3)_2]$ complexes, and the literature data for the $[\text{Fe}(\text{L}^{\text{pytH}})_2(\text{NCBH}_3)_2]$ complex,¹⁰⁵ in CDCl_3 solution, from 243 to 313 K, in intervals of 5 K, by the Evans NMR method. Data (points) are fitted (curves) to the regular solution model^{119, 216-217} (see text and Appendix for details).

In detail: $[\text{Fe}(\text{L}^{\text{pytCF}_3})_2(\text{NCBH}_3)_2]$ (Figure 2.5, purple) has by far the highest $T_{1/2}$ value (374 K), as well as the highest *meta*- Z (CF_3) Hammett parameter; however, the error on the calculated $T_{1/2}$ using the regular SCO model fitting is particularly large (23.3 K, Figure A2.79 and Table A2.10) as it involves huge extrapolation because a very little of the SCO occurred within the measured T range.^{119, 217}

Next in order of decreasing $T_{1/2}$ is, as expected given that it has the *meta*-substituent with the next highest Hammett parameter, is the complex with $Z = \text{Br}$ (Figure 2.5, blue), with $T_{1/2} = 294$ K (error in fitting ± 0.2 K; as the midpoint of the SCO occurs in the T range studied). For these two cases, the biggest difference between solid state and solution phase SCO is observed: for $Z = \text{CF}_3$, the $T_{1/2}$ in the solid state is 208 K (with *hysteresis*, $\Delta T_{1/2} = 10$ K) vs. 374 K in solution; for $Z = \text{Br}$, in the solid state it remains LS up

to 400 K vs. $T_{1/2} = 294$ K in solution. For $Z = \text{Br}$, the size of the crystalline cell in solid state (assuming similar packing for the two solvatomorphs) is very likely responsible for inhibiting the SCO transition. Crystallographic data show evidences of a very small cell, with limited amount of *free* space; this condition would make the cell unable of hosting the largest size of the HS $[\text{Fe}(\text{L}^{\text{pytBr}})_2(\text{NCBH}_3)_2]$, prohibiting the SCO transition. This condition is not existing in solution phase; then, SCO transition can occur.

Table 2.2. The $T_{1/2}$ values observed for the family of five $[\text{Fe}(\text{L}^{\text{pytZ}})_2(\text{NCBH}_3)_2]$ complexes in the solid state and in CDCl_3 solution (detail in Sections A2.11-A2.12), along with $\sigma_{\text{m}^+}(\text{Z})$, and the N_A chemical shift values for the four new L^{pytZ} ligands, plus the literature unsubstituted analogue L^{pytH} ,⁸³ obtained by calculation using the improved protocol described herein and by experimental measurement (*d* = direct method, *i* = indirect method), along with the % error (calculated vs measured).

	$T_{1/2}$ (K) solid	$T_{1/2}$ (K) CDCl_3	$\sigma_{\text{m}^+}(\text{Z})$	$\delta(\text{N}_\text{A})$ (ppm) Meas. (Calc.)	$\delta(\text{N}_\text{A})$ Err. %
L^{pytMe}	300	279	-0.07	312(d) (310)	0.6%
L^{pytH}	309 ¹⁰⁵	288 ¹⁰⁵	0	311(d/i) ⁸³ (308)	1.0%
L^{pytF}	290	281	+0.35	320(i) (315)	1.6%
L^{pytBr}	LS	294	+0.41	317(d/i) (312)	1.8%
$\text{L}^{\text{pytCF}_3}$	203↓ 213↑	374	+0.52	314(d) (307)	2.1%

The reference complex characterised earlier by some of us, with $Z = \text{H}$, is next, with $T_{1/2} = 288$ K,¹⁰⁵ despite having a Hammett parameter that lies between those of $Z = \text{F}$ and Me . The last two complexes, with $Z = \text{F}$ ($T_{1/2} = 281$, Figure 2.5, red) and $Z = \text{Me}$ ($T_{1/2} = 279$ K, Figure 2.5, black) present indistinguishable solution SCO behaviour. They were also similar to one another in the solid state ($T_{1/2} = 290$ and 300 K); albeit interestingly the $T_{1/2}$ values are lower in the solution phase than in the solid state.

2.3.6. Experimental and Calculated ¹⁵N_A Chemical Shift of Ligands

In a previous 2017 study,⁷⁷ there was a good match (average error 4.0%; max. error 6.6%, Table A2.10) between the theoretical (*DFT*) and experimental values (measured directly or indirectly) of the ¹⁵N NMR chemical shift, δN_A , of the coordinating N of the ligand, N_A .⁸³ Nevertheless an improved *DFT* protocol, that maintains low computational costs, is described herein. It is built on benchmark studies reported by Neese *et al.*,²¹⁹⁻²²⁰ so employs a *meta*-GGA functional (*TPSS*)²²¹ and a special basis set for NMR chemical shifts optimised by Jensen (*pcSseg-2*).²²²

Application of the new protocol to the five ligands in the *L^{azine}* family⁸³ confirmed the expected improvement, with the average error in δN_A (*obs.* vs *calc.*) dropping from 4.0 to 1.4%, and the max. error from 6.6% to 3.9% (Table A2.14). Therefore it was used to update δN_A for the fourteen of the over twenty-five previously studied⁸³ **bpp**^{x,y} ligands for which the [Fe(**bpp**^{x,y})₂]²⁺ SCO transition was studied in acetone solvent (Table A2.18). The changes in δN_A are minor, so unsurprisingly the reported ¹⁵N_A vs $T_{1/2}$ correlations for these two families continue to hold (see below, Figures 2.6 and 2.7, $R^2 = 0.98$ and 0.79 respectively).⁸³

Next the new computational protocol was employed to calculate δN_A for the free ligands in the three new families (Figure 2.1) used as further tests of the generality of the δN_A vs $T_{1/2}$ correlation approach: (a) our new *meta*-substituted *L^{pytz}* bidentate ligands (experimental ¹⁵N NMR data are also shown in Table 2.2), (b) the twelve literature **pybox**^x tridentate ligands varying in *para*-substituents (Table A2.16) and (c) the seven literature **pytacn**^x tetradentate ligands varying in *para*-substituents (Table A2.17).

2.3.7. ¹⁵N NMR vs $T_{1/2}$ Correlations in Five Different Fe^{II} SCO Families

The δN_A vs $T_{1/2}$ plot for the five complexes with bidentate L^{pytZ} ligands varying *meta*-substituted pyridine, $[\text{Fe}(L^{pytZ})_2(\text{NCBH}_3)_2]$ (Figure 2.1d), is shown Figure 2.6. There are two main observations.

Firstly, the calculated δN_A values span a very small range, 307-315 ppm ($\Delta\delta = 8$ ppm), due to the (expected) low impact of changes in a *meta* substituent. *Meta* substituents provide a much narrower range of electronic effects (Hammett¹²⁵ σ_m^+ -0.07 to +0.67) compared with *para* substituents (Hammett¹²⁵ σ_p^+ -1.70 to +0.79) (details in *Subsection 1.4.1*).

Secondly, δN_A is not correlated with $T_{1/2}$ (green line, $R^2 = 0.37$) for these *meta-Z* substituted complexes. Interestingly, the attempted correlation line has negative slope, similar to that seen by Halcrow in the $T_{1/2}$ with σ_m^+ correlation plot for the *meta-Y* substituted $[\text{Fe}^{\text{II}}(\mathbf{bpp}^Y)_2]^{2+}$ complexes,²³ but opposite to both of the previously reported correlations,⁸³ despite the similar structures of the $[\text{Fe}(L)_2(\text{NCBH}_3)_2]$ complexes of L^{pytZ} and L^{azine} . But it must be pointed out that the correlation is very poor, so almost any line could have been drawn through these data points. The shared member, L^{pytH} , of these two families is not a diazine, which should make it more similar to the new L^{pytZ} family than to the previously reported L^{azine} family, but it fits into both correlation lines reasonably well.

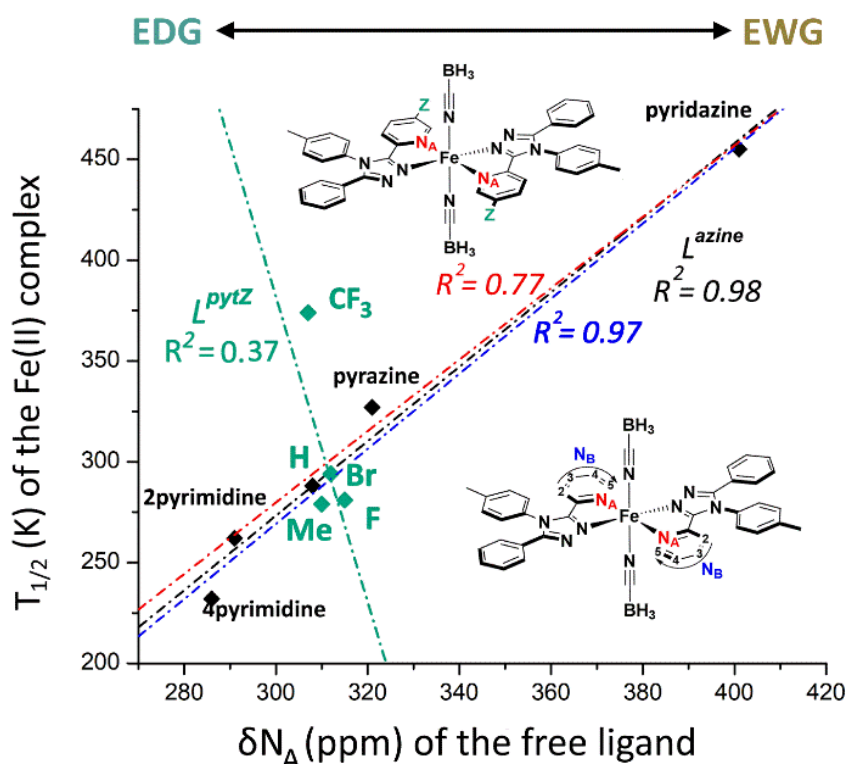


Figure 2.6. Correlations between the calculated ^{15}N chemical shift δN_A of the free ligand L and the switching temperature $T_{1/2}$ of the respective $[\text{Fe}(\text{L})_2(\text{NCBH}_3)_2]$ complex. Poor correlation for the five L^{pytZ} ($R^2 = 0.37$, green line, $\delta\text{N}_A = -7.56 \cdot \sigma^+ + 2649.28$); extremely good correlations for the five L^{azine} ($R^2 = 0.98$, black line, $\delta\text{N}_A = 1.84 \cdot \sigma^+ - 280.61$); good correlations for the eight $[\text{Fe}(\text{L})_2(\text{NCBH}_3)_2]$ complexes ($L = L^{\text{azine}}$ and L^{pytZ} , $R^2 = 0.77$, red line, $\delta\text{N}_A = 1.86 \cdot \sigma^+ - 289.13$); extremely good correlations for the seven $[\text{Fe}(\text{L})_2(\text{NCBH}_3)_2]$ complexes (except L^{pytCF_3}) ($R^2 = 0.97$, blue line, $\delta\text{N}_A = 1.77 \cdot \sigma^+ - 251.41$).

Indeed, combining the two subfamilies into one big family of nine compounds ($L = L^{\text{azine}} + L^{\text{pytZ}}$) results are in a good correlation (red line, $R^2 = 0.77$), whereas if $[\text{Fe}(L^{\text{pytCF}_3})_2(\text{NCBH}_3)_2]$ is excluded the remaining eight compounds give an excellent correlation (blue line, $R^2 = 0.97$) – but this is in large part because the four remaining L^{pytZ} systems are not discriminating as they are clustered around L^{pytH} . It is not easy to identify a good reason to exclude the $[\text{Fe}(L^{\text{pytCF}_3})_2(\text{NCBH}_3)_2]$ complex, but perhaps it fails to correlate with the rest of the family due to the presence of an additional intramolecular H-bond between the two opposing ligands, involving the CF_3 substituent (Figure 2.3).

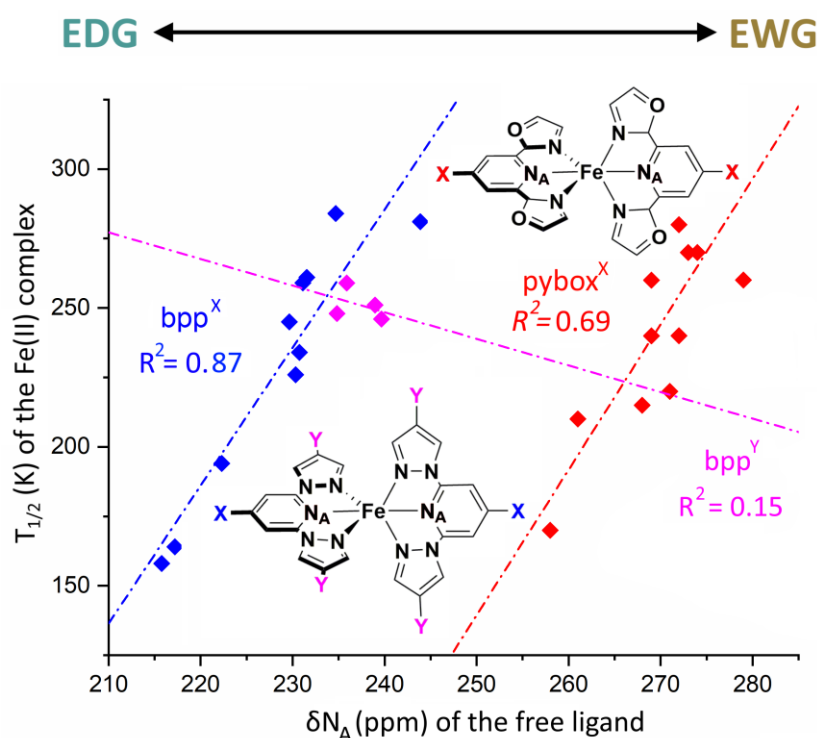


Figure 2.7. Correlations found between the calculated ^{15}N chemical shift δN_A of the twelve tridentate pybox^X ligands and the switching temperature $T_{1/2}$ of the respective $[\text{Fe}(\text{pybox}^X)_2]^{2+}$ complexes ($T_{1/2} = 5.23 \cdot \delta N_A - 1169.24$) versus the fourteen bpp^X ligands (split into eleven X-substituted) and the switching temperature $T_{1/2}$ of the respective $[\text{Fe}(\text{bpp}^X)_2]^{2+}$ ($T_{1/2} = 5.23 \cdot \delta N_A - 1169.24$) complexes. Finally, the four bpp^Y ligands (split into four Y-substituted) and the switching temperature $T_{1/2}$ of the respective $[\text{Fe}(\text{bpp}^Y)_2]^{2+}$ ($T_{1/2} = -0.96 \cdot \delta N_A - 478.37$) complexes.

Next the twelve members of the $[\text{Fe}^{\text{II}}(\text{pybox}^X)_2]^{2+}$ family, reported in 2017 then studied in depth in 2018 by Kimura and Ishida,^{22, 141} which contain tridentate ligands with a range of pyridine *para*-substituents **X**, and $T_{1/2}$ values in acetone ranging from 170 K (**X** = **OMe**) to 310 K (**X** = **4-pyridine**), have been examined. A modest δN_A versus $T_{1/2}$ correlation ($R^2 = 0.69$) is observed (Figure 2.7, red line).

This family of twelve $[\text{Fe}^{\text{II}}(\text{pybox}^X)_2]^{2+}$ (red line in Figure 2.7) is closely related to the family of eleven $[\text{Fe}^{\text{II}}(\text{bpp}^X)_2]^{2+}$ discussed above (blue line). Higher values of δN_A are consistently observed for the pybox^X ligands (258-279 ppm, $\Delta\delta = 21$ ppm) than for the bpp^X ligands (216-244 ppm, $\Delta\delta = 28$ ppm), due to pybox^X having oxazole rings flanking the

pyridine ring on both sides, rather than the flanking pyrazole rings found in **bpp**^x. The two δN_A versus $T_{1/2}$ correlation lines have similar slopes (5.08 for **bpp**^x vs 5.23 for **pybox**^x), confirming the comment in 2018 by Kimura and Ishida that the magnitude of the influence of **X** on the electron density, $\rho(\text{N}_A)$ - which in our studies (herein and in 2017⁸³) is reflected in δN_A - on the observed $T_{1/2}$ is similar for both of these families.¹⁴¹

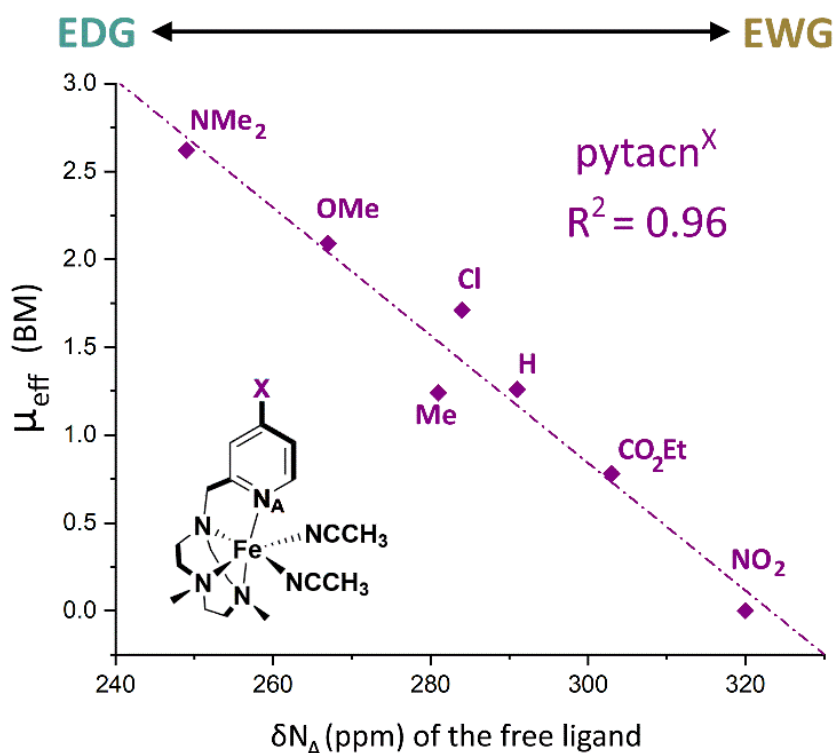


Figure 2.8. Correlations found between the calculated ^{15}N chemical shift δN_A of the free ligand and the effective magnetic moment (μ_{eff}) measured at 298 K in acetonitrile of the respective Fe(II) complex for the **pytacn**^x family ($\mu_{\text{eff}} = -0.04 \cdot \delta\text{N}_A - 11.74$).

Next the literature family of seven $[\text{Fe}(\text{pytacn}^x)(\text{NCCH}_3)_2]^{2+}$ complexes of the *tetradentate* **pytacn**^x ligands, reported by Costas *et al.*²⁴ is examined. The effective magnetic moment (μ_{eff}) at 298 K was determined for these complexes in acetonitrile, and ranged from 2.62 (BM) for **X** = **NMe**₂ to 0.00 BM for **X** = **NO**₂. These values of μ_{eff} (298 K) only provide a snapshot of the *SCO* behaviour but as this occurs around RT it is a valuable one, as μ_{eff} (298 K) is strongly correlated ($R^2 = 0.96$) with

δN_A (Figure 2.8). Note the negative slope in this case is simply due to increasing $T_{1/2}$ corresponding to decreasing μ_{eff} (298 K).

In summary, the same trend is observed for all of the *para*-**X** substituted families, $[\text{Fe}(\text{bpp}^{\text{X}})_2]^{2+}$, $[\text{Fe}(\text{pybox}^{\text{X}})_2]^{2+}$ and $[\text{Fe}(\text{pytacn}^{\text{X}})(\text{NCCH}_3)_2]^{2+}$.²²⁻²³

2.3.8. Hammett vs ^{15}N NMR Correlations for the Five Families

As introduced in *Subsection 1.4.1* and discussed above, the Hammett parameter is the most common parameter used to describe the electronic effects that substituents have on the electron density of aromatic rings. Given that both σ^+ and δN_A have shown correlations with $T_{1/2}$, it seemed reasonable to expect that σ^+ and δN_A would also be correlated. A δN_A vs. σ^+ plot for each of the five families of complexes with **X**, **Y** or **Z**-substituents ($\sigma_{\text{p/m}^+}$ in Figures 2.9 and $\sigma_{\text{p/m}}$ in Figure A2.86) is revealing.

For the three families of complexes of *para*-**X** substituted ligands (σ_{p^+}), all have positive and good-to-excellent correlations, with R^2 values as follows: **pybox**^X = 0.76, **bpp**^X = 0.87, **pytacn**^X = 0.94. In contrast, for the two families of complexes of *meta*-**Y** or **Z** substituted ligands (σ_{m^+}), they both have negative and weak correlations, with R^2 values as follows: L^{pytZ} = 0.02 and **bpp**^Y = 0.25. These findings are consistent with conclusions of Deeth and Halcrow, as summarised in the introduction.²³

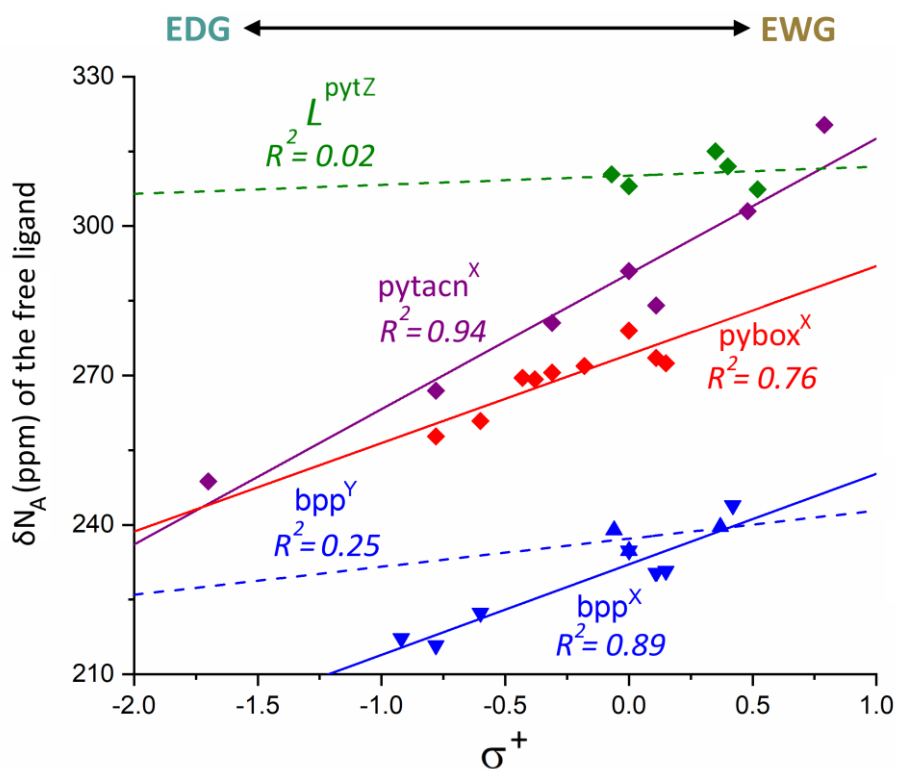


Figure 2.9. Correlation between the calculated ^{15}N chemical shift δN_A of the free ligand for each of the families reported in this study against the relative value of the Hammett parameter σ^+ of the substituent on the pyridine ring (note: a substituent with a positive Hammett parameter is EWG, whilst one with a negative value is EDG; H is by definition 0). Solid lines for ligands with para substituents (σ_{p}^+ is used in this case); dashed lines for ligands with meta substituents (σ_{m}^+ is used in this case). Good correlation found for a family of eleven bpp^{X} ligands (blue, up-faced triangles; $\delta\text{N}_\text{A} = 26.73 \cdot \sigma^+ - 226.18$); seven pytacn^{X} ligands (purple, diamonds; $\delta\text{N}_\text{A} = 27.16 \cdot \sigma^+ - 290.04$) and twelve pybox^{X} (red, diamonds; $\delta\text{N}_\text{A} = 17.77 \cdot \sigma^+ - 274.20$); poor correlation found for four bpp^{Y} ligands (blue, down-faced triangles; $\delta\text{N}_\text{A} = 5.63 \cdot \sigma^+ - 237.24$) and five L^{pytZ} (green, diamonds; $\delta\text{N}_\text{A} = 18.17 \cdot \sigma^+ - 232.08$).

2.4. Conclusions

The synthesis of four new ligands and four $[\text{Fe}^{\text{II}}(\text{L}^{\text{pytZ}})_2(\text{NCBH}_3)_2]$ complexes is reported. Solid state and solution phase (in CDCl_3) SCO activity is investigated under the perspective of employing *meta* substituents as electronic tuners of the ligand field strength. Unfortunately, no correlation was found between the Hammett parameter σ_{m^+} with the measured SCO $T_{1/2}$ both in solid and solution phase. This lack of predictability, and the much narrower range of electronic effects for *meta* substituents (Hammett¹²⁵ σ_{m^+} -0.07 to +0.67) compared with *para* substituents (Hammett¹²⁵ σ_{p^+} -1.70 to +0.79), make *meta* substituents far less valuable tools for $T_{1/2}$ tuning.

The approach previously developed by Brooker *et al.* in predicting the SCO $T_{1/2}$ in iron(II) complex from the δN_A chemical shift in the free ligand is: (a) applied to three new families, bringing the total to five; (b) revealed very promising results for *para* substituted ligands (**bpp**^x, $R^2 = 0.87$; **pybox**^x, $R^2 = 0.69$; **pytacn**^x, $R^2 = 0.96$) but not for *meta* substituted ligands (**L**^{pytZ}, $R^2 = 0.37$; **bpp**^y, $R^2 = 0.15$); (c) proved to be just as effective as the Hammett constant σ_{p^+} in describing substituent effects, with the significant advantage that it is easily accessible when Hammett values are missing. It also enables studies of CH/N or N/O ligand substitutions and can be experimentally verified.

2.5. Experimental Section

For general experimental and full instrument details please see Appendix A1. The MS and NMR (Section A2.2-A2.9), the structure determination (Section A2.10), magnetic measurements (Section A2.11-A2.12) and UV-vis spectra (Section A2.13) are provided in Appendix (Appendix A2).

2.5.1. Organic Synthesis

The four pyridine carboxylic acids (AK Scientific) and 80% aqueous hydrazine hydrate (Sigma Aldrich) were used as supplied. The required N-(4-methylphenyl)benzenethioamide⁶³ and ethyl N-(4-methylphenyl)benzenethiocarboximidothioate⁶³ were synthesised as previously reported, as was $[\text{Fe}^{\text{II}}(\text{pyridine})_4(\text{NCBH}_3)_2]$.⁸⁸ Ethanol and 1-butanol were reagent grade. Dry methanol was prepared by distilling absolute methanol with Mg/I₂.

5-Trifluoromethane-pyridine-2-methylcarboxylate. To a green suspension of 5-trifluoromethane-picolinic acid (1.70 g, 8.94 mmol) in dry methanol (30 mL), SOCl₂ (2.50 mL, 30.10 mmol) was added dropwise. The resulting green solution was stirred at RT for 24 h in air before being taken to dryness under reduced pressure. The green solid residue was taken up in, and neutralised with, sat. NaHCO₃ aqueous solution (10 mL), then extracted with dichloromethane (3 x 25 mL). The DCM phase was taken to dryness under reduced pressure, giving the ester as green powder that was used without further purification. (1.78 g, 8.68 mmol, 97%). C₈H₆NOF₃ (M=205.05 g mol⁻¹), calc. C 46.84% N 6.38% H 2.95%; found C 47.05% N 6.60% H 2.86%. ¹H NMR (400 MHz, CDCl₃) δ(ppm) = 9.00 (t, 1H); 8.26 (m, 1H); 8.10 (m, 1H); 4.00 (s, 3H). Synthesis of this compound was previously reported, by a different method in a lower yield, by Warren *et al.* in 2019.²¹²

5-Bromo-pyridine-2-methylcarboxylate. To a colourless suspension of 5-bromo-picolinic acid (0.50 g, 2.48 mmol) in dry methanol (10 mL), SOCl_2 (0.40 mL, 4.81 mmol) was added dropwise. The resulting colourless solution was stirred at RT for 24 h in air before being taken to dryness under reduced pressure. The white solid residue was taken up in, and neutralised with, sat. NaHCO_3 aqueous solution (5 mL), then extracted with dichloromethane (3 x 10 mL). The combined DCM phase was taken to dryness under reduced pressure, giving the ester as a white powder that was used without further purification (0.46 g, 2.21 mmol, 89%). $\text{C}_7\text{H}_6\text{NOBr}$ ($M=215.94 \text{ g mol}^{-1}$): calc. C 38.92% N 6.48% H 2.80%; found C 39.25% N 6.26% H 2.65%. ^1H NMR (400 MHz, CDCl_3) $\delta(\text{ppm}) = 8.79$ (m, 1H); 8.00 (m, 1H); 7.99 (m, 1H); 4.00 (s, 3H). The same synthetic procedure was previously reported by Krauss *et al.* in 2013, with similar yield obtained.²¹³

5-Fluoro-pyridine-2-methylcarboxylate. To a pale green coloured suspension of 5-fluoro-picolinic acid (1.70 g, 12.11 mmol) in dry methanol (30 mL), SOCl_2 (3.5 mL, 42.12 mmol) was added dropwise. The resulting pale green solution was stirred at RT for 24 h in air before being taken to dryness under reduced pressure. The pale green solid residue was taken up in, and neutralised with, sat. NaHCO_3 aqueous solution (10 mL), then extracted with dichloromethane (3 x 25 mL). The combined DCM phase was taken to dryness under reduced pressure, giving the ester as a pale green powder that was used without further purification (1.82 g, 11.7 mmol, 97%). $\text{C}_7\text{H}_6\text{NOF}$ ($M=155.03 \text{ g mol}^{-1}$): calc. C 54.20% N 9.03% H 3.90%; found C 53.95% N 8.71% H 3.90%. ^1H NMR (400 MHz, CDCl_3) $\delta(\text{ppm}) = 8.56$ (t, 1H); 8.18 (m, 1H); 7.52 (m, 1H); 4.00 (s, 3H).

5-Methyl-pyridine-2-methylcarboxylate. To a green coloured suspension of 5-methyl-picolinic acid (1.00 g, 7.41 mmol) in dry methanol (10 mL), SOCl_2 (2.50 mL, 30.09 mmol) was added dropwise. The resulting pale green

solution was stirred at 100°C for 24 h in air before being taken to dryness under reduced pressure. The light green solid residue was taken up in, and neutralised, with sat. NaHCO₃ aqueous solution (5 mL), then extracted with dichloromethane (3 x 20 mL). The combined DCM phase was taken to dryness under reduced pressure, giving the ester as a pale green product that was used without further purification (0.75 g, 4.97 mmol, 67%). C₈H₉NO₂ (M=151.17 g mol⁻¹): calc. C 63.56% N 9.27% H 6.00%; found C 63.48% N 9.06% H 6.22%. ¹H NMR (400 MHz, CDCl₃) δ(ppm) = 8.56 (s, 1H); 8.03 (d, 1H); 7.63 (d, 1H); 4.00 (s, 3H); 2.38 (s, 3H).

5-Trifluoromethyl-pyridine-2-carbohydrazide. *Caution! Hydrazine hydrate is potentially explosive. Perform the reaction behind a blast screen in a fume hood. Dispose of hydrazine hydrate residues appropriately.* Behind a blast shield, to a green EtOH (10 mL) solution of 5-trifluoromethyl-pyridine-2-methylcarboxylate (0.53 g, 2.6 mmol) at room temperature was added dropwise 80% aqueous N₂H₄·H₂O (0.5 mL, 10 mmol). The resulting pale green mixture was refluxed in air for 30 min at 80°C, then allowed to cool down to RT, which caused a white precipitate to form. The precipitate was filtered off, washed with cold EtOH (5 mL), and air dried, giving the carbohydrazide as a white solid that was used without further purification (0.28 g, 1.37 mmol, 53%). C₇H₆N₃OF₃ (M=205.05 g mol⁻¹), calc. C 40.99% N 20.48% H 2.95%; found C 41.11% N 20.09% 3.03%. ¹H NMR (400 MHz, CDCl₃) δ(ppm) = 8.94 (m, 1H); 8.81 (m, 1H); 8.29 (m, 1H); 8.10 (m, 1H); 4.07 (m, 2H).

5-Bromo-pyridine-2-carbohydrazide. *Caution! Hydrazine hydrate is potentially explosive. Perform the reaction behind a blast screen in a fume hood. Dispose of hydrazine hydrate residues appropriately.* Behind a blast shield, to a colourless EtOH (10 mL) solution of 5-bromo-pyridine-2-methylcarboxylate (0.46 g, 2.14 mmol) at room temperature was added dropwise 80% aqueous N₂H₄·H₂O (0.2 mL, 4 mmol). The resulting

colourless solution was stirred in air at RT until a white precipitate was formed (approx. 5 min), then kept stirring for 15 min longer. The white precipitate was filtered off, washed with cold EtOH (5 mL) and air dried, giving the carbohydrazide as a white solid that was used without further purification (0.41 g, 1.90 mmol, 89%). C₆H₆N₃OBr (M=216.04 g mol⁻¹), calc. C 33.33% N 19.44% H 2.78%; found C 33.08% N 19.21% 2.88%. ¹H NMR (400 MHz, CDCl₃) δ(ppm) = 8.84 (s, 1H); 8.60 (m, 1H); 8.01 (m, 1H); 7.98 (m, 1H); 3.96 (s, 2H). The same synthetic procedure was previously reported by Noel *et al.* in 2015 with a similar yield.²¹⁴

5-Fluoro-pyridine-2-carbohydrazide. *Caution! Hydrazine hydrate is potentially explosive. Perform the reaction behind a blast screen in a fume hood. Dispose of hydrazine hydrate residues appropriately.* Behind a blast shield, to a pale green EtOH (10 mL) solution of 5-fluoro-pyridine-2-methylcarboxylate (0.96 g, 6.19 mmol) at room temperature was added dropwise 80% aqueous N₂H₄·H₂O (1 mL, 20 mmol). The resulting colourless solution was stirred in air at RT until a white precipitate was formed (approx. 5 min), then kept stirring for 15 min longer. The precipitate was filtered off, washed with cold EtOH (5 mL), and air dried, giving the carbohydrazide as a white solid that was used without further purification (0.67g, 4.32 mmol, 70%). C₆H₆N₃OF (M=155.05 g mol⁻¹), calc. C 46.45% N 27.09% H 3.90%; found C 46.42% N 27.33% 3.82%. ¹H NMR (400 MHz, CDCl₃) δ(ppm) = 8.79 (s, 1H); 8.38 (m, 1H); 8.19 (m, 1H); 7.53 (m, 1H); 3.91 (s, 2H).

5-Methyl-pyridine-2-carbohydrazide. *Caution! Hydrazine hydrate is potentially explosive. Perform the reaction behind a blast screen in a fume hood. Dispose of hydrazine hydrate residues appropriately.* Behind a blast shield, to a pale green EtOH (2 mL) solution of 5-methyl-pyridine-2-methylcarboxylate (0.50 g, 2.14 mmol) at room temperature was added dropwise 80% aqueous N₂H₄·H₂O (4 mL, 80 mmol). The resulting green

mixture was refluxed for 30 min at 80°C, then the resulting solution was carefully taken to dryness using a gentle air flow, then dried under vacuum for 48 h. The resulting white solid was used without further purification (0.5g, 2.14 mmol, 99%). $\text{C}_7\text{H}_9\text{N}_3\text{O}$ ($M=151.17\text{ g mol}^{-1}$), calc. C 55.62% N 27.80% H 6.00%; found C 55.40% N 27.55% H 5.82%. ^1H NMR (400 MHz, CDCl_3) $\delta(\text{ppm}) = 8.91$ (s, 1H); 8.36 (s, 1H); 8.04 (d, 1H); 7.64 (d, 1H). The same synthetic procedure was previously reported by Noel *et al.* in 2015, with a similar yield.²¹⁴

3-(2-(5-Trifluoromethyl-pyridyl))-4-tolyl-5-phenyl-1,2,4-triazole (L^{pytCF_3}).

Crude ethyl N-(4-methylphenyl)-benzenecarboximidothioate (1 g, 4.5 mmol) and 5-trifluoromethyl-pyridine-2-carbohydrazide (0.61 g, 3.0 mmol) were dissolved in 1-butanol (15 mL) and refluxed for 3 d at 145 °C under argon. After cooling down to RT no precipitate was observed, so the reaction mixture was taken to dryness. The resulting white solid was suspended in water (20 mL) filtered off, and then washed with cold diethyl ether (3 x 5 mL) to remove unreacted reagents, (as L^{pytCF_3} ligand shows low solubility in diethyl ether. The resulting white powder was air dried (0.47g, 1.24 mmol, 42%). $\text{C}_{21}\text{H}_{15}\text{N}_4\text{F}_3$ ($M=380.37\text{ g mol}^{-1}$), calc. C 66.31.% N 17.73% H 3.98%; found C 66.35% N 17.50% H 4.08%. ^1H NMR (400 MHz, CDCl_3) $\delta(\text{ppm}) = 8.58$ (s, 1H, H₁); 8.34 (d, 2H, H₃); 7.99 (d, 1H, H₂); 7.46 (m, 2H, H₉); 7.36 (m, 1H, H₇); 7.29 (m, 2H, H₈); 7.19 (d, 2H, H₄); 7.09 (d, 2H, H₅); 2.41 (s, 3H, H₆). ^{13}C NMR (400 MHz, CDCl_3) $\delta(\text{ppm}) = 156.3$ (C₆); 152.6 (C₁₂); 150.3 (C₅); 145.7 (C₁); 139.4 (C₁₆); 133.8 (q, C₁₇); 133.0 (C₁₀); 129.9 (C₉); 129.8 (C₇); 128.8 (C₁₄); 128.38 (C₁₅); 127.6 (C₈); 126.6 (C₂); 124.6 (C₃); 123.7 (C₄); 121.9 (C₁₃); 21.2(C₁₁). ^{15}N NMR (500 MHz, CDCl_3) $\delta(\text{ppm}) = 320.9$ (N₂); 313.8 (N₁); 315.1 (N₃); 177.2 (N₄). HR-ESI-MS (acetone) m/z: $[\text{H}(\text{C}_{21}\text{H}_{15}\text{N}_4\text{F}_3)]^+$, calc. 381.13, exp. 381.13; $[\text{Na}(\text{C}_{21}\text{H}_{15}\text{N}_4\text{F}_3)]^+$, calc. 403.11, exp. 403.11; $[\text{K}(\text{C}_{21}\text{H}_{15}\text{N}_4\text{F}_3)]^+$, calc. 419.08, exp. 419.08; $[\text{Na}(\text{C}_{21}\text{H}_{15}\text{N}_4\text{F}_3)_2]^+$, calc. 783.23, exp. 783.23.

3-(2-(5-Bromo-pyridyl))-4-tolyl-5-phenyl-1,2,4-triazole (L^{pytBr}). Crude ethyl N-(4-methylphenyl)-benzenecarboximidothioate (0.70 g, 3.3 mmol) and 5-bromo-pyridine-2-carbohydrazide (0.90 g, 4.0 mmol) were dissolved in 1-butanol (20 mL) and refluxed for 5 d at 145 °C under argon. After cooling down to RT no precipitate was observed, so the reaction mixture was taken to dryness. The resulting white solid was suspended in water (20 mL) filtered off, and then washed with cold diethyl ether (3 x 5 mL) to remove unreacted reagents, (like for the L^{pytCF_3} ligand, L^{pytBr} has low solubility in diethyl ether). The resulting white powder was recrystallised from EtOH and air dried, to give L^{pytBr} as an analytically pure white powder (0.47g, 1.24 mmol, 42%). (0.13 g, 0.34 mmol 11%). $C_{20}H_{15}N_4Br$ ($M=391.27$ g mol⁻¹), calc. C 61.39% N 14.32% H 3.86%; found C 60.91% N 14.28% 3.86%. ¹H NMR (400 MHz, CDCl₃) δ (ppm) = 8.40 (s, 1H, H₁); 8.07 (d, 2H, H₃); 7.88 (d, 1H, H₂); 7.45 (m, 2H, H₉); 7.35 (m, 1H, H₇); 7.18 (d, 2H, H₄); 7.18 (m, 2H, H₈); 7.07 (d, 2H, H₅); 2.40 (s, 3H, H₆). ¹³C NMR (400 MHz, CDCl₃) δ (ppm) = 155.85 (C₁₂); 152.98 (C₆); 150.0 (C₁); 145.5 (C₅); 139.3 (C₇); 139.2 (C₃); 133.0 (C₁₀); 129.8 (C₁₆); 129.7 (C₉); 128.8 (C₁₄); 128.4 (C₁₅); 127.6 (C₈); 126.7 (C₁₃); 125.3 (C₄); 121.4 (C₂); 21.2 (C₁₁). ¹⁵N NMR (500 MHz, CDCl₃) δ (ppm) = 318.1 (N₂); 317.8 (d), 317.0 (i) (N₁); 313.8 (N₃); 176.8 (d), 176.0 (i) (N₄). HR-ESI-MS (acetone) m/z: [H(C₂₀H₁₅N₄Br)]⁺, calc. 391.05, exp. 391.06; [Na(C₂₀H₁₅N₄Br)]⁺, calc. 413.04, exp. 413.04; [K(C₂₀H₁₅N₄Br)]⁺, calc. 431.00, exp. 431.00; [Na(C₂₀H₁₅N₄Br)₂]⁺, calc. 805.08, exp. 805.08.

3-(2-(5-Fluoro-pyridyl))-4-tolyl-5-phenyl-1,2,4-triazole (L^{pytF}). Crude ethyl N-(4-methylphenyl)-benzenecarboximidothioate (0.55 g, 2.2 mmol) and 4-methoxyl-pyridazine-2-carbohydrazide (0.33 g, 1.96 mmol) were dissolved in 1-butanol (20 mL) and refluxed for 3 d at 145 °C under argon. After cooling down to RT the desired product only partially precipitated, so the reaction mixture was taken to dryness, the solid suspended in water (25 mL), filtered off, and then washed with cold diethyl ether (3 x 5 mL) to remove unreacted reagents as the L^{pytF} ligand shows low solubility in

diethyl ether. The resulting white powder was recrystallised from MeOH, and air dried, to give L^{pytF} as analytically pure white fluffy crystals (0.4 g, 1.2 mmol, 61%). $\text{C}_{20}\text{H}_{15}\text{N}_4\text{F}$ ($M=330.36\text{ g mol}^{-1}$), calc. C 72.71% N 16.96% H 4.58%; found C 72.68% N 16.72% H 4.69%. ^1H NMR (400 MHz, CDCl_3) δ (ppm) = 8.19 (m, 1H, H_1); 8.11 (m, 2H, H_3); 7.46 (m, 1H, H_2); 7.44 (m, 2H, H_9); 7.32 (m, 1H, H_7); 7.27 (m, 2H, H_8); 7.15 (d, 2H, H_4); 7.06 (d, 2H, H_5); 2.38 (s, 3H, H_6). ^{13}C NMR (400 MHz, CDCl_3) δ (ppm) = 159.3 (d, C_2); 155.7 (C_{12}); 153.1 (C_6); 143.5 (d, C_5); 139.2 (C_7); 137.4 (d, C_1); 133.0 (C_{10}); 129.8 (C_9); 129.7 (C_{16}); 128.8 (C_{14}); 128.4 (C_{15}); 127.7 (C_8); 126.8 (d, C_4); 125.7 (C_{13}); 123.5 (d, C_3); 21.3 (C_{11}). HR- ^{15}N NMR (500 MHz, CDCl_3) δ (ppm) = 319.9 (N_1); 176.0 (N_4). ESI-MS (acetone) m/z: $[\text{H}(\text{C}_{20}\text{H}_{15}\text{N}_4\text{F})]^+$, calc. 331.13, exp. 331.13; $[\text{Na}(\text{C}_{20}\text{H}_{15}\text{N}_4\text{F})]^+$, calc. 353.12, exp. 353.12; $[\text{K}(\text{C}_{20}\text{H}_{15}\text{N}_4\text{F})]^+$, calc. 369.09, exp. 369.09; $[\text{Na}(\text{C}_{20}\text{H}_{15}\text{N}_4\text{F})_2]^+$, calc. 683.24, exp. 683.24.

3-(2-(5-Methyl-pyridyl))-4-tolyl-5-phenyl-1,2,4-triazole (L^{pytMe}). Crude ethyl N-(4-methylphenyl)-benzenecarboximidothioate (0.58 g, 2.57 mmol) and 4-methyl-pyridine-2-carbohydrazide (0.5 g, 2.14 mmol) were dissolved in 1-butanol (10 mL) and refluxed for 4 d at 145 °C under argon. After cooling down to RT the resulting precipitate was filtered off and washed with a copious volume of water (approx. 100 mL), then with a copious volume of diethyl ether (approx. 100 mL) to remove the unreacted reagents as the L^{pytMe} does not show any solubility in either solvent. The powder was then crystallised from MeOH, and air dried, to give L^{pytMe} as an analytically pure white powder (0.62g, 1.9 mmol, 58%). $\text{C}_{21}\text{H}_{18}\text{N}_4$ ($M=326.4\text{ g mol}^{-1}$), calc. C 77.28% N 17.17% H 5.56%; found C 77.58% N 16.91% H 5.49%. ^1H NMR (400 MHz, CDCl_3) δ (ppm) = 8.20 (s, 1H, H_1); 7.90 (d, 2H, H_3); 7.52 (d, 1H, H_2); 7.44 (m, 2H, H_9); 7.33 (m, 2H, H_8); 7.28 (m, 1H, H_7); 7.12 (d, 2H, H_4); 7.06 (d, 2H, H_5); 2.37 (s, 3H, H_6); 2.29 (s, 3H, H_{10}). ^{13}C NMR (400 MHz, CDCl_3) δ (ppm) = 155.4 (C_{12}); 154.0 (C_6); 149.5 (C_1); 144.4 (C_5); 139.0 (C_7); 136.9 (C_4); 133.2 (C_3); 130.5 (C_{10}); 129.7 (C_9); 129.5 (C_{16}); 128.8 (C_{14}); 128.3 (C_{15}); 127.7 (C_8); 127.1 (C_{13}); 123.9 (C_2); 21.3 (C_{11}); 18.4 (C_{17}). ^{15}N NMR (500 MHz, CDCl_3)

δ (ppm) = 313.7 (N₂); 312.2 (N₁); 311.6 (N₃); 175.8 (N₄). HR-ESI-MS (acetone) m/z: [H(C₂₁H₁₈N₄)]⁺, calc. 327.16, exp. 327.16; [Na(C₂₁H₁₈N₄)]⁺, calc. 349.14, exp. 349.14; [K(C₂₁H₁₈N₄)]⁺, calc. 365.11, exp. 365.12; [Na(C₂₁H₁₈N₄)₂]⁺, calc. 675.30, exp. 675.29.

2.5.2. Inorganic Synthesis

[Fe^{II}(*L*^{pytCF3})₂(NCBH₃)₂] \cdot 0.5H₂O. Nitrogen gas was bubbled into a clear solution of *L*^{pytCF3} (13 mg, 34.2 μ mol) in CHCl₃ (12.5 mL) for five minutes, then solid [Fe^{II}(pyridine)₄(NCBH₃)₂] (7.6 mg, 16.2 μ mol) was added causing immediately the solution to turn purple. Vapour diffusion of diethyl ether into the reaction solution, in air, resulted in the formation of a dark purple polycrystalline precipitate which was filtered off, washed with diethyl ether, and air dried to give [Fe^{II}(*L*^{pytCF3})₂(NCBH₃)₂] (7.4 mg, 8.0 μ mol, yield 49.4%). C₄₂H₃₆N₁₀B₂F₆Fe \cdot 0.5H₂O (M=914.3 g mol⁻¹), calc. C 57.74% N 15.30% H 4.20%; found C 57.66% N 15.32% 4.06%. TGA (3.14 mg, 100°C for 240 min) calculated weight loss for removal of H₂O: 1.0%. Found weight loss on heating: 0.5%. HR-ESI-MS (acetone) m/z: [H(C₂₁H₁₅N₄F₃)]⁺, calc. 381.13, exp. 381.13; [Na(C₂₁H₁₅N₄F₃)]⁺, calc. 403.11, exp. 403.11; [Fe(C₂₁H₁₅N₄F₃)₂]²⁺, calc. 408.09, exp. 408.09; [K(C₂₁H₁₅N₄F₃)]⁺, calc. 419.08, exp. 419.08; [Fe(C₂₁H₁₅N₄F₃)(CH₃OH-H)]⁺, calc. 467.08, exp. 467.08; [Fe(C₂₁H₁₅N₄F₃)₃]²⁺, calc. 598.15, exp. 598.15; [Na(C₂₁H₁₅N₄F₃)₂]⁺, calc. 783.23, exp. 783.23; [Fe(C₂₁H₁₅N₄F₃)₂(NCBH₃)]⁺, calc. 856.22, exp. 856.22. Dark purple single crystals of [Fe^{II}(*L*^{pytCF3})₂(NCBH₃)₂] \cdot 2CHCl₃, suitable for SCXRD, were obtained by recrystallisation from chloroform by diethyl ether diffusion.


[Fe^{II}(*L*^{pytBr})₂(NCBH₃)₂] \cdot 0.5H₂O. Nitrogen gas was bubbled into a clear solution of *L*^{pytBr} (10.6 mg, 27.1 μ mol) in DCM (5 mL) for five minutes, [Fe^{II}(pyridine)₄(NCBH₃)₂] (6.5 mg, 13.8 μ mol) was then added causing the solution to turn dark red. Vapor diffusion of diethyl ether into the reaction solution, in air, resulted in the formation of dark red polycrystalline

precipitate which was filtered off, washed with diethyl ether, and air dried to give with formula $[\text{Fe}^{\text{II}}(\text{L}^{\text{pytBr}})_2(\text{NCBH}_3)_2]$ (7.5 mg, 7.2 μmol , yield 52.2%). $\text{C}_{42}\text{H}_{36}\text{N}_{10}\text{B}_2\text{Br}_2\text{Fe}\cdot 0.5\text{H}_2\text{O}$ ($M=1045.49$ g mol $^{-1}$), calc. C 54.41% N 15.11% H 4.02%; found C 54.27% N 14.90% 3.79%. TGA (2.56 mg, 100°C for 240min) calculated weight loss for removal of H_2O : 1.0%. Found weight loss on heating: 0.5%. HR-ESI-MS (acetone) m/z : $[\text{H}(\text{C}_{20}\text{H}_{15}\text{N}_4\text{Br})]^+$, calc. 391.05, exp. 391.06; $[\text{Na}(\text{C}_{20}\text{H}_{15}\text{N}_4\text{Br})]^+$, calc. 413.04, exp. 413.04; $[\text{Fe}(\text{C}_{20}\text{H}_{15}\text{N}_4\text{Br})_2]^{2+}$, calc. 419.01, exp. 419.01; $[\text{K}(\text{C}_{20}\text{H}_{15}\text{N}_4\text{Br})]^+$, calc. 431.00, exp. 431.00; $[\text{Fe}(\text{C}_{20}\text{H}_{15}\text{N}_4\text{Br})(\text{CH}_3\text{OH}-\text{H})]^+$, calc. 477.00, exp. 477.00; $[\text{Fe}(\text{C}_{20}\text{H}_{15}\text{N}_4\text{Br})_3]^{2+}$, calc. 615.04, exp. 615.04; $[\text{Na}(\text{C}_{20}\text{H}_{15}\text{N}_4\text{Br})_2]^+$, calc. 805.08, exp. 805.08; $[\text{Fe}(\text{C}_{20}\text{H}_{15}\text{N}_4\text{Br})_2(\text{NCBH}_3)]^+$, calc. 878.06, exp. 878.06. Dark red single crystals of $[\text{Fe}^{\text{II}}(\text{L}^{\text{pytBr}})_2(\text{NCBH}_3)_2]\cdot 2\text{CHCl}_3$, suitable for SCXRD, were obtained by recrystallisation from acetonitrile by diethyl ether diffusion.

$[\text{Fe}^{\text{II}}(\text{L}^{\text{pytF}})_2(\text{NCBH}_3)_2]\cdot 1\text{H}_2\text{O}$. Nitrogen gas was bubbled into a clear solution of L^{pytF} (15.2 mg, 45.3 μmol) in DCM (25 mL) for five minutes, $[\text{Fe}^{\text{II}}(\text{pyridine})_4(\text{NCBH}_3)_2]$ (10.1 mg, 21.3 μmol) was then added causing the solution to turn bright red. Vapor diffusion of diethyl ether into the reaction solution, in air, resulted in the formation of red polycrystalline precipitate which was filtered off, washed with diethyl ether, and air dried to give with formula $[\text{Fe}^{\text{II}}(\text{L}^{\text{pytF}})_2(\text{NCBH}_3)_2]$ (8 mg, 9.7 μmol , yield 45.6%). $\text{C}_{42}\text{H}_{36}\text{N}_{10}\text{B}_2\text{F}_2\text{Fe}\cdot \text{H}_2\text{O}_2$ ($M=814.28$ g mol $^{-1}$), calc. C 62.32% N 17.22% H 4.51%; found C 62.24% N 16.96% 4.71%. TGA (3.84 mg, 100°C for 240min) calculated weight loss for removal of H_2O : 2.2%. Found weight loss on heating: 1.5%. ESI-MS (acetone) m/z : $[\text{H}(\text{C}_{20}\text{H}_{15}\text{N}_4\text{F})]^+$, calc. 331.13, exp. 331.13; $[\text{Na}(\text{C}_{20}\text{H}_{15}\text{N}_4\text{F})]^+$, calc. 353.12, exp. 353.12; $[\text{Fe}(\text{C}_{20}\text{H}_{15}\text{N}_4\text{F})_2]^{2+}$, calc. 358.09, exp. 358.09; $[\text{K}(\text{C}_{20}\text{H}_{15}\text{N}_4\text{F})]^+$, calc. 369.09, exp. 369.09; $[\text{Fe}(\text{C}_{20}\text{H}_{15}\text{N}_4\text{F})(\text{CH}_3\text{OH}-\text{H})]^+$, calc. 417.08, exp. 417.08; $[\text{Fe}(\text{C}_{20}\text{H}_{15}\text{N}_4\text{F})_3]^{2+}$, calc. 523.16, exp. 523.16; $[\text{Na}(\text{C}_{20}\text{H}_{15}\text{N}_4\text{F})_2]^+$, calc. 683.24, exp. 683.24; $[\text{Fe}(\text{C}_{20}\text{H}_{15}\text{N}_4\text{F})_2(\text{NCBH}_3)]^+$, calc. 756.23, exp. 756.23. Orange single crystals

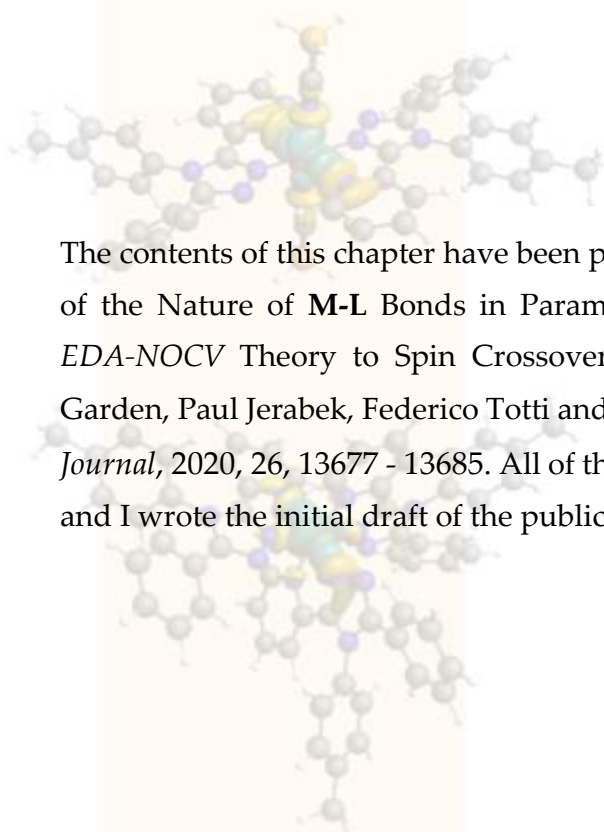
of $[\text{Fe}^{\text{II}}(\text{L}^{\text{pytF}})_2(\text{NCBH}_3)_2] \cdot 2\text{CH}_3\text{NO}_2$, suitable for SCXRD, were obtained by recrystallisation from nitromethane by diethyl ether diffusion.

$[\text{Fe}^{\text{II}}(\text{L}^{\text{pytMe}})_2(\text{NCBH}_3)_2] \cdot 0.5\text{H}_2\text{O}$. Nitrogen gas was bubbled into a clear solution of L^{pytMe} (20 mg, 61.3 μmol) in CHCl_3 (5 mL) for five minutes, $[\text{Fe}^{\text{II}}(\text{pyridine})_4(\text{NCBH}_3)_2]$ (14.9 mg, 31.7 μmol) was then added causing the solution to turn bright red. Vapor diffusion of diethyl ether into the reaction solution, in air, resulted in the formation of light red polycrystalline precipitate which was filtered off, washed with diethyl ether, and air dried to give with formula $[\text{Fe}^{\text{II}}(\text{L}^{\text{pytMe}})_2(\text{NCBH}_3)_2] \cdot 0.5\text{H}_2\text{O}$ (15 mg, 18.6 μmol , yield 58.7%). $\text{C}_{44}\text{H}_{42}\text{N}_{10}\text{B}_2\text{Fe} \cdot \text{H}_2\text{O}$ ($M=797.35 \text{ g mol}^{-1}$), calc. C 66.57% N 17.36% H 5.21%; found C 66.00% N 16.88% 5.23%. TGA (3.07 mg, 100°C for 240min) calculated weight loss for removal of H_2O : 1.1%. Found weight loss on heating: 1.5%. HR-ESI-MS (acetone) m/z : $[\text{H}(\text{C}_{21}\text{H}_{18}\text{N}_4)]^+$, calc. 327.16, exp. 327.16; $[\text{Na}(\text{C}_{21}\text{H}_{18}\text{N}_4)]^+$, calc. 349.14, exp. 349.14; $[\text{Fe}(\text{C}_{21}\text{H}_{18}\text{N}_4)_2]^{2+}$, calc. 354.11, exp. 354.11; $[\text{K}(\text{C}_{21}\text{H}_{18}\text{N}_4)]^+$, calc. 365.11, exp. 365.12; $[\text{Fe}(\text{C}_{21}\text{H}_{18}\text{N}_4)(\text{CH}_3\text{OH}-\text{H})]^+$, calc. 413.10, exp. 413.10; $[\text{Fe}(\text{C}_{21}\text{H}_{18}\text{N}_4)_3]^{2+}$, calc. 517.20, exp. 517.20; $[\text{Fe}(\text{C}_{21}\text{H}_{18}\text{N}_4)_2(\text{NCBH}_3)]^+$, calc. 748.28, exp. 748.28. Red single crystals of $[\text{Fe}^{\text{II}}(\text{L}^{\text{pytMe}})_2(\text{NCBH}_3)_2] \cdot 2\text{CHCl}_3$, suitable for SCXRD, were obtained by recrystallisation from chloroform by diethyl ether diffusion.

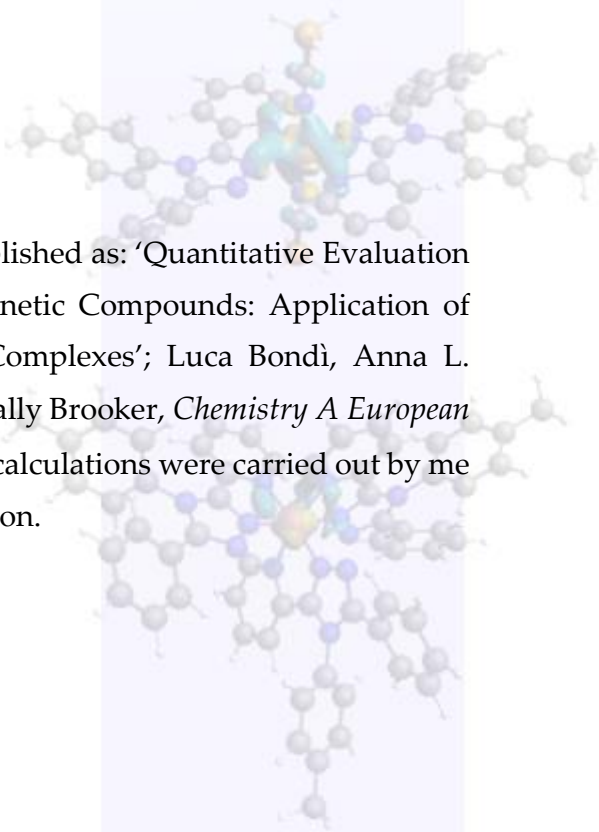


Quantitative Evaluation of the Nature of M-L Bonds in Paramagnetic Compounds: Application of EDA-NOCV Theory to Spin Crossover Complexes

σ -bonding



π -bonding



The contents of this chapter have been published as: 'Quantitative Evaluation of the Nature of M-L Bonds in Paramagnetic Compounds: Application of EDA-NOCV Theory to Spin Crossover Complexes'; Luca Bondi, Anna L. Garden, Paul Jerabek, Federico Totti and Sally Brooker, *Chemistry A European Journal*, 2020, 26, 13677 - 13685. All of the calculations were carried out by me and I wrote the initial draft of the publication.

3.1. Abstract

With the aim of improving understanding of **M-L** bonds in *3d* transition metal complexes, quantitative analysis by Energy Decomposition Analysis and Natural Orbital for Chemical Valence model (*EDA-NOCV*) is done on octahedral spin crossover (*SCO*) complexes, as the transition temperature ($T_{1/2}$) is sensitive to subtle changes in **M-L** bonding. *EDA-NOCV* analysis of Fe-N bonds in 5 $[\text{Fe}^{\text{II}}(\text{L}^{\text{azine}})_2(\text{NCBH}_3)_2]$, in both low spin (*LS*) and paramagnetic high spin (*HS*) states, led to (a) development of a general, widely applicable, corrected **M+L₆** fragmentation, tested against a family of 5 *LS* $[\text{Fe}^{\text{II}}(\text{L}^{\text{azine}})_3(\text{BF}_4)_2]$, confirming that 3 *L^{azine}* are stronger ligands ($\Delta E_{\text{orb},\sigma+\pi} \approx -370$ kcal/mol) than 2 *L^{azine}* + 2 NCBH_3 (≈ -335 kcal/mol), as observed; (b) analysis of **Fe-L** bonding on *LS* \rightarrow *HS*, reveals more ionic (ΔE_{elstat}) and less covalent (ΔE_{orb}) character ($\Delta E_{\text{elstat}}:\Delta E_{\text{orb}}$ 55:45 *LS* \rightarrow 64:36 *HS*), mostly due to a big drop in σ - ($\Delta E_{\text{orb},\sigma}$ \downarrow 50%; -310 \rightarrow -145 kcal/mol), and a drop in π - contributions ($\Delta E_{\text{orb},\pi}$ \downarrow 90%; -30 \rightarrow -3 kcal/mol); (c) strong correlation of observed $T_{1/2}$ and $\Delta E_{\text{orb},\sigma+\pi}$, for both *LS* and *HS* families ($R^2 = 0.99$ *LS*, $R^2 = 0.95$ *HS*), but no correlation of $T_{1/2}$ and $\Delta \Delta E_{\text{orb},\sigma+\pi}(\text{LS-HS})$ ($R^2 = 0.11$). Overall, this study has established and validated a generally applicable fragmentation and computational protocol for *EDA-NOCV* **M-L** bonding analysis of any diamagnetic or paramagnetic, homoleptic or heteroleptic, octahedral transition metal complex.

3.2. Introduction

3.2.1. General Overview

The function of metalloenzymes,¹⁹¹⁻¹⁹² catalysts^{194, 223} and materials¹⁹⁵⁻¹⁹⁶ is often utterly dependent on the finely tuned properties of a first row transition metal ion(s), **M**, at the active site. Fine-tuning the **M-L** interactions^{175, 224-225} – and hence the size of Δ_o – in a predictable manner,^{22-23, 83, 126, 133, 153, 159, 163, 226-228} is generally done by a series of small modifications to a particular ligand skeleton, such as varying a substituent or exchanging a CH for an N atom in a heterocycle, within a family of related complexes.^{18, 23-24, 83, 141} Herein we trial a new *in silico* approach to improving our detailed understanding of **M-L** interactions in *any* octahedral complex,²⁰ in particular aiming to address this in *paramagnetic 3d* complexes.

Specifically, Energy Decomposition Analysis (*EDA*) and the Natural Orbital for Chemical Valence theory (*NOCV*),¹⁸⁶⁻¹⁸⁷ are used in combination¹⁸³⁻¹⁸⁴ in order to provide a full, quantitative and chemically intuitive *ab initio* description of the **M-L** interactions during bond formation: the various contributions to the total interaction energy (ΔE_{int}) are assessed by the use of *EDA*, and then a breakdown of the orbital contribution (ΔE_{orb}) to quantitatively assess the **M-L** bond character is achieved by the use of the *NOCV* scheme (*Subsection 1.6.6*).

Whilst *EDA-NOCV* methodology has been extensively used to study diamagnetic systems,²²⁹⁻²³² it has rarely been applied to paramagnetic transition metal complexes,²³³⁻²⁴⁰ lanthanide/actinide complexes,²⁴¹⁻²⁴³ or indeed to other open-shell radical systems;²⁴⁴⁻²⁴⁷ the somewhat related *ALMO-EDA* has been used to investigate pressure-induced *SCO*.²⁴⁸ Nevertheless there were no systematic studies that could provide guidance with respect to a general fragmentation scheme (i.e. $\mathbf{M}^{n+} + \mathbf{L}_6$ vs $\mathbf{ML}_5^{n+} + \mathbf{L}$ for a general \mathbf{ML}_6 complex) suitable for *EDA*-based bonding analyses and

direct comparison of *any* metal complex - so we rigorously, and successfully, address this issue herein.

Our first, and key, step was therefore to establish a suitable, generally applicable fragmentation and computational protocol for EDA-NOCV analysis of any diamagnetic or paramagnetic, homoleptic or heteroleptic, octahedral transition metal complex. A detailed description of the EDA-NOCV model is provided in *Subsection 1.6.6*.

3.2.2. Choice of Test System

Spin crossover (SCO) active complexes^{30, 32, 249-253} provide a very sensitive experimental probe of subtle changes in **M-L** bonds as **L** is modified, as the transition temperature ($T_{1/2}$) at which the complex switches between the low spin (*LS*) and high spin (*HS*) states in solution is sensitive to these changes.^{18, 22-23, 83} Hence a family of five $[\text{Fe}^{\text{II}}(\text{L}^{\text{azine}})_2(\text{NCBH}_3)_2]$ complexes which vary in the choice of the azine ring (Figure 3.1), for which a linear correlation of the $T_{1/2}$ with the ^{15}N NMR chemical shift of the coordinating azine nitrogen atom in the respective ligand,⁸³ was chosen as the test system to trial this new approach to improving our detailed understanding of **M-L** interactions in octahedral complexes.²⁰

Application of the resulting new protocol to this family of SCO-active complexes then enabled us to evaluate the changes in the bonding properties across the family, obtained by EDA-NOCV calculations,^[10] such as the σ -donor and π -acceptor character of the respective ligands, against the trend in the observed $T_{1/2}$ values of the complexes. Doing this enabled us to determine whether or not the theoretical findings are consistent with experiment, and hence provide quantitative and chemically intuitive insights into the nature of the **M-L** bonds under consideration.

Finally, the optimised EDA-NOCV protocol, developed for the SCO-active $[\text{Fe}^{\text{II}}(\text{L}^{\text{azine}})_2(\text{NCBH}_3)_2]$ complexes, was then used for the closely related $[\text{Fe}^{\text{II}}(\text{L}^{\text{azine}})_3(\text{BF}_4)_2]$ family of *LS* complexes,^[16] where our calculations

showed that 3 L^{azine} ligands produce a stronger octahedral ligand field than a combination of 2 L^{azine} + 2 $NCBH_3$, which is in line with experimental findings.

Overall, this study has established and validated a generally applicable fragmentation and computational protocol for EDA-NOCV M-L bonding analysis of any diamagnetic or paramagnetic, homoleptic or heteroleptic, octahedral transition metal complex.

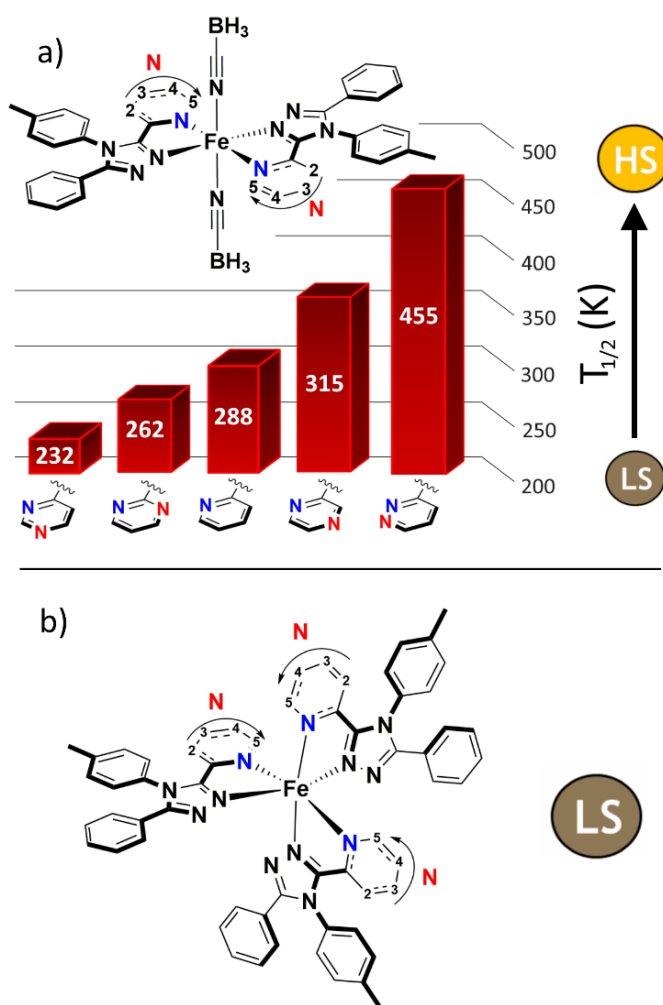


Figure 3.1. The two families of complexes studied herein: a) five SCO-active complexes, $[Fe^{II}(L^{azine})_2(NCBH_3)_2]$, shown in order of increasing $T_{1/2}$ in $CDCl_3$ solution as a function of the azine i.e. position of non-coordinated N (red): absent ($L^{pyridine}$); or present in the 2-position ($L^{2pyrimidine}$), 3-position ($L^{pyrazine}$), 4-position ($L^{4pyrimidine}$), or 5-position ($L^{pyridazine}$)⁸³ and b) five LS $[Fe^{II}(L^{azine})_2(BF_4)_2]$ complexes.²⁵⁴

3.3. Fragmentation Dilemma

Interpretation of *EDA-NOCV* results is known to be highly dependent on the choice of fragmentation of the molecule.¹⁷⁵⁻¹⁸⁰ Moreover, complexes involving 3d metal ions pose a special challenge as it is desirable to reflect physically meaningful orbital occupations and energies in both possible situations: the bound complex and the isolated fragments. In the latter case, oftentimes the best representation would be achieved with fractionally occupying the energetically lower-lying 3d orbitals of the metal,²⁵⁵ while in the former the occupation of the appropriate antibonding molecular orbitals with *d* character at the metal centre is mandatory. To find a balance between meaningful reference states, chemically intuitive orbital occupations and computational feasibility, a series of systematic *EDA-NOCV* calculations with various fragmentation schemes and additional computational protocols have been performed which are detailed in the following.

The family of five *SCO*-active $[\text{Fe}^{\text{II}}(\text{L}^{\text{azine}})_2(\text{NCBH}_3)_2]$ complexes comprise of one metal ion (Fe^{2+}), two constant axial anionic co-ligands (NCBH_3) and two varying equatorial neutral bidentate L^{azine} ligands. In the first step, a full test of five possible fragmentations that the *LS* $[\text{Fe}^{\text{II}}(\text{L}^{\text{azine}})_2(\text{NCBH}_3)_2]$ complexes could be broken into (**1-5**, Figure 3.2) was carried out, as these being diamagnetic led to easier wavefunction convergence and clearer visual analysis of the *NOCV* results than for the analogous *paramagnetic high spin* state complexes. To our knowledge, a systematic study of fragmentation schemes, at the level presented here, is a novelty in the *EDA-NOCV*-based bonding analysis of transition metal complexes with *d* orbital configurations other than d^0 and d^{10} .²³⁴⁻²³⁵

Fragmentations **1** and **2** (Figure 3.2) represent the most commonly used fragmentation types in the *EDA-NOCV* literature when *diamagnetic* transition metal ions (*LS* d^6 or d^{10}) are present, removal of a single ligand.^{176,}
²⁵⁶ Here either $\text{L} = [\text{NCBH}_3]^-$ (fragmentation **1**) or $[\text{L}^{\text{azine}}]$ (fragmentation **2**) is

removed, so these provide detailed information on a single type of Fe-L interaction. However, the presence of another ligand of the same type in the other, iron-containing, fragment makes these two fragmentation choices less than ideal here. Hence fragmentations 3 and 4 (Figure 3.2), in which a pair of identical ligands are removed, either both $[2 \times \text{NCBH}_3]$ (fragmentation 3) or both $[2 \times \text{L}^{\text{azine}}]$ (fragmentation 4) ligands, should provide a cleaner analysis of the details of the different types of Fe-L bonds. These fragmentation schemes are described in detail in the Supporting Information (Subsections A3.3.1-A3.3.4).

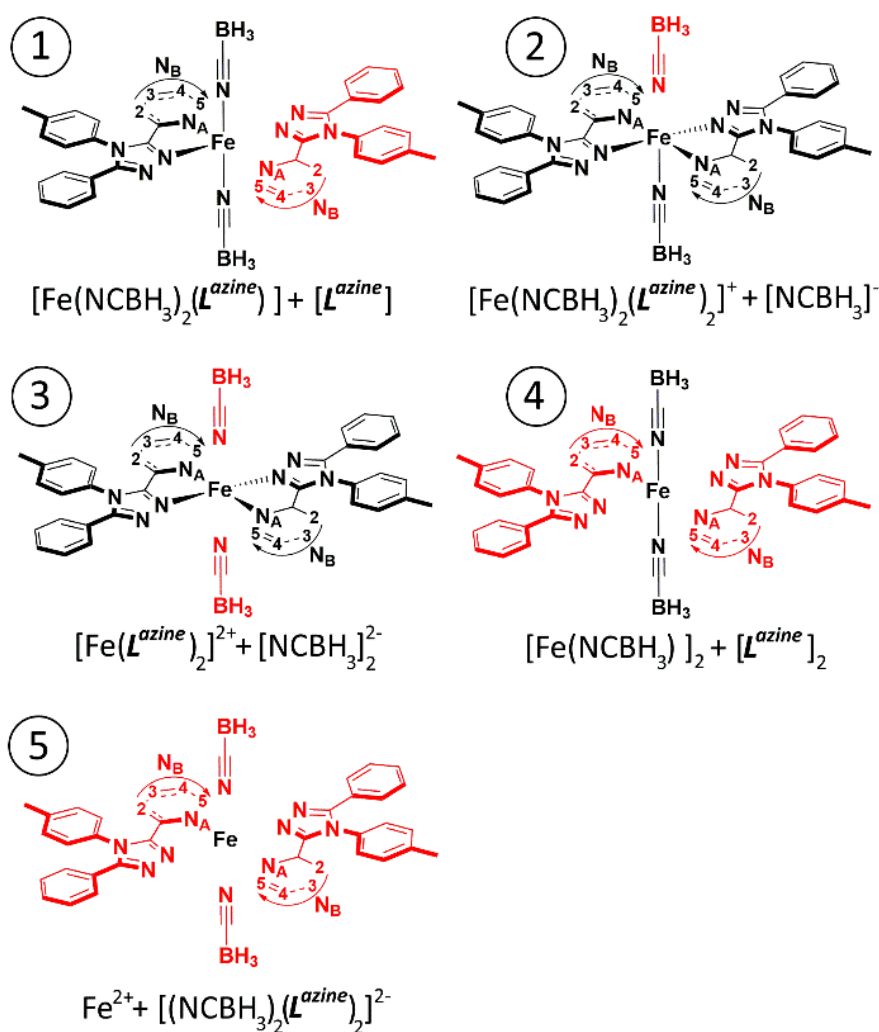


Figure 3.2. The five fragmentations 1-5 (top to bottom) trialed for EDA-NOCV analysis of the five LS $[\text{Fe}(\text{L}^{\text{azine}})_2(\text{NCBH}_3)_2]$ complexes (fragment 1 in black; fragment 2 in red).

However, all four of these fragmentations, **1-4**, would only really be useful for examining trends within a family of very closely analogous complexes - confidently comparing very different coordination environments around **M** will be rather difficult, as the fragmentation is not general enough for that: The remaining metal-bound ligands will surely affect the electronic environment of the metal ion so will subsequently influence the **M-L** bonding character. In light of this, fragmentation **5** (Figure 3.2), in which all of the ligands are removed from the metal centre, is the most unbiased of all of these fragmentation options, and opens up the general application of the *EDA-NOCV* analysis to any monometallic complex of similar structure.

Whilst the Fe *d* orbital energies in fragmentations **1-4** are comparable to the frontier orbital energies of the ligands, as expected within Hoffman's MOs diagram (see Figure A3.1), this is not the case in fragmentation **5**. Due to the absence of partial ligand fields, which are induced by lone-pair containing ligands surrounding the metal ion containing fragment in the other fragmentation schemes (**1-4**), the attractive potential of the Fe²⁺ centre is not "buffered" by electron density in the vicinity anymore and is therefore fully experienced by the *d* electrons. So, although using Fe²⁺ instead of Fe⁰ as a fragment appears intuitive and convenient at first, the resulting Fe²⁺ *d* atomic energies for fragmentation **5a** (no corrections, Subsection A3.2.9 and Table A3.4), are very low in energy (approx. -26.0 eV, see Tables 3.1 and A3.4), compared to the energies of the frontier orbitals of the ligands (between -4.0 and +4.0 eV, see Table A3.5). This strongly challenges the physical justification for this description of **M-L** bonding interactions because of the poor match in energies between interacting frontier orbitals. To overcome this dilemma, the free ion **Mⁿ⁺** of **5a** was surrounded by varying amounts of negative charges (described as **5b-5d** in Appendix A3, Subsection A3.2.9) in order to emulate the electron density of the ligand lone-pairs. A slightly different approach was taken with scheme **5e**: Here the electron density of the isolated Fe²⁺ AOs was mapped onto the

neutral Fe⁰ AOs. All treatments effectively rescaled the Fe²⁺ *d* orbitals towards more positive energy levels.

We found that through the computational protocols **5b** and **5e** the Fe²⁺ orbital energies were brought closest to the energy levels of Fe⁰ in spherical symmetry (Tables 3.1 and A3.4), and hence also to the ligand frontier orbital energies, which in turn yields a more chemically intuitive MO diagram for fragmentation into the isolated metal ion and the surrounding ligands with much better matching orbital energies.

Fragmentations **5b** and **5e** were found to have different advantages and disadvantages (*vide infra*; and see Sections A3.9 and A3.5 for more details) so both were applied for in depth analysis of the complexes depending on the quantity in question. Specifically, **5b** allowed for identification of chemically intuitive bonding interactions via NOCV analysis but underestimated the Pauli repulsion (ΔE_{Pauli}) in the EDA, whereas for **5e** it is the other way around.

Table 3.1. The calculated energy of the Fe(AOs) frontier orbitals (eV) was used to establish the most appropriate way to deal with the very low energy observed for Fe²⁺ (ca. -26 eV) relative to Fe⁰ (ca. -8.0 eV) so that EDA-NOCV analyses could be carried out for fragmentation 5 (M+L₆) for the LS [Fe^{II}(L^{azine})₂(NCBH₃)₂] complexes. Note: the energy levels of the ligand frontier orbitals range from -4.0 to +4.0 eV.

LS Fe(AOs)	T _{2g}	E _g	ΔE (E _g -T _{2g})	Energy (H)	Frag.
Fe ⁰ (Spherical Symmetry)	-7.93	-7.93	0.0	-1263.66	-
Fe ²⁺ (no charges)	-26.05	-25.61	0.56	-1262.74	5a
Fe ²⁺ (6x -0.425e)	-8.00	-7.61	0.39	-1262.75	5b
Fe ²⁺ on Fe ⁰ (AOs)	-7.96 [†]	-7.78 [†]	0.18 [†]	-1263.66	5e

Subsequently, we have employed scheme **5e** to obtain information about the contributions to the intrinsic bond energy (ΔE_{elstat} , ΔE_{Pauli} , ΔE_{orb} , ΔE_{disp}) and **5b** – in separate calculations – to gain deeper insight into orbital interactions and the relative contributions within by decomposition via NOCV scheme, respectively. As the purpose of this work is to provide a robust computational protocol to enable the application of EDA-NOCV analysis to any monometallic complex, regardless of spin state or the exact nature of the coordination pocket provided by the coordinating ligands, a detailed description of the results of applying these two general fragmentations, **5b/5e** (i.e., corrected $\mathbf{M}^{n+} + \mathbf{L}_6$), in the EDA-NOCV analysis of three families of complexes follows.

3.4. Results and Discussion

As noted above, ΔE_{elstat} and ΔE_{orb} (Equation 1.13) are the *EDA* quantities that give indications of the *ionic* and *covalent* character of the chemical bonds formed between the two fragments (**5e**; $M^{n+} + L_6$).

The term (fragmentation **5b**; $M^{n+}+L_6$) that is expected to be most sensitive to the differences in the **M-L^{azine}** bonds (due to the 5 different azines), and hence reflects the changes in the *SCO* properties, is ΔE_{orb} (Equation 1.29), in particular the σ - and π -contributions that involve the metal ion (Equation 1.29; $\Delta E_{orb,\sigma}$ and $\Delta E_{orb,\pi}$). Visual representations of all the σ - and π -contributions to the **M-L** bonding are provided by the *NOCV* deformation densities $\Delta\rho^{(i)}$ for each of the fragmentations employed. It should be noted that the general appearance is the same for the other four complexes in the respective family (treated with the same fragmentation), regardless of the different *L^{azine}* ligands.

These key parameters are presented for both the *LS* (Figure 3.3 and A3.27) and *HS* (Figure A3.28) state families of $[Fe(L^{pyridine})_2(NCBH_3)_2]$ and for the *LS* family of $[Fe(L^{pyridine})_3]^{2+}$ (see later, Figures 3.7 and A3.30).

3.4.1. *LS* $[Fe^{II} (L^{azine})_2(NCBH_3)_2]$

As expected, due to the charged nature of the $NCBH_3^-$ co-ligand, *EDA* using fragmentation **5e** reveals that the bonding interaction is mainly ionic ($\Delta E_{elstat}:\Delta E_{orb} = 55:45$; Figure 3.4).

Furthermore, *NOCV* analysis using fragmentation **5b** reveals the ratio of σ - and π -contributions to ΔE_{orb} is about 90:10 ($\Delta E_{orb,\sigma}:\Delta E_{orb,\pi}$) (Figure 3.5, Table A3.21). Focusing first on the **M←L** σ -interactions, those involving the Fe^{2+} *p* and *s* orbitals provide a constant stabilisation energy across the entire family (Table A3.21 and Figure A3.27). Hence, as expected, the

variation in $\Delta E_{orb,\sigma}$ as the L^{azine} changes from $L^{4pyrimidine}$ to $L^{pyrazine}$ is due to changes in the σ -interactions formed by the Fe^{2+} d_{z^2} and $d_{x^2-y^2}$ orbitals ($\Delta\rho_1$ and $\Delta\rho_2$, Figures 3.3 and A3.27). Unsurprisingly, these $\Delta E_{orb,\sigma}$ values do not fit the experimental observations (order of $T_{1/2}$ values). The $L^{pyridazine}$ complex shows significantly smaller d_{z^2} (-102 kcal/mol) and $d_{x^2-y^2}$ (-110 kcal/mol) orbital interactions than are seen in the other complexes (-113 to -114, and -116 to -119 kcal/mol respectively; Figure A3.27, Table A3.21).

Focusing next on the analysis of the three $M \rightarrow L$ π -back donation contributions, $\Delta E_{orb,\pi}$, reveals: $\Delta\rho_3$ is mainly associated with the interaction of M with the *diazine* ring in the yz -plane ($\Delta E_{orb,3}$ about -1 to -30 kcal/mol across the family); while $\Delta\rho_4$ is mainly associated with the interaction of M with the *triazole* ring in the xz -plane ($\Delta E_{orb,4}$ constant at -11 kcal/mol across the family). $\Delta\rho_5$ lies in the L^{azine} plane (xy) so both the *diazine* ring and the *triazole* ring of each L^{azine} ligand participates in this bond ($\Delta E_{orb,5}$ constant at -15 kcal/mol across the family) (Figure A3.27, Table A3.21).

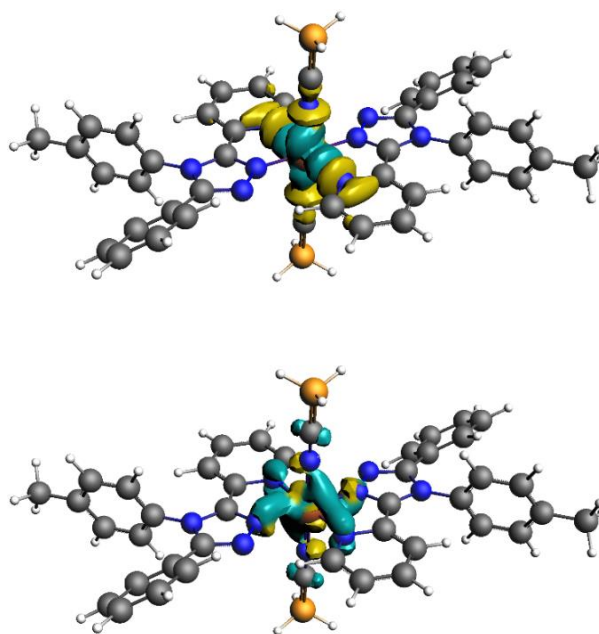


Figure 3.3. Plot of the deformation densities $\Delta\rho_{(i)}$ (reported using cut-off on $\Delta\rho_{(i)}$ of 0.003) obtained for fragmentation **5b** EDA-NOCV analysis of LS $Fe(L^{pyridine})_2(NCBH_3)_2$. These correspond to: (top) $\Delta\rho_2$, $Fe(d_{x^2-y^2}) \leftarrow$ ligand σ -donation and (bottom) $\Delta\rho_4$, $Fe(d_{zx}) \rightarrow$ ligand π -back donation. Direction of charge flow: yellow \rightarrow turquoise.

As for the $\Delta E_{orb,\sigma}$ values, the $\Delta E_{orb,\pi}$ values do not parallel the order of $T_{1/2}$ values: again, the $L^{pyridazine}$ complex is the outlier, with a significantly bigger $\Delta E_{orb,3}$ (-30 kcal/mol) than the rest (-1 to -4 kcal/mol).

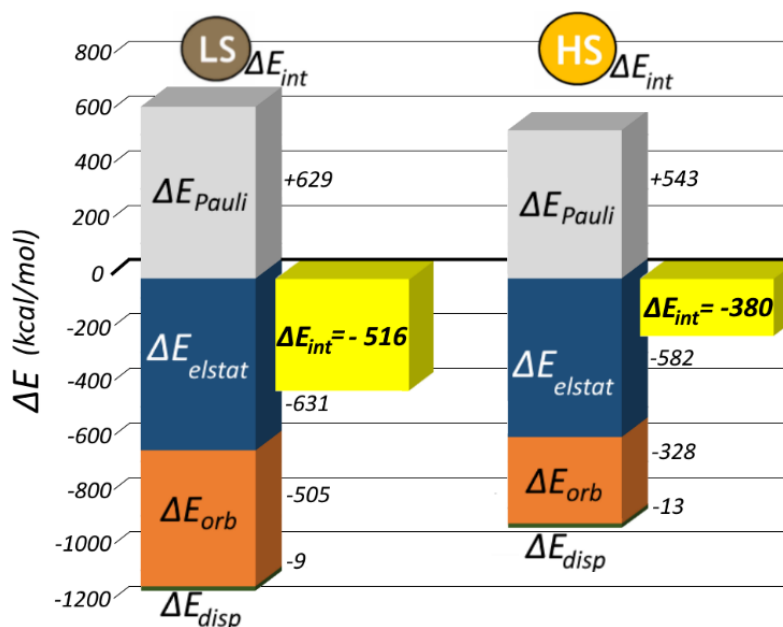


Figure 3.4. Results of EDA for LS (left) vs HS (right) $[Fe(L^{pyridine})_2(NCBH_3)_2]$ using fragmentation 5e. For each spin state the pair of bar graphs shows the four components of ΔE_{int} and the sum of them (ΔE_{int} , yellow). Energies are in kcal/mol.

3.4.2. HS $[Fe^{II} (L^{azine})_2(NCBH_3)_2]$

Moving to the HS family of $[Fe(L^{azine})_2(NCBH_3)_2]$ complexes (again using fragmentations 5b/5e Subsections A3.2.9 and A3.3.6), unsurprisingly, the change in Fe^{II} spin state dramatically affects the M-L interactions. The EDA (fragmentation 5e) shows that on going from LS to HS the ΔE_{int} stabilisation for the $[Fe(L^{azine})_2(NCBH_3)_2]$ family (Table A3.22) decreases by ca. 25%, from about -500 to -370 kcal/mol. The exact values depend on the L^{azine} present; those for $L^{pyridine}$ are shown in Figure 3.4.

This is consistent with the *HS* state being less stable enthalpically than the *LS* state, as expected as the *HS* state only becomes more stable than the *LS* state at higher temperatures when the entropic contributions become large enough to outweigh the enthalpic term. The three main contributions to ΔE_{int} (ΔE_{orb} , ΔE_{Pauli} and ΔE_{elstat} ; Equation 1.16, Figure 3.4, Table A3.22) are also reduced in magnitude when changing from *LS* to *HS*. Of them, the largest reduction is observed for ΔE_{orb} (from about -500 to about -330 kcal/mol).

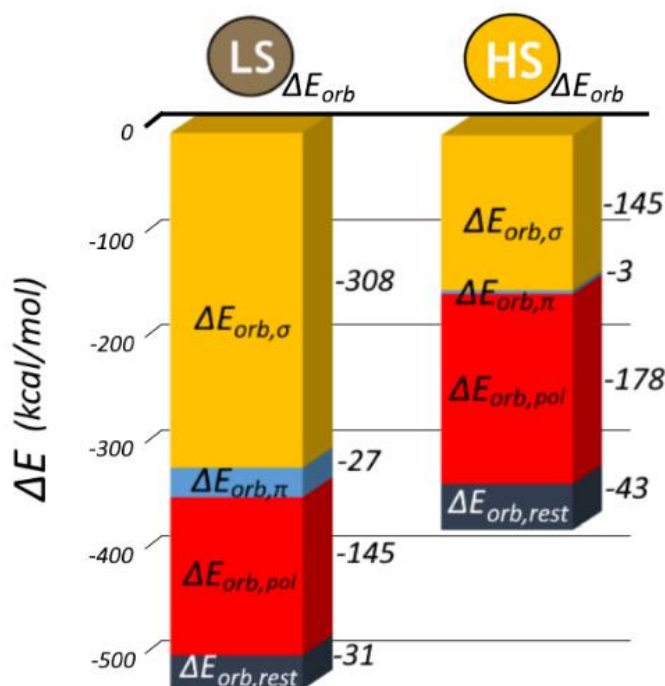


Figure 3.5. Results of NOCV decomposition of ΔE_{orb} for *LS* (left) vs *HS* (right) $[Fe_2(L_{pyridine})_2(NCBH_3)]$ using fragmentation **5b**. For each spin state the bar graph shows the four components of ΔE_{orb} . Energies are in kcal/mol.

In addition, the $\Delta E_{orb}:\Delta E_{elstat}$ ratio goes from 44:55 for *LS* to 35:63 for *HS*, values consistent with the *HS* state being less covalent and more ionic than the *LS* state. This quantitative analysis confirms the significant change in the nature of the **M-L** interactions that is anticipated on change of spin state.

More details of the changes in **M-L** bonding on changing spin state are revealed by comparison of the results of the NOCV analysis (fragmentation **5b**) for both spin states (Figures 3.5, 3.6 and A3.28, Table A3.22). The $\Delta E_{orb,\sigma+\pi}$ for *LS* [Fe(*L*^{azine})₂(NCBH₃)₂] lies between -330 and -350 kcal/mol and almost two-thirds of this orbital interaction is provided by $\Delta E_{orb,\sigma}$, in particular by the formation of **M-L** σ -bonds involving the **M** d_{z^2} and $d_{x^2-y^2}$ (unoccupied) orbitals ($\Delta E_{orb,\sigma} > 100$ kcal/mol each).

In contrast, in *HS* [Fe(*L*^{azine})₂(NCBH₃)₂] these two orbitals are now half-occupied so **M-L** anti-bonding interactions are also present, dropping the $\Delta E_{orb,\sigma}$ stabilisation energy values to less than -35 kcal/mol each; consequently, the total $\Delta E_{orb,\sigma+\pi}$ stabilisation energy drops to between -145 and -160 kcal/mol in the *HS* state (Figure 3.6). As for the *LS* analogues, a constant contribution to $\Delta E_{orb,\sigma}$, almost unaffected by the spin state, is observed for the contributions where *s* and *p* of Fe²⁺ are involved, i.e., $\Delta E_{orb,\sigma}(s, p_x, p_y, p_z)$ (Figure A3.28, Table A3.22).

Whilst the π -contributions ($\Delta E_{orb,\pi}$) to $\Delta E_{orb,\sigma+\pi}$ are small in both spin states (Figure 3.5; *LS* -27 kcal/mol vs *HS* -3 kcal/mol), those involving the t_{2g} orbitals donating electron density back to the ligands show a large reduction in magnitude of stabilisation on going from *LS* to *HS* (see Figure A3.28 | $v_{24} | \alpha$) due to the lower number of electrons present in them. In contrast, the fragment polarisation contributions ($\Delta E_{orb,pol}$) provide greater stabilisation in the *HS* state, by about -30 kcal/mol (Figure 3.5), regardless of *L*^{azine}. In a nutshell, as expected by the occupation of anti-bonding orbitals, spin state switching from *LS* to *HS* (Figures 3.4-3.6) greatly reduces the orbital contributions (ΔE_{orb}) between **M** and **L**, by ca 50%, while the electrostatic interactions (ΔE_{elstat}) only drop by $\approx 10\%$, reflecting the reduction in the hardness of the metal ion as the radius increases (from 0.75 Å *LS* to 0.95 Å *HS*).²⁵⁷ This is consistent with the classical view, that on switching from *LS* to *HS* the **M-L** bond becomes more ionic and less covalent, with longer and weaker bonds due to decreases in both the σ - and π -interactions.

3.4.3. Correlation of *EDA-NOCV* Parameters with $T_{1/2}$

Given the above, the $\Delta E_{orb,\sigma+\pi}$ values obtained from the *EDA-NOCV* analysis were expected to correlate with the ligand field strength of the bonds formed between the fragments M^{n+} and L_6 . This is a useful test of whether or not this approach can provide a useful, general, quantitative and predictive tool for predicting $T_{1/2}$ for an *SCO* system.

A very good correlation ($R^2 = 0.95$) between the *EDA-NOCV* calculated $\Delta E_{orb,\sigma+\pi}$ and the experimentally observed $T_{1/2}$ is observed, regardless of whether the family of *LS* and *HS* state complexes is examined (Figure 3.6 and A3.29). This indicates that the new computational protocol is pleasingly sensitive, which is quite remarkable given that computed *EDA-NOCV* $\Delta E_{orb,\sigma+\pi}$ values for *L*⁴*pyrimidine*, *L*²*pyrimidine*, *L**pyridine* in particular lie within fractions of kcal/mol of each other. No correlation between $T_{1/2}$ and the small difference between the $\Delta E_{orb,\sigma+\pi}$ values for the *LS* and *HS* states ($\Delta_{LS-HS}\Delta E_{orb,\sigma+\pi}$) is observed ($R^2 = 0.12$, Figure A3.29). Rather, the single spin state trend (*LS* is the easier of the two to calculate) should be used, as it appears to be a good predictive tool.

In summary, it is evident from these results that the change of *L*^{azine} induces different alterations in the σ - and π - interactions, which only correlate (extremely well) with the $T_{1/2}$ values when the synergy of the two contributions ($\Delta E_{orb,\sigma+\pi}$) is considered (Figure 3.6). The results also confirm the expected extreme difficulty in foreseeing the effect of a ligand on the $T_{1/2}$ of a complex on the basis of simple consideration of σ - or π -contributions.

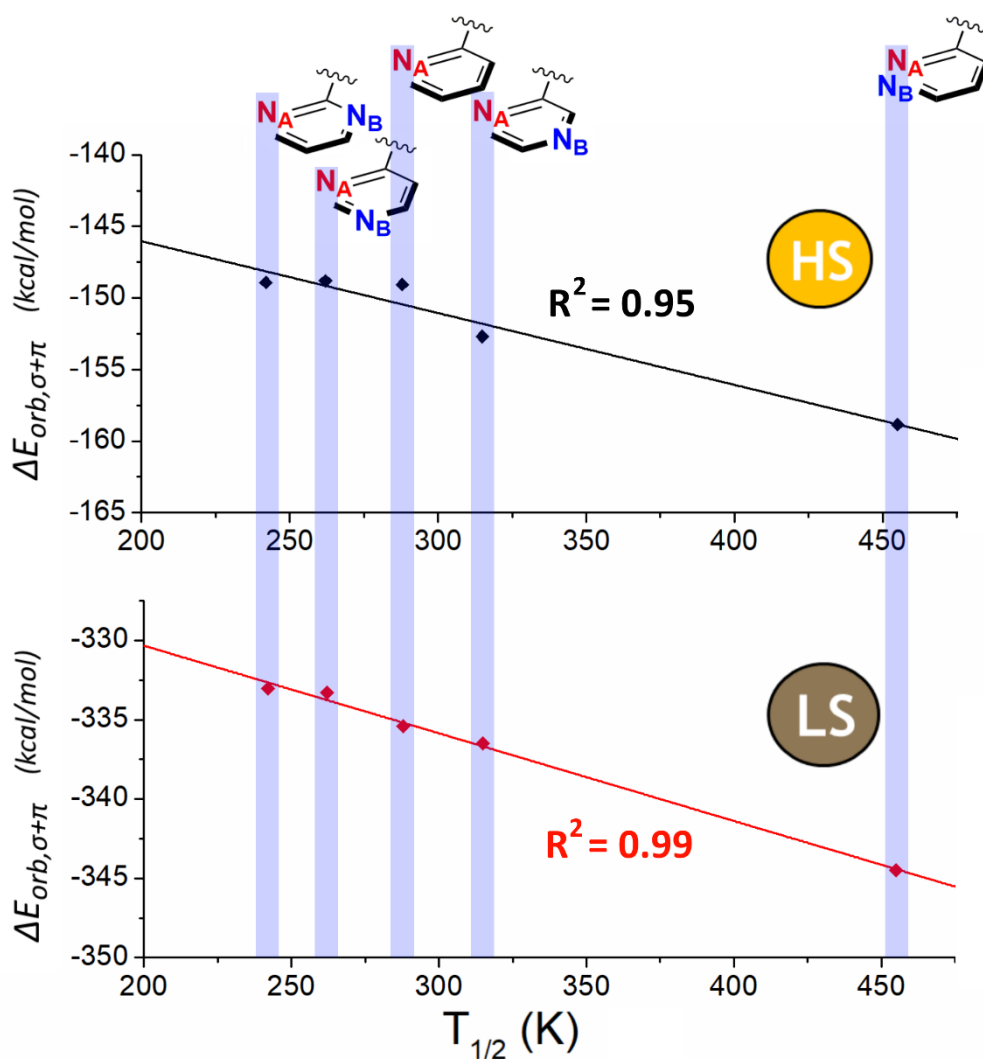


Figure 3.6. Strong correlations are seen between $\Delta E_{orb,\sigma+\pi}$ (calculated using fragmentation **5b**) and $T_{1/2}$, for both the LS state complexes ($R^2 = 0.99$) and the HS state complexes ($R^2 = 0.95$), but there is no correlation between the difference, $\Delta_{LS-HS}\Delta E_{orb,\sigma+\pi}$, and $T_{1/2}$ ($R^2 = 0.12$; see Figure A3.29).

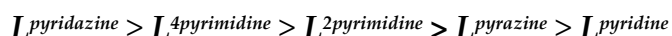
3.4.4. $LS [Fe^{II}(L^{azine})_3]^{2+}$

Application EDA-NOCV ($M^{n+} + L_6$; based on **5b/5e**) to the closely related family of $LS [Fe(L^{azine})_3]^{2+}$ complexes (Figure 3.7) provided a new set of charged candidates to start to test the generality of these protocols. For the $LS [Fe(L^{azine})_3]^{2+}$ family the EDA revealed a $\Delta E_{elstat}:\Delta E_{orb}$ ratio of about 45:55

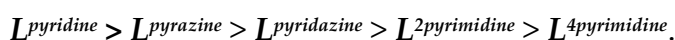
(Figure A3.30, Table A3.23), revealing greater covalent than ionic bonding, in contrast to the *LS* $[\text{Fe}(\text{L}^{\text{azine}})_2(\text{NCBH}_3)_2]$ complexes in which this ratio is reversed ($\Delta E_{\text{elstat}}:\Delta E_{\text{orb}} = 55:45$) (Table A3.23).

This is not surprising as in the present case none of the ligands are charged, whereas in the $[\text{Fe}(\text{L}^{\text{azine}})_2(\text{NCBH}_3)_2]$ complexes two anions are involved. This results, when going from $[\text{Fe}(\text{L}^{\text{azine}})_2(\text{NCBH}_3)_2]$ to $[\text{Fe}(\text{L}^{\text{azine}})_3]^{2+}$ (Table A3.23), in a large decrease in ΔE_{elstat} stabilisation (approx. -620 to -400 kcal/mol) and a slight increase in ΔE_{orb} stabilisation (≈ -15 to -20 kcal/mol). The same magnitude of increase in stability observed for the ΔE_{orb} term is observed as an increase in ΔE_{Pauli} stabilisation ($\approx +15$ to $+20$ kcal/mol). This is consistent with the general trend that these two terms, ΔE_{orb} and ΔE_{Pauli} , are intimately connected in describing the covalent bonding between fragments (Table A3.23).

The NOCV analysis reveals that on stepping across the five $\underline{\text{L}}^{\text{azine}}$ ligand from $\text{L}^{\text{4pyrimidine}}$ (weakest field strength, least negative $\Delta E_{\text{orb},\sigma+\pi}$) to $\text{L}^{\text{pyridazine}}$ (strongest field strength, most negative $\Delta E_{\text{orb},\sigma+\pi}$) that: (a) the σ -bonds ($\Delta E_{\text{orb},\sigma}$) involving the d_{z^2} and $d_{x^2-y^2}$ orbitals strengthen by about -5 to -10 kcal/mol per bond per step and (b) the π -backbonds ($\Delta E_{\text{orb},\pi}$) involving the d_{xy} , d_{zx} , d_{zy} orbitals strengthen by about -5 to -15 kcal/mol per bond per step (Figures 3.7 and A3.30, Table A3.23). On the other hand, as before, the bonds involving s , p_x , p_y and p_z orbitals show marginal differences (Figure A3.23, Table A3.30). Analysis of the σ - and π -contributions shows that the σ -interaction is almost eight times larger than the π -interaction regardless of L^{azine} . The σ -strength ($\Delta E_{\text{orb},\sigma}$) of the L^{azine} ligands follows the order:



Interestingly the order of the π -strength ($\Delta E_{\text{orb},\pi}$) of the L^{azine} ligands differs (and the values are far from showing a monotonic trend):



Adding those two contributions together gives $\Delta E_{orb,\sigma+\pi}$ and this puts the complexes into the same order as was observed experimentally for the $[\text{Fe}(\text{NCBH}_3)_2(\text{L}^{azine})_2]$ family, with an average magnitude decrease in $\Delta E_{orb,\sigma+\pi}$ stability of about 30 kcal/mol between *LS* $[\text{Fe}(\text{L}^{azine})_3]^{2+}$ and *LS* $[\text{Fe}(\text{L}^{azine})_2(\text{NCBH}_3)_2]$ (Table A3.21 and Table A3.23):

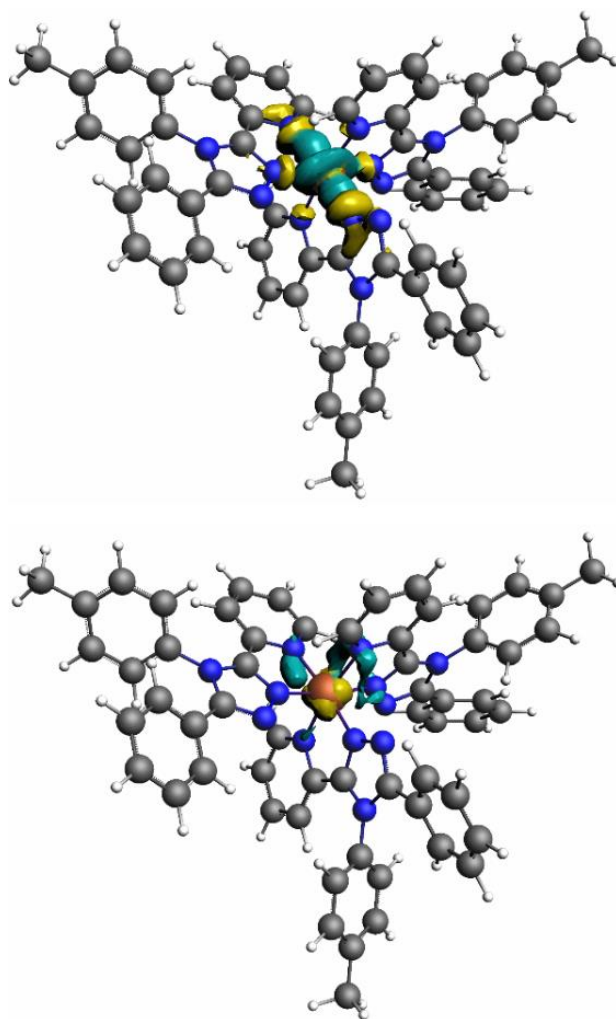


Figure 3.7. Plot of the deformation densities $\Delta\rho_{(i)}$ in fragmentation **5b** ($\text{M} + \text{L}_6$) of the $[\text{Fe}(d_{z^2})] \leftarrow$ ligand σ -donation (left) and the $[\text{Fe}(d_{xz})] \rightarrow$ ligand π -donation in reference complex *LS* $[\text{Fe}(\text{L}^{\text{pyridine}})_3]^{2+}$. The direction of the charge flow is yellow \rightarrow turquoise. The eigenvalues $|v_i|$ indicate the relative size of the charge flow. Cut-off on $\Delta\rho_{(i)} = 0.003$.

3.4.5. L^{azine} vs 2NCBH_3 : Ligand Field Strength Comparison

The above results enable another test of whether or not this *EDA-NOCV* protocol ($\mathbf{M} + \mathbf{L}_6$) can provide a useful, general, quantitative and predictive tool – in this case to compare the field strength of a pair of ligands in different types of complexes (Figure 3.8).

In contrast to the *SCO*-active $[\text{Fe}^{\text{II}}(\text{L}^{azine})_2(\text{NCBH}_3)_2]$ family,⁸³ the related family of $[\text{Fe}(\text{L}^{azine})_3](\text{BF}_4)_4$ complexes are all *LS*,²⁵⁴ which implies that the replacement of two NCBH_3^- anions by one bidentate L^{azine} ligand increases the ligand field experienced by the iron centre. The $\Delta E_{orb,\sigma+\pi}$ values (Figure 3.8) for $[\text{Fe}(\text{L}^{azine})_2(\text{NCBH}_3)_2]$ (-335 kcal/mol) and $[\text{Fe}(\text{L}^{azine})_3]^{2+}$ (-368 kcal/mol) show that replacement of $2x\text{NCBH}_3^-$ by one L^{azine} leads to an increase in the stabilisation ($\Delta\Delta E_{orb,\sigma+\pi}$) of -33 kcal/mol (Figure 3.8), which is consistent with the experimental observation that the $[\text{Fe}(\text{L}^{azine})_2(\text{NCBH}_3)_2]$ family are *SCO*-active whereas the $[\text{Fe}(\text{L}^{azine})_3]^{2+}$ family are solely *LS*.

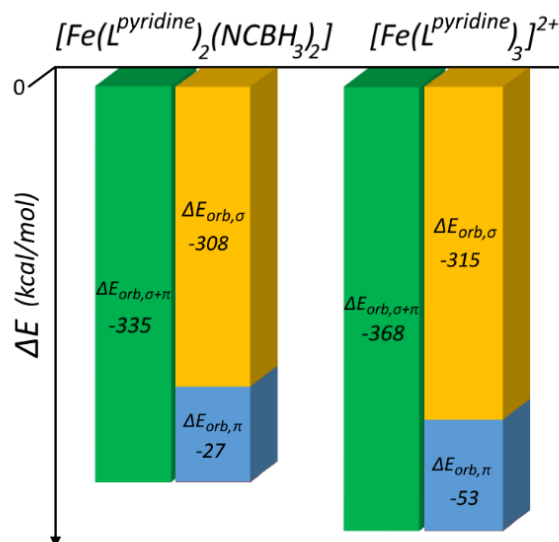


Figure 3.8. Comparison of $\Delta E_{orb,\sigma+\pi}$ (and components), calculated for *LS* $[\text{Fe}(\text{L}^{pyridine})_2(\text{NCBH}_3)_2]$ (left) and *LS* $[\text{Fe}(\text{L}^{pyridine})_3]^{2+}$ (right) using corrected $\mathbf{M} + \mathbf{L}_6$ (**5b** for NOCV), is consistent with the former being *SCO* active and the latter remaining *LS*.

3.5. Conclusions

In this study we aimed to provide new insights into the details of the nature of **M-L** bonds. To do so, *EDA-NOCV* has been employed. First a range of fragmentations of the complexes was considered, starting from the usual literature fragmentation used (loss of one ligand). That, and the related fragmentations (loss of pairs of ligands) were found to be unsatisfactory, and also lacked generality, i.e., the potential to be used for any complex regardless of ligand type or charge. Hence a protocol that enables robust and general *EDA-NOCV* analysis of any coordination complex, by fragmentation into $\mathbf{M}^{n+} + \mathbf{L}_6$, has been developed.

A family of *SCO*-active Fe^{II} complexes, $[\text{Fe}(\mathbf{L}^{\text{azine}})_2(\text{NCBH}_3)_2]$, was chosen as the test system for this study as the experimentally observed solution switching temperatures ($T_{1/2}$) provided the order of $\mathbf{L}^{\text{azine}}$ ligand field strengths. Also, the chance to work on both spin states, diamagnetic *LS* and paramagnetic *HS*, enabled us to increase the number of reports of *EDA-NOCV* analysis of paramagnetic transition metal complexes from three²³³⁻²³⁵ to four and, above all, to critically tackle this class of systems in depth for the first time. Moreover, this work is also the first to focus on *SCO*-active complexes.

Regardless of whether the *LS* or *HS* family of $[\text{Fe}(\mathbf{L}^{\text{azine}})_2(\text{NCBH}_3)_2]$ complexes were examined by *EDA-NOCV*, the analysis identified a good correlation (R^2 : *LS* 0.99; *HS* 0.95) between decreasing $T_{1/2}$ and increasing ligand field strength as quantified by the $\Delta E_{\text{orb},\sigma+\pi}$ term. In addition, comparison of the results for $[\text{Fe}(\mathbf{L}^{\text{azine}})_2(\text{NCBH}_3)_2]$ with those subsequently obtained on the *LS* $[\text{Fe}(\mathbf{L}^{\text{azine}})_3(\text{BF}_4)_2]$ complexes revealed that only the corrected $\mathbf{M}^{n+} + \mathbf{L}_6$ fragmentation provides a general protocol suitable for comparing different types of complexes.

In conclusion, the *EDA-NOCV* protocol developed herein employs a new and general fragmentation type ($\mathbf{M}^{n+} + \mathbf{L}_6$) which provides a clear and quantitative description of the **M-L** bonds in these *paramagnetic* and

diamagnetic transition metal complexes. This protocol should be widely applicable, a point we are currently testing further, in order to prove it is general and hence has great promise as predictive tool. It should be noted that the above analysis neglects any entropic contributions, which are known to be key in *SCO*, so the next big step in the development of this approach will be the understanding of how the inclusion of computed entropic contributions can be included so that the unbiased determination of the $T_{1/2}$ values on the basis of the *EDA* values will be possible.

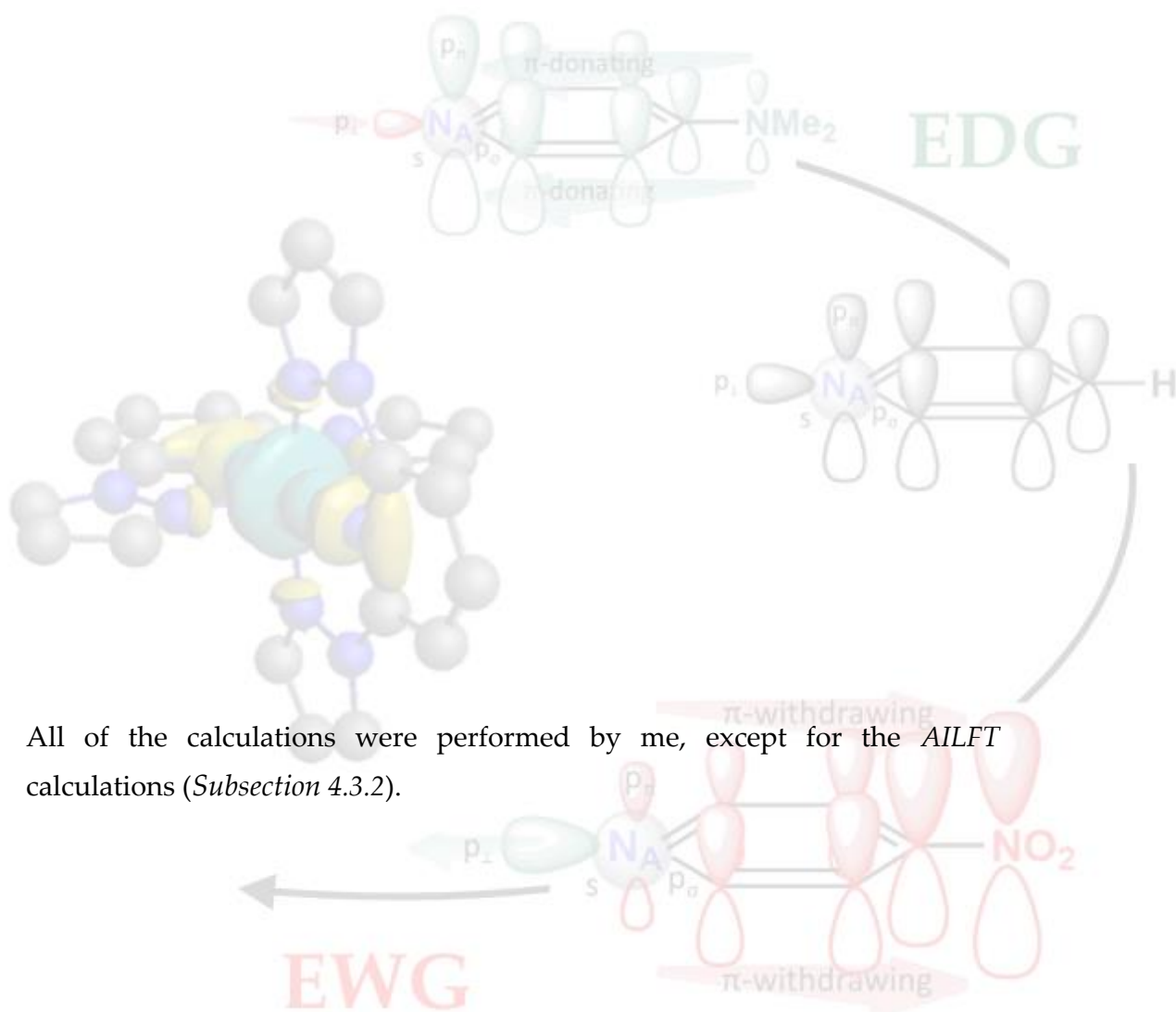
3.6. Computational Protocol

As a first step, accurate structures for these five $[\text{Fe}^{\text{II}}(\text{L}^{\text{azine}})_2(\text{NCBH}_3)_2]$ complexes in both the low-spin (*LS*) and high-spin (*HS*) states are required, so *DFT* structure optimisations of the complexes were performed with the ORCA 4.1 software package.²⁵⁸ After testing several computational features (details in *Appendix A3: Subsection A3.1.1*, Table A3.1-A3.3 and Figures A3.2-A3.9), the level of theory with the best overall performance was identified to be RI-BP86-D3(BJ)/def2-TZVPP+CPCM(CHCl_3).²⁵⁹⁻²⁶⁷ i.e. usage of the BP86 functional²⁶³⁻²⁶⁴ together with the resolution of identity (RI) approximation,²⁶⁶⁻²⁶⁷ Grimme's D3 dispersion correction (including BJ damping),²⁵⁹⁻²⁶⁰ a def2-TZVPP basis set²⁶¹ and implicit CPCM-solvent model.²⁶⁵

Using this protocol all of the calculated structures, for both the *LS* and *HS* complexes, are in good agreement with the available experimental X-ray crystallographic data for the *LS* and *HS* states of the $[\text{Fe}^{\text{II}}(\text{L}^{\text{pyridine}})_2(\text{NCBH}_3)_2]$ complex,¹⁰⁵ (Table A3.3). The $[\text{Fe}^{\text{II}}(\text{L}^{\text{azine}})_3(\text{BF}_4)_2]$ complexes had been previously optimised using the same protocol.²⁵⁴ These sets of optimised structures were then used in single-point calculations for the subsequent *EDA-NOCV* analyses performed using the ADF program package (Version 2018.106) at the BP86-D3(BJ)/TZ2P level of theory.²⁶⁸⁻²⁶⁹ A detailed introduction to the *EDA-NOCV* model is presented in *Subsection 1.6.6*.



Quantitative Assessment of the Energetic Contribution on the M-L Interaction in Fe(II) 2,6-Di(Pyrazol-1-yl)Pyridine



4.1. Abstract

The effect of the *para*-substituent **X** on the electronic structure of a literature family of sixteen tridentate **bpp^X** ligands (**bpp^X** = 4-**X**-2,6-di(pyrazol-1-yl)-pyridine)) and the corresponding *solution* spin crossover (SCO) active [Fe(**bpp^X**)₂]²⁺ complexes is further investigated, with the aim of supplying further insights into the σ -donor and π -acceptor properties of the **bpp^X** ligand. Halcrow, Deeth *et al.* concluded their study on [Fe(**bpp^X**)₂]²⁺ by proposing the extremely good correlation of $T_{1/2}$ vs. $\sigma_p^+(\mathbf{X})$ ($R^2 = 0.92$) was due to the **EDG** \rightarrow **EWG** causing an increasing **M** \rightarrow **L** π -backdonation, which causes an increasing ligand field strength and a $T_{1/2}$ increase.

Herein, *AILFT* is employed to calculate Δ_o values for the sixteen *LS* [Fe(**bpp^X**)₂]²⁺ complexes, resulting in good correlations with the experimental $T_{1/2}$ ($R^2 = 0.78$) and with $\sigma_p^+(\mathbf{X})$ ($R^2 = 0.93$).

EDA-NOCV analysis of the sixteen *LS* [Fe(**bpp^X**)₂]²⁺ complexes revealed that neither $\Delta E_{orb,\sigma+\pi}$ ($R^2 = 0.48$) nor $\Delta E_{orb,\pi}$ ($R^2 = 0.31$) correlated with the experimental $T_{1/2}$ values, but that $\Delta E_{orb,\sigma}$ correlates well ($R^2 = 0.82$). This implies that as **EDG** \rightarrow **EWG**, somehow the ligand field is becoming a better σ -donor and that this is causing the increasing ligand field strength and $T_{1/2}$. This is counter-intuitive and contrasts with the finding for *Lazine* ($T_{1/2}$ vs. $\Delta E_{orb,\pi}$; $R^2 = 0.95$), and with the hypothesis of Deeth, Halcrow's *et al.* that **M** \rightarrow **L** π -backbonding is what dominates in this family.

But Mulliken charge analysis of the population of the ($\mathbf{N}_A(sp^2(Fe))$) involved in the Fe-N σ -bond *versus* the perpendicular $\mathbf{N}_A(p\pi)$ employed in the aromatic π -system of the ligand reveals that the electronic effects triggered by the **X** substituent as **EDG** \rightarrow **EWG** are felt in opposite ways. Whilst the electron population on $\mathbf{N}_A(p\pi)$ decreases, the electron population in $\mathbf{N}_A(sp^2(Fe))$ increasing, leading to a stronger σ -bond and increasing the $T_{1/2}$ as observed. Finally, correlations identified in this study have been used to estimate the value of σ_p^+ for two **X** substituents, **SOMe** (0.26) and **SO₂Me** (0.60), not available in literature.

4.2. Introduction

Predictable fine tuning of the electronic structure of metal complexes is highly desirable, not least in order to optimise them for use in practical applications, such as molecular electronics,⁴⁸⁻⁵⁰ emissive devices,⁵¹⁻⁵³ catalysis¹⁹⁴ or photovoltaics.²⁷⁰ The choice of substituent (in this study, **X** for *para* and **Y** for *meta* substituents) present in a 5- or 6-membered aromatic ring is an important and frequently employed tool for fine-tuning the electronic structure of *organic* and *inorganic* metal compounds.

Substituent effects are commonly parametrised using the Hammett constant, which encompasses two different electronic effects: (a) *inductive effects* (through σ -bonds) and (b) *resonance effects* (through π -bonds).¹²⁴ Hammett parameters for *para*-**X** substituents, $\sigma_p^+(\mathbf{X})$, range from those for very Electron Donating Groups (**EDG**, **X** = **NMe₂**, $\sigma_p^+ = -1.70$) to those for very Electron Withdrawing Groups (**EWG**, **X** = **NO₂**, $\sigma_p^+ = 0.70$); whereas for *meta*-**Y** substituents $\sigma_m^+(\mathbf{Y})$ a much narrower range is observed: **EDG** (**X** = **Me**, $\sigma_p^+ = -0.07$) to **EWG** (**X** = **NO₂**, $\sigma_p^+ = 0.52$) (see also *Subsection 1.4.1*).^{125, 271}

Many studies have tried, with varying success, to rationalise how ligand substituent modifications affect the molecular orbital (*MO*) energies, redox potentials, spin crossover switching temperatures ($T_{1/2}$, as the temperature whereas 50:50 ratio between *HS:LS*), etc.

Herein the focus is on the use of **X** to modify the $T_{1/2}$ of spin crossover active (*SCO*) metal complexes.^{22-23, 83, 89, 133, 159, 272-276} *SCO* occurs when the metal ion **M** (usually $3d^4$ to $3d^7$ electronic configuration in octahedral geometry) can be switched between the high spin (*HS*) and low spin (*LS*) states through a trigger stimulus as temperature, pressure, host-guest interaction, external magnetic field or light irradiation (*Section 1.2*).^{7, 30, 250-251, 253, 277-279} Systems showing thermal *SCO* in the solution phase are particularly suitable candidates for monitoring the **X** (or **Y**) effects on the **M-L** bond, as they are not complicated by the effects of crystal packing or solvatomorphs,²⁸⁰ so variations in the ligand field strength, due to **X** (or **Y**) substituent, are more clearly observed^{22-24, 83} than in the solid state *SCO*.¹²⁶⁻

¹³² For thermal SCO, the switching temperature $T_{1/2}$ is measured in order to monitor these variations.^{23, 83, 133} The most complete study on the effects of *para*-**X** (and *meta*-**Y**) on *solution* SCO reported to date was carried out by Deeth, Halcrow *et al.* in 2017²³ on the large family of $[\text{Fe}^{\text{II}}(\text{bpp}^{\text{X,Y}})_2]^{2+}$ complexes ($\text{bpp}^{\text{X,Y}} = 4\text{-X-2,6-di(pyrazol-3-Y-1-yl)-pyridine}$, Figure 4.1), prepared by various authors across the years (See also *Subsections 1.4.3* and *1.6.3*).^{107, 132, 134-137} Follow up studies were published by them in 2018⁸⁹ and 2019,²⁸⁰ but with a smaller impact than the most relevant 2017 study.²³ In 2017,²³ they set a milestone in explaining the effects of changing a *para* **X** substituent on the pyridyl ring or a *meta* **Y**-substituent on the pyrazolyl rings of the $\text{bpp}^{\text{X,Y}}$ ligand on the $T_{1/2}$ of the complex in solution (Figures 1.12-1.22). Firstly, they found a strong $\sigma_{\text{p}}^+(\text{X})$ vs. $T_{1/2}$ correlation ($R^2 = 0.92$) and a weaker $\sigma_{\text{m}}(\text{Y})$ vs. $T_{1/2}$ correlation ($R^2 = 0.61$). Secondly, they found that the ΔE_{HL} gap correlated strongly with $\sigma_{\text{p}}^+(\text{X})$ ($R^2 = 0.89$) and less strongly with $\sigma_{\text{m}}(\text{Y})$ ($R^2 = 0.67$) (Figure 1.25).²³ Thirdly, they found that the Hammett parameter $\sigma_{\text{p}}^+/\sigma_{\text{m}}$ correlated the $E(t_{2g})$ and $E(e_g)$ energy levels calculated with DFT for LS $[\text{Fe}^{\text{II}}(\text{bpp}^{\text{X,Y}})_2]^{2+}$ (Figure 1.12) ($\sigma_{\text{p}}^+(\text{X})$: $E(t_{2g})$, $R^2 = 0.94$ and $E(e_g)$, $R^2 = 0.93$; $\sigma_{\text{m}}(\text{Y})$: $E(t_{2g})$, $R^2 = 0.99$ and $E(e_g)$, $R^2 = 0.98$). They concluded, through close examination of the effects of EDG \rightarrow EWG substituents on $E(t_{2g})$ and $E(e_g)$, that Fe \rightarrow N π -back bonding effects dominate for **X** (*para*) substituents as this strengthens the ligand field strength and increases $T_{1/2}$, whereas the Fe \leftarrow N σ -bonding effects dominate for **Y** (*meta*) substituents, causing the opposite effect, decreasing the ligand field strength and the $T_{1/2}$ (more details in *Subsections 1.4.3* and *1.6.3*).^{23, 138}

The present study was motivated by the above findings and by the promise shown in our first use of EDA-NOCV theory – which is combination of EDA model (Energy Decomposition Analysis),^{175, 185} with NOCV model (Natural Orbitals for Chemical Valence)¹⁸⁶⁻¹⁸⁷ (introduced in *Subsection 1.6.7*) – on a *solution* SCO system, specifically on a family of five $[\text{Fe}^{\text{II}}(\text{L}^{\text{azine}})_2(\text{NCBH}_3)_2]$ (*Chapter Three*).⁹¹ The latter study established (i) a computational protocol for evaluating **M-L** bond strength in any kind of metal complex (*diamagnetic* or *paramagnetic*) and (ii) a strong correlation

between the $\Delta E_{orb,\sigma+\pi}$ term for the family of five $[\text{Fe}^{\text{II}}(\text{L}^{\text{azine}})_2(\text{NCBH}_3)_2]$ complexes with the experimental $T_{1/2}$ for SCO in solution ($R^2 = 0.99$).⁹¹

In this study, sixteen of the available *para*-**X** substituted $[\text{Fe}(\text{bpp}^{\text{X}})_2]^{2+}$ complexes are studied using AILFT and EDA-NOCV in order to (a) determine Δ_o , (b) determine the relative importance of the σ - and π -contributions to the M-L bonds and (c) use the observed correlations to predict the Hammett parameter σ_p^+ for the two substituents **X** for which it is not available in literature (**X** = **SOMe** or **SO₂Me**).

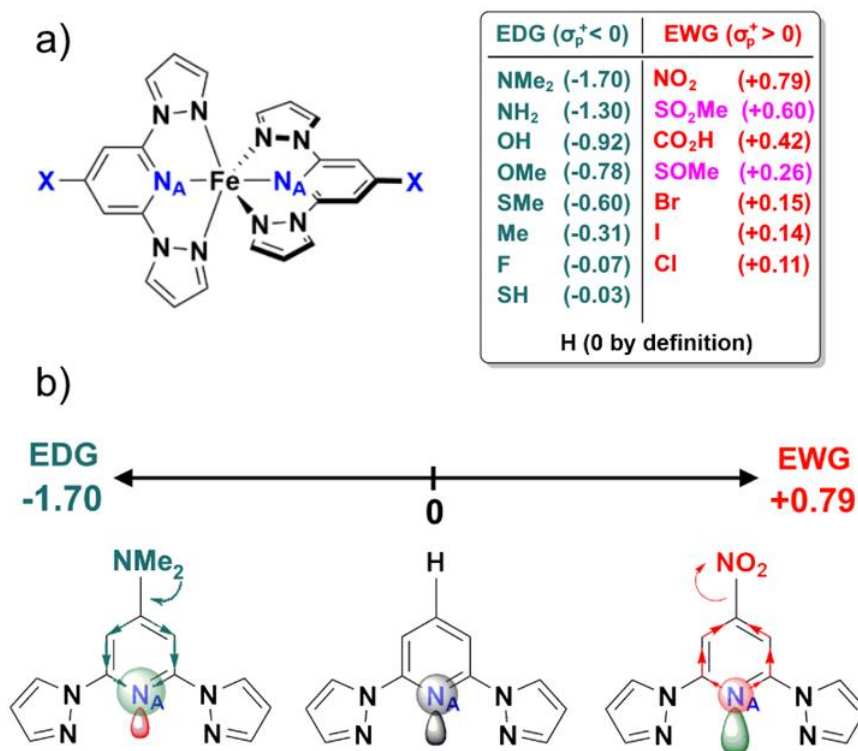


Figure 4.1. Representations of (a) the members of the $\text{Fe}(\text{bpp}^{\text{X}})_2^{2+}$ family studied herein; (b & c) electrostatic effects on the pyridine nitrogen donor atom, N_A , by either (b) electron donating group (EDG) or (c) electron withdrawing group (EWG) substituent (σ_p^+) in $\text{Fe}(\text{bpp}^{\text{X}})_2^{2+}$. Pink text for the two **X** for which σ_p^+ is not known but is estimated from the correlations presented herein (Subsection 4.3.7, Table A4.14).

4.3. Results and Discussion

4.3.1. DFT optimisation of $[\text{Fe}(\text{bpp}^{\text{X}})_2]^{2+}$ (*LS* and *HS*)

The computational protocol employed for the sixteen *LS* and sixteen *HS* $[\text{Fe}^{\text{II}}(\text{bpp}^{\text{X}})_2]^{2+}$ complexes was chosen based on the functional screen performed previously by Brooker *et al.* (as described in *Chapter Three*).⁹¹ The same computational protocol was applied to all of the candidates, in the same CPCM solvent, acetone, albeit the *LS* forms of the $\text{X} = \text{NMe}_2$ or NH_2 complexes are not observed experimentally. Calculating Root-Mean-Square-Deviation (*RMSD*) of each atomic position (Equation A4.1) confirmed that the variation of the *para*-substituent X in the bpp^{X} ligands causes no significant deviations of these structures from that of the respective *LS* or *HS* parent complex $[\text{Fe}(\text{bpp}^{\text{H}})_2]^{2+}$ (*RMSD* < 0.01 Å in all cases, Table A4.1).

The six out of the sixteen $[\text{Fe}(\text{bpp}^{\text{X}})_2]^{2+}$ complexes where the experimental $T_{1/2}$ values were measured in nitromethane solvent (Table A4.1) were subjected to a new geometry optimisation process, and then to an *RMSD* evaluation between the final geometries calculated in acetone *vs* nitromethane. Again, the *RMSD* for each atomic position confirmed that, as expected, changing the dielectric constant in the CPCM model,²⁸¹ from acetone to nitromethane, has a negligible effect on the optimised structures obtained in these two different solvents (*RMSD* < 0.01 Å in all cases, Table A4.1).

4.3.2. AILFT Analysis Effect of X on Δ_o for LS $[\text{Fe}(\text{bpp}^{\text{X}})_2]^{2+}$

The octahedral ligand field splitting energy (Δ_o) was calculated using Ab-Initio Ligand Field Theory (AILFT), as reported in *Subsection 1.6.1* and *Section 4.6*, for the sixteen LS $[\text{Fe}(\text{bpp}^{\text{X}})_2]^{2+}$ complexes, by our collaborator Paul Jerabek (Helmholz-Geesthacht, Germany), to observe the variation in Δ_o as X is varied. As expected, the calculated value of Δ_o increases as the experimental $T_{1/2}$ of the $[\text{Fe}(\text{bpp}^{\text{X}})_2]^{2+}$ complexes increases. Indeed, a good $T_{1/2}$ vs. Δ_o correlation ($R^2 = 0.78$) is observed (blue dotted line, Figure 4.2).

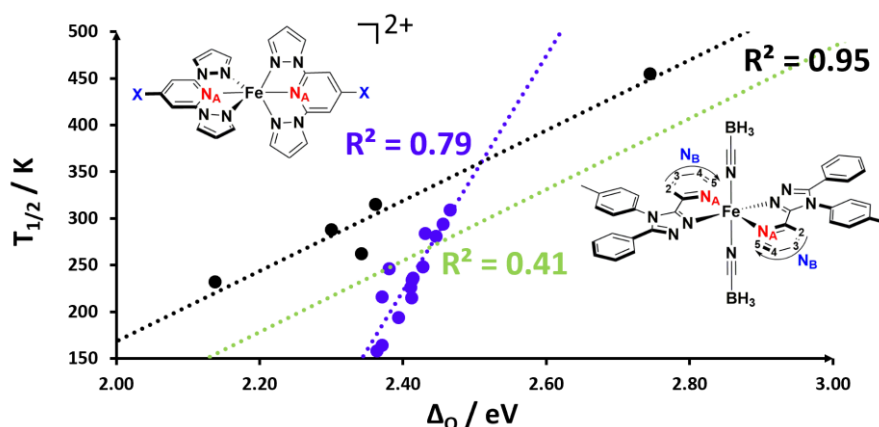


Figure 4.2. Observed correlation of the experimental $T_{1/2}$ vs. the calculated Δ_o (using AILFT) for the fourteen LS $[\text{Fe}(\text{bpp}^{\text{X}})_2]^{2+}$ complexes (blue, $R^2 = 0.78$; X = NH_2 , NMe_2 are absent) and the five LS $[\text{Fe}^{\text{II}}(\text{L}^{\text{azine}})_2(\text{NCBH}_3)_2]$ complexes (black, $R^2 = 0.95$) and for all the nineteen complexes (green, $R^2 = 0.41$; X = NH_2 , NMe_2 are absent). $1 \text{ eV} = 23 \text{ kcal/mol} = 8100 \text{ cm}^{-1}$.

For comparison, AILFT was also used to calculate Δ_o for the family of five LS $[\text{Fe}^{\text{II}}(\text{L}^{\text{azine}})_2(\text{NCBH}_3)_2]$ complexes,^{83, 91} and these also correlated strongly with $T_{1/2}$ ($R^2 = 0.95$, black dotted line, Figure 4.2). So, the calculated Δ_o values represent a solid and reliable assessment of the relative size of the experimental $e_g - t_{2g}$ gap (*Subsection 1.6.2*) and hence expected *solution* $T_{1/2}$ order. This easy – albeit rather simplistic – interpretation of Δ_o as the only key parameter for *solution* SCO is expected to lead to a shared correlation

line for $T_{1/2}$ vs. Δ_o , regardless the family. But this is not observed (Figure 4.2, green dotted line, $R^2 = 0.41$); rather, the $\text{Fe}(\text{bpp}^{\text{X}})_2^{2+}$ family ($R^2 = 0.78$) lies on a different correlation line to that of the $[\text{Fe}^{\text{II}}(\text{L}^{\text{azine}})_2(\text{NCBH}_3)_2]$ family ($R^2 = 0.95$). Very likely, the different entropic effects associated with the different classes of ligands employed (coordination pocket, charge) are responsible for the different correlation lines (and so the different sensitivities of the iron(II) complex to the electronic effects of X).

As well, an excellent correlation is observed between Δ_o and $\sigma_{\text{p}}^+(\text{X})$ ($R^2 = 0.93$, Figure 4.3): from **EDG** \rightarrow **EWG**, the $t_{2g-e.g.}$ gap gets bigger and the Δ_o gets bigger – further confirming the above results.

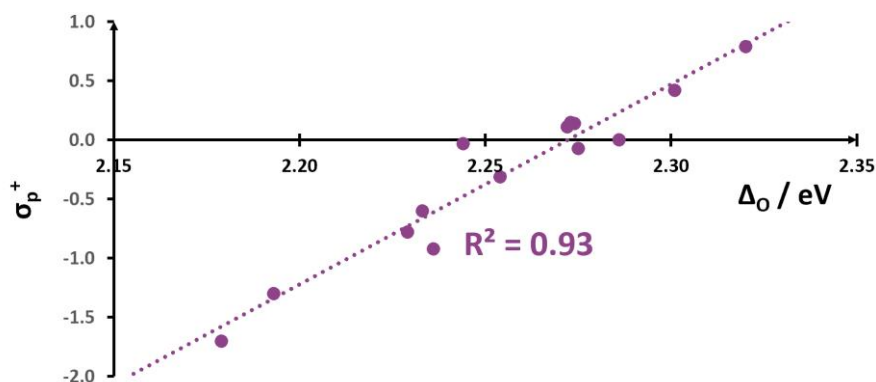


Figure 4.3. Extremely good correlation ($R^2 = 0.93$) of the Hammett parameter $\sigma_{\text{p}}^+(\text{X})$ with the Δ_o calculated for the sixteen LS $[\text{Fe}(\text{bpp}^{\text{X}})_2]^{2+}$ complexes using ALLFT,¹⁴⁵ following procedure reported in Subsection 1.6.1 ($\text{X} = \text{SOMe}, \text{SO}_2\text{Me}$ are absent, Table A4.8). $1 \text{ eV} = 23 \text{ kcal/mol} = 8100 \text{ cm}^{-1}$.

4.3.3. EDA Analysis of Effects of X in $[\text{Fe}(\text{bpp}^{\text{X}})_2]^{2+}$ (LS and HS)

EDA (Energy Decomposition Analysis)^{175, 185} – using fragmentation **5e** ($\text{M}+\text{L}_6$) in Figure 3.2⁹¹ – was applied to the sixteen HS and sixteen LS $[\text{Fe}^{\text{II}}(\text{bpp}^{\text{X}})_2]^{2+}$ complexes (Figure A4.1). This quantified the overall interaction energy, ΔE_{int} , which accounts for the strength of the grip applied by the coordination sphere on the iron(II) centre. The ΔE_{int} contribution for HS was half that for LS $[\text{Fe}^{\text{II}}(\text{bpp}^{\text{X}})_2]^{2+}$ complexes (Table 4.1). This is

consistent with the *HS* state being less enthalpically stable than the *LS* state; note these results are obtained at absolute zero. Furthermore, as σ_{p^+} increases (EDG \rightarrow EWG, $\text{NMe}_2 \rightarrow \text{NO}_2$), the stabilising energy ΔE_{int} drops by about 50 kcal/mol in all cases, from about -250 to -200 kcal/mol for the *LS* complexes ($\text{NMe}_2 \rightarrow \text{NO}_2$) and from -120 to -70 kcal/mol ($\text{NMe}_2 \rightarrow \text{NO}_2$) for the *HS* complexes (Figure 4.4 and Table 4.1 and A4.1; details in Subsection 1.6.7).

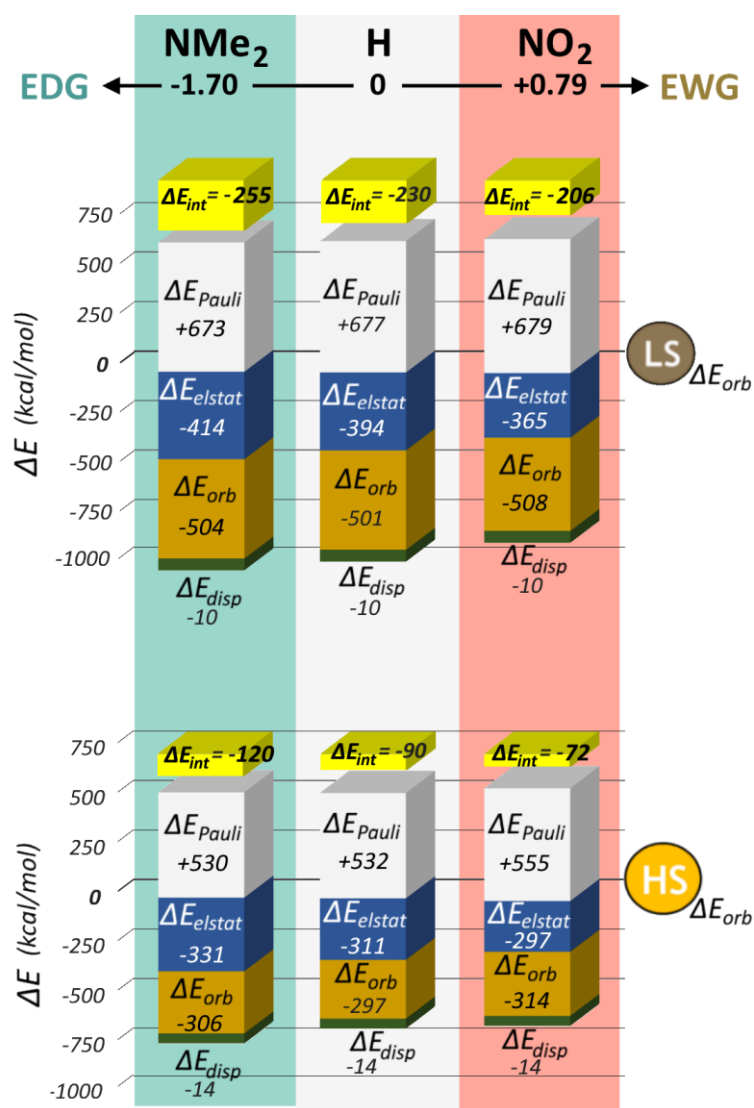


Figure 4.4. Results of EDA analysis for LS (top) vs HS (bottom) $[\text{Fe}(\text{bpp}^{\text{H}})_2]^{2+}$ using fragmentation 5e. For each spin state the bar graphs show the four components of ΔE_{int} (Subsection 1.6.6) and the sum of them (ΔE_{int} , yellow). Energies are in kcal/mol. $1 \text{ eV} = 23 \text{ kcal/mol} = 8100 \text{ cm}^{-1}$.

Table 4.1. EDA-NOCV results (using fragmentation **5e**, Section 3.3) for the sixteen LS and HS $[\text{Fe}(\text{bpp}^{\text{X}})_2]^{2+}$ complexes: all energies are reported in kcal/mol. Results are presented in order of increasing Hammett parameter (σ_{p^+}). * values estimated in Subsection 4.3.7.

X	$T_{1/2}$	σ_{p^+}	State	ΔE_{int}	ΔE_{elstat}	ΔE_{orb}
NMe₂	<i>HS</i>	-1.70	<i>LS</i>	-255.0	-413.8	-305.5
			<i>HS</i>	-120.1	-330.6	-503.9
NH₂	<i>HS</i>	-1.30	<i>LS</i>	-246.7	-409.4	-309.1
			<i>HS</i>	-113.0	-338.2	-409.4
OH	164	-0.92	<i>LS</i>	-232.0	-396.2	-307.7
			<i>HS</i>	-98.1	-325.0	-499.5
OMe	158	-0.78	<i>LS</i>	-238.9	-401.2	-310.6
			<i>HS</i>	-104.0	-328.7	-501.6
SMe	194	-0.60	<i>LS</i>	-239.6	-397.1	-310.6
			<i>HS</i>	-104.4	-326.5	-507.0
Me	216	-0.31	<i>LS</i>	-235.6	-397.9	-306.7
			<i>HS</i>	-101.5	-314.3	-502.8
F	215	-0.31	<i>LS</i>	-219.5	-385.0	-296.9
			<i>HS</i>	-83.0	-302.9	-499.3
SH	246	-0.03	<i>LS</i>	-231.6	-390.7	-314.0
			<i>HS</i>	-98.5	-320.1	-505.6
H	248	0.00	<i>LS</i>	-229.1	-393.7	-296.6
			<i>HS</i>	-89.9	-310.7	-501.3
Cl	226	+0.11	<i>LS</i>	-221.7	-383.1	-311.8
			<i>HS</i>	-88.2	-312.4	-504.0
I	236	+0.14	<i>LS</i>	-224.5	-382.5	-304.1
			<i>HS</i>	-86.9	-300.5	-508.4
Br	234	+0.15	<i>LS</i>	-222.9	-383.1	-301.8
			<i>HS</i>	-85.5	-301.1	-505.6
CO₂H	281	+0.42	<i>LS</i>	-223.7	-383.4	-314.2
			<i>HS</i>	-89.0	-313.2	-508.3
NO₂	309	+0.79	<i>LS</i>	-205.7	-365.4	-508.7
			<i>HS</i>	-71.6	-296.6	-314.9
SOMe*	284	+0.26*	<i>LS</i>	-224.4	-368.0	-515.0
			<i>HS</i>	-81.0	-300.8	-305.5
SO₂Me*	294	+0.60*	<i>LS</i>	-215.4	-359.1	-515.8
			<i>HS</i>	-90.1	-303.2	-314.8

In the detailed analysis of the various energetic contributions to the ΔE_{int} term, the ΔE_{elstat} term – which accounts for the *ionic* bonding between the fragments (details in *Subsection 1.6.7*) – is observed to correlate well with $\sigma_p^+(\mathbf{X})$ for *LS* $[\text{Fe}^{\text{II}}(\mathbf{bpp}^{\mathbf{X}})_2]^{2+}$ ($R^2 = 0.89$, Table A4.3, Figure A4.2) and moderately well for *HS* $[\text{Fe}^{\text{II}}(\mathbf{bpp}^{\mathbf{X}})_2]^{2+}$ ($R^2 = 0.73$, Table A4.4 and Figure A4.3). In both cases, this behaviour can be understood as follows: as \mathbf{X} becomes more electron poor (σ_p^+ increases) it drains more electron density away from the coordinating nitrogen (Figure 4.1), decreasing the favourable electrostatic interactions with the Fe^{2+} ion (Tables A4.3-A4.4). From $\mathbf{X} = \text{NMe}_2$ to $\mathbf{X} = \text{NO}_2$, ΔE_{elstat} decreases by just -60 kcal/mol (+15%) in the *LS* $[\text{Fe}^{\text{II}}(\mathbf{bpp}^{\mathbf{X}})_2]^{2+}$ and decreasing by just -35 kcal/mol (+12%) in the *HS* $[\text{Fe}^{\text{II}}(\mathbf{bpp}^{\mathbf{X}})_2]^{2+}$ complexes. In contrast, the ΔE_{orb} interaction – which accounts for the *covalent* bonding between the fragments (details in *Subsection 1.6.6*) – remains almost constant across the whole range of σ_p^+ values: from $\mathbf{X} = \text{NMe}_2$ to $\mathbf{X} = \text{NO}_2$, ΔE_{orb} increases by just +20 kcal/mol (+3.5%) in the *LS* $[\text{Fe}^{\text{II}}(\mathbf{bpp}^{\mathbf{X}})_2]^{2+}$ and decreasing by just -5 kcal/mol (-1.5%) in the *HS* $[\text{Fe}^{\text{II}}(\mathbf{bpp}^{\mathbf{X}})_2]^{2+}$ complexes.

Comparing these *EDA* results with those for the $[\text{Fe}^{\text{II}}(\mathbf{L}^{azine})_2(\text{NCBH}_3)_2]$ family ($\mathbf{L}^{azine} = 3\text{-(2-aziny1)-4-tolyl-5-phenyl-1,2,4-triazole}$; (*Chapter Three*, Table 4.2),⁹¹ the ΔE_{int} energies, that for the $[\text{Fe}^{\text{II}}(\mathbf{L}^{azine})_2(\text{NCBH}_3)_2]$ family are twice the size of those for the $[\text{Fe}^{\text{II}}(\mathbf{bpp}^{\mathbf{X}})_2]^{2+}$ family,⁹¹ but yet, the ΔE_{orb} values are almost the same (Table 4.2). The cause of the big difference in ΔE_{int} values is the big drop in magnitude for the ΔE_{elstat} term in the $[\text{Fe}^{\text{II}}(\mathbf{bpp}^{\mathbf{X}})_2]^{2+}$ family *vs* the $[\text{Fe}^{\text{II}}(\mathbf{L}^{azine})_2(\text{NCBH}_3)_2]$ family. This is due to the fact that the two BF_4^- (or two PF_6^-) anions are not directly bonded at the iron(II) ion in $[\text{Fe}^{\text{II}}(\mathbf{bpp}^{\mathbf{X}})_2]^{2+}$; whereas the two NCBH_3^- anions are directly bonded to the iron(II) ion in $[\text{Fe}^{\text{II}}(\mathbf{L}^{azine})_2(\text{NCBH}_3)_2]$ (Table 4.2).²³

Finally, it should be noted that the ratio between *ionic* and *covalent* contributions ($\Delta E_{elstat}:\Delta E_{orb}$ ratio) is important in describing the bonding between fragments.²⁷⁶ For the $[\text{Fe}(\mathbf{bpp}^{\text{H}})_2]^{2+}$ complex the *ionic:covalent* ratio becomes more *ionic* on going from *LS* (44:55) to *HS* (50:47). This is very

different from $[\text{Fe}(\text{L}^{\text{pyridine}})_2(\text{NCBH}_3)_2]$ complex where the *ionic* bonding is already dominating in the *LS* state ($\Delta E_{\text{elstat}}:\Delta E_{\text{orb}}$, 55:45), and this further increases in the *HS* state (65:35) (Table 4.2).

In conclusion, the *EDA* analysis showed to be already able to correctly catch in details the origin of the change in nature of the coordinative bond in the charged and neutral families.⁹¹

Table 4.2. Range of ΔE_{int} , ΔE_{elstat} and ΔE_{orb} values obtained from *EDA* analysis, in both *HS* and *LS* spin states (using fragmentation **5e**), of the sixteen $[\text{Fe}(\text{bpp}^{\text{x}})_2]^{2+}$ complexes, compared with those previously obtained for five $[\text{Fe}^{\text{II}}(\text{L}^{\text{azine}})_2(\text{NCBH}_3)_2]$ complexes:⁹¹ all energies are reported in kcal/mol. 1 eV = 23 kcal/mol = 8100 cm⁻¹.

	State	ΔE_{int} (kcal/mol)	ΔE_{elstat} (kcal/mol)	ΔE_{orb} (kcal/mol)
$[\text{Fe}^{\text{II}}(\text{bpp}^{\text{x}})_2]^{2+}$	<i>LS</i>	-250 / -200	-415 / -365 (~45%)	-510 / -500 (~55%)
	<i>HS</i>	-120 / -70	-330 / -290 (~55%)	-315 / -295 (~45%)
$[\text{Fe}^{\text{II}}(\text{L}^{\text{azine}})_2(\text{NCBH}_3)_2]^{91}$	<i>LS</i>	-530 / -500	-635 / -620 (~55%)	-520 / -500 (~45%)
	<i>HS</i>	-385 / -370	-585 / -570 (~65%)	-330 / -325 (~35%)
bpp^{H} vs $\text{L}^{\text{pyridine}}$	<i>LS</i>	-53% / -60%	-35%	-0.5%
	<i>HS</i>	-59% / -81%	-40%	-5%

4.3.4. NOCV Analysis of the effects of X vs σ - and π - Bonding Terms of $[\text{Fe}(\text{bpp}^{\text{X}})_2]^{2+}$ (LS and HS)

The full EDA-NOCV results obtained using fragmentation **5b** (Section 3.3)⁹¹ are reported in Tables A4.5-A4.6, with selected results shown and discussed in the following sections. From the breakdown of the ΔE_{orb} term, the nine **M+L₆** bonding interactions (described by Hoffman theory²¹) can be identified by visual inspection and *quantitatively* assessed (Figure A4.1): six σ - ($\Delta E_{\text{orb},\sigma}$), and three π -contributions ($\Delta E_{\text{orb},\pi}$) to the **ML₆** interactions are sought (Figure 4.5, Table 4.3 and A4.5; details in Subsection 1.6.6). For both spin states of the sixteen complexes the $\Delta E_{\text{orb},\sigma(s,p_x,p_y,p_z)}$ contribution remains constant as X varies (Table 4.2-4.3, Figures A4.7-A4.9).

For all sixteen LS $[\text{Fe}(\text{bpp}^{\text{X}})_2]^{2+}$ complexes, the six σ -bonds ($\Delta E_{\text{orb},\sigma}$) account for about 85% of the $\Delta E_{\text{orb},\sigma+\pi}$ contribution to **M-L** bonding, leaving only 15% of the stabilisation energy to come from the three π -bonds. The same is observed for all sixteen HS $[\text{Fe}(\text{bpp}^{\text{X}})_2]^{2+}$ complexes ($\Delta E_{\text{orb},\sigma}:\Delta E_{\text{orb},\pi} = 85:15$; Tables 4.3 and A4.6-A4.7).

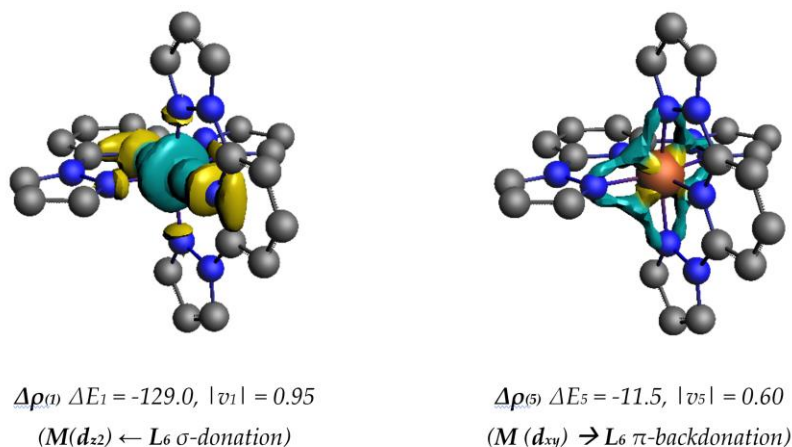


Figure 4.5. Plot of the deformation densities $\Delta\rho(i)$ (Subsections A4.1.2-A4.1.3) with corresponding energy contribution to the total orbital term ΔE_i (given in kcal/mol) of the $\text{M}(\text{d}_{z^2}) \leftarrow \text{L}_6 \sigma\text{-donation}$ (right), the $\text{M}(\text{d}_{xy}) \rightarrow \text{L}_6 \pi\text{-backdonation}$ (right) in the LS $[\text{Fe}(\text{bpp}^{\text{H}})_2]^{2+}$ complexes. The direction of the charge flow is yellow \rightarrow turquoise. The eigenvalues $|v_i|$ indicate the relative size of the charge flow (reported values for $|v_i| > 0.1$; $\rho < 0.003$).

In the *LS* state the overall σ -strength is mostly due to the two $\mathbf{M} \leftarrow \mathbf{L}$ σ -bonds formed by the Fe^{2+} d_{z^2} and $d_{x^2-y^2}$ orbitals ($\Delta E_{(i)} < -100$ kcal/mol; $v_i > 0.90$; Figure 4.5(left) and Figures A4.4-A4.6). In *MO* picture, such interaction corresponds only to the σ bonding $\mathbf{M} \leftarrow \mathbf{L}$ interactions where \mathbf{L} character is predominant, whereas the σ^* anti-bonding interaction, where the Fe^{2+} d_{z^2} and $d_{x^2-y^2}$ character is now dominant, are empty. In the sixteen *HS* $[\text{Fe}(\text{bpp}^{\text{X}})_2]^{2+}$ complexes – where these two *e.g.*, anti-bonding orbitals are half-occupied, not empty – the $\Delta E_{\text{orb},\sigma}$ stabilisation energy drops by 55% relative to the analogous *LS* state complex (Tables 4.3 and A4.6-A4.7).

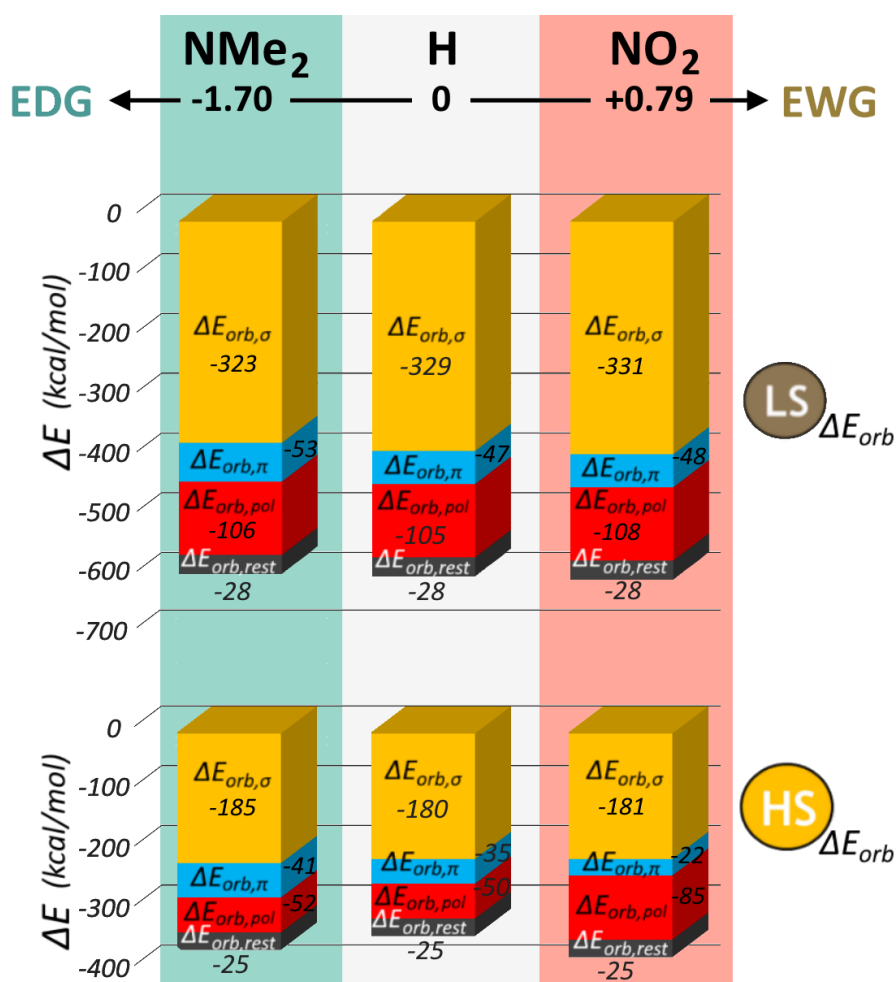


Figure 4.6. Results of NOCV decomposition of ΔE_{orb} for *LS* (top) vs *HS* (bottom) $[\text{Fe}(\text{bpp}^{\text{H}})_2]^{2+}$ using fragmentation **5b**. For each spin state the bar graph shows the four components of ΔE_{orb} (Subsection 1.6.6). Energies are in kcal/mol.

In comparison, in the *LS* [Fe(*L^{azine}*)₂(NCBH₃)₂] complexes the six σ -bonds ($\Delta E_{orb,\sigma}$) account for even more, about 92%, of the $\Delta E_{orb,\sigma+\pi}$, the only exception for *L^{azine}* = *L^{pyrdt}* were the σ -contribution drops to 84%; this is very likely due to a mixing between the σ - and π - contribution, Table A3.21. As well, in *HS* [Fe(*L^{azine}*)₂(NCBH₃)₂] complexes an even more inhomogeneity between $\Delta E_{orb,\sigma}$ and $\Delta E_{orb,\pi}$ is observed ($\Delta E_{orb,\sigma}:\Delta E_{orb,\pi} = 98:2$). The three π -acceptor **M**→**L** bonds are composed by two stronger degenerate π -bonds involving the iron(II) d_{xz}/d_{yz} orbitals (Figures A4.4-A4.6), and a weaker π -bond involving the iron(II) d_{xy} orbital (Figures A4.4-A4.6). For *LS* [Fe(**bpp^x**)₂]²⁺, these three π (**M** → **L₆**) interactions (slightly bonding *MOs*) contribute -47 kcal/mol. For *HS* [Fe(**bpp^x**)₂]²⁺ these three π (**M** → **L₆**) bonds contribute only -25 kcal/mol due to the *SCO* from *LS* → *HS* reducing the population of the *t_{2g}*-like orbitals, which reduces the π -backdonation. Overall, on *LS* → *HS*, stabilisation by $\Delta E_{orb,\pi}$ drops by about 40% and the overall $\Delta E_{orb,\sigma+\pi}$ it drops by about 50%. In comparison, for the [Fe(*L^{azine}*)₂(NCBH₃)₂] complexes the $\Delta E_{orb,\sigma}$ term drops by about 50%, $\Delta E_{orb,\pi}$ drops by about 90%, and the overall $\Delta E_{orb,\sigma+\pi}$ drops by about 60%.

Table 4.3. EDA-NOCV results (using fragmentation **5b**, Section 3.3) for the sixteen LS and HS $[\text{Fe}(\text{bpp}^{\text{x}})_2]^{2+}$ complexes: all energies are reported in kcal/mol. Results are presented in order of increasing Hammett parameter (σ_{p^+}). * values estimated in Subsection 4.3.7.

X	$T_{1/2}$	σ_{p^+}	State	$\Delta E_{\text{orb},\sigma+\pi}$	$\Delta E_{\text{orb},\sigma}$	$\Delta E_{\text{orb},\pi}$
NMe₂	<i>HS</i>	-1.70	<i>LS</i>	-378.5	-323.2	-52.5
			<i>HS</i>	-167.7	-142.1	-25.5
NH₂	<i>HS</i>	-1.30	<i>LS</i>	-374.8	-324.6	-50.1
			<i>HS</i>	-161.9	-135.8	-26.0
OH	164	-0.92	<i>LS</i>	-374.6	-325.9	-48.4
			<i>HS</i>	-168.9	-145.6	-23.3
OMe	158	-0.78	<i>LS</i>	-376.1	-326.4	-49.6
			<i>HS</i>	-156.3	-130.9	-25.3
SMe	194	-0.60	<i>LS</i>	-378.5	-326.1	-52.4
			<i>HS</i>	-165.9	-141.7	-24.1
Me	216	-0.31	<i>LS</i>	-376.2	-327.7	-48.2
			<i>HS</i>	-170.6	-147.4	-23.1
F	215	-0.31	<i>LS</i>	-374.4	-326.7	-48.5
			<i>HS</i>	-169.2	-142.4	-26.7
SH	246	-0.03	<i>LS</i>	-378.6	-327.6	-51.0
			<i>HS</i>	-170.2	-145.9	-24.3
H	248	0.00	<i>LS</i>	-376.0	-328.7	-47.3
			<i>HS</i>	-168.9	-142.3	-26.6
Cl	226	+0.11	<i>LS</i>	-376.9	-327.9	-49.0
			<i>HS</i>	-169.1	-145.7	-23.3
I	236	+0.14	<i>LS</i>	378.9	-328.5	-50.4
			<i>HS</i>	-169.7	-142.8	-26.8
Br	234	+0.15	<i>LS</i>	-377.6	-327.9	-49.6
			<i>HS</i>	-169.7	-142.9	-26.8
CO₂H	281	+0.42	<i>LS</i>	-379.7	-331.1	-48.5
			<i>HS</i>	-171.7	-148.3	-23.3
NO₂	309	+0.79	<i>LS</i>	-379.7	-331.8	-48.78
			<i>HS</i>	-171.5	-147.7	-23.7
SOMe*	284	+0.26*	<i>LS</i>	-375.8	-328.5	-49.7
			<i>HS</i>	-165.2	-142.5	-22.6
SO₂Me*	294	+0.60*	<i>LS</i>	-378.2	-330.3	-47.8
			<i>HS</i>	-170.1	-147.7	-22.9

4.3.5. Correlations of NOCV Results with $T_{1/2}$, σ_p^+ , δN and Δ_o

NOCV Results vs $T_{1/2}$

Deeth, Halcrow *et al.*²³ reported that as the Hammett constant $\sigma_p^+(\mathbf{X})$ increases, so too does the experimental $T_{1/2}$ for the *solution* SCO of $[\text{Fe}(\text{bpp}^{\mathbf{X}})_2]^{2+}$. Herein, EDA-NOCV analysis reveals that the increase of the switching temperature is in extremely good correlation with $\Delta E_{\text{orb},\sigma}$ for LS $[\text{Fe}(\text{bpp}^{\mathbf{X}})_2]^{2+}$ (Figure 4.7, red line, $R^2 = 0.82$ and Figure A4.8). On the other hand, $T_{1/2}$ does not correlate with $\Delta E_{\text{orb},\pi}$ ($R^2 = 0.09$ Figure A4.9), and only very weakly correlates with $\Delta E_{\text{orb},\sigma+\pi}$ ($R^2 = 0.48$ Figure A4.10). However, it should be recalled (see above) that $\Delta E_{\text{orb},\sigma}$ provides 85% of the overall bonding stabilisation ($\Delta E_{\text{orb},\sigma+\pi}$).

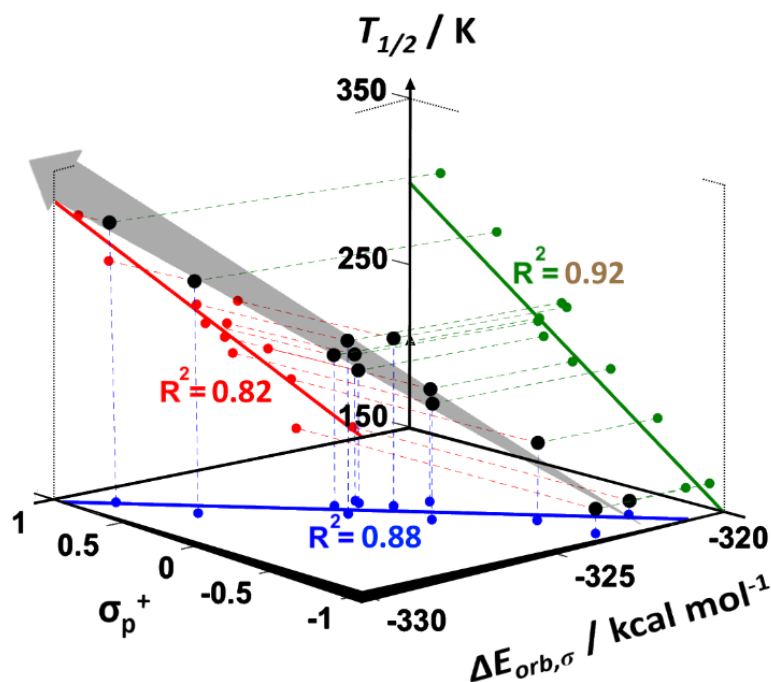


Figure 4.7. Three strong pairwise correlations (blue, red and green lines), and a cross-correlation (black dots; grey arrow is only a guide to the eye) between the ligand donation properties ($\Delta E_{\text{orb},\sigma}$; calculated by EDA-NOCV for the LS complexes using fragmentation **5b**), the Hammett constant $\sigma_p^+(\mathbf{X})$, and the switching temperature ($T_{1/2}$) for the twelve SCO-active complexes for which $\sigma_p^+(\mathbf{X})$ is known in this family of $[\text{Fe}(\text{bpp}^{\mathbf{X}})_2]^{2+}$ complexes ($\mathbf{X} = \text{SOMe}, \text{SO}_2\text{Me}, \text{NH}_2, \text{NMe}_2$ are absent, as $\sigma_p^+(\mathbf{X})$ is not known for the first two, and the last two remain HS).

In contrast, for the *HS* $[\text{Fe}(\mathbf{bpp}^{\mathbf{X}})_2]^{2+}$ complexes none of the $\Delta E_{orb,i}$ terms ($i = \sigma, \pi, \sigma+\pi$) shows promising correlations with the $T_{1/2}$ values: $\Delta E_{orb,\sigma}$ ($R^2 = 0.36$, Figure A4.17), $\Delta E_{orb,\pi}$ ($R^2 = 0.07$, Figure A4.18) and $\Delta E_{orb,\sigma+\pi}$ ($R^2 = 0.31$, Figure A4.19).

This is consistent with the *LS* state being the key spin state where it is possible to observe the electronic effect of \mathbf{X} on the bonding properties of the $[\text{Fe}(\mathbf{bpp}^{\mathbf{X}})_2]^{2+}$ complex through the correlations of $\Delta E_{orb,\sigma}$ versus $T_{1/2}$ (Figure 4.7, red line, $R^2 = 0.82$) and $\Delta E_{orb,\sigma}$ versus σ_{p^+} (Figure 4.7, blue line, $R^2 = 0.88$) and $T_{1/2}$ versus σ_{p^+} (Figure 4.7, green line, $R^2 = 0.92$).²³ The cross-correlations reported in Figure 4.7 explain from a molecular to macroscopic level the effect that the \mathbf{X} substituent has on the $[\text{Fe}(\mathbf{bpp}^{\mathbf{X}})_2]^{2+}$ complex. The finding that only $\Delta E_{orb,\sigma}$, not $\Delta E_{orb,\pi}$, correlates with $T_{1/2}$ is not consistent with the hypothesis by Deeth, Halcrow *et al.*²³ that $\mathbf{M} \rightarrow \mathbf{L}$ π -backbonding dominates the tuning by \mathbf{X} . This key issue is discussed further in the following pages, and is resolved in *Subsection 4.3.6*.

These results for the $[\text{Fe}(\mathbf{bpp}^{\mathbf{X}})_2]^{2+}$ complexes did not lead to the same conclusions as those observed in *Chapter Three* for the $[\text{Fe}(\mathbf{L}^{azine})_2(\text{NCBH}_3)_2]^{2+}$ family where a strong correlation was observed for $\Delta E_{orb,\sigma+\pi}$ vs. $T_{1/2}$ ($R^2 = 0.99$, Figure 3.7, *Subsection 3.4.3*) and weakly for $\Delta E_{orb,\sigma}$ vs. $T_{1/2}$ ($R^2 = 0.76$), $\Delta E_{orb,\pi}$ vs. $T_{1/2}$ ($R^2 = 0.88$). However, a comparison of the *EDA-NOCV* results between the $[\text{Fe}(\mathbf{bpp}^{\mathbf{X}})_2]^{2+}$ and the $[\text{Fe}(\mathbf{L}^{azine})_2(\text{NCBH}_3)_2]^{2+}$ families might be too early, as they are the only two *SCO* families studied using the *EDA-NOCV* model to date. Indeed, they are very different families (as also discussed in the previous analysis in *Subsection 4.3.3*) and the ‘tuning’ operating within each family (\mathbf{X} substituent vs. $\mathbf{CH/N}$ replacement) is quite different. Such results also indicate that *EDA-NOCV* analysis works much better when the number of unpaired electrons is limited.

In these regards, some general indications to *EDA-NOCV* analysis approach can be derived. Indeed, comparing the results obtained for the *SCO* families under study emerges that the *LS* $[\text{Fe}(\mathbf{bpp}^{\mathbf{X}})_2]^{2+}$ spin states show a much better correlation vs $T_{1/2}$. This can be related to smaller

variations of the electronic and entropic terms expected for *LS* [Fe(**bpp**^X)₂]²⁺ state than for *HS* [Fe(**bpp**^X)₂]²⁺ along the series. This explains the reason why *EDA-NOCV* analysis, not completely recovering such contributions if not indirectly, shows these limits more evidently for the *HS* state than for the *LS* [Fe(**bpp**^X)₂]²⁺.

NOCV Results vs $\sigma_p^+(\mathbf{X})$

For the *LS* [Fe(**bpp**^X)₂]²⁺ family, when the Hammett constant $\sigma_p^+(\mathbf{X})$ changes from EDG ($\mathbf{X} = \text{NMe}_2$) to EWG ($\mathbf{X} = \text{NO}_2$), a strong correlation is observed with $\Delta E_{orb,\sigma}$ ($R^2 = 0.88$, Figure 4.8a), a weak correlation is observed with $\Delta E_{orb,\pi}$ (see Table A4.5 for detail; $R^2 = 0.31$, Figure 4.8b), and a poor correlation is observed with the overall $\Delta E_{orb,\sigma+\pi}$ ($R^2 = 0.43$, Figure 4.8c). No correlations are observed for the *HS* [Fe(**bpp**^X)₂]²⁺ complexes: σ_p^+ vs $\Delta E_{orb,\sigma}$ ($R^2 = 0.30$, Figure A4.14); $\Delta E_{orb,\pi}$ ($R^2 = 0.01$, Figure A4.15); $\Delta E_{orb,\sigma+\pi}$ ($R^2 = 0.34$, Figure A4.16).

Compared to the previous studies²³ the effects of \mathbf{X} on π -backdonation ($\Delta E_{orb,\pi}$) in this *LS* [Fe(**bpp**^X)₂]²⁺ family are less linear and predictable than for the σ -donation, $\Delta E_{orb,\sigma}$. $\Delta E_{orb,\pi}$ shows a weak and opposite trend with the Hammett constant $\sigma_p^+(\mathbf{X})$. This result was unexpected, as Deeth, Halcrow *et al.* in 2017²³ had proposed an intuitively reasonable explanation of the effect of the \mathbf{X} substituents, that effect of \mathbf{X} primarily operates on the $\mathbf{M} \rightarrow \mathbf{L}$ π -backdonation. Hence a $\Delta E_{orb,\pi}$ vs σ_p^+ and $T_{1/2}$ correlation had been expected, but not observed. It is important to note that this divergence is not linked with the employed level of theory, as both studies employed the same *DFT* theory. Their conclusions were obtained by the analysis of the *MO* energy levels of the [Fe(**bpp**^X)₂]²⁺ complexes, the σ_p^+ values and the observed $T_{1/2}$. In this study, the conclusions are based on the variation in the $\mathbf{M-L}$ bonding quantified by the *EDA-NOCV* analysis (i.e., the σ - and π - stabilising energies that results from the $\mathbf{M-L}$ bond engagement).

Herein, as **X** varied **EDG**→**EWG** (-1.70 → +0.79) a *quantitative* $\Delta\Delta E_{orb,\sigma}$ stabilisation of about 5 kcal/mol is observed, along with a *qualitative* $\Delta\Delta E_{orb,\pi}$ destabilisation of about 1.5 kcal/mol (Tables 4.3, A4.6-A4.7). Not surprisingly, the σ -donor properties again dominate the π -acceptor properties, with the latter playing only a secondary role in the ligand field tuning operated by the **X** substituent.

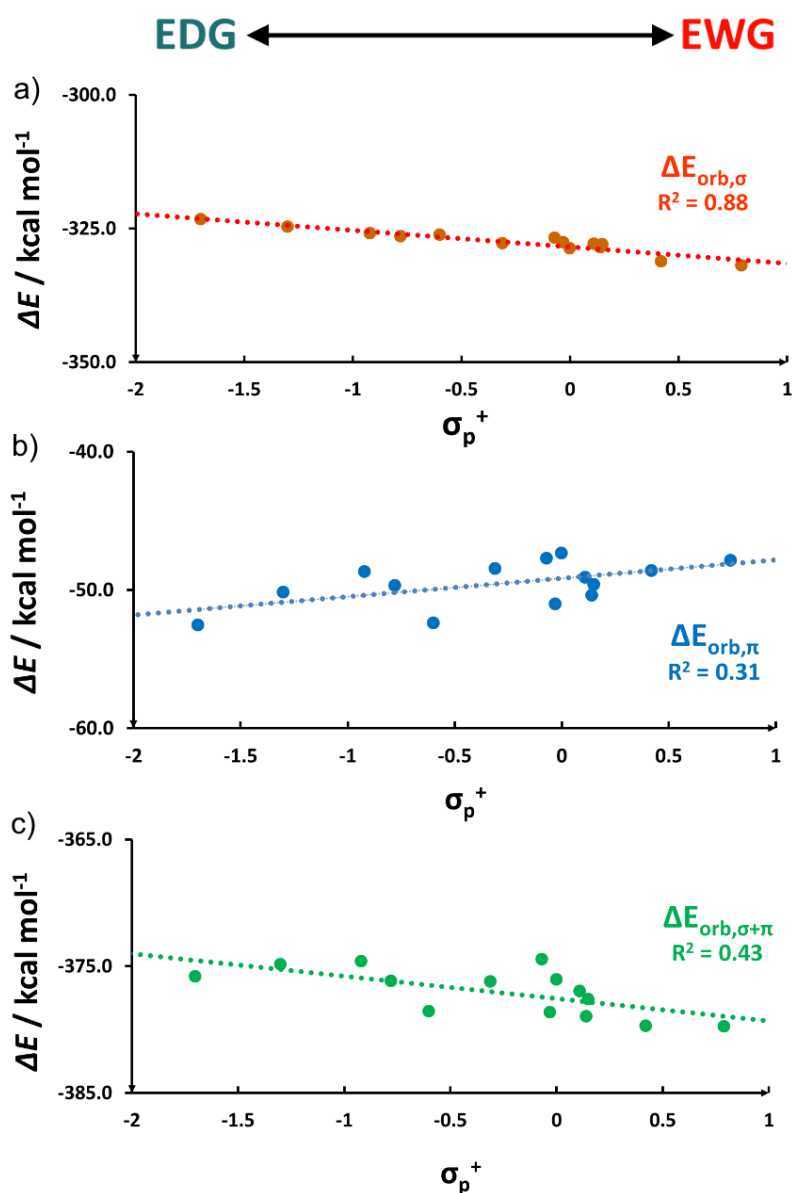


Figure 4.8. (a) Correlation of σ_p^+ Hammett parameter with (a) $\Delta E_{orb,\sigma}$ ($R^2 = 0.91$); (b) $\Delta E_{orb,\pi}$ ($R^2 = 0.31$) and (c) $\Delta E_{orb,\sigma+\pi}$ ($R^2 = 0.43$) for the family of fourteen **bpp^x** ligands (**X** = **SOMe**, **SO₂Me** are absent as σ_p^+ is not available from literature).

These different interpretations of the basis of the effect of **X** are obtained by theoretical analysis of two different molecular properties (*MO* energy vs bond strength), between which there is no established correlation, i.e., it is not known yet how increasing bond strength ($\Delta E_{orb,\sigma}$, $\Delta E_{orb,\pi}$ or $\Delta E_{orb,\sigma+\pi}$) affects the energy of the $[\text{Fe}(\text{bpp}^{\text{X}})_2]^{2+}$ *MOs* or *vice versa*.

Therefore, even if the conclusions by Deeth, Halcrow *et al.* versus those reported herein appear divergent, the full picture is not yet fully understood and both perspectives should be kept open in order to further evaluate how the **X** substituent truly operates on the ligand and hence the complex electronic structure. In a further probe of the effect of **X** on the **M-L** bonding in this $[\text{Fe}(\text{bpp}^{\text{X}})_2]^{2+}$ family, a Mulliken charge analysis was performed, with illuminating results, which are described below (*Subsection 4.3.6*).

NOCV Results vs δ_{N_A}

Finally, correlations of NOCV results with another parameter, the δ_{N_A} chemical shift of the free **bpp**^X ligand (as reported by Brooker *et al.* in 2017⁸³) not yet explicitly discussed in this study, are discussed next.

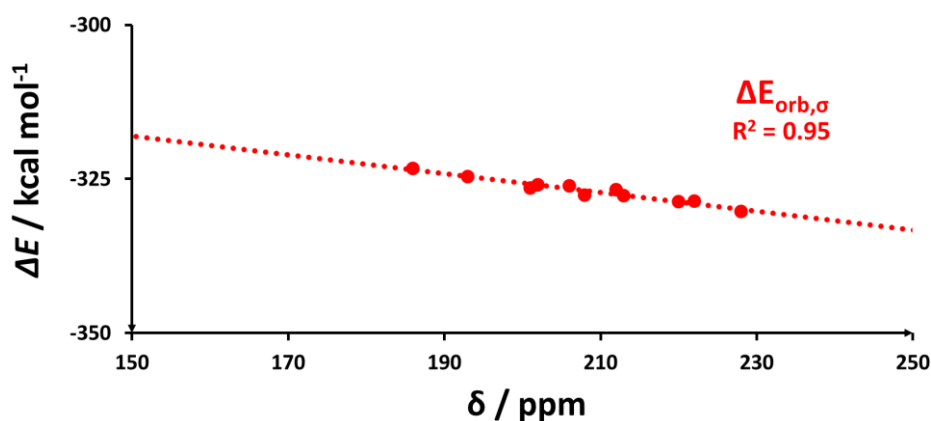


Figure 4.9. Strong correlation ($R^2 = 0.95$) of $\Delta E_{orb,\sigma}$ with δ_{N_A} in the family of sixteen LS $\text{Fe}(\text{bpp}^{\text{X}})_2^{2+}$ complexes.

For *LS* [Fe(**bpp**^X)₂]²⁺, δN_A shows an extremely good correlation only against $\Delta E_{orb,\sigma}$ ($R^2 = 0.95$ Figures 4.9 and A4.11); and a weak correlation against $\Delta E_{orb,\pi}$ ($R^2 = 0.39$ Figure A4.12) or $\Delta E_{orb,\sigma+\pi}$ ($R^2 = 0.23$ Figure A4.13).⁸³ This mirrors the findings that above, only $\Delta E_{orb,\sigma}$ correlated strongly with the observed solution $T_{1/2}$.

For *HS* [Fe(**bpp**^X)₂]²⁺, no correlations are observed for δN_A vs. any $\Delta E_{orb,i}$ ($i=\sigma; \pi; \sigma+\pi$) term: $\Delta E_{orb,\sigma}$ ($R^2 = 0.35$, Figures A4.20), $\Delta E_{orb,\pi}$ ($R^2 = 0.04$, Figures A4.21) and $\Delta E_{orb,\sigma+\pi}$ ($R^2 = 0.30$, Figures A4.22).

In summary, the calculation of the nitrogen chemical shift δN_A of the ligand is confirmed again to be an easy and quick way to estimate the strength of the ligand field applied when the ligand coordinates the metal ion.⁸³

4.3.6. EDA-NOCV results explained by Mulliken charges

The *EDA-NOCV* results just reported (*Subsections 4.3.3-4.3.4*), project a different interpretation of the experimental results than that proposed by Deeth, Halcrow *et al.* in 2017.²³ They concluded that **X** changing **EDG**→**EWG** caused increasing in **M**→**L** π -backdonation, and hence increasing the ligand field splitting (Δo) and the observed solution $T_{1/2}$ values. In contrast, the above *EDA-NOCV* analysis indicates, rather counter-intuitively at first glance, that as **EDG**→**EWG** the main effect is an increase in the **M**←**L** σ -donation and hence increasing the ligand field splitting and the observed solution $T_{1/2}$ values (Figure 4.10).

In order to try to understand how **X** changing **EDG**→**EWG** could increase the ability of the N-donor to act as a stronger σ -donor to Fe(II), here the changes in the population of the coordinating nitrogen (N_A) valence orbitals when the **X** substituent changes from **EDG** (**NMe**₂, $\sigma_{p^+} = -1.70$) to **EWG** (**NO**₂, $\sigma_{p^+} = +0.79$) are probed. This analysis is performed by looking at the Mulliken charges.

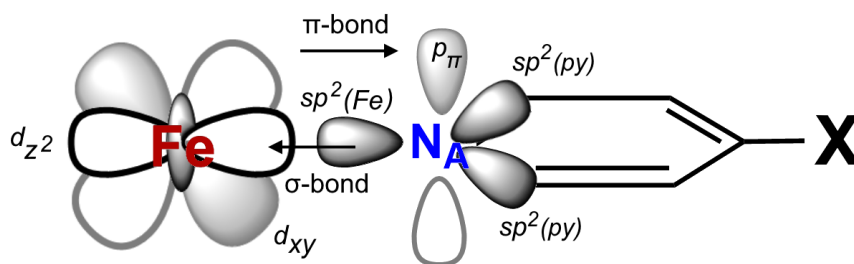


Figure 4.10. Simplified representation of the atomic orbitals of Fe(II) and the coordinating N_A nitrogen in the Fe-N bonding for described Mulliken population analysis.

This is one of the most common – even if not the most accurate – methods to evaluate the atomic charges in any *DFT* calculation. This investigation was performed on the geometry optimised free ligands, using the same basis set employed for the related iron(II) complexes. The population of the individual valence orbitals on N_A can uncover information otherwise lost when attention is focused on the *overall* electron density, as is case when looking at the overall atomic charge ($\rho(N_A)$)²² or at ¹⁵N-NMR chemical shift (δN_A).⁸³ Mulliken charges were calculated for *each* valence orbital on the N_A -donor atom. The coordinating N atom is sp^2 hybridised (Figure 4.10) and the spare p orbital (p_π), perpendicular to the sp^2 orbitals, is involved in the pyridine aromatic π -system (and in the π -backdonation in $[Fe^{II}(\mathbf{bpp}^X)_2]^{2+}$). Two out of the three hybrid sp^2 orbitals ($sp^2(py)$) are involved in C-N σ -bonds within the ligand backbone and the last sp^2 orbital ($sp^2(Fe)$) is responsible for the Fe-N σ -bond (Figures 4.10-4.11).

Firstly – not surprisingly – σ_{p^+} vs. $N_A(sp^2(py))$ shows low correlation ($R^2 = 0.27$, Figure 4.11a) and that **X** has an almost negligible substituent effect on the $N_A(sp^2(py))$ orbital ($\Delta e = -0.001$, $NMe_2 \rightarrow NO_2$). Secondly, as expected, the Hammett parameter σ_{p^+} correlates extremely well with $N_A(p_\pi)$ ($R^2 = 0.90$, Figure 4.11b): from **EDG** to **EWG** substituents, the $N_A(p_\pi)$ population decreases, as expected due to the increasing electron withdrawing properties of *para*-substituted **X** ($\Delta e = +0.08$, $NMe_2 \rightarrow NO_2$). Thirdly, and most interestingly, the Hammett parameter σ_{p^+} vs. $N_A(sp^2(Fe))$ also correlated ($R^2 = 0.79$, Figure 4.11c) but with the opposite trend to that seen for $N_A(p_\pi)$ ($\Delta e = -0.03$, $NMe_2 \rightarrow NO_2$).

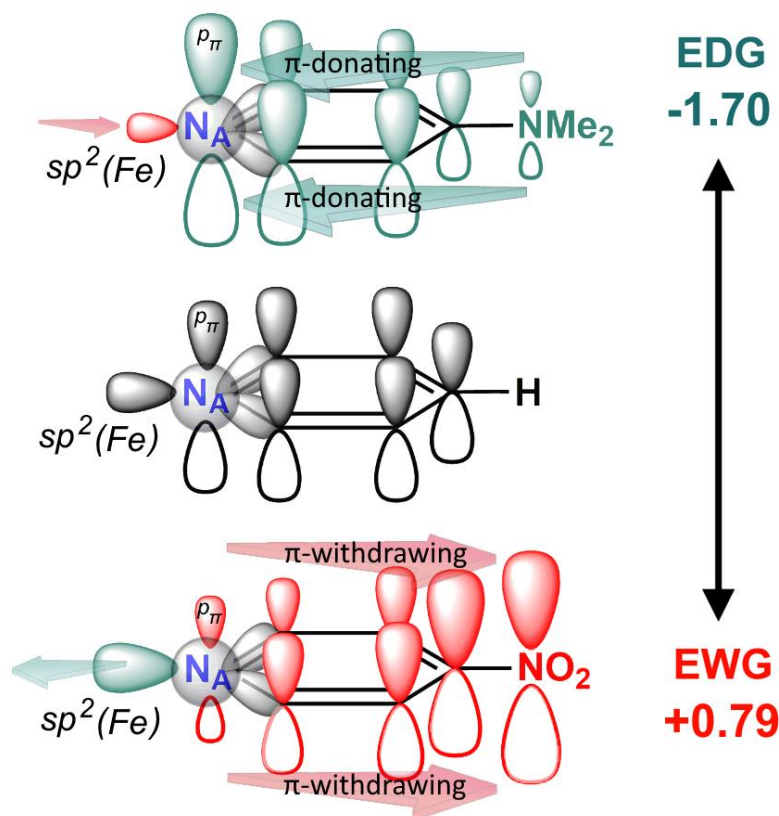


Figure 4.11. Representation of the N_A (AOs) of the pyridyl ring in the referenced $[Fe(\mathbf{bpp}^H)_2]^{2+}$ complex (centre) and at the substituted ligands at the ending of the Hammett scale ($[Fe(\mathbf{bpp}^{NMe_2})_2]^{2+}$, $\sigma_p^+ = -1.70$ (top); $[Fe(\mathbf{bpp}^{NO_2})_2]^{2+}$, $\sigma_p^+ = +0.79$ (bottom)). Arrows describe directionality of the resonance effects: toward the N_A for $[Fe(\mathbf{bpp}^{NMe_2})_2]^{2+}$ and away from the N_A for $[Fe(\mathbf{bpp}^{NO_2})_2]^{2+}$ and the complementary effects on the $p_\perp(N_A)$: enriching for $p_\perp(N)$ in $[Fe(\mathbf{bpp}^{NMe_2})_2]^{2+}$ and impoverishing for $p_\perp(N)$ in $[Fe(\mathbf{bpp}^{NO_2})_2]^{2+}$.

Therefore, whilst the $N_A(p_\pi)$ population is decreased as the **X** substituent becomes more **EWG**, the $N_A(sp^2(Fe))$ population is increased. The spatial orthogonality of the two orbitals. This charge enrichment in $N_A(sp^2(Fe))$ increases the ligand field strength of the Fe-N σ -bonding and hence $T_{1/2}$ is also increased – in alignment with interpretation from crystal field theory first principles (Figure 4.12). In previous studies it was observed that δN_A is intimately connected with $T_{1/2}^{ref83}$ and σ_p^+ (Chapter Two).

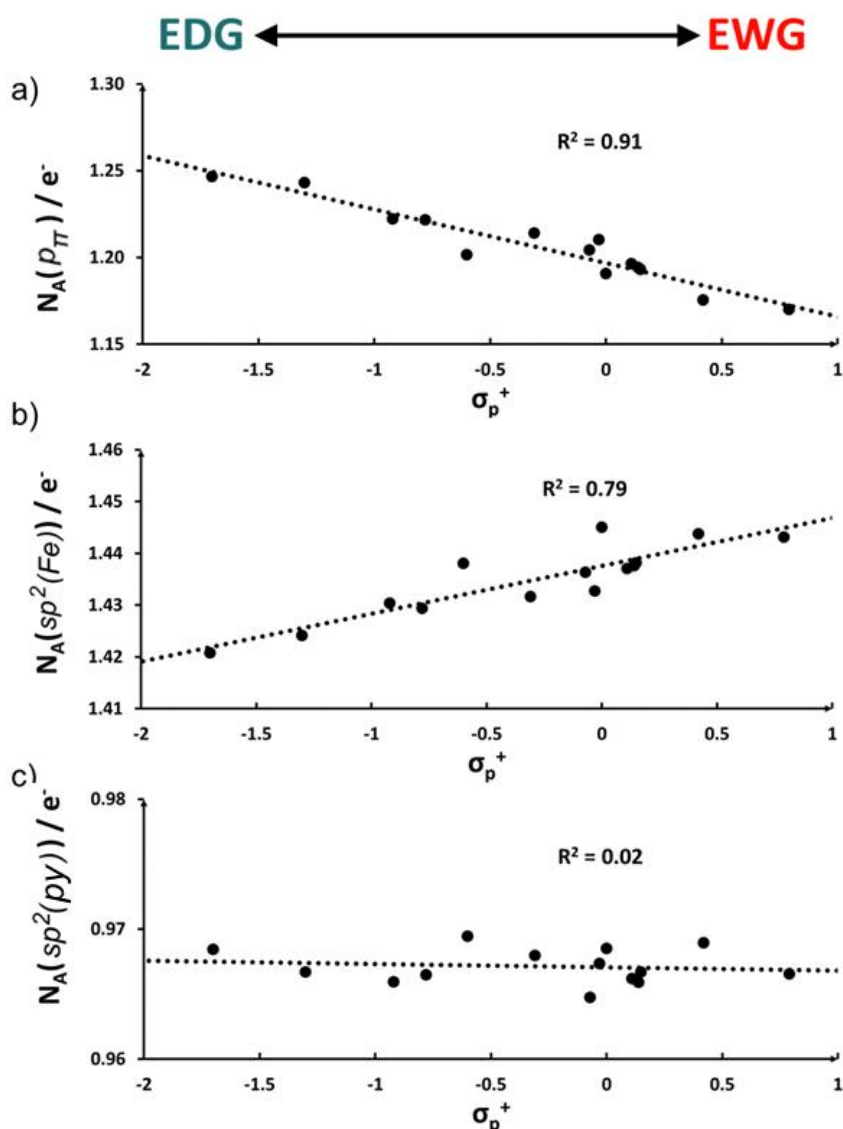


Figure 4.12. (a) Correlation of σ_p^+ Hammett parameter with (a) $N_A(p_\pi)$ ($R^2 = 0.91$); (b) $N_A(sp^2(Fe))$ ($R^2 = 0.79$) and (c) $N_A(sp^2(py))$ ($R^2 = 0.02$) for the family of fourteen **bpp^X** ligands (**X** = **SOMe**, **SO₂Me** are absent as σ_p^+ is not available from literature).

Hence herein, possible relationships of $\delta N_A(\mathbf{bpp}^X)$ with the Mulliken population analysis results are probed. A strong *increasing* trend of δN_A with decreasing $N_A(p_\pi)$ ($R^2 = 0.99$) contrasts with a strong *increasing* trend of δN_A with *increasing* $N_A(sp^2(Fe))$ ($R^2 = 0.93$) are observed. No correlation ($R^2 = 0.01$) is observed between δN_A and $N_A(sp^2(py))$ (Figure 4.13).

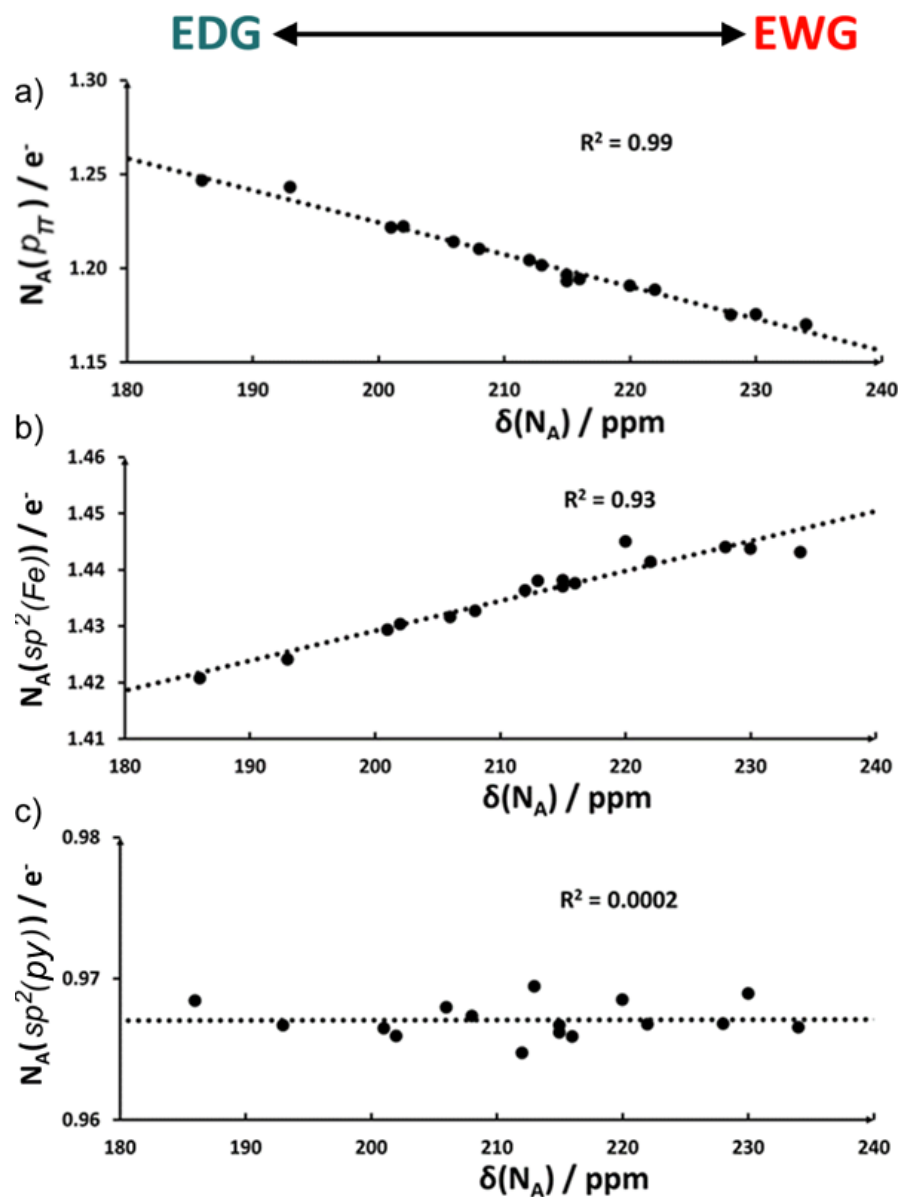


Figure 4.13. (a) Correlation of the $^{15}\text{N}_A$ chemical shift with (a) $N_A(p_\pi)$ ($R^2 = 0.99$); (b) $N_A(sp^2(Fe))$ ($R^2 = 0.93$) and (c) $N_A(sp^2(py))$ ($R^2 = 0.0002$) for the family of fourteen bpp^X ligands ($X = \text{SOMe}, \text{SO}_2\text{Me}$ are absent as σ_{p^+} is not available from literature).

4.3.7. Predicted σ_p^+ Parameter for X = SOME, SO₂Me

The set of seven correlations identified in this study enabled prediction of the Hammett parameter σ_p^+ for the two X substituents for which the values are not available in literature (X = SOME and X = SO₂Me).

To do so, the seven observed correlations (Equations 4.1-4.7) are involved at micro- or macroscopic level with the effect of X on the properties of the sixteen [Fe(**bpp**^X)₂]²⁺ complexes studies (Table 4.4) were used to calculate the missing values of σ_p^+ (X) (Table A4.9). This gives the calculated values for X = SOME and X = SO₂Me as, respectively, 0.26±0.16 and 0.60±0.08 (Table 4.4).

Table 4.4. Predicted values of σ_p^+ for the two X substituents for which this value is not reported in literature, using the correlations identified in this study with the best correlation factor, followed by the weighted average value highlighted in yellow (average without the pink value is in brackets).

vs.	σ_p^+		
	X = SOME	X = SO ₂ Me	R ²
$N_A(p_\pi)$	0.23	0.64	0.99
$\Delta_o(AILFT)$	0.29	0.67	0.93
$N_A(sp^2(Fe))$	0.23	0.48	0.93
$\delta(^{15}N-NMR)$	0.27	0.58	0.92
$T_{1/2}$	0.58	0.70	0.92
ΔE_{elstat}	0.19	0.65	0.89
$\Delta E_{orb,\sigma}$	0.01	0.50	0.88
$\langle \sigma_p^+ \rangle$	0.26	0.60	-

$$\Delta_o = 0.061 \cdot \sigma_{p^+} - 2.41 \quad (4.1)$$

$$N_A(p_\pi) = -0.02 \cdot \sigma_{p^+} + 6.32 \quad (4.2)$$

$$\delta N = 16.56 \cdot \sigma_{p^+} + 215.06 \quad (4.3)$$

$$T_{1/2} = 0.011 \cdot \sigma_{p^+} - 2.57 \quad (4.4)$$

$$\Delta E_{elstat} = 17.12 \cdot \sigma_{p^+} - 386.60 \quad (4.5)$$

$$\Delta E_{orb,\sigma} = -3.10 \cdot \sigma_{p^+} - 328.39 \quad (4.6)$$

$$N_A(p_\perp) = 0.009 \cdot \sigma_{p^+} + 1.44 \quad (4.7)$$

4.4. Conclusion

Inspired by the 2017 study of Deeth, Halcrow *et al.*,²³ the effect of the *para*-substituent **X** on the electronic structure of sixteen *solution* SCO active $[\text{Fe}(\mathbf{bpp}^{\mathbf{X}})_2]^{2+}$ complexes was investigated in more depth, employing different levels of theory (including *AILFT*, *EDA-NOCV* and Mulliken charges). The $\Delta_o(\text{AILFT})$ analysis shows extremely good correlation of Δ_o with the $\sigma_p^+(\mathbf{X})$ ($R^2 = 0.93$) and the experimental $T_{1/2}$ ($R^2 = 0.78$). But analogous of the *L^{azine}* family reveals that *AILFT* cannot uniquely connect the $T_{1/2}$ with the actual ligand field strength imposed on a metal ion by any ligand family.

The *EDA-NOCV* results revealed a strong correlation between the σ -donor strength ($\Delta E_{orb,\sigma}$) of the $\mathbf{bpp}^{\mathbf{X}}$ ligand with $\sigma_p^+(\mathbf{X})$ ($R^2 = 0.88$), the measured $T_{1/2}([\text{Fe}(\mathbf{bpp}^{\mathbf{X}})_2]^{2+})$ ($R^2 = 0.82$), the ^{15}N NMR chemical shift ($\delta\text{N}_A(\mathbf{bpp}^{\mathbf{X}})$, $R^2 = 0.95$). Results obtained by correlating the *EDA-NOCV* analysis, the *LS* $[\text{Fe}(\mathbf{bpp}^{\mathbf{X}})_2]^{2+}$ showed that an incredibly better agreement with experimental observable than the *HS* $[\text{Fe}(\mathbf{bpp}^{\mathbf{X}})_2]^{2+}$. This result can be explained with the smaller entropic contributions (electronic and geometrical) present in *LS* $[\text{Fe}(\mathbf{bpp}^{\mathbf{X}})_2]^{2+}$ that the *EDA-NOCV* can include only indirectly. A more in-depth investigation of this link between the computed σ -donor strength ($\Delta E_{orb,\sigma}$) of the $\mathbf{bpp}^{\mathbf{X}}$ ligand with all the mentioned experimental evidences was performed through the analysis of the Mulliken charges for the N_A valence orbitals. From **EDG** to **EWG** substituents, the analysis of the Mulliken charges showed that at the portion of p_π -electron in the $\text{N}_A(p_\pi)$ orbital decreases (as delocalised in the ligand π -system towards the **X** substituent), whilst the electron occupation in the Nitrogen lone pair, $\text{N}_A(p(\text{Fe}))$ and orthogonal to the $\text{N}_A(p_\pi)$, increases. This effect enhances the reach out of the N_A when the $\mathbf{bpp}^{\mathbf{X}}$ ligand coordinates the iron(II) ion in the relative $[\text{Fe}(\mathbf{bpp}^{\mathbf{X}})_2]^{2+}$ complex.

Finally, this study led to the estimation of the value of σ_p^+ for two **X** substituents: **SOMe** (0.26) and **SO₂Me** (0.60), not available in literature.

4.5. Computational Protocol

Calculations were performed using ORCA 4.1²⁵⁸ and ADF (version 2018.106) code.²⁶⁹ The ORCA code was used to optimise the structure of sixteen of the $[\text{Fe}(\mathbf{bpp}^{\text{x}})_2]^{2+}$ complexes (in both *HS* and *LS* states); the absence of negative eigenvalues for the Hessian matrix confirmed the all computed geometries are in real minima.

Firstly, using the atomic coordinates of the sixteen *LS* and sixteen *HS* $[\text{Fe}^{\text{II}}(\mathbf{bpp}^{\text{x}})_2]^{2+}$ complexes available from the *DFT* study at RI-BP86-D3(BJ)/def2-SVP/J+COSMO(acetone) level of theory in the paper by Deeth, Halcrow *et al.*,²³ a geometry re-optimisation was performed using different RI-BP86-D3(BJ)/def2-TZVPP+CPCM(acetone) level of theory:²⁵⁹⁻²⁶⁷ i.e. RI = resolution of identity²⁶⁶⁻²⁶⁷ with a BP86 functional,²⁶³⁻²⁶⁴ with D3 dispersion correction (including BJ damping),²⁵⁹⁻²⁶⁰ def2-TZVPP basis set,²⁶¹ and the solvent modelled by CPCM.²⁶⁵ The same was done for the sixteen free \mathbf{bpp}^{x} ligands. The optimised geometries were then used for two different kinds of studies.

Secondly, the optimised structures were used for Ab-initio Ligand Field Theory (*AILFT*) analysis (details in *Subsection 1.6.1*),¹⁴⁵ as implemented in ORCA 4.1, computed at the *NEVPT2* level of theory with def2-SV(P)/BP86/def2-TZVPP, and utilising auxiliary basis sets for the RI approximation. The active space for the underlying State-Averaged Complete Active Space Self-consistent Field (*SA-CASSCF*).¹⁴⁴ The methodology employed in this study proceed with displacing the six *d*-electrons over the five *MOs* with pronounced *d*-shape. All the possible rearrangements, until maximum spin multiplicity of quintet (singlet, triplet and quintet), were screened; through this procedure, various Δ_{o} ($\Delta_{\text{o}}(\text{singlet})$, $\Delta_{\text{o}}(\text{triplet})$, $\Delta_{\text{o}}(\text{quintet})$) are so calculated and, therefore, they are weight-averaged to give the overall Δ_{o} ; this weight-averaging is calculated from the relative stability of each wavefunction (obtained for each spin state), vs. the ground state. To reduce the computational costs in the *N*-

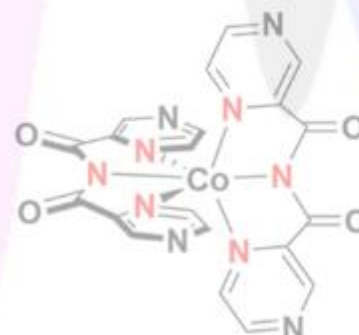
Electron Valence State Perturbation Theory (*NEVPT*) procedure,¹⁴⁹⁻¹⁵² the Domain-based Local Pair Natural Orbital (*DLPNO*)²⁸² treatment was employed. *AILFT* analysis is employed on the sixteen final structures of *LS* [Fe(**bpp**^X)₂]²⁺ complexes and on the five optimised structures of the five *LS* [Fe^{II}(*L*^{azine})₂(NCBH₃)₂] complexes (from studies in *Chapter Three*).

Thirdly, the optimised structures were used for the *EDA-NOCV*¹⁸³⁻¹⁸⁴ method combines classical *EDA*,^{175, 185} with *NOCV*,¹⁸⁶⁻¹⁸⁷ which were performed using the ADF program package at the BP86-D3(BJ)/TZ2P level of theory.²⁶⁸⁻²⁶⁹ It should be noted that neither the *AILFT* nor the *EDA-NOCV* models are implemented including any solvation modelling included (i.e., CPCM). Detailed description of the *EDA-NOCV* model is reported in *Subsection 1.6.6*.



Accurate Prediction of Pressure and Temperature $T_{1/2}$ Variation in Solid State Spin Crossover by Ab Initio Methods: The $[\text{Co}^{\text{II}}(\text{dpzca})_2]$ Case

The contents of this chapter are at an advanced stage of preparation for submission to *Journal of the American Chemical Society* as: 'Accurate Prediction of Pressure and Temperature $T_{1/2}$ Variation in Solid State Spin Crossover by Ab Initio Methods: The $[\text{Co}^{\text{II}}(\text{dpzca})_2]$ Case'. All of the calculations were performed by me. The manuscript and supporting information were entirely drafted by me.



5.1. Abstract

The spin crossover (SCO) phenomenon is among the most complicated second-order transitions to be modelled from first principles. Some *ad hoc* strategies have been successful for modelling *solution* SCO, but this is rare for *solid state* SCO because of the added complexity coming from (a) interacting molecules and (b) packing effects. In this study, the solid state SCO transition of solvent-free crystalline $[\text{Co}^{\text{II}}(\text{dpzca})_2]$ is modelled through the calculation of the transition temperature ($T_{1/2}$) under a range of different physical conditions. This candidate complex undergoes both thermal and pressure-activated SCO (quoted $T_{1/2}$ values obtained at $\gamma_{\text{HS}} = 0.5$): from pressures of 1 to 2100 bar, the SCO is mostly *abrupt* (*gradual:abrupt* = 20:80; 173 K < $T_{1/2}$ < 189 K); from 2500 bar a progressively increasing fraction of *gradual*-SCO replaces the last part of the *abrupt* transition (*gradual:abrupt* = 60:40; $T_{1/2} = 202$ K); at 4300 bar, the conversion to *gradual* SCO is almost complete (*gradual:abrupt* = 80:20; $T_{1/2} = 235$ K). In the first part of this study, a computational protocol was established that reproduces the experimental properties of crystalline high spin (HS) and low spin (LS) $[\text{Co}^{\text{II}}(\text{dpzca})_2]$ at the pressure of 1 bar. Then, this protocol was trailed at six different pressures, up to 4300 bar, and it accurately reproduced the available crystallographic data (HS [1 bar]; LS [1 bar and 4300 bar]) and the electronic structure (density of states; DOS). Extremely good predictions of $T_{1/2}$ were obtained, with deviations from the observed values of less than 10 K, up to a pressure of 2100 bar, i.e. whilst crystalline $[\text{Co}^{\text{II}}(\text{dpzca})_2]$ undergoes mostly an *abrupt* SCO transition. Above 2500 bar, when the *abrupt* part of the SCO transition becomes increasingly *gradual*, the divergence between the experimental data and theoretical predictions increases. Considering the numerous degrees of freedom involved in *ab initio* SCO modelling, the results obtained for $[\text{Co}^{\text{II}}(\text{dpzca})_2]$ at pressures up to 2500 bar are very encouraging. The observed divergence for $p > 2500$ bar is likely due to a crystal transition or phase change of the HS $[\text{Co}^{\text{II}}(\text{dpzca})_2]$ unit cell, as the only available crystallographic data in this pressure range (LS $[\text{Co}^{\text{II}}(\text{dpzca})_2]$ at 4300 bar) are in excellent agreement with the computed ones

5.2. Introduction

When transition metal ions with d^4 to d^7 electronic configurations are coordinated in (pseudo-) octahedral environments they can adopt either the High Spin (*HS*) or Low Spin (*LS*) state, based on the strength of the coordinating ligands. When these two spin states are both *thermodynamically* accessible (*Chapter One*), these metal complexes can undergo a Spin Crossover (*SCO*) transition. Such complexes are of particular interest, as sensors for monitoring physical/chemical environmental changes (i.e., temperature or pressure),^{10, 53, 69-70} as active components for spintronics and molecule-based data storage devices,²⁸³⁻²⁸⁶ and in innovative devices profiting from additional features obtained by combining *SCO* with other functionalities.^{203, 287} The *SCO* transition can be described from this thermodynamic perspective, by looking at the enthalpy (ΔH) and entropy (ΔS) terms which are involved in the spin state switch. The enthalpic gap between the *HS* and the *LS* states favours the *LS* state ($\Delta H_{\text{HS-LS}} > 0$), but as the temperature increases, this is progressively overcome by the entropy difference ($\Delta S_{\text{HS-LS}} > 0$) which drives the spin-state switching and *gradually* populates the entropically favoured *HS* state. For a complete one step $\text{LS} \rightarrow \text{HS}$ thermal *SCO*, the transition temperature ($T_{1/2}$) is defined as the temperature where the condition $\Delta H_{\text{HS-LS}} = T_{1/2} \Delta S_{\text{HS-LS}}$ is respected, and corresponds to a fraction *HS*, γ_{HS} , of 0.5 (*Subsection 1.2.2*).

In solution, the modelling of the spin switching, where molecules are surrounded by solvent molecules and cooperative effects between the metal ions are inhibited, has been already attempted. Despite the more limited number of degrees of freedom, with respect to the solid state, successful examples of predictivity are still limited.^{164, 170, 173} In solid state *SCO*, packing effects are crucial for modelling a spin state transition. Within the term ‘packing effects’ are many factors, the unit cell symmetry, the number of molecules, the presence of counterions or solvent molecules and, hence, all of the *intermolecular* interactions between the *SCO* centre and

its surroundings, mediated by H-bonds,^{79, 102-103} π - π stacking¹⁰⁹ and dipolar/VdW dispersion forces.^{79, 110} Therefore, in order to reproduce the $T_{1/2}$ within an error of few Kelvins, it is mandatory to have a protocol that is able to accurately reproduce (i) the electronic structure of the SCO complex itself; (ii) the *intra*- and *intermolecular* interactions (iii) in the case of pressure-induced SCO, the variation of the unit cell parameters for both the LS and HS states.

A computational protocol able to satisfy these demands and, hence, reliably predict the thermal and pressure-activated SCO behaviour across a range of temperatures, would represent a step change in the field, as it would provide a useful pre-synthetic screening step. Literature studies report the use of a range of theoretical models in attempts to rationalise various aspects of the SCO phenomenon.²⁸⁸⁻²⁹⁴ A key focus of those studies was on screening functionals to identify the one best candidate able to accurately reproduce the $\Delta H_{el,HS-LS}$ gap (previously also called ΔE_{HL} in *Chapter One*, the electronic enthalpy change between the two spin states, Figure 1.2).^{143, 159, 295}

In just a few cases, first principles calculations were employed to calculate the thermodynamic contributions $\Delta H_{vib,HS-LS}$, $\Delta S_{vib,HS-LS}$, $\Delta H_{el,HS-LS}$ and $\Delta S_{el,HS-LS}$ which are associated with the SCO phenomenon for isolated molecules (*Section 1.6*).^{164, 170} A remarkable study was published in 2012 when Cirera and Paesani¹⁶⁴ modelled the SCO transition using a Boltzmann-like transition after screening several DFT functionals (*Subsection 1.6.3*). The employed approach enabled *qualitative* reproduction of the experimental data, but with a considerable error for the best fit *vs* experimental $T_{1/2}$ values ($\Delta T_{1/2} \cong 50$ -100 K).

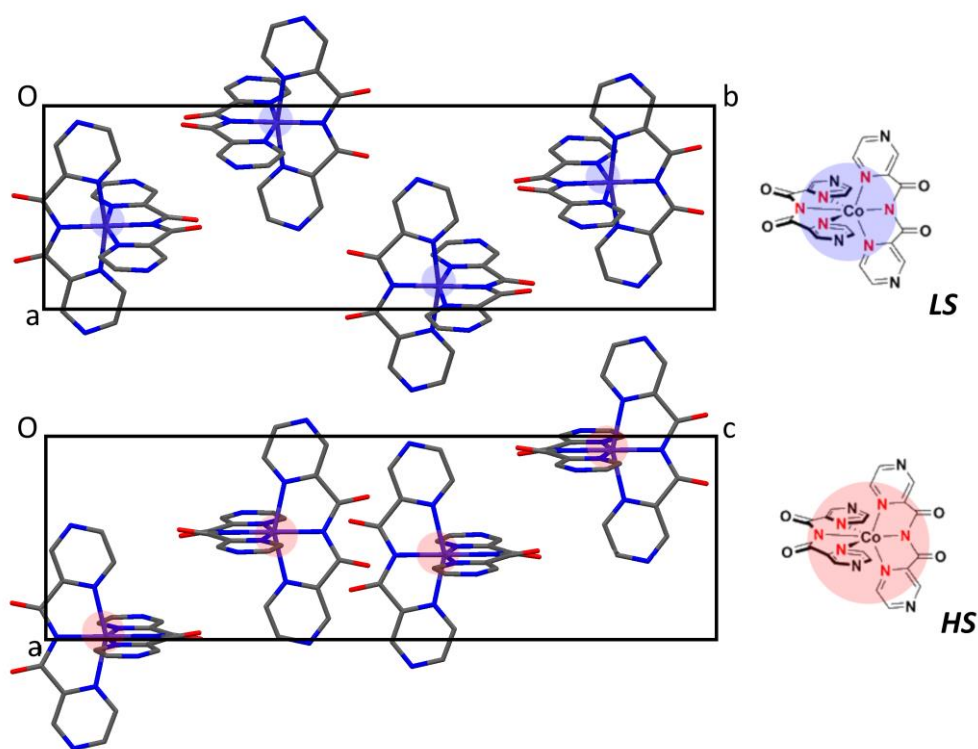


Figure 5.1. Unit cells of $1_{\text{cryst,LS,1bar,90K}}$ (90 K, top, $P2_1/c$) and $1_{\text{cryst,HS}}$ (298 K, bottom, $I4_1/a$) $[\text{Co}^{\text{II}}(\text{dpzca})_2]$ obtained from single X-ray structure determination at ambient pressure by some of us in 2012;¹⁰⁴ we subsequently reported single X-ray structure determinations under a range of pressures at 293 K in 2015, including $1_{\text{cryst,LS,4300bar,293K}}$.¹⁹

In the solid state, to our knowledge, the accurate estimation of $T_{1/2}$ via periodic *ab initio* methods, for any class of compounds, or for a single system at different pressures, has never been achieved. It is worth noting that in performing fully periodic calculations, cooperative effects are intrinsically added to a certain extent by allowing other than gradual (following simple Boltzmann distribution law) transitions, i.e. abrupt ones, too. Transitions with *hysteresis* can, at the moment, only be added in a further step with *ad hoc* parameterization as reported by Slichter (1972)²¹⁶ and Sorai (1974).²⁹⁶ These are explicitly not considered in the present study, as neither method can supply general results that can be extended to other systems.

With the aim of tackling this challenge, as a first step to a more general picture, the thermal and pressure-activated SCO complex, $[\text{Co}^{\text{II}}(\text{dpzca})_2]$, $\mathbf{1}_{\text{cryst}}$ (LS , $S = 1/2$ to HS , $S = 3/2$ per molecule; LS , $S = 2$ to HS , $S = 6$ per unit cell), is used as a test system for developing this computational protocol (Figure 5.1, Section 1.5).^{19, 104}

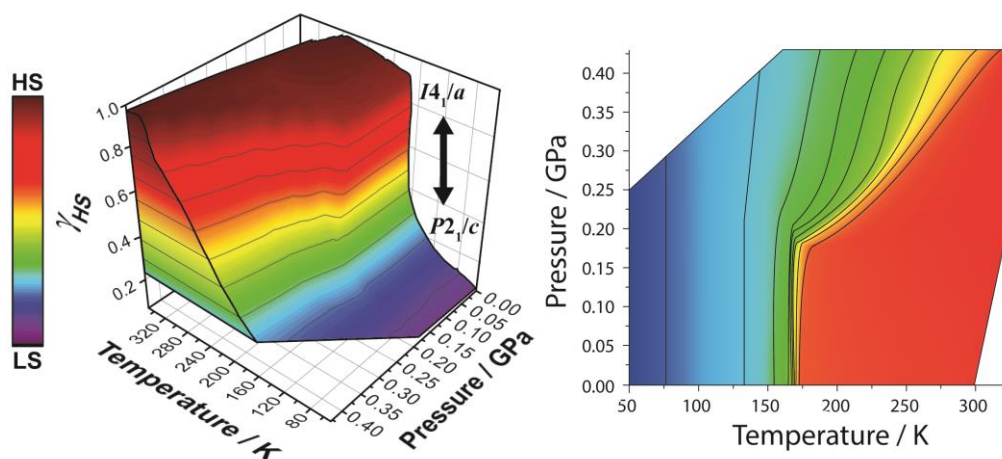


Figure 5.2. (left) Two different representations of the 3D temperature and pressure dependence of the HS fraction (γ_{HS}) during the SCO in $\mathbf{1}_{\text{cryst}}$, as monitored by magnetic measurements. Note that the colours on the cut-through (left wall) are only guides for the eyes. (right) Projection of the surface shown in the left panel. The tight bunching of contour lines denoting γ_{HS} (colour scale similar to that used for the left image) corresponds to the abrupt structural phase transition from $P2_1/c$ to $I4_1/a$ due to phase-change at low pressures ($p < 0.20$ GPa).^{19, 104} $1 \text{ bar} = 10^{-4} \text{ Pa}$. Figure reproduced with modifications from ref.¹⁹

Solvent-free $\mathbf{1}_{\text{cryst}}$ is a neutral $\text{Co}(\text{II})$ complex, coordinated by two tridentate anionic imide ligands, with no counter ion or solvent inclusion in the crystalline lattice. Variable temperature (VT) and variable pressure (VP) magnetic measurements of $\mathbf{1}_{\text{cryst}}$ are shown in Figure 5.2. All of the experimental and theoretical $T_{1/2}$ values in this paper correspond to the temperature where γ_{HS} , the fraction of $\mathbf{1}_{\text{cryst}}$ in the high spin state, is 0.5 (Figure 5.2).¹⁹

At ambient pressure ($p = 1 \text{ bar}$), $\mathbf{1}_{\text{cryst},1\text{bar}}$ shows mostly *abrupt* SCO with $T_{1/2} = 173 \text{ K}$ and a small *thermal hysteresis* (Figure 1.31).¹⁰⁴ When the

pressure is increased up to 4300 bar, the $T_{1/2}$ increases to 235 K and the composition of the transition curve changes: the mostly *abrupt* shape gets replaced by a progressively more *gradual* transition. The *gradual:abrupt* SCO ratio increases from 20:80 at 1 bar to 60:40 at 2500 bar then to 80:20 at 4300 bar (Section 1.6, Figure 5.2, Figure 1.31). The SCO transition was also monitored through Raman spectroscopy at room temperature, at the range of pressures from 1 to 5700 bar (Figure 1.31).¹⁰⁴

For $\mathbf{1}_{\text{cryst,LS}}$, crystallographic data are available at both $T = 90 \text{ K}$, $p = 1 \text{ bar}$ ($\mathbf{1}_{\text{cryst,LS,1bar,90K}}$),¹⁹ and $T = 293 \text{ K}$, $p = 4300 \text{ bar}$ ($\mathbf{1}_{\text{cryst,LS,4300bar,293K}}$).¹⁰⁴ At both pressures (1 bar, 4300 bar), the unit cell includes four molecules of $\mathbf{1}_{\text{cryst,LS}}$ (one complex per asymmetric unit, $Z = 4$, $P2_1/c$; Figure 5.1, Table 1.1). These crystallographic results are of great importance since it is experimental confirmation that the space group for the $\mathbf{1}_{\text{cryst,LS}}$ species does not undergo any further change as the pressure changes from 1 to 4300 bar. This is not true for $\mathbf{1}_{\text{cryst,HS}}$. Indeed, crystallographic data were collected uniquely at the pressure of 1 bar and 298 K ($\mathbf{1}_{\text{cryst,HS,1bar,298K}}$).¹⁹ As for $\mathbf{1}_{\text{cryst,LS}}$, four molecules are included in the unit cell of $\mathbf{1}_{\text{cryst,HS}}$ ($1/4$ of the complex per asymmetric unit, $Z = 16$, $I4_1/a$; Figure 5.1, Table 1.1).¹⁹ For the pressure of 4300 bar, the full population of $\mathbf{1}_{\text{cryst,HS}}$ ($\gamma_{\text{HS}} = 1.0$) is only expected to be reached above 320 K (Figure 5.2).¹⁰⁴

Collecting crystallographic data under such conditions is extremely challenging: (a) the quality of crystallographic data decreases at high temperatures due to increase in the molecular vibrations and (b) the use of anvil cells (required for XRD at high pressures) dramatically reduces the number of collectable reflections and makes temperature control challenging (hence pressure XRD is usually performed at ambient temperature, as in the present case).^{19, 104} Hence, no structural experimental evidence is available to show whether or not $\mathbf{1}_{\text{cryst,HS}}$ preserves the same $I4_1/a$ crystalline phase across all of the studied pressure range. The possible occurrence of a phase change as the pressure is increased would be far from being uncommon, since there are several cases in literature of solid state

SCO where one of the two spin states go through a crystallographic phase change at higher pressures or temperatures.²⁹⁷⁻³⁰⁴ The Raman spectra, performed on $\mathbf{1}_{\text{cryst}}$ along all the pressure series (see later),¹⁰⁴ also fail to provide clarity on this issue. So we are left blind with respect to reliable monitoring of the structural evolution, and any possible phase transition, of $\mathbf{1}_{\text{cryst,HS}}$ as a function of the applied pressure.

The aim of the present study is to establish a computational protocol grounded in, and tuned by, the structural and magnetic experimental data available for $\mathbf{1}_{\text{cryst,1bar}}$, which can accurately predict $T_{1/2}$ values up to the pressure of 4300 bar. To do so, the fully periodic $DFT+U$ ³⁰⁵ approach (*Subsection 1.6.4*) was employed for the determination of all of the structural and energetic degrees of freedom of the $\mathbf{1}_{\text{cryst}}$ systems, leading to a clean and homogeneous computational protocol that can largely recover the molecule-molecule and molecule-lattice interactions needed for an accurate description of the SCO transition (*Section 5.6*).

5.3. Methodology: Modelling a SCO Transition

Each unit cell of $\mathbf{1}_{\text{cryst}}$ includes four molecules: therefore, for $\mathbf{1}_{\text{cryst,LS}}$, a spin $S = 2$ ($S = 1/2 \cdot 4$ $[\text{Co}(\text{dpzca})_2]$ molecules) was set while $S = 6$ for $\mathbf{1}_{\text{cryst,HS}}$ ($S = 3/2 \cdot 4$ $[\text{Co}(\text{dpzca})_2]$ molecules); i.e., all of the results below are presented per unit cell. Intermediate spins deriving from the flip of a single molecule were not considered since it would have increased considerably the number of calculations and, above all, because we are focused on the straight value of $T_{1/2}$ for which only $S = 2$ and $S = 6$ states are sufficient. A thermally-driven spin transition can be rationalised as the overcoming of the enthalpy of the *LS* state ($\Delta H_{\text{HS-LS}} > 0$) by the entropy contribution of the *HS* state as the temperature increases ($\Delta S_{\text{HS-LS}} > 0$). When the SCO reaches $T_{1/2}$, $\gamma_{\text{LS}} = \gamma_{\text{HS}} = 0.5$ and the $\Delta G_{\text{HS-LS}}$ ($\Delta G_{\text{HS-LS}} = G_{\text{HS}} - G_{\text{LS}} = \Delta H_{\text{HS-LS}} - T\Delta S_{\text{HS-LS}}$) becomes equal to zero; therefore, $T_{1/2}$ can be obtained as:

$$T_{1/2} = \frac{\Delta H_{\text{HS-LS}}(T_{1/2})}{\Delta S_{\text{HS-LS}}(T_{1/2})} \quad (5.1)$$

$$\Delta H_{\text{vib,HS-LS}}(T) = \Delta H_{\text{vib,HS-LS}}(T) + \Delta H_{\text{el,HS-LS}} \quad (5.2)$$

$$\Delta S_{\text{vib,HS-LS}}(T) = \Delta S_{\text{vib,HS-LS}}(T) + \Delta S_{\text{el,HS-LS}} \quad (5.3)$$

Where $H_{\text{vib,HS-LS}}(T)$ and $S_{\text{vib,HS-LS}}(T)$ terms can be evaluated, for both spin states, from first principles if the vibrational normal modes of the system are available. In the approach herein proposed, vibrations were calculated at the Γ (gamma) point of the first Brillouin zone; therefore, only $3N-3$ values are obtained, with no phonon dispersions. In this regard, the frequencies of the acoustic modes were approximated as the lowest optical ones.³⁰⁶ In such a framework, it is possible to express the $H_{\text{vib,HS-LS}}(T)$ and

$S_{vib,HS-LS}(T)$ as derivation from the partition function for a crystalline solid:³⁰⁷ in detail, the calculated integral in the partition function is substituted by the sum over the vibrational degrees of freedom (Equations 5.4-5.5).¹⁶⁶

$$H_{vib,HS-LS}(T) = \sum_{i=1}^{N_{vib}} \left(\frac{1}{2} h\nu_i + \frac{h\nu_i e^{-h\nu_i/k_bT}}{1 - e^{-h\nu_i/k_bT}} \right) \quad (5.4)$$

$$S_{vib,HS-LS}(T) = \sum_{i=1}^{N_{vib}} \left(\frac{h\nu_i}{T} \frac{1}{e^{-h\nu_i/k_bT} - 1} - k_b T \ln(1 - e^{-h\nu_i/k_bT}) \right) \quad (5.5)$$

In Equation 5.6 is reported how the electronic entropy (S_{el}) was calculated. The $S_{el,HS-LS}$ term depends by the number of allowed microstates whereby the unpaired electron can get access to. It is uniquely related to the spin multiplicity of the investigated system.

$$S_{el,HS-LS} = R \ln(2S + 1) \quad (5.6)$$

Finally, the electronic enthalpy term, $\Delta H_{el,HS-LS}$, accounts for the absolute energy difference between $\mathbf{1}_{\text{cryst},LS}$ and $\mathbf{1}_{\text{cryst},HS}$. This term collects energetic contributions coming from the *molecular structure*, *dispersion forces* and *periodic interactions* between the $[\text{Co}(\text{dpzca})_2]$ molecules in the $\mathbf{1}_{\text{cryst}}$ crystalline lattice. Such a term is highly dependent on the choice of the functional and it is accurately tuned by the employment of the *Hubbard U* term (U_{eff}). This strategy led to a preliminary step in which the *Hubbard U* term was finely tuned. Following the approach reported in ref³⁰⁸, the U_{eff} values have been tuned using experimental data of $\mathbf{1}_{\text{cryst},HS}$ at the pressure of 1 bar. The tuned protocol was then applied at the other pressures (p = 1800 bar, 2100 bar, 2500 bar, 2900 bar, 3900 bar, 4300 bar) where a procedure of cell optimisation was performed, in the hypothesis that both spin states do not go through crystallographic phase change.

5.4. Results and Discussion

5.4.1. Fine Tuning of the U_{eff} term

The prediction of the pressure-temperature induced SCO activity of $\mathbf{1}_{\text{cryst}}$ represents a real computational challenge since several different observables need to be reproduced within the same computational framework (structural and electronic properties, dispersion forces, periodic interactions). This means that the computational protocol must account for electronic correlation contributions, such as periodic packing effects, at the same time as a function of the applied pressure. Therefore, the only accessible strategy is the employment of a *DFT+U* theory, parameterized from the largest available experimental dataset rather than extracting the values from higher level post-*HF* calculations (Section 1.6). In such a framework, the calculation of $T_{1/2}$ values at certain pressures requires the unit cell to be fully optimised along with the molecules within it.

Such a step is far from trivial and it could be even more challenging in the absence of experimental structural data. It is worth noting that the robustness of this proposed computational protocol depends on the maintenance of the space group of the unit cell (a condition not proven for $\mathbf{1}_{\text{cryst,HS}}$), as a phase change is still an unresolved issue at the computational level, above all when molecular crystals are considered. The procedure to tune the U_{eff} term(s) consisted of several steps of trial and error in order to get the needed accuracy in reproducing observables such as molecular structure parameters, cell parameters and $\Delta H_{\text{el,HS-LS}}$ of $\mathbf{1}_{\text{cryst,1bar}}$. In this regard, a first guess was obtained by starting on a procedure of geometry optimisation, without tweaking the cell parameters. At the end of this procedure, when a $U_{\text{eff}} = 2.35 \text{ eV}$ was applied on the Co(*d*) orbitals, good agreement was reached between the molecular structures (*RMSD*, Equation A5.1; *HS*: 0.13 Å; *LS*: 0.10 Å) and the SCO $T_{1/2}$ (*th.* 175 K vs *exp.* 171

K, Table A5.1, Figure A5.2). In a second step, the procedure of cell optimisation was undertaken, starting from the results obtained in the first step. Taking advantage of the previous U_{eff} tuning for $\text{Co}(d)$, this procedure was able to be sped up. Unfortunately, extending the optimisation procedure not only to molecular structures but also to cell parameters, forced the application of different U_{eff} or the various atomic species (N, C, O, H) in both $\mathbf{1}_{\text{cryst,LS}}$ and $\mathbf{1}_{\text{cryst,HS}}$ ($p = 1 \text{ bar}$) (Tables A5.2-A5.3). This showed that the $\text{N}(p)$ had to be corrected to accurately reproduce the atomic positions and the unit cell parameters (a - b - c and α - β - γ) ($U_{\text{eff}}(\text{N}(p)) = 3.00 \text{ eV}$). Consequently, to this perturbation, the U_{eff} for $\text{Co}(d)$ was reoptimized ($U_{\text{eff}}(\text{Co}(d)) = 1.15 \text{ eV}$, Figure A5.3, Tables A5.4-A5.5) in order to produce a new and accurate representation of the $T_{1/2}$ value.

With the new set of U_{eff} values, the computed $T_{1/2}$ is, therefore, strikingly reproduced with 171 K ($T_{1/2}(\text{exp}) = 171 \text{ K}$), and the following are also fulfilled: (i) the errors between calculated and measured cell parameters for $\mathbf{1}_{\text{cryst,1bar}}$ all fell below 4%: *max error* equals to 3.5% in $\mathbf{1}_{\text{cryst,LS,1bar,90K}}$ and 2.7% in $\mathbf{1}_{\text{cryst,HS,1bar,293K}}$; *average error* equals to 1.1% in $\mathbf{1}_{\text{cryst,LS,1bar,90K}}$ (Table A5.5) and 1.3% in $\mathbf{1}_{\text{cryst,HS,1bar,293K}}$ (Table A5.5); (ii) the *RMSD* for the atomic coordinates (Equation A5.1) a very good agreement with the experimental crystallographic data ($\mathbf{1}_{\text{cryst,HS}}$: 0.23 Å; $\mathbf{1}_{\text{cryst,LS}}$: 0.24 Å). It is worth mentioning that for this full range of $U_{\text{eff}}(\text{Co}(d))$, $\Delta H_{\text{el,HS-LS}}$ varies by about 2.20 eV. This small variation is more than enough to change the magnetic response of $\mathbf{1}_{\text{cryst,1bar}}$: at $U_{\text{eff}}(\text{Co}(d)) > 1.75 \text{ eV}$ $\mathbf{1}_{\text{cryst,1bar}}$ is *HS* at all temperatures and at $U_{\text{eff}}(\text{Co}(d)) < 0.50 \text{ eV}$ $\mathbf{1}_{\text{cryst,1bar}}$ is *LS* at all temperatures (Figure A5.3). In between 0.50 eV and 1.75 eV $\mathbf{1}_{\text{cryst,1bar}}$ is *SCO*, with the $T_{1/2}$ tuned to higher temperatures as $U_{\text{eff}}(\text{Co}(d))$ drops. $U_{\text{eff}}(\text{Co}(d)) = 1.15 \text{ eV}$ gives $T_{1/2}(\text{calc.}) = T_{1/2}(\text{exp.}) = 171 \text{ K}$ (Figure A5.3, Table A5.4).

The most striking result obtained in this “tuning” part of the computational setup, is the observation that the introduction of the functional corrections only on the cobalt ion ($U_{\text{eff}}(\text{Co}(d))$) is not sufficient to accurately reproduce the packing interactions. But, just by adding

functional corrections to the nitrogen atoms ($U_{\text{eff}}(\text{N}(p))$), a good agreement between all of the computed and experimental sets of data is achieved. Such a result also suggests that when post-*HF* calculations are used to calculate the $\Delta H_{\text{el,HS-LS}}$ splitting, the inclusion of only the *d* metal orbitals for the Complete Active Space Self Consistent Field (CASSCF) calculation may result in oversimplification.

Table 5.1. Unit cell parameters (*a*, *b*, *c*, α , β , γ , *V*) for $1_{\text{cryst,LS}}$ (top section) and $1_{\text{cryst,HS}}$ (bottom section) obtained experimentally at ambient pressure (*exp* data entries, in bold italics; LS at 90 K, 1 bar and at 293 K, 4300 bar; HS at 298 K, 1 bar) or calculated after unit cell optimisation at a range of different pressures, *p* (bar), and the temperature of 0 K.

LS		Cell Parameters					
pressure	<i>a</i> / Å	<i>b</i> / Å	<i>c</i> / Å	α / °	β / °	γ / °	<i>V</i> / Å³
<i>exp</i>	8.668	27.656	8.514	90.00	91.52	90.00	2040.277
1	8.366	27.536	8.357	89.971	90.925	89.901	1925.081
1800	8.328	27.473	8.334	90.156	90.945	89.727	1906.641
2100	8.323	27.464	8.330	90.145	90.923	89.670	1903.710
2500	8.322	27.442	8.321	90.153	90.852	89.579	1899.975
2900	8.311	27.421	8.312	90.233	90.972	89.687	1893.814
3900	8.329	27.137	8.309	88.025	89.908	82.939	1883.451
4300	8.300	27.355	8.282	89.868	90.849	89.729	1879.991
<i>exp</i>	8.795	8.795	27.918	90.00	90.00	90.00	2159.514
1	8.556	8.555	27.342	89.979	90.065	89.969	2001.271
1800	8.512	8.525	27.276	89.442	90.398	89.73	1978.911
2100	8.509	8.525	27.224	89.404	90.526	89.778	1974.626
2500	8.501	8.519	27.213	89.42	90.548	89.739	1970.445
2900	8.605	8.355	27.253	88.731	91.379	91.076	1958.018
3900	8.415	8.454	27.259	85.676	91.996	87.125	1956.776
4300	8.294	8.389	27.489	85.868	94.868	87.671	1906.644

Therefore, the inclusion of the contributions of *MOs* localised on the donor atoms of the coordinating ligands must be pursued to calculate the dynamic correlation through perturbative approaches (*CASPT2*, *NEVPT2*).^{144, 150-152} Indeed, *SCO* systems are characterised by a coordinative bond which is in large part covalent. This explains why the orbitals accounting for the first coordination sphere are so important to properly describe the electronic structure of the *SCO* complex

5.4.2. Structural Distortions in $[\text{Co}(\text{dpzca})_2]$ Unit Cell

$\mathbf{1}_{\text{cryst,LS}}$ is packed in the $P2_1/c$ space group at conditions of $p = 1$ bar and $T = 90$ K, as well as at $p = 4300$ bar at $T = 293$ K; whereas crystalline $\mathbf{1}_{\text{cryst,HS}}$ is packed in the $I4_1/a$ space group at conditions of $p = 1$ bar and $T = 298$ K. On the basis of these data, it is reasonable to assume that the space group of the unit cell of the *LS* species does not undergo any change as the pressure changes. However, this cannot be said for $\mathbf{1}_{\text{cryst,HS}}$, as the only experimental data available is at $p = 1$ bar. Hence, whilst conscious of the intrinsic limits, the geometries of crystalline $\mathbf{1}_{\text{cryst,LS}}$ and $\mathbf{1}_{\text{cryst,HS}}$ were calculated at the other six experimental pressures (from 1800 to 4300 bar, Table 5.1).

For $\mathbf{1}_{\text{cryst,LS}}$, from $p = 1$ bar to $p = 4300$ bar no significant distortions in the unit cell are observed, but rather a *gradual* reduction of the cell volume of 45 \AA^3 (-2.3%, Table 5.1, Table A5.6) due to the shortening of the cell axes (about -4.6%, Table 5.1, Table A5.6). The crystallographic data collected at the pressure of 4300 bar are in very good agreement with the calculated ones, confirming the robustness of the protocol employed from $p = 1$ bar to $p = 4300$ bar (Table 5.1). The only exception is that, at the pressure of 3900 bar, an out of trend distortion was obtained. This will be discussed shortly (Figure 5.3). For $\mathbf{1}_{\text{cryst,HS}}$, the structural overview was more complicated: as the pressure increases (from 1 bar to 4300 bar), an overall shrinking of the calculated *HS* unit cell volume is observed, mostly due to cell angles tilting

(-2.1%; Table 5.1, Table A5.5). From the pressure of 2900 bar and above, a strong distortion involving the cell angles (α , β and γ) ultimately changes the tetragonal cell into a monoclinic one. This distortion of α , β , γ increases progressively: from $[-1.2^\circ, +1.4^\circ, +1.1^\circ]$ (2900 bar) to $[-3.4^\circ, +4.0^\circ, -2.7^\circ]$ (3900 bar) until $[-4.2^\circ, +4.8^\circ, -2.3^\circ]$ (4300 bar) (Table 5.1). Such distortions lead to a much more intense shrinking of the cell HS unit volume, by 95 \AA^3 (-4.7%, from $p = 1 \text{ bar}$ to $p = 4300 \text{ bar}$, Table 5.1, Table A5.6). An out of trend distortion is observed both for $\mathbf{1}_{\text{cryst,HS}}$ and $\mathbf{1}_{\text{cryst,LS}}$ at the pressure of 3900 bar (Figure 5.3). All the computed unit cell parameters were correlated with the pressure and the experimental $T_{1/2}$ values (Table A5.7, Figures A5.4-A5.27). Only one parameter, c , significantly correlates with them ($R^2(p) = 0.93$, $R^2(T_{1/2}(\text{exp})) = 0.86$, Table A5.7 and Figures A5.20-A5.21), while all the others present poor or very poor R^2 values. For this reason, structural data cannot be used as an easy-to-hand tool to rationalise or predict the pressure induced SCO behaviour.

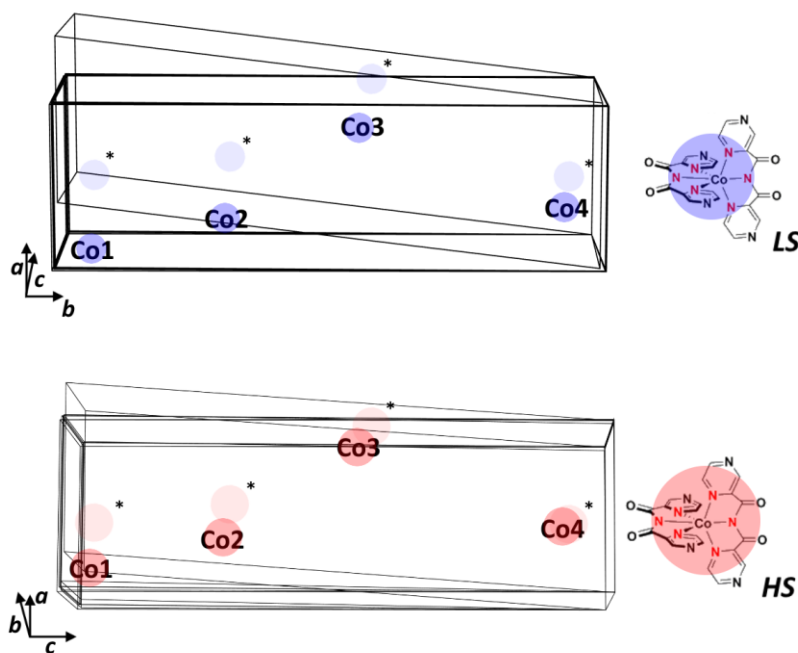


Figure 5.3. Superimposed calculated unit cells at the seven different pressures for $\mathbf{1}_{\text{cryst,LS}}$ (top) and $\mathbf{1}_{\text{cryst,HS}}$ (bottom), along with three of the sets of positions for the four Co^{II} ions. For $p = 3900 \text{ bar}$ (0.39 GPa; $1 \text{ bar} = 10^5 \text{ Pa}$) of external pressure an exceptional distortion is observed at the end of the cell optimization routine (this is also the only unit cell that does not closely overlay the other six unit cells); the stars highlight the positions of the four Co^{II} ions in this case.

5.4.1. Pressure Effects on Molecular Structure of $[\text{Co}(\text{dpzca})_2]$ Complexes

The effects of the unit cell shrinking as the pressure increases were monitored by looking at the variation of several structural parameters. Firstly, the *intermolecular* distances of three Co(II)-Co(II) distances (Co1-Co2, Co2-Co3, Co3-Co4) among the four $[\text{Co}(\text{dpzca})_2]$ molecules included in the crystalline cell (Figure 5.4, Table A5.8-S9). A clear trend is evident for both spin states only for the $d(\text{Co2-Co3})$. In this case, a monotonic decrease of both the *LS* and *HS* distances is observed and, interestingly, a difference of $\approx 2.5 \text{ \AA}$ is consistently conserved on passing between $\mathbf{1}_{\text{cryst,LS}}$ and $\mathbf{1}_{\text{cryst,HS}}$ (Figure 5.4, middle) regardless of the pressure value. A shorter $d(\text{Co2-Co3})$ value for the $\mathbf{1}_{\text{cryst,HS}}$ can be explained by the larger volume of the $[\text{Co}(\text{dpzca})_2]$ molecules in $\mathbf{1}_{\text{cryst,HS}}$, which is not compensated by the increased volume of the cell ($\mathbf{1}_{\text{cryst,HS}}$, 2001 \AA^3 vs $\mathbf{1}_{\text{cryst,LS}}$, 1953 \AA^3 at 1 bar, Table 5.1). For all distances, the four Co(II) ions in $\mathbf{1}_{\text{cryst,LS}}$ get steadily closer, $\Delta d(\text{Co-Co}) \approx -0.6-0.09\%$, from 1 to 4300 bar (Figure 5.4, blue).

However, the $d(\text{Co1-Co2})$ and $d(\text{Co3-Co4})$ in $\mathbf{1}_{\text{cryst,HS}}$ show no clear trend as the pressure increases from 1 to 4300 bar. The maximal variations are 0.07 \AA and 0.2 \AA for the former and the latter distances, respectively. In particular, an abrupt and substantial elongation of $d(\text{Co3-Co4})$ is observed for $\mathbf{1}_{\text{cryst,HS}}$ between 2500 bar and 2900 bar. This elongated value remains steady up to the final pressure of 4300 bar. The effects of the unit cell shrinking were also monitored by looking at the angular distortions within the complex, using a variety of parameters (Equations A5.1-A5.6 and Table A5.10). From $\mathbf{1}_{\text{cryst,LS}}$ to $\mathbf{1}_{\text{cryst,HS}}$, each distortion parameter (Σ , Θ , Ω) increased, in agreement with the marked deviation from a perfect octahedron as a consequence of the spin switch from *LS* to *HS* (Table A5.10; details in Section 5.6).

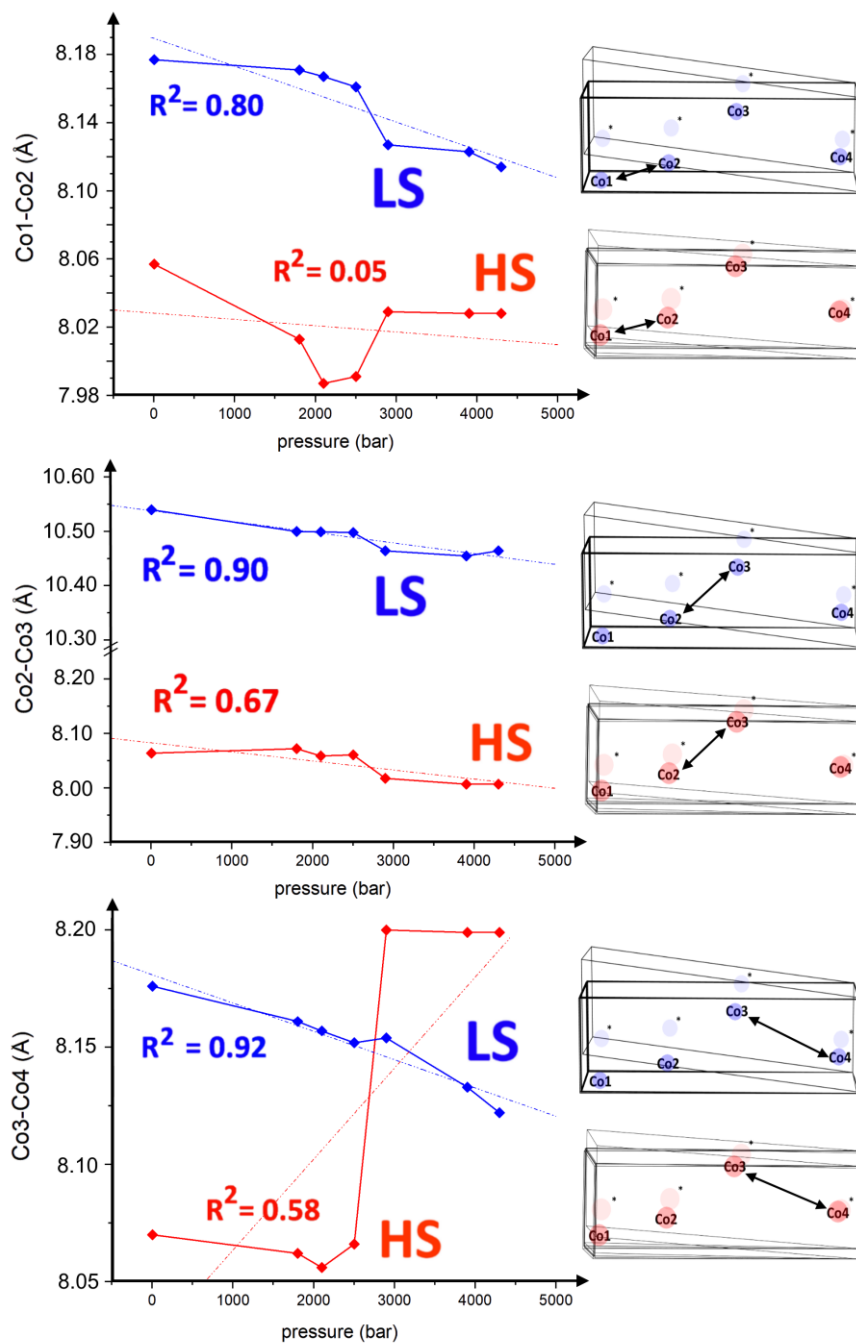


Figure 5.4. Calculated variations of the Co-Co intermolecular distances in 1_{cryst} (Å) from the pressure of 1 bar to 4300 bar. Three Co-Co distances (Co1-Co2; Co2-Co3; Co3-Co4) between neighbour molecules within the same crystalline cell are reported (solid lines are a guide to the eye and simply join the datapoints). Dotted trend lines report the correlation factor for $1_{\text{cryst,HS}}$ (red; (top) $R^2(\text{Co1-Co2}) = 0.05$; (middle) $R^2(\text{Co2-Co3}) = 0.67$; (bottom) $R^2(\text{Co3-Co4}) = 0.58$) and $1_{\text{cryst,LS}}$ (blue; (top) $R^2(\text{Co1-Co2}) = 0.80$; (middle) $R^2(\text{Co2-Co3}) = 0.90$; (bottom) $R^2(\text{Co3-Co4}) = 0.92$). 1 bar = 10^5 Pa.

The difference, $\Delta\Theta$, between the *HS* and *LS* states, of the trigonal distortion (Θ , defined as the degree of twist away from a perfect octahedron towards a trigonal prism, Equation A5.5), has been claimed to be a key parameter for the spin transition in $\text{ML}_6^{\text{n}+}$ complexes, with an inverse dependence with the $T_{1/2}$ observed.³⁰⁹ But this is not the case here.

The *RMSD* relates to how smoothly the $\mathbf{1}_{\text{cryst,HS}}$ and $\mathbf{1}_{\text{cryst,LS}}$ structures deviate with the increase of pressure with respect to the structure at 1 bar. *RMSD* is the only parameter that shows a monotonic variation with pressure increase, for both spin states. A particularly smooth growth of *RMSD* is observed for $\mathbf{1}_{\text{cryst,LS}}$ ($R^2 = 0.92$, Figure 5.5(left)). This is very likely due to the smaller volume of the $\mathbf{1}_{\text{cryst,LS}}$, which suffers less from progressive cell shrinking due to the pressure increase. For $\mathbf{1}_{\text{cryst,HS}}$, the behaviour is different: an *RMSD* trend similar to $\mathbf{1}_{\text{cryst,LS}}$ is observed up to 2500 bar, whereas a much steeper increase is observed at higher pressures ($R^2 = 0.95$, Figure 5.5(right)).

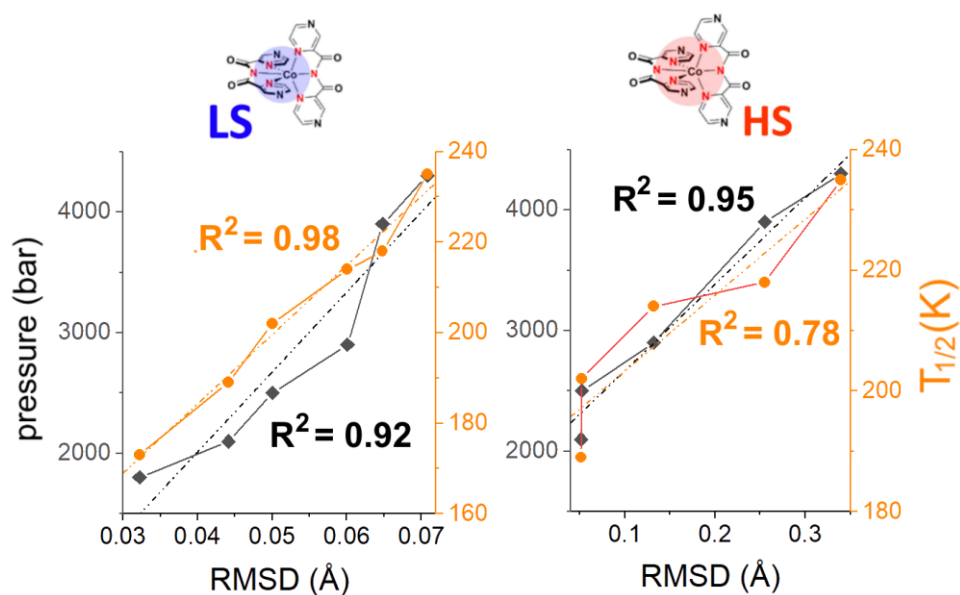


Figure 5.5. (left) For $\mathbf{1}_{\text{cryst,LS}}$, reported effects on the *RMSD* parameter (solid lines are a guide to the eyes and simply join the datapoints) of the pressure increase (black diamonds, $R^2 = 0.92$) and of the experimental $T_{1/2}$ values (orange circles, $R^2 = 0.98$). (right) For $\mathbf{1}_{\text{cryst,HS}}$, reported effects on the *RMSD* parameter (solid lines are a guide to the eyes and simply join the datapoints) of the pressure increase (black diamonds, $R^2 = 0.95$) and of the experimental $T_{1/2}$ values (orange circles, $R^2 = 0.78$).

Such different behaviour could be due to limits related to the employed computational protocol or, more intriguingly, to a possible significant change in the experimental crystallographic cell and/or space group for $\mathbf{1}_{\text{cryst,HS}}$.

Unfortunately, none of the above computed parameters showed any clear indication that could be useful to rationalise the deformations of the octahedron associated with the pressure-induced spin transition (Table A5.10, Figures A5.28-A5.46). On the basis of these results, the rationalisation of the evolution of the SCO transition produced by the change of the pressure by simple geometrical criteria appears elusive, at least if considering the whole pressure range. Once again, this is a demonstration of how complicated it is to reduce the rationalization of the SCO phenomenon to simple structural considerations.

5.4.2. Pressure Effects on $[\text{Co}(\text{dpzca})_2]$ Density of States

With the aim of finding easy-to-read observables suited to the rationalisation of the pressure induced SCO effects, the electronic structure was analysed through the computed Total Density of States (*TDOS*) for $\mathbf{1}_{\text{cryst,LS}}$ and $\mathbf{1}_{\text{cryst,HS}}$. *TDOS* curves report the orbital contribution of each atomic species to the electronic structure of $\mathbf{1}_{\text{cryst,LS}}$ and $\mathbf{1}_{\text{cryst,HS}}$ at various pressures (Figure 5.6). The overall electronic structures of $\mathbf{1}_{\text{cryst,LS}}$ and $\mathbf{1}_{\text{cryst,HS}}$ does not show very significant changes in any of the main features as the pressure is increased from 1 to 4300 bar (Figure 5.6). More interestingly, to disclose a specific contribution to band changes in $\mathbf{1}_{\text{cryst,LS}}$ and $\mathbf{1}_{\text{cryst,HS}}$ as the pressure increases, the projected components (*PDOS*) of the Co(II) *d*-orbitals were also computed (Figures A5.72-A5.78), as well as the N and C *s*- and *p*-orbitals (Figures A5.83-A5.86). This important step is compulsory in order to verify energy shifts in Co(II) *d*-orbitals, as the overall contributions of the Co(II) *d*-orbitals to the *TDOS* are marginal (as Co(II) ions are numerically lower than other atomic species). Small but distinguishable intensity variations can be seen for a few main peaks present in *TDOS* at -1.9 eV, -2.6 eV and -3.2 eV for $\mathbf{1}_{\text{cryst,LS}}$; and at energies of -0.5 eV, -0.7 eV, and -1.9 eV for $\mathbf{1}_{\text{cryst,HS}}$ (Table A5.11). It is worth noting that the band variation at -1.9 eV is common to both spin states.

Interestingly, but not unexpectedly, these variations are strongly (to moderately) correlating both with the applied pressures (min. 1 bar; max. 4300 bar) and the experimental $T_{1/2}$ values (min. 173 K; max. 235 K) (Table A5.11, Figure A5.60-A5.71), respectively. Very high correlation R^2 values for the three bands energy variation *vs* pressure are observed for $\mathbf{1}_{\text{cryst,LS}}$ ($R^2(-1.9 \text{ eV}) = 0.84$, $R^2(-2.6 \text{ eV}) = 0.97$, and $R^2(-3.2 \text{ eV}) = 0.97$, Table A5.11) while for $\mathbf{1}_{\text{cryst,HS}}$ a slightly lower correlations are observed ($R^2(-0.5 \text{ eV}) = 0.84$, $R^2(-0.7 \text{ eV}) = 0.97$, and $R^2(-1.9 \text{ eV}) = 0.77$, Table A5.11).

An overall lower correlation for the three bands energy variation vs $T_{1/2}$ was also obtained (Table A5.11). Indeed, very good correlation are found for $\mathbf{1}_{\text{cryst,LS}}$ ($R^2(-1.9 \text{ eV}) = 0.92$, $R^2(-2.6 \text{ eV}) = 0.74$, and $R^2(-3.2 \text{ eV}) = 0.74$, Table A5.11) and for $\mathbf{1}_{\text{cryst,HS}}$ ($R^2(-0.5 \text{ eV}) = 0.52$, $R^2(-0.7 \text{ eV}) = 0.73$, and $R^2(-1.9 \text{ eV}) = 0.87$, Table A5.11). The obtained results indicate that the employed computational protocol can be confidently used to monitor and predict the pressure effect on the overall electronic spectra. The most striking result is the very high correlation values are found for the -1.9eV peak variation vs $T_{1/2}$, which shows variations both for $\mathbf{1}_{\text{cryst,LS}}$ ($R^2 = 0.92$, Figure A5.60) and $\mathbf{1}_{\text{cryst,LS}}$ ($R^2 = 0.87$, Figure A5.69).

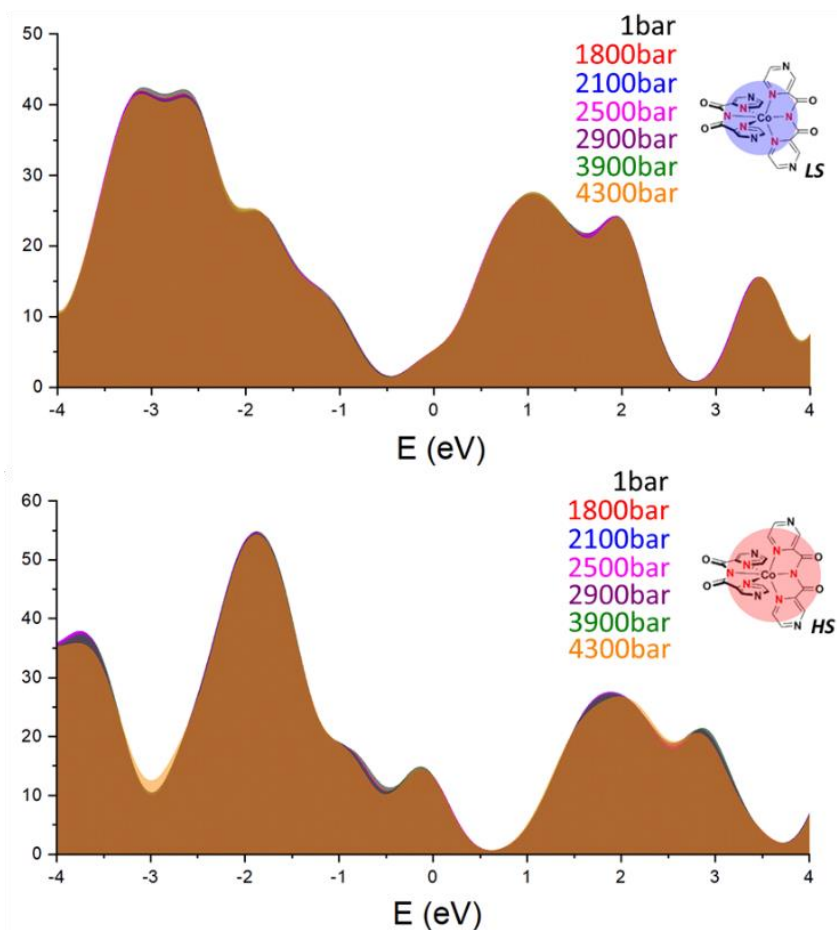


Figure 5.6. Reported TDOS for $\mathbf{1}_{\text{cry,LS}}$ (top) and to $\mathbf{1}_{\text{cry,HS}}$ (bottom) across the whole pressure range ($1 \text{ bar} < p < 4300 \text{ bar}$) in the energy range between -4 eV and $+4 \text{ eV}$. Colour code: 1 bar (black), 1800 bar (red), 2100 bar (blue), 2500 bar (magenta), 2900 bar (purple), 3900 bar (olive), 4300 bar (orange).

In practice, this means that once the *TDOS* are calculated the values of $T_{1/2}$ vs pressure can be reliably predicted. It is important to mention that, at the experimental level, computed tiny variations in the electronic structure are only interpreted with difficulty.

The *TDOS* profile in the -3.0eV to -0.5eV range deserves a deeper discussion. For $\mathbf{1}_{\text{cryst,LS}}$, the inter-band minimum (bottom at -2.1eV) between the two peaks at -2.6eV and -1.9eV suffers the most from the effect of the pressure increase. Conversely, in $\mathbf{1}_{\text{cryst,HS}}$ a decrease of the maximum of the peak at -1.9eV is observed. For both cases, a large part of the computed *TDOS* profile variation (25-35%) can be ascribed to a blue-shift of *MOs* bands with *d*-bonding/non-bonding metal character (Table A5.12, Figure 5.7, Figures A5.87-A5.88). Indeed, e_g -bonding like orbitals were observed for $\mathbf{1}_{\text{cryst,LS}}$; e_g bonding and non-bonding t_{2g} -like *MOs* for $\mathbf{1}_{\text{cryst,HS}}$. When the *MO* energies were trialled against the experimental pressure values, good to excellent correlations were found (Figures A5.89-A5.109). The correlation factor improves further if the only out-of-trend results for $\mathbf{1}_{\text{cryst,LS,3900bar}}$ and $\mathbf{1}_{\text{cryst,HS,3900bar}}$ are excluded (Figure 5.3). As well, a very good correlation was also found between the *MO* energies at different pressures and the measured $T_{1/2}$ in the same conditions (Figures A5.107-A5.124).

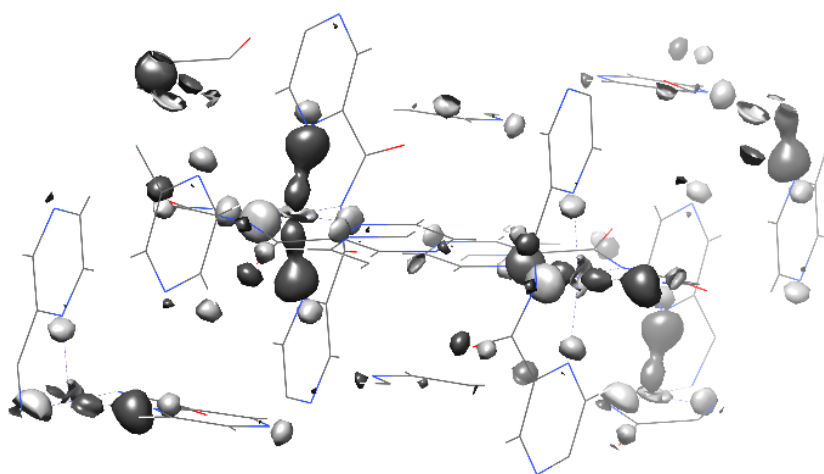


Figure 5.7. Plot showing the e_g bonding *MOs* 277β (e_g shaped; $E = -2.10\text{eV}$ at $p = 1\text{ bar}$, $E = -1.73\text{eV}$ at $p = 4300\text{bar}$) for the 4 molecules of $\mathbf{1}_{\text{cryst,HS}}$ in the unit cell, calculated at the pressure of 1 bar ($\rho_{\text{cutoff}} = 0.04$).

Such results can be rationalized as follows: the increasing pressure reduces the volume of the crystalline cell with consequent shrinking of the volume of $[\text{Co}(\text{dpzca})_2]$ molecules and shortening of the Co-N bonds (Table A5.10). A net increase in interelectronic repulsion is therefore expected with σ -bonding MOs being less stabilized and an increase of the overall $[\text{Co}(\text{dpzca})_2]$ MOs energy ladder is observed. However, the pressure induced changes on the overall electronic structure are far from being massive (Table A5.11), but with respect to the geometrical observables (Table A5.10), they are more evident and readable. This is because the electronic structure can act as a collective magnifier of the sum of all the tiny geometrical changes.

Finally, as it is often reported in literature,^{159,164} the energy gap at the Fermi level ($\Delta E_{\text{HOMO,LUMO}}$) for both $\mathbf{1}_{\text{cryst,HS}}$ and $\mathbf{1}_{\text{cryst,LS}}$ (Table A5.13) was also considered. Unfortunately, poor correlations were observed between the $\Delta E_{\text{HOMO,LUMO}}$ with the pressure or the experimental $T_{1/2}$ values (Table A5.13, Figures A5.127-S130). Such results indicate that the *HOMO-LUMO* gap cannot be considered as a reliable parameter for predicting the SCO behaviour, since it represents just one of the ingredients of the whole SCO process.

5.4.3. Pressure effects on IR and Raman spectra of $[\text{Co}(\text{dpzca})_2]$

Given the robust results obtained in reproducing both the geometry and the electronic structure, the vibrational structure of the $[\text{Co}(\text{dpzca})_2]$ molecule was then calculated in isolated conditions (named $\mathbf{1}_{\text{iso,LS}}$ and $\mathbf{1}_{\text{iso,HS}}$; see Section 5.6) and in a $3 \times 3 \times 1$ supercell charge field (named $\mathbf{1}_{\text{cf,LS}}$ and $\mathbf{1}_{\text{cf,HS}}$; see Section 5.6) for all of the experimentally applied pressures ($p = 1, 1800, 2100, 2500, 2900, 3900$ bar). Raman and IR spectra were calculated for $\mathbf{1}_{\text{cf,LS}}$ and $\mathbf{1}_{\text{cf,HS}}$ at the different pressure values and are compared with the results obtained experimentally by some of us (Figure 5.8).¹⁰⁴ Simulated IR/Raman

spectra were computed both for the whole unit cell in the presence of periodic conditions and on an isolated molecule in a Madelung field with the charges computed at the periodic level (Figure A5.133; see Section 5.6). The agreement between the IR spectra simulated with the two approaches is extremely good for $1_{\text{cf},\text{LS}}$ and good for $1_{\text{cf},\text{HS}}$ (Figures A5.133-A5.134). In Figure 5.8a, the experimental Raman spectra¹⁰⁴ are reported for 1_{cryst} at three different pressures: 1 bar (10^{-4} GPa, mostly $1_{\text{cryst},\text{HS}}$), 3200 bar (0.32 GPa, mixed $1_{\text{cryst},\text{HS};\text{LS}}$) and 5700 bar (0.57 GPa, fully $1_{\text{cryst},\text{LS}}$). Before getting into the analysis of the main features of the simulated 1_{cf} systems (Figure 5.8b-5.8d), it is worth mentioning that the Raman spectra simulated for optimised isolated molecules of $[\text{Co}(\text{dpzca})_2]$ (Figures 5.8c-5.8d, light grey plot) reveal only very small differences between the simulated spectra in the two different scenarios (isolated *vs.* crystalline). From Figure 5.8b, the main features of the calculated Raman spectra of purely $1_{\text{cf},\text{HS}}$ (red) and $1_{\text{cf},\text{LS}}$ (blue) at $p = 1$ bar can be compared. Particularly interesting is the observed blueshift of the most intense peak at 1250 cm^{-1} passing from $1_{\text{cf},\text{HS}}$ to $1_{\text{cf},\text{LS}}$. Such a result suggests that the experimental spectrum obtained at ambient pressure (Figure 5.8a, red plot) may not be 100% $1_{\text{cf},\text{HS}}$, as a small but significant percentage (about 10%) of $1_{\text{cf},\text{LS}}$ appears to still be present. This percentage value was derived by testing different ratios of $1_{\text{cf},\text{HS}}$ to $1_{\text{cf},\text{LS}}$ to reproduce the spectrum (Figure A5.134). The transition in the Raman spectrum from $1_{\text{cf},\text{LS}}$ to $1_{\text{cf},\text{HS}}$ can also be monitored by looking at the peaks at 1700 cm^{-1} and 1000 cm^{-1} where an overall change in the peak shape is observed and confirmed experimentally. Simulated spectra at higher pressures maintain the characteristic peaks reported for $1_{\text{cf},\text{LS}}$ (Figure 5.8c) and $1_{\text{cf},\text{HS}}$ (Figure 5.8d). This important result confirms that Raman spectroscopy can only be used to *qualitatively* monitor the spin state switching between the two spin states.

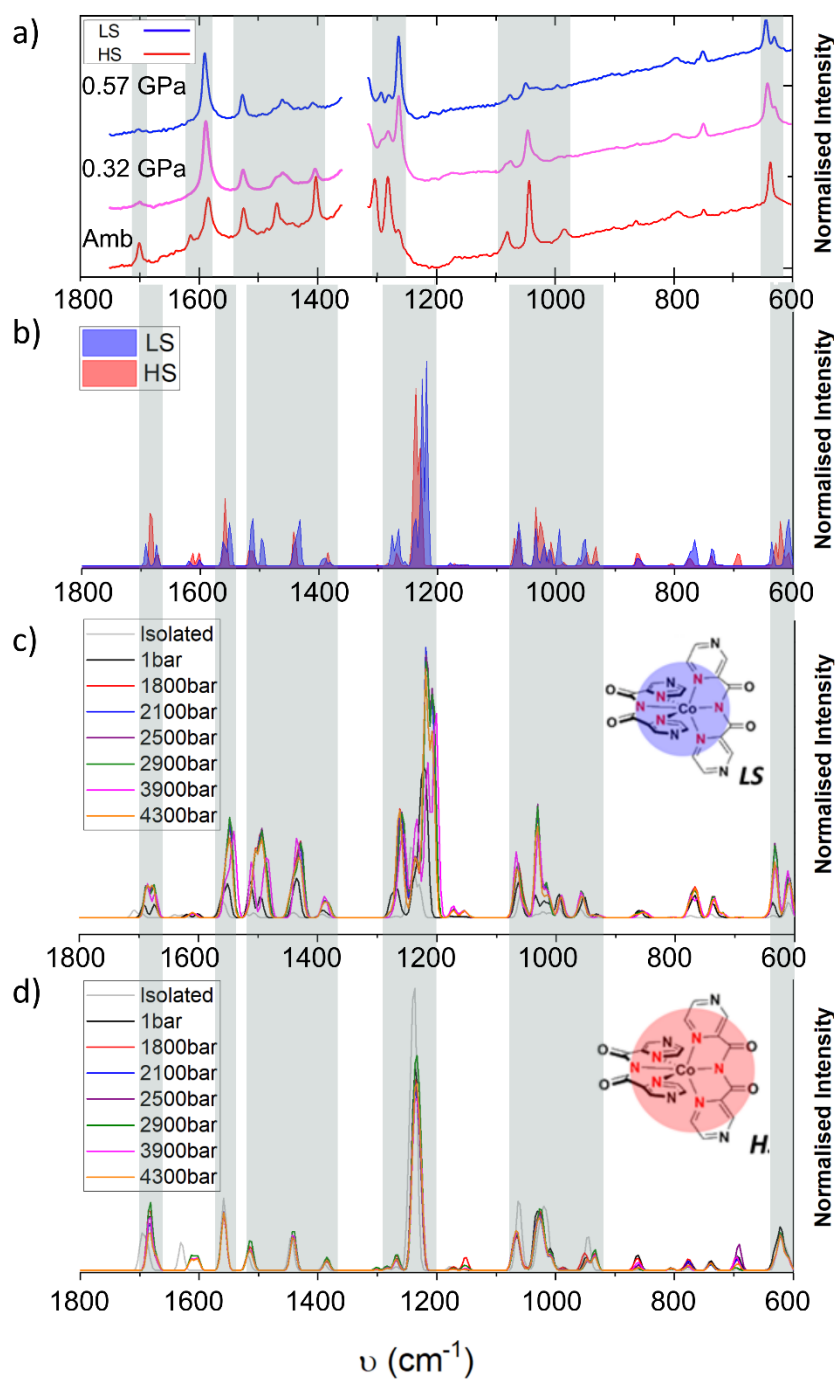


Figure 5.8. (a) Experimental Raman spectra measured at 298 K at three different pressures: $p = 10^{-4}$ GPa, $1_{\text{cryst,LS}}$ (blue); $p = 0.32$ GPa, mixed $1_{\text{cryst,LS/HS}}$ (magenta); $p = 0.57$ GPa, $1_{\text{cryst,HS}}$ (red).³¹ (b) Calculated Raman spectra for $1_{\text{cf,LS}}$ and $1_{\text{cf,HS}}$ at $p = 1$ bar ($w = 5$). (c) Calculated Raman spectra for $1_{\text{cf,LS}}$ at seven different pressures (1, 1800, 2100, 2500, 2900, 3900, 4300 bar; $w = 10$). (d) Calculated Raman spectra for $1_{\text{cf,HS}}$ at seven different pressures (1, 1800, 2100, 2500, 2900, 3900, 4300 bar, $w = 10$). Figure reproduced with modifications from ref.³¹ 1 bar = 10^4 Pa.

Indeed, a *quantitative* description of the ratio of $\mathbf{1}_{\text{cf,HS}}$ to $\mathbf{1}_{\text{cf,LS}}$ is difficult in absence of a spectrum of the pure *HS* species (experimental or computed), as the observed changes cannot be easily ascribed to one of the spin species (Figure 5.8b and Figure A5.134). Whilst the good agreement between experimental and computed spectra indicates that Raman spectroscopy can be used as a probe of the local molecular geometries, it cannot be used for monitoring the evolution of the unit cell.

5.4.4. Calculation of $T_{1/2}$ for SCO transition for $[\text{Co}(\text{dpzca})_2]$

Strong With strong agreement between the computed geometrical, vibrational, and electronic data with the corresponding experimental data in hand, the final step is to calculate the temperature induced SCO transition at different pressures. Using Equations 1-5, the spin switching curves were computed (Figure 5.9). The calculated SCO $T_{1/2}$ values (at $\gamma_{\text{HS}} = 0.5$) are compared with the measured values from reported earlier by some of us (Table 5.2).¹⁹ The $T_{1/2}$ SCO values are accurately reproduced ($\Delta T_{1/2} < 10$ K) for pressures of 1 bar to 2100 bar. This is a remarkable result considering that these values are obtained *ab initio* from scratch (i.e. relying only on the computational set up developed for $\mathbf{1}_{\text{cryst}}$ at 1 bar) with no experimental geometrical data supporting the high-pressure modelling. Unfortunately, the experimental order is not fully reproduced, but it is worth stressing that the calculated $T_{1/2}$ value is only 7 K lower than the average experimental $T_{1/2}$ at 1800 bar. The computed $T_{1/2} = 190$ K at 2100 bar is, instead, in strikingly good agreement with the average experimental $T_{1/2} = 189$ K. These results are very promising, especially if compared with previous studies reported in literature,^{164, 173} where an error larger than 50 K was reported at best; moreover, no claims of being predictive were proposed, in contrast to the method developed herein. At the pressure of 2500 bar, the error in the computed SCO transition, even if still lower than

the ones reported in other literature studies,^{164, 173} increases significantly ($\Delta T_{1/2} = 30$ K). At yet higher pressures, the computational protocol fails. Indeed, for pressures of 2900 and 3900 bar, the LS state is predicted to be the ground state up to 400 K (Figure 5.9). For $p = 4300$ bar, the calculated vibrational frequencies are not available, as it was not possible to reach sufficiently tight levels of convergence that are required for the calculation of $T_{1/2}$. As the pressure increases, the largest variation is observed for $\Delta H_{el,HS-LS}$: 0.32 eV (1 bar) to 1.64 eV (4300 bar) (see also Table A5.12). The $\Delta H_{el,HS-LS}$ term is ≈ 0.32 eV up to 2500 bar while at higher pressures, a widening of the $\Delta H_{el,HS-LS}$ gap is observed. On the basis of the considerations that neither the electronic nor the vibrational spectra show an *abrupt* change in their features, the computed discrepancies between experimental and computed $T_{1/2}$ likely reside in the reproduction of the $\mathbf{1}_{\text{cryst,HS}}$ unit cell.

Table 5.2. Values of $T_{1/2}$ (K) for the $\mathbf{1}_{\text{cryst}}$ SCO transition calculated in this study (at $\gamma_{\text{HS}} = 0.5$), along with the experimental values for the SCO obtained by some of us (at $\gamma_{\text{HS}} = 0.5$),³⁰ and the difference between the experimental and the calculated results.

p / bar	Calc. $T_{1/2}$ ($\gamma_{\text{HS}} = 0.5$)	Exp. $T_{1/2}$ ($\gamma_{\text{HS}} = 0.5$)			Calc. vs Exp.
	$T_{1/2}$ (Gradual SCO)	$T_{1/2}$ (av.)	$T_{1/2}$ (up)	$T_{1/2}$ (down)	$\Delta T_{1/2} / \langle \Delta T_{1/2} \rangle$
1	171	171	173	169	2-2 / 2
1800	164	171	173	168	9-4 / 6
2100	190	189	189	188	1-2 / 1
2500	173	202	202	202	30-30 / 30
2900	LS	214	214	214	-
3900	LS	218	218	218	-
4300	-	235	235	235	-

However, considering the agreement with the experimental findings obtained for the 1800 and 2100 bar, it is also likely that $\mathbf{1}_{\text{cryst,HS}}$ might go through a crystallographic phase change, as already observed for other systems.²⁹⁷⁻³⁰⁴ This eventuality cannot be excluded due to the absence of experimental structural data and the limited information provided by the Raman spectra. Another possible explanation is reaching the computational and protocol limits to reproducing the eventual change of the crystallographic symmetry or of the space group for $\mathbf{1}_{\text{cryst,HS}}$. The prediction of the latter is a general challenge that remains open in the literature, and is outside the scope of this work. Above 2500 bar, the $\Delta H_{\text{el,HS-LS}}$ gap gets wider: 2900 bar ($\Delta H_{\text{el,HS-LS}} = 1.08 \text{ eV}$); 3900 bar ($\Delta H_{\text{el,HS-LS}} = 1.08 \text{ eV}$) and 4300 bar ($\Delta H_{\text{el,HS-LS}} = 1.64 \text{ eV}$) (Table A5.14). This wider gap is driven by a steeper increase in the $\Delta H_{\text{el,HS-LS}}$ energy of the $\mathbf{1}_{\text{cryst,HS}}$ (destabilising effects of pressure, Table A5.14); for $\mathbf{1}_{\text{cryst,LS}}$ a linear increase of $\Delta H_{\text{el,HS-LS}}$ is observed from pressure 1 bar to pressure 4300 bar (Table A5.14).

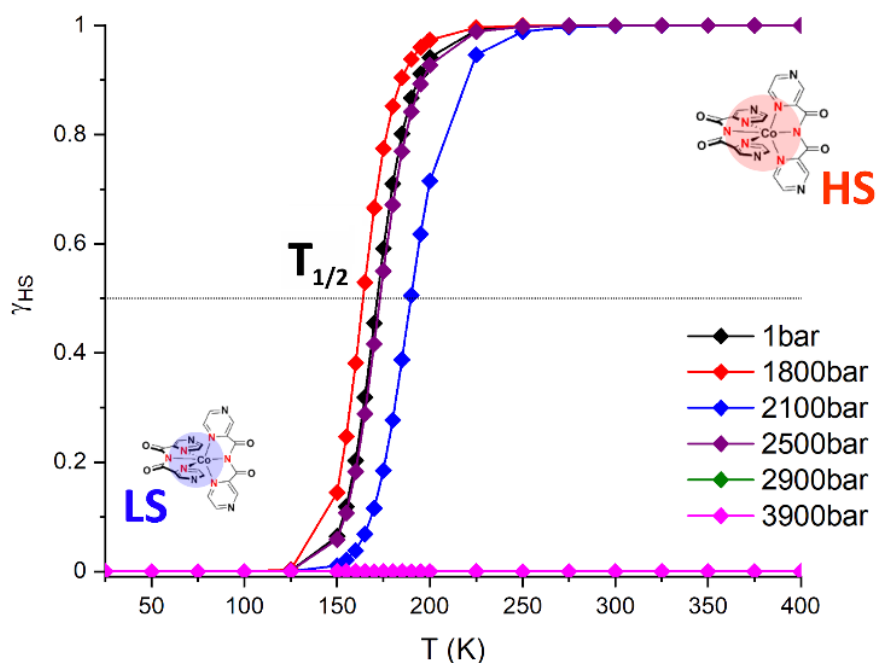


Figure 5.9. Calculated results of the Boltzmann transition (regular SCO) of $\mathbf{1}_{\text{cryst}}$ at external pressures from 1 to 3900 bar. The thermal SCO transition curve was obtained by using the model published by Ribas-Arino et al. in 2014.⁴³

This energy increase (*destabilisation*) is expected when the crystalline cell experiences strong external pressures that are able to reduce the crystal cell volume and force the molecules into more distorted geometries.¹⁹

As the pressure increases, the variation in $\Delta H_{\text{vib,HS-LS}}$ term reveals tiny changes in the order of magnitude of meV (Table A5.16-S17). Similar trends are observed for the $\Delta S_{\text{vib,HS-LS}}$ and $\Delta S_{\text{el,HS-LS}}$ terms, but the changes are even more negligible (or even absent) (Tables A5.18-A5.19). Therefore, as expected, the crucial parameters for the derivation of $T_{1/2}$ are $\Delta H_{\text{el,HS-LS}}$, while all the others contribute only marginally. However, it is worth noticing that $\Delta H_{\text{el,HS-LS}}$ does not follow a linear trend with the increase of the pressure.

5.5. Conclusions

The computational protocol developed herein to model thermal and pressure-active $\text{SCO } \mathbf{1}_{\text{cryst}}$ in the solid state proved to be able to reach an extremely good agreement with the experimental data, accurately reproducing the SCO behaviour up to a pressure of 2100 bar with an error on $\Delta T_{1/2}(\text{exp. vs. th.}) < 10$ K. From the pressure of 2500 bar, the agreement between experimental and theoretical results drops to $\Delta T_{1/2}(\text{exp. vs. th.}) < 30$ K, while for even higher pressures, $\mathbf{1}_{\text{cryst,LS}}$ is expected to be the ground state at least up to 400 K. In the absence of structural experimental findings of $\mathbf{1}_{\text{cryst,HS}}$ at these high pressures, it is possible that this deviation between the computed and the experimental $T_{1/2}$ at higher pressures is due to a crystallographic phase change right for $\mathbf{1}_{\text{cryst,HS}}$.²⁹⁷⁻³⁰⁴ Such an eventuality is supported by the accuracy reached by our computational protocol in the reproduction of the structural, vibrational, and electronical experimental findings for $\mathbf{1}_{\text{cryst}}$. Since the X-ray determination of $\mathbf{1}_{\text{cryst,HS}}$ at high temperatures and pressures presents several significant challenges, the presented computational protocol can be used to propose that there may be an intrinsic change of the unit cell symmetry. In summary, the obtained results are very promising, providing far more accurate $T_{1/2}$ values than ever before reported in the literature,^{164, 173} and showing an unprecedented predictive power. The $\Delta H_{\text{el,HS-LS}}$ gap is proven to be the crucial parameter in the SCO transition, but also that entropic and packing effects, and accurate calculations of them, must be taken into account to reach the fine tuning of the $T_{1/2}$. Of particular interest going forwards from here is the very good correlation between experimental $T_{1/2}$ at a range of pressure values with specific features observed in the calculated TDOS plots (i.e. with Co-L e_g -bonding and t_{2g} -non-bonding interactions). Inter alia, the variation of DOS profiles at -1.9eV , present in both species, showed a high correlation value with the $T_{1/2}$ values. This result paves the way toward the possible use of TDOS for predicting the change in the $T_{1/2}$ of the SCO transition as a function of the applied pressure, but only if an accurate computational protocol like this one is available. Overall, these results represent a very promising step forward in predicting the SCO phenomenon in the solid state

5.6. Computational Protocol

All periodic calculations were performed with the CP2K 6.1 quantum chemistry software,³¹¹ which employs the Gaussian-plane waves formalism (GPW). Norm-conserving Goedecker-Tetter Hutter (GTH) pseudopotentials³¹²⁻³¹⁴ along with double zeta basis set with polarisation functions (DZVP-MOLOPT-SR) were employed for C, N, O, H atoms and DZVP-MOLOPT-SR-GTH basis set was applied to Co atoms. A cut-off of 450 Ry was applied for the plane wave expansion.³¹⁵

The Anasimov simplified version¹⁶⁸ of the DFT+U approach³⁰⁵ was used (U_{eff}). The U_{eff} parameters were chosen to match the experimental X-ray data observables (cell parameters and atomic positions) of both $\mathbf{1}_{\text{cryst,LS}}$ and $\mathbf{1}_{\text{cryst,HS}}$ at 1 bar of pressure along with the corresponding $T_{1/2}$ value (*abrupt* $T_{1/2}\uparrow$ from ref¹⁹). Tests on U_{eff} values for Co, N, C, O, and H atoms were performed with revPBE functional³¹⁶ with rVV10³¹⁷⁻³¹⁸ as non-local VdW correlation functional. The exact reproduction of the average $T_{1/2}$ value (171 K) for the *abrupt* component of the SCO at 1 bar proved be very sensitive to the U_{eff} values chosen for the d orbitals of the cobalt ion (Co(d)) whilst the reproduction of the crystallographic parameters was needed to tune the U_{eff} on the p -orbitals on the nitrogen atoms (N(p); Tables A5.2-A5.3). In such a framework, the best computational set up was achieved with $U_{\text{eff}}(\text{Co}(d)) = 1.15 \text{ eV}$ and $U_{\text{eff}}(\text{N}(p)) = 3.0 \text{ eV}$. Cell optimisations were performed to very tight levels of convergence for the wavefunction (1.0×10^{-9} Hartree) and for the atomic forces (1.0×10^{-8} Hartree bohr⁻¹).

Hessian matrices were calculated and checked to ensure that no imaginary eigenvalues values were present. Being performed at the Γ point, 3N-3 frequencies (optical modes) were computed and used to calculate the thermodynamic quantities (see below, Tables A5.14-A5.19).

This procedure was repeated for six out the seven pressures (1800, 2100, 2500, 2900, 3900 bar) reported in ref¹⁹ at which the experimental SCO activity of $\mathbf{1}_{\text{cryst}}$ was measured. For $p = 4300$ bar, $\mathbf{1}_{\text{cryst,HS}}$ did not reach satisfying convergence criteria. Finally, IR/Raman spectra were calculated for $\mathbf{1}_{\text{cryst,LS}}$ and

$\mathbf{1}_{\text{cryst,HS}}$ in vacuum and in the charge field built over the optimised structures obtained at the end of the calculations performed with CP2K6.1 package and re-run with ORCA4.1 code,²⁵⁸ using PBE functional³¹⁹ and def2-TZVPP basis sets.^{261-262, 320} Two different kind of calculations were performed: (i) re-optimising the isolated $[\text{Co}^{\text{II}}(\text{dpzca})_2]$ ($\mathbf{1}_{\text{iso,LS}}$ and $\mathbf{1}_{\text{iso,HS}}$) molecules in vacuum and (ii) re-optimising the structures of one $[\text{Co}(\text{dpzca})_2]$ molecule in a charge field ($\mathbf{1}_{\text{cf,LS}}$ and $\mathbf{1}_{\text{cf,HS}}$) produced by the $3 \times 3 \times 1$ supercell obtained at the end of the cell optimisation with CP2K6.1 code for each pressure. The charge field was set by replacing each atom kind with the respective Mulliken charge at the Potential Energy (*PES*) minima; the $3 \times 3 \times 1$ supercell was obtained by replicating the original crystalline unit cells nine times. For both $\mathbf{1}_{\text{cf,LS}}$ and $\mathbf{1}_{\text{cf,HS}}$: three times along the shorter *a*- and *c*-axes and once along the longer *b*-axes.

The effects of the cell shrinking were monitored by looking at the angular distortions within the complex, using a variety of parameters (Equations S1-S6 and Table A5.10); *RMSD* measures the average divergence between atomic position when the studied system is compared to a reference (in this study, the molecules in $\mathbf{1}_{\text{cryst,LS}}$ and $\mathbf{1}_{\text{cryst,HS}}$ at $p = 1$ bar) (Equation A5.1); $\langle \mathbf{D} \rangle$ describes the average Co-N bond distance). ζ is the sum of the differences between individual Co-N bond distance *vs.* the mean Co-N bond (Equation A5.2);³²¹ Δ is the average of the differences between individual Co-N bond distance *vs.* the mean Co-N bond (Equation A5.3);³²² Σ describes the local angular deviation from the *cis* octahedral angles of 90° (Equation A5.4);³²³ Θ measures the trigonal torsion, which is defined as the degree of twist from a perfect octahedron towards trigonal prismatic: it is obtained by the sum of the differences of the absolute value of all 24 unique angles (Equation A5.5).³²⁴ Finally, Ω measures the three angles, ω , of each of the eight triangles (24 angles in total) found in a perfect octahedron (Equation A5.6).³⁰⁹ For a perfect octahedral geometry, all the distortion parameters (Σ , Θ , Ω) are equal to zero. $\langle \mathbf{D} \rangle$, ζ , Δ , Σ , Θ , were calculated using OctaDist 2.6.1 software;³²⁵ *RMSD* was calculated using VMD software.³²⁶



Final Remarks

This PhD project aimed to investigate a range of methods potentially capable of predicting molecular properties of new SCO complexes in the early stages of the synthetic design. Achieving this would make synthetic strategies more efficient, reducing unsuccessful attempts and enabling targeting of a complex with the expected properties.

This goal was pursued by operating through three main strategies: (i) the employment of the δN_A chemical shift to predict the experimental $T_{1/2}$ for iron(II) solution SCO complexes (discussed in *Chapter Two*), (ii) the *quantitative* assessment of the **M-L** bond energy in iron(II) solution SCO complexes by using the *EDA-NOCV* model (discussed in *Chapter Three* and *Chapter Four*) and (iii) the development of an approach based on periodic *DFT* to predict the solid state SCO behaviour in $[\text{Co}^{\text{II}}(\text{dpzca})_2]$ at different pressures (discussed in *Chapter Five*).

In *Chapter Two*, the δN_A vs. $T_{1/2}$ correlations previously established in 2017 by Brooker *et al.*⁸³ for two families of iron(II) solution SCO complexes, of *Lazine* and **bpp**^{X,Y} ligands, are successfully extended to two further literature families, of **pybox**^X and **pytacn**^X ligands, and to a new family of *L^{pytZ}* ligands synthesised in this thesis for the first time (a total of forty-two iron(II) complexes and five families). The new *L^{pytZ}* ligand family, composed of four new members **Z** = **CF**₃, **Br**, **F**, **Me** (in addition to *L^{pytH}* which was already reported in literature¹⁰⁵), was synthesised and characterised for the first time in this thesis (Figure 6.1a). As well, the corresponding four new $[\text{Fe}(\text{L}^{\text{pytZ}})_2(\text{NCBH}_3)_2]$ complexes were synthesised and characterised, including single crystal X-ray structure determination on all four complexes (Figure 6.1b). All four of the $[\text{Fe}^{\text{II}}(\text{L}^{\text{pytZ}})_2(\text{NCBH}_3)_2]$ complexes showed SCO behaviour around room temperature in both solid and solution, revealing potential applications at room temperature for most of the candidates (Figure 6.2).

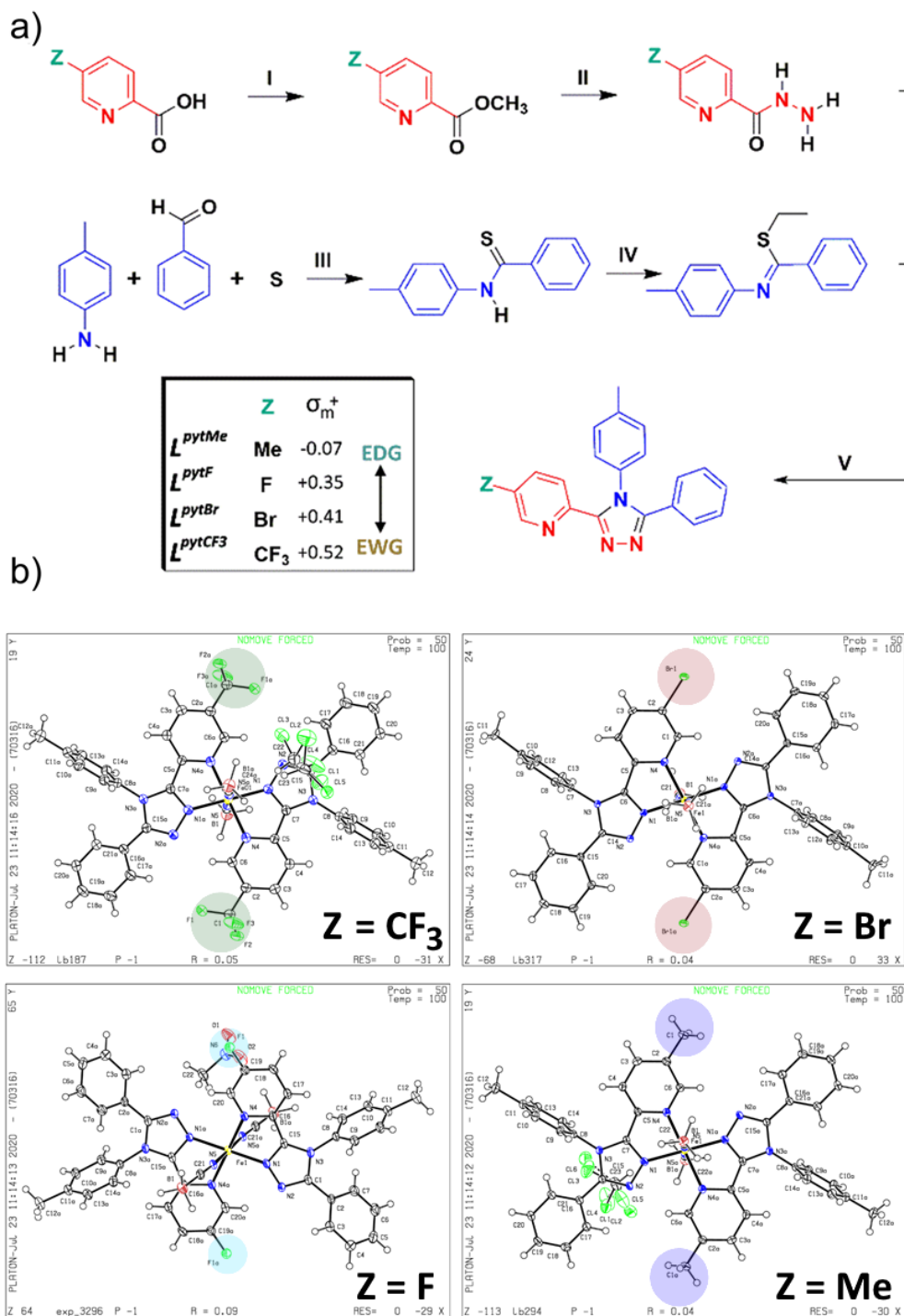


Figure 6.1. (a) Multistep synthesis of the four new Z -pyridyl-ring substituted L^{py^Z} ligands; the L^{py^H} ligand was reported previously.⁸³ (b) Solved crystallographic structures of the four newly synthesised $[Fe(L^{py^Z})_2(NCBH_3)_2]$ -solvents ($Z = CF_3, Br, F, Me$).

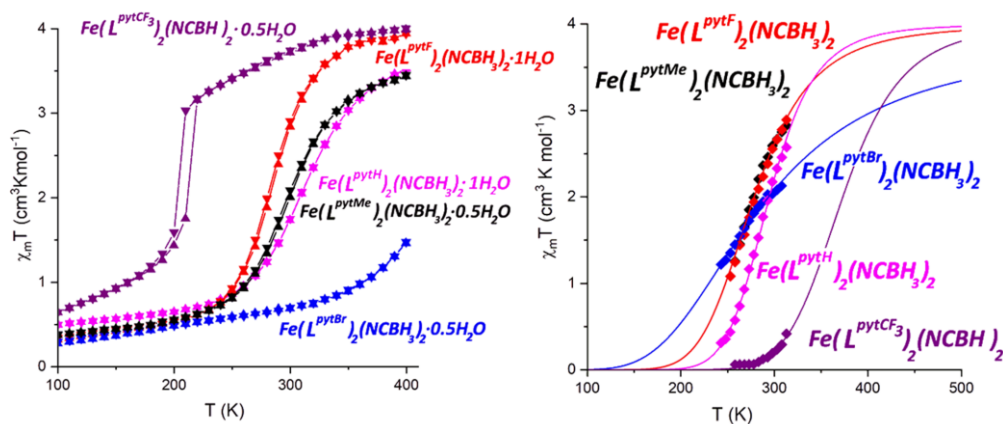


Figure 6.2. Solid state measurements (right) and solution phase measurements in CDCl_3 solution (left) of $\chi_{\text{M}}T$ vs temperature (T) for all four new $[\text{Fe}(\text{L}^{\text{pytZ}})_2(\text{NCBH}_3)_2] \cdot n\text{H}_2\text{O}$ complexes and the literature data for the $[\text{Fe}(\text{L}^{\text{pytH}})_2(\text{NCBH}_3)_2]$ complex.¹⁰⁵

This study also proved that the $\delta\text{N}_{\text{A}}$ chemical shift can be more generally used as a predictive tool for fine tuning solution $T_{1/2}$ values by choice of *para*-**X** substituent: good to extremely $\delta\text{N}_{\text{A}}$ vs. $T_{1/2}$ (Figure 6.3a-c) are observed for both new cases, the literature families of **pybox**^x ($R^2 = 0.69$) and **pytacn**^x ($R^2 = 0.96$), similar to that reported for **bpp**^x ($R^2 = 0.87$) previously.⁸³ But in the case of *meta* substituents (**Y**, **Z**), only weak correlations are observed between the $\delta\text{N}_{\text{A}}$ chemical shift of the free ligand and the experimental $T_{1/2}$ of the related iron(II) complex: L^{pytZ} ($R^2 = 0.37$), literature **bpp**^y ($R^2 = 0.15$) (Figure 6.3a-c).

Next, consideration was given to the use of the easily calculated, experimentally verifiable, $\delta\text{N}_{\text{A}}$ as an alternative to the Hammett constant σ_{p}^+ as a measure of the EDG/EWG effect of a change in substituent. Good to extremely good $\delta\text{N}_{\text{A}}$ vs. σ_{p}^+ correlations were found for the *para*-**X** substituted families: (**bpp**^x ($R^2 = 0.89$), **pybox**^x ($R^2 = 0.76$), **pytacn**^x ($R^2 = 0.94$), Figure 6.3d). So $\delta\text{N}_{\text{A}}$ can be used in place of σ_{p}^+ for *para*-**X** substituents. This means that any substituent, including those for which σ_{p}^+ is not available, can be used. The use of $\delta\text{N}_{\text{A}}$ also enables comparison of other types of ligand modification, such as N/O/S/CH substitutions.

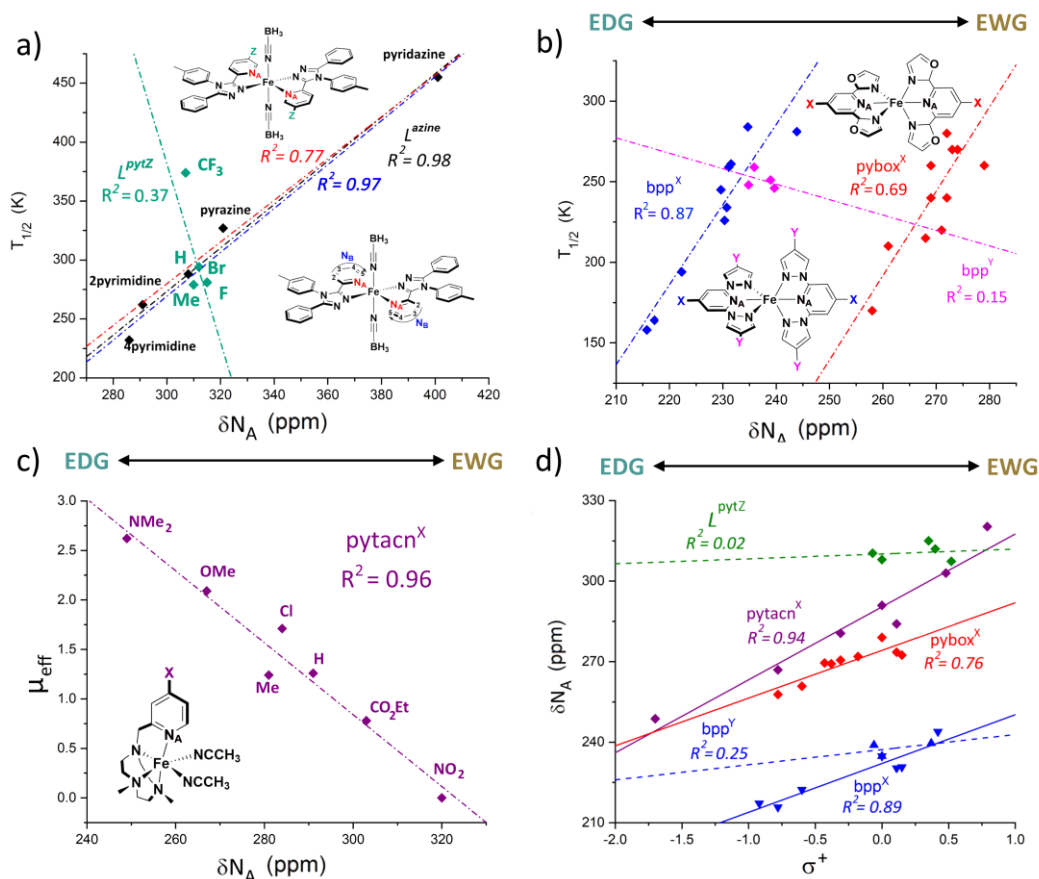


Figure 6.3. (a) Correlation between $\delta N_A(L)$ vs. solution $T_{1/2}([Fe(L)_2(NCBH_3)_2])$. Poor correlation for the five L^{pytZ} ($R^2 = 0.37$, green line); extremely good correlations for the five L^{azine} ($R^2 = 0.98$, black line); good correlations for the eight $[Fe(L)_2(NCBH_3)_2]$ complexes ($L = L^{azine}$ and L^{pytZ} , $R^2 = 0.77$, red line); extremely good correlations for the seven $[Fe(L)_2(NCBH_3)_2]$ complexes (except L^{pytCF_3}) ($R^2 = 0.97$, blue line). (b) Good correlation between $\delta N_A(pybox^X)$ vs. $T_{1/2}([Fe(pybox^X)_2]^{2+})$ ($R^2 = 0.69$, red line); extremely good correlation between $\delta N_A(bpp^X)$ vs. $T_{1/2}([Fe(bpp^X)_2]^{2+})$ ($R^2 = 0.87$, blue line); poor good correlation between $\delta N_A(bpp^Y)$ vs. $T_{1/2}([Fe(bpp^Y)_2]^{2+})$ ($R^2 = 0.15$, magenta line). (c) Extremely good correlation between $\delta N_A(pytacn^X)$ vs. $T_{1/2}([Fe(pytacn^X)(NCCH_3)_2]^{2+})$ ($R^2 = 0.96$, purple line) (d) Correlation between $\delta N_A(\text{ligands})$ vs. the Hammett parameter σ^+ (note: EWG: $\sigma^+ > 0$, EDG: $\sigma^+ < 0$). X (para) substituents are reported with solid lines, Y (meta) substituents are reported with dashed lines. All the reported δN_A values are calculated.

Not surprisingly, the *meta* substituents did not give good correlations of δN_A vs. σ_m^+ : (bpp^Y ($R^2 = 0.25$), L^{pytZ} ($R^2 = 0.02$)) (Figure 6.3d), so δN_A cannot be used in place of σ_m^+ for *meta* substituents.

This comparison between the use of the Hammett parameter (σ/σ^+) and the δN_A chemical shift is another key take-home message of this study: δN_A can be easily calculated for any ligand or any substituent, and it can be experimentally validated – whereas the Hammett parameters are not always available, or indeed appropriate (e.g., **CH/N/O/S** substitutions).

In *Chapters Three and Four*, EDA-NOCV theory was applied to SCO compounds for the first time. Implementation of this model enables the details of the energetic profile of the **M-L** bonds to be quantified (Figure 6.4(left)). The focus was on developing and validating a protocol that would enable a *quantitative* study of the variation in σ -donor and π -acceptor properties of families in any kind of metal complex.

In order to develop a solid and generalisable protocol, five different fragmentation schemes for $[\text{Fe}(\text{L}^{\text{azine}})_2(\text{NCBH}_3)_2]$ were examined in *Chapter Two* (Figure 6.4(left)). A corrected description of fragmentation **5** was selected as (i) it establishes a constant reference level able to maximise differences occurring from different ligands and (ii) it generalises the approach so that it is applicable to any **ML₆** complex, independent of the choice of the metal ion, spin state or oxidation state. Using this fragmentation protocol, the EDA-NOCV analysis of the five $[\text{Fe}^{\text{II}}(\text{L}^{\text{azine}})_2(\text{NCBH}_3)_2]$ complexes (Figure 6.4(right)) revealed a very strong correlation between the σ and π **M-L** bond strength ($\Delta E_{\text{orb},\sigma+\pi}$) and the experimental *solution* $T_{1/2}$ of the complexes ($R^2 = 0.99$; Figure 6.4(right)). This is consistent with the impact of varying the coordinated azine being felt synergistically, through both the σ and π components of the Fe-N bonds.

In *Chapter Four*, EDA-NOCV analysis of sixteen of the members of the literature solution SCO $[\text{Fe}(\text{bpp}^{\text{X}})]^{2+}$ family was used to quantify the σ - and π -bonding strength of the Fe-N bonds as *para*-**X** varied. This enabled an in-depth analysis of how the *para* substituent **X** affects the σ - and π -bonding strength in Fe-N bonding as **X** changed from electron donating (EDG, e.g., **X** = **NMe₂**) to electron withdrawing (EWG, e.g., **X** = **NO₂**).

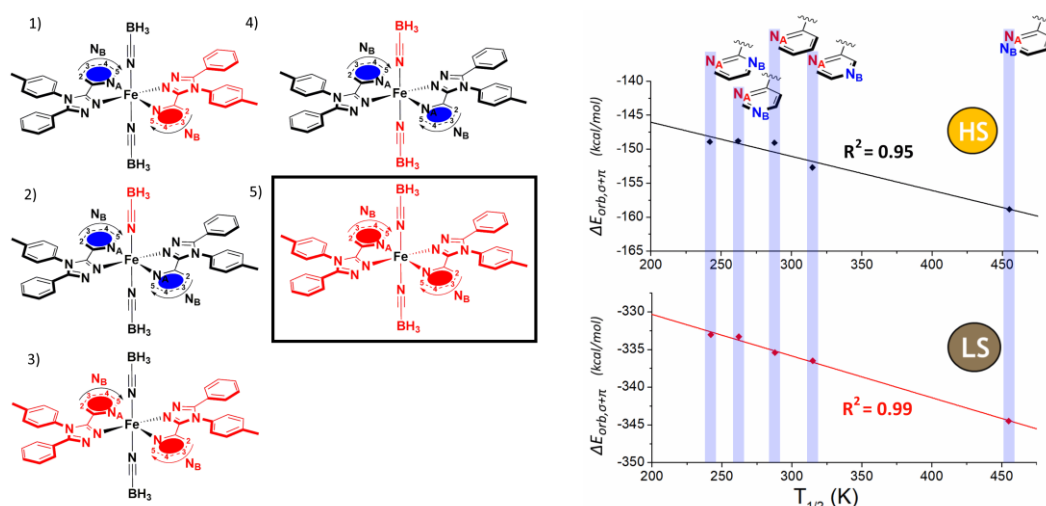


Figure 6.4. (left) The five fragmentations 1-5 (top to bottom) trialled for EDA-NOCV analysis of the five LS $[Fe(Lazine)_2(NCBH_3)_2]$ complexes (fragment A in black; fragment B in red). (right) Strong correlations are seen between $\Delta E_{orb,\sigma+\pi}$ (calculated using fragmentation 5, details in Section 3.3) and solution $T_{1/2}$, for both the LS state complexes ($R^2 = 0.99$) and the HS state complexes ($R^2 = 0.95$).

Surprising results were obtained: it was observed that as **X** changes from **EDG** \rightarrow **EWG** properties (σ_p^+ increases), the σ -donor capability of the **bpp^X** ligand in coordinating to the iron(II) ion increases, as reflected in $\Delta E_{orb,\sigma}$ becoming more negative (stable). Furthermore, $\Delta E_{orb,\sigma}$ correlated well with the Hammett parameter σ_p^+ ($R^2 = 0.88$, Figure 6.5(left)) and with the experimental $T_{1/2}$ solution ($R^2 = 0.82$, Figure 6.5(left)) of the $[Fe(\mathbf{bpp}^X)_2]^{2+}$ complex. The surprising result, that **EDG** \rightarrow **EWG** on the **bpp^X** ligand actually increases the **Fe** \leftarrow **N_A** σ -bond strength, was explained through Mulliken analysis of the population of the valence orbitals of the coordinating nitrogen atom **N_A** in the **bpp^X** ligand (Figure 6.5(right)).

Indeed, it is observed that – as the nitrogen lone pair involved in the **Fe** \leftarrow **N_A** σ -bond and the nitrogen π -electrons involved in the aromatic ring and the **Fe** \rightarrow **N_A** π -backdonation are mutually orthogonal (Figure 6.5(right)) – an opposite polarisation links the increase in electron withdrawal over the π -system with an increase in electron charge on the nitrogen lone pair

involved in the $\text{Fe} \leftarrow \text{N}_A$ σ -bond (Figure 6.5(right)). The *EDA-NOCV* results, in combination with the Mulliken charge analysis, explain at a deep molecular level the effect that the substituent X has on the ligand electronic structure. Finally, the correlations found in this study were used to predict the Hammett parameter (σ_p^+) for two substituents ($\sigma_p^+(\text{SOMe}) = 0.26$, $\sigma_p^+(\text{SO}_2\text{Me}) = 0.60$) for which it is not yet available in the literature.

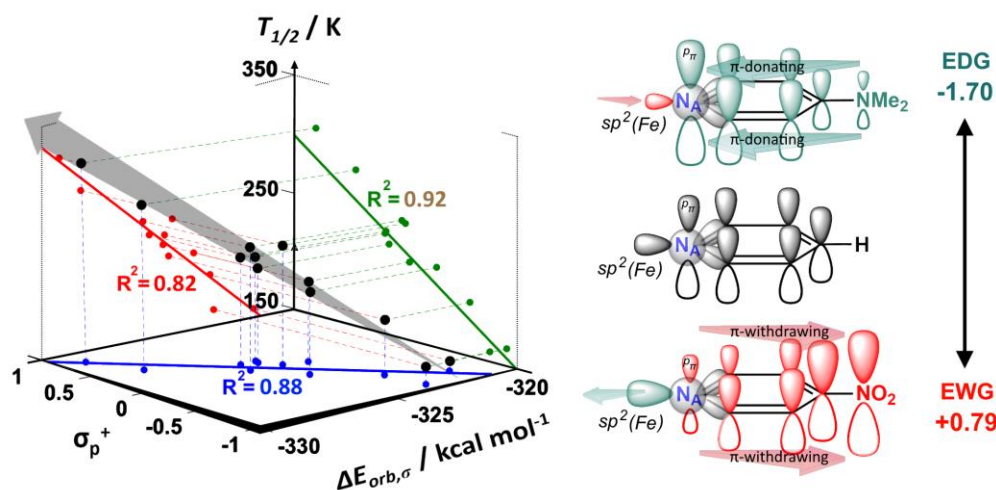


Figure 6.5. (a) Three strong pairwise correlations (blue, red and green lines), and a cross-correlation (black dots; grey arrow is only a guide to the eye) between the ligand donation properties ($\Delta E_{\text{orb},\sigma}$; calculated by *EDA-NOCV* for the LS complexes using fragmentation **5b**), the Hammett constant of X (σ_p^+), and the solution switching temperature ($T_{1/2}$) for the twelve SCO-active complexes for which $\sigma_p^+(\text{X})$ is known in this family of $[\text{Fe}(\text{bpp}^{\text{X}})_2]^{2+}$ complexes ($\text{X} = \text{SOMe}, \text{SO}_2\text{Me}, \text{NH}_2, \text{NMe}_2$ are absent, as $\sigma_p^+(\text{X})$ is not known for the first two, and the last two remain HS). (b) Representation of the $\text{N}_A(\text{AOs})$ of the pyridyl ring in the referenced $[\text{Fe}(\text{bpp}^{\text{H}})_2]^{2+}$ complex (centre) and at the substituted ligands at the ending of the Hammett scale ($[\text{Fe}(\text{bpp}^{\text{NMe}_2})_2]^{2+}$, $\sigma_p^+ = -1.70$ (top); $[\text{Fe}(\text{bpp}^{\text{NO}_2})_2]^{2+}$, $\sigma_p^+ = +0.79$ (bottom)). Arrows describe directionality of the resonance effects on $\text{N}_A(p\pi)$ and $\text{N}_A(sp^2(\text{Fe}))$, determined by Mulliken charge analysis.

Finally, in *Chapter Five* (the last project in this PhD thesis), a robust computational protocol was established and applied on the temperature/pressure induced SCO complex **1_{cy}** at the solid state for which experimental data were collected by Brooker *et al.* in 2012¹⁰⁴ and 2015¹⁹ (Figure 6.6(right)). The protocol was tuned for the atmospheric pressure, 1

bar (Figure 6.6(right), blue curve) to be applied, afterward, to other six pressures. This protocol was able to predict the SCO behaviour of 1_{cry} as the pressure was increased up to 2100 bar with very high accuracy ($\Delta T_{1/2} < 10$ K), far above the one previously reported in the few works present in literature.^{164, 173} However, for higher values of pressure, the accuracy drops. On the bases of the computed trends for structural, electronic, and vibrational observables, a possible explanation of this divergence from experimental results at higher pressures may be ascribed to crystallographic changes for $1_{\text{cry,HS}}$ unit cell.

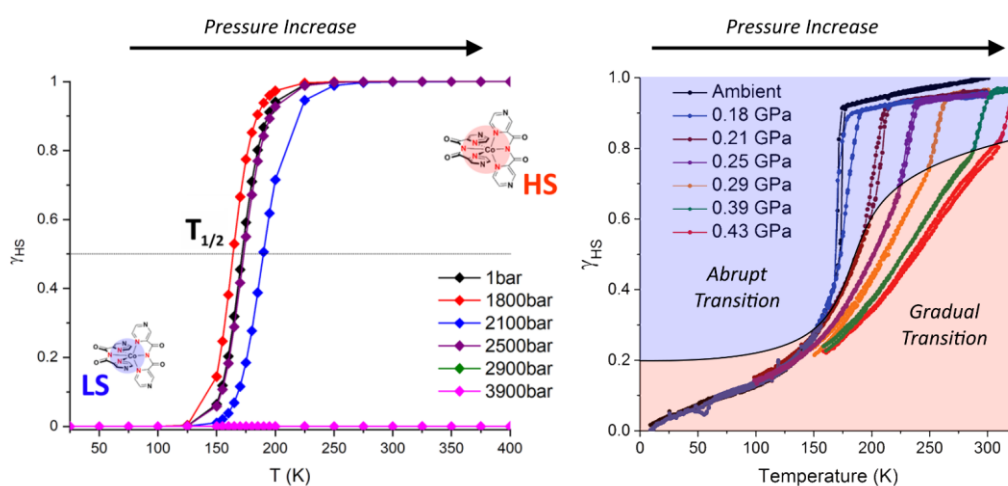


Figure 6.6. (left) Calculated curves for gradual transition of 1_{cry} from external pressure of bar to 1 bar to 3900 bar (10⁻⁴ to 0.39 GPa). SCO transition curves were obtained by using the model published by Ribas-Arino et al. in 2014.¹⁶⁶ (right) Fraction HS (γ_{HS}) versus temperature for 1_{cry} , obtained from VT magnetic data collected in the solid state as a function of increasing pressure for selected isobars from ambient to 4300 bar (0.43 GPa). Figure reproduced with modifications from ref¹⁹.

In support to this, experimental data (Figure 6.6(right)) show a change in the SCO behaviour for 1_{cry} above 2500 bar from *abrupt* to *gradual* (SCO *gradual:abrupt* 20:80 at $p = 1$ bar; SCO *gradual:abrupt* 80:20 at $p = 4300$ bar). This is consistent with the possibility that the $1_{\text{cry,HS}}$ undergoes to some crystallographic change at higher pressures (Figure 6.6). This hypothesis cannot be tested against experiment, as to obtain the $1_{\text{cry,HS}}$ at 4300 bar

would require temperatures about 350 K and only room temperatures ($T = 293$ K) data was collected in the diamond cell.¹⁹

In conclusion, the overall results presented in *Chapter Five*, prove that our robust computational protocol is able to account structural, electronic, and packing effects paving the way for a reliable prediction the SCO effect at the solid state.

A1 | Additional Details

A1.1. Experimental Section: General Procedures

Elemental analyses (C, H, N, S) were measured at the Campbell Microanalytical Laboratory, University of Otago.

Evans method NMR measurements were carried out on a Varian 500MHz NMR spectrometer, using a OneProbe with a variable temperature controller, between 243 to 313 K in intervals of 5 K, with expected error in T of ± 1 K. A diamagnetic correction for the sample ($-M \times 0.5 \times 10^{-6} \text{ cm}^3 \text{ mol}^{-1}$),¹¹⁹ and a correction for the variation of the viscosity of the solvent with temperature,¹²⁰ were applied to each dataset (Table A2.2). The least squares fittings were obtained by modelling each dataset as a *gradual* and complete *SCO* using the regular solution model (equation A2.1),^{216-217, 327} with good fits obtained, providing the derived parameters ΔH and ΔS , and hence access to $T_{1/2}(\Delta H/\Delta S)$ (Table A2.1). This was carried out using OriginPro version 9.1.0 from OriginLab Corporation. For all fits, the maximum χ_{MT} value ($\chi_{\text{MT}}(\text{max})$) was set to $3.5 \text{ cm}^3 \cdot \text{K} \cdot \text{mol}^{-1}$ in Equation A2.1,^{216-217, 327} the expected value for a *HS* iron(II) centre.^{23, 92}

Single-crystal X-ray diffraction data were collected on an Oxford Diffraction SuperNova diffractometer with Atlas CCD, equipped with a Cryostream N₂ open-flow cooling device,³²⁸ using mirror monochromated micro-focus Cu-K α radiation at 100 K. The series of scans was performed in such a way as to collect a complete set of unique reflections to a maximum resolution of 0.80 Å. Raw frame data (including data reduction, inter-frame scaling, unit cell refinement and absorption corrections)³²⁹ for all structures were processed using CrysAlis Pro.³³⁰

Structures were solved using SUPERFLIP³³¹ and refined using full-matrix least-squares on F^2 and refined against F^2 using all data by full-matrix

least-squares techniques with SHELXS-2014³³² and refined using full-matrix least-squares on F2 within the X-Seed graphical user interface Olex2-1.2. All hydrogen atoms were inserted at calculated positions with $U(H) = 1.2 U$ (attached atom), and rode on the atoms to which they were attached. Further details of the refinements, including modelling disordered solvent of crystallisation, and additional tables are provided in the ESI (Tables A2.1-A2.6).

All solid state magnetic susceptibilities were measured under a magnetic field of 0.1 T on a Quantum Design Physical Property Measurement System (PPMS) equipped with a vibrating sample mount (VersaLab). Four 50–400–50 K cycles were obtained for each $[\text{Fe}^{\text{II}}(\text{L}^{\text{pytZ}})_2(\text{NCBH}_3)_2] \cdot x\text{H}_2\text{O}$, to check for reproducibility. In the first three cycles data were obtained in 10 K steps, then in the fourth and final cycle in 2.5 K steps either side (± 20 K) of the observed $T_{1/2}$ for two of the complexes, $[\text{Fe}(\text{L}^{\text{pytZ}})_2(\text{NCBH}_3)_2] \cdot x\text{H}_2\text{O}$ where **Z** = **F** or **Me**), in all cases ramping between steps at 2 K min^{-1} .

These measurements are obtained in settle mode (the instrument considers the temperature “settled” after 1 min of the temperature being within the smaller value of $\pm 0.5 \text{ K}$ or $\pm 0.5\%$ of the target value). Due to the observation of thermal *hysteresis*, a scan rate (at 20, 10, 5, 2 and 0.2 K min^{-1}) study of $\chi_{\text{M}}T$ vs T was carried out for $[\text{Fe}(\text{L}^{\text{pytCF}_3})_2(\text{NCBH}_3)_2] \cdot 0.5\text{H}_2\text{O}$, from 150 to 250 K, in sweep mode (data collected continuously as T swept at specified rate). All of the data were corrected for the diamagnetism of the capsule and of the sample ($-M \times 0.5 \times 10^{-6} \text{ cm}^3\text{mol}^{-1}$).¹¹⁹

Solution UV-Vis spectra of a 1:6 ratio of $\text{Fe}(\text{pyridine})_4(\text{NCBH}_3)_2$: L^{pytZ} (Subsection A2.1.14), in HPLC grade CHCl_3 that was first neutralised by filtering it through a pad of Al_2O_3 , and were 0.5 mM in Fe(II), were recorded at room temperature on a PerkinElmer Lambda 950 UV-Vis/NIR.

A1.2. Theoretical Background

A1.2.1. Schrödinger Equation

The history of the modern quantum chemistry had birth in 1927 when Erwin Schrödinger published for the first time his time-independent equation (Equation A1.1) for describing the properties of any quantum mechanical system.³³³

$$\hat{H}_{TOT}\psi_{TOT}(R_{\alpha}, r_i) = E_{TOT}\psi_{TOT}(R_{\alpha}, r_i) \quad (\text{A1.1})$$

Where the \hat{H}_{TOT} operator includes the all set of operators which describe the energy of the system (*kinetic, potential energy*); ψ_{TOT} is the total wavefunction of the system, determined by each electronic position (r_i) and each nuclear position (R_{α}).

Considering those two terms ($r_i; R_{\alpha}$) almost independent each other, the total wavefunction $\psi_{TOT}(R_{\alpha}, r_i)$ can be written as a product of two semi-independent wavefunctions which describe the nuclei $\psi_{nucl}(R_{\alpha})$ and the electrons $\psi_{el}(R_{\alpha}, r_i)$. Consequently, to this wavefunction splitting, the full Hamiltonian \hat{H}_{TOT} can be also split into its two fundamental terms - the nuclear contribution \hat{H}_{nucl} and the electronic contribution \hat{H}_{el}

$$\hat{H}_{TOT} = \hat{H}_{nucl} + \hat{H}_{el} \quad (\text{A1.2})$$

$$\psi_{TOT}(R_{\alpha}, r_i) = \psi_{nucl}(R_{\alpha})\psi_{el}(R_{\alpha}, r_i) \quad (\text{A1.3})$$

Solving equation A1.3 as follow:

$$\hat{H}_{TOT}(R_{\alpha}, r_i)\psi_{TOT}(R_{\alpha}, r_i) = [\hat{H}_{nucl}(R_{\alpha}) + \hat{H}_{el}(R_{\alpha}, r_i)]\psi_{nucl}(R_{\alpha})\psi_{el}(R_{\alpha}, r_i) \quad (\text{A1.4})$$

$$= (\hat{H}_{nucl}(R_\alpha) + \hat{H}_{el}(R_\alpha, r_i))\psi_{nucl}(R_\alpha) + \hat{H}_{el}(R_\alpha, r_i)\psi_{el}(R_\alpha, r_i) + \hat{H}_{nucl}(R_\alpha)\psi_{el}(R_\alpha, r_i) \quad (A1.5)$$

Reported Equation A1.4 shows a dependency of $\psi_{el}(R_\alpha, r_i)$ by the nuclear Hamiltonian $\hat{H}_{nucl}(R_\alpha)$ which does not allow to treat the electronic structure as completely independent by the nuclear wavefunction. In other words, the $\hat{H}_{nucl}(R_\alpha)\psi_{el}(R_\alpha, r_i)$ term is the mathematical description of the physical phenomenon of coupling between electronic and vibrational wavefunctions. In 1927, Born and Oppenheimer demonstrated that, in most of the cases,³³⁴ this contaminated term can be neglected and the two wavefunctions can be treated as independent; this is due to the huge speed difference between electrons motion and nuclei motion (about 10^6 ms^{-1}) which make any electronic rearrangement almost instantaneous in the nuclei reference system.

The last term of Equation A1.5 can be so neglected and the two wavefunction considered completely independent for fixed values of R_α (nuclei position).³³⁴

$$\hat{H}_{TOT}(R_\alpha, r_i)\psi_{TOT}(R_\alpha, r_i) = \hat{H}_{TOT}\psi_{nucl}(R_\alpha) + \hat{H}_{el}\psi_{el}(R_\alpha, r_i) \quad (A1.6)$$

The Electronic Hamiltonian \hat{H}_{el} so defined can be further decomposed in the each of his components as reported in Equation A1.7.

$$\hat{H}_{el} = \hat{T}(r_i) + \hat{V}(R_\alpha, r_i) + \hat{W}(r_i, r_j) \quad (A1.7)$$

Where $\hat{T}(r_i)$ is the kinetic energy operator, $\hat{V}(R_\alpha, r_i)$ includes the nuclei-electron repulsion and the nuclei-electron attraction; $\hat{W}(r_i, r_j)$ is the term accounting for electron-electron repulsion; nuclei-nuclei repulsion is added to $\hat{W}(r_i, r_j)$ term as a constant (for fixed positions). The most problematic term in Equation A1.7 is the inter-electronic term $\hat{W}(r_i, r_j)$ which makes the Schrödinger equation impossible to be exactly solved for system which more than one electron. Therefore, two main theory were developed across the years

to try to get a good approximation of the Schrödinger equation: Hartree-Fock Theory (*HF*) and Density Functional Theory (*DFT*). These theories are very different in the way they treat electrons; consequently, both have advantages and disadvantages. The inter-electronic term $\widehat{W}(r_i, r_j)$ includes some important energetic terms, treated differently in *HF* and *DFT*, defined as *correlation energies* which describe the magnitude of the ‘awareness’ a single electron has of all the other ones. There are two different kind of correlations:

1. *STATIC CORRELATION*. This term comes out when a system has a ground state which can be described by more than one wavefunction, i.e., more than one electronic rearrangement in degenerate or *quasi*-degenerate structures (as the resonance forms in aromatic systems or the allocation of *d*-electrons in quasi-degenerate t_{2g} orbitals in metal ions). This error arises when the applied theory does not consider both the equivalent electronic structure but just one of them, with a consequent increase of the energy of the final system. This correlation is missing both in *HF* theory and *DFT* theory whereby both the wavefunctions are single determinantal (one single wavefunction).³³⁵
2. *DYNAMIC CORRELATION*. This term describes the spatial and spin restrictions when the interaction between two electrons is considered. This term is completely neglected in *HF* theory where the two body interaction is replaced by the interaction with an average potential.³³⁶ Instead, it is empirically treated in *DFT*, as discussed in the next section.

A1.2.2. Density Functional Theory

In order to understand why *DFT* is so widely used to compared with *HF* it is necessary to recall principal issues related with this previous approach. In Hatree-Fock theory each electron is treated singularly in an average potential

field produced by all the other electrons. In this approach each electron is thus described using a single-electron wavefunction. Moreover, each single-electron wavefunction is then mathematically combined together to respect properties of anti-symmetry and normalisation of the system, to give the overall molecular wavefunction.

The final mathematical description of this molecular wavefunction is called a *Slater determinant*. The size of the *Slater determinant* increases exponentially with the increase of the number of electrons, providing some expectable major limits about the system size. The *HF* wavefunction depends on $3N$ variable (with N number of electrons and x_i, y_i, z_i cartesian coordinates for each electron) plus the spin state (σ_i). It can be easily understood how quickly any kind of *HF* calculation become demanding.

In 1965 Hohenberg and Sham set the basis of *DFT* proving two important theorems: the first one establishes the connection between the system electronic properties and its electronic density; with this theorem the wavefunction is not necessary anymore and the electronic structure can be studied without the tedious problem of the demanding costs imposed by the *Slater determinant*,³³⁷ instead using an electron density of only three variables.

The second theorem states that the theory respects the variational theorem, i. e. any approximation of the electron density, which leads to a less accurate solution of the Schrödinger equation describes a system higher in energy than the real one.³³⁷ This new approach which works with a system dependent by only three variables (x, y, z coordinates of the electron density), instead of $3N$ variables, assures the chance to move beyond the size limits imposed by *HF* theory.

In Equation A1.8 is reported the total energy of the system $E[\rho]$ as a functional of the density ρ ; in the right side of the equation the same energetic terms described previously in the chapter are reported as well in terms of functionals of the density ρ . Functional is a mathematical transformation which produces a number from a function.

$$E[\rho] = T[\rho] + W[\rho] + V[\rho] \quad (\text{A1.8})$$

If we look more in depth to each of these terms, *DFT* limits will easily emerge. In a system composed by *interacting* particles (as any real one) the kinetic term $T[\rho]$ is impossible to be calculated exactly. This issue addressed many years later and its solution, a reasonably strong approximation in the new-born method, is still in place today. In 1965 – after the Hohenberg and Sham theorems were published – a new method developed by Kohn and Sham gave to this theory a chance to get real applications. This new method arises from two statements:

1. Definition of the density through the use of orbitals.
2. Treating of the system as *non-interacting*.

Those two strong approximations were able to give a first very approximated solution to the *DFT* applicability problem. The use of a *non-interacting* system leads to easily calculate the kinetic term $T_{NI}[\rho]$. If a set of orbitals is introduced in a *non-interacting* system the solution can be calculated exactly (as in the *HF* theory).

$$T_{NI}[\rho] = \sum_{i=1}^N \left\langle \varphi_i \left| -\frac{1}{2} \nabla^2 \right| \varphi_i \right\rangle \quad (\text{A1.9})$$

Where φ_i are the all orbitals which describe our system. Therefore, as calculated for *non-interacting* system, the resulting functional just approximate the real $T_I[\rho]$. $T_{NI}[\rho]$ captures the majority of $T_I[\rho]$ except for a small term.

The second term in Equation A1.8 ($W[\rho]$) carries with it another unsolved problem. This term depends on the interaction of two electrons, consequently the term is a functional of $\rho(r_1, r_2)$ where r_1 and r_2 are the spatial position of two electrons. We can approximate this functional to the electrostatic repulsion between two densities $\rho(r_1)$ and $\rho(r_2)$ which interact classically as follows.

$$J[\rho] = \frac{1}{2} \iint \frac{\rho(r_1)\rho(r_2)}{r_{12}} \partial r_1 \partial r_2 \quad (\text{A1.10})$$

Unfortunately, also with this trick we are just introducing another approximation by neglecting two important terms:

1. The exchange term of the interaction energy. The simple shift of the electronic density as a diffuse charge does not account for the different description between fermions and bosons.
2. The *self-interaction* term which comes from the approximation that ρ is not calculated as a sum of particles but a spread charge. This approximation includes the interaction of a particle with itself and it must be corrected.

The classical approximation for this second term is corrected by changing the definition of the total density $\rho(r_1, r_2)$.

$$\rho(r_1, r_2) = \rho(r_1)\rho(r_2)(1 + h_{xc}(r_1, r_2)) \quad (\text{A1.11})$$

Where inside the new term $h_{xc}(r_1, r_2)$ all of the errors introduced by a classical electron treatment (points 1 and 2 above) are collected. Therefore, the new expression of $W[\rho]$ would be:

$$W[\rho] = J[\rho] + \frac{1}{2} \int \rho(r_1) v_{xc}(r_1) \partial r_1 \quad (\text{A1.12})$$

Where the function $v_{xc}(r_1)$ is defined as follow.

$$v_{xc}(r_1) = \frac{1}{2} \int \frac{\rho(r_2) h_{xc}(r_1, r_2)}{r_{12}} \partial r_2 \quad (\text{A1.13})$$

The $v_{xc}(r_1)$ term becomes the bridge from the classical to the quantum treatment of the problem with the inclusion of the exchange and correlation effects.

Finally, the last functional in Equation A1.8 ($V[\rho]$) does not need other approximations and it can be calculated exactly. If we re-write Equation A1.8 using the approximations presented so far, the new description is:

$$E[\rho] = T_{NI}[\rho] + T_I[\rho] - T_{NI}[\rho] + J[\rho] + W[\rho] - J[\rho] + V[\rho] \quad (\text{A1.14})$$

Which can be summarised in Equation A1.15:

$$E[\rho] = T_{NI}[\rho] + J[\rho] + V[\rho] + E_{XC}[\rho] \quad (\text{A1.15})$$

Where $E_{XC}[\rho]$ includes all of the approximations.

$$E_{XC}[\rho] = T_I[\rho] - T_{NI}[\rho] + W[\rho] - J[\rho] \quad (\text{A1.16})$$

Gathering all the approximations into a single functional makes this approach ‘theoretically’ exact. In fact, by discovering the exact function $v_{xc}(r_1)$, the equation leads to exact answer. Unfortunately, the exact description of $v_{xc}(r_1)$ is unknown. On the years many approaches have tried to approximate, as close as possible, the real potential v_{XC} , required to obtain the exact functional $E_{XC}[\rho]$.

The first class of functionals are called *Local Density Functionals (LDA)* because they do not depend from the gradient $\nabla\rho$, by just the density ρ . The first historical attempt to define a functional of this type is the Thomas-Fermi (*TF*) functional (1926)³³⁸ which describes exactly the XC functional of a uniform gas of *non-interacting* particles. This first example is further improvement by Dirac (1930) with the inclusion of the exchange term which was not considered in the *TF* description.

In 1935, an important step forward was made by Von Weizsacker³³⁹ when he tried for the first time to introduce the density gradient $\nabla\rho$ into v_{XC} . This first example did not yield particularly good results but it formed the basis for the new generation of functional.

During the 1980 and 1990 years, a huge effort was made in order to find a good expression for the v_{XC} term to turn *DFT* in better theory than *HF*.

A new family of functional was called *Generalised Gradient Functional* (*GGA*); functionals such as BP86,^{263-264, 339} PBE³⁴⁰ or PW91³⁴¹ belong to this family. Despite the fact that they just belong to just second generation of *DFT* functionals, and recently more sophisticated functionals have been discovered, some of the early *GGA* functionals are still widely used. Some of them, such as PBE, have been subject of re-parameterisation across the years to better face more specific problems (revPBE, RPBE).³⁴²

In order to conclude this overview, the following step in the functional evolution is shortly mentioned. The new functional generation is called *Hybrid* because they came out from a mixing between *DFT* theory and *HF* theory. In *HF* theory the exchange-correlation term (E_{XC}) is more accurately calculated than in *DFT*, based on theory hypothesis. Then, the new generation of functionals included different percentages of the *HF* exchange term. Unfortunately, this approach did not lead to any definitive improvement but to a new series of functional which show just a different set of pros and cons as the *GGA* ones. It is important to mention B3LYP³⁴³⁻³⁴⁴ as one of the most famous and the newer version of PBE with the inclusion of 25% of the exact *HF* exchange called PBE0.³⁴²

A2 | Testing the Generality of $T_{1/2}$ of Spin Crossover Complex vs Ligand ^{15}N NMR Chemical Shift Correlations: Towards Predictable Tuning

A2.1. Computational Details

Calculations were performed using ORCA4.1.²⁵⁸ The computational protocol used to optimise the structures of the ligands was RIJCOSX-TPSS-D3(BJ)/*pcSseg-2*+CPCM.^{221-222, 259-260, 266-267} i.e. use of the *TPSS* functional⁴⁹ together with the resolution of identity (RIJCOSX) approximation,²⁶⁶⁻²⁶⁷ Grimme's D3 dispersion correction (including BJ damping),²⁵⁹⁻²⁶⁰ a *pcSseg-2* basis set⁵⁰ and implicit CPCM-solvent model. Finally, ^{15}N NMR calculations were performed on the *DFT* optimised structures through a single point calculation. Different CPCM models were applied, based on the solvent used experimentally to measure the *SCO* phenomenon: CDCl_3 for *L*^{azine} and *L*^{pytZ}; acetone for **pybox**^x and **bpp**^{x,y}, acetonitrile for **pytacn**^x.

A2.2. NMR and MS Figures for L^{pytCF_3} Ligand

^1H -NMR Spectrum

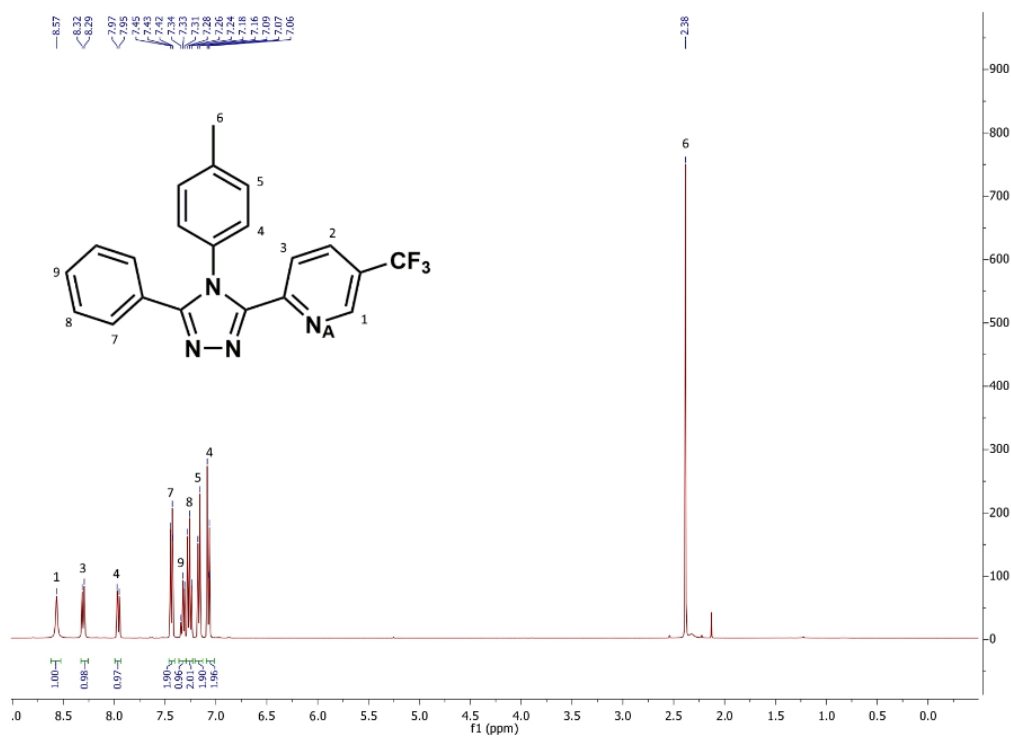


Figure A2.1. The full range ^1H NMR spectrum of ligand L^{pytCF_3} in CDCl_3 at 298 K.

^{13}C -NMR Spectrum

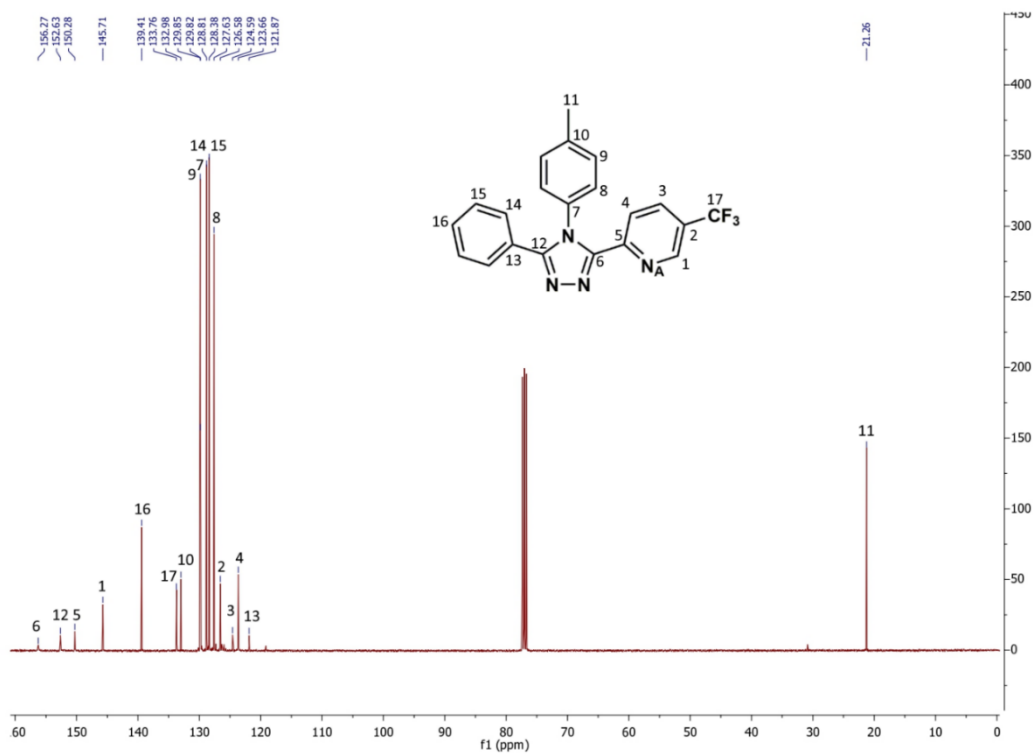


Figure A2.2. The full range ^{13}C NMR spectrum of ligand $\text{L}^{\text{pytCF}_3}$ in CDCl_3 at 298 K.

HSQCAD Spectrum

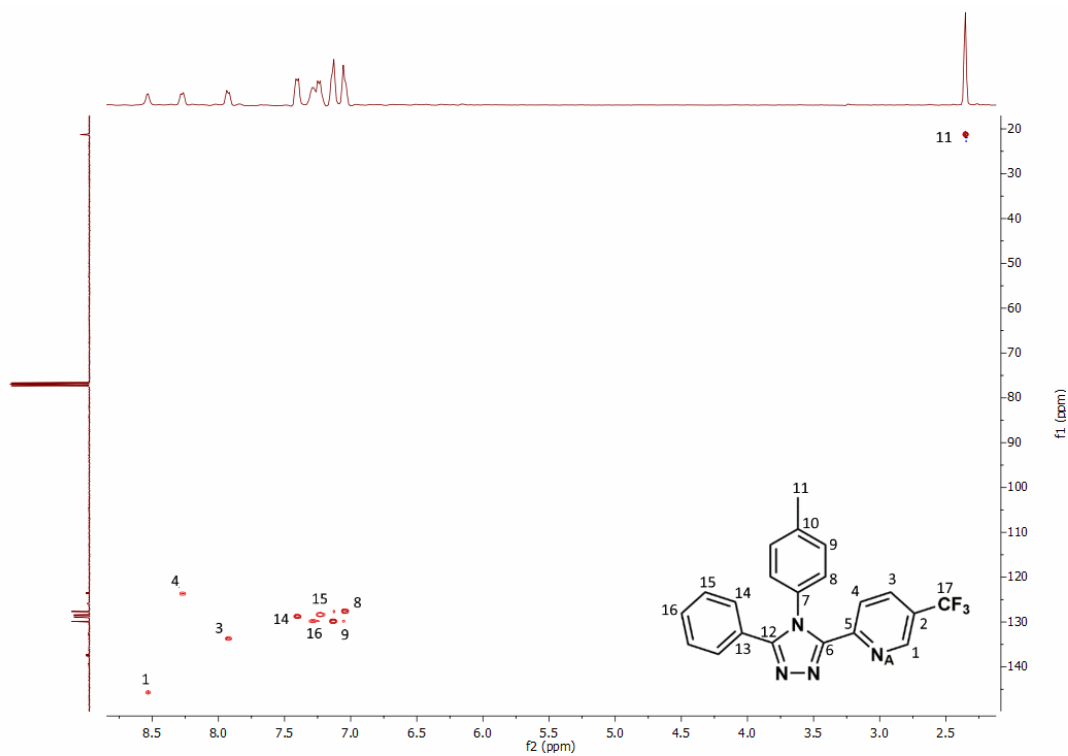


Figure A2.1. Heteronuclear ^1H - ^{13}C NMR spectrum of ligand LpytCF_3 in CDCl_3 at 298 K.

^{15}N -NMR Spectrum

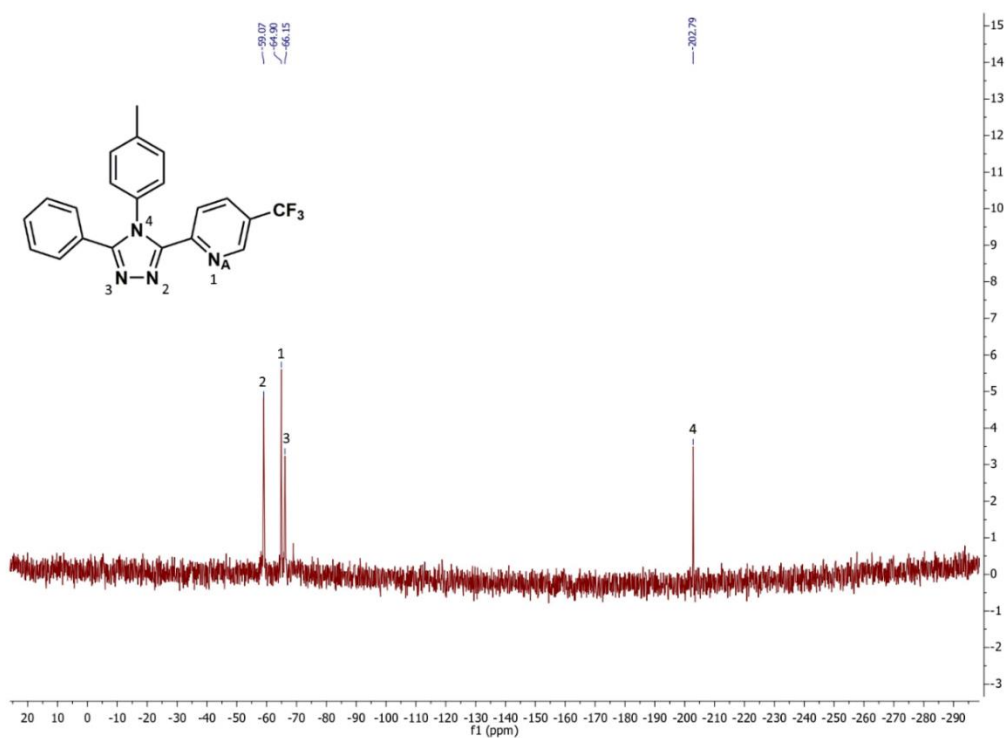


Figure A2.4. The full range ^{15}N NMR spectrum (direct measurement) of ligand L^{pytCF_3} in CDCl_3 at 298 K.

Mass Spectrum

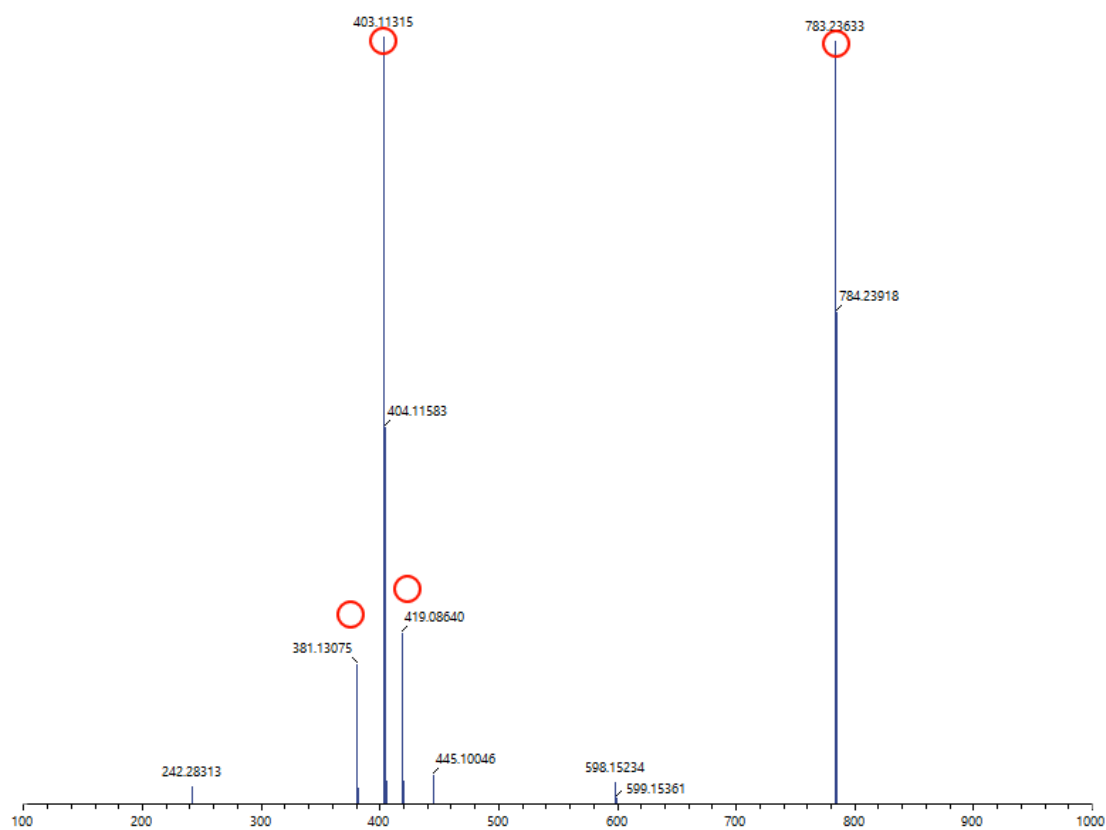


Figure A2.5. Complete mass spectrum of L_{pytCF_3} . Reported circles refer to zoomed regions reported below.

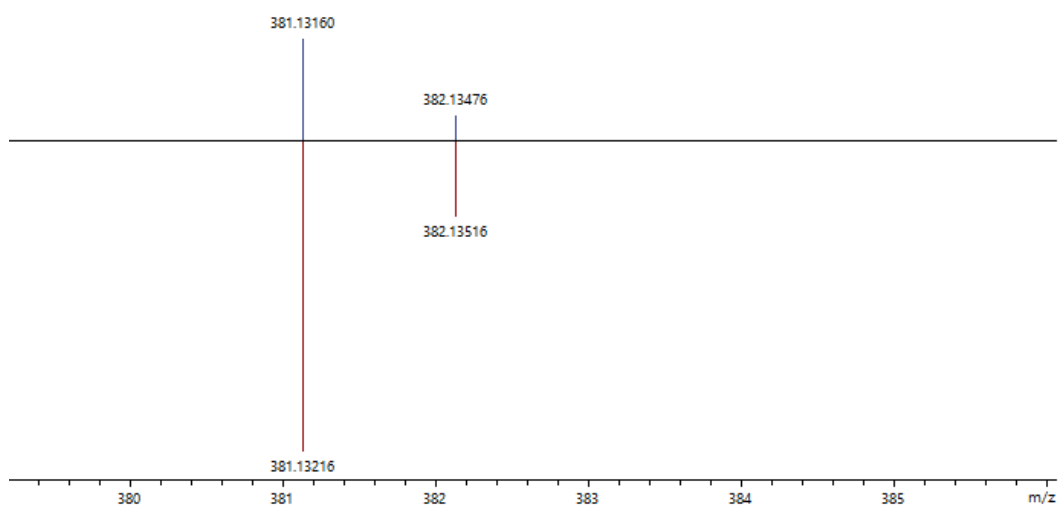


Figure A2.6. Fit of a peak in the mass spectrum of $[\text{L}^{\text{pytCF}_3}+\text{H}]^+$ experimental (blue) and simulated pattern (red).

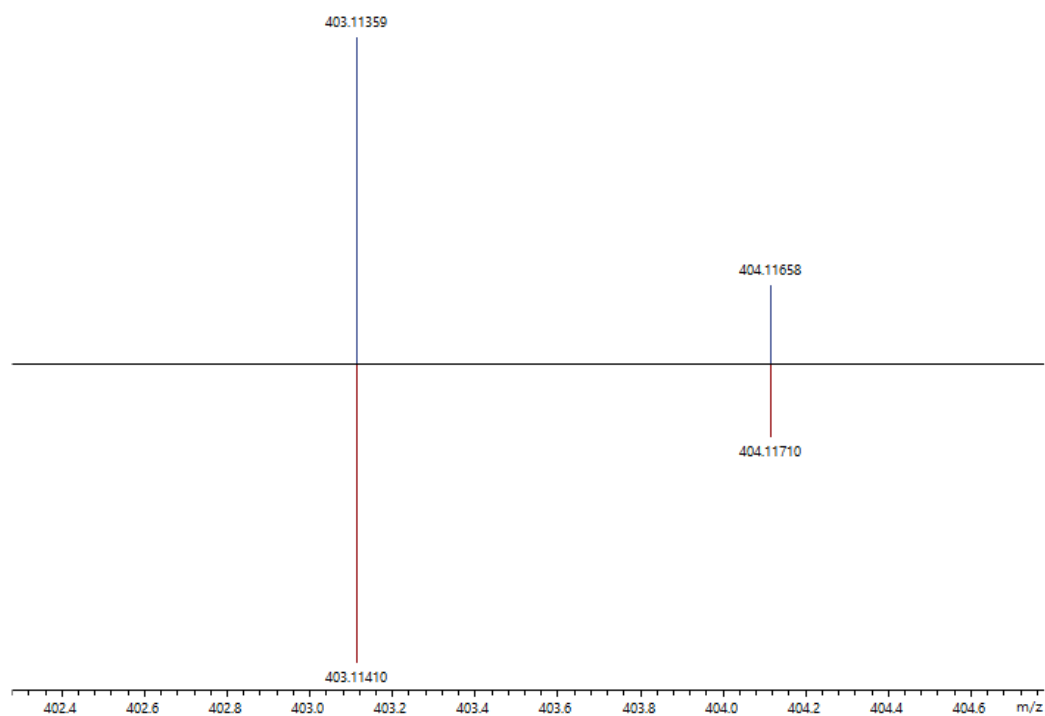


Figure A2.7. Fit of a peak in the mass spectrum of $[\text{L}^{\text{pytCF}_3}+\text{Na}]^+$ experimental (blue) and simulated pattern (red).

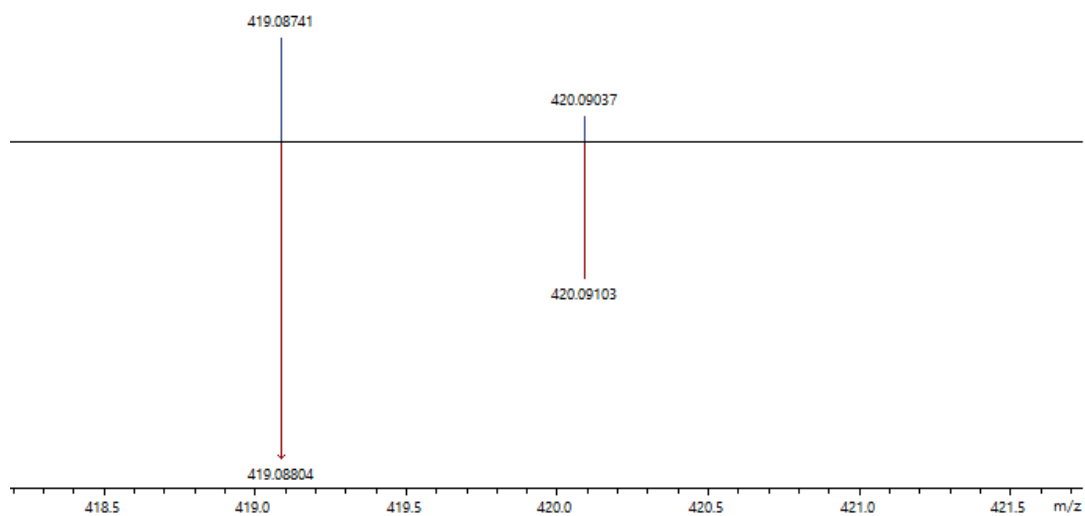


Figure A2.8. Fit of a peak in the mass spectrum of $[\text{L}^{\text{pytCF}_3}+\text{K}]^+$ experimental (blue) and simulated pattern (red).

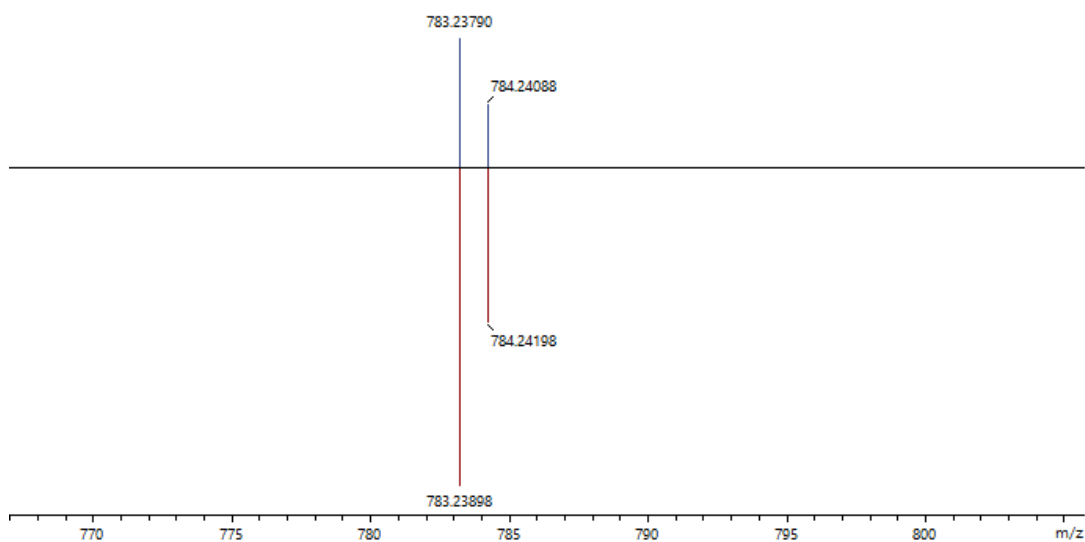


Figure A2.9. Fit of a peak in the mass spectrum of $[2\text{L}^{\text{pytCF}_3}+\text{Na}]^+$ experimental (blue) and simulated pattern (red).

A2.3. MS Figures for $[\text{Fe}(\text{L}^{\text{pytCF}_3})_2(\text{NCBH}_3)_2]$ Complex

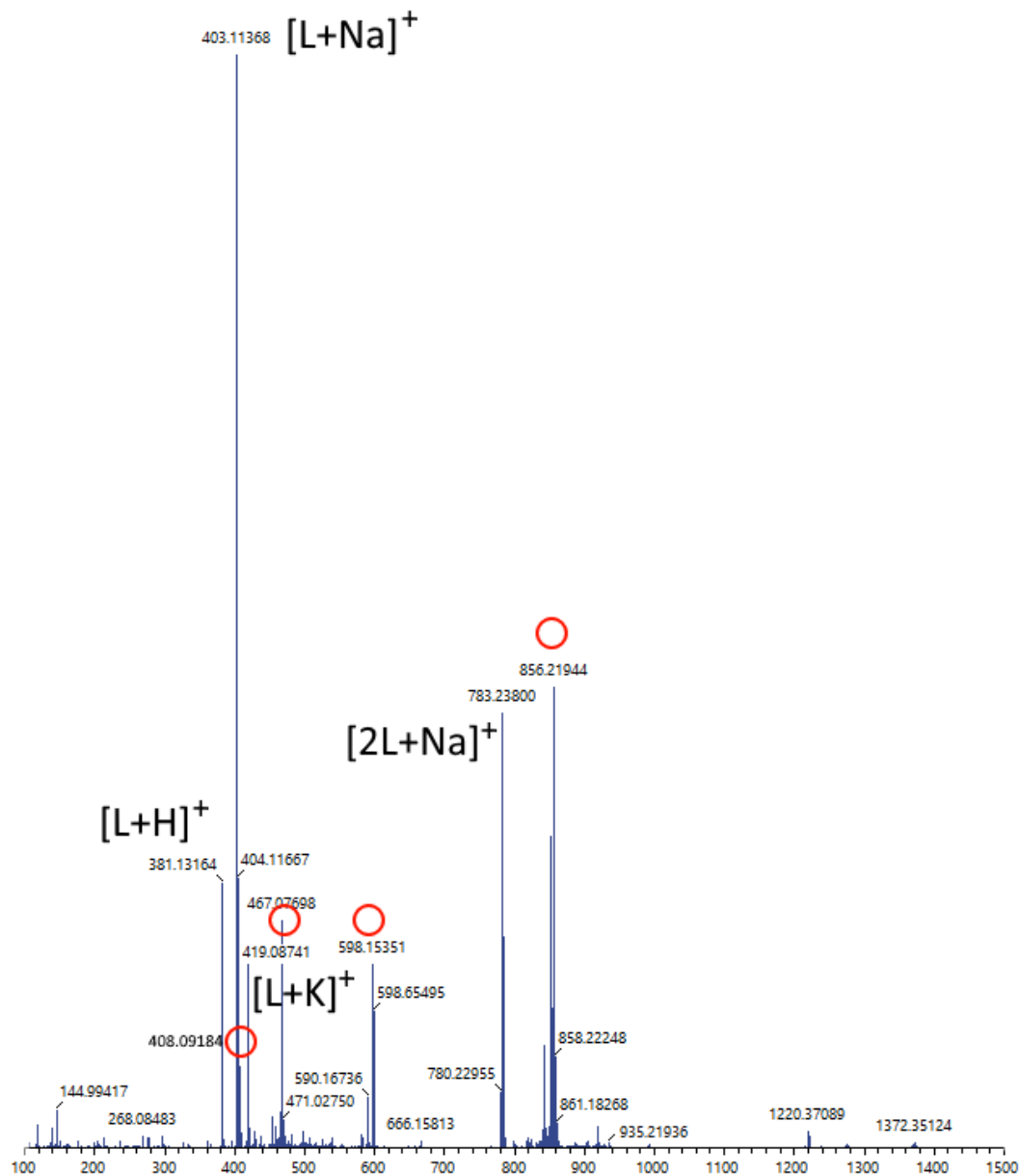


Figure A2.10. Complete mass spectrum of $[\text{Fe}(\text{L}^{\text{pytCF}_3})_2(\text{NCBH}_3)_2]$. Reported circles refer to zoomed regions reported below.

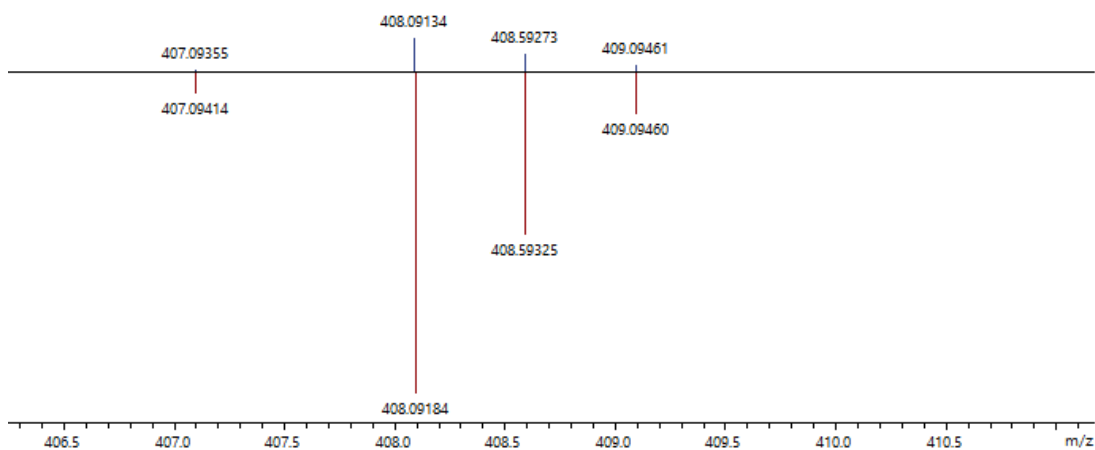


Figure A2.11. Fit of a peak in the mass spectrum of $[\text{Fe}(\text{LpytCF}_3)_2]^{2+}$ experimental (blue) and simulated pattern (red).

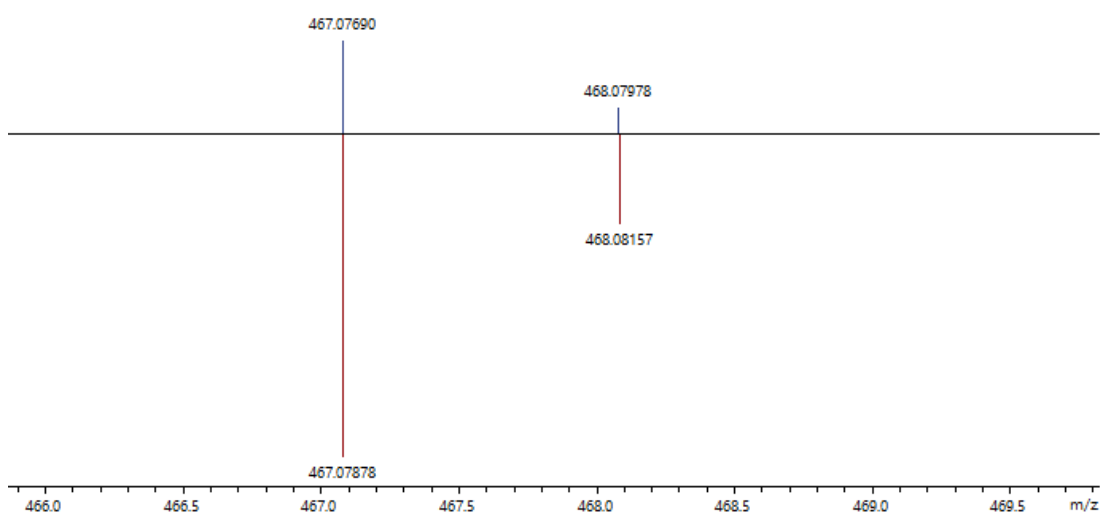


Figure A2.12. Fit of a peak in the mass spectrum of $[\text{Fe}(\text{LpytCF}_3)(\text{MeOH})-\text{H}]^+$ experimental (blue) and simulated pattern (red).

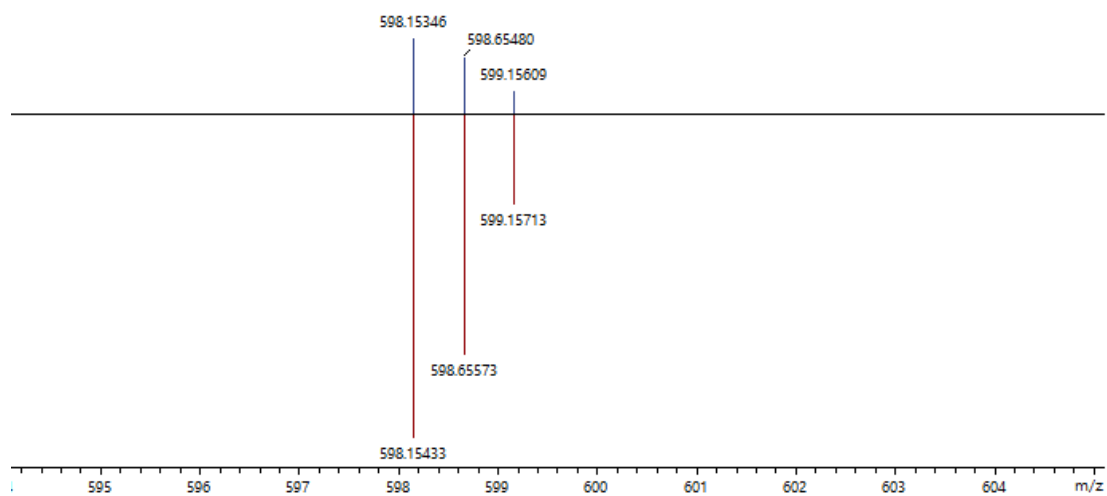


Figure A2.13. Fit of a peak in the mass spectrum of $[\text{Fe}(\text{L}^{\text{pytCF}_3})_3]^{2+}$ experimental (blue) and simulated pattern (red).

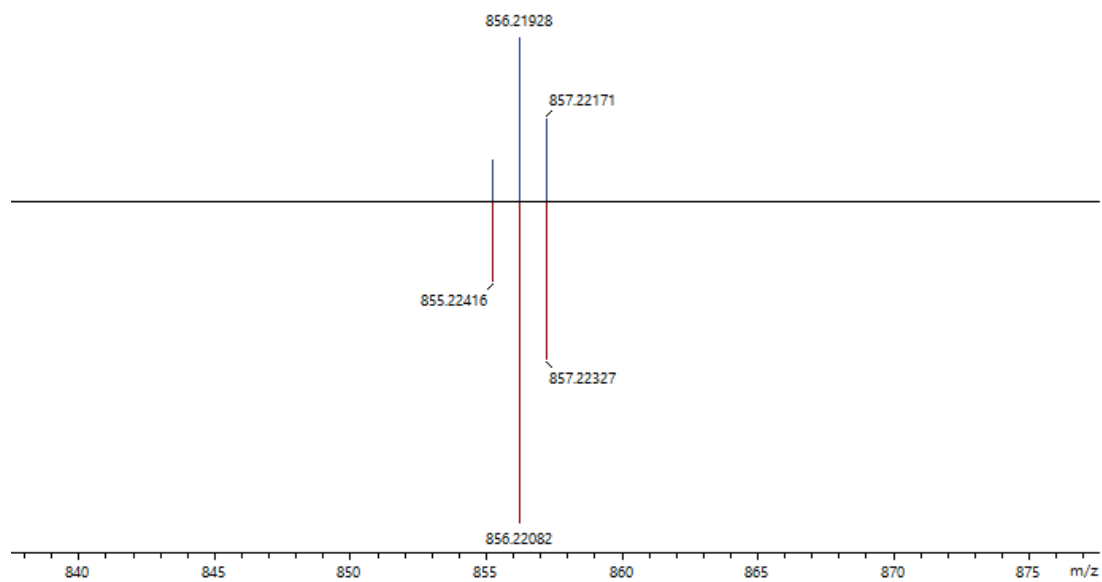


Figure A2.14. Fit of a peak in the mass spectrum of $[\text{Fe}(\text{L}^{\text{pytCF}_3})_2(\text{NCBH}_3)]^+$ experimental (blue) and simulated pattern (red).

A2.4. NMR and MS Figures for L^{pytBr} Ligand

^1H -NMR Spectrum

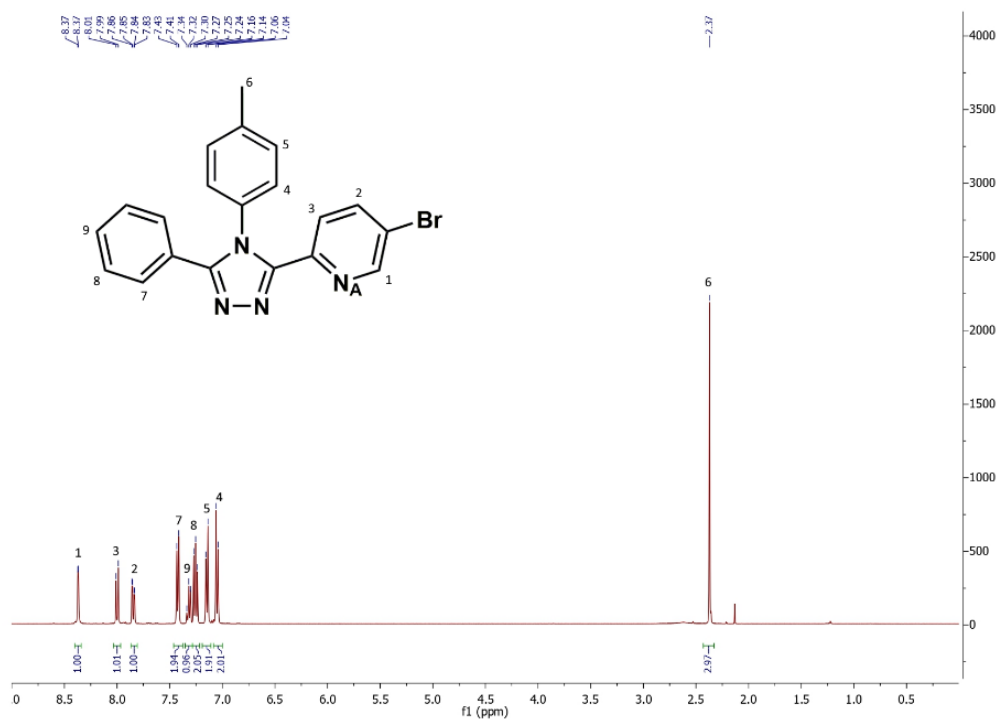


Figure A2.15. The full range ^1H NMR spectrum of ligand L^{pytBr} in CDCl_3 at 298 K.

^{13}C -NMR Spectrum

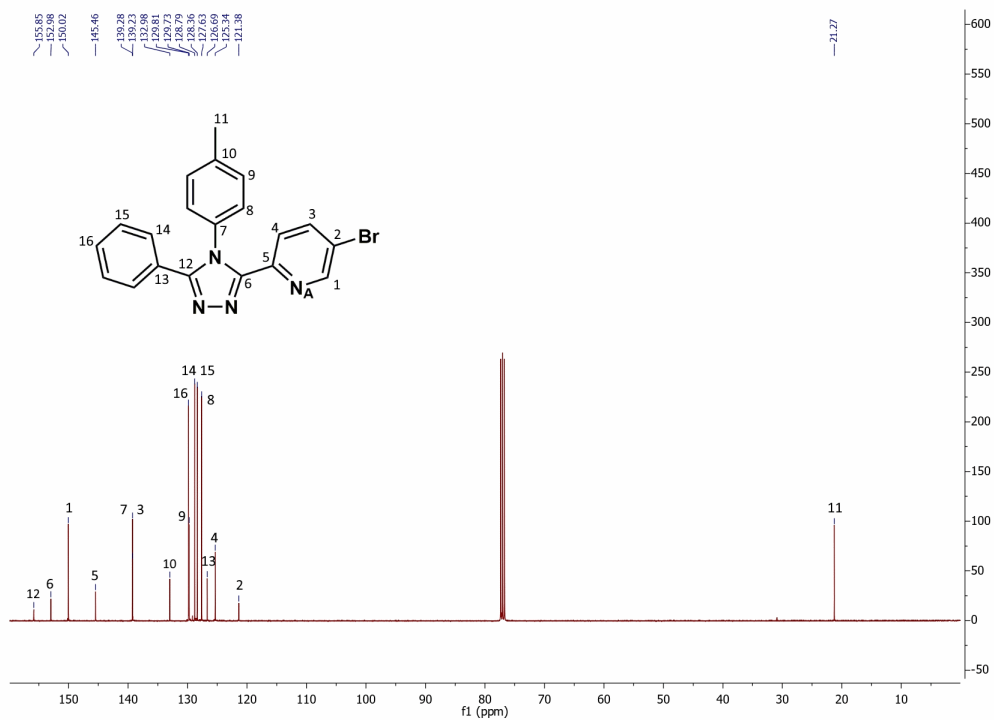


Figure A2.16. The full range ^{13}C NMR spectrum of ligand L^{pytBr} in CDCl_3 at 298 K.

HSQCAD Spectrum

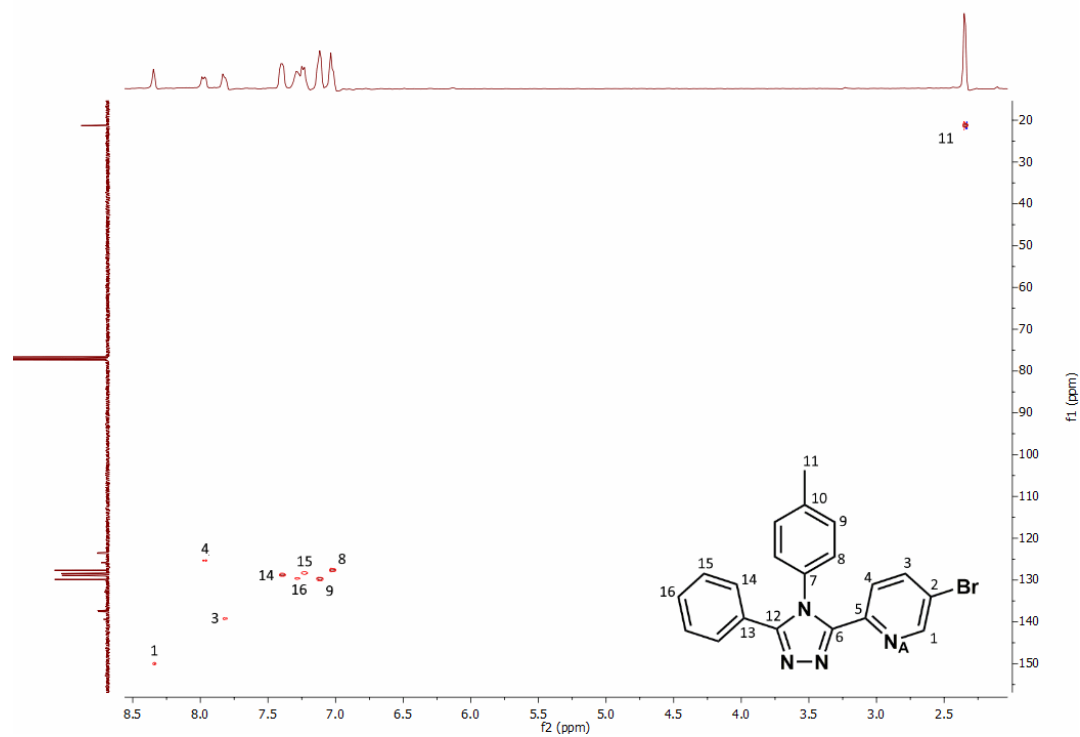


Figure A2.17. Heteronuclear ^1H - ^{13}C NMR spectrum of ligand L_{pytBr} in CDCl_3 at 298 K.

^{15}N -NMR Spectrum

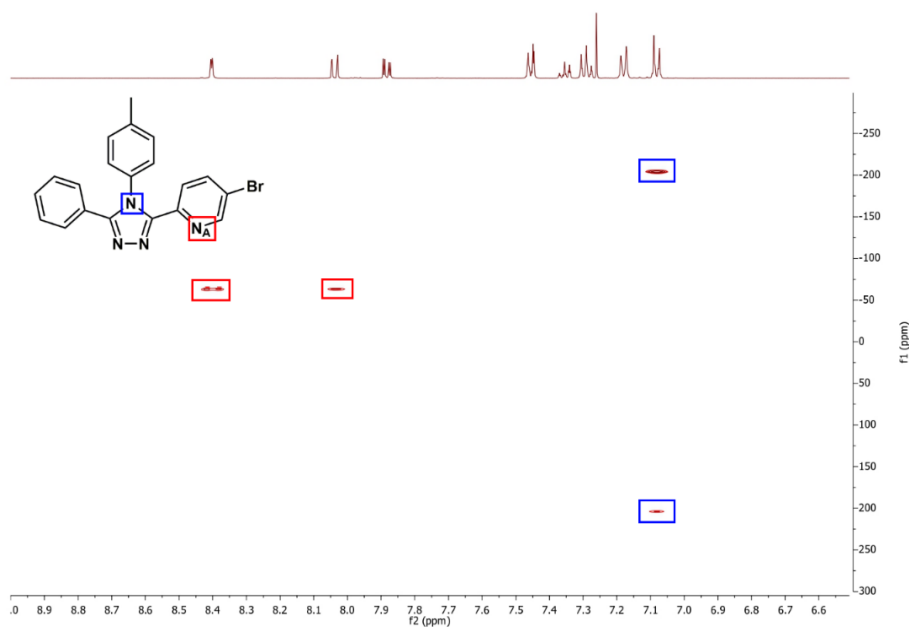


Figure A2.18. The full range CIGARD ^1H - ^{15}N NMR spectrum (indirect measurement) of ligand L^{pytBr} in CDCl_3 at 298 K.

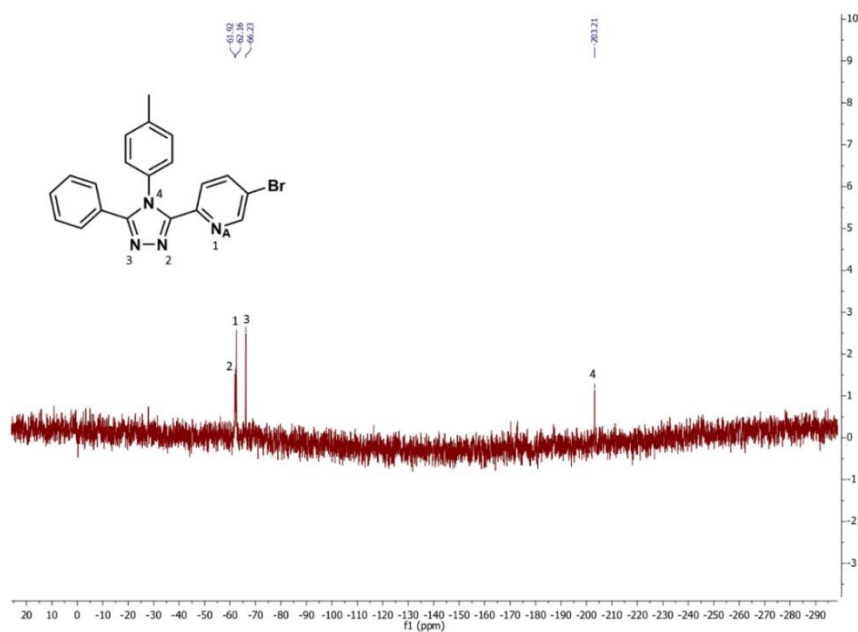


Figure A2.19. The full range ^{15}N NMR spectrum (direct measurement) of ligand L^{pytBr} in CDCl_3 at 298 K.

Mass Spectrum

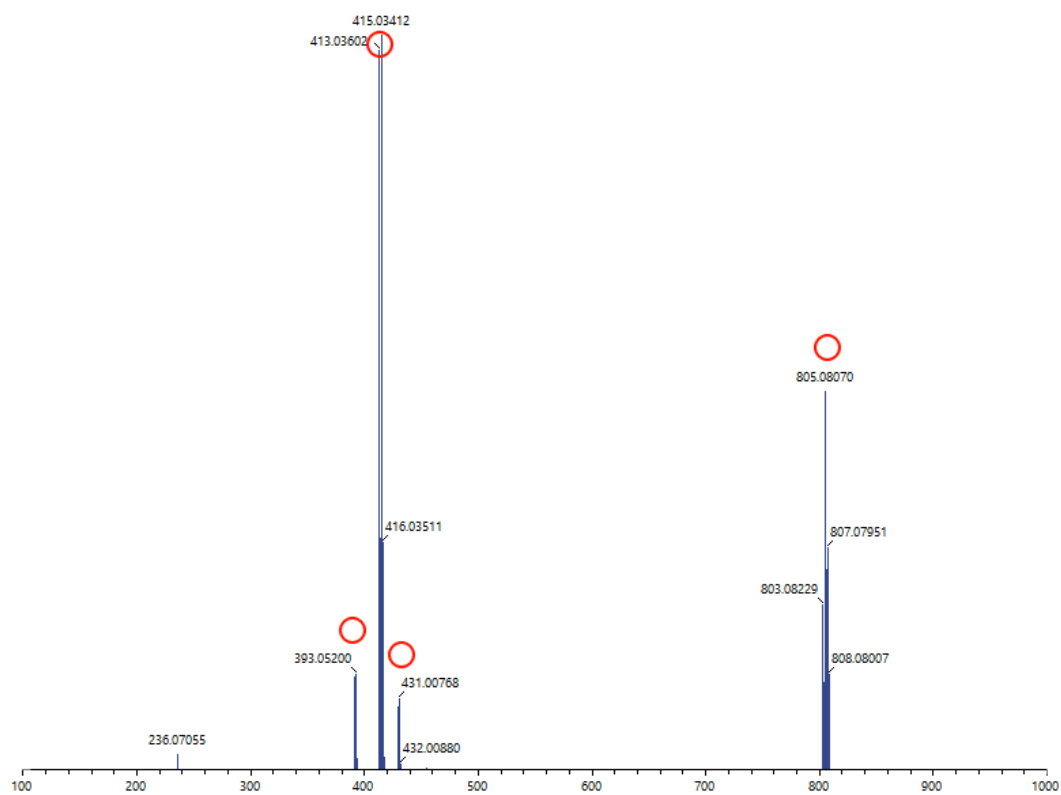


Figure A2.20. Complete mass spectrum of L^{pytBr} . Reported circles refer to zoomed regions reported below.

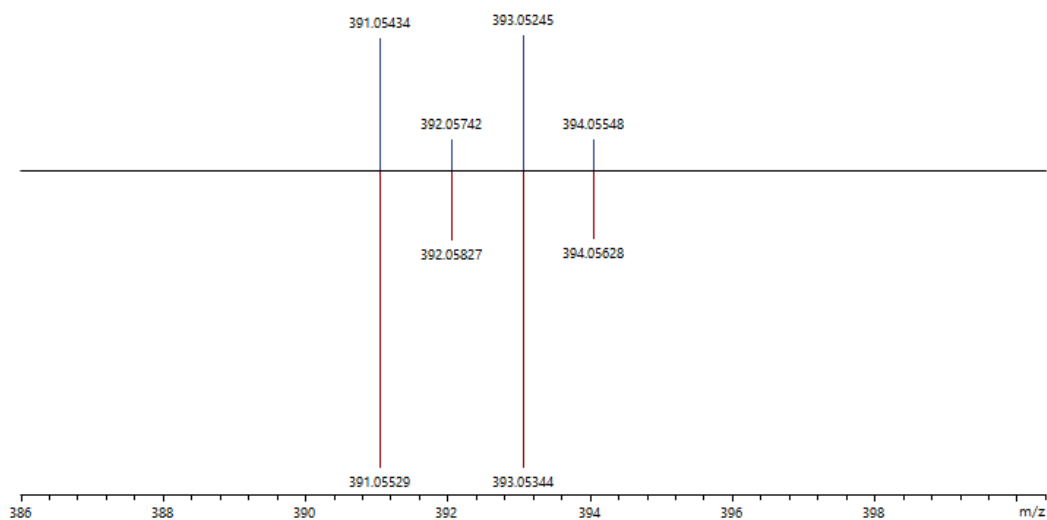


Figure A2.21. Fit of a peak in the mass spectrum of $[L^{pytBr}+H]^+$ experimental (blue) and simulated pattern (red).

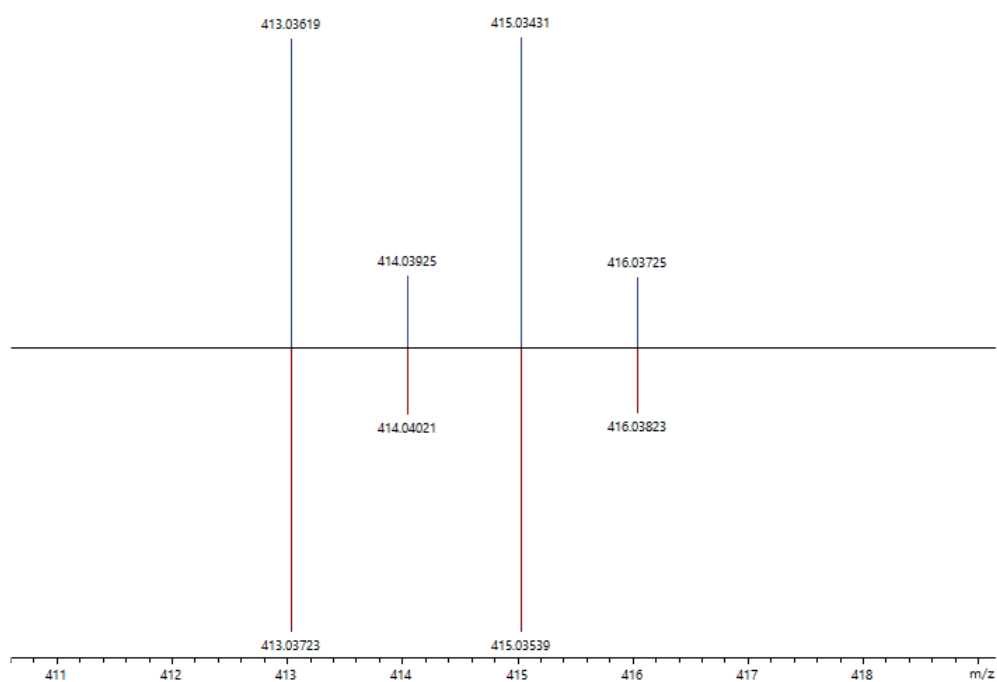


Figure A2.22. Fit of a peak in the mass spectrum of $[L^{pytBr}+Na]^+$ experimental (blue) and simulated pattern (red).

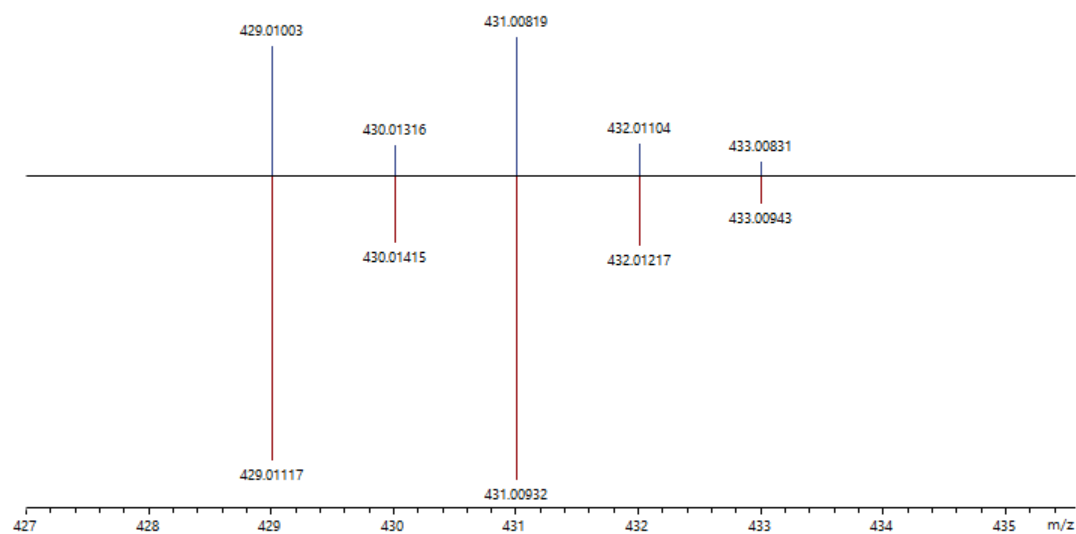


Figure A2.23. Fit of a peak in the mass spectrum of $[\text{L}^{\text{py}}\text{tBr}+\text{K}]^+$ experimental (blue) and simulated pattern (red).

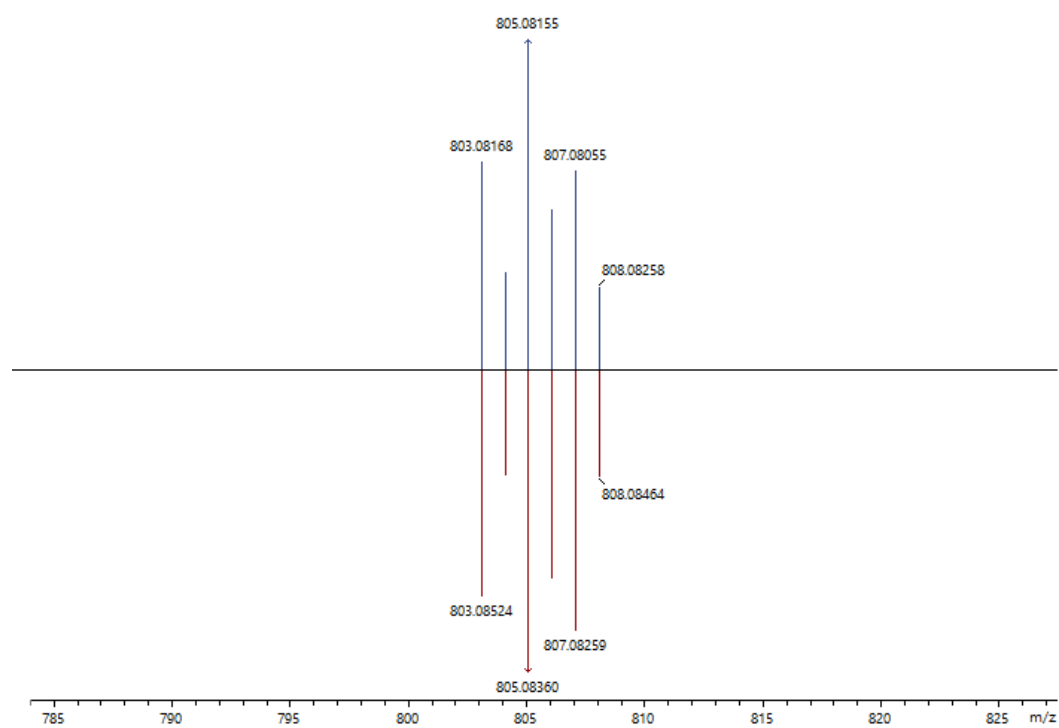


Figure A2.24 Fit of a peak in the mass spectrum of $[(\text{L}^{\text{py}}\text{tMe})_2+\text{Na}]^+$ experimental (blue) and simulated pattern (red).

A2.5. MS Figures for $[\text{Fe}(\text{L}^{\text{pytBr}})_2(\text{NCBH}_3)_2]$ Complex

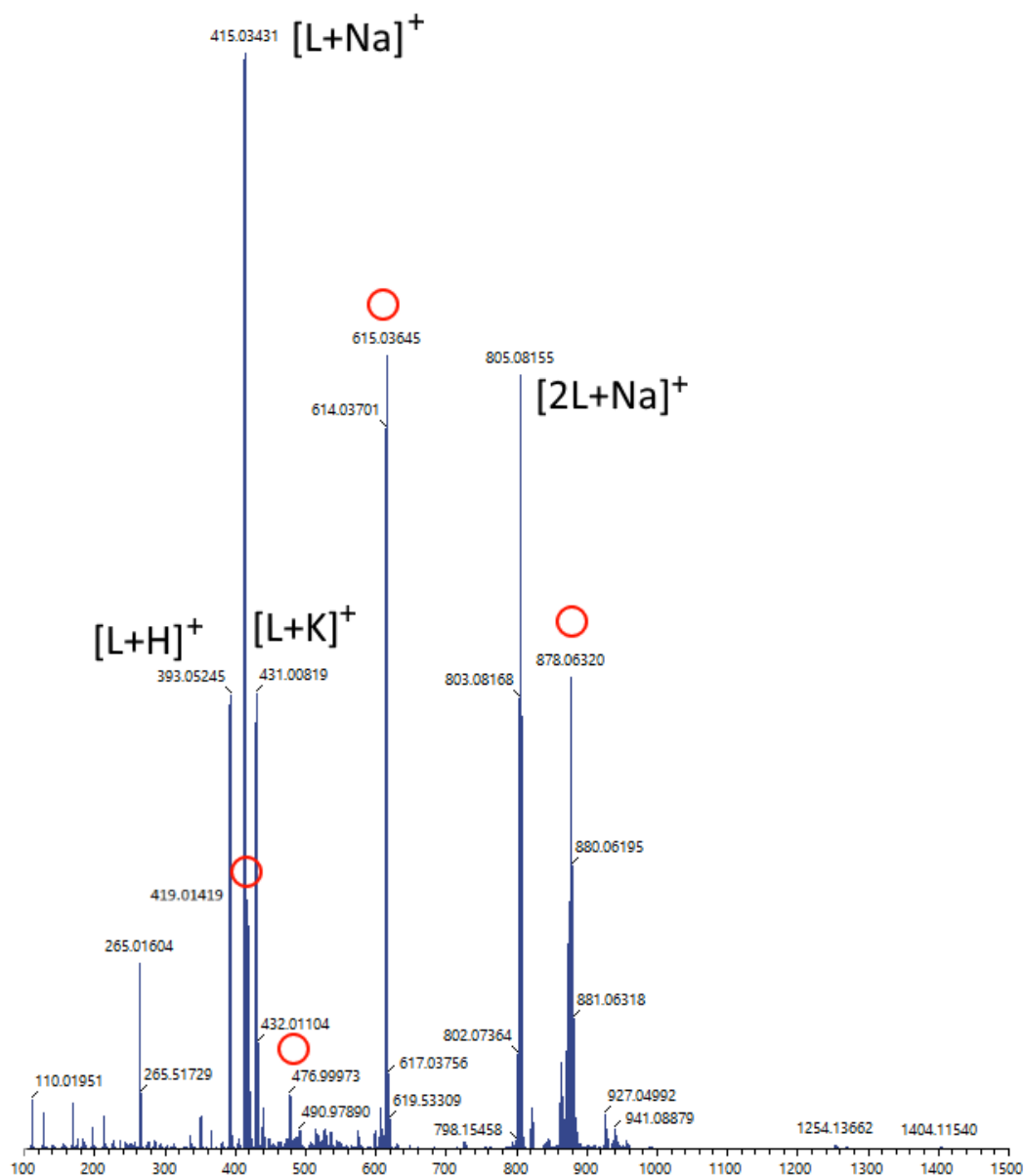


Figure A2.25. Complete mass spectrum of $[\text{Fe}(\text{L}^{\text{pytBr}})_2(\text{NCBH}_3)_2]$. Reported circles refer to zoomed regions reported below.

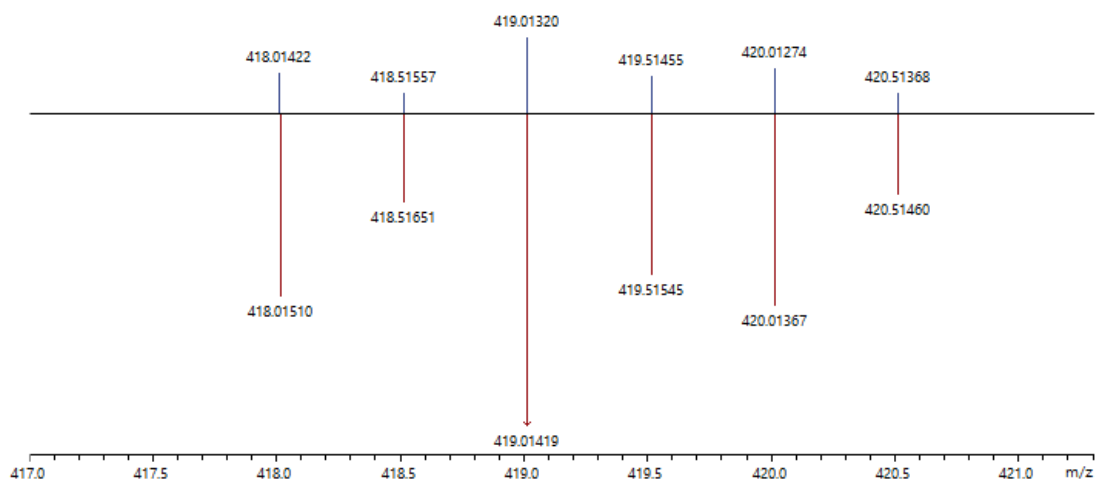


Figure A2.26. Fit of a peak in the mass spectrum of $[\text{Fe}(\text{L}^{\text{pytBr}})_2]^{2+}$ experimental (blue) and simulated pattern (red).

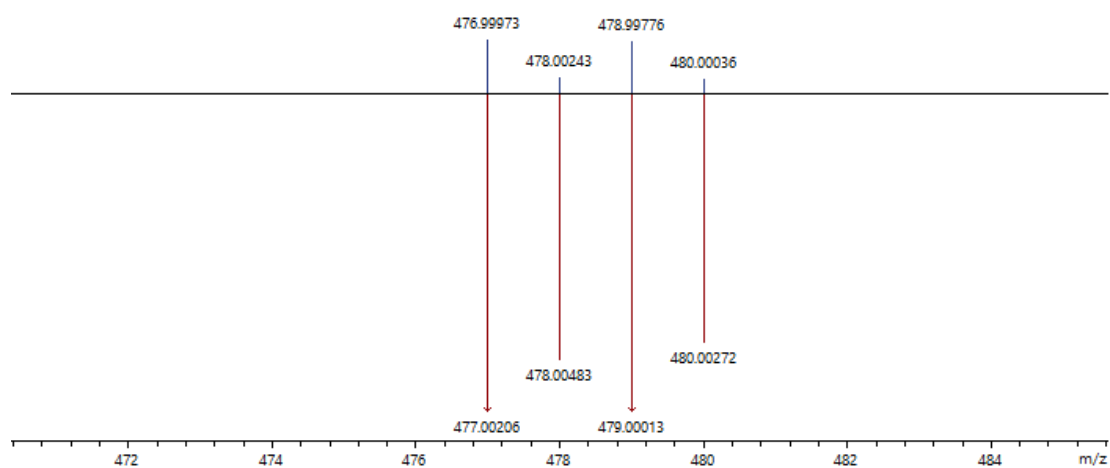


Figure A2.27. Fit of a peak in the mass spectrum of $[\text{Fe}(\text{L}^{\text{pytBr}})(\text{MeOH})-\text{H}]^+$ experimental (blue) and simulated pattern (red).

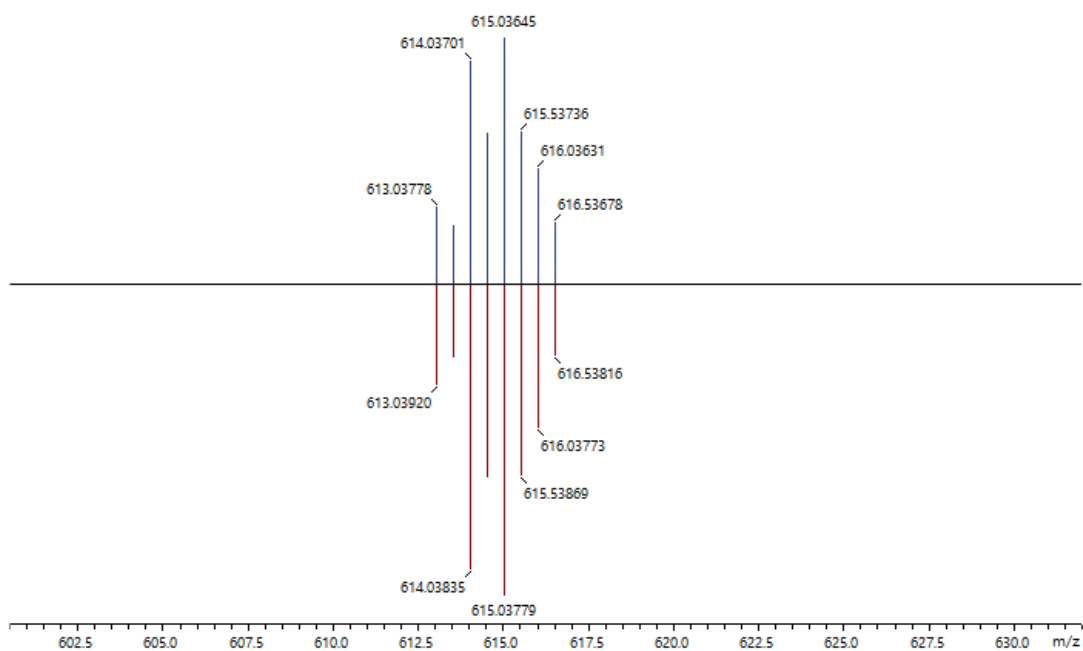


Figure A2.28. Fit of a peak in the mass spectrum of $[\text{Fe}(\text{L}^{\text{pytBr}})_3]^{2+}$ experimental (blue) and simulated pattern (red).

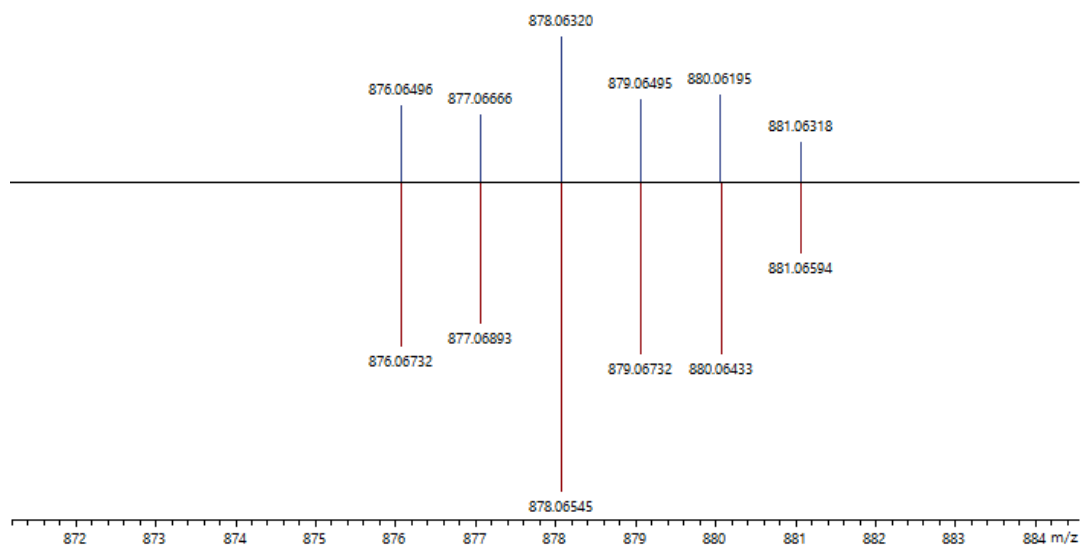


Figure A2.29. Fit of a peak in the mass spectrum of $[\text{Fe}(\text{L}^{\text{pytBr}})_2(\text{NCBH}_3)]^+$ experimental (blue) and simulated pattern (red).

A2.6. NMR and MS Figures for L^{pytF} Ligand

^1H -NMR Spectrum

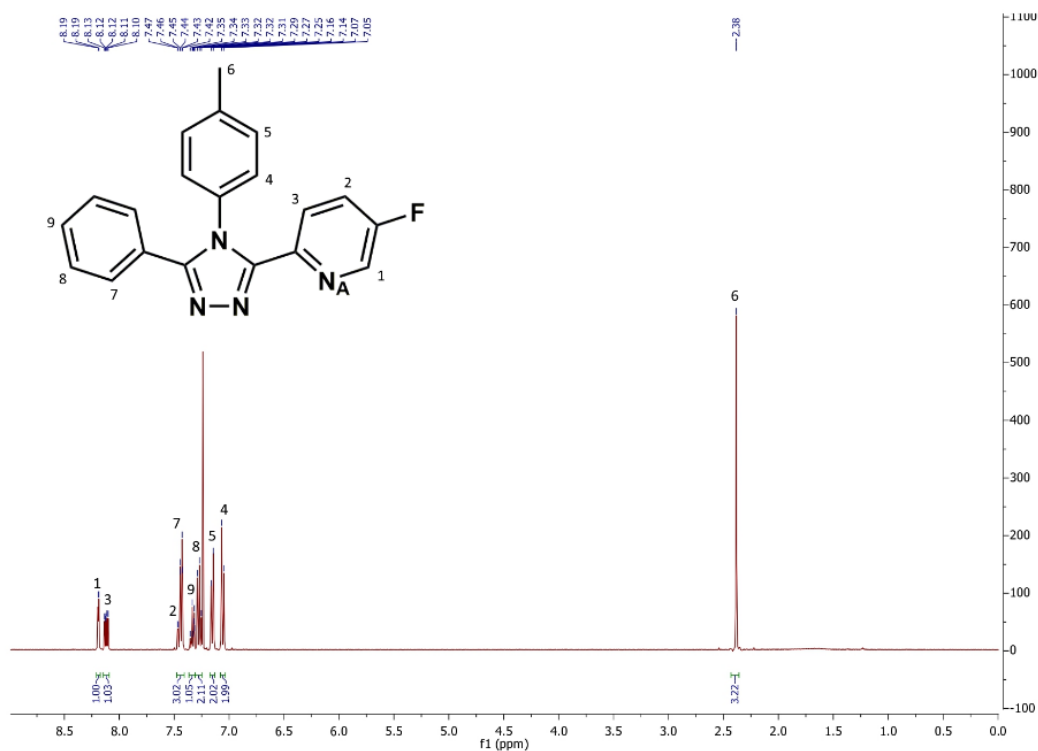


Figure A2.30. The full range ^1H NMR spectrum of ligand L^{pytF} in CDCl_3 at 298 K.

^{13}C -NMR Spectrum

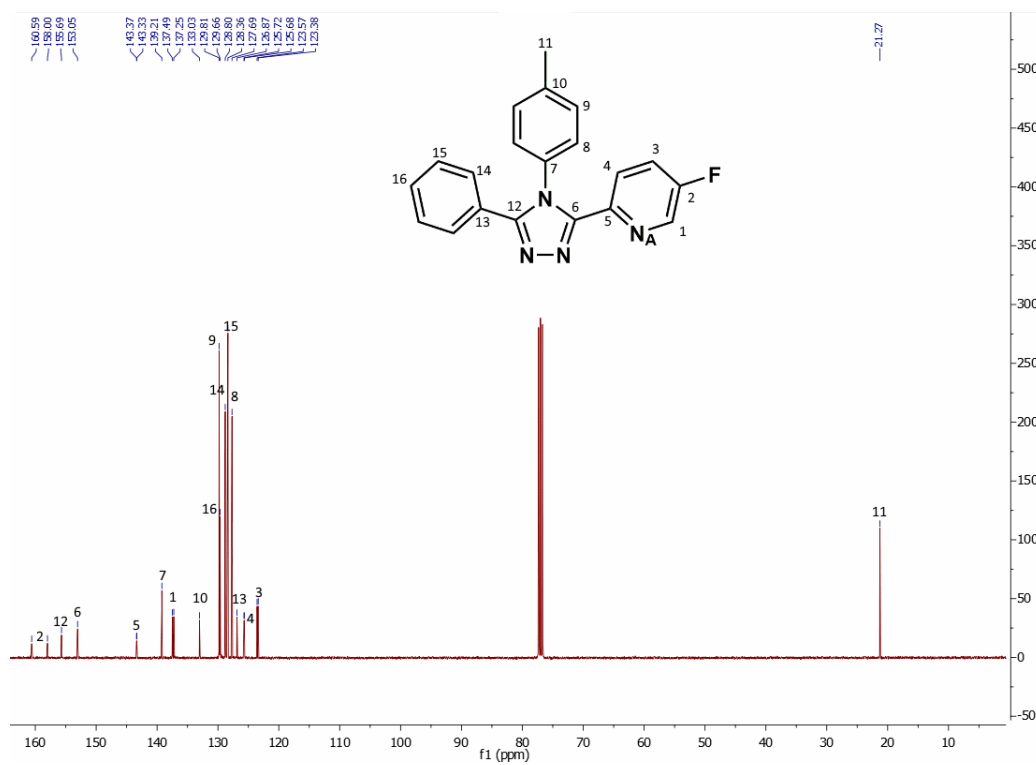


Figure A2.31. The full range ^{13}C NMR spectrum of ligand L_{pytF} in CDCl_3 at 298 K.

HSQCAD Spectrum

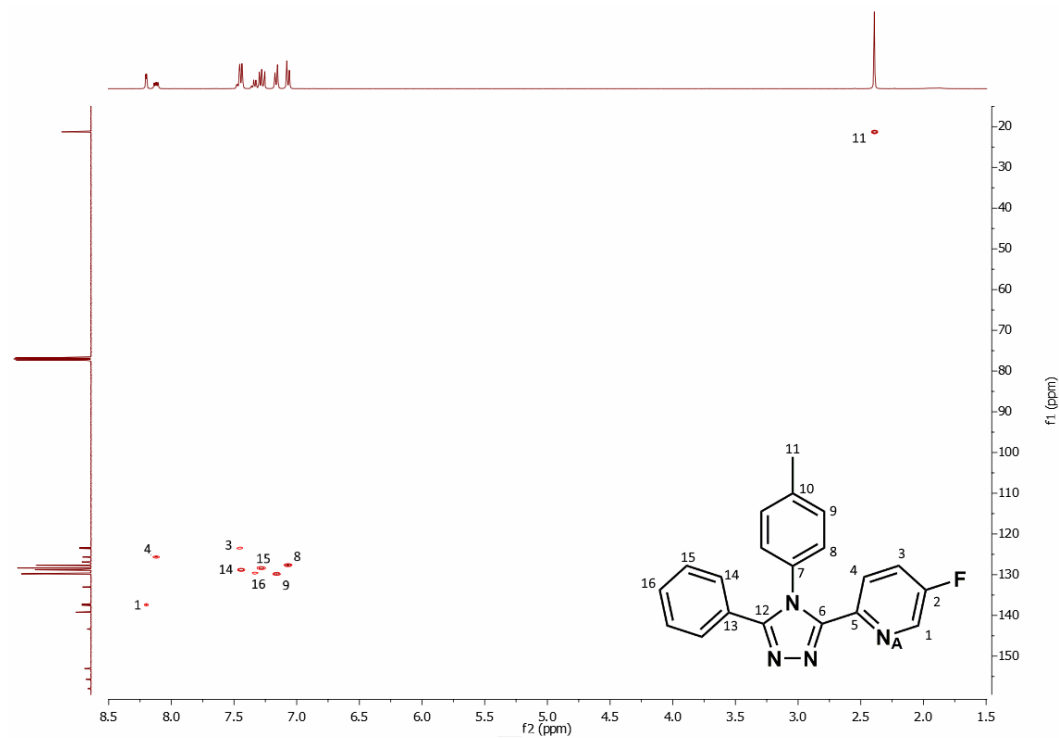


Figure A2.32. Heteronuclear ^1H - ^{13}C NMR spectrum of ligand L^{py^tF} in CDCl_3 at 298 K.

^{15}N -NMR Spectrum

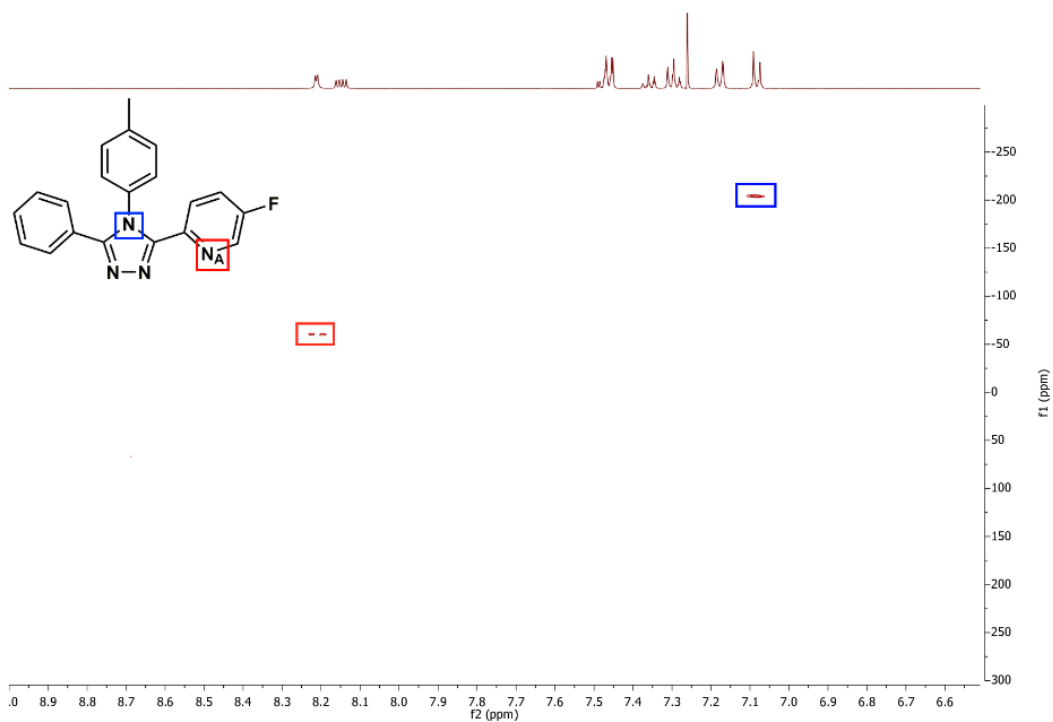


Figure A2.33. The full range CIGARD ^1H - ^{15}N NMR spectrum (indirect measurement) of ligand L^{pytF} in CDCl_3 at 298 K.

Mass Spectrum

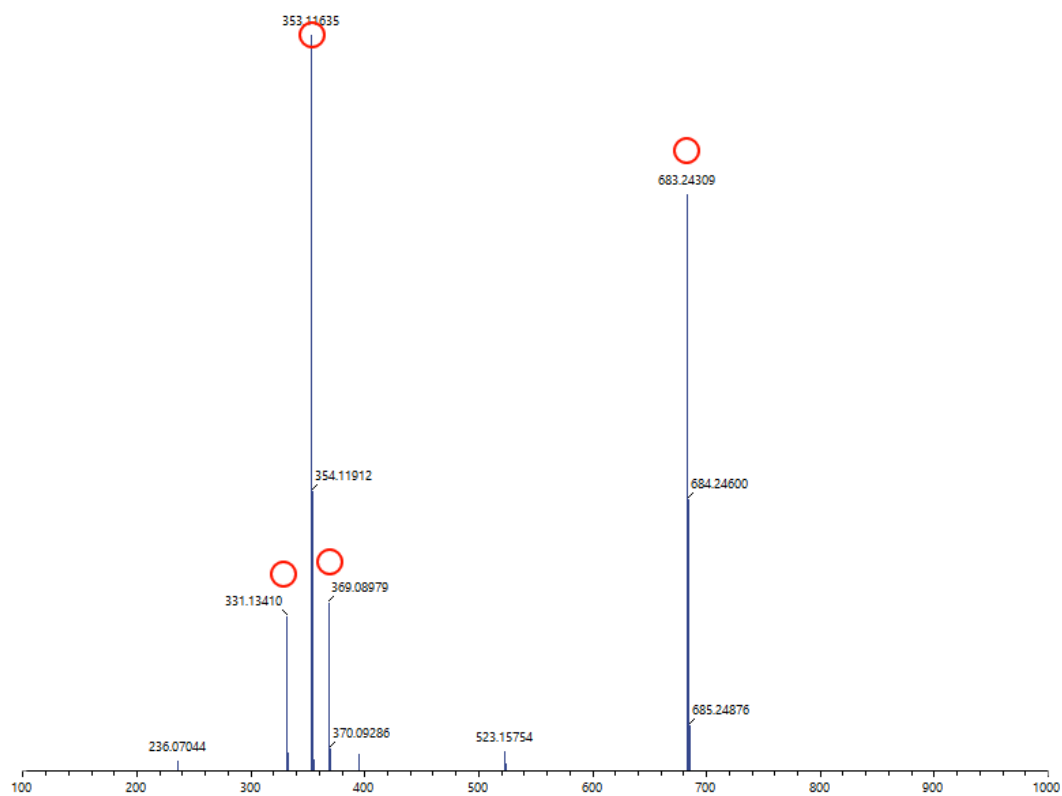


Figure A2.34. Complete mass spectrum of Lpy^{EF} . Reported circles refer to zoomed regions reported below.

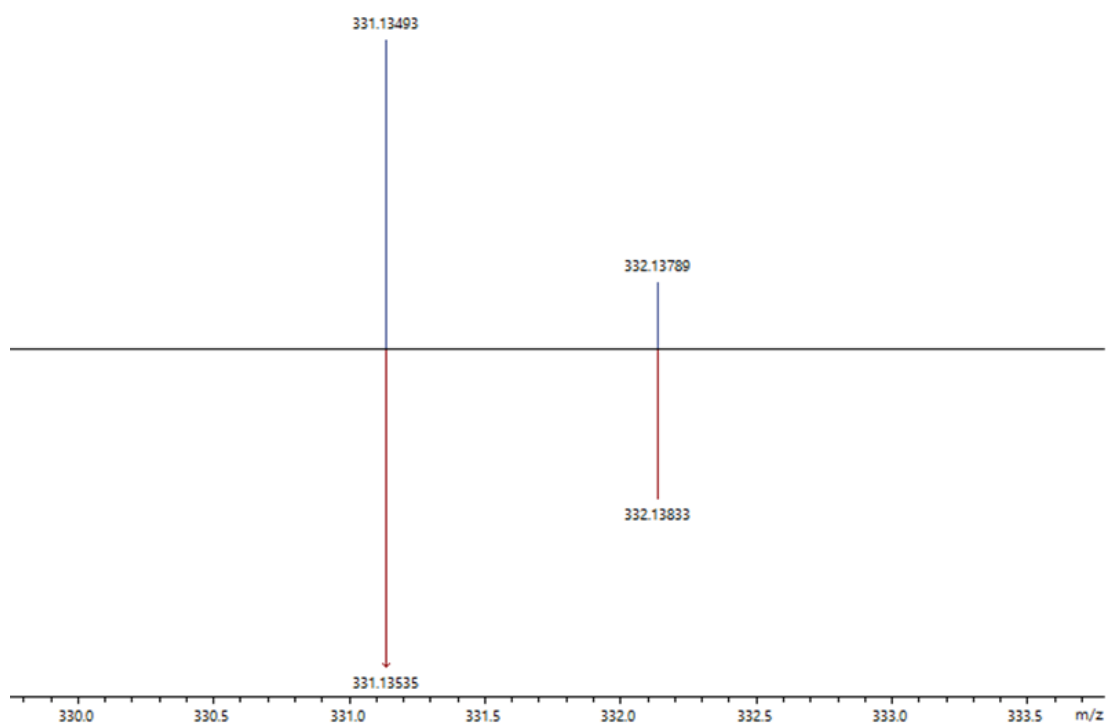


Figure A2.35. Fit of a peak in the mass spectrum of $[\text{Lpy}^{\text{TF}}+\text{H}]^+$ experimental (blue) and simulated pattern (red).

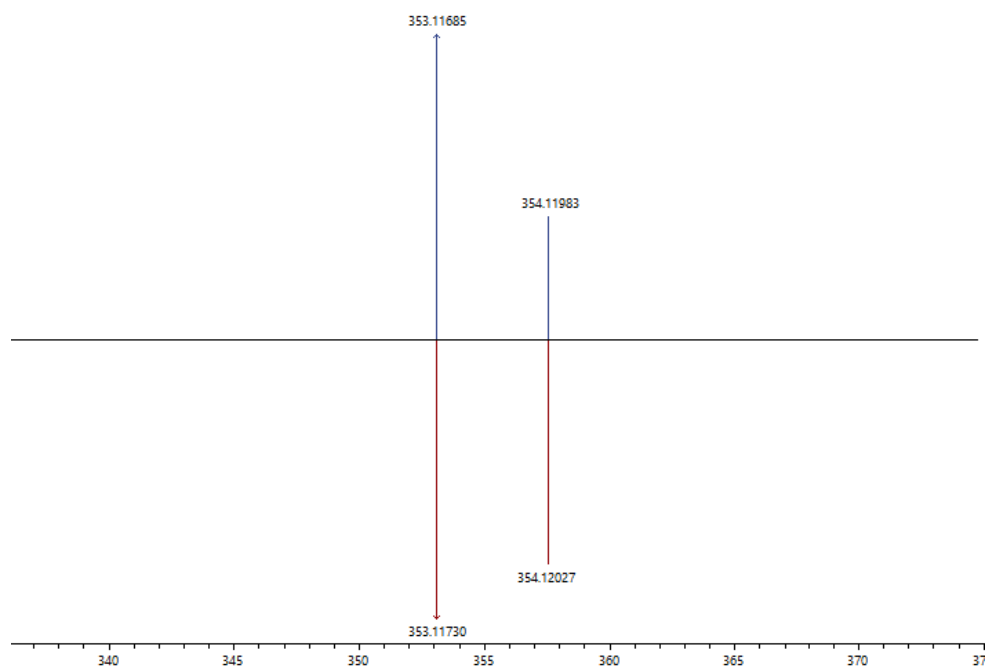


Figure A2.36. Fit of a peak in the mass spectrum of $[\text{Lpy}^{\text{TF}}+\text{Na}]^+$ experimental (blue) and simulated pattern (red).

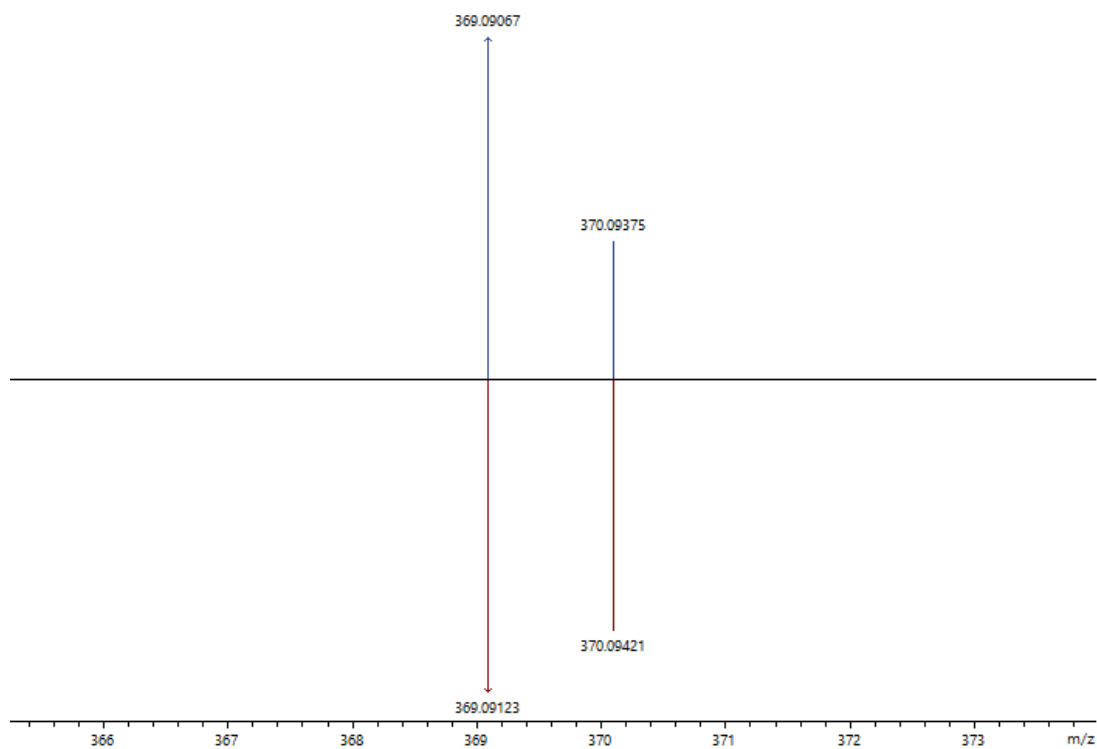


Figure A2.37. Fit of a peak in the mass spectrum of $[\text{LpytF}+\text{K}]^+$ experimental (blue) and simulated pattern (red).

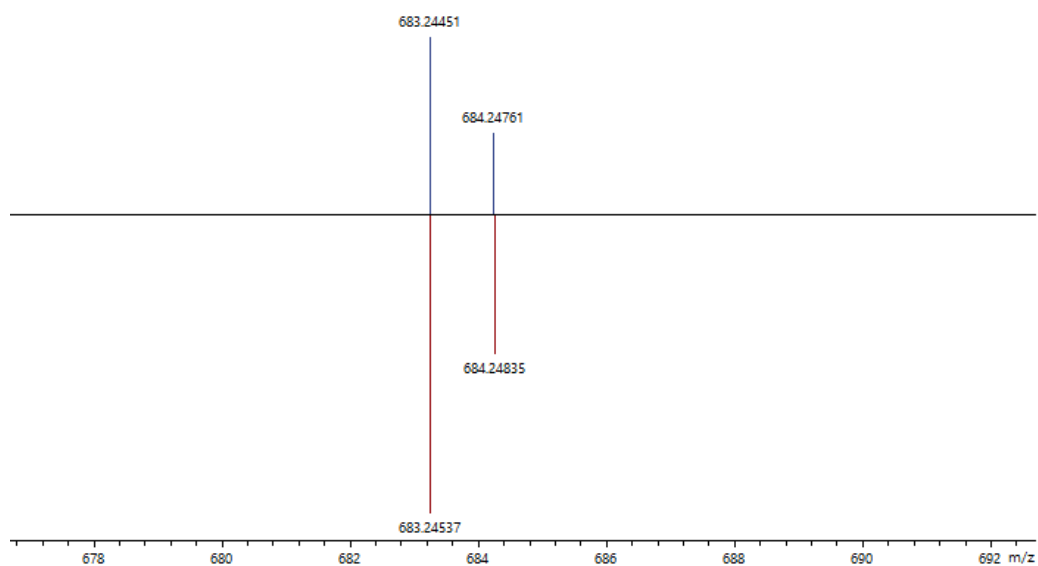


Figure A2.38. Fit of a peak in the mass spectrum of $[(\text{LpytF})_2+\text{Na}]^+$ experimental (blue) and simulated pattern (red).

A2.7. MS Figures for $[\text{Fe}(\text{L}^{\text{pytF}})_2(\text{NCBH}_3)_2]$ Complex

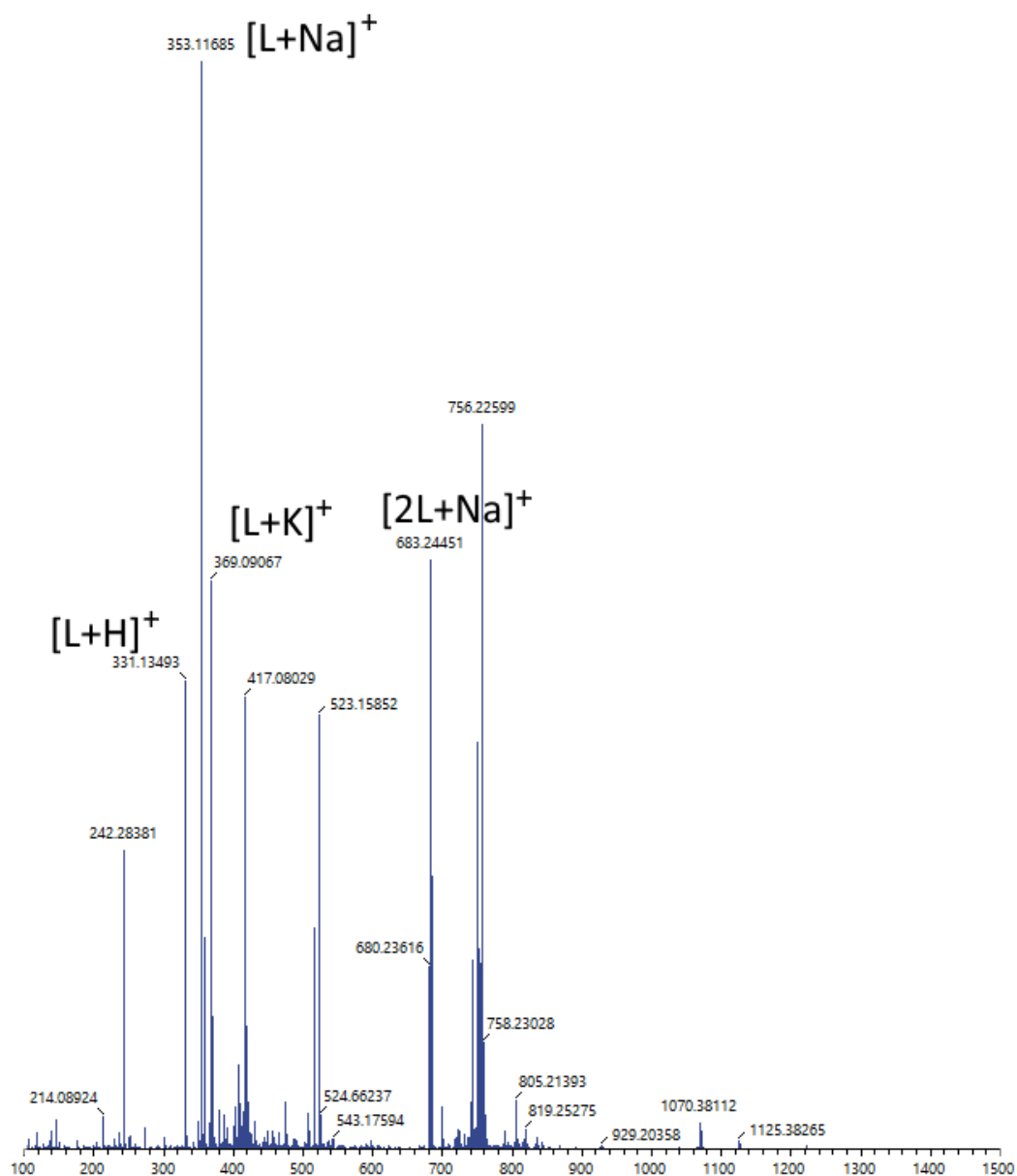


Figure A2.39. Complete mass spectrum of $[\text{Fe}(\text{L}^{\text{pytF}})_2(\text{NCBH}_3)_2]$. Reported circles refer to zoomed regions reported below.

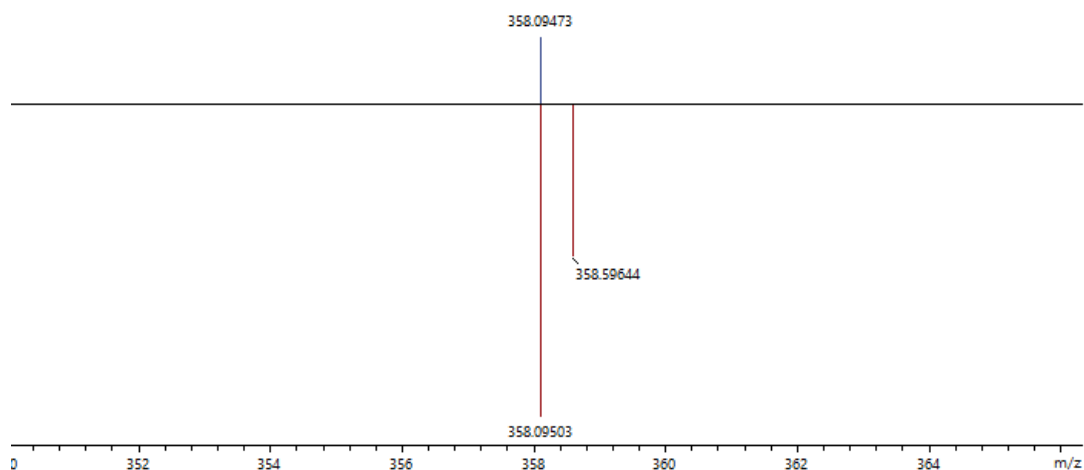


Figure A2.40. Fit of a peak in the mass spectrum of $[\text{Fe}(\text{L}^{\text{pytF}})_2]^{2+}$ experimental (blue) and simulated pattern (red).

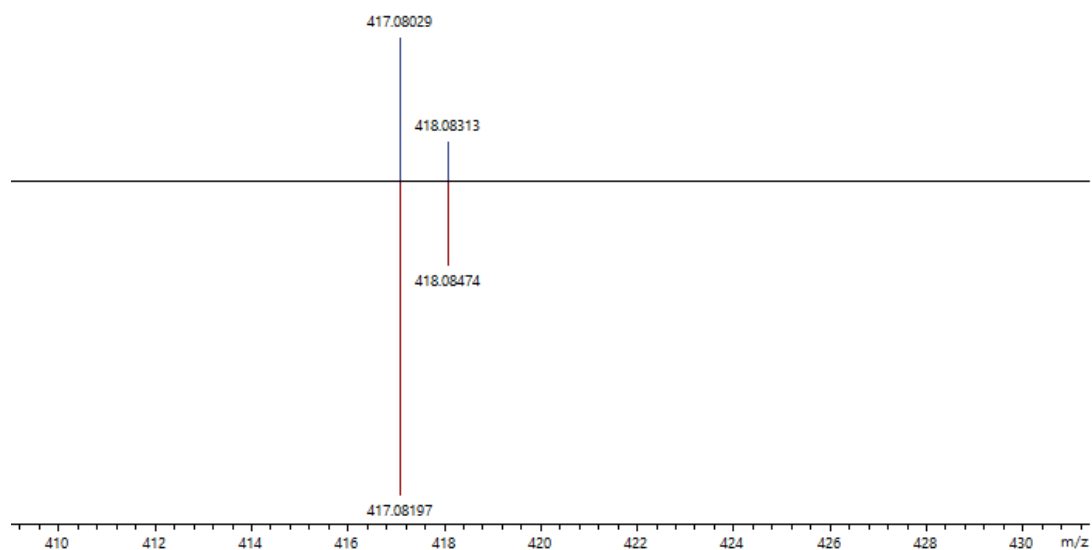


Figure A2.41. Fit of a peak in the mass spectrum of $[\text{Fe}(\text{L}^{\text{pytF}})(\text{MeOH})-\text{H}]^+$ experimental (blue) and simulated pattern (red).

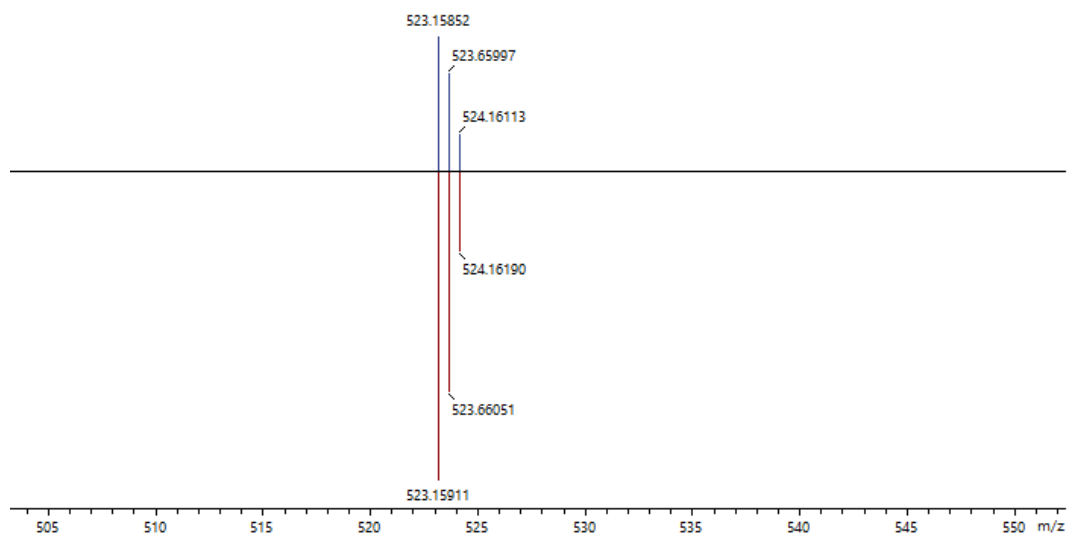


Figure A2.42. Fit of a peak in the mass spectrum of $[\text{Fe}(\text{L}^{\text{pytF}})_3]^{2+}$ experimental (blue) and simulated pattern (red).

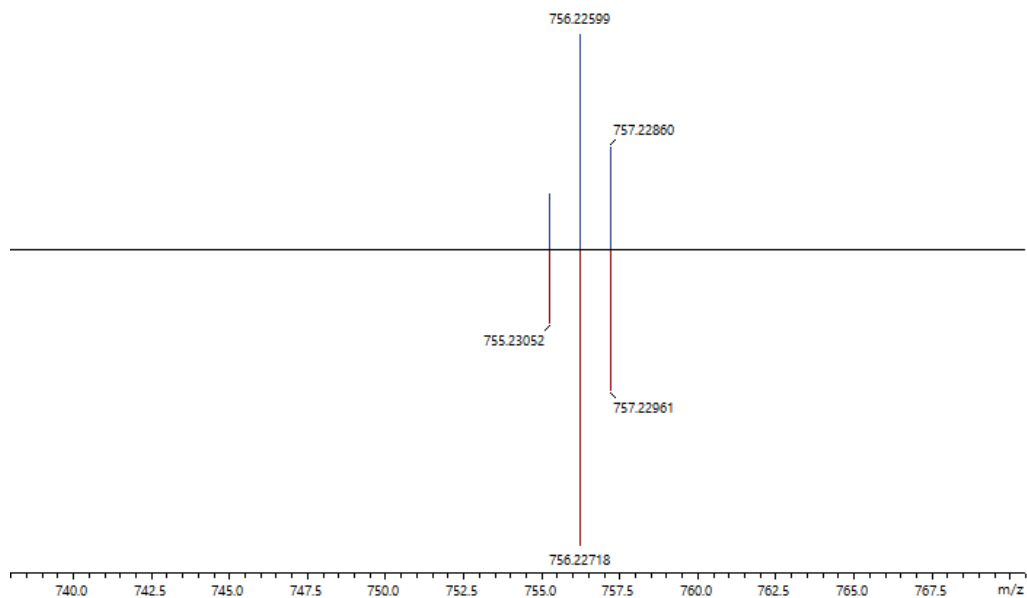


Figure A2.43. Fit of a peak in the mass spectrum of $[\text{Fe}(\text{L}^{\text{pytF}})_2(\text{NCBH}_3)]^+$ experimental (blue) and simulated pattern (red).

A2.8. NMR and MS Figures for L^{pytMe} Ligand

^1H -NMR Spectrum

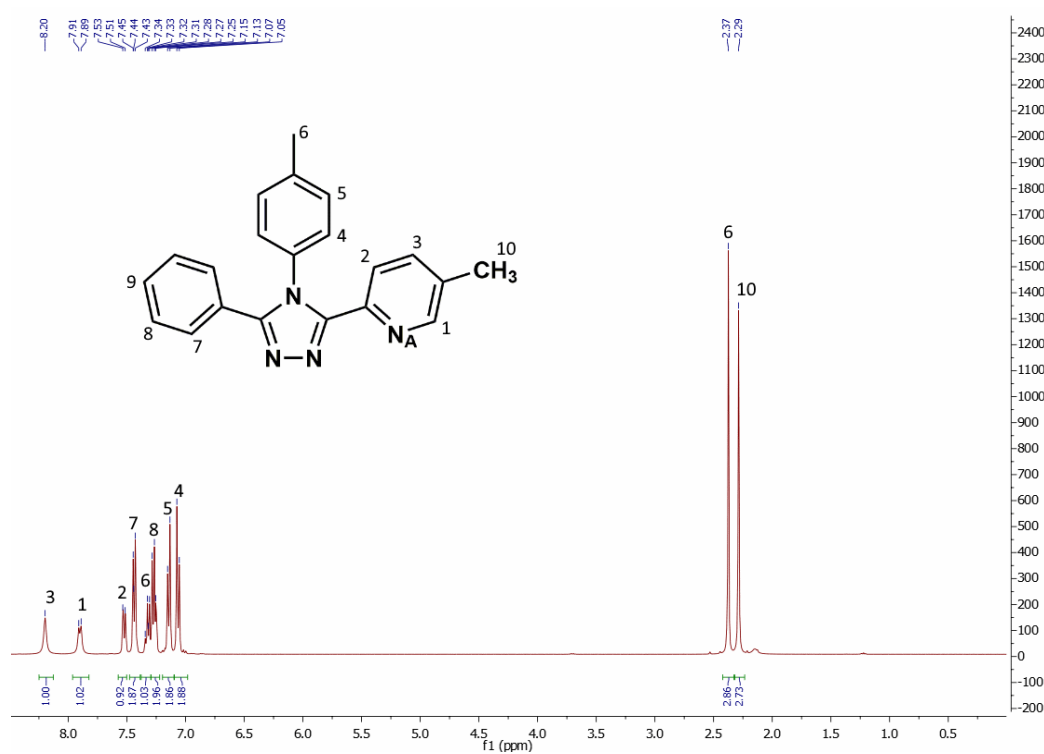


Figure A2.44. The full range ^1H NMR spectrum of ligand L^{pytMe} in CDCl_3 at 298 K.

^{13}C -NMR Spectrum

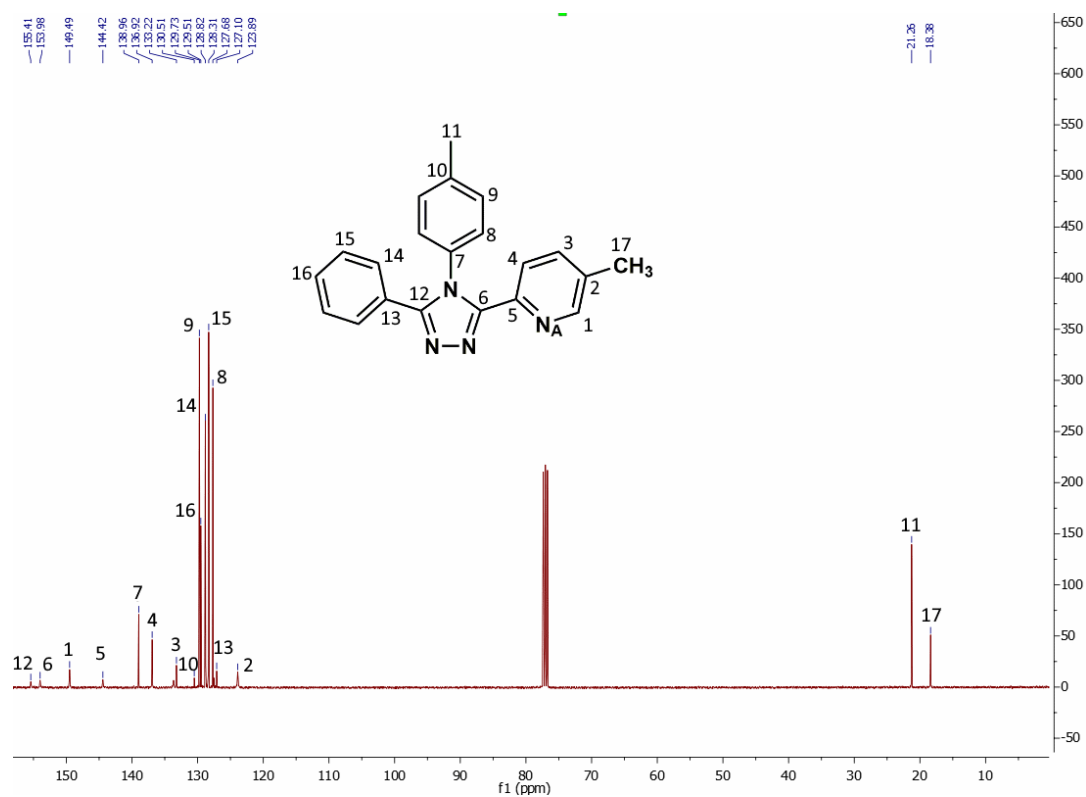


Figure A2.45. The full range ^{13}C NMR spectrum of ligand L_{pytMe} in CDCl_3 at 298 K.

HSQCAD Spectrum

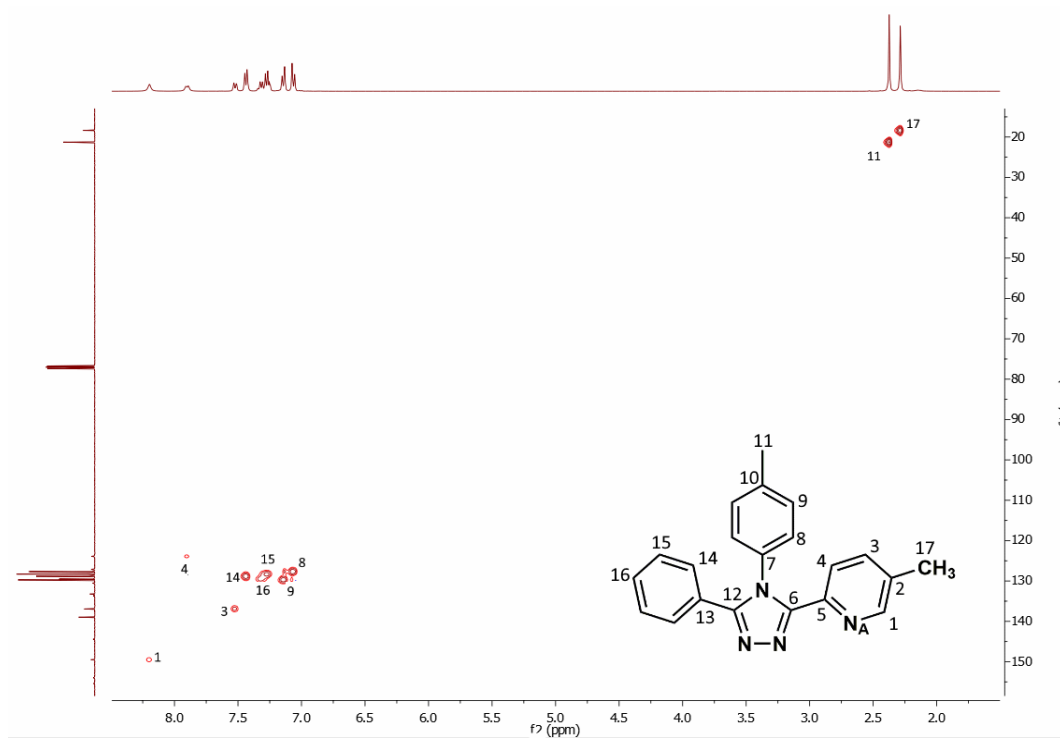


Figure A2.46. Heteronuclear ^1H - ^{13}C NMR spectrum of ligand L^{pytMe} in CDCl_3 at 298 K.

^{15}N -NMR Spectrum

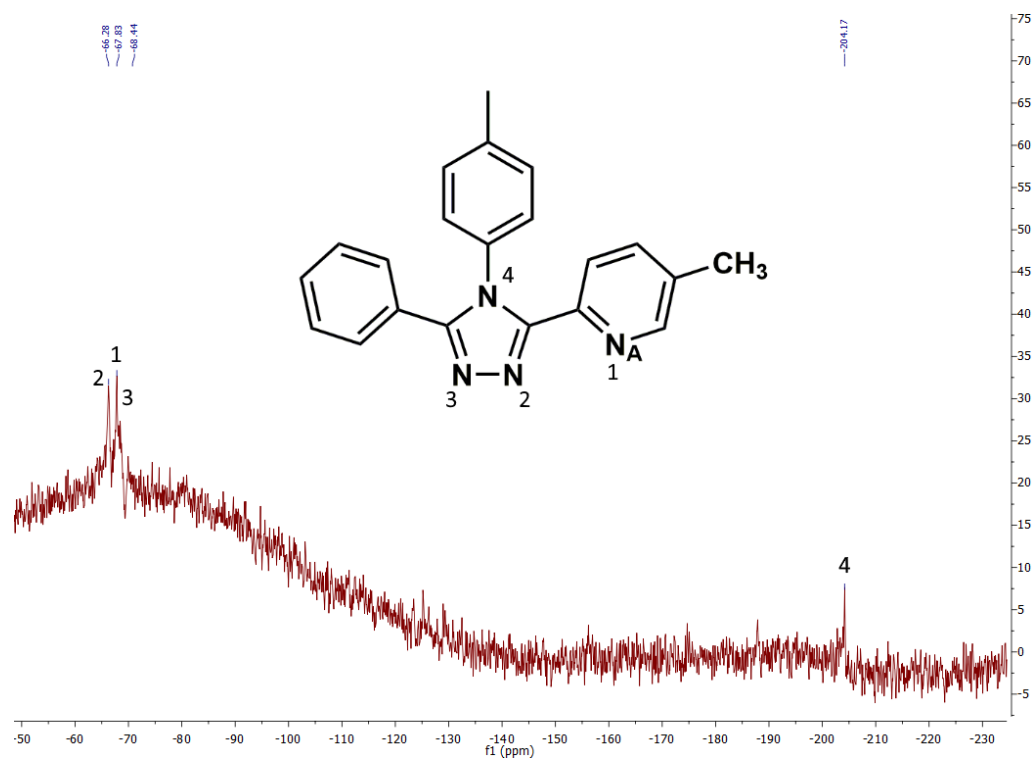


Figure A2.47. The full range ^{15}N NMR spectrum (direct measurement) of ligand L^{pytMe} in CDCl_3 at 298 K.

Mass Spectrum

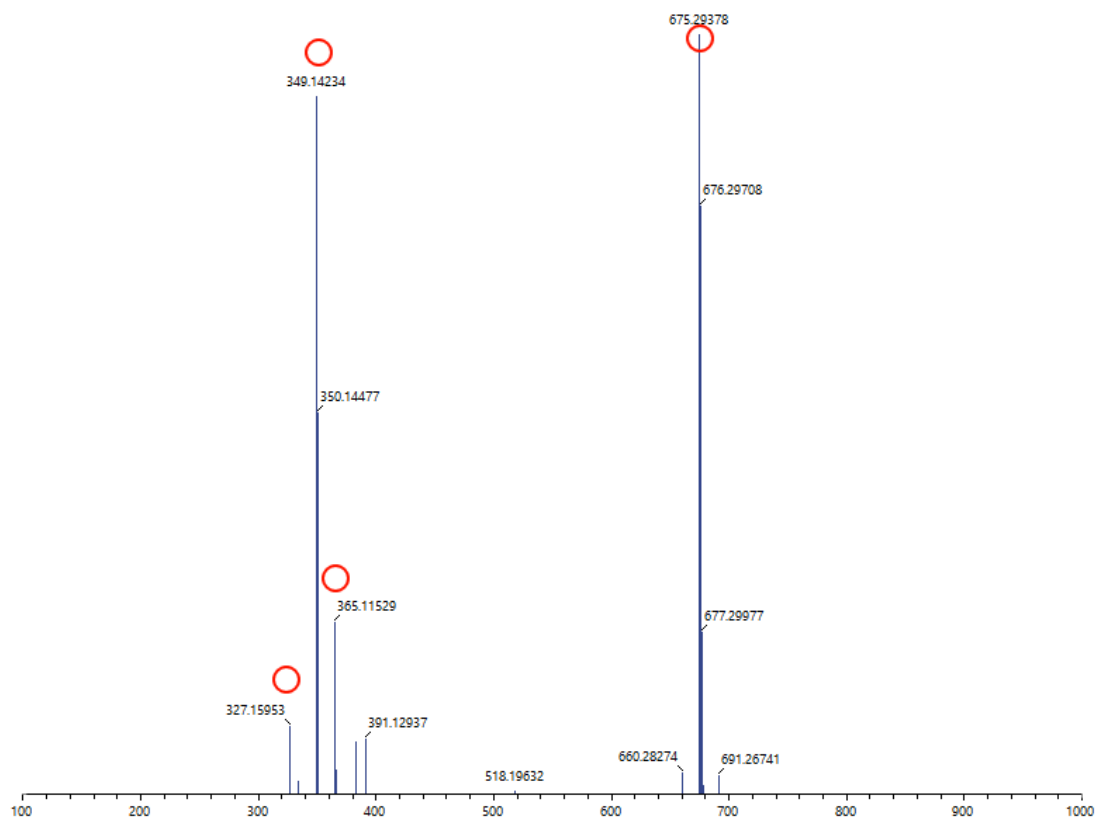


Figure A2.48. Complete mass spectrum of L^{pytMe} . Circled peaks are those reported and fitted in the following figures.

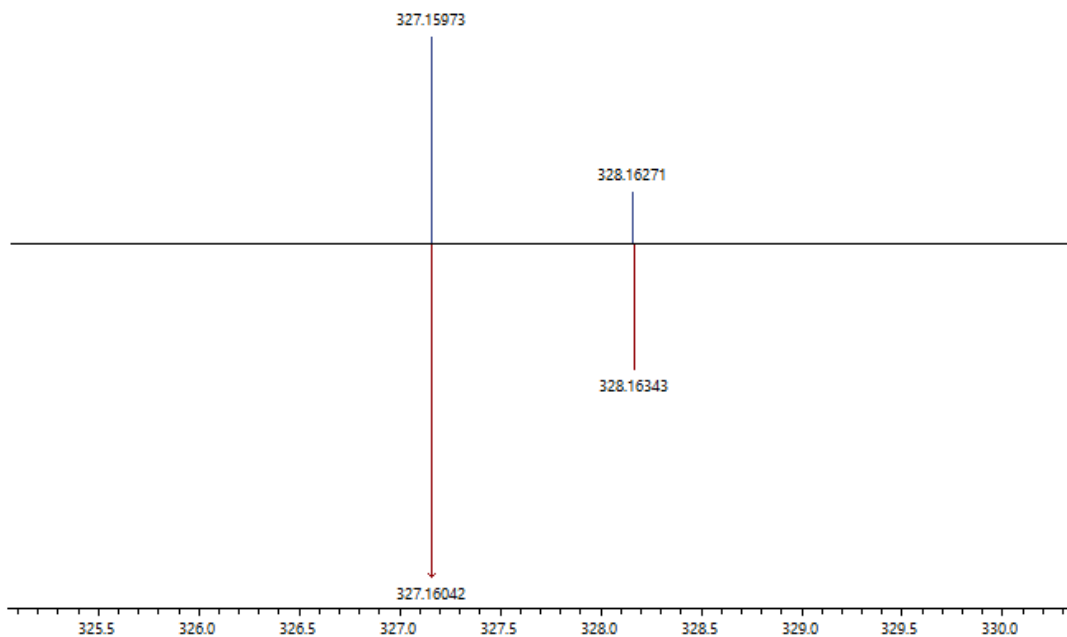


Figure A2.49. Fit of a peak in the mass spectrum of $[\text{L}^{\text{pytMe}}+\text{H}]^+$ experimental (blue) and simulated pattern (red).

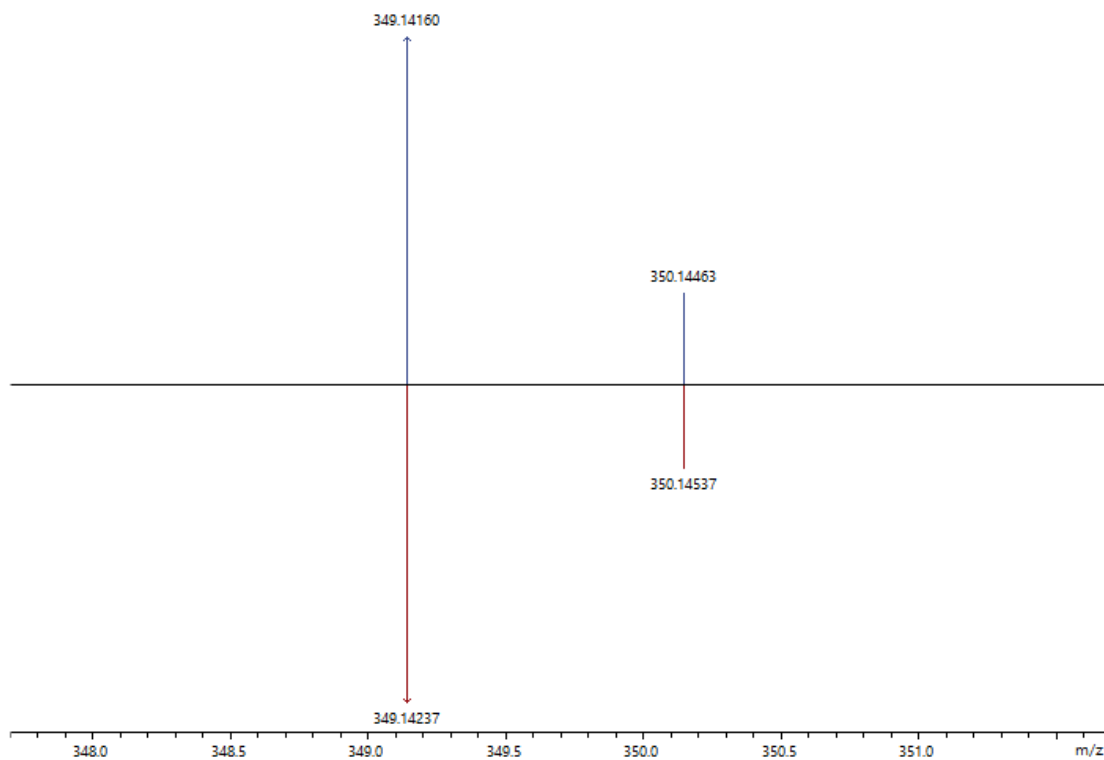


Figure A2.50. Fit of a peak in the mass spectrum of $[\text{L}^{\text{pytMe}}+\text{Na}]^+$ experimental (blue) and simulated pattern (red).

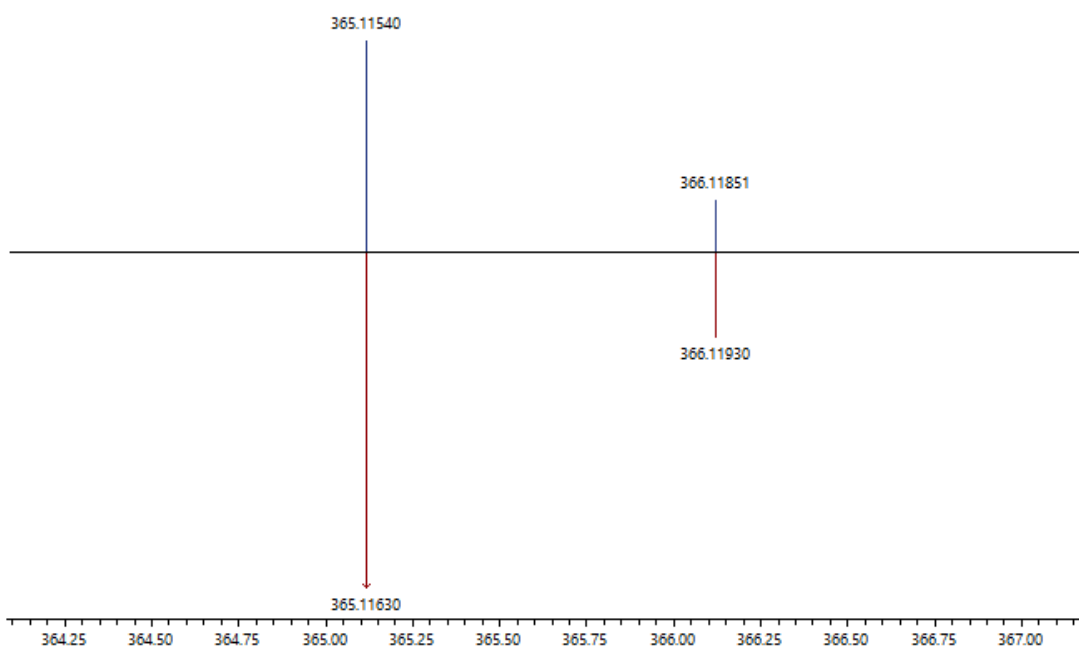


Figure A2.51. Fit of a peak in the mass spectrum of $[\text{LpytMe}+\text{K}]^+$ experimental (blue) and simulated pattern (red).

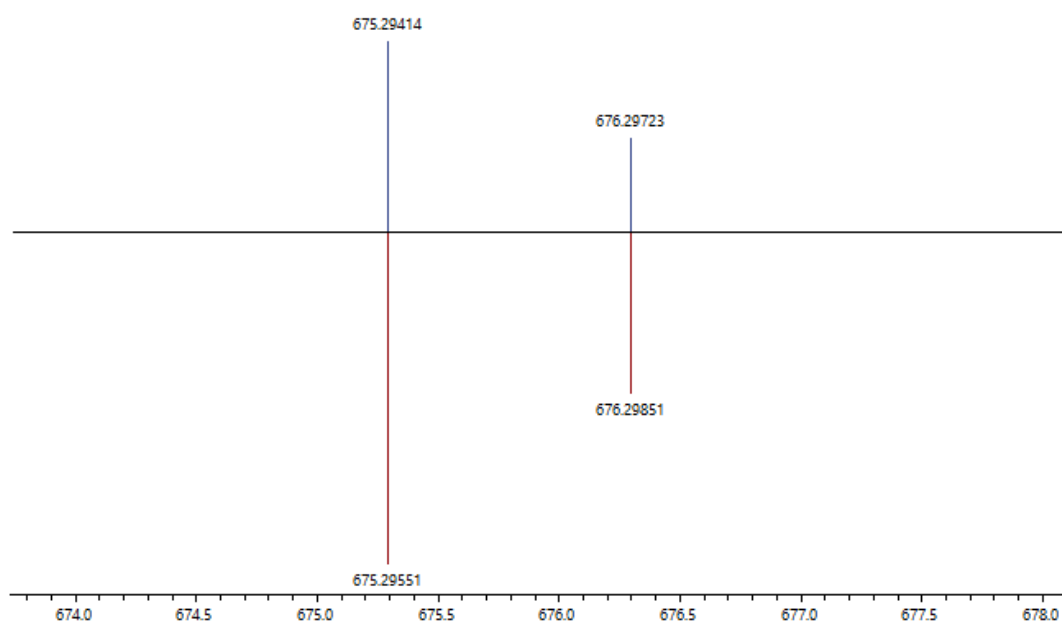


Figure A2.52. Fit of a peak in the mass spectrum of $[(\text{LpytMe})_2+\text{Na}]^+$ experimental (blue) and simulated pattern (red).

A2.9. MS Figures for $[\text{Fe}(\text{L}^{\text{pytMe}})_2(\text{NCBH}_3)_2]$ Complex Spectra

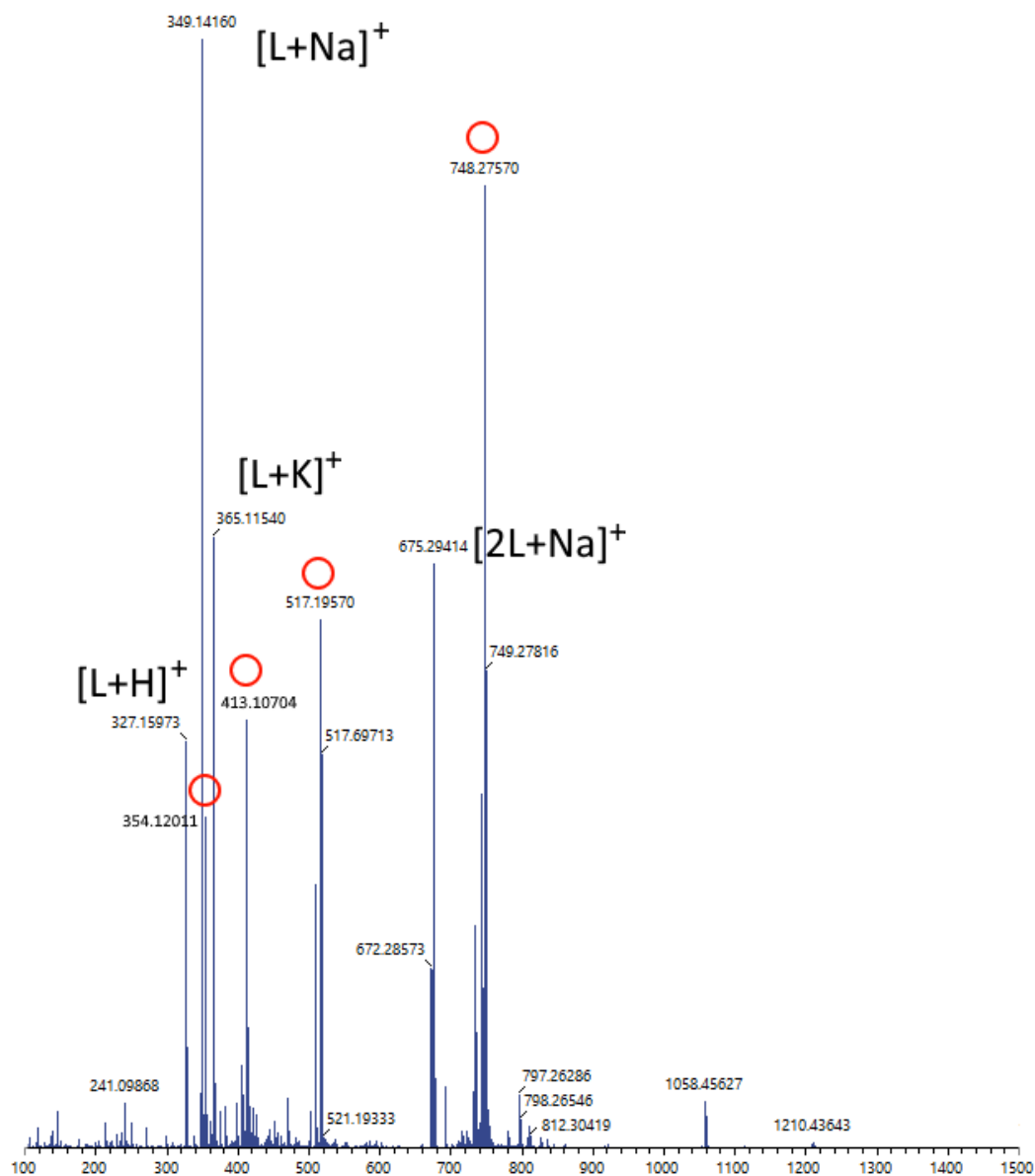


Figure A2.53. Complete mass spectrum of $[\text{Fe}(\text{L}^{\text{pytMe}})_2(\text{NCBH}_3)_2]$. Reported circles refer to zoomed regions reported below.

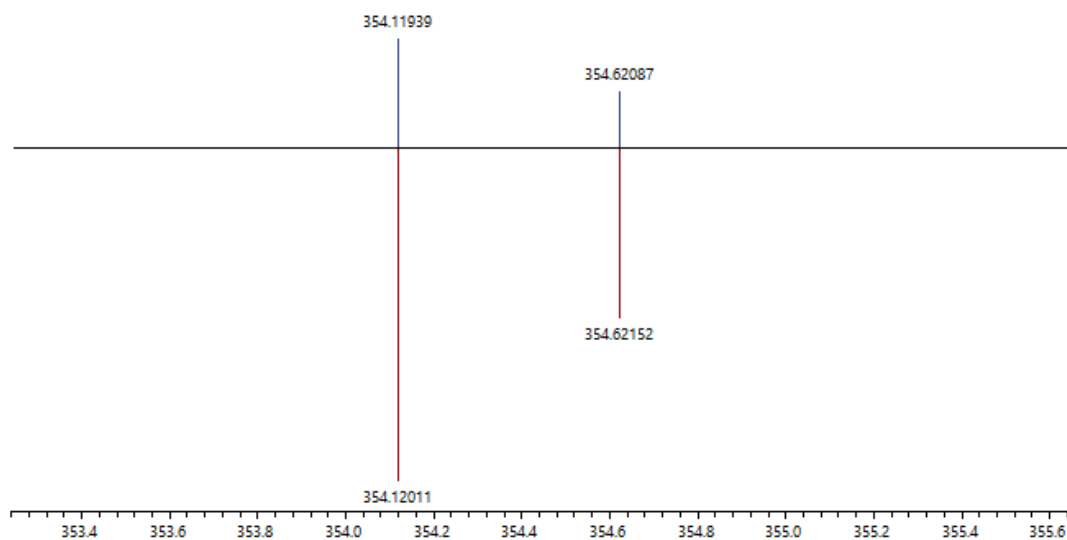


Figure A2.54. Fit of a peak in the mass spectrum of $[\text{Fe}(\text{L}^{\text{pytMe}})_2]^{2+}$ experimental (blue) and simulated pattern (red).

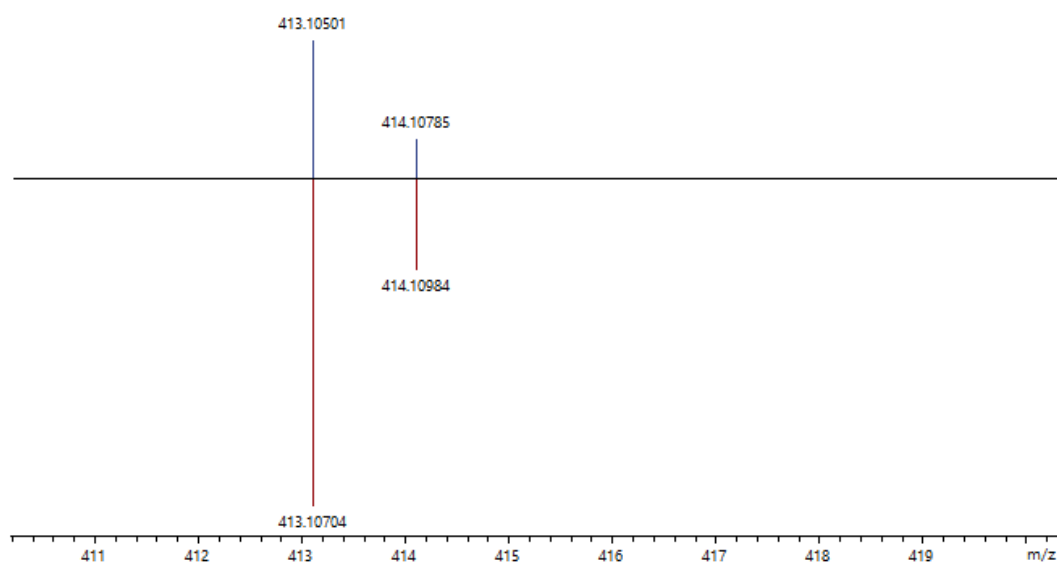


Figure A2.55. Fit of a peak in the mass spectrum of $[\text{Fe}(\text{L}^{\text{pytMe}})(\text{MeOH})-\text{H}]^+$ experimental (blue) and simulated pattern (red).

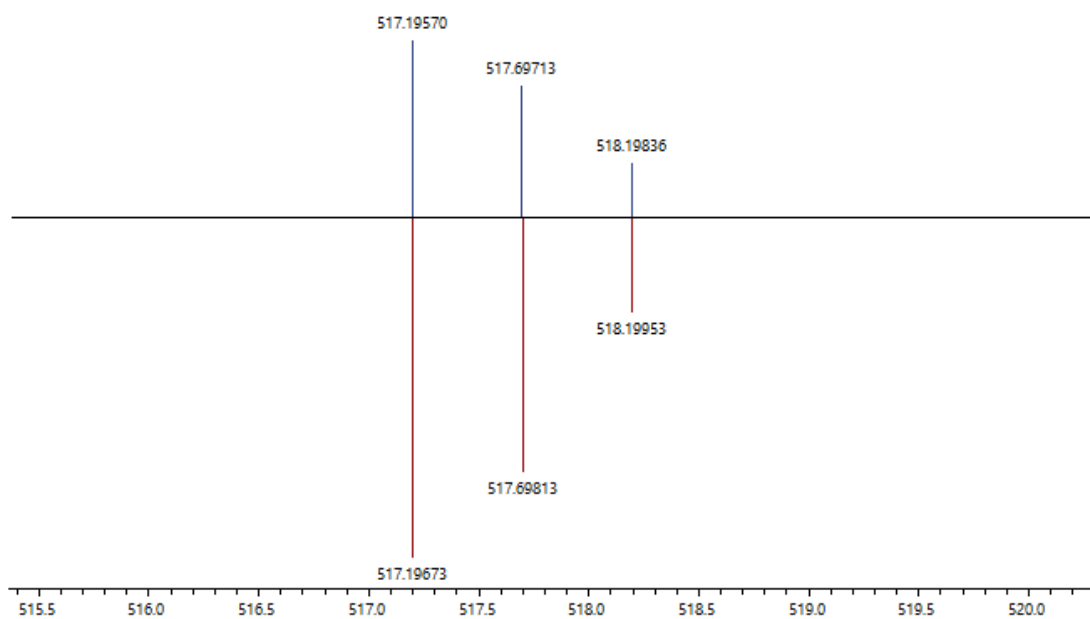


Figure A2.56. Fit of a peak in the mass spectrum of $[\text{Fe}(\text{L}^{\text{pytMe}})_3]^{2+}$ experimental (blue) and simulated pattern (red).

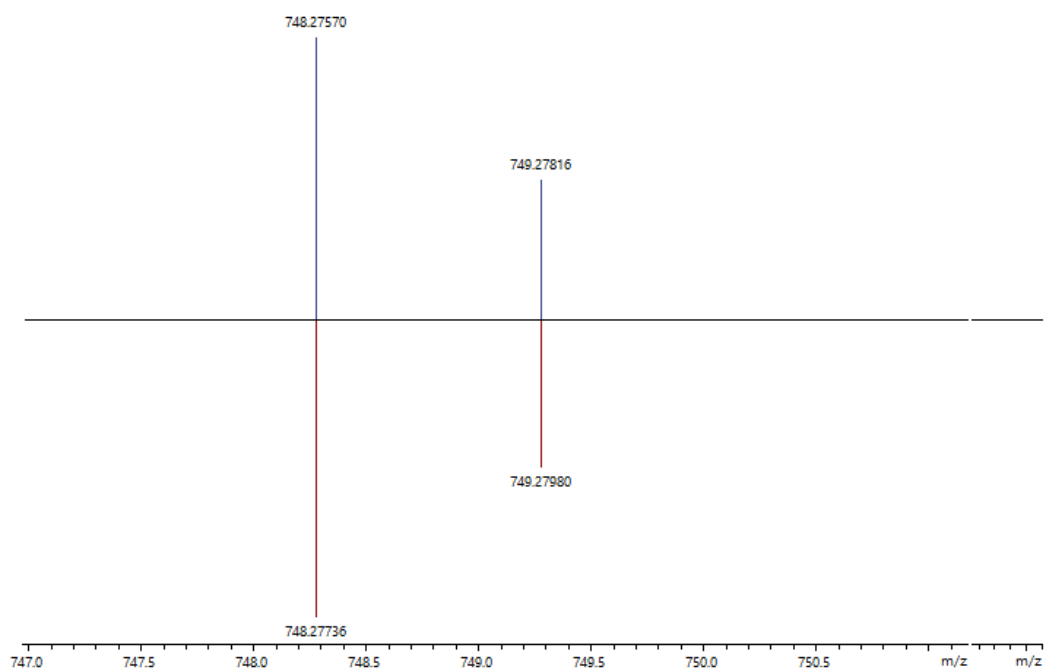


Figure A2.57. Fit of a peak in the mass spectrum of $[\text{Fe}(\text{L}^{\text{pytMe}})_2\text{NCBH}_3]^+$ experimental (blue) and simulated pattern (red).

A2.10. Single Crystal X-Ray Data

The four $[\text{Fe}^{\text{II}}(\text{L}^{\text{pytZ}})_2(\text{NCBH}_3)_2]$ complexes are isomorphous, all having crystallised in the triclinic space group P-1 (Table A2.1), with half of the complex in the asymmetric unit and the other half generated by an inversion centre located at the iron(II) centre. One solvent molecule of crystallisation was present in the asymmetric unit in three cases: in both $[\text{Fe}(\text{L}^{\text{pytCF}_3})_2(\text{NCBH}_3)_2] \cdot 2\text{CHCl}_3$ and $[\text{Fe}(\text{L}^{\text{pytMe}})_2(\text{NCBH}_3)_2] \cdot 2\text{CHCl}_3$ the CHCl_3 molecule was disordered over two sites (Figures A2.59-A2.65); in $[\text{Fe}(\text{L}^{\text{pytF}})_2(\text{NCBH}_3)_2] \cdot 2\text{CH}_3\text{NO}_2$ whereas the nitromethane molecule was ordered (Figures A2.62- A2.63). The average Fe–N length for the iron(II) centres at 100 K is 1.98 Å (Table 5.1) as expected for related *LS* complexes of **Rat/Rdpt** complexes (1.93-2.02 Å).

For the three ($[\text{Fe}(\text{L}^{\text{pytZ}})_2(\text{NCBH}_3)_2]$ -solvents first (**Z** = **CF₃**, **Br**, **Me**) and then ($[\text{Fe}(\text{L}^{\text{pytF}})_2(\text{NCBH}_3)_2] \cdot 2\text{CH}_3\text{NO}_2$). These three iron(II) have a quite homogeneous structure: firstly, octahedral distortion parameter Σ (the sum of the deviations of the 12 *cis* N–Fe–N angles from 90°) for three of the complexes lies in the range 43-45°, which is at the bottom end of the range usually seen for related *LS* complexes of **Rat/Rdpt** complexes (42.5–65.7°);^{4, 139} then, the azine ring is expected to be close to being coplanar with the triazole ring due to the restrictions imposed by coordination of both of them to the iron(II) centre, as seen in related **Rat/Rdpt**-based complexes,^{4, 139} and this is also seen here (0.2-3.1°). Whilst the dihedral angle between the phenyl and triazole ring is not constrained in this way it too is usually not far from being co-planar (0°-25°),^{4, 139} whereas the tolyl ring is usually closer to perpendicular to the triazole ring due to steric factors.

Finally, the Fe–NC(BH₃) bond is extremely close to being linear (174.7-178.6°). $[\text{Fe}(\text{L}^{\text{pytF}})_2(\text{NCBH}_3)_2] \cdot 2\text{CH}_3\text{NO}_2$ reveal a very intense distortion ($\Sigma=70.8^\circ$ vs 43.0-45.0° for the other three members of the family); this value is beyond reported range for *LS* complexes of **Rdpt** complexes (42.5–65.7°)^{4, 139} but not yet in the range seen for related complexes in the *HS* state (92.9°-112.2°).^{4, 84, 105, 139}

Moreover, the azine-triazole dihedral angles shows an important deviation from plane (6.1°); along with phenyl-triazole dihedral angles (41.5°). Last but not least, [Fe(*L^{pytF}*)₂(NCBH₃)₂] \cdot 2CH₃NO₂ reports an Fe-NCBH₃ angle which is very far from linearity (166.4°).

All the four structures [Fe(*L^{pytZ}*)₂(NCBH₃)₂] \cdot solvents (**Z = CF₃, Br, F, Me**) show one crystallographically independent non-classical³⁴⁵⁻³⁴⁷ *intramolecular* N \cdots HC H-bond occurring between the pair of equatorial *L^{pytZ}* ligands, and involves the non-coordinated triazole nitrogen atom and the pyridine CH of the opposite *L^{pytZ}* ligand (C1-H1 \cdots N2 3.07-3.12 Å; Figures A2.58, A2.60, A2.62, A2.64 and Table A2.3-A2.6).

When solvent is present (**Z = CF₃** and **Me**), H-bonds between CH in the tolyl ring and the Cl of in the CHCl₃ molecule are observed (for **Z = CF₃**: C14-H14 \cdots Cl1 3.57 Å, Figures A2.58-A2.59 and Table A2.3; for **Z = Me**: C8-H8 \cdots Cl1 3.48 Å, Figures A2.64-A2.65 and Table A2.6). When **Z = CF₃** a long interaction occurs between the adjacent one of the F on the *meta*-CF₃ substituent, and one of the of the phenyl ring of the opposite *L^{pytCF3}* ligand (C17-H17 \cdots F1 3.78 Å, Figures A2.58 and Table A2.3), of the opposite *L^{pytCF3}* ligand. When **Z = Me** a second, longer interaction occurs between the CH in the pyridyl ring with the same non-coordinated triazole nitrogen atom of the opposite *L^{pytMe}* ligand (C20-H20 \cdots N2 3.61 Å, Figures A2.64 and Table A2.6). When **Z = F**, three H-bonds are directly engaged by the fluorine substituents with three different CH (C9-H9 \cdots F1 3.42 Å, C12-H12 \cdots F1 3.31 Å, C17-H17 \cdots F1 3.61 Å, Figures A2.62 and Table A2.5). Three more are engaged by the CH₃NO₂ solvent molecule: from CH₃ ending in nitromethane is H-bonded by non-coordinating triazole nitrogen (C23-H23B \cdots N2 3.46 Å) and NCBH₃ nitrogen atom (C23-H23C \cdots N5 3.60 Å); also, a H-bond between is observed between the oxygen atom from the NO₂ ending and the substituted pyridyl ring (C4-H4 \cdots O1 3.31 Å, Figures A2.62-A2.63 and Table A2.5).

Table A2.1. Crystal data and structure refinement details for the four $[\text{Fe}(\text{L}^{\text{pytZ}})_2(\text{NCBH}_3)_2] \cdot 2\text{CHCl}_3$.

Empirical formula	$[\text{Fe}(\text{L}^{\text{pytCF}_3})_2(\text{NCBH}_3)_2] \cdot 2\text{CHCl}_3$	$[\text{Fe}(\text{L}^{\text{pytBr}})_2(\text{NCBH}_3)_2]$	$[\text{Fe}(\text{L}^{\text{pytF}})_2(\text{NCBH}_3)_2] \cdot 2\text{CH}_3\text{NO}_2$	$[\text{Fe}(\text{L}^{\text{pytMe}})_2(\text{NCBH}_3)_2] \cdot 2\text{CHCl}_3$
Formula weight	1135.03	918.10	918.36	1027.08
Temperature/K	100(2)	100(2)	100(2)	100(2)
Crystal system	triclinic	triclinic	triclinic	triclinic
Space group	P-1	P-1	P-1	P-1
a [Å]	9.5845(3)	8.9066(4)	8.3350(6)	9.3639(4)
b [Å]	11.4336(8)	9.4038(3)	11.0887(8)	11.3127(4)
c [Å]	11.7405(7)	13.0691(6)	12.5957(6)	11.9801(4)
α [°]	91.135(5)	70.425(4)	90.610(5)	91.075(3)
β [°]	94.601(4)	75.239(4)	92.312(5)	95.484(3)
γ [°]	100.639(4)	82.491(3)	106.356(7)	102.546(3)
Volume [Å ³]	1259.61(12)	996.08(8)	1115.83(13)	1232.07(8)
Z	1	1	1	1
ρ_{calc} [g/cm ³]	1.496	1.531	1.367	1.384
μ [mm ⁻¹]	5.907	5.744	3.258	5.797
F(000)	576.0	464.0	476.0	528.0
Crystal size [mm ³]	0.19 × 0.07 × 0.07	0.009 × 0.05 × 0.08	0.004 × 0.007 × 0.012	0.008 × 0.01 × 0.013
Radiation	CuK α ($\lambda = 1.54184$)	CuK α ($\lambda = 1.54184$)	CuK α ($\lambda = 1.54184$)	CuK α ($\lambda = 1.54184$)
2 θ range [°]	7.558-145.322	10.210-152.546	8.312-154.182	10.608 -152.186
Reflections collected	8656	6308	7840	9638
Independent reflections	4834	4026	4482	4993
Data/restraints /parameters	4834/ 0/ 362	4026/ 0/ 272	4482/ 0/ 317	4993/ 0/ 340
Goof [F ²]	1.046	1.010	1.068	1.203
R ₁ [$I > 2\sigma(I)$]	0.0547	0.0351	0.0886	0.0398
wR ₂ [all data]	0.1479	0.1114	0.2610	0.1329
Largest diff. peak/hole [eÅ ⁻³]	1.35 to -0.89	0.8 to -0.85	2.1 to -0.86	0.49 to -0.68

Table A2.2. Summary of key structural parameters for the four $[\text{Fe}(\text{L}^{\text{pytZ}})_2(\text{NCBH}_3)_2] \cdot \text{solvent}$ complexes.

	$[\text{Fe}(\text{L}^{\text{pytCF}_3})_2(\text{NCBH}_3)_2] \cdot 2\text{CHCl}_3$	$[\text{Fe}(\text{L}^{\text{pyBr}})_2(\text{NCBH}_3)_2]$	$[\text{Fe}(\text{L}^{\text{pyF}})_2(\text{NCBH}_3)_2] \cdot 2\text{CH}_3\text{NO}_2$	$[\text{Fe}(\text{L}^{\text{pyMe}})_2(\text{NCBH}_3)_2] \cdot 2\text{CHCl}_3$
av. Fe-N _{triazole} (Å)	1.957 Å	1.959 Å	1.982 Å	1.974 Å
av. Fe-N _{pyridine} (Å)	1.999 Å	1.987 Å	2.005 Å	2.010 Å
av. Fe-N _{NCBH₃} (Å)	1.933 Å	1.945 Å	1.945 Å	1.938 Å
av. Fe-N (Å)	1.963 Å	1.964 Å	1.977 Å	1.974 Å
Distortion angle (Σ°)	44.9°	44.9°	70.8°	43.0°
Temperature	100 K	100 K	100 K	100 K
Spin State	<i>LS</i>	<i>LS</i>	<i>LS</i>	<i>LS</i>
N _{triazole} -Fe-N _{azine} angle (°)	80.2°	80.1°	79.9°	80.3°
N _{triazole} -Fe-N _{azine} dihedral angle (°)	3.06°	0.24°	6.21°	0.91°
Fe-NCBH ₃ angle (°)	178.3°	174.7°	166.37°	178.6°
triazole-tolyl ring dihedral angle (°)	78.7°	76.0°	75.2°	73.0°
triazole-phenyl ring dihedral angle (°)	24.2°	3.6°	41.5°	21.6°

Table A2.3. Non-classical H-bonds observed in $[\text{Fe}(\text{L}^{\text{pytCF}_3})_2(\text{NCBH}_3)_2] \cdot 2\text{CHCl}_3$. Q = -x, -y, -z. R = 1-x, -y, -z. S = -x, 1-y, -z. T = -x, -y, 1-z.

D-H...A	D-A (Å)	H...A (Å)	D-H...A (°)
C20Q-H20Q...F1	3.775	2.980	144.3
C1-H1...N2Q	3.070	2.266	144.4
C8-H8...Cl1	3.569	2.825	137.8

Table A2.4. Non-classical H-bonds observed in $[\text{Fe}(\text{L}^{\text{pytBr}})_2(\text{NCBH}_3)_2]$. Q = -x, -y, -z. R = 1-x, -y, -z. S = -x, 1-y, -z. T = -x, -y, 1-z.

D-H...A	D-A (Å)	H...A (Å)	D-H...A (°)
C1-H1... N2S	3.070	2.266	144.4
C20T-H20T... Br1	4.690	3.864	149.7

Table A2.5. Non-classical H-bonds observed in $[\text{Fe}(\text{L}^{\text{pytF}})_2(\text{NCBH}_3)_2] \cdot 2\text{CH}_3\text{NO}_2$. Q = -x, -y, -z. R = 1-x, -y, -z. S = -x, 1-y, -z. T = -x, -y, 1-z.

D-H...A	D-A (Å)	H...A (Å)	D-H...A (°)
C17-H17...F1T	3.607	2.736	156.4
C9-H9...F1R	3.423	2.812	124.3
C12-H12...F1Q	3.314	2.592	134.8
C1-H1...N2S	3.117	2.331	141.9
C22-H22B...N2S	3.461	2.533	162.6
C22-H22C...N5S	3.604	2.953	126.3
C4-H4...O1Q	3.305	2.533	140.7
C20S-H20S...F1	5.590	5.207	109.4

Table A2.6. Non-classical H-bonds observed in $[\text{Fe}(\text{L}^{\text{pytMe}})_2(\text{NCBH}_3)_2] \cdot 2\text{CHCl}_3$. Q = -x, -y, -z. R = 1-x, -y, -z. S = -x, 1-y, -z. T = -x, -y, 1-z.

D-H...A	D-A (Å)	H...A (Å)	D-H...A (°)
C1-H1...N2Q	3.107	2.276	145.6
C19T-H19T...N2	3.612	2.998	123.7
C13-H13...Cl1	3.480	2.741	144.5

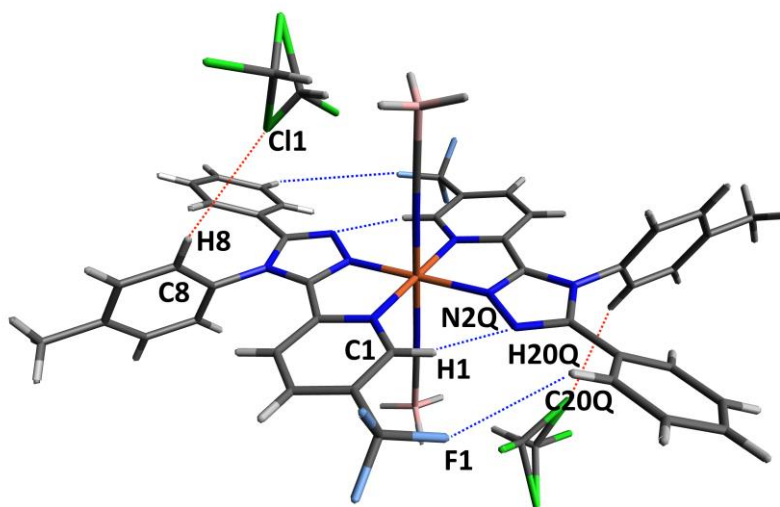


Figure A2.58. Crystal structure of $[\text{Fe}(\text{L}^{\text{pytCF}_3})_2(\text{NCBH}_3)_2] \cdot 2\text{CHCl}_3$. Blue dotted lines report the non-classical C-H...X H-bond interactions (intramolecular H-bonds: C1-H1...N2Q and C20Q-H20Q...F1); red dotted lines report complex-solvent H-bond interactions (intermolecular H-bonds: C8-H8...Cl1). See Table S3. Colour code: Fe orange, N blue, C black, Cl green, F light blue, B pink, H white.

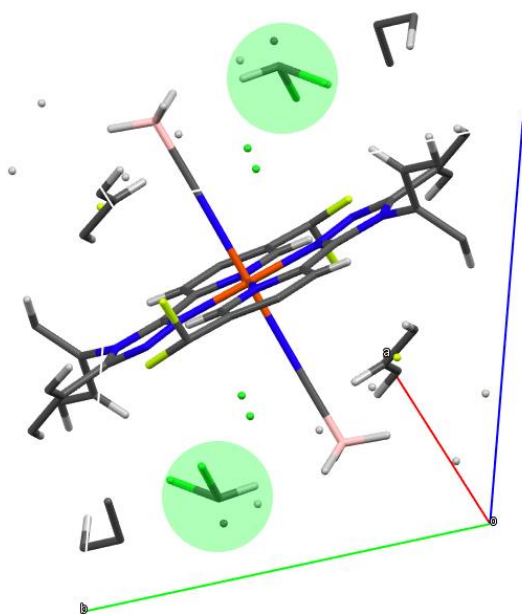


Figure 2.59. Unit cell crystal packing of $[\text{Fe}(\text{L}^{\text{pytCF}_3})_2(\text{NCBH}_3)_2] \cdot 2\text{CHCl}_3$, one mononuclear complex per unit cell. Two disordered half molecules of CHCl_3 are highlighted in green. Colour code: Fe orange, N blue, C black, Cl green, F light blue, B pink, H white.

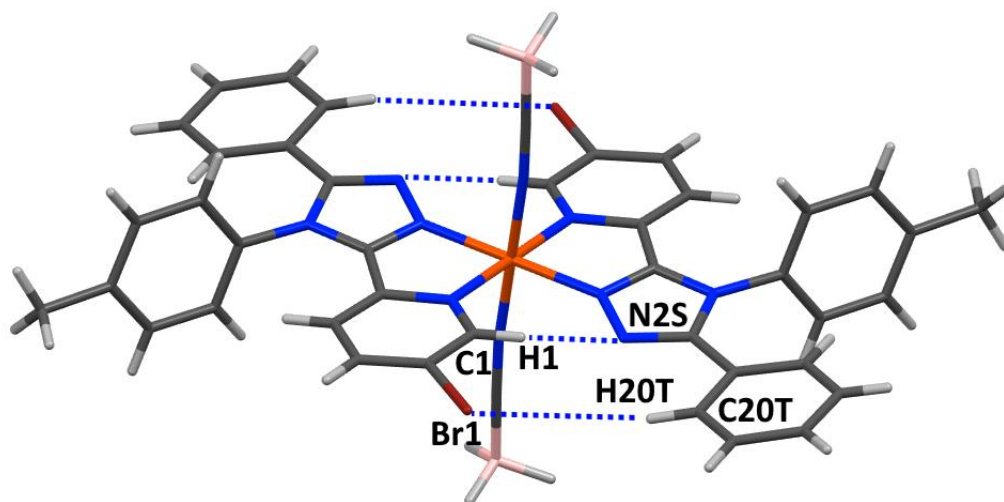


Figure A2.60. Crystal structure of $[\text{Fe}(\text{L}^{\text{pyt}^{\text{Br}}})_2(\text{NCBH}_3)_2]$. Blue dotted lines report the non-classical C-H...X H-bond interactions (intramolecular H-bond: C1-H1...N2S). Details in Table S4. Note: C20T-H20T...Br1 3.864 Å, C20T...Br1 4.690 Å, C20T-H20T...Br1 149.67°, so is at best a weak intramolecular interaction in this case (cf the Z = CF₃ case, Figure S58). Colour code: Fe orange, N blue, C black, Br crimson, B pink, H white.

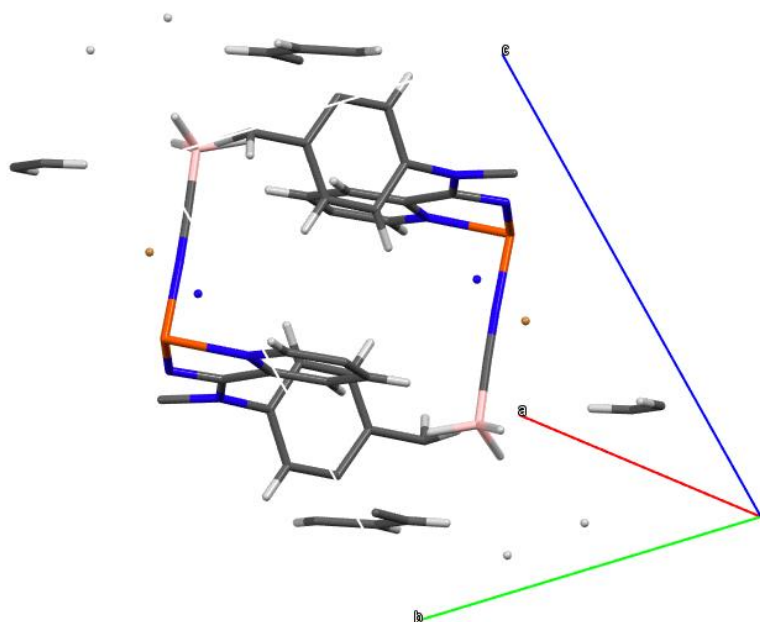


Figure A2.61. Unit cell crystal packing of $[\text{Fe}(\text{L}^{\text{pyt}^{\text{Br}}})_2(\text{NCBH}_3)_2]$, one mononuclear complex per unit cell. Colour code: Fe orange, N blue, C black, Br crimson, B pink, H white.

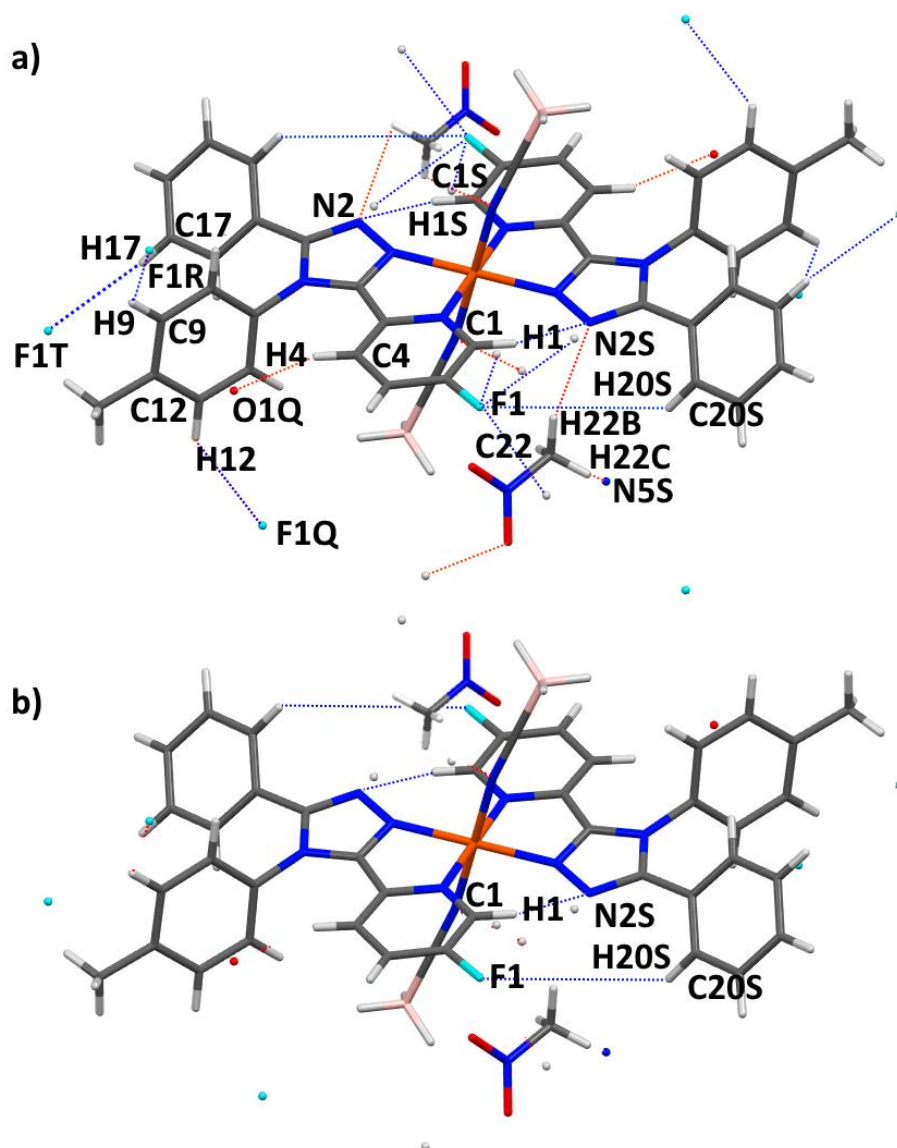


Figure A.262. Crystal structure of $[\text{Fe}(\text{L}^{\text{py}^{\text{F}}})_2](\text{NCBH}_3)_2 \cdot 2\text{CH}_3\text{NO}_2$. (a) Blue dotted lines report the non-classical C-H...X interactions (intramolecular H-bonds: C1-H1...N2S; intermolecular H-bonds: C9-H9...F1R, C12-H12...F1Q, C17-H17...F1T); red dotted lines report complex-solvent H-bond interactions (H-bonds: C22-H22B...N2S, C22-H22C...N5S, C4-H4...O1Q). See Table S5. (b) Blue dotted lines highlight the intermolecular non classical H-bonds made by the Z = F substituents (C20S-H20S...F1 5.207 Å, C20S...F1 5.590 Å, C20S...F1 109.4°), which contrast with the intramolecular non classical H-bonds made by the Z = CF₃ substituents (Figure S58, Table S3) and Z = Br substituents (Figure S60, Table S4). Colour code: Fe orange, N blue, C black, F light blue, B pink, H white, O red.

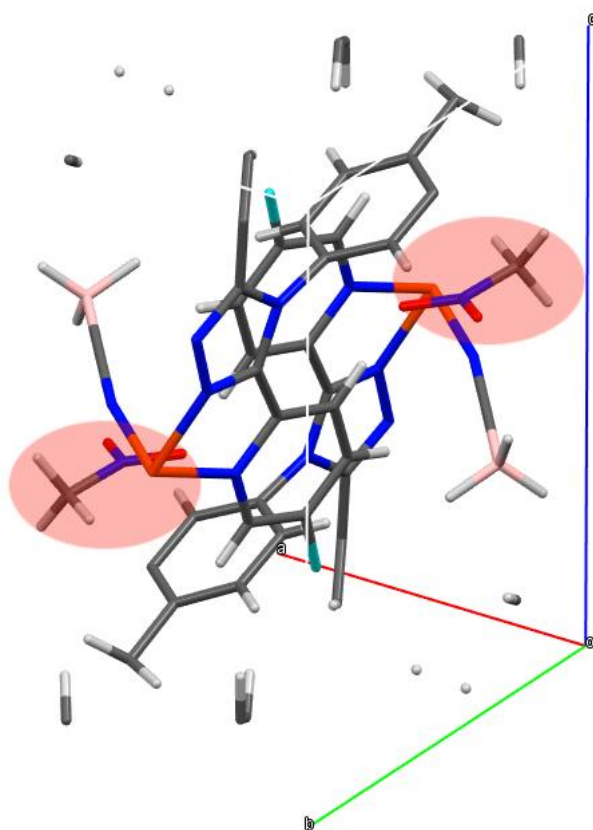


Figure A2.63. Unit cell crystal packing of $[\text{Fe}(\text{L}^{\text{pyrF}})_2(\text{NCBH}_3)_2]$, two mononuclear complex per unit cell. Two disordered half molecules of CH_3NO_2 are highlighted in red. Colour code: Fe orange, N blue, C black, F light blue, B pink, H white, O red.

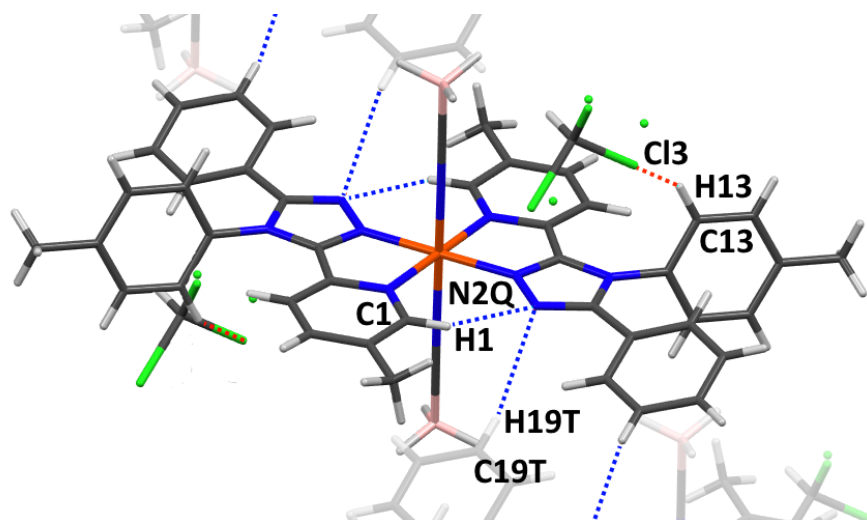


Figure A2.64. Crystal structure of $[\text{Fe}(\text{L}^{\text{pytMe}})_2(\text{NCBH}_3)_2] \cdot 2\text{CHCl}_3$. Blue dotted lines report the non-classical C-H...X interactions (intramolecular H-bonds: C1-H1...N2Q; intermolecular H-bonds: C19T-H19T...N2); red dotted lines report complex-solvent H-bond interactions (H-bonds: C13-H13...Cl3). See Table S6. Colour code: Fe orange, N blue, C black, Cl green, B pink, H white.

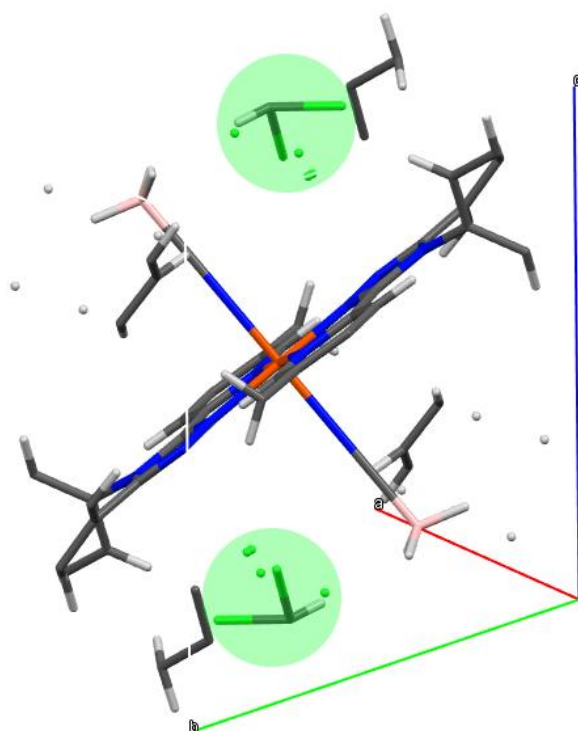


Figure A2.65. Unit cell crystal packing of $[\text{Fe}(\text{L}^{\text{pytMe}})_2(\text{NCBH}_3)_2] \cdot 2\text{CHCl}_3$, one mononuclear complex per unit cell. Two disordered molecules of CHCl_3 are highlighted in green. Colour code: Fe orange, N blue, C black, Cl green, B pink, H white.

A2.11. Solid State Magnetic Measurements

The solid state magnetic susceptibilities were measured from 50–400–50 K for each $[\text{Fe}^{\text{II}}(\text{L}^{\text{pytZ}})_2(\text{NCBH}_3)_2] \cdot n\text{H}_2\text{O}$ (measuring in 10 K steps, ramping between steps at 2 K min^{-1}). These measurements are obtained in settle mode (the instrument considers the temperature “settled” after 1 min of the temperature being within the smaller value of ± 0.5 K or $\pm 0.5\%$ of the target value). Scan rate study of $\chi_{\text{M}}T$ vs T for $[\text{Fe}(\text{L}^{\text{pytCF}_3})_2(\text{NCBH}_3)_2] \cdot 0.5\text{H}_2\text{O}$ from 150 to 250 K was obtained in sweep mode. In this instrumental set up, $\chi_{\text{M}}T$ measurements are collected continuously as the temperature was swept at different rates (20, 10, 5, 2 and 0.2 K min^{-1}). Measurements were obtained by applying a magnetic field of 0.1 T with a Quantum Design Physical Property Measurement System equipped with a vibrating sample mount (VersaLab). The data were corrected for the diamagnetism of the capsule and of the sample $((-M \times 0.5) \times 10^{-6} \text{ cm}^3\text{mol}^{-1})$.¹¹⁹

Table A2.7. Reported obtained $T_{1/2}$ from solid state measurements on $[\text{Fe}(\text{L}^{\text{pytZ}})_2(\text{NCBH}_3)_3] \cdot x\text{H}_2\text{O}$ family.

$[\text{Fe}(\text{L}^{\text{pytZ}})_2(\text{NCBH}_3)_2] \cdot x\text{H}_2\text{O}$	$T_{1/2}$ (K)
$[\text{Fe}(\text{L}^{\text{pytCF}_3})_2(\text{NCBH}_3)_2] \cdot 0.5\text{H}_2\text{O}$	$T_{1/2\downarrow} = 203$ K, $T_{1/2\uparrow} = 213$ K; $\Delta T_{1/2} = 10$ K
$[\text{Fe}(\text{L}^{\text{pytBr}})_2(\text{NCBH}_3)_2] \cdot 0.5\text{H}_2\text{O}$	LS
$[\text{Fe}(\text{L}^{\text{pytF}})_2(\text{NCBH}_3)_2] \cdot 1\text{H}_2\text{O}$	290
$[\text{Fe}(\text{L}^{\text{pytMe}})_2(\text{NCBH}_3)_2] \cdot 0.5\text{H}_2\text{O}$	300

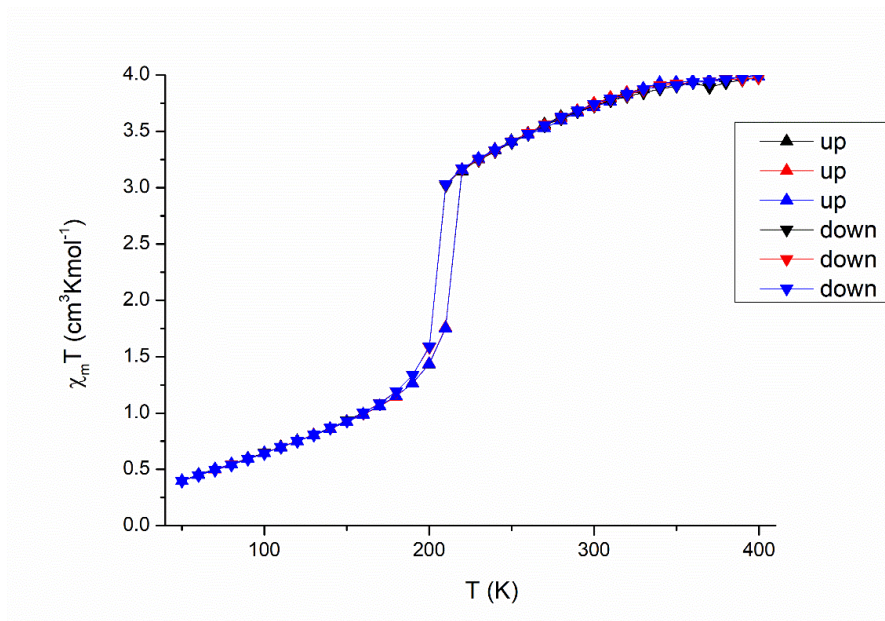


Figure A2.66. $\chi_M T$ versus T plot for a solid sample of $[\text{Fe}(\text{L}^{\text{pytCF}_3})_2(\text{NCBH}_3)_2] \cdot 0.5\text{H}_2\text{O}$ from 50 to 400 K. Cycle was performed by cooling first (down triangles), then heating (up triangles) for three cycles, in 10 K steps, changing temperatures at 2 K min^{-1} , in settle mode.

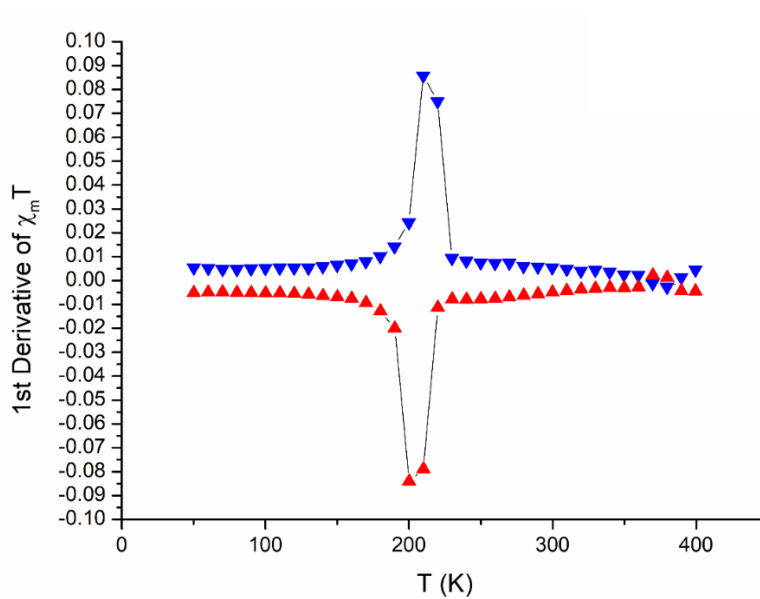


Figure A2.67. First derivative of $\chi_M T$ versus T plot for a solid sample of $[\text{Fe}(\text{L}^{\text{pytCF}_3})_2(\text{NCBH}_3)_2] \cdot 0.5\text{H}_2\text{O}$ from 50 to 400 K. Cycle was performed by cooling first (down triangles), then heating (up triangles) in 10 K steps, changing temperatures at 2 K min^{-1} , in settle mode.

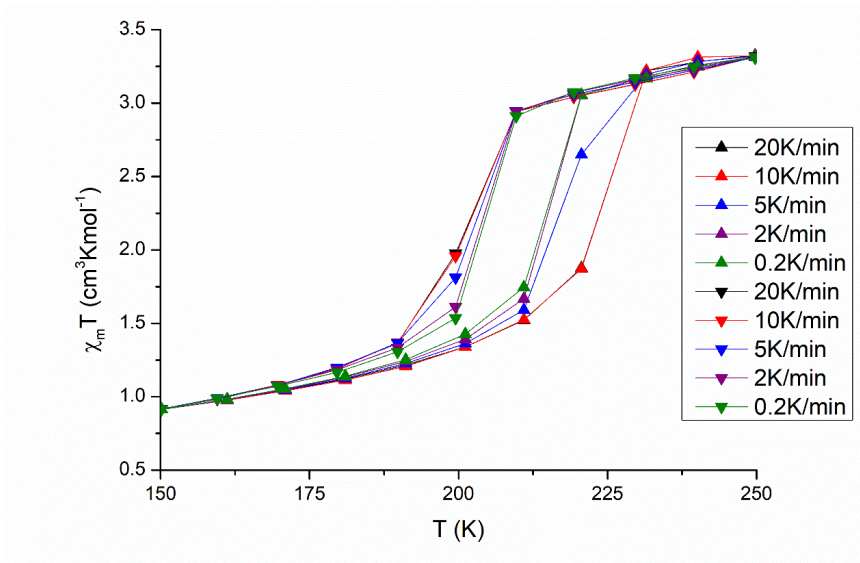


Figure A2.68. Scan rate study (20 to 0.2 K min^{-1}) of $\chi_{\text{M}}T$ vs T for $[\text{Fe}(\text{L}^{\text{pytCF}_3})_2(\text{NCBH}_3)_2] \cdot 0.5\text{H}_2\text{O}$ from 150 to 250 K in sweep mode.

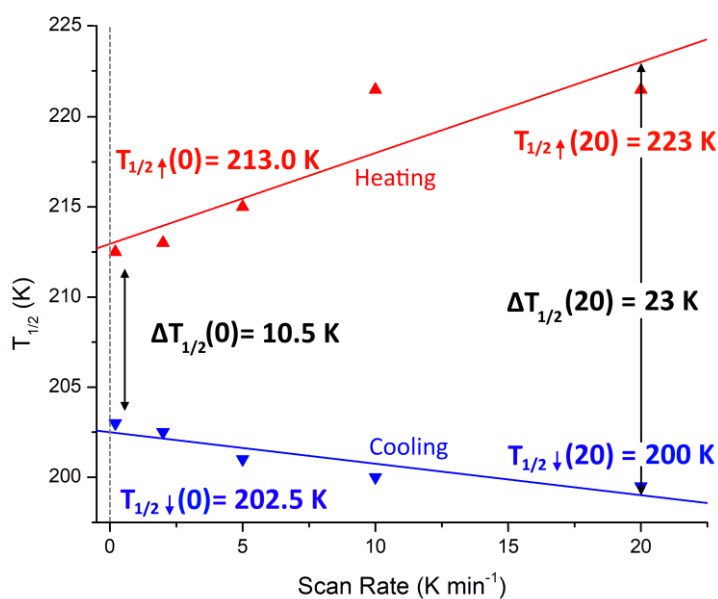


Figure A2.69. Plots of $T_{1/2}$ values obtained from the cooling (blue, at 20 K min^{-1} ($T_{1/2}\downarrow(20)$) and extrapolated at limit speed of 0 K min^{-1} ($T_{1/2}\downarrow(0)$) and heating (red, at 20 K min^{-1} ($T_{1/2}\uparrow(20)$) and extrapolated at limit speed of 0 K min^{-1} ($T_{1/2}\uparrow(0)$) modes from magnetic experiments run at different scan rates (in sweep mode) for $[\text{Fe}(\text{L}^{\text{pytCF}_3})_2(\text{NCBH}_3)_2] \cdot 0.5\text{H}_2\text{O}$. The lines shown were obtained by linear fitting of the magnetic data, as reported by Brooker et al.⁹⁵⁻⁹⁶

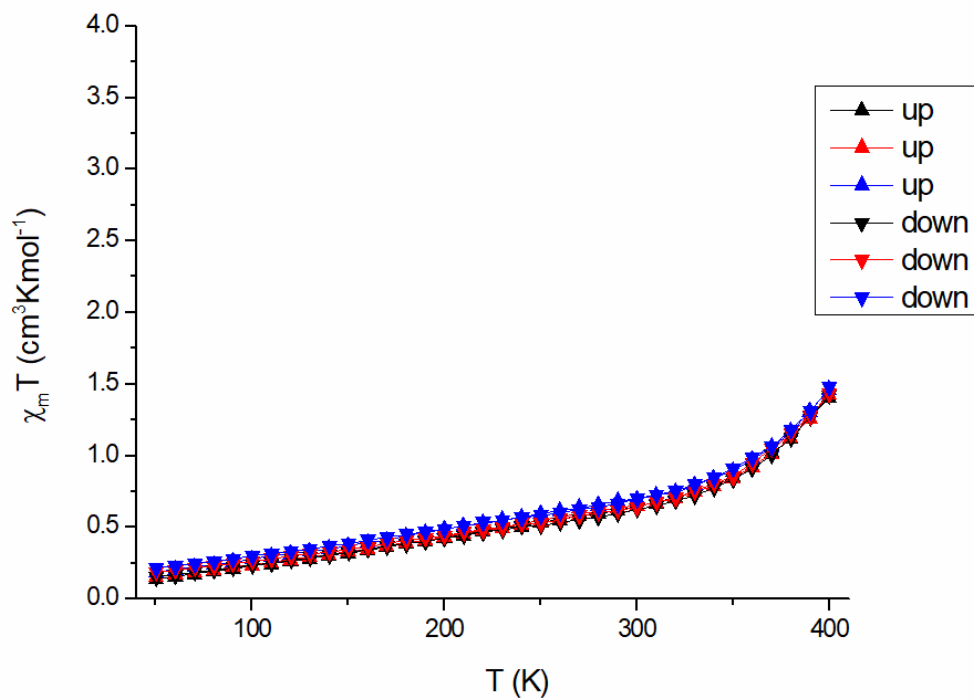


Figure A2.70. $\chi_M T$ versus T plot for a solid sample of $[\text{Fe}(\text{Lpy}^{\text{tBr}})_2(\text{NCBH}_3)_2] \cdot 0.5\text{H}_2\text{O}$ from 50 to 400 K. Cycle was performed by cooling first (down triangles), then heating (up triangles) for three cycles, in 10 K steps, changing temperatures at 2 K min^{-1} , in settle.

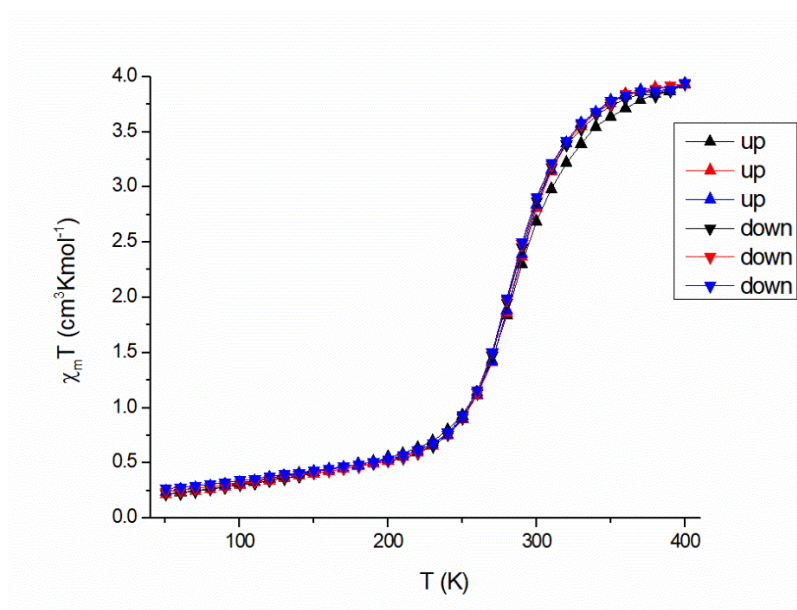


Figure A2.71. $\chi_M T$ versus T plot for a solid sample of $[\text{Fe}(\text{L}^{\text{pyr}^{\text{Hf}}})_2(\text{NCBH}_3)_2] \cdot 1\text{H}_2\text{O}$ from 50 to 400 K. Cycle was performed by cooling first (down triangles), then heating (up triangles) for three cycles, in 10 K steps, changing temperatures at 2 K min^{-1} , in settle mode.

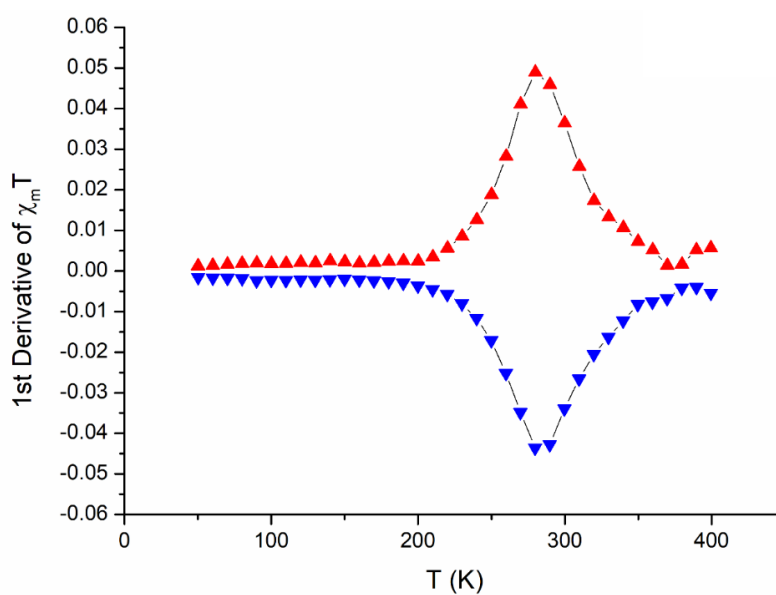


Figure A2.72. First derivative of $\chi_M T$ versus T plot for a solid sample of $[\text{Fe}(\text{L}^{\text{pyr}^{\text{Hf}}})_2(\text{NCBH}_3)_2] \cdot 1\text{H}_2\text{O}$ from 50 to 400 K. Cycle was performed by cooling first (down triangles), then heating (up triangles) in 10 K steps, changing temperatures at 2 K min^{-1} , in settle mode.

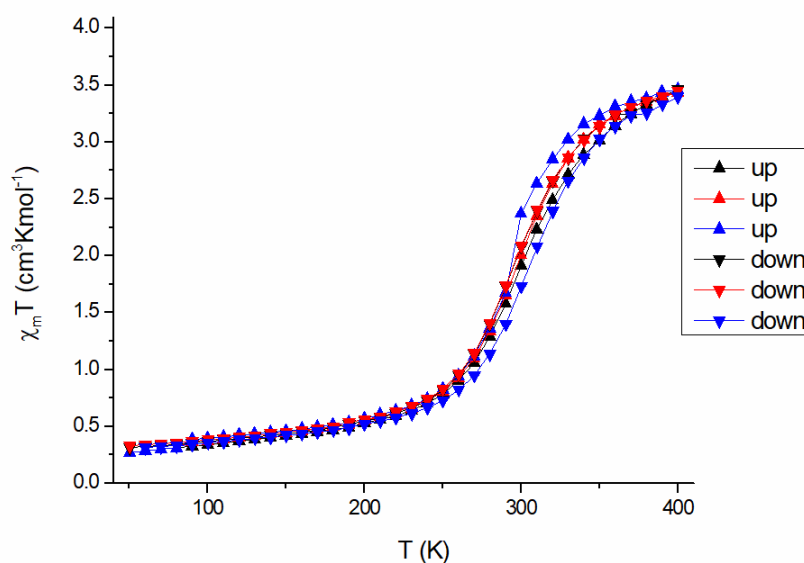


Figure A2.73. $\chi_M T$ versus T plot for a solid sample of $[\text{Fe}(\text{L}^{\text{PytMe}})_2(\text{NCBH}_3)_2] \cdot 0.5\text{H}_2\text{O}$ from 50 to 400 K. Cycle was performed by cooling first (down triangles), then heating (up triangles) for three cycles, in 10 K steps, changing temperatures at 2 K min^{-1} , in settle mode.

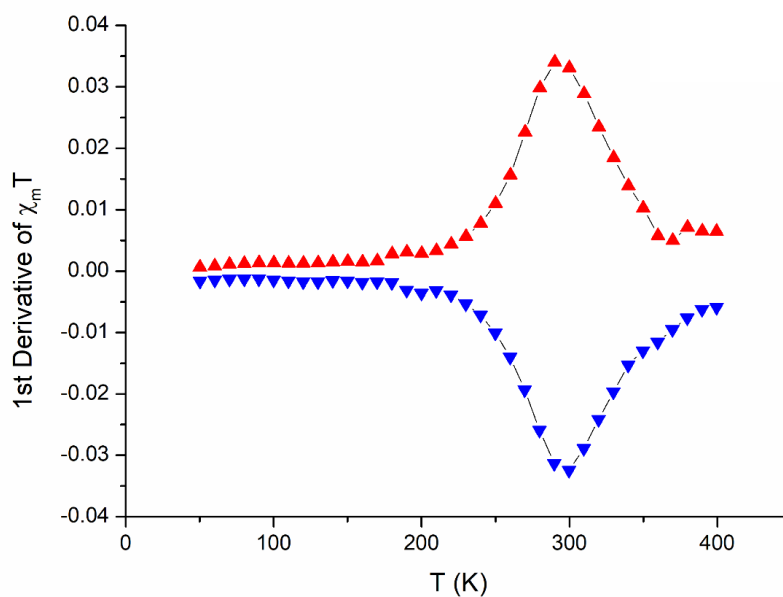


Figure A2.74. First derivative of $\chi_M T$ versus T plot for a solid sample of $[\text{Fe}(\text{L}^{\text{PytMe}})_2(\text{NCBH}_3)_2] \cdot 0.5\text{H}_2\text{O}$ from 50 to 400 K. Cycle was performed by cooling first (down triangles), then heating (up triangles) in 10 K steps, changing temperatures at 2 K min^{-1} , in settle mode.

A2.12. Solution Phase Magnetic Measurements

The complex solutions for this study were prepared by reacting a precisely known mass of $[\text{Fe}^{\text{II}}(\text{pyridine})_4(\text{NCBH}_3)_2]$ in 0.500 mL of CDCl_3 with the corresponding L^{pytz} ligand in a 6:1 L^{pytz} / iron(II) ratio.⁸³ Solution magnetic susceptibility data were obtained from these CDCl_3 solutions using the Evans ¹H-NMR method³⁴⁸ on a Varian500 AR with a 5 mm OneProbe with a variable temperature controller between 243 to 313 K in intervals of 5 K.

A diamagnetic correction for the sample (-0.5×10^{-6}),¹¹⁹ and a correction for the variation of the density of the solvent with temperature,¹²⁰ were applied to each dataset (Table A2.9). The derived parameters, i.e., ΔH , ΔS , and the least squares fittings were obtained by modelling each dataset as a *gradual* and complete *SCO* using the regular solution model (Equation A2.1)^{119, 216-217} with good fits obtained. These were carried out using OriginPro version 9.1.0 from OriginLab Corporation. For all data, a maximum χ_{MT} value ($\chi_{\text{MT}}(\text{MAX})$) of $3.5 \text{ cm}^3 \cdot \text{K} \cdot \text{mol}^{-1}$ was used in Equation A2.1.^{119, 216-217}

Note that the expected error in temperature in an VT-NMR instrument is ± 1 K, and error associated with the Evan's method determination of $\chi_{\text{MT}}(\text{T})$ is 5%, so significant errors are expected in the derived parameters (Table A2.8).⁹²

Excel was also employed, to determine 95% confidence intervals and help assign appropriate errors to the parameters obtained from the fit (Figures A2.83-A2.87). This error analysis in the gradual *SCO* fitting was evaluated using the non-linear regression of the experimental data as reported by Brown and co-workers.³⁴⁹

$$\chi_M T(T) = \frac{\chi_M T(\text{MAX})}{1 + \exp\left(\frac{\Delta H}{RT} - \frac{\Delta S}{R}\right)} \quad (\text{A2.1})$$

$$T_{1/2} = \frac{\Delta H}{\Delta S} \quad (\text{A2.2})$$

A2.12.1. Evans Method VT ^1H -NMR Spectra

Table A2.8. Reported results obtained by fitting points obtained by Evan's method measurement on regular solution SCO phenomenon. First line report values of change in enthalpy (ΔH); in the second line the change in entropy (ΔS) is reported. In the bottom line the correlation factor R^2 for the fitting curves is reported.

	$[\text{Fe}(\text{L}^{\text{pytCF}_3})_2$ (NCBH ₃) ₂]	$[\text{Fe}(\text{L}^{\text{pytBr}})_2$ (NCBH ₃) ₂]	$[\text{Fe}(\text{L}^{\text{pytF}})_2$ (NCBH ₃) ₂]	$[\text{Fe}(\text{L}^{\text{pytMe}})_2$ (NCBH ₃) ₂]
$\Delta H / \text{J mol}^{-1}$	-35806.0±3353.7	-9645.8±292.4	-22095.1±201.6	-20526.4±807.1
$\Delta S / \text{J mol}^{-1}$	-95.7±10.44	-32.8±1.1	-78.7±0.7	-73.7±2.9
$T_{1/2}$	374.1±23.3	293.9±0.2	280.6±3.5	278.5±1.0
R^2	0.96	0.99	0.99	0.99

Table A2.9. Molar magnetic susceptibility ($\chi_{\text{M}}T$ in $\text{cm}^3\cdot\text{K}\cdot\text{mol}^{-1}$) values calculated from ¹H NMR data by Evans method at different temperatures in CDCl₃ solution. Note that all concentrations are based on moles of [Fe(pyridine)₄(NCBH₃)₂], and each solution has a L^{pyz} /iron(II) ratio of 6:1 equivalents (see Section A2.11). Evans method has a relative error of 5%,⁹² therefore significant errors associated with the data fitting discussed (Figures A2.83-A2.86). Second column from the left reports the viscosity of CDCl₃ solvent at in the range of temperatures employed for the ¹H NMR measurements.

T	η	$\chi_{\text{M}}T$ ($\text{cm}^3\cdot\text{K}\cdot\text{mol}^{-1}$)			
		CF ₃	Br	F	Me
313	1451.73	0.41658		2.89185	2.82624
308	1461.09	0.29182	2.34856	2.77622	2.75084
303	1470.35	0.2342	2.29631	2.66389	2.66911
298	1479.52	0.19241	2.24484	2.55476	2.59229
293	1488.6	0.14416	2.23836	2.38442	2.46143
288	1497.6	0.12363	2.14607	2.23578	2.36266
283	1506.51	0.08985	2.0756	2.09228	2.20489
278	1515.35	0.06519	1.99741	1.93878	1.99378
273	1524.1	0.06402	1.90116	1.76164	1.85119
268	1532.78	0.06285	1.8043	1.5628	1.65362
263	1541.39	0.06167	1.70355	1.44317	1.4549
258	1549.93	0.0605	1.59594	1.24642	1.25553
253	1558.4		1.49046	1.08198	
248	1566.8		1.40171		
243	1575.14		1.34283		

VT ^1H -NMR of $\text{Fe}^{\text{II}}(\text{L}^{\text{pytCF}_3})_2(\text{NCBH}_3)_2$

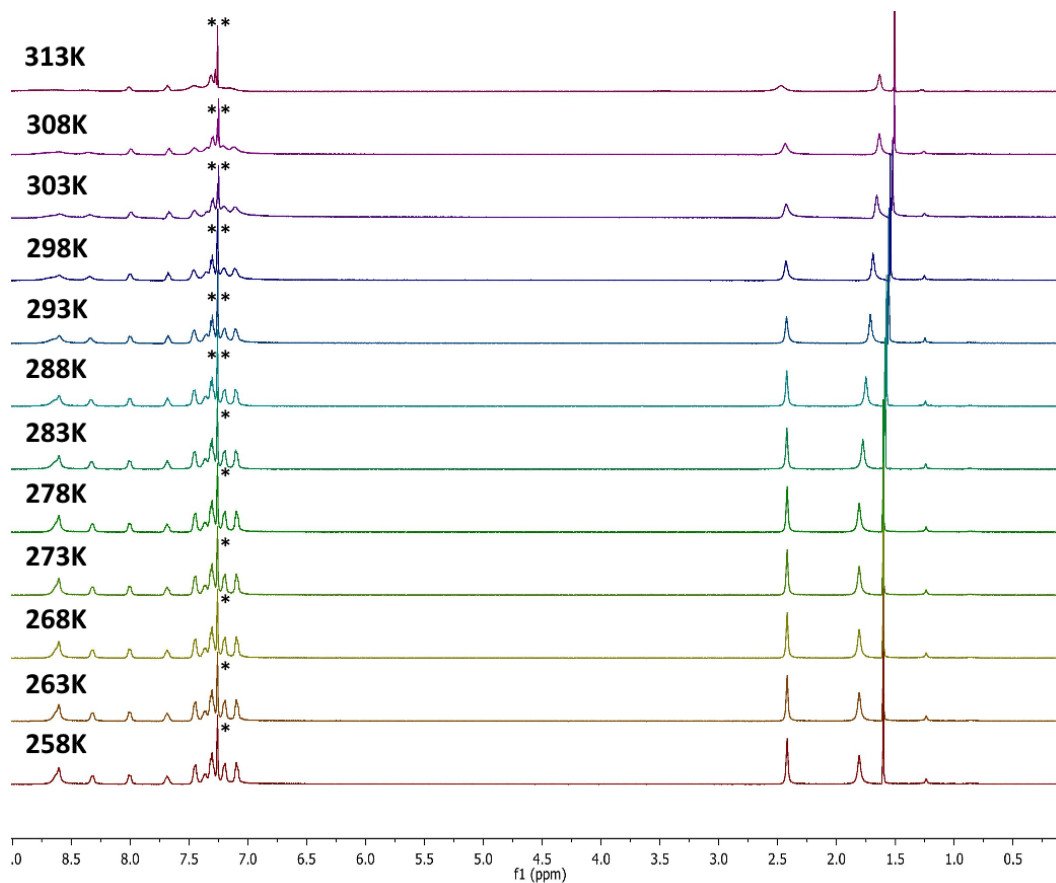


Figure A2.79. Stacked spectra, obtained by the Evans ^1H NMR method, from 258 to 313 K for complex $[\text{Fe}^{\text{II}}(\text{L}^{\text{pytCF}_3})_2(\text{NCBH}_3)_2]$. Note that the solution was prepared using 6 equivalents of $\text{L}^{\text{pytCF}_3}$ ligand per equivalents of $\text{Fe}(\text{II})$.

VT ^1H -NMR of $\text{Fe}^{\text{II}}(\text{L}^{\text{pytBr}})_2(\text{NCBH}_3)_2$

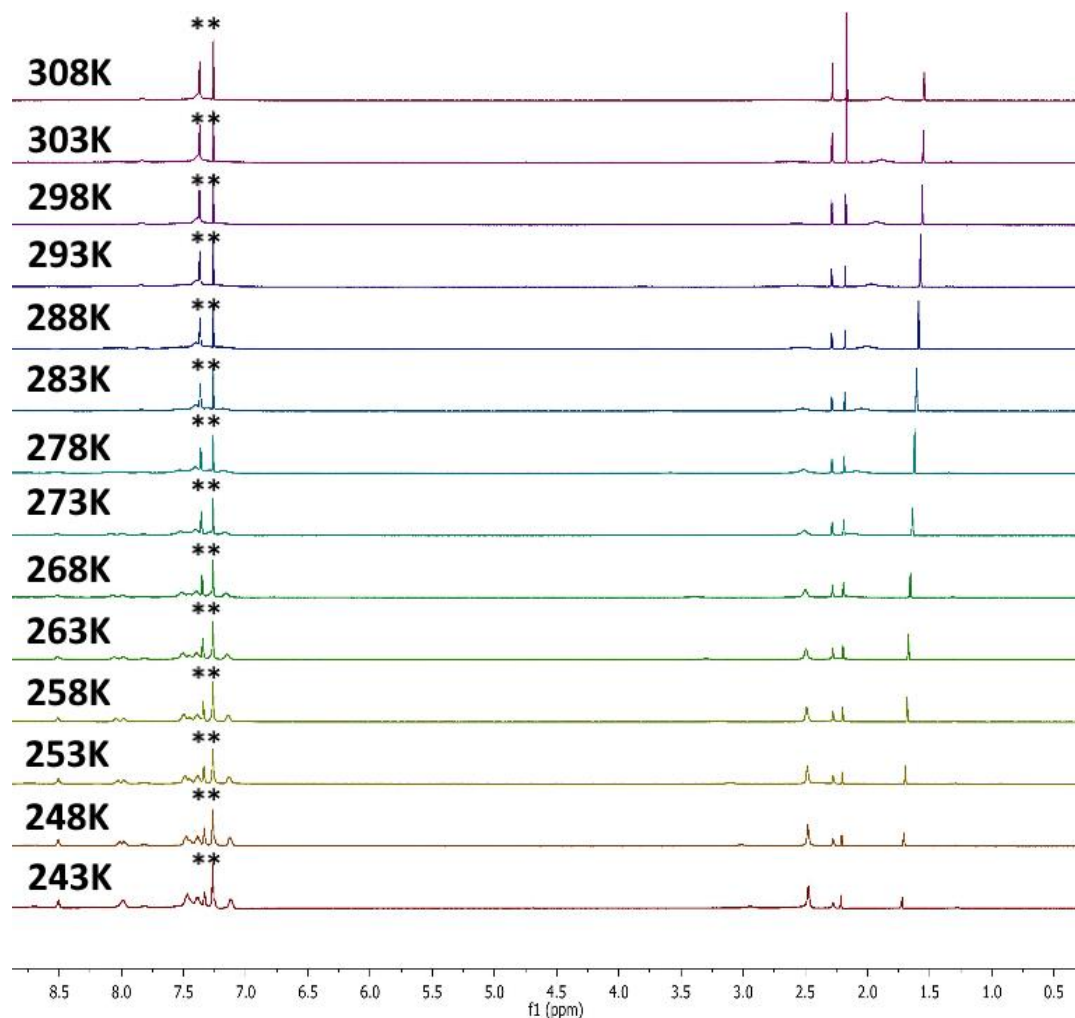


Figure A2.80. Stacked spectra, obtained by the Evans ^1H NMR method, from 243 K to 308 K for complex $[\text{Fe}^{\text{II}}(\text{L}^{\text{pytBr}})_2(\text{NCBH}_3)_2]$. Note that the solution was prepared using 6 equivalents of L^{pytBr} ligand per equivalents of $\text{Fe}(\text{II})$.

VT ^1H -NMR of $\text{Fe}^{\text{II}}(\text{L}^{\text{pytF}})_2(\text{NCBH}_3)_2$

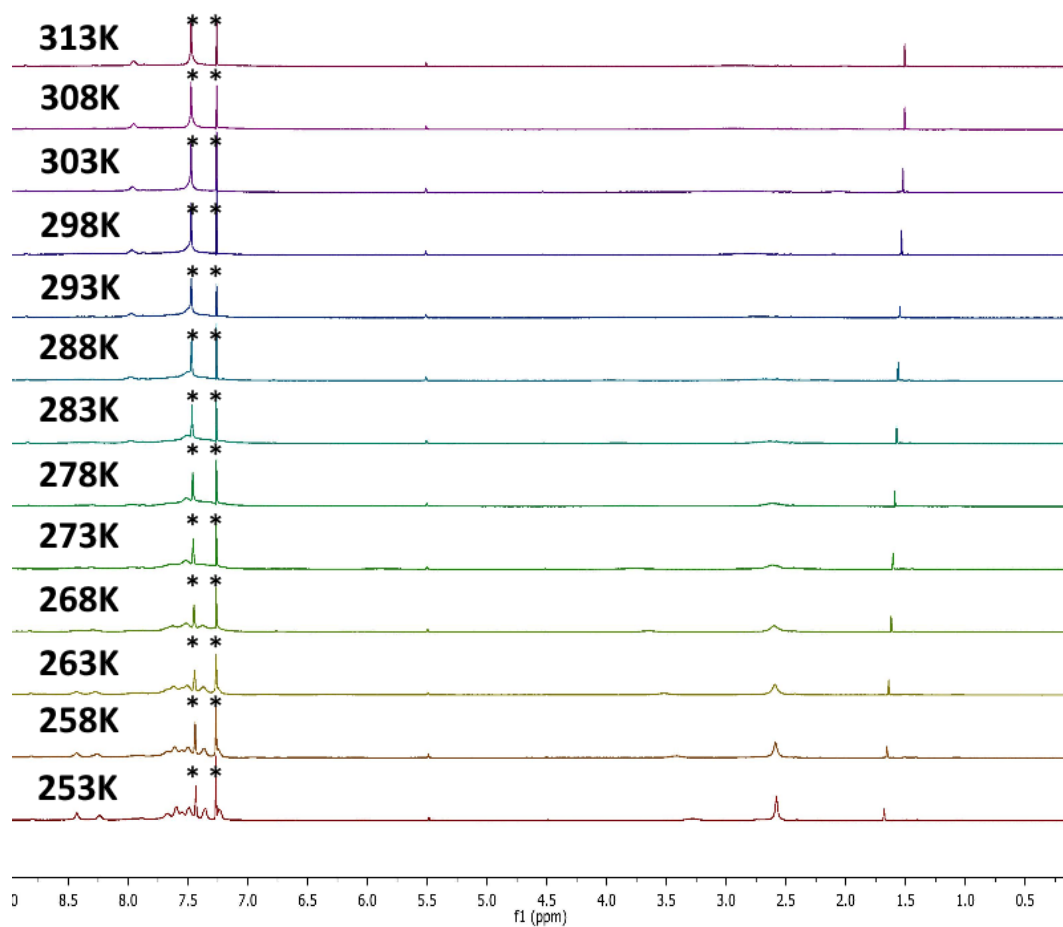


Figure A2.81. Stacked spectra, obtained by the Evans ^1H NMR method, from 253 K to 313 K for complex $[\text{Fe}^{\text{II}}(\text{L}^{\text{pytF}})_2(\text{NCBH}_3)_2]$. Note that the solution was prepared using 6 equivalents of L^{pytF} ligand per equivalents of $\text{Fe}(\text{II})$.

VT ^1H -NMR of $\text{Fe}^{\text{II}}(\text{L}^{\text{pytMe}})_2(\text{NCBH}_3)_2$

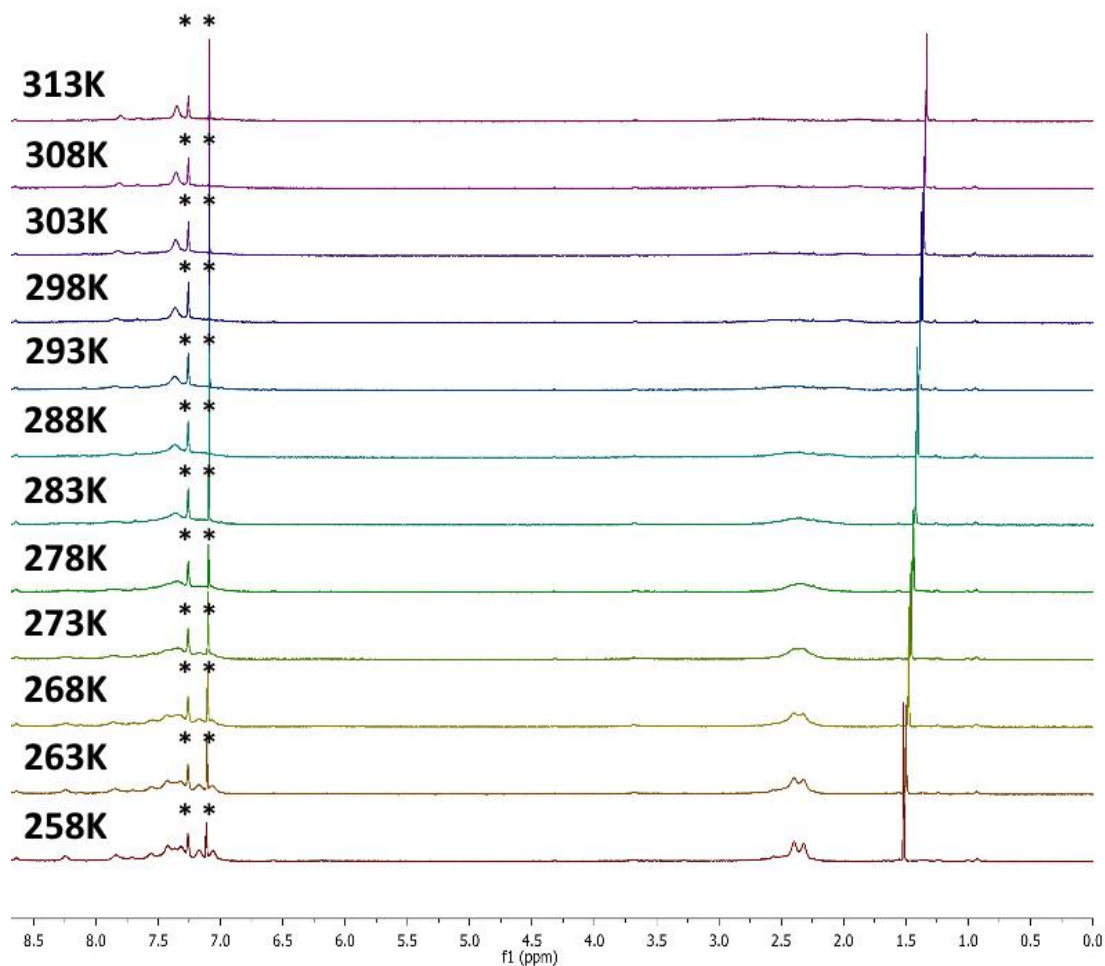


Figure A2.82. Stacked spectra, obtained by the Evans ^1H NMR method, from 258 K to 313 K for complex $[\text{Fe}^{\text{II}}(\text{L}^{\text{pytMe}})_2(\text{NCBH}_3)_2]$. Note that the solution was prepared using 6 equivalents of L^{pytMe} ligand per equivalents of $\text{Fe}(\text{II})$.

A2.12.2. Evans Method: Error Analysis

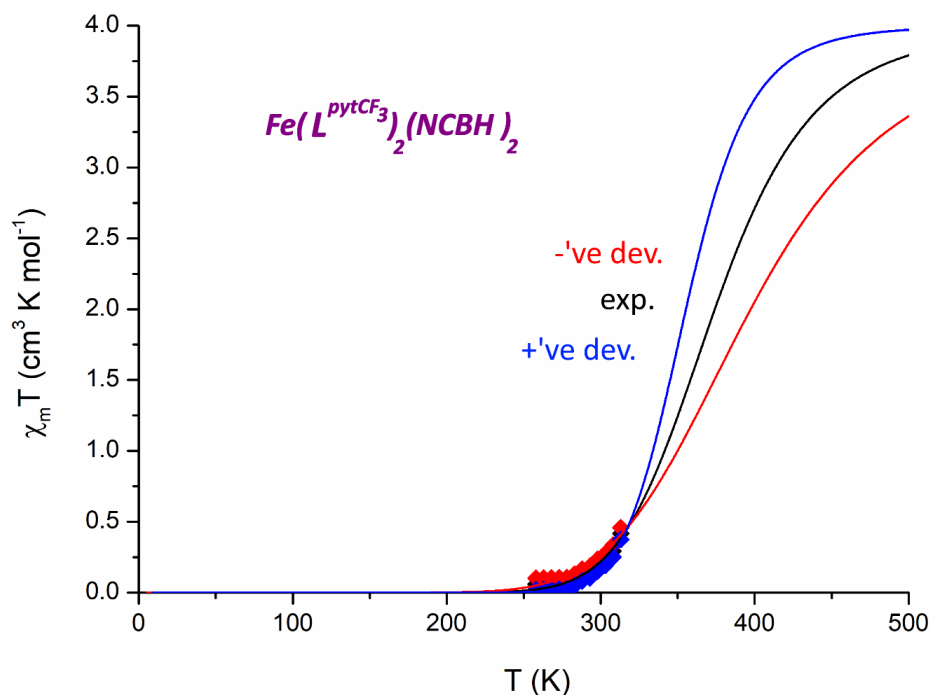


Figure A2.83. $\chi_{\text{m}}T$ vs T for $[\text{Fe}^{\text{II}}(\text{L}^{\text{pytCF}_3})_2(\text{NCBH}_3)_2]$ in CDCl_3 solution from Evans NMR method studies (500 MHz); this graph displays the experimental data points (black squares), and the 95% confidence intervals (red and blue) around the fit.

Table A2.10. Derived parameters obtained by fitting of regular SCO transition (Equation A2.1) in $\chi_{\text{m}}T$ vs T for $[\text{Fe}^{\text{II}}(\text{L}^{\text{pytCF}_3})_2(\text{NCBH}_3)_2]$ in CDCl_3 solution from Evans NMR method studies (500 MHz) reported in Figure A2.83. Energies are reported in J mol^{-1} .

	+ 've deviation	experimental	- 've deviation
ΔH	-26729.9±3019.4	-35806.0±3353.6	-50453.9±2938.4
ΔS	-67.3±9.6	-95.7±10.4	-142.0±8.8
T	397.4	374.1	355.3
R^2	0.92	0.96	0.99

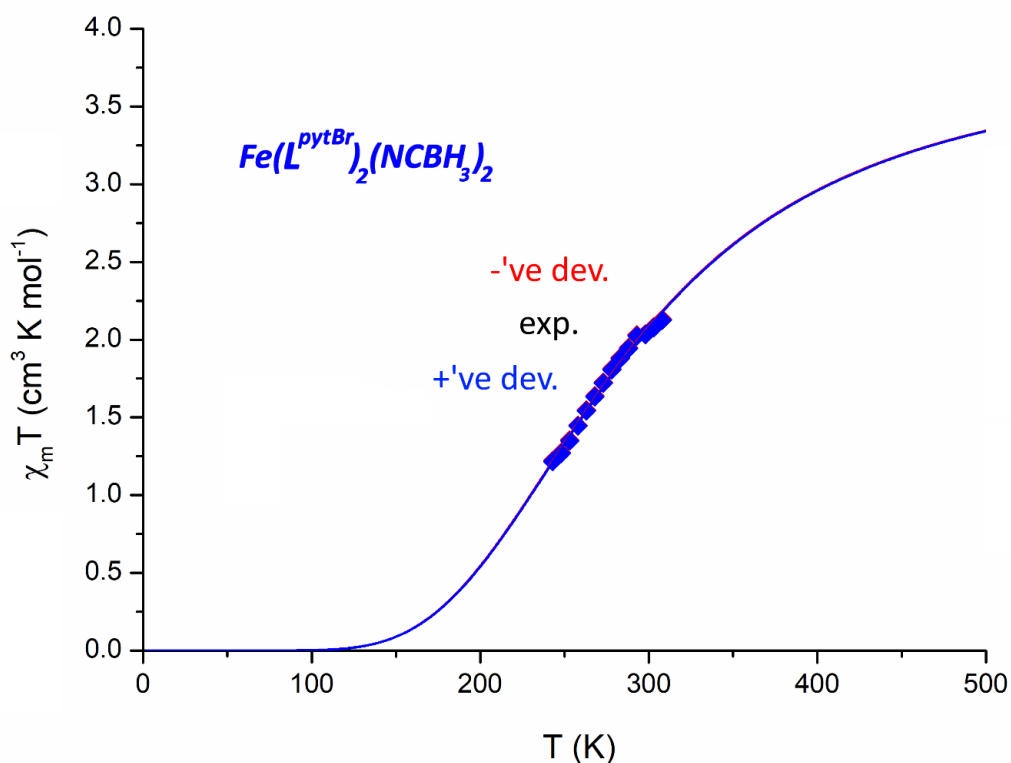


Figure A2.84. $\chi_{\text{m}}T$ vs T for $[\text{Fe}^{\text{II}}(\text{L}^{\text{pytBr}})_2(\text{NCBH}_3)_2]$ in CDCl_3 solution from Evans NMR method studies (500 MHz); this graph displays the experimental data points (black squares), and the 95% confidence intervals (red and blue) around the fit.

Table A2.11. Derived parameters obtained by fitting of regular SCO transition (Equation A2.1) in $\chi_{\text{m}}T$ vs T for $[\text{Fe}^{\text{II}}(\text{L}^{\text{pytBr}})_2(\text{NCBH}_3)_2]$ in CDCl_3 solution from Evans NMR method studies (500 MHz) reported in Figure A2.84. Energies are reported in J mol^{-1} .

	+ve deviation	experimental	-ve deviation
ΔH	-9641.2±291.7	-9645.8±292.4	-9650.4±293.1
ΔS	-32.8±1.1	-32.8±1.1	-32.8±1.1
T	293.7	293.9	294.1
R^2	0.99	0.99	0.99

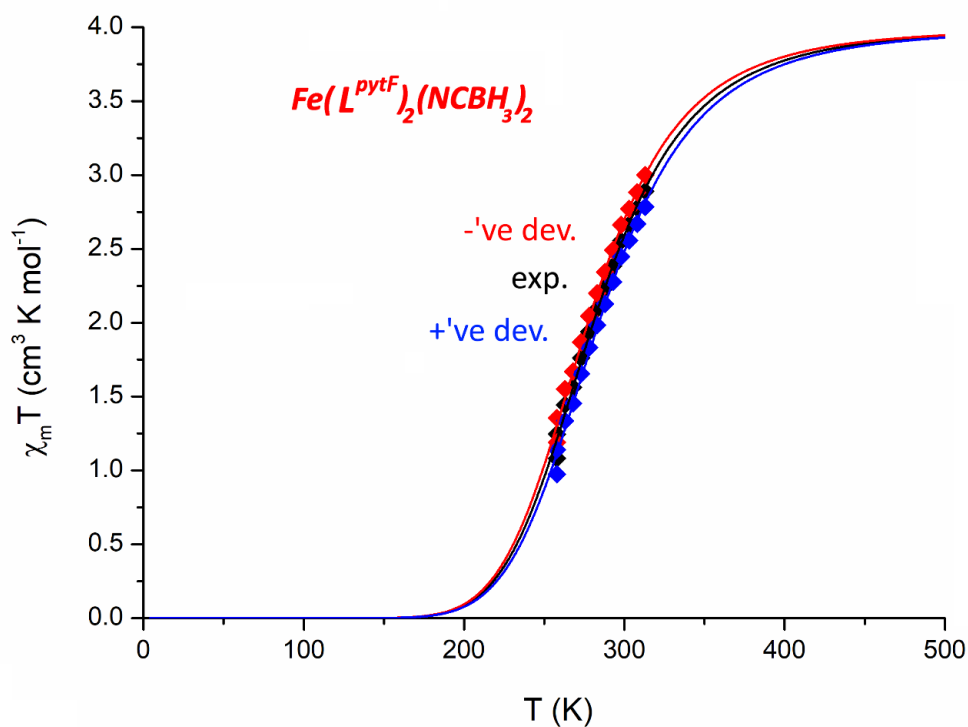


Figure A2.85. χ_{mT} vs T for $[\text{Fe}^{\text{II}}(\text{L}^{\text{pytF}})_2(\text{NCBH}_3)_2]$ in CDCl_3 solution from Evans NMR method studies (500 MHz); this graph displays the experimental data points (black squares), and the 95% confidence intervals (red and blue) around the fit.

Table A2.12. Derived parameters obtained by fitting of regular SCO transition (Equation A2.1) in χ_{mT} vs T for $[\text{Fe}^{\text{II}}(\text{L}^{\text{pytF}})_2(\text{NCBH}_3)_2]$ in CDCl_3 solution from Evans NMR method studies (500 MHz) reported in Figure A2.85. Energies are reported in J mol^{-1} .

	+ve deviation	experimental	-ve deviation
ΔH	-22221.9 ± 671.8	-22095.1 ± 705.9	-22089.0 ± 764.8
ΔS	-80.2 ± 2.4	-78.7 ± 2.5	-77.7 ± 2.7
T	277.3	280.6	284.1
R^2	0.99	0.99	0.99

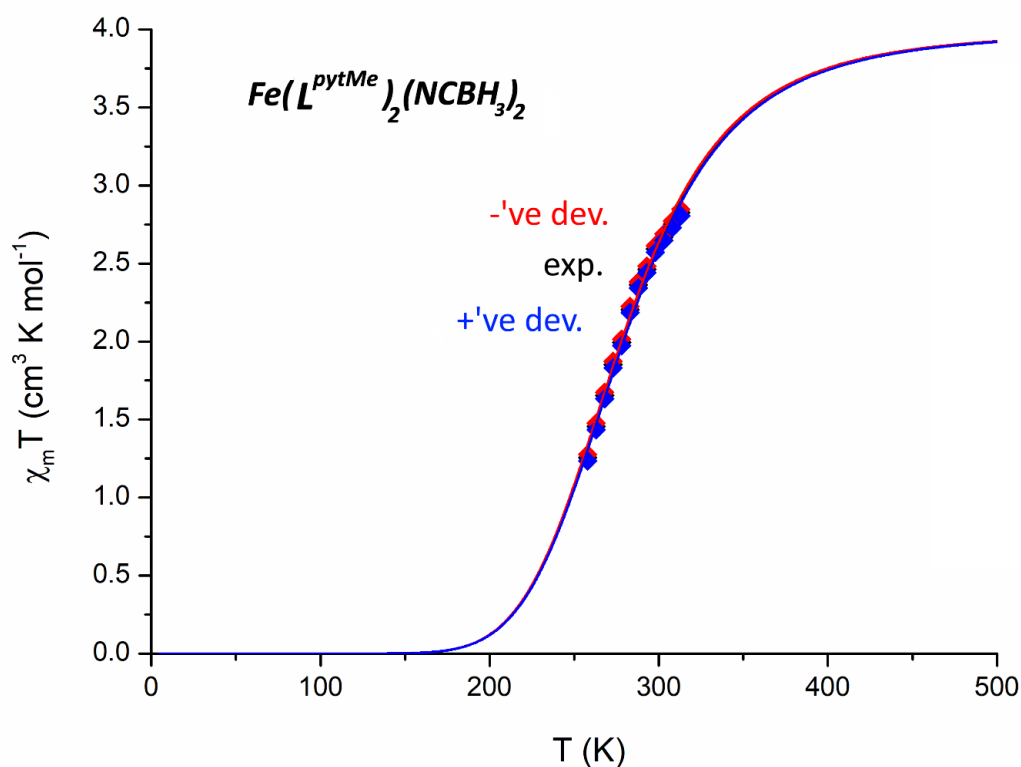


Figure A2.86. $X_M T$ vs T for $[Fe^{II}(L^{pytMe})_2(NCBH_3)_2]$ in $CDCl_3$ solution from Evans NMR method studies (500 MHz); this graph displays the experimental data points (black squares), and the 95% confidence intervals (red and blue) around the fit.

Table A2.13. Derived parameters obtained by fitting of regular SCO transition (Equation A2.1) in $X_M T$ vs T for $[Fe^{II}(L^{pytMe})_2(NCBH_3)_2]$ in $CDCl_3$ solution from Evans NMR method studies (500 MHz) reported in Figure A2.86. Energies are reported in J mol^{-1} .

	+ve deviation	experimental	-ve deviation
ΔH	-20571.0 \pm 789.4	-20526.4 \pm 807.2	-20488.6 \pm 825.2
ΔS	-74.1 \pm 2.9	-73.7 \pm 2.9	-73.4 \pm 2.9
T	277.8	278.5	279.2
R^2	0.99	0.99	0.99

A2.13. UV-Vis Spectra of $[\text{Fe}(\text{L}^{\text{pytZ}})_2(\text{NCBH}_3)_2]$

UV-Vis studies for all the complexes were carried out in chloroform (Figure A2.87). The concentration of samples was 0.04 mM. $[\text{Fe}(\text{L}^{\text{pytF}})_2(\text{NCBH}_3)_2]$ shows λ_{max} at 411 and 506 nm; $[\text{Fe}(\text{L}^{\text{pytCF}_3})_2(\text{NCBH}_3)_2]$ shows λ_{max} at 520 and 566 nm; $[\text{Fe}(\text{L}^{\text{pytBr}})_2(\text{NCBH}_3)_2]$ shows λ_{max} at 495 and 531 nm; $[\text{Fe}(\text{L}^{\text{pytMe}})_2(\text{NCBH}_3)_2]$ shows λ_{max} at 450 and 500 nm. The all four other $[\text{Fe}(\text{L}^{\text{pytZ}})_2(\text{NCBH}_3)_2]$ shows an extinction coefficient between 1500 and 2500 $\text{M}^{-1}\text{cm}^{-1}$ for the higher energy transition and between 2000 and 6000 $\text{M}^{-1}\text{cm}^{-1}$ for the lower energy transition. For all complexes, bands observed in the visible region, originate from charge transfer (CT), with large value of molar extinction coefficient.

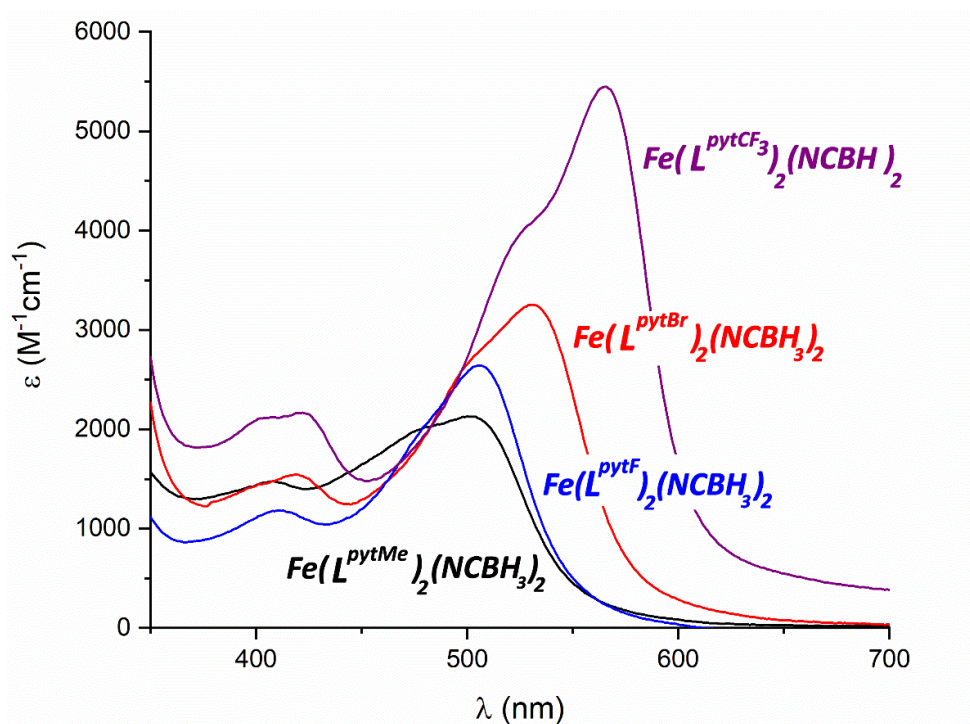


Figure A2.87. UV-visible spectra (700nm to 350 nm) collected using a 1:6 ratio of $[\text{Fe}(\text{pyridine})_4(\text{NCBH}_3)_2] : \text{L}^{\text{pytZ}}$, with $[\text{Fe}] = 0.5 \text{ mM}$.

A2.14. Computational Details

A2.14.1. Ligand Structures

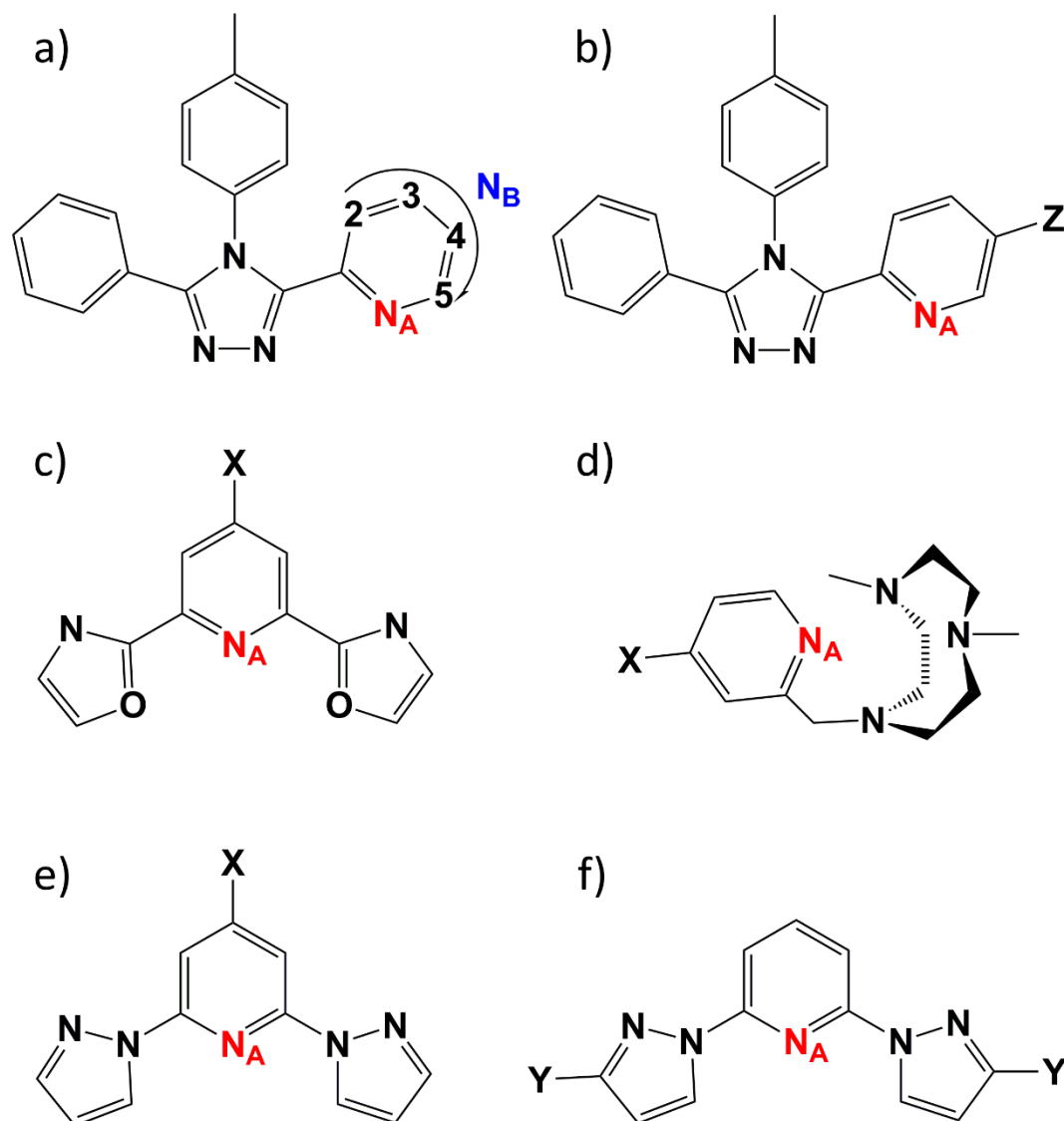


Figure A2.88. Five families of ligands focussed on in this study. (a) five of L^{azine} ; (b) five of L^{pytz} ; (c) twelve of $pybox^X$; (d) seven of $pytacn^X$; (e) eleven of bpp^X ; (f) four of bpp^Y .

A2.14.2. Calculated N_A -NMR Chemical Shifts

Table A2.14. Summary table reporting comparison between Brooker et al. previous study (central column) and the one applied in this study. Deviation to experimental ^{15}N NMR chemical shift is also reported for both the computational protocols.

	Measured ^{15}N -NMR	B3LYP/ 6-31G(d) CPCM(CHCl_3)		TPSS/pcSseg-2-aug-cc-pVTZ/ RIJCOSX/D3BJ/CPCM(CH_3Cl)		$T_{1/2}$ (K)
		^{15}N NMR	Err%	^{15}N NMR	Err%	
<i>L</i> ⁴ pyrimidine	288	269	6.6%	286	0.7%	232 ⁸³
<i>L</i> ² pyrimidine	290	282	2.8%	291	0.3%	242 ⁸³
<i>L</i> ^{pytH}	311	300	3.9%	308	1.0%	288 ⁸³
<i>L</i> ^{pyrazine}	334	315	5.7%	321	3.9%	315 ⁸³
<i>L</i> ^{pyridazine}	398	402	1.0%	401	0.8%	455 ⁸³

Table A2.15. Reported values of the N_A chemical shift for the new four L^{pytZ} ligands obtained by calculation using improved protocol (TPSS/pcSseg-2/aug-cc-pVTZ/ RIJCOSX/D3BJ/CPCM(CHCl_3)) and by experimental measurement (d = direct method, i = indirect method), to the respective $[\text{Fe}(L^{pytZ})(\text{NCBH}_3)_2]$ complex.

	Solvent	δN_A	δN_A	Err%	$T_{1/2}$
		(ppm) Measured	(ppm) Calculated		
L^{pytMe}	CDCl_3	312 (d)	310	0.6%	279
L^{pytF}	CDCl_3	319 (i)	315	1.3%	281
L^{pytBr}	CDCl_3	318 (d/i)	312	1.6%	294
L^{pytCF_3}	CDCl_3	314 (d)	307	2.2%	374

Table A2.16. Results calculated δN_A (ppm) for the twelve $pybox^X$ family calculated using the TPSS/pcSseg-2/aug-cc-pVTZ/ RIJCOSX/D3BJ/CPCM(Acetone) computational protocol.

	Solvent	δN_A (ppm)	$T_{1/2}$
$pybox-X-4Py$	$\text{CO}(\text{CD}_3)_2$	277	310 ²²
$pybox-X-3Py$	$\text{CO}(\text{CD}_3)_2$	273	270 ²²
$pybox-X-2Th$	$\text{CO}(\text{CD}_3)_2$	269	260 ²²
$pybox-X-3Th$	$\text{CO}(\text{CD}_3)_2$	269	240 ²²
$pybox-X-Cl$	$\text{CO}(\text{CD}_3)_2$	274	270 ²²
$pybox-X-Br$	$\text{CO}(\text{CD}_3)_2$	272	280 ²²
$pybox-X-H$	$\text{CO}(\text{CD}_3)_2$	279	260 ²²
$pybox-X-OMe$	$\text{CO}(\text{CD}_3)_2$	258	170 ²²
$pybox-X-Ph$	$\text{CO}(\text{CD}_3)_2$	272	240 ²²
$pybox-X-SMe$	$\text{CO}(\text{CD}_3)_2$	261	210 ²²
$pybox-X-N_3$	$\text{CO}(\text{CD}_3)_2$	268	215 ²²
$pybox-X-Me$	$\text{CO}(\text{CD}_3)_2$	271	220 ²²

Table A2.17. Results calculated δN_A (ppm) for the seven *pytacn*^x family calculated using the TPSS/pcSseg-2/aug-cc-pVTZ/ RIJCOSX/D3BJ/CPCM(Acetonitrile) computational protocol.

Name	Solvent	δN_A (ppm)	μ_{eff}
<i>Pytacn-X-NO₂</i>	CD ₃ CN	320	0.00 ²⁴
<i>Pytacn-X-CO₂Et</i>	CD ₃ CN	303	0.78 ²⁴
<i>Pytacn-X-Me</i>	CD ₃ CN	281	1.24 ²⁴
<i>Pytacn-X-H</i>	CD ₃ CN	291	1.26 ²⁴
<i>Pytacn-X-Cl</i>	CD ₃ CN	284	1.71 ²⁴
<i>Pytacn-X-OMe</i>	CD ₃ CN	267	2.09 ²⁴
<i>Pytacn-X-NMe₂</i>	CD ₃ CN	249	2.62 ²⁴

Table A2.18. Results calculated δN_A (ppm) for the fourteen **bpp**^{X,Y} family calculated using the TPSS/pcSseg-2/aug-cc-pVTZ/ RIJCOSX/D3BJ/CPCM(CH₃Cl) computational protocol.

	Solvent	δN_A (ppm)	$T_{1/2}$
bpp-X-H	CO(CD ₃) ₂	235 ¹⁸⁹	248
bpp-X-Br	CO(CD ₃) ₂	23 ²³	234
bpp-X-CCPh-CN	CO(CD ₃) ₂	23 ²³	259
bpp-X-CCPh	CO(CD ₃) ₂	230 ²³	245
bpp-X-CCPh-NO₂	CO(CD ₃) ₂	232 ²³	261
bpp-X-Cl	CO(CD ₃) ₂	230 ²³	226
bpp-X-CO₂H	CO(CD ₃) ₂	244 ²³	281
bpp-X-OH	CO(CD ₃) ₂	217 ²³	164
bpp-X-OMe	CO(CD ₃) ₂	216 ²³	158
bpp-X-SMe	CO(CD ₃) ₂	222 ³⁵⁰	194
bpp-X-SOMe	CO(CD ₃) ₂	235 ³⁵⁰	284
Bpp-Y-H	CO(CD ₃) ₂	235 ²³	248
bpp-Y-CO₂Et	CO(CD ₃) ₂	240 ²³	246
bpp-Y-tBu	CO(CD ₃) ₂	239 ²³	251
bpp-Y-CH₂OH	CO(CD ₃) ₂	236 ²³	259

A2.15. Correlations

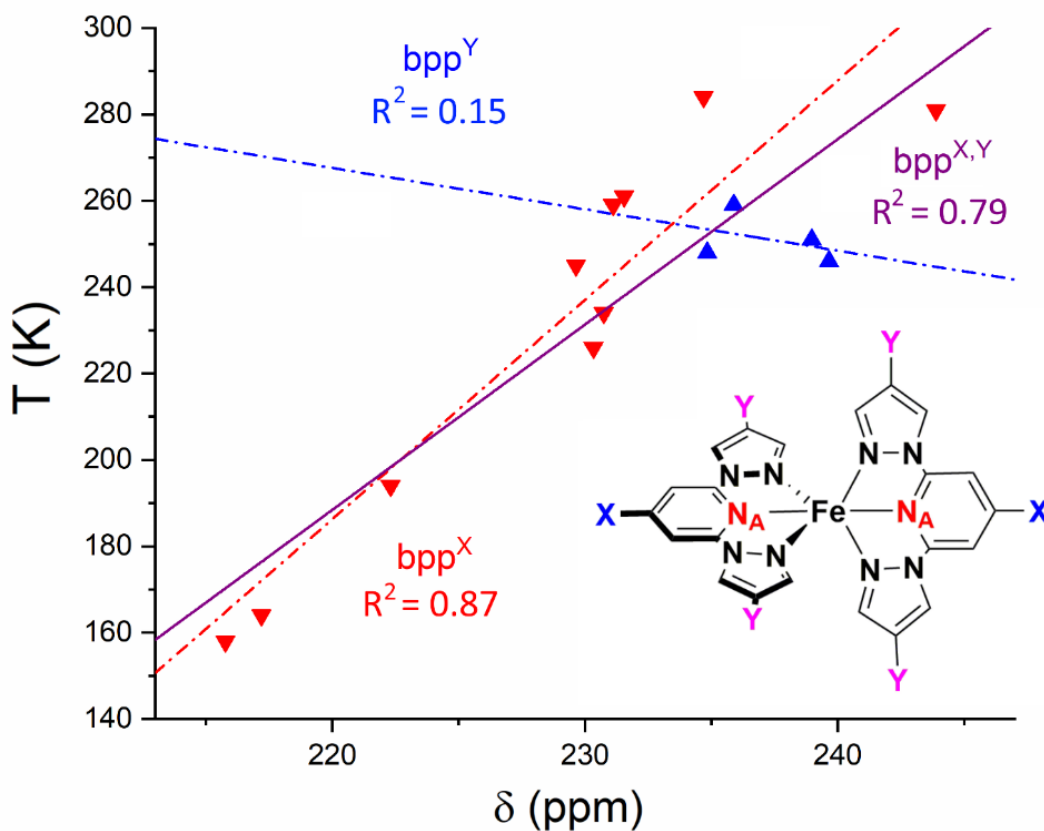


Figure A2.89. Correlations between the $T_{1/2}$ of the $[\text{Fe}^{\text{II}}(\text{bpp}^{\text{X,Y}})_2]^{2+}$ complexes and the measured δN_A chemical shift for the corresponding tridentate ligand $\text{bpp}^{\text{X,Y}}$. Correlation lines are shown for: (purple) for all fourteen compounds with no distinction made between X and Y substituents ($R^2 = 0.80$; $T_{1/2} = 4.29 \cdot \delta\text{N}_A - 756.29$); and then taking in account only the (blue; $T_{1/2} = -0.96 \cdot \delta\text{N}_A - 478.37$) four Y-substituted ($R^2 = 0.15$) and the (red; $T_{1/2} = 5.23 \cdot \delta\text{N}_A - 1169.24$) eleven X-substituted ($R^2 = 0.87$) compounds.

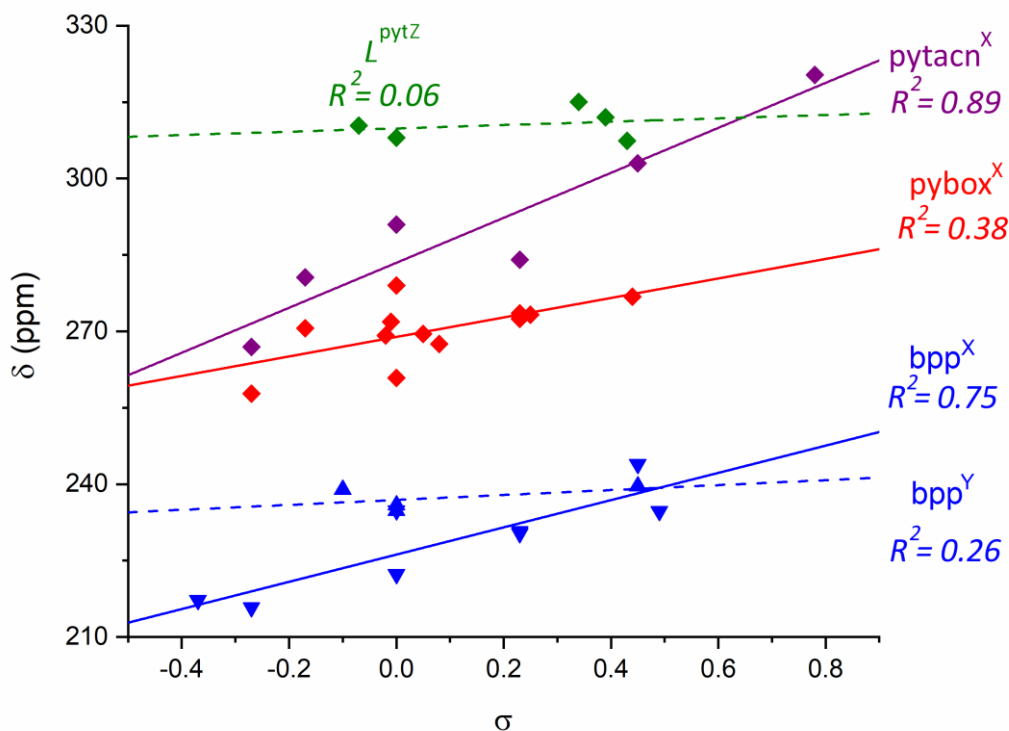


Figure A2.90. Correlation between the calculated ^{15}N chemical shift δN_A of the free ligand for each of the families reported in this study against the relative value of the Hammett parameter σ^+ of the substituent on the pyridine ring (note: a substituent with a positive Hammett parameter is **EWG**, whilst one with a negative value is **EDG**; H is by definition 0). Solid lines for ligands with para substituents (σ_p is used in this case); dashed lines for ligands with meta substituents (σ_m is used in this case). Good correlation found for a family of eleven bpp^x ligands ($\delta\text{N}_A = 26.73 \cdot \sigma - 226.18$) and seven pytacn^x ligands ($\delta\text{N}_A = 44.13 \cdot \sigma - 283.46$); poor correlation found for four bpp^y ligands ($\delta\text{N}_A = 4.85 \cdot \sigma - 236.91$); twelve pybox^x ($\delta\text{N}_A = 19.13 \cdot \sigma - 268.90$) and five L^{pyt^z} ($\delta\text{N}_A = 3.28 \cdot \sigma - 309.84$).

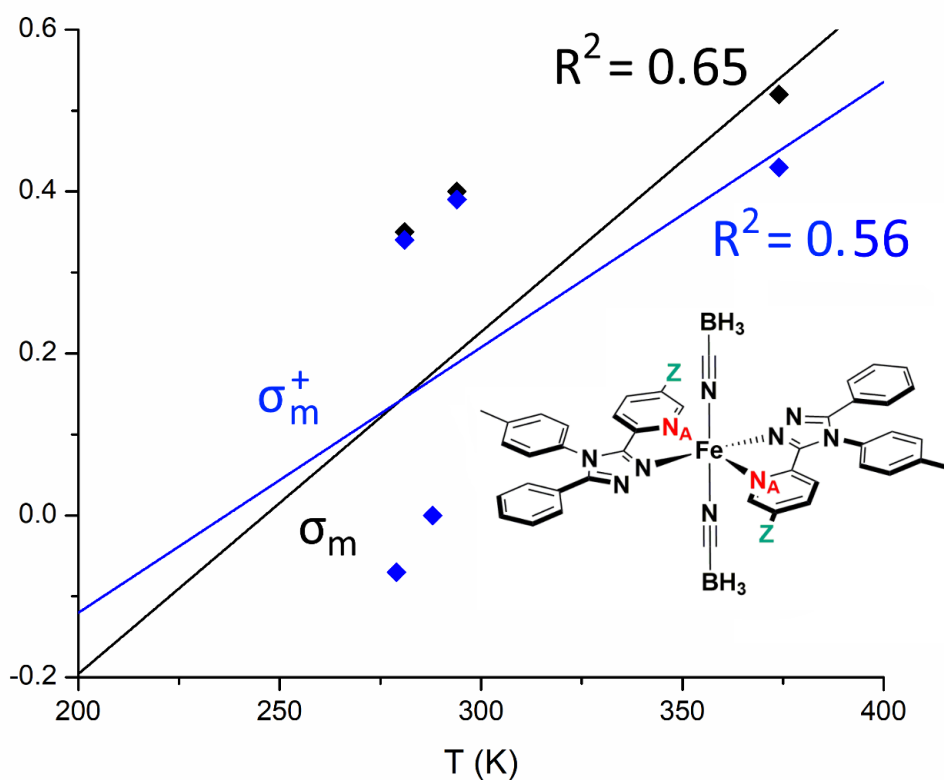


Figure A2.91. Reported correlation between the measured $T_{1/2}$ for the new family of L^{pytZ} versus the relative value of Hammett parameter σ_m (blue dots, $R^2 = 0.22$, $\sigma_m = 0.003 \cdot T_{1/2} - 0.78$) and the Hammett parameter σ_m^+ (black dots, $R^2 = 0.32$, $\sigma_m^+ = 0.004 \cdot T_{1/2} - 1.04$).

**A3 | Quantitative Evaluation of
the Nature of M-L Bonds in
Paramagnetic Compounds:
Application of *EDA-NOCV*
Theory to Spin Crossover
Complexes**

A3.1. Geometry Optimisation Protocol

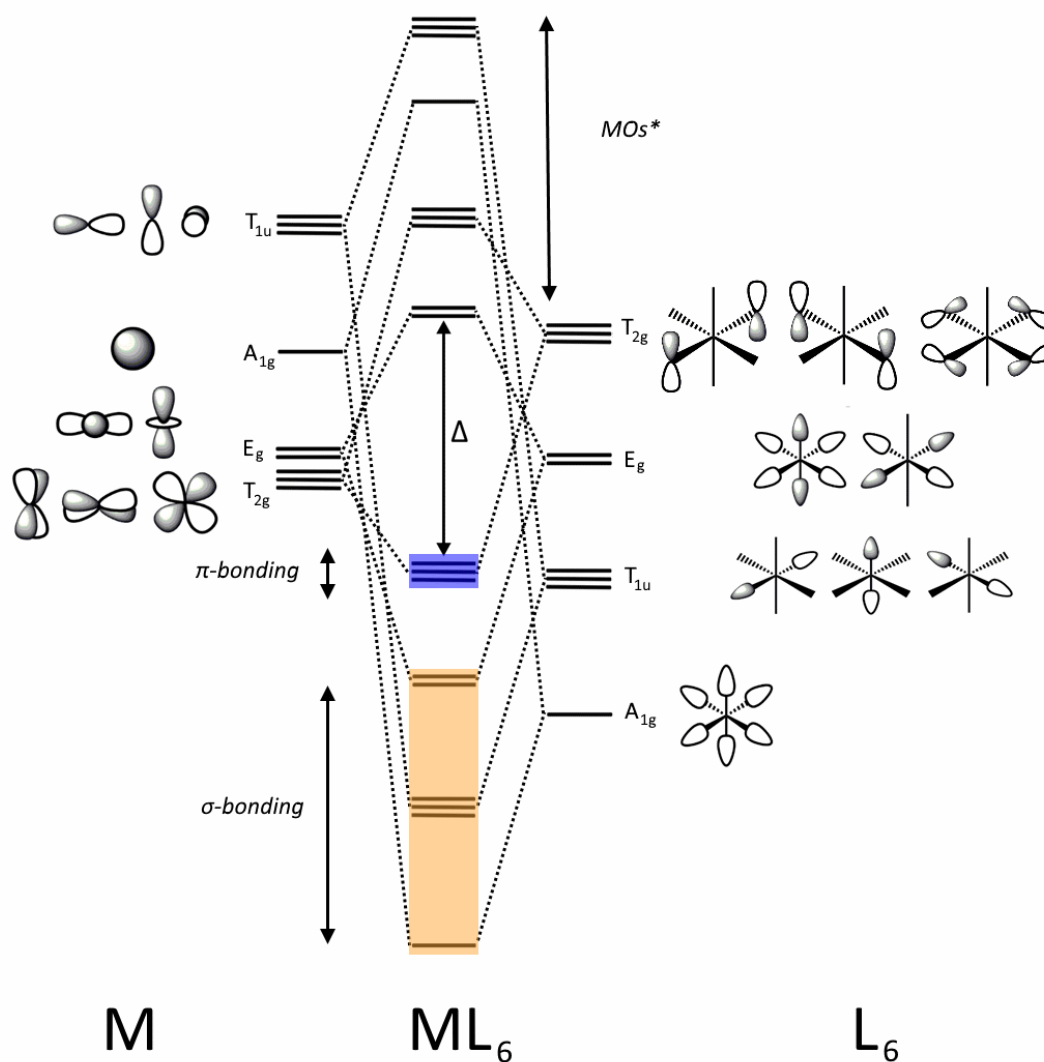


Figure A3.1. Classic qualitative representation of the ladder of σ - and π -MO energies (centre) for a perfect octahedral (O_h symmetry) ML_6 complex which results from overlap of the valence AOs of M (left) with the L_6 MOs of the same symmetry (right). For the sake of readability: on the left the M AO's are shown as already split into E_g and T_{2g} (but should be degenerate), and on the right the six L_6 symmetry adapted linear combinations (SALCs) forming the σ -bonds with M are not shown as energetically degenerate (but should be).

As a first step, accurate structures for these complexes in both the low-spin (*LS*) and high-spin (*HS*) states are required, so density functional theory (*DFT*) calculations were performed, with the ORCA 4.1 software package,²⁵⁸ to determine the optimal computational setup required to obtain these (Table A3.1, Figure 3.2).¹⁰⁵ Four different functionals (B3LYP, BP86, revPBE, RPBE)¹⁵⁹ were tested, as well as the possible inclusion of dispersion effects, *via* a D3 dispersion correction including Becke-Johnson damping (BJ),³¹⁵ and of solvent effects (CHCl₃), by using the conductor-like polarizable continuum model (CPCM).²⁶⁵ To determine the best combination of these, the optimised structures obtained were compared to the single-crystal X-ray structure data available for [Fe^{II}(*L*pyridine)₂(NCBH₃)₂] in both the *LS* and *HS* states,¹⁰⁵ with particular attention given to three key parameters: Fe-N distance, Fe-N≡C(BH₃) angle and the root-mean-square-deviation (RMSD) of all coordinates (Table A3.2). Deviations from the experimentally observed linear Fe-N≡C(BH₃) were observed for most of the tested combinations, especially when the complex was in the paramagnetic *HS* state (see Table A3.2 and Figures A3.2-A3.9). The best combination was determined to be BP86-D3(BJ)/def2-TZVPP+CPCM(CHCl₃).^{263, 341} i.e. use of a BP86 functional, with D3 dispersion correction (including BJ damping), def2-TZVPP basis set,²⁶¹⁻²⁶² and the solvent modelled by CPCM. This protocol was therefore the one used to provide all of the optimised structures used as the start point for the subsequent *EDA-NOCV* analyses performed using ADF package²⁶⁹ (Tables A3.1-A3.3).

Table A3.1. Summary of the combinations of computational features used to determine the best computational set up for the geometry optimisation using ORCA code, with the best combination highlighted.

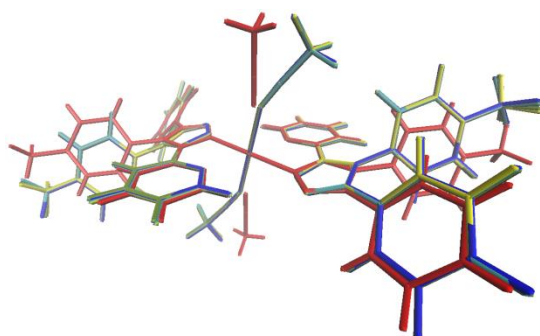
Name	DFT Functional				Basis Set	Dispersion Model	CPCM Solvent
	B3LYP	BP86	revPBE	RPBE			
T.B3	X				X		
T.B3.D	X				X	X	
T.B3.D.s	X				X	X	X
T.BP		X			X		
T.BP.D		X			X	X	
T.BP.s		X			X		X
T.BP.D.s		X			X	X	X
T.RV			X		X		
T.RV.D			X		X	X	
T.RV.s			X		X		X
T.RV.D.s			X		X	X	X
T.RP				X	X		
T.RP.D				X	X	X	
T.RP.s				X	X		X
T.RP.D.s				X	X	X	X

Table A3.2. RMSD values (Å) and Fe-NCBH₃ Axial Angle – referred to crystal structure of both candidates – of the final optimised structures of [Fe(L_{pyridine})₂(NCBH₃)₂] in both the HS and LS states, with the method of choice highlighted in blue.

Name	HS		LS	
	RMSD	Fe-NC(BH ₃) Angle	RMSD	Fe-(NCBH ₃) Angle
REF	-	175.44	-	177.61
T.B3	0.1867	156.6	0.2187	166.98
T.B3.D	0.1876	156.8	0.2976	153.37
T.B3.s	0.1807	155.6	0.2357	171.45
T.B3.D.s	0.1827	155.7	0.2491	169.44
T.BP	0.3970	156.72	0.2959	174.39
T.BP.D	0.3218	149.39	0.4893	179.07
T.BP.s	0.1978	177.50	0.2457	153.41
T.BP.D.s	0.2142	178.97	0.2602	177.99
T.RV	0.3977	158.54	0.3615	169.13
T.RV.D	0.3254	141.00	0.4893	154.35
T.RV.s	0.2019	177.71	0.2374	179.24
T.RV.D.s	0.3371	152.84	0.2477	177.15
T.RP	0.1815	158.16	0.2959	168.68
T.RP.D	0.1787	148.79	0.4893	157.19
T.RP.s	0.1027	177.70	0.2457	179.38
T.RP.D.s	0.2602	153.20	0.1152	178.28

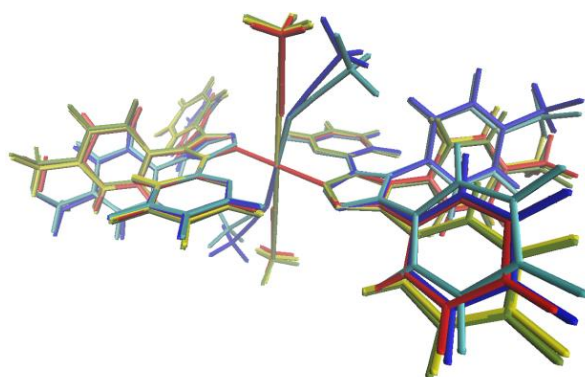
Table A3.3. Fe-N bond distances (\AA) and Fe-N=C(BH₃) angles in the LS (HS) states of the experimentally determined structures of $[\text{Fe}(\text{Lpyridine})_2(\text{NCBH}_3)_2]$ and in the calculated structures of all five $[\text{Fe}(\text{L}^{\text{azine}})_2(\text{NCBH}_3)_2]$ complexes obtained by DFT at the BP86-D3(B)/def2-TZVPP (+CPCM) level of theory, along with the observed $T_{1/2}$ and calculated δN_A chemical shift.

<i>L</i> ^{azine}	Spin State		Fe-N _A (\AA)	Fe-N _{tr} (\AA)	Fe-NCBH ₃ (\AA)	Fe-N≡CBH ₃ ($^\circ$)	$T_{1/2}$ (K)	δN_A (ppm)
<i>L</i> pyridine	HS	Exp.	2.02	1.98	1.95	177.6	288 ⁸³	300
		Calc.	(2.18)	(2.12)	(2.14)	(175.3)		
<i>L</i> pyridine	LS	Exp.	1.99	1.95	1.90	178.2	232 ⁸³	269
		Calc.	(2.15)	(2.13)	(2.10)	(179.2)		
<i>L</i> ⁴ pyrimidine	LS	Exp.	1.99	1.94	1.90	179.3	262 ⁸³	282
		Calc.	(2.16)	(2.13)	(2.09)	(179.2)		
<i>L</i> ² pyrimidine	LS	Exp.	1.98	1.94	1.90	179.0	327 ⁸³	327
		Calc.	(2.15)	(2.13)	(2.09)	(179.0)		
<i>L</i> pyrazine	LS	Exp.	1.97	1.95	1.90	178.3	455 ⁸³	402
		Calc.	(2.15)	(2.13)	(2.09)	(179.3)		
<i>L</i> pyridazine	LS	Exp.	1.95	1.95	1.90	177.6		
		Calc.	(2.15)	(2.15)	(2.09)	(179.3)		



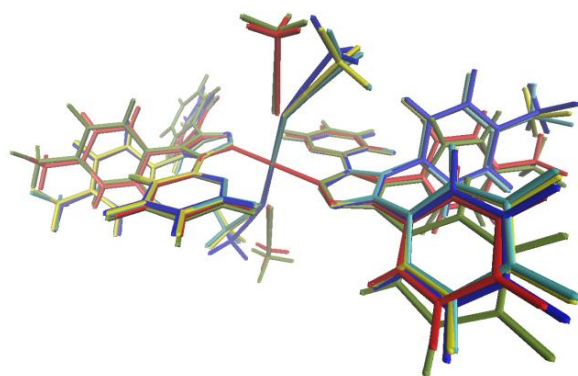
Legend:
RED – crystalline structure
YELLOW – B3.D.s
BLUE – B3
CYANO – B3.D
GREEN – B3.s

Figure A3.2. Superimposed structures for HS $[\text{Fe}(\text{Lpyridine})_2(\text{NCBH}_3)_2]$. The experimentally determined single crystal X-ray structure (**red**) is compared with those calculated by DFT using the def2-TZVPP basis set and a B3LYP density functional alone (**blue**), or in combination with other terms: worst combination B3LYP+D3(BJ) (**cyan**); B3LYP +CPCM (**yellow**); optimal combination B3LYP + D3(BJ)+CPCM (**green**).



Legend:
RED – crystalline
YELLOW – BP.D.s
BLUE – BP
CYANO – BP.D
GREEN – BP.s

Figure A3.3. Superimposed structures for HS $[\text{Fe}(\text{Lpyridine})_2(\text{NCBH}_3)_2]$. The experimentally determined single crystal X-ray structure (**red**) is compared with those calculated by DFT using the def2-TZVPP basis set and a BP86 density functional alone (**blue**), or in combination with other terms: worst combination BP86+D3(BJ) (**cyan**); BP86+CPCM (**yellow**); optimal combination BP86+ D3(BJ)+CPCM (**green**).



Legend:

RED – crystalline structure

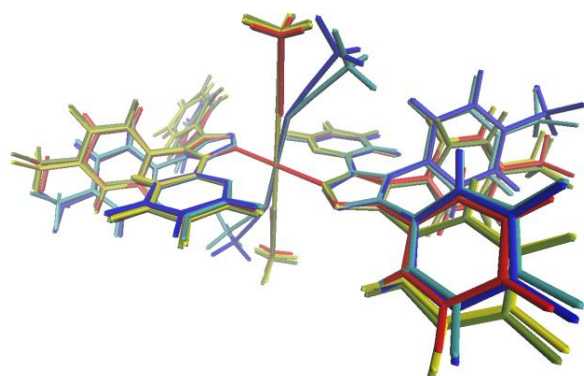
YELLOW – RV.D.s

BLUE – RV

CYANO – RV.D

GREEN – RV.s

Figure A3.4. Superimposed structures for HS [Fe(L_{pyridine})₂(NCBH₃)₂]. The experimentally determined single crystal X-ray structure (**red**) is compared with those calculated by DFT using the def2-TZVPP basis set and a revPBE density functional alone (**blue**), or in combination with other terms: worst combination revPBE+D3(BJ) (**cyan**); revPBE+CPCM (**yellow**); optimal combination BP86+ D3(BJ)+CPCM (**green**).



Legend:

RED – crystalline structure

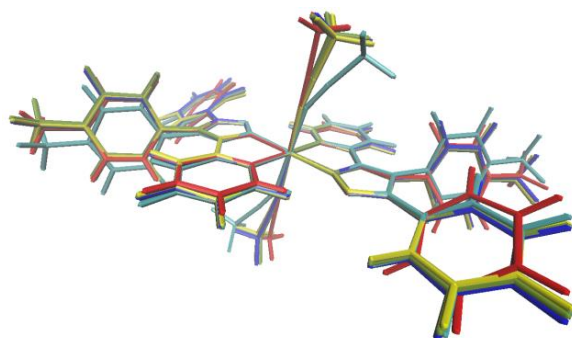
YELLOW – B3.D.s

BLUE – B3

CYANO – B3.D

GREEN – B3.s

Figure A3.5. Superimposed structures for HS [Fe(L_{pyridine})₂(NCBH₃)₂]. The experimentally determined single crystal X-ray structure (**red**) is compared with those calculated by DFT using the def2-TZVPP basis set and a RPBE density functional alone (**blue**), or in combination with other terms: worst combination RPBE+D3(BJ) (**cyan**); RPBE+CPCM (**yellow**); optimal combination RPBE + D3(BJ)+CPCM (**green**).



Legend:

RED – crystalline structure

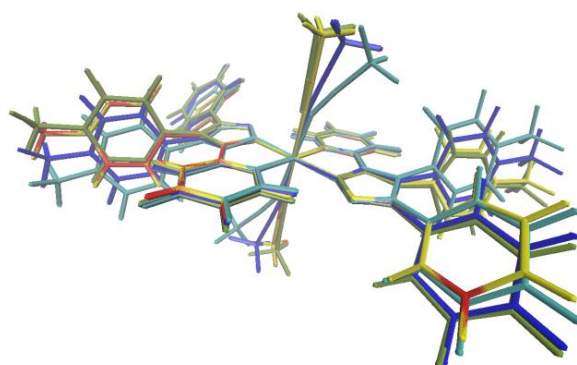
YELLOW – B3.D.s

BLUE – B3

CYANO – B3.D

GREEN – B3.s

Figure A3.6. Superimposed structures for LS $[\text{Fe}(\text{Lpyridine})_2(\text{NCBH}_3)_2]$. The experimentally determined single crystal X-ray structure (**red**) is compared with those calculated by DFT using the def2-TZVPP basis set and a B3LYP density functional alone (**blue**), or in combination with other terms: worst combination B3LYP+D3(BJ) (**cyan**); B3LYP +CPCM (**yellow**); optimal combination B3LYP + D3(BJ)+CPCM (**green**).



Legend:

RED – crystalline structure

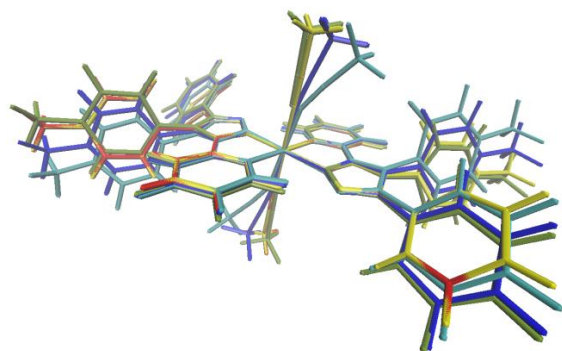
YELLOW – BP.D.s

BLUE – BP

CYANO – BP.D

GREEN – BP.s

Figure A3.7 Superimposed structures for LS $[\text{Fe}(\text{Lpyridine})_2(\text{NCBH}_3)_2]$. The experimentally determined single crystal X-ray structure (**red**) is compared with those calculated by DFT using the def2-TZVPP basis set and a BP86 density functional alone (**blue**), or in combination with other terms: worst combination BP86+D3(BJ) (**cyan**); BP86+CPCM (**yellow**); optimal combination BP86+ D3(BJ)+CPCM (**green**).



Legend:

RED – crystalline structure

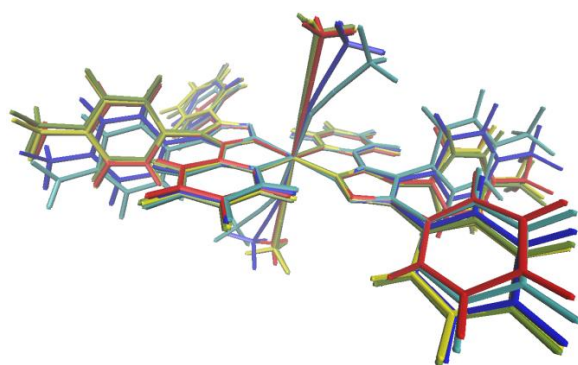
YELLOW – B3.D.s

BLUE – B3

CYANO – B3.D

GREEN – B3.s

Figure A3.8. Superimposed structures for LS $[\text{Fe}(\text{Lpyridine})_2(\text{NCBH}_3)_2]$. The experimentally determined single crystal X-ray structure (**red**) is compared with those calculated by DFT using the def2-TZVPP basis set and a revPBE density functional alone (**blue**), or in combination with other terms: worst combination revPBE+D3(BJ) (**cyan**); revPBE+CPCM (**yellow**); optimal combination BP86+ D3(BJ)+CPCM (**green**).



Legend:

RED – crystalline structure

YELLOW – B3.D.s

BLUE – B3

CYANO – B3.D

GREEN – B3.s

Figure A3.9. Superimposed structures for LS $[\text{Fe}(\text{Lpyridine})_2(\text{NCBH}_3)_2]$. The experimentally determined single crystal X-ray structure (**red**) is compared with those calculated by DFT using the def2-TZVPP basis set and a RPBE density functional alone (**blue**), or in combination with other terms: worst combination RPBE+D3(BJ) (**cyan**); RPBE+CPCM (**yellow**); optimal combination RPBE + D3(BJ)+CPCM (**green**).

A3.2. EDA-NOCV Optimisation Protocol Development

A3.2.1. First Application of EDA-NOCV to Paramagnetic Complexes

For the first time, EDA-NOCV analysis is applied here to an open shell (paramagnetic) metal system – specifically to the family of $[\text{Fe}^{\text{II}}(\text{L}^{\text{azine}})_2(\text{NCBH}_3)_2]$ complexes in the *high spin* state. Here this is done in order to observe the changes which occur as a result of a spin state change; here from diamagnetic *LS* Fe^{II} ($S=0$) to paramagnetic *HS* Fe^{II} ($S=4$). But the general approach developed herein should be applicable to other paramagnetic complexes. In contrast to the *LS* Fe^{II} systems (above), the treatment of the open-shell *HS* Fe^{II} systems requires the use of separate *alpha* and *beta* electrons during all of the calculations. Hence, the NOCV deformation densities $\Delta\rho_i$ are also split into *alpha*- and *beta*- contributions (Figure A3.28); they are then merged to obtain the final values (as reported in Table A3.22).

A3.2.2. Convergence Troubleshooting

Convergence issues were met in attempts to prepare the $[\text{Fe}(\text{L}^{\text{azine}})_2]^{2+}$ and $[\text{Fe}(\text{NCBH}_3)_2]$ fragments (for fragmentations 3 and 4) with the correct occupancy of the *d* orbitals. To overcome this problem, fractional charges (0.2 e^- , distance from Fe 2.00 Å) were introduced and placed at the coordinates, relative to Fe(II), of the coordinating N of the NCBH_3^- and L^{azine} ligands.

A3.2.3. Symmetry Constraint in [FeI(L^{azine})₂(NCBH₃)₂] Family

Starting from the ideal and correct description of the M-L bond in Hoffman's theory²¹ where fragments are treated in their native electronic state and chargeless, EDA-NOCV imposes two method constraints which have forced the authors to introduce approximations in order to perform a bond analysis using this model. Firstly, according to the Hoffmann M-L bond description,^{21, 255} metal fragment should be treated in its own native state (Fe^0). This condition is impossible to be applicable in EDA-NOCV analysis as the model imposes agreement between the oxidation state between each fragment and the final system; consequently Fe^{2+} species must be used instead of Fe^0 . A possible 'trick' to overcome this constraint is reported below in fragmentation 5e. Secondly, according to the Hoffmann M-L bond description,^{21, 255} in the most faithful description of the M(AOs) prior to bonding the five metal d orbitals would be degenerate each other (spherical symmetry). Unfortunately, in order to provide the correct d -orbital occupancies, in EDA-NOCV analysis a symmetry reduction must be imposed. For all the LS species into this study where a ($d_{xy}^2 d_{xz}^2 d_{yz}^2 d_{x^2-y^2}^0 d_{z^2}^0$) electronic structure is requested a symmetry fall from *total spherical* to O_h is enough (Table A3.4). This symmetry applied to the uncoordinated metal ion introduces a small bias, due to introduction of a t_{2g} -e.g., gap this earlier stage. Moreover, in the case of HS systems the use of O_h symmetry is not enough, as it does not grant a unique allocation of the only *beta* electron in the former t_{2g} orbitals. Due to this necessity to allocate univocally electrons into fragments orbitals, the Fe^{2+} fragment was prepared by further reducing the symmetry to C_{2v} and choosing to assign the double occupation to the d_{xy} orbital ($d_{xy}^2 d_{xz}^1 d_{yz}^1 d_{x^2-y^2}^1 d_{z^2}^1$) (Table A3.6). This choice is justified by the fact that the d_{xy} orbital is found to be the lowest orbital in the d set in the final complex.

A3.2.4. Frag. 1 - LS [Fe^{II} (Lazine)₂(NCBH₃)₂]

This fragmentation (removal of one NCBH₃⁻) enables the details of the bonding between the ML₅ fragment and a single NCBH₃⁻ co-ligand to be probed. ΔE_{elstat} and ΔE_{orb} are quantities that give indications of the *ionic* and *covalent* character of the chemical bond(s) formed between the two fragments, respectively. As expected, due to the charged nature of the NCBH₃⁻ co-ligand, the interaction is mainly ionic ($\Delta E_{elstat}:\Delta E_{orb} = \text{ca. } 70:30$) (Figure A3.11 and Table A3.17). Furthermore, the σ - and π -contributions to ΔE_{orb} are 75:25 $\Delta E_{orb,\sigma}:\Delta E_{orb,\pi}$. The EDA-NOCV analysis reveals three interactions (deformation densities $\Delta\rho_{(i)}$), forming one σ -type-bond and two π -type-bonds between the LS Fe^{II} and NCBH₃⁻ anion (Figure A3.10 and Figure A3.23, Table A3.17). The σ -interaction (Figure A3.10, left) occurs between the unoccupied ML₅ (MOs) with high Fe(d_{z^2}) character and the occupied NCBH₃⁻ (MOs) with high N_{NCBH₃} lone pair character. The two π -acceptor interactions (Figure A3.10, right, 1 of these) occur between the occupied ML₅ (MOs) with high Fe(d_{xz} and d_{yz}) character and the unoccupied NCBH₃⁻ (MOs).

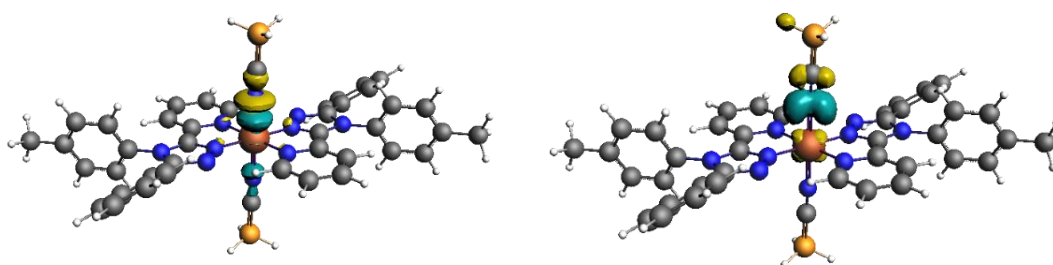


Figure A3.10. Plot of the deformation densities $\Delta\rho_{(i)}$ (reported using cut-off on $\Delta\rho_{(i)}$ of 0.003) in fragmentation 1 of LS [Fe(Lpyridine)₂(NCBH₃)₂] corresponding to the [TM]←ligand σ -donation (top), the [TM]→ligand π -backdonation (bottom). The direction of the charge flow is yellow → turquoise.

The total of σ - and π -type orbital interactions $\Delta E_{orb,\sigma+\pi}$ found for the NCBH₃⁻ co-ligand is practically constant at 50-51 kcal/mol across the entire family (independent of the choice of *L^{azine}*). Hence the role of the NCBH₃⁻ apical ligands in the modulation of the SCO process appears constant, as expected given that it is *L^{azine}* that is being varied (Figure A3.23, Table A3.17).

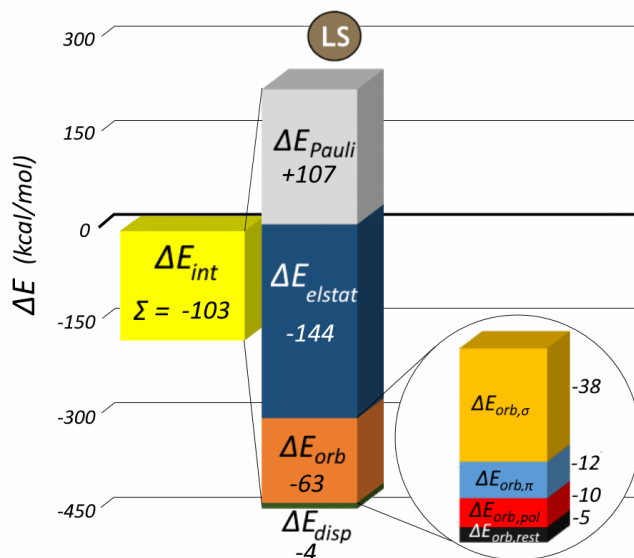


Figure A3.11. Results of EDA-NOCV for LS [Fe(Lpyridine)₂(NCBH₃)₂] using fragmentation 1: (left) yellow column is total ΔE_{int} and middle column is components of ΔE_{int} ; (right) expansion showing contributions to ΔE_{orb} (Equation A3.2). Energies are in kcal/mol.

A3.2.5. Frag. 2 - LS [Fe^{II} (L^{azine})₂(NCBH₃)₂]

Fragmentation 2 considers the removal of a single neutral bidentate *L^{azine}* ligand (Figure A3.24, Table A3.18). Clearly, this fragmentation was expected to be the most valuable with regard to establishing the relative ligand field strength of each of these five *L^{azine}* ligands. Indeed, EDA-NOCV analysis appears to detect the differences in the electronic structure in the *L^{azine}* ligands (Figure A3.24, Table A3.18), but the differences in energy are very small (4 kcal/mol), so should be taken with caution. The $\Delta E_{\text{orb},\sigma+\pi}$ values show a trend consistent with the expected ligand field increases across the series (Table A3.18), with the *L^{4pyrimidine}* complex (lowest $T_{1/2}$) experiencing the weakest (-85.2 kcal/mol) and the *L^{pyridazine}* complex (highest $T_{1/2}$) the strongest ligand field (-89.0 kcal/mol) (Figure A3.24, Table A3.18), respectively. Both the σ - and π -contributions, $\Delta E_{\text{orb},\sigma}$ and $\Delta E_{\text{orb},\pi}$, also follow this trend (Figure A3.24, Table A3.18), with both steadily increasing on going from *L^{4pyrimidine}* across to *L^{pyridazine}*, again consistent with the experimentally observed steadily increasing $T_{1/2}$ (and

hence ligand field). The $L^{pyridine}$ ligand is out of line with this trend, by about 2 kcal/mol, but this is not surprising, as it is not simply an isomer of the other azines: While four of the others are *diazines*, pyridine contains only one N atom in the six-membered ring. The ratio of $\Delta E_{orb,\sigma}$ and $\Delta E_{orb,\pi}$ is about 75:25, regardless of the L^{azine} involved in the $M-L^{azine}$ bonds being formed (Figure A3.24, Table A3.18).

A3.2.6. Frag. 3 - $LS [Fe^{II} (L^{azine})_2(NCBH_3)_2]$

To avoid spurious contributions to the EDA coming from the presence of additional ligands of the same kind still being present in the ML_x fragment, fragmentations 3 and 4 were trialled. In the case of fragmentation 3 (removal of both $NCBH_3$, Figure A3.25, Table A3.19), the energies of the $Fe(d)$ orbitals only experience the different strength of the L^{azine} ligands *within* the ML_2^{azine} fragment, not *between* the two fragments. The minimal differences observed for fragmentation 1 are enhanced enough in fragmentation 3 to give a clearer trend of field strength for the family of L^{azine} complexes. Specifically, $\Delta E_{orb,\sigma+\pi}$ is observed to steadily decrease from $L^{4pyrimidine}$ (-95.7 kcal/mol) through to $L^{pyridazine}$ (-98.1 kcal/mol) as expected from the trend in $T_{1/2}$ (Figure 3.1, Figure A3.25, Table A3.19), with just $L^{pyridine}$ (-95.0 kcal/mol) representing a discontinuity in the trend, as it is not a *diazine*.

A3.2.7. Frag. 4 - $LS [Fe^{II} (L^{azine})_2(NCBH_3)_2]$

Moving forward to fragmentation 4 we expect better results, as it better reflects the chemical point of view¹⁰⁵ - as experimentally $Fe(NCBH_3)_2$ reacts with two equivalents of L^{azine} - and it should enhance the differences between the members of the L^{azine} family, whilst maintaining a constant electronic structure for the other fragment, $ML_2 = Fe(NCBH_3)_2$. Analysis of the σ - and π -contributions (Figure A3.12, Figure A3.26, Table A3.20) shows that the σ -

interaction is almost three times larger than the π -interaction regardless of L^{azine} . The σ -strength ($\Delta E_{orb,\sigma}$) of the L^{azine} ligands follows the order (Table A3.20):

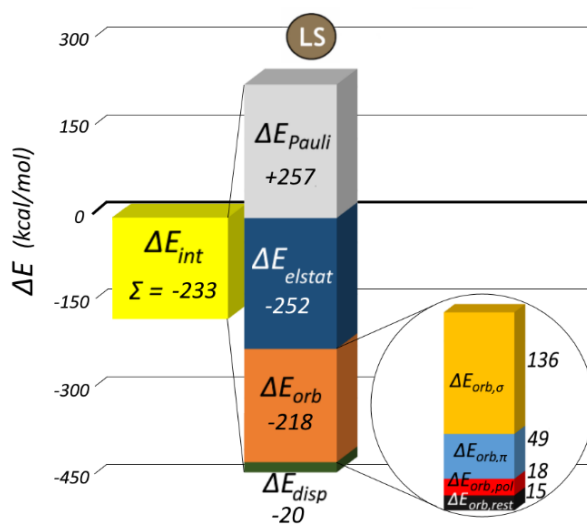
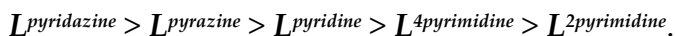
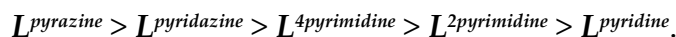
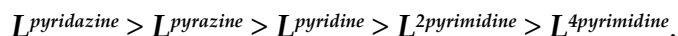


Figure A3.12. Results of EDA-NOCV for LS $[Fe(L^{pyridine})_2(NCBH_3)_2]$ using fragmentation 4: (left) yellow column is total ΔE_{int} and middle column is components of ΔE_{int} (Equation A3.1); (right) expansion showing contributions to ΔE_{orb} (Equation A3.2). Energies are in kcal/mol.

This matches the observed order of $T_{1/2}$ until the pyrimidines are considered; they are in the reverse order (Figure 3.1).⁸³ Interestingly the order of the π -strength ($\Delta E_{orb,\pi}$) of the L^{azine} ligands differs (and the values are far from showing a monotonic trend):



This order bears no relationship to the observed order of $T_{1/2}$ values (Figure 3.1, Table A3.20). Crucial is the collective contribution of $\Delta E_{orb,\sigma}$ and $\Delta E_{orb,\pi}$, $\Delta E_{orb,\sigma+\pi}$, as this describes the total effect of the pair of L^{azine} ligands on the metal ion in the final complex correctly (Figure A3.12, Figure A3.26, Table A3.20):



Indeed, an extremely strong correlation between the $\Delta E_{\text{orb},\sigma+\pi}$ term and the experimental $T_{1/2}$ values ($R^2 = 0.99$) is observed (Figure A3.13 red).

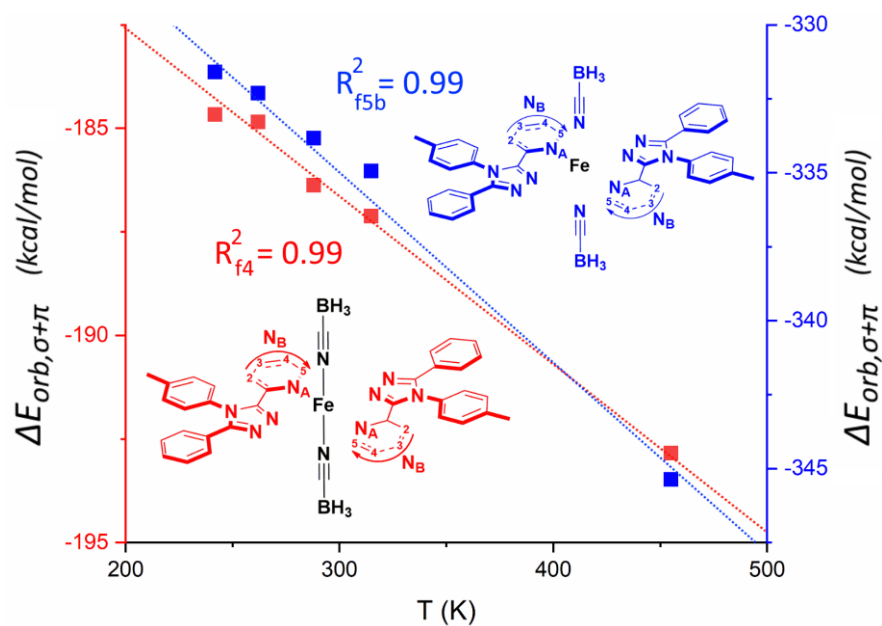


Figure A3.13. Linear correlation between the experimental $T_{1/2}$ values of the LS $[\text{Fe}(\text{L}^{\text{pyridine}})_2(\text{NCBH}_3)_2]$ complexes and the $\Delta E_{\text{orb},\sigma+\pi}$ values (sum of σ - and π - character orbital interactions between the fragments), using fragmentations **4** (red, $R^2 = 0.99$) and **5b** (blue, $R^2 = 0.99$).

A3.2.8. L^{azine} vs 2NCBH_3 in Frag. 1 - 4

Regardless of L^{azine} , comparisons of $\Delta E_{orb,\sigma+\pi}$ for fragmentations 1 (NCBH_3^- : -48 to -49 kcal/mol) vs 2 (L^{azine} : -85 to -89 kcal/mol) vs 3 ($2\times\text{NCBH}_3^-$: -95 to -98 kcal/mol) vs 4 ($2\times L^{azine}$: -183 to -193 kcal/mol), consistently show that the $\Delta E_{orb,\sigma+\pi}$ for two NCBH_3^- ligands (-95 to -98 kcal/mol) contributes a similar or slightly larger stabilisation energy than one bidentate L^{azine} (-85 to -97 kcal/mol) does (Figures A3.14). This is inconsistent with the above experimental observations, which clearly show that bidentate L^{azine} actually possesses a stronger ligand field ligand than $2\times\text{NCBH}_3^-$ (monodentate). This disagreement between the theoretical results and experimental data highlights why fragmentations 1-4 are not good choices for such a comparison. It occurs because of these fragmentation choices not sharing a constant reference fragment (and hence lacking generality). If the strength of a ligand is to be assessed then this can be done only if the rest of the coordination sphere is maintained unaltered. This is achieved by employing fragmentation 5, in the form of 5b, to obtain $\Delta E_{orb,\sigma+\pi}$.

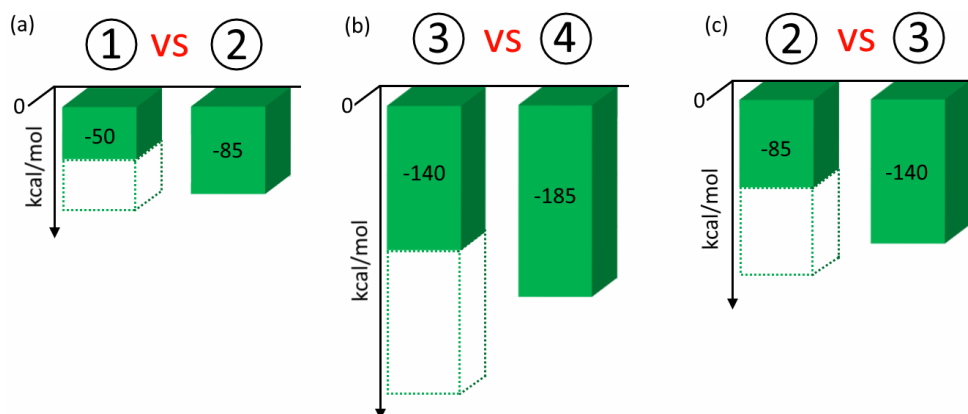


Figure A3.14. $\Delta E_{orb,\sigma+\pi}$ results (kcal/mol) across fragmentation 1-4; scheme leads comparing theoretical results versus experimental evidences on the ligand strength of NCBH_3^- versus L^{azine} for LS $[\text{Fe}(\text{Lpyridine})_2(\text{NCBH}_3)_2]$ complex. Results are consistent for all the other four LS $[\text{Fe}(L^{azine})_2(\text{NCBH}_3)_2]$. (a) $\Delta E_{orb,\sigma+\pi}$ comparison between fragmentation 1 and 2. (b) $\Delta E_{orb,\sigma+\pi}$ comparison between fragmentation 3 and 4. (c) $\Delta E_{orb,\sigma+\pi}$ comparison between fragmentation 2 and 3. Dotted boxes help to visualise twice the amount of $\Delta E_{orb,\sigma+\pi}$ for specific fragmentation.

A3.2.9. Frag. 5a-5e: correct Fe²⁺ Energy Levels in LS [Fe^{II}(L^{azine})₂(NCBH₃)₂] Family

Whilst the energies of the Fe *d* orbitals in fragmentations 1-4 have comparable energies to the valence orbitals of the ligands, as expected within Hoffman's MO diagram (see Figure A3.1), thanks to the partial ligand fields induced by the ligands included in the fragments, this does not happen in fragmentation 5. In this case, the Fe²⁺ *d* atomic energies, for fragmentation 5a (no modifications/corrections) are calculated to be unrealistically low in energy, approx. -26.0 eV (Table A3.4), with respect to the MO energies of the ligands, -4.0 to +4.0 eV (Table A3.5). This huge difference in energy is unacceptable in Hoffman's MO diagram, and may well present a bias in the EDA analysis. So, to overcome this problem the free ion Mⁿ⁺ in 5a was instead treated by four different methods 5b to 5e in order to determine which generated the most appropriate Fe²⁺ *d* atomic energy levels:

- Fragmentation 5a. Fe²⁺ (*t*_{2g} : -26.0 eV; *e*_g : -25.6 eV).
- Fragmentation 5b. Fe²⁺ + 6x -0.425e (*t*_{2g} : -8.0 eV; *e*_g : -7.61 eV).
- Fragmentation 5c. Fe²⁺ + 6x -1.0e (*t*_{2g} : +16.4 eV; *e*_g : +16.9 eV).
- Fragmentation 5d. Fe²⁺ +6x -2.0e (*t*_{2g} : +58.7 eV; *e*_g : +59.6 eV).
- Fragmentation 5e. Fe²⁺ density mapped onto Fe⁰(AOs) (*t*_{2g} : -8.0 eV; *e*_g : -7.8 eV).

In three of these fragmentations, 5b-5d, six negative charges are placed octahedrally around the Fe²⁺ ion at a distance of 2.00 Å. The magnitude of the charges was tuned (from -0.425e to -1e to -2e each) in order to obtain Fe²⁺(AO) energies closer to the ligand MO energies (Table A3.5); the best fragmentation is 5b (approx. -8.0 eV). This occurs at the cost of introducing a small *t*_{2g}-*e*_g splitting but this has the advantage of ensuring the correct occupancy of the *d*-orbitals in the final complex with marginal effects on the final absolute energy

of the Fe^{2+} fragment (Table A3.4). But, fragmentation of **5b** suffers from underestimating the ΔE_{Pauli} (see later) so an additional fragmentation, **5e**, was also developed. Here the wavefunction obtained by calculation of the Fe^0 in an octahedral symmetry (Table A3.4) was manually manipulated to simply remove two electrons from 4s orbital, *i.e.*, $\text{Fe}^0(3d^64s^2)$ to $\text{Fe}^{2+}(3d^64s^0)$, whilst retaining the calculated energy levels (which are appropriate in Hoffman's MO diagram), in preparation for EDA-NOCV analysis.

To our knowledge, such a fragmentation at the level we present it here represents a novelty in the EDA-NOCV analysis of transition metal complexes. Indeed, to apply this approach successfully, first the problem of accurate representation of the *d* orbitals energies had to be addressed and hence several computational setups were trialled for fragmentation **5** (see also above). In fragmentations **5a-5e** comparison each term of the EDA-NOCV analysis was proved a full understanding of the relationship between Fe orbitals and EDA-NOCV energy terms. Fragmentations **5a-5d** (octahedral negative charges from 0e to 2e) do not show substantial changes in any of the EDA-NOCV (Tables A3.7-A3.16 and Figures A3.15-A3.21) terms: ΔE_{int} and ΔE_{Pauli} are shifted by charges inclusion in the Fe^{2+} fragment, but regardless of this the trend across the family is maintained (Tables A3.12-A3.16 and Figures A3.15-A3.16).

In contrast, for ΔE_{orb} and ΔE_{elstat} a trend inversion is reported: increasing the charge intensity around the metal ion caused ΔE_{orb} to decrease slightly, whilst ΔE_{elstat} rose (Tables A3.12-A3.16 and Figures A3.17-A3.18). This trend inversion only introduces differences of around 1-2% so is not significant. Similarly, $\Delta E_{\text{orb},\sigma}$ decreased and $\Delta E_{\text{orb},\pi}$ increased as the octahedral charge intensity around the $\text{Fe}^{2+}(\text{AOs})$ was increased by charge inclusion (Tables A3.12-A3.16 and Figures A3.19-A3.20). Once the $\text{Fe}^{2+}(\text{AOs})$ energies were raised above reasonable levels (fragmentations **5c-5d**) $\Delta E_{\text{orb},\pi}$ becomes extremely small (almost negligible) or even positive (Tables A3.12-A3.16 and Figures A3.20) consistent with a shift of the formally "*t_{2g}*" *d* orbitals far above the *diazine* π^* orbital energies, inhibiting π -back donation and leading to σ -only interactions. Interestingly, the $\Delta E_{\text{orb},\sigma+\pi}$ term maintains a stable value

across fragmentations **5a-5d** (Tables A3.12-A3.16 and Figure A3.21) despite the variations in single constitutive $\Delta E_{orb,\pi}$ and $\Delta E_{orb,\sigma}$ contributions which change due to the different setups (partial charges) used to handle the Fe^{2+} ion.

Hence fragmentation **5e**, in which the density of the $\text{Fe}^{2+}(\text{AOs})$ was mapped onto the $\text{Fe}^0(\text{AOs})$, to emulate a molecular orbital interaction in Hoffmann's framework,²¹ was also trialled. The EDA-NOCV analysis results from this fragmentation are very different from those observed for all of the previous fragmentations **5a-5d**. A remarkable difference was observed in the ΔE_{Pauli} contribution, which rises from about 250 kcal/mol (fragmentations **5a-5d**) to more than 600 kcal/mol (Tables A3.16 and Figure A3.15).

Consequently, ΔE_{int} decreases considerably, indicating the quality of the new densities (Tables A3.16 and Figure A3.15), since smaller ΔE_{int} indicates smaller dissociation energies for the involved fragments, and, therefore, fragment densities that are closer to the final one. The same range of ΔE_{int} values as found in **5a-5e** have been reported in a previous study in literature when M^0 or M^{2+} are used. Furthermore, in the same study the authors point out that the use of a M^{2+} fragment in EDA can introduce a bias into the results. The choice of the correct representation of ΔE_{Pauli} energy should be the one where the calculated amount is comparable (often higher) than ΔE_{elstat} . $\Delta E_{elstat} + \Delta E_{Pauli}$ can be considered as the lost energy (consequently with positive (+) contribution) to be overtaken by ΔE_{orb} to engage a new bond. From this angle, fragmentation **5e** gives the most correct representation in the EDA analysis as it avoids to underestimate ΔE_{Pauli} as for fragmentation **5b**.

On other hand, when results obtained from NOCV are analysed considerable error is observed. Deformation density $\Delta\rho_3$ (identified as a d_{xz} π -backdonation) unphysically positive and considerably stronger than the two other π -interactions (occurring through d_{yz} and d_{xy}) (Table A3.11, Table A3.16). This result would drop to zero the entire π -strength of the coordination sphere with unique contribution of the metal ion through σ -bonds (except for $[\text{Fe}(\text{Lpyridazine})_2(\text{NCBH}_3)_2]$). A similar error in this π -interaction (as that specific interaction would be de-stabilising term) was observed, indeed, in

fragmentation **5d** when Fe^{2+} are risen to +50 eV (Table A3.15). However, $\Delta E_{orb,\sigma+\pi}$ values are in line with the ones computed in any **5** fragmentation (Figure A3.21). The correlation established earlier in fragmentation **4** between $\Delta E_{orb,\sigma+\pi}$ and the experimental $T_{1/2}$ is reported also for fragmentations **5** where, despite the fluctuations observed into σ - and π -interactions when Fe^{2+} is treated differently, the correlation shows $R^2 > 0.95$ for all the **5** fragmentations (Figure A3.21).

In summary, considering all of the data reported above, fragmentations **5b** and **5e** appear to be the most accurate for two different types of analysis: fragmentation **5b** shows the best results for the NOCV analysis – but the error in the underestimation of the ΔE_{Pauli} has to be reported. On the other hand, fragmentation **5e** corrects this error and it provides the best EDA analysis in order to get information on the energies of bond(s) formed between the fragments. They should both be employed, as together this provides the best description of EDA **5e** and NOCV **5b** analysis.

Table A3.4. Results reported for the analysis of the LS Fe(AOs) energies (eV) frontier orbitals used for establish the most correct EDA-NOCV analysis in the $M+L_6$ fragmentation. The best are fragmentations are **5b** and **5e** as the Fe^{2+} orbital energies are close to those of the L (-4.0 to 4.0 eV; Table A3.5). †Energy levels for **5e** come directly from those calculated for Fe^0 (O_H); the only difference is that the 2 s electrons have been manually removed in preparation for EDA-NOCV analysis.

LS Fe (O_H)	T_{2g}	E_g	ΔE ($E_g - T_{2g}$)	Energy (H)	Fragmentation
Fe^0 (Spherical Sym.)	-7.93	-7.93	0.0	-1263.66	-
Fe^0 (O_H)	-7.96 [†]	-7.78 [†]	0.18 [†]	-1263.66	-
Fe^{2+} (no charges)	-26.05	-25.61	0.56	-1262.74	5a
Fe^{2+} (6x -0.425e)	-8.00	-7.61	0.39	-1262.75	5b
Fe^{2+} (6x -1.0e)	+16.37	+16.94	0.57	-1262.75	5c
Fe^{2+} (6x -2.0e)	+58.68	+59.55	0.87	-1262.74	5d
Fe^{2+} on Fe^0 (AOs)	-7.96 [†]	-7.78 [†]	0.18 [†]	-1263.66	5e

Table A3.5. Reported energies (eV) of the MO of the L6 coordination sphere who interact with Fe(AOs). Each MO(L₆) is paired with the relative Fe(AOs) in bracket. MOs pairing was obtained by analysis of the contributing SFOs from density flowing ($\Delta\rho(i)$) in EDA-NOCV analysis.

	MO ($d_{x^2-y^2}$)	MO (d_{z^2})	MO (d_{xz})	MO (d_{zy})	MO (d_{xy})	MO (p_x)	MO (p_y)	MO (p_z)	MO (s)
L ⁴ pyrimidine	0.20	0.53	2.62	3.26	-	-0.73	-0.37	-0.35	-2.98
L ² pyrimidine	0.27	0.54	2.78	2.93	-	-0.66	-0.35	-0.35	-1.55
Lpyridine	0.41	0.74	3.47	3.10	-	-0.56	-0.23	-0.23	-1.71
Lpyrazine	0.19	0.48	2.58	3.07	-	-0.75	-0.43	-0.42	-3.19
Lpyridazine	0.99	0.53	2.94	2.91	-	-0.39	0.14	-0.23	-1.13

Table A3.6. Results reported for the analysis of the HS Fe(AOs) energies (eV) frontier orbitals used for establish the most correct EDA-NOCV analysis in the M+L₆ fragmentation.

HS Fe (C _{2v})	d_{xy}	d_{xz}	d_{zy}	$d_{x^2-y^2}$	d_{z^2}	Fragmentation
Fe ⁰ (Spherical Symmetry)	-7.93	-7.93	-7.93	-7.93	-7.93	-
Fe ²⁺ (no charges)	- 26.05	-26.31	-26.31	-25.46	-26.58	5a
Fe ²⁺ (6x -0.425e)	-7.28	-8.13	-8.13	-7.13	-8.25	5b
Fe ²⁺ on Fe ⁰ (AOs)	-7.42	-8.23	-8.23	-7.44	-8.47	5e

Table A3.7. EDA -NOCV results (kcal/mol) across the five fragmentations 5a-5e for the treatment of the isolated metal ion M. Results for LS [Fe(L⁴pyrimidine)₂(NCBH₃)₂] are reported. Decomposition in specific contribution of ΔE_{int} (top), and ΔE_{orb} (bottom) are reported.

	5a	5b	5c	5d	5e
ΔE_{int}	-865.6	-865.8	-866.7	-870.3	-505.1
ΔE_{Pauli}	264.4	263.9	263.1	261.4	631.0
ΔE_{elstat}	-609.1	-610.6	-612.8	-617.1	-622.4
ΔE_{orb}	-511.3	-509.6	-507.4	-505.0	-504.1
$\Delta E_{orb,\sigma}$	-301.9	-304.4	-308.0	-314.9	-321.3
$\Delta E_{orb,\pi}$	-33.1	-28.7	-22.8	-12.9	-0.2
$\Delta E_{orb,\sigma+\pi}$	-334.9	-333.0	-330.8	-327.7	-321.5

Table A3.8. EDA -NOCV results (kcal/mol) across the five fragmentations **5a-5e** for the treatment of the isolated metal ion **M**. Results for LS [Fe(L²pyrimidine)₂(NCBH₃)₂] are reported. Decomposition in specific contribution of ΔE_{int} (top), and ΔE_{orb} (bottom) are reported.

	5a	5b	5c	5d	5e
ΔE_{int}	-865.9	-866.1	-867.0	-870.3	-505.5
ΔE_{Pauli}	265.9	265.5	264.6	-262.9	632.3
ΔE_{elstat}	-611.4	-612.9	-615.1	-619.4	-624.7
ΔE_{orb}	-510.9	-509.1	-507.0	-504.6	-503.6
$\Delta E_{orb,\sigma}$	-303.5	-305.9	-312.1	-315.7	-322.1
$\Delta E_{orb,\pi}$	-31.7	-27.4	-21.4	-15.3	0.6
$\Delta E_{orb,\sigma+\pi}$	-335.2	-333.3	-333.5	-331.0	-321.4

Table A3.9. EDA -NOCV results (kcal/mol) across the five fragmentations **5a-5e** for the treatment of the isolated metal ion **M**. Results for LS [Fe(L¹pyridine)₂(NCBH₃)₂] are reported. Decomposition in specific contribution of ΔE_{int} (top), and ΔE_{orb} (bottom) are reported.

	5a	5b	5c	5d	5e
ΔE_{int}	-876.7	-876.9	-877.8	-881.4	-516.0
ΔE_{Pauli}	262.7	262.9	262.1	-260.3	630.0
ΔE_{elstat}	-618.7	-619.5	-621.7	-625.9	-631.1
ΔE_{orb}	-511.2	-510.6	-508.5	-506.2	-505.2
$\Delta E_{orb,\sigma}$	-302.2	-308.1	-311.6	-318.2	-325.0
$\Delta E_{orb,\pi}$	-33.8	-27.3	-21.6	-12.2	0.1
$\Delta E_{orb,\sigma+\pi}$	-335.9	-335.4	-333.2	-330.4	-324.9

Table A3.10. EDA -NOCV results (kcal/mol) across the five fragmentations **5a-5e** for the treatment of the isolated metal ion **M**. Results for LS [Fe(Lpyrazine)₂(NCBH₃)₂] are reported. Decomposition in specific contribution of ΔE_{int} (top), and ΔE_{orb} (bottom) are reported.

	5a	5b	5c	5d	5e
ΔE_{int}	-864.3	-864.5	-865.4	-869.0	-503.9
ΔE_{Pauli}	268.0	267.6	266.8	-265.0	634.5
ΔE_{elstat}	-607.5	-609.1	-611.3	-615.6	-620.9
ΔE_{orb}	-515.2	-513.4	-511.2	-508.8	-507.8
$\Delta E_{orb,\sigma}$	-304.6	-307.3	-311.1	-317.9	-324.2
$\Delta E_{orb,\pi}$	-33.7	-29.2	-23.0	-13.0	-0.7
$\Delta E_{orb,\sigma+\pi}$	-338.3	-336.5	-341.3	-330.9	-324.9

Table A3.11. EDA -NOCV results (kcal/mol) across the five fragmentations **5a-5e** for the treatment of the isolated metal ion **M**. Results for LS [Fe(Lpyridazine)₂(NCBH₃)₂] are reported. Decomposition in specific contribution of ΔE_{int} (top), and ΔE_{orb} (bottom) are reported.

	5a	5b	5c	5d	5e
ΔE_{int}	-885.4	-883.0	-883.9	-887.5	-522.4
ΔE_{Pauli}	268.4	-271.11	-270.3	-268.6	-638.0
ΔE_{elstat}	-607.7	-623.0	-625.3	-629.6	-634.9
ΔE_{orb}	-515.4	-521.6	-519.5	-517.1	-516.1
$\Delta E_{orb,\sigma}$	-290.9	-289.1	-292.8	-301.4	-308.5
$\Delta E_{orb,\pi}$	-55.4	-55.4	-48.5	-37.1	-23.4
$\Delta E_{orb,\sigma+\pi}$	-346.2	-344.5	-341.3	-338.4	-331.9

Table A3.12. EDA -NOCV results (kcal/mol) reported for fragmentation 5a for all the five LS $[Fe(L^{azine})_2(NCBH_3)_2]$ systems. First section (top) reports ΔE_{int} energy splitting; second section (middle) reports ΔE_{orb} energy splitting; third section (bottom) reports all the nine orbital interaction due to M + L_6 interaction.

	L 4pyrimidine	L 2pyrimidine	L pyridine	L pyrazine	L pyridazine
ΔE_{int}	-865.6	-865.9	-876.7	-864.3	-885.4
ΔE_{Pauli}	265.9	265.9	262.7	268.0	268.4
ΔE_{elstat}	-609.1 (53.9%)	-611.4 (54.0%)	-618.7 (54.3%)	-607.5 (53.6%)	-607.7 (53.7%)
ΔE_{orb}	-511.3 (45.2%)	-510.9 (45.1%)	-511.2 (44.8%)	-515.2 (45.5%)	-515.4 (45.5%)
ΔE_{disp}	-9.6 (0.9%)	-9.5 (0.9%)	-9.7 (0.9%)	-9.6 (0.9%)	-9.4 (0.8%)
$\Delta E_{orb,\sigma}$	-301.9 (59.1%)	-303.5 (59.3%)	-302.2 (59.1%)	-304.6 (59.2%)	-290.9 (56.5%)
$\Delta E_{orb,\pi}$	-33.1 (6.5%)	-31.7 (6.3%)	-33.8 (6.7%)	-33.7 (6.6%)	-55.4 (10.8%)
$\Delta E_{orb,\sigma+\pi}$	-334.9 (65.6%)	-335.2 (65.6%)	-335.9 (65.8%)	-338.3 (65.8%)	-346.2 (67.3%)
$\Delta E_{orb,pol}$	-146.6 (28.8%)	-148.9 (29.2%)	-145.9 (28.6%)	-147.2 (28.5%)	-158.7 (30.9%)
$\Delta E_{orb,rest}$	-29.8 (5.6%)	-29.8 (5.2%)	-29.4 (5.8%)	-29.4 (5.7%)	-31.2 (5.8%)
$\Delta E_{orb,dz2}$	-112.7	-112.3	-113.0	-111.3	-111.5
$\Delta E_{orb,dx2-y2}$	-115.2	-116.6	-114.6	-118.1	-103.0
$\Delta E_{orb,dzx}$	-5.3	-4.5	-6.0	-5.2	-26.9
$\Delta E_{orb,dzy}$	-12.1	-11.4	-12.4	-12.8	-12.0
$\Delta E_{orb,dxy}$	-15.7	-15.8	-15.4	-15.7	-16.4
$\Delta E_{orb,s}$	-23.3	-23.1	-23.6	-23.6	-23.2
$\Delta E_{orb,pz}$	-18.8	-19.3	-19.3	-19.7	-21.2
$\Delta E_{orb,px}$	-18.5	-19.0	-18.2	-19.1	-18.9
$\Delta E_{orb,py}$	-13.3	-13.2	-13.4	-12.8	-13.1

Table A3.13. EDA -NOCV results (kcal/mol) reported for fragmentation **5b** for all the five LS $[\text{Fe}(\text{L}^{\text{azine}})_2(\text{NCBH}_3)_2]$ systems. First section (top) reports ΔE_{int} energy splitting; second section (middle) reports ΔE_{orb} energy splitting; third section (bottom) reports all the nine orbital interaction due to $M + L_6$ interaction.

	$L^4\text{pyrimidine}$	$L^2\text{pyrimidine}$	L^{pyridine}	L^{pyrazine}	$L^{\text{pyridazine}}$
ΔE_{int}	-866.1	-876.9	-864.5	-883.0	-866.1
ΔE_{Pauli}	265.5	262.9	267.6	271.11	265.5
ΔE_{elstat}	-610.6 (54.0%)	-612.8 (54.1%)	-619.5 (54.4%)	-609.1 (53.7%)	-623.0 (53.8%)
ΔE_{orb}	-509.6 (45.1%)	-509.1 (45.0%)	-510.6 (44.7%)	-513.4 (45.4%)	-521.6 (45.4%)
ΔE_{disp}	-9.6 (0.9%)	-9.5 (0.9%)	-9.7 (0.9%)	-9.6 (0.9%)	-9.4 (0.8%)
$\Delta E_{\text{orb},\sigma}$	-304.3 (59.6%)	-305.9 (60.1%)	-308.1 (60.3%)	-307.3 (60.4%)	-289.1 (56.4%)
$\Delta E_{\text{orb},\pi}$	-28.7 (5.7%)	-27.4 (5.3%)	-27.3 (5.3%)	-29.2 (4.7%)	-55.4 (8.8%)
$\Delta E_{\text{orb},\sigma+\pi}$	-333.0 (65.3%)	-333.3 (65.4%)	-335.4 (65.6%)	-336.5 (65.1%)	-344.5 (65.2%)
$\Delta E_{\text{orb},\text{pol}}$	-146.5 (28.6%)	-145.8 (28.7%)	-145.2 (28.4%)	-146.9 (24.1%)	-146.6 (23.6%)
$\Delta E_{\text{orb},\text{rest}}$	-30.6 (5.9%)	-33.5 (5.9%)	-31.6 (6.0%)	-30.5 (5.8%)	-31.3 (4.9%)
$\Delta E_{\text{orb},dz^2}$	-113.8	-113.4	-112.8	-112.5	-102.2
$\Delta E_{\text{orb},dx^2-y^2}$	-116.3	-117.7	-120.4	-119.3	-110.3
$\Delta E_{\text{orb},d_{zx}}$	-3.4	-2.6	-1.3	-3.2	-29.2
$\Delta E_{\text{orb},d_{zy}}$	-10.8	-10.1	-11.2	-11.5	-10.9
$\Delta E_{\text{orb},d_{xy}}$	-14.6	-14.7	-14.9	-14.6	-15.3
$\Delta E_{\text{orb},s}$	-23.4	-23.2	-23.8	-23.6	-23.3
$\Delta E_{\text{orb},pz}$	-18.8	-19.4	-19.3	-19.8	-21.3
$\Delta E_{\text{orb},px}$	-18.6	-19.0	-19.3	-19.1	-19.0
$\Delta E_{\text{orb},py}$	-13.4	-13.3	-13.5	-12.9	-13.1

Table A3.14. EDA-NOCV results (kcal/mol) reported for fragmentation **5c** for all the five LS $[\text{Fe}(\text{L}^{\text{azine}})_2(\text{NCBH}_3)_2]$ systems. First section (top) reports ΔE_{int} energy splitting; second section (middle) reports ΔE_{orb} energy splitting; third section (bottom) reports all the nine orbital interaction due to $M + L_6$ interaction.

	$L^4\text{pyrimidine}$	$L^2\text{pyrimidine}$	L^{pyridine}	L^{pyrazine}	$L^{\text{pyridazine}}$
ΔE_{int}	-867.0	-877.8	-865.4	-883.9	-867.0
ΔE_{Pauli}	263.1	264.6	262.0	266.7	270.3
ΔE_{elstat}	-612.8 (54.2%)	-615.1 (54.3%)	-621.6 (54.6%)	-611.3 (53.9%)	-625.3 (54.0%)
ΔE_{orb}	-507.4 (44.9%)	-507.0 (44.8%)	-508.5 (44.5%)	-511.2 (45.2%)	-519.5 (45.2%)
ΔE_{disp}	-9.6 (0.9%)	-9.5 (0.9%)	-9.7 (0.9%)	-9.6 (0.9%)	-9.4 (0.8%)
$\Delta E_{\text{orb},\sigma}$	-308.0 (60.7%)	-312.1 (61.5%)	-311.6 (61.4%)	-311.1 (60.9%)	-292.8 (56.3%)
$\Delta E_{\text{orb},\pi}$	-22.7 (3.8%)	-21.5 (3.4%)	-21.6 (4.3%)	-23.0 (4.5%)	-48.5 (9.3%)
$\Delta E_{\text{orb},\sigma+\pi}$	-330.8 (64.5%)	-333.5 (64.9%)	-333.2 (65.7%)	-334.2 (65.4%)	-341.3 (65.6%)
$\Delta E_{\text{orb},\text{pol}}$	-146.6 (29.0%)	-143.4 (28.2%)	-145.4 (28.5%)	-147.1 (28.8%)	-148.2 (28.5%)
$\Delta E_{\text{orb},\text{rest}}$	-31.4 (6.5%)	-33.6 (6.9%)	-29.3 (6.8%)	-30.9 (6.8%)	-31.3 (6.9%)
$\Delta E_{\text{orb},dz^2}$	-115.6	-115.0	-114.3	-114.3	-105.1
$\Delta E_{\text{orb},dx^2-y^2}$	-117.9	-119.3	-122.0	-121.1	-111.6
$\Delta E_{\text{orb},d_{zx}}$	-0.7	-0.1	+1.2	-0.3	-25.6
$\Delta E_{\text{orb},d_{zy}}$	-9.0	-8.2	-9.4	-9.7	-9.1
$\Delta E_{\text{orb},d_{xy}}$	-13.1	-13.2	-13.4	-13.1	-13.7
$\Delta E_{\text{orb},s}$	-23.4	-23.2	-23.9	-23.7	-23.3
$\Delta E_{\text{orb},pz}$	-18.9	-19.5	-19.4	-19.9	-20.4
$\Delta E_{\text{orb},px}$	-18.7	-19.2	-18.4	-19.2	-19.1
$\Delta E_{\text{orb},py}$	-13.5	-16.0	-13.6	-13.0	-13.2

Table A3.15. EDA-NOCV results (kcal/mol) reported for fragmentation **5d** for all the five LS $[\text{Fe}(\text{L}^{\text{azine}})_2(\text{NCBH}_3)_2]$ systems. First section (top) reports ΔE_{int} energy splitting; second section (middle) reports ΔE_{orb} energy splitting; third section (bottom) reports all the nine orbital interaction due to $M + L_6$ interaction.

	$L^4\text{pyrimidine}$	$L^2\text{pyrimidine}$	L^{pyridine}	L^{pyrazine}	$L^{\text{pyridazine}}$
ΔE_{int}	-870.6	-881.4	-869.0	-887.5	-870.6
ΔE_{Pauli}	261.4	262.9	260.3	265.0	268.6
ΔE_{elstat}	-617.1 (54.5%)	-619.4 (54.6%)	-625.9 (54.9%)	-615.6 (54.2%)	-629.6 (54.3%)
ΔE_{orb}	-505.0 (44.6%)	-504.6 (44.5%)	-506.2 (44.2%)	-508.8 (44.9%)	-517.1 (45.5%)
ΔE_{disp}	-9.6 (0.9%)	-9.5 (0.9%)	-9.7 (0.9%)	-9.6 (0.9%)	-9.4 (0.8%)
$\Delta E_{\text{orb},\sigma}$	-314.9 (62.4%)	-315.7 (62.6%)	-318.2 (62.8%)	-317.9 (62.5%)	-301.4 (58.2%)
$\Delta E_{\text{orb},\pi}$	-12.9 (2.6%)	-15.3 (3.0%)	-12.2 (2.4%)	-13.0 (2.6%)	-37.1 (7.1%)
$\Delta E_{\text{orb},\sigma+\pi}$	-327.7 (65.0%)	-331.0 (65.6%)	-330.4 (65.2%)	-330.9 (65.1%)	-338.4 (65.3%)
$\Delta E_{\text{orb},\text{pol}}$	-147.3 (29.1%)	-143.6 (28.5%)	-145.8 (28.9%)	-147.9 (29.1%)	-148.6 (28.8%)
$\Delta E_{\text{orb},\text{rest}}$	-31.0 (5.9%)	-33.8 (5.9%)	-30.8 (5.9%)	-30.9 (5.8%)	-31.6 (5.9%)
$\Delta E_{\text{orb},d_{z^2}}$	-118.9	-118.0	-117.1	-117.6	-110.4
$\Delta E_{\text{orb},d_{x^2-y^2}}$	-121.0	-122.5	-125.1	-124.4	-114.3
$\Delta E_{\text{orb},d_{zx}}$	+3.9	+4.3	+5.5	+4.5	-19.4
$\Delta E_{\text{orb},d_{zy}}$	-6.1	-5.3	-6.5	-6.8	-6.2
$\Delta E_{\text{orb},d_{xy}}$	-10.6	-14.3	-11.2	-10.7	-11.4
$\Delta E_{\text{orb},s}$	-23.4	-23.1	-24.0	-23.7	-23.3
$\Delta E_{\text{orb},pz}$	-19.0	-19.1	-19.6	-19.6	-20.5
$\Delta E_{\text{orb},px}$	-18.9	-19.4	-18.6	-19.5	-19.4
$\Delta E_{\text{orb},py}$	-13.7	-13.6	-13.8	-13.2	-13.4

Table A3.16. EDA-NOCV results (kcal/mol) reported for fragmentation **5e** for all the five LS $[Fe(L^{azine})_2(NCBH_3)_2]$ systems. First section (top) reports ΔE_{int} energy splitting; second section (middle) reports ΔE_{orb} energy splitting; third section (bottom) reports all the nine orbital interaction due to $M + L_6$ interaction.

	$L^{4pyrimidine}$	$L^{2pyrimidine}$	$L^{pyridine}$	$L^{pyrazine}$	$L^{pyridazine}$
ΔE_{int}	-505.1	-505.5	-516.0	-503.9	-522.4
ΔE_{Pauli}	631.0	632.3	630.0	634.5	638.0
ΔE_{elstat}	-622.4 (54.9%)	-624.7 (55.0%)	-631.1 (55.3%)	-620.9 (54.6%)	-634.9 (54.7%)
ΔE_{orb}	-504.1 (44.5%)	-503.6 (44.4%)	-505.2 (44.1%)	-507.8 (44.8%)	-516.1 (44.4%)
ΔE_{disp}	-9.6 (0.9%)	-9.5 (0.9%)	-9.7 (0.9%)	-9.6 (0.9%)	-9.4 (0.8%)
$\Delta E_{orb,\sigma}$	-321.3 (63.7%)	-322.1 (63.8%)	-325.0 (64.4%)	-324.2 (63.8%)	-308.5 (59.7%)
$\Delta E_{orb,\pi}$	-0.2 (0.0%)	+0.6 (- 0.1%)	+0.1 (0.0%)	-0.7 (- 0.1%)	-23.4 (4.5%)
$\Delta E_{orb,\sigma+\pi}$	-321.5 (63.7%)	-321.4 (63.7%)	-324.9 (64.4%)	-324.9 (63.7%)	-331.9 (64.1%)
$\Delta E_{orb,pol}$	-152.5 (30.4%)	-152.2 (30.2%)	-150.3 (29.7%)	-156.3 (30.7%)	-164.6 (32.0%)
$\Delta E_{orb,rest}$	-31.4 (5.9%)	-35.5 (5.9%)	-31.1 (5.9%)	-31.2 (5.6%)	-32.0 (5.9%)
$\Delta E_{orb,dz^2}$	-124.2	-123.2	-122.1	-122.9	-117.1
$\Delta E_{orb,dx^2-y^2}$	-126.3	-128.0	-130.5	-130.0	-119.2
$\Delta E_{orb,dzx}$	+10.2	+10.5	+11.7	+11.1	-12.2
$\Delta E_{orb,dzy}$	-2.3	-1.3	-2.7	-3.0	-2.4
$\Delta E_{orb,dxy}$	-8.1	-8.5	-8.9	-8.9	-8.7
$\Delta E_{orb,s}$	-23.0	-22.7	-24.1	-23.5	-23.3
$\Delta E_{orb,pz}$	-19.2	-19.8	-19.7	-19.6	-19.6
$\Delta E_{orb,px}$	-14.8	-14.7	-14.6	-14.9	-16.0
$\Delta E_{orb,py}$	-13.8	-13.7	-13.9	-13.3	-13.4

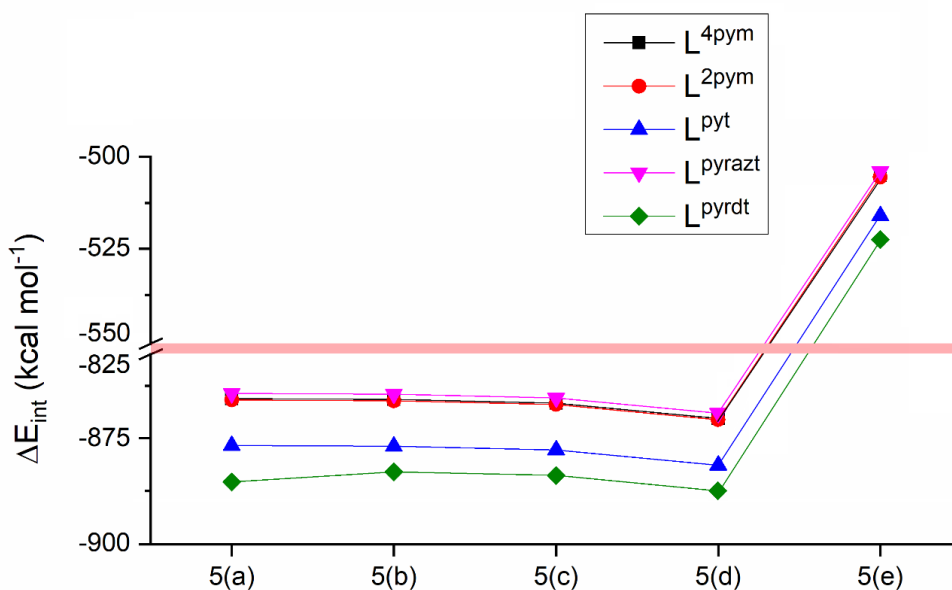


Figure A3.15. Trend of ΔE_{int} energy contribution (kcal/mol) for each of the five LS $[\text{Fe}(\text{L}^{\text{azine}})_2(\text{NCBH}_3)_2]$ systems across the five sub fragmentations 5a-5e.

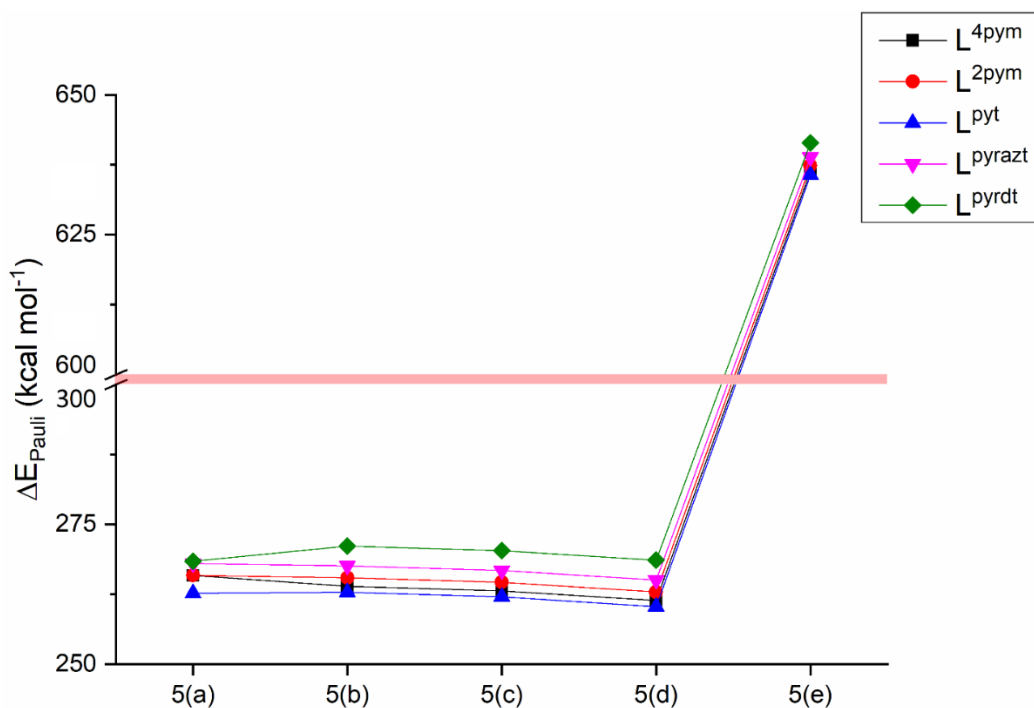


Figure A3.16. Trend of ΔE_{Pauli} energy contribution (kcal/mol) for each of the five LS $[\text{Fe}(\text{L}^{\text{azine}})_2(\text{NCBH}_3)_2]$ systems across the five sub fragmentations 5a-5e.

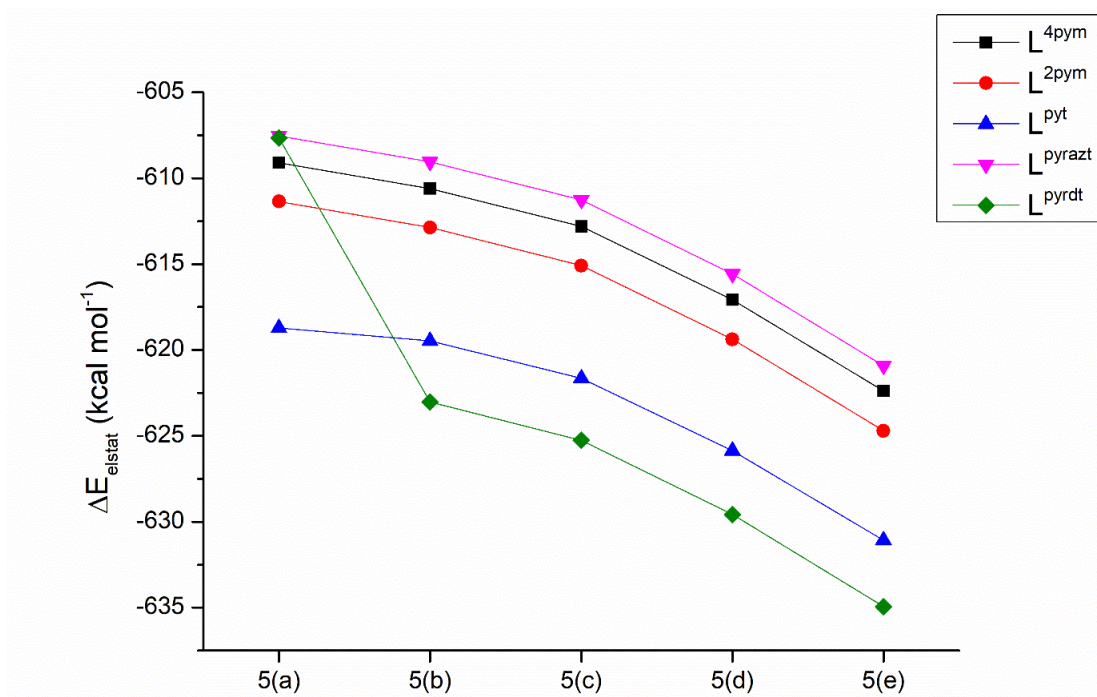


Figure A3.17. Trend of ΔE_{elstat} energy contribution (kcal/mol) for each of the five LS $[Fe(L^{azine})_2(NCBH_3)_2]$ systems across the five sub fragmentations 5a-5e.

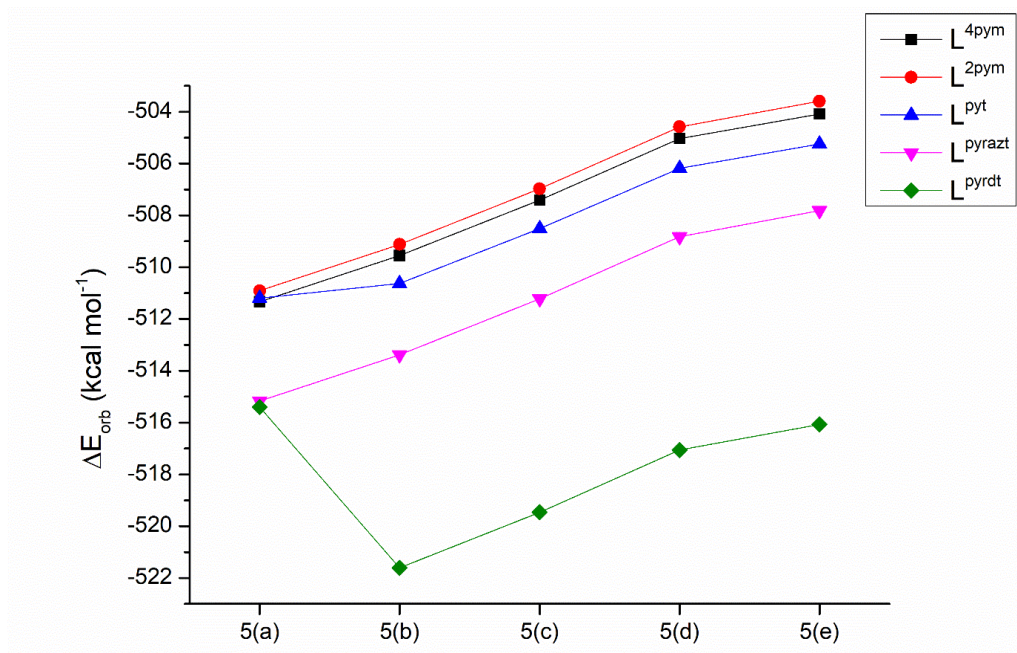


Figure A3.18. Trend of ΔE_{orb} energy contribution (kcal/mol) for each of the five LS $[Fe(L^{azine})_2(NCBH_3)_2]$ systems across the five sub fragmentations 5a-5e.

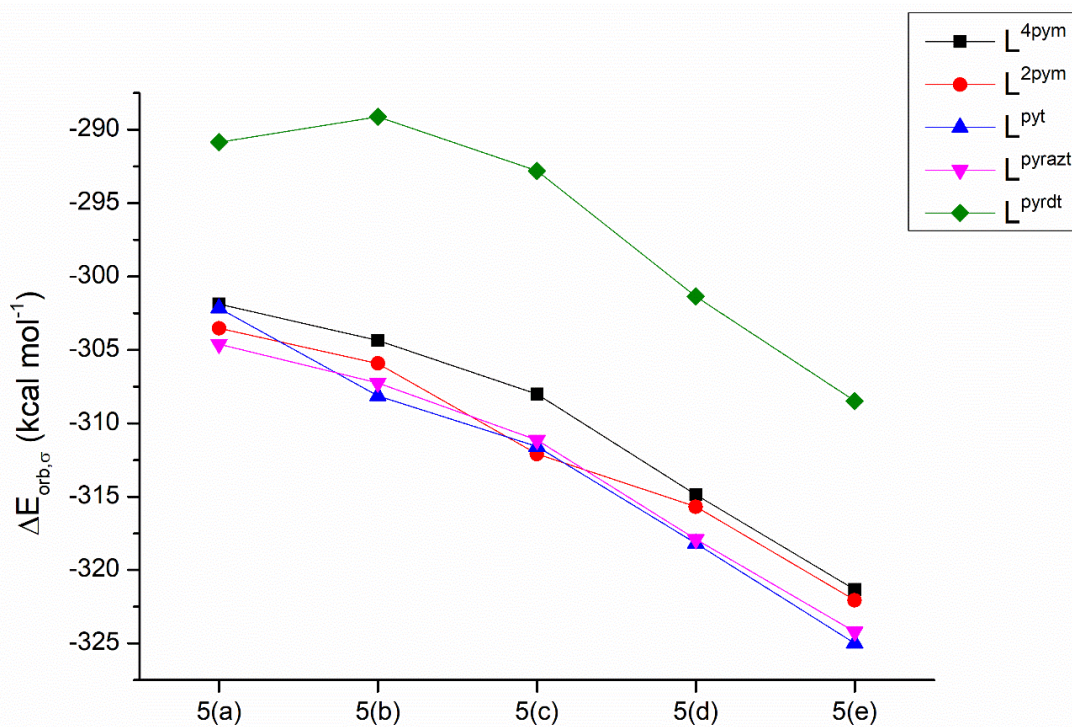


Figure A3.19. Trend of $\Delta E_{orb,\sigma}$ energy contribution (kcal/mol) for each of the five LS $[\text{Fe}(\text{L}^{azine})_2(\text{NCBH}_3)_2]$ systems across the five sub fragmentations 5a-5e.

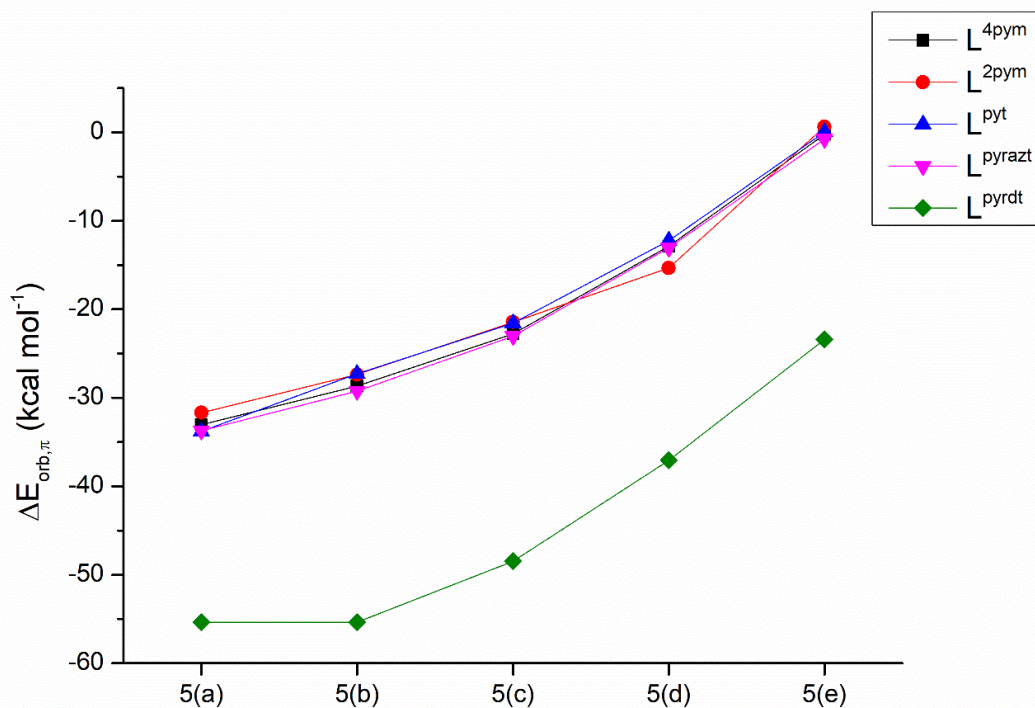


Figure A3.20. Trend of $\Delta E_{orb,\pi}$ energy contribution (kcal/mol) for each of the five LS $[\text{Fe}(\text{L}^{azine})_2(\text{NCBH}_3)_2]$ systems across the five sub fragmentations 5a-5e.

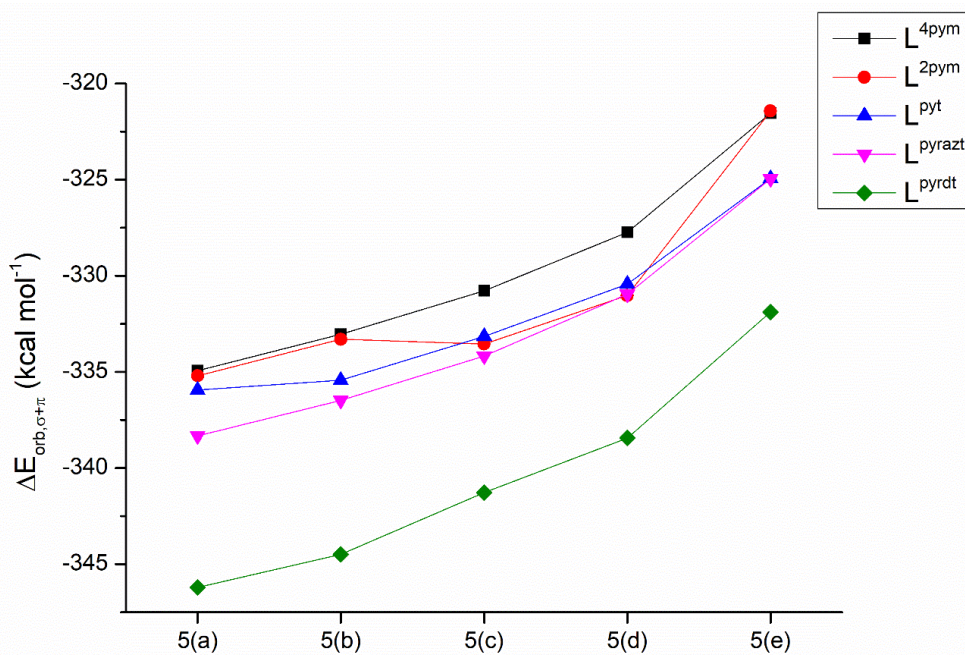


Figure A3.21. Trend of $\Delta E_{orb,\sigma+\pi}$ energy contribution (kcal/mol) for each of the five LS $[Fe(L^{azine})_2(NCBH_3)_2]$ systems across the five sub fragmentations 5a-5e.

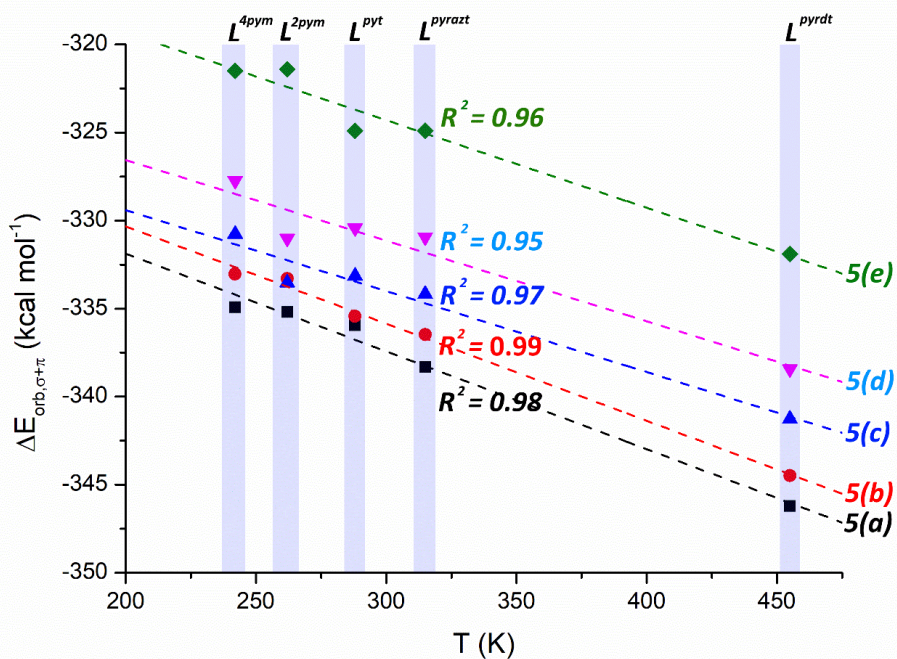


Figure A3.22. Correlation lines observed for $\Delta E_{orb,\sigma+\pi}$ energy contribution (kcal/mol) across the LS $[Fe(L^{azine})_2(NCBH_3)_2]$ family in the five sub fragmentations 5a-5e.

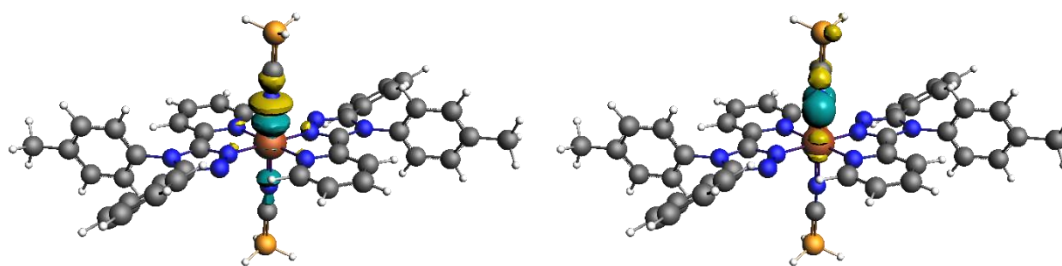
A3.3. EDA-NOCV Results

A3.3.1. Frag. 1 - LS Fe^{II}(L^{azine})₂(NCBH₃)₂

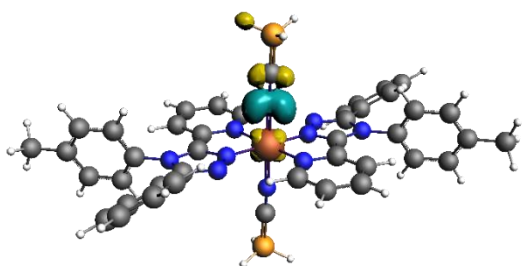
Table A3.17. Summary EDA-NOCV results (kcal/mol) for fragmentation 1 for all the five LS [Fe(L^{azine})₂(NCBH₃)₂] systems. Fragmentation 1 describes interaction between one of the axial coligands NCBH₃ with the remaining ML₅ system. First section (top) reports ΔE_{int} energy splitting; second section (middle) reports ΔE_{orb} energy splitting; third section (bottom) reports all the orbital interaction due to ML₅ + L interaction.

	L ⁴ pyrimidine	L ² pyrimidine	L ^{pyridine}	L ^{pyrazine}	L ^{pyridazine}
ΔE_{int}	-108.1	-108.3	-103.4	-110.0	-105.0
ΔE_{Pauli}	106.9	106.9	107.2	107.0	106.5
ΔE_{elstat}	-147.2 (68.4%)	-147.5 (68.4%)	-143.6 (68.1%)	-148.8 (68.8%)	-143.7 (67.7%)
ΔE_{orb}	-63.5 (29.5%)	-63.5 (29.5%)	-62.7 (30.0%)	-64.0 (29.5%)	-63.4 (29.9%)
ΔE_{disp}	-4.2 (2.1%)	-4.2 (2.1%)	-4.3 (2.9%)	-4.3 (1.8%)	-4.4 (2.4%)
$\Delta E_{orb,\sigma}$	-36.0 (56.3%)	-36.0 (56.3%)	-35.6 (57.1%)	-36.4 (56.3%)	-36.3 (57.1%)
$\Delta E_{orb,\pi}$	-12.3 (19.4%)	-12.3 (19.4%)	-12.3 (19.6%)	-12.2 (19.4%)	-11.9 (19.4%)
$\Delta E_{orb,\sigma+\pi}$	-48.3 (75.7%)	-48.3 (75.7%)	-47.9 (76.7%)	-48.6 (75.7%)	-48.2 (76.5%)
$\Delta E_{orb,pol}$	-7.9 (13.2%)	-8.4 (13.4%)	-9.7 (13.3%)	-8.5 (13.2%)	-7.8 (12.4%)
$\Delta E_{orb,rest}$	-7.3 (11.1%)	-6.8 (10.9%)	-5.1 (10.0%)	-6.9 (11.1%)	-7.4 (11.1%)
$\Delta E_{orb,dz^2}$	-36.0	-36.0	-35.6	-36.4	-36.3
$\Delta E_{orb,dzx}$	-6.3	-6.3	-6.3	-6.3	-6.1
$\Delta E_{orb,dzy}$	-6.0	-6.0	-6.0	-6.0	-5.8

Figure A3.23. Plot of the deformation densities $\Delta\rho^{(i)}$ in fragmentation **1** with corresponding energy contribution to the total orbital term ΔE (given in kcal/mol) of the $[TM]\leftarrow$ ligand σ -donation, the $[TM]\rightarrow$ ligand π -backdonation in reference complex LS $[\text{Fe}(\text{L}^{\text{pyridine}})_2(\text{NCBH}_3)_2]$. The direction of the charge flow is yellow \rightarrow turquoise. The eigenvalues $|v_i|$ indicate the relative size of the charge flow. Deformation densities describing bond interaction are reported using cut-off on $\Delta\rho^{(i)}=0.003$. The choice of cut-off on deformation densities used to produce these images does not affect the results; as EDA-NOCV analysis are performed by applying default cut-off on NOCVs energies (0.5 kcal/mol) and individual SFO contribution (0.001).



$$\Delta\rho^{(1)} \Delta E_1 = -35.6, |v_1| = 0.57 (d_{[TM]\leftarrow\text{ligand}} \sigma) \quad \Delta\rho^{(2)} \Delta E_2 = -6.3, |v_2| = 0.25 (d_{[TM]\rightarrow\text{ligand}} \pi)$$



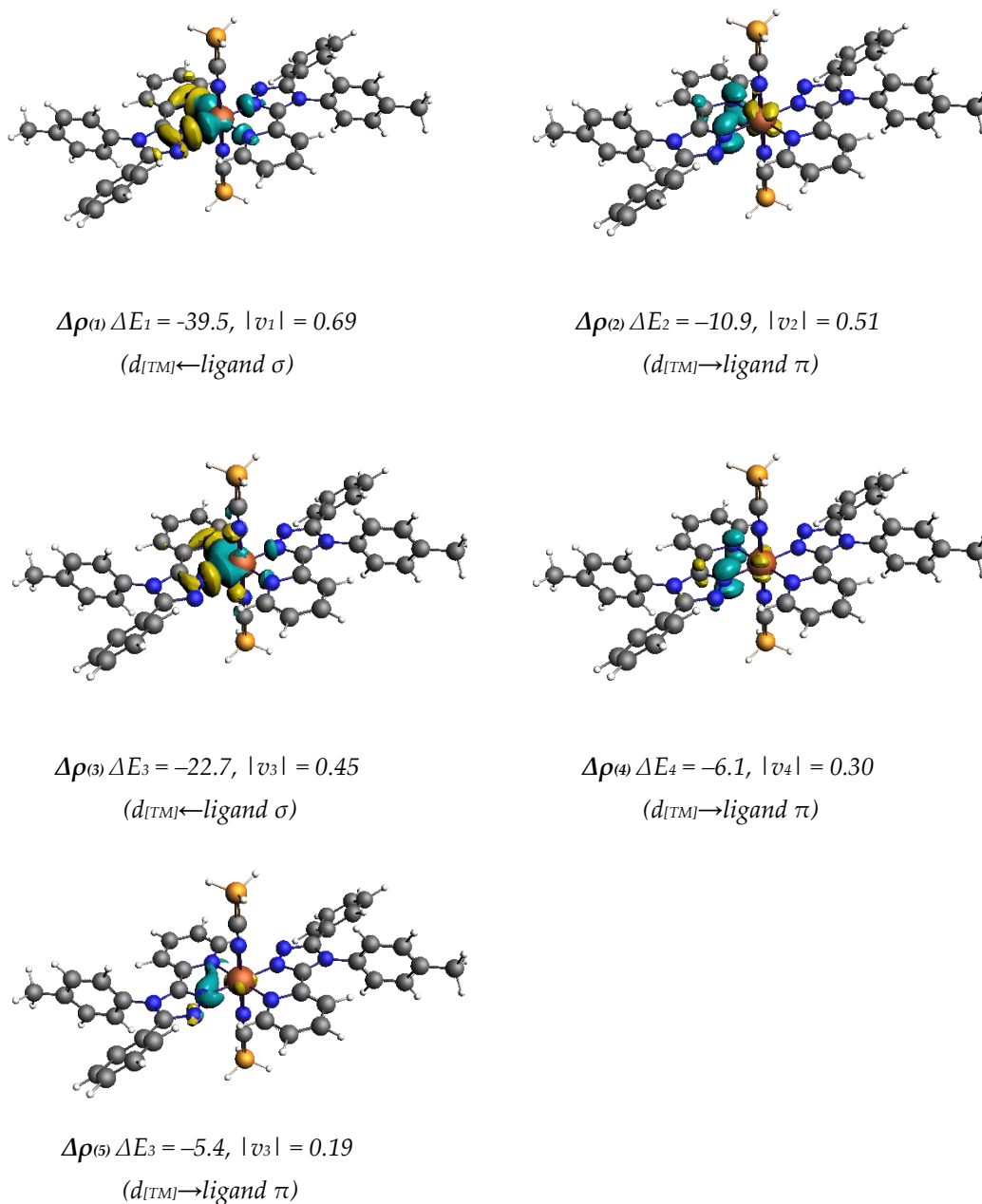
$$\Delta\rho^{(3)} \Delta E_3 = -6.0, |v_3| = 0.24 (d_{[TM]\rightarrow\text{ligand}} \pi)$$

A1.2.3. Frag. 2 - LS Fe^{II}(L^{azine})₂(NCBH₃)₂

Table A3.18. Summary EDA-NOCV results (kcal/mol) for fragmentation 2 for all the five LS [Fe(L^{azine})₂(NCBH₃)₂] systems. Fragmentation (2) describes interaction between one of the equatorial ligands L^{azine} with the remaining ML₅ system. First section (top) reports ΔE_{int} energy splitting; second section (middle) reports ΔE_{orb} energy splitting; third section (bottom) reports all the orbital interaction due to ML₄ + L₂ interaction.

	L ⁴ pyrimidine	L ² pyrimidine	Lpyridine	Lpyrazine	Lpyridazine
ΔE_{int}	-89.4	-91.0	-90.3	-91.2	-83.4
ΔE_{Pauli}	174.2	175.6	174.1	178.4	168.7
ΔE_{elstat}	-148.2 (56.3%)	-150.2 (56.4%)	-148.7 (56.4%)	-151.3 (55.9%)	-138.3 (55.0%)
ΔE_{orb}	-101.3 (38.4%)	-102.4 (38.3%)	-101.5 (38.3%)	-104.2 (38.5%)	-100.8 (39.8%)
ΔE_{disp}	-14.0 (5.3%)	-14.0 (5.3%)	-14.3 (5.3%)	-14.2 (5.6%)	-12.9 (5.2%)
$\Delta E_{orb,\sigma}$	-62.6 (62.4%)	-62.9 (61.8%)	-62.2 (60.8%)	-63.7 (61.3%)	-64.3 (63.6%)
$\Delta E_{orb,\pi}$	-22.6 (22.3%)	-22.9 (22.5%)	-22.4 (21.6%)	-23.5 (22.1%)	-24.7 (24.7%)
$\Delta E_{orb,\sigma+\pi}$	-85.2 (84.7%)	-85.7 (84.3%)	-84.6 (82.4%)	-87.2 (83.4%)	-89.0 (88.3%)
$\Delta E_{orb,pol}$	11.1 (10.3%)	12.0 (11.1%)	12.1 (12.9%)	15.3 (7.8%)	7.1 (7.0%)
$\Delta E_{orb,rest}$	-5.0 (5.0%)	-4.7 (4.6%)	-4.8 (4.7%)	-4.7 (4.8%)	-4.7 (4.7%)
$\Delta E_{orb,dz^2}$	-22.8	-22.8	-22.7	-23.0	-22.8
$\Delta E_{orb,dx^2-y^2}$	-39.9	-40.1	-39.5	-40.7	-41.5
$\Delta E_{orb,dzx}$	-11.0	-10.8	-10.9	-11.4	-12.4
$\Delta E_{orb,dzy}$	-6.1	-6.5	-6.1	-6.5	-6.6
$\Delta E_{orb,dxy}$	-5.6	-5.5	-5.4	-5.5	-5.7

Figure A3.24. Plot of the deformation densities $\Delta\rho^{(i)}$ in fragmentation 2 with corresponding energy contribution to the total orbital term ΔE (given in kcal/mol) of the $[\text{TM}]\leftarrow\text{ligand}$ σ -donation, the $[\text{TM}]\rightarrow\text{ligand}$ π -backdonation in reference complex LS $[\text{Fe}(\text{Lpyridine})_2(\text{NCBH}_3)_2]$. The direction of the charge flow is yellow \rightarrow turquoise. The eigenvalues $|v|$ indicate the relative size of the charge flow. Deformation densities describing bond interaction are reported using cut-off on $\Delta\rho^{(i)}=0.003$. The choice of cut-off on deformation densities used to produce these images does not affect the results; as EDA-NOCV analysis are performed by applying default cut-off on NOCVs energies (0.5 kcal/mol) and individual SFO contribution (0.001).

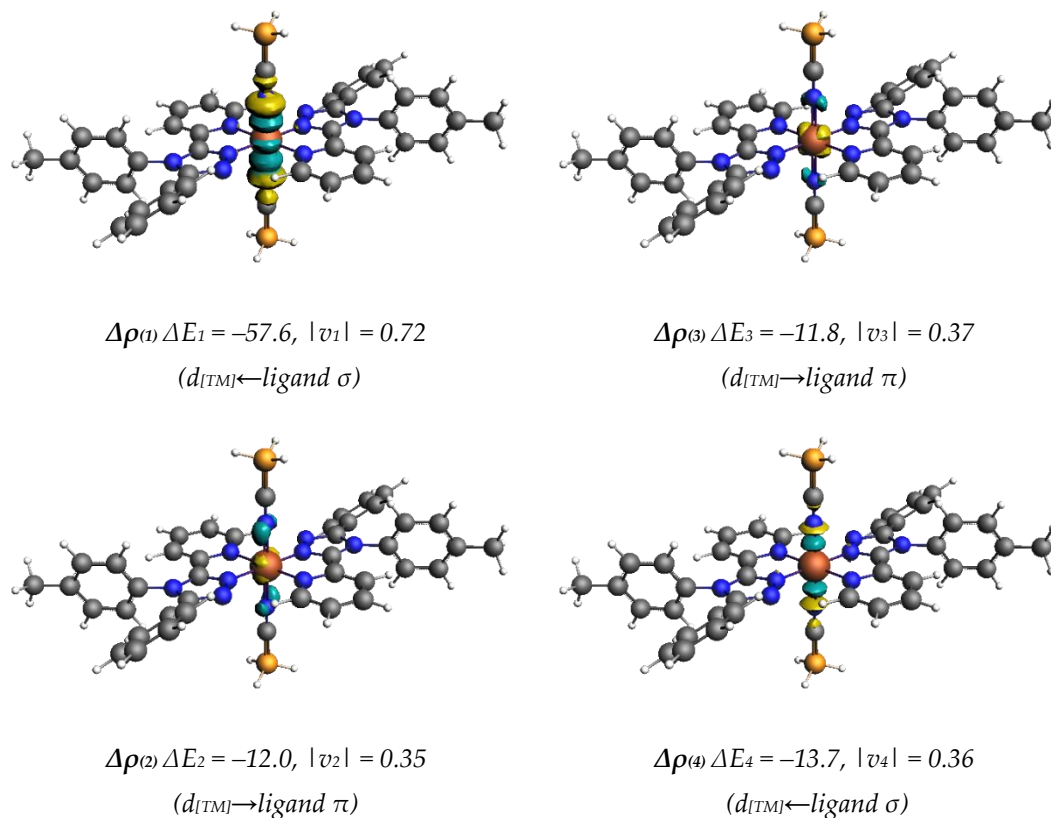


A3.3.2. Frag. 3 - LS Fe^{II}(Lazine)₂(NCBH₃)₂

Table A3.19. Summary EDA-NOCV results (kcal/mol) for fragmentation 3 for all the five LS [Fe(L^{azine})₂(NCBH₃)₂] systems. Fragmentation (3) describes interaction between one of both axial coligands 2xNCBH₃ with the remaining ML₄ system. First section (top) reports ΔE_{int} energy splitting; second section (middle) reports ΔE_{orb} energy splitting; third section (bottom) reports all the orbital interaction due to ML₄ + L₂ interaction.

	L ⁴ pyrimidine	L ² pyrimidine	L ^{pyridine}	L ^{pyrazine}	L ^{pyridazine}
ΔE _{int}	-345.9	-346.1	-335.9	-349.7	-337.7
ΔE _{Pauli}	176.1	176.4	170.6	177.6	179.4
ΔE _{elstat}	-377.4 (72.2%)	-378.0 (72.3%)	-370.3 (72.1%)	-380.7 (72.1%)	-370.8 (71.8%)
ΔE _{orb}	-132.3 (25.3%)	-132.4 (25.2%)	-129.9 (25.3%)	-134.4 (25.7%)	-134.2 (25.9%)
ΔE _{disp}	-12.2 (2.5%)	-12.2 (2.5%)	-12.3 (2.6%)	-12.3 (2.2%)	-12.1 (2.3%)
ΔE _{orb,σ}	-72.4 (54.8%)	-72.3 (54.6%)	-71.3 (54.6%)	-74.2 (55.2%)	-75.0 (55.9%)
ΔE _{orb,π}	-23.3 (17.4%)	-23.6 (17.8%)	-23.8 (18.3%)	-23.5 (17.5%)	-23.1 (17.2%)
ΔE _{orb,σ+π}	-95.7 (72.2%)	-95.9 (72.4%)	-95.0 (72.9%)	-97.7 (72.7%)	-98.1 (72.1%)
ΔE _{orb,pol}	28.3 0 (21.6%)	28.3 (21.6%)	27.4 (21.1%)	27.6 (20.8%)	27.1 (21.2%)
ΔE _{orb,rest}	8.2 (6.2%)	8.2 (6.2%)	-7.6 (5.8%)	-8.7 (6.5%)	-9.0 (6.7%)
ΔE _{orb,dz2}	-58.4	-58.4	-57.6	-60.0	-61.1
ΔE _{orb,dzx}	-11.3	-11.8	-11.8	-11.6	-11.5
ΔE _{orb,dzy}	-12.0	-11.8	-12.0	-11.9	-11.5
ΔE _{orb,pz}	-14.0	-13.9	-13.7	-14.2	-14.0

Figure A3.25. Plot of the deformation densities $\Delta\rho^{(i)}$ in fragmentation 4 with corresponding energy contribution to the total orbital term ΔE (given in kcal/mol) of the $[TM]\leftarrow$ ligand σ -donation, the $[TM]\rightarrow$ ligand π -backdonation in reference complex LS $[\text{Fe}(\text{L}^{\text{pyridine}})_2(\text{NCBH}_3)_2]$. The direction of the charge flow is yellow \rightarrow turquoise. The eigenvalues $|v|$ indicate the relative size of the charge flow. Deformation densities describing bond interaction are reported using cut-off on $\Delta\rho^{(i)}=0.003$. The choice of cut-off on deformation densities used to produce these images does not affect the results; as EDA-NOCV analysis are performed by applying default cut-off on NOCVs energies (0.5 kcal/mol) and individual SFO contribution (0.001).

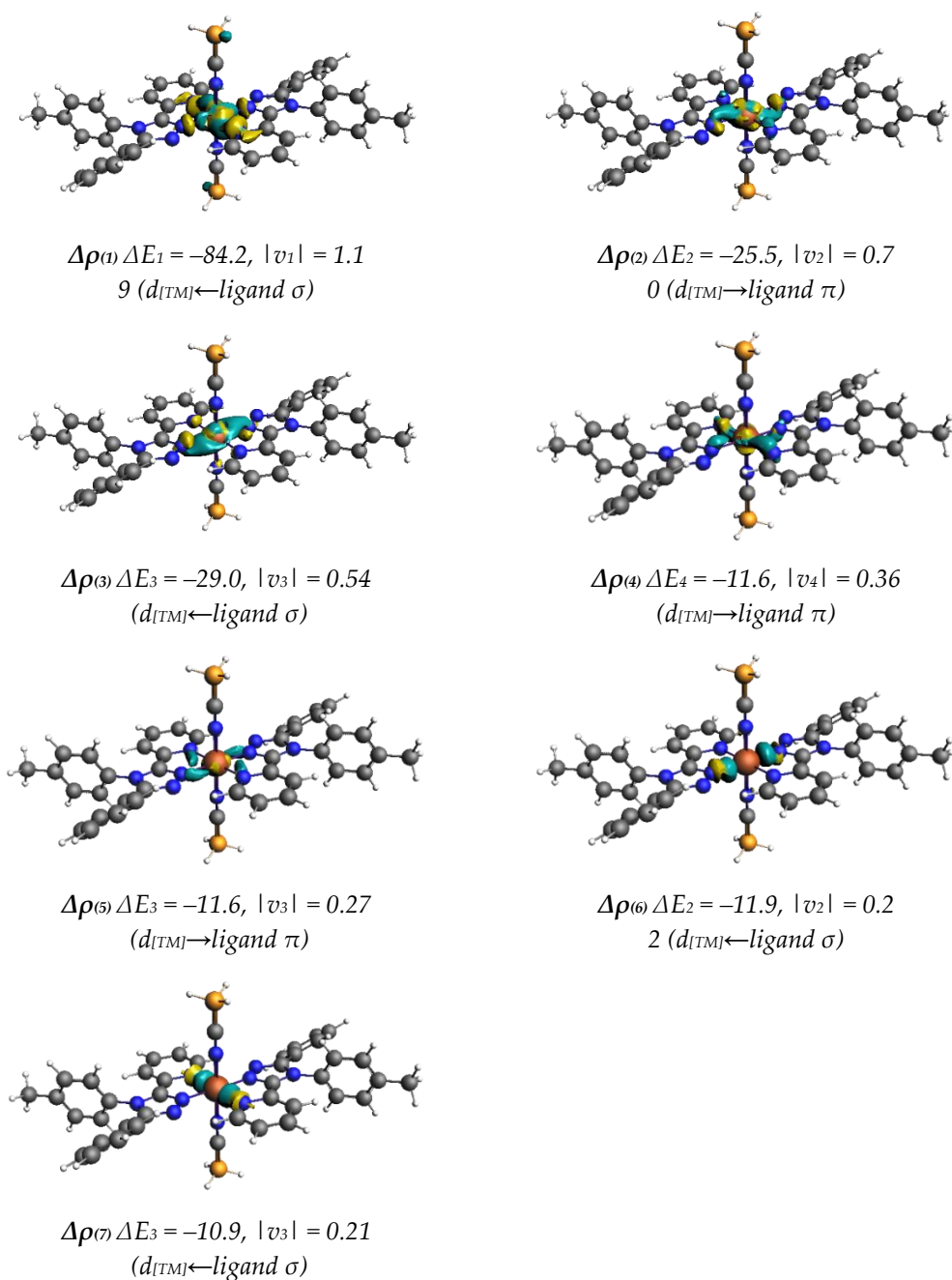


A3.3.3. Frag. 4 - LS Fe^{II}(L^{azine})₂(NCBH₃)₂

Table A3.20. Summary EDA-NOCV results (kcal/mol) for fragmentation 4 for all the five LS [Fe(L^{azine})₂(NCBH₃)₂] systems. Fragmentation 4 describes interaction between one of both equatorial ligands 2xL^{azine} with the remaining ML₄ system. First section (top) reports ΔE_{int} energy splitting; second section (middle) reports ΔE_{orb} energy splitting; third section (bottom) reports all the orbital interaction due to ML₂ + L₄ interaction.

	L ⁴ pyrimidine	L ² pyrimidine	L ^{pyridine}	L ^{pyrazine}	L ^{pyridazine}
ΔE _{int}	-228.1	-228.3	-233.0	-229.7	-238.8
ΔE _{Pauli}	260.7	262.6	257.5	265.3	270.7
ΔE _{elstat}	-250.9 (51.4%)	-252.3 (51.3%)	-252.3 (51.3%)	-253.1 (51.1%)	-259.3 (40.1%)
ΔE _{orb}	-218.4 (44.7%)	-219.1 (44.6%)	-218.3 (44.4%)	-222.2 (44.8%)	-231.0 (45.4%)
ΔE _{disp}	-19.4 (3.9%)	-19.5 (4.1%)	-19.7 (4.3%)	-19.7 (4.1%)	-19.2 (4.6%)
ΔE _{orb,σ}	-134.9 (61.8%)	-134.6 (61.5%)	-136.0 (62.4%)	-139.4 (62.7%)	-141.9 (61.4%)
ΔE _{orb,π}	-48.8 (22.3%)	-49.6 (22.6%)	-49.2 (22.6%)	-46.6 (21.0%)	-51.6 (22.3%)
ΔE _{orb,σ+π}	-183.6 (84.1%)	-184.2 (84.1%)	-185.2 (85.0%)	-186.0 (83.7%)	-193.5 (83.7%)
ΔE _{orb,pol}	-19.6 (9.0%)	-19.8 (9.0%)	-18.1 (8.3%)	-20.7 (9.3%)	-21.4 (9.3%)
ΔE _{orb,rest}	-15.2 (6.9%)	-15.1 (6.9%)	-15.0 (6.9%)	-15.5 (7.0%)	-16.1 (7.0%)
ΔE _{orb,dz2}	-30.1	-29.2	-29.0	-33.4	-33.0
ΔE _{orb,dx2-y2}	-82.8	-83.6	-84.2	-84.6	-87.2
ΔE _{orb,dzx}	-24.5	-24.0	-25.5	-21.5	-26.8
ΔE _{orb,dzy}	-12.2	-11.9	-11.6	-12.1	-11.3
ΔE _{orb,dxy}	-12.1	-11.9	-11.6	-12.1	-11.3
ΔE _{orb,px}	-12.0	-11.9	-11.9	-11.5	-11.2
ΔE _{orb,py}	-10.1	-9.9	-10.9	-9.9	-10.5

Figure A3.26. Plot of the deformation densities $\Delta\rho^{(i)}$ in fragmentation (4) with corresponding energy contribution to the total orbital term ΔE (given in kcal/mol) of the $[TM]\leftarrow$ ligand σ -donation, the $[TM]\rightarrow$ ligand π -backdonation in reference complex LS $[\text{Fe}(\text{Lpyridine})_2(\text{NCBH}_3)_2]$. The direction of the charge flow is yellow \rightarrow turquoise. The eigenvalues $|v_i|$ indicate the relative size of the charge flow. Deformation densities describing bond interaction are reported using cut-off on $\Delta\rho^{(i)}=0.003$. The choice of cut-off on deformation densities used to produce these images does not affect the results; as EDA-NOCV analysis are performed by applying default cut-off on NOCVs energies (0.5 kcal/mol) and individual SFO contribution (0.001).

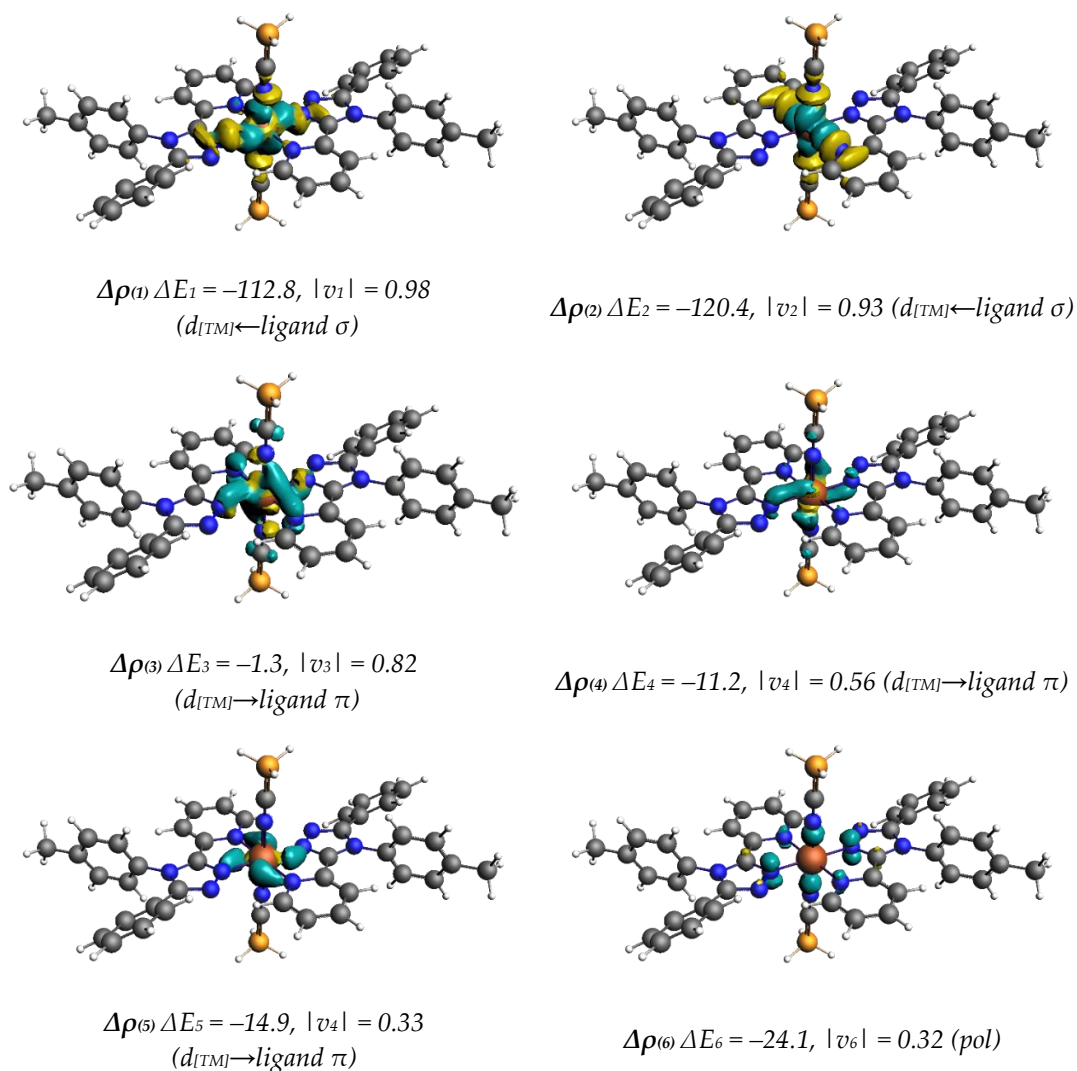


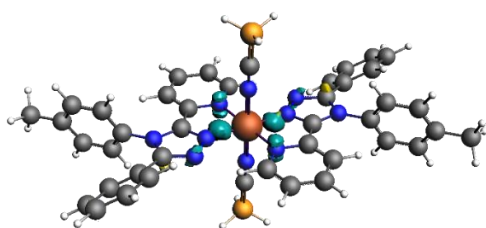
A3.3.4. Frag. 5b/5e - LS Fe^{II}(L^{azine})₂(NCBH₃)₂

Table A3.21. EDA-NOCV results (kcal/mol) reported for fragmentation 5b-5e for all the five LS Fe^{II}(L^{azine})₂(NCBH₃)₂ systems. First section (top) reports ΔE_{int} energy splitting 5e; second section (middle) reports ΔE_{orb} energy splitting; third section (bottom) reports all the nine orbital interaction due to M - L₆ interaction 5b.

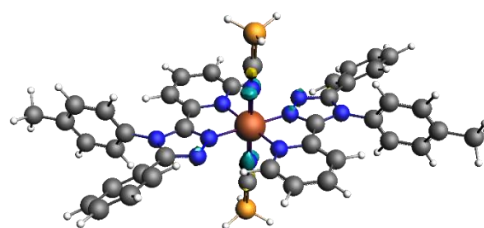
	L ⁴ pyrimidine	L ² pyrimidine	L ¹ pyridine	L ¹ pyrazine	L ¹ pyridazine
ΔE_{int}	-505.1	-505.5	-516.0	-503.9	-522.4
ΔE_{Pauli}	631.0	632.3	630.0	634.5	638.0
ΔE_{elstat}	-622.4 (54.9%)	-624.7 (55.0%)	-631.1 (55.3%)	-620.9 (54.6%)	-634.9 (54.7%)
ΔE_{orb}	-504.1 (44.5%)	-503.6 (44.4%)	-505.2 (44.1%)	-507.8 (44.8%)	-516.1 (44.4%)
ΔE_{disp}	-9.6 (0.6%)	-9.5 (0.6%)	-9.7 (0.6%)	-9.6 (0.6%)	-9.4 (0.9%)
$\Delta E_{orb,\sigma}$	-304.3 (59.6%)	-305.9 (60.1%)	-308.1 (60.3%)	-307.3 (60.4%)	-289.1 (56.4%)
$\Delta E_{orb,\pi}$	-28.7 (5.7%)	-27.4 (5.3%)	-27.3 (5.3%)	-29.2 (4.7%)	-55.4 (8.8%)
$\Delta E_{orb,\sigma+\pi}$	-333.0 (65.3%)	-333.3 (65.4%)	-335.4 (65.6%)	-336.5 (65.1%)	-344.5 (65.2%)
$\Delta E_{orb,pol}$	-146.5 (28.6%)	-145.8 (28.7%)	-145.2 (28.4%)	-146.9 (24.1%)	-146.6 (23.6%)
$\Delta E_{orb,rest}$	-30.6 (5.9%)	-33.5 (5.9%)	-31.6 (6.0%)	-30.5 (5.8%)	-31.3 (4.9%)
$\Delta E_{orb,dz2}$	-113.8	-113.4	-112.8	-112.5	-102.2
$\Delta E_{orb,dx2-y2}$	-116.3	-117.7	-120.4	-119.3	-110.3
$\Delta E_{orb,dzx}$	-3.4	-2.6	-1.3	-3.2	-29.2
$\Delta E_{orb,dzy}$	-10.8	-10.1	-11.2	-11.5	-10.9
$\Delta E_{orb,dxy}$	-14.6	-14.7	-14.9	-14.6	-15.3
$\Delta E_{orb,s}$	-23.4	-23.2	-23.8	-23.6	-23.3
$\Delta E_{orb,pz}$	-18.8	-19.4	-19.3	-19.8	-21.3
$\Delta E_{orb,px}$	-18.6	-19.0	-19.3	-19.1	-19.0
$\Delta E_{orb,py}$	-13.4	-13.3	-13.5	-12.9	-13.1

Figure A3.27. Plot of the deformation densities $\Delta\rho^{(i)}$ in fragmentation **5b** with corresponding energy contribution to the total orbital term ΔE (given in kcal/mol) of the $[TM]\leftarrow$ ligand σ -donation, the $[TM]\rightarrow$ ligand π -backdonation and polarisation in reference complex LS $[\text{Fe}(\text{Lpyridine})_2(\text{NCBH}_3)_2]$. The direction of the charge flow is yellow \rightarrow turquoise. The eigenvalues $|v_i|$ indicate the relative size of the charge flow. Figures are reported using until $|v_i| = 0.1$ with cut-off on $\Delta\rho^{(i)}=0.003$. The choice of cut-off on deformation densities used to produce these images does not affect the results; as EDA-NOCV analysis are performed by applying default cut-off on NOCVs energies (0.5 kcal/mol) and individual SFO contribution (0.001).

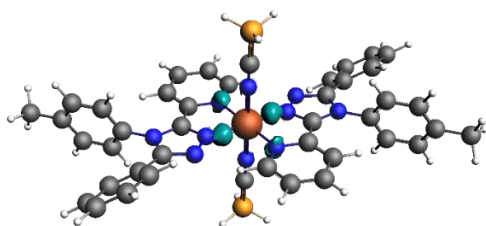




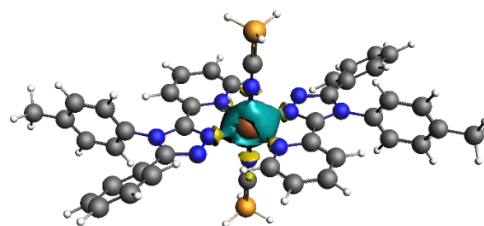
$$\Delta\rho_{(7)} \Delta E_7 = -20.2, |v_7| = 0.30 \text{ (pol)}$$



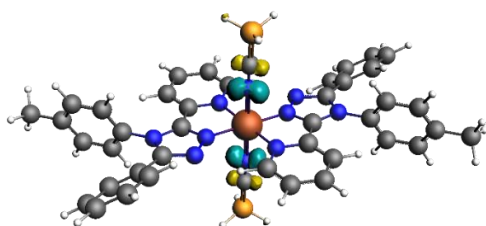
$$\Delta\rho_{(8)} \Delta E_8 = -16.1, |v_8| = 0.27 \text{ (pol)}$$



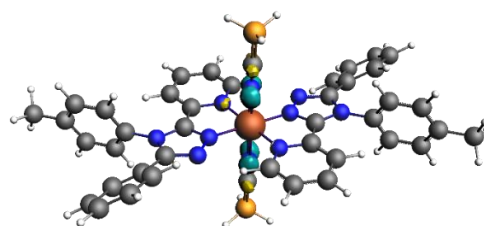
$$\Delta\rho_{(9)} \Delta E_9 = -19.3, |v_9| = 0.26 \\ (p_{[TM]} \leftarrow \text{ligand } \sigma)$$



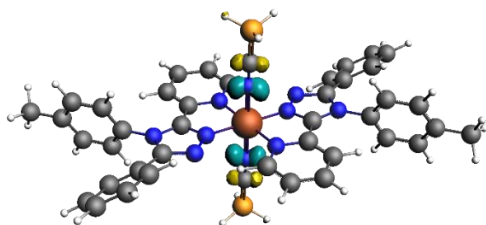
$$\Delta\rho_{(10)} \Delta E_{10} = -23.8, |v_{10}| = 0.24 \text{ (} p_{[TM]} \leftarrow \text{ligand } \sigma)$$



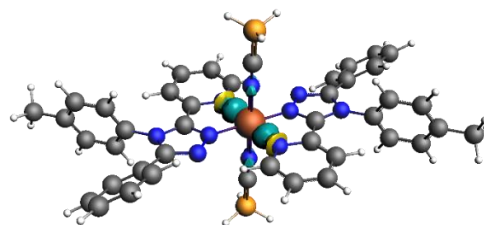
$$\Delta\rho_{(11)} \Delta E_{11} = -15.5, |v_{11}| = 0.23 \text{ (pol)}$$



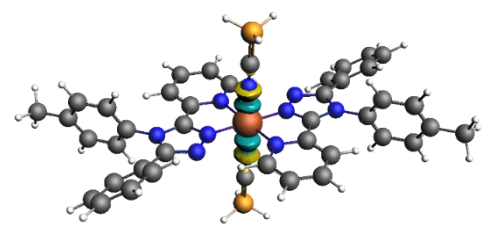
$$\Delta\rho_{(12)} \Delta E_{12} = -17.0, |v_{12}| = 0.22 \text{ (pol)}$$



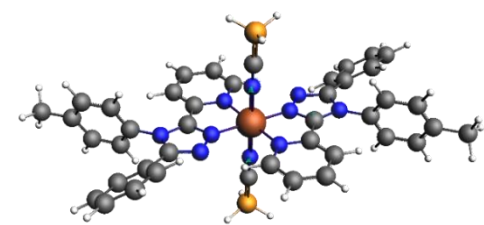
$$\Delta\rho_{(13)} \Delta E_{13} = -16.0, |v_{13}| = 0.22 \text{ (pol)}$$



$$\Delta\rho_{(14)} \Delta E_{14} = -17.0, |v_{14}| = 0.21 \\ (p_{[TM]} \leftarrow \text{ligand } \sigma)$$



$$\Delta\rho_{(15)} \Delta E_{15} = -13.5, |v_{15}| = 0.17 \\ (p_{[TM]} \leftarrow \text{ligand } \sigma)$$



$$\Delta\rho_{(16)} \Delta E_{16} = -6.3, |v_{16}| = 0.15 \text{ (pol)}$$

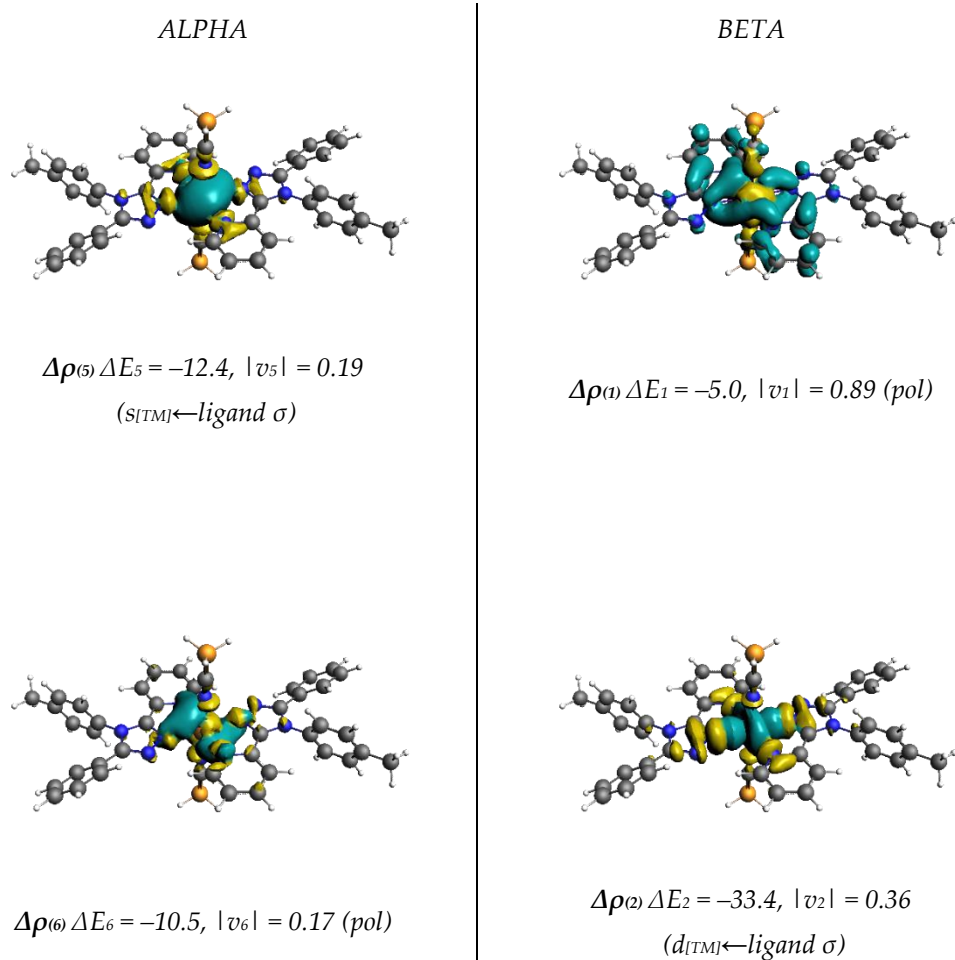
A3.3.5. Frag. 5b/5e - HS Fe^{II}(L^{azine})₂(NCBH₃)₂

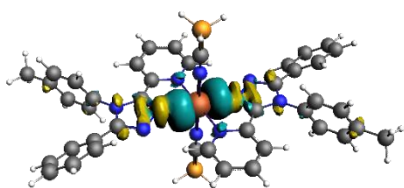
Table A3.22. EDA-NOCV results (kcal/mol) reported for fragmentation 5b-5e for all the five HS Fe(L^{azine})₂(NCBH₃)₂. First section (top) reports ΔE_{int} energy splitting 5e; second section (middle) reports ΔE_{orb} energy splitting; third section (bottom) reports all the nine orbital interaction due to M - L₆ interaction 5b.

	L ⁴ pyrimidine	L ² pyrimidine	L ^{pyridine}	L ^{pyrazine}	L ^{pyridazine}
ΔE_{int}	-370.29	-369.34	-380.45	-367.96	-385.49
ΔE_{Pauli}	544.31	544.33	543.52	547.15	539.3
ΔE_{elstat}	-573.4 (62.7%)	-574.3 (62.9%)	-582.4 (63.0%)	-571.8 (62.5%)	-583.5 (63.10%)
ΔE_{orb}	-327.9 (35.9%)	-326.2 (35.7%)	-328.1 (35.5%)	-329.9 (36.1%)	-328.4 (35.5%)
ΔE_{disp}	-13.3 (1.48%)	-13.2 (1.48%)	-13.4 (1.48%)	-13.4 (1.49%)	-12.9 (1.42%)
$\Delta E_{orb,\sigma} [\alpha+\beta]$	-145.5 (44.61%)	-145.4 (44.80%)	-145.6 (44.60%)	-149.4 (45.49%)	-155.6 (47.68%)
$\Delta E_{orb,\pi} [\alpha+\beta]$	-3.4 (1.04%)	-3.4 (1.06%)	-3.5 (1.06%)	-3.34 (1.02%)	-3.2 (0.98%)
$\Delta E_{orb,\sigma+\pi} [\alpha+\beta]$	-148.9 (45.65%)	-148.8 (45.86%)	-149.1 (45.66%)	-152.7 (46.51%)	-158.8 (48.66%)
$\Delta E_{orb,pol}$	-178.3 (54.66%)	-176.7 (54.45%)	-178.4 (54.64%)	-176.6 (53.79%)	-168.6 (51.66%)
$\Delta E_{orb,rest}$	-42.8 (13.12%)	-46.7 (14.39%)	-43.3 (13.27%)	-43.5 (13.26%)	-42.8 (13.11%)
$\Delta E_{orb,dz^2} [\alpha+\beta]$	-34.1	-33.8	-33.4	-34.8	-34.6
$\Delta E_{orb,dx^2-y^2} [\alpha+\beta]$	-30.7	-30.5	-31.0	-31.4	-31.7
$\Delta E_{orb,dxz} [\alpha+\beta]$	-	-	-	-	-
$\Delta E_{orb,dzy} [\alpha+\beta]$	-	-	-	-	-
$\Delta E_{orb,dxy} [\alpha+\beta]$	-3.4	-3.4	-3.5	-3.3	-3.2
$\Delta E_{orb,s} [\alpha+\beta]$	-27.1	-27.1	-25.9	-27.0	-29.6
$\Delta E_{orb,pz} [\alpha+\beta]$	-21.2	-20.1	-21.4	-21.7	-23.1
$\Delta E_{orb,px} [\alpha+\beta]$	-18.2	-17.6	-18.1	-18.9	-19.5
$\Delta E_{orb,py} [\alpha+\beta]$	-15.8	-15.8	-15.8	-15.8	-15.8

$\Delta E_{orb,dz2} [\alpha]$	-	-	-	-	-
$\Delta E_{orb,dx2-y2} [\alpha]$	-	-	-	-	-
$\Delta E_{orb,dzx} [\alpha]$	-	-	-	-	-
$\Delta E_{orb,dzy} [\alpha]$	-	-	-	-	-
$\Delta E_{orb,dxy} [\alpha]$	-3.4	-3.4	-3.5	-3.3	-3.2
$\Delta E_{orb,s} [\alpha]$	-13.5	-13.5	-12.4	-13.2	-15.4
$\Delta E_{orb,pz} [\alpha]$	-11.3	-11	-11.5	-11.7	-12.0
$\Delta E_{orb,px} [\alpha]$	-9.9	-9.2	-9.0	-9.8	-9.4
$\Delta E_{orb,py} [\alpha]$	-6.8	-8.9	-8.3	-8.5	-9.3
$\Delta E_{orb,pol} [\alpha]$	-93.1	-91.4	-93.3	-93.2	-90.8
$\Delta E_{orb,rest} [\alpha]$	-21.5	-23.5	-21.8	-22	-21.8
$\Delta E_{orb,dz2} [\beta]$	-34.1	-33.8	-33.4	-34.8	-34.6
$\Delta E_{orb,dx2-y2} [\beta]$	-30.7	-30.5	-31.0	-31.4	-31.7
$\Delta E_{orb,dzx} [\beta]$	-	-	-	-	-
$\Delta E_{orb,dzy} [\beta]$	-	-	-	-	-
$\Delta E_{orb,dxy} [\beta]$	-	-	-	-	-
$\Delta E_{orb,s} [\beta]$	-13.6	-13.6	-13.5	-13.8	-14.2
$\Delta E_{orb,pz} [\beta]$	-9.8	-9.1	-9.9	-10.0	-11.2
$\Delta E_{orb,px} [\beta]$	-8.3	-8.4	-9.1	-9.1	-10.1
$\Delta E_{orb,py} [\beta]$	-7.6	-7.4	-7.6	-7.0	-7.7
$\Delta E_{orb,pol} [\beta]$	-85.2	-85.3	-85.1	-83.4	-77.8
$\Delta E_{orb,rest} [\beta]$	-21.3	-23.2	-21.5	-21.5	-21.0

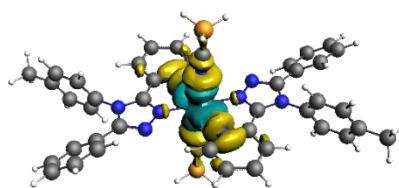
Figure A3.28. Plot of the deformation densities $\Delta\rho^{(i)}$ in fragmentation **5b** with corresponding energy contribution to the total orbital term ΔE (given in kcal/mol) of the $[TM]\leftarrow$ ligand σ -donation, the $[TM]\rightarrow$ ligand π -backdonation and polarisation in reference complex HS $[\text{Fe}(\text{Lpyridine})_2(\text{NCBH}_3)_2]$. The direction of the charge flow is yellow \rightarrow turquoise. The eigenvalues $|v_i|$ indicate the relative size of the charge flow. On the left column are reported $\Delta\rho^{(i)}$ for alpha electrons; on the right are reported $\Delta\rho^{(i)}$ for beta electrons. Figures are reported using until $|v_i| = 0.05$ with cut-off on $\Delta\rho^{(i)}=0.0003$. The choice of cut-off on deformation densities used to produce these images does not affect the results; as EDA-NOCV analysis are performed by applying default cut-off on NOCVs energies (0.5 kcal/mol) and individual SFO contribution (0.001).





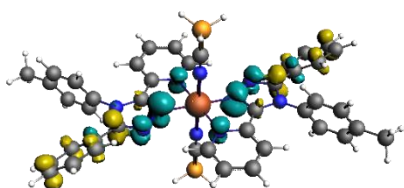
$$\Delta\rho^{(8)} \Delta E_8 = -11.5, |v_8| = 0.15$$

($p_{[TM]} \leftarrow \text{ligand } \sigma$)

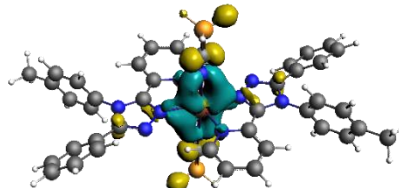


$$\Delta\rho^{(3)} \Delta E_3 = -31.0, |v_3| = 0.3$$

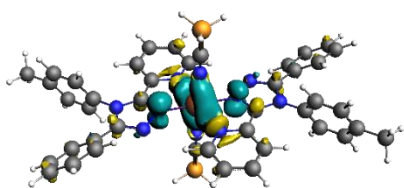
6 ($d_{[TM]} \leftarrow \text{ligand } \sigma$)



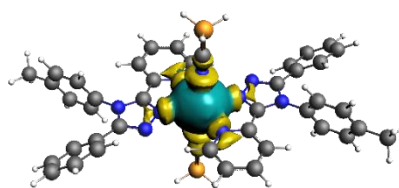
$$\Delta\rho^{(10)} \Delta E_{10} = -6.7, |v_{10}| = 0.13 \text{ (pol)}$$



$$\Delta\rho^{(4)} \Delta E_4 = -11.9, |v_4| = 0.22 \text{ (pol)}$$

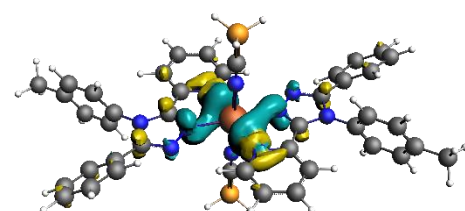


$$\Delta\rho^{(11)} \Delta E_{11} = -8.7, |v_{11}| = 0.13 \text{ (pol)}$$



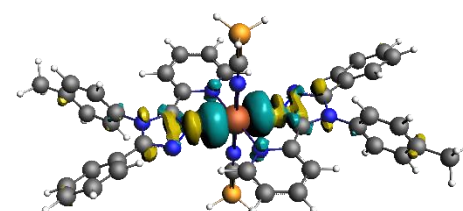
$$\Delta\rho^{(7)} \Delta E_7 = -13.5, |v_7| = 0.15$$

($s_{[TM]} \leftarrow \text{ligand } \sigma$)



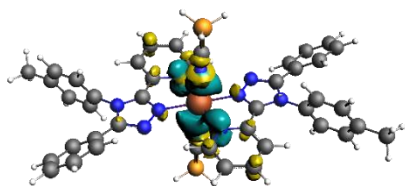
$$\Delta\rho^{(12)} \Delta E_{12} = -9.0, |v_{12}| = 0.13$$

($p_{[TM]} \leftarrow \text{ligand } \sigma$)



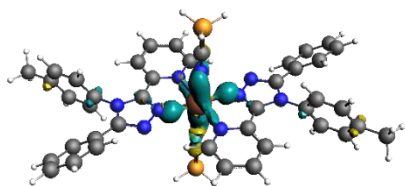
$$\Delta\rho^{(9)} \Delta E_9 = -9.9, |v_9| = 0.14$$

($s_{[TM]} \leftarrow \text{ligand } \sigma$)

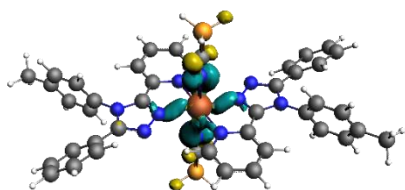


$$\Delta\rho_{(15)} \Delta E_{15} = -8.3, |v_{15}| = 0.12$$

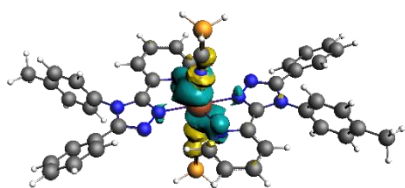
($p_{[TM]} \leftarrow \text{ligand } \sigma$)



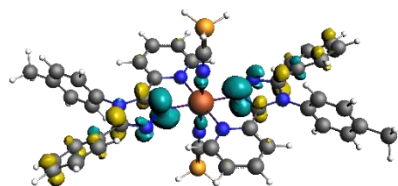
$$\Delta\rho_{(19)} \Delta E_{19} = -5.8, |v_{19}| = 0.11 \text{ (pol)}$$



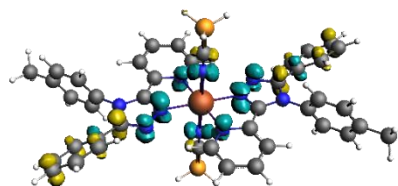
$$\Delta\rho_{(20)} \Delta E_{20} = -5.4, |v_{20}| = 0.10 \text{ (pol)}$$



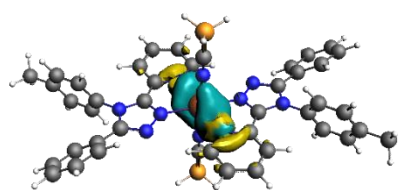
$$\Delta\rho_{(21)} \Delta E_{21} = -6.8, |v_{21}| = 0.10 \text{ (pol)}$$



$$\Delta\rho_{(13)} \Delta E_{13} = -7.0, |v_{13}| = 0.13 \text{ (pol)}$$

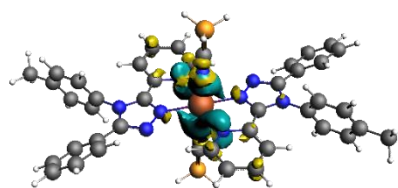


$$\Delta\rho_{(14)} \Delta E_{14} = -6.2, |v_{14}| = 0.12 \text{ (pol)}$$

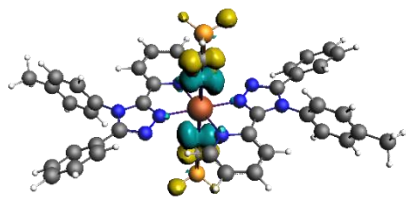


$$\Delta\rho_{(16)} \Delta E_{16} = -9.1, |v_{16}| = 0.12$$

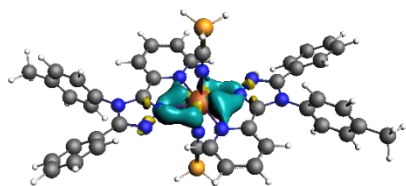
($p_{[TM]} \leftarrow \text{ligand } \sigma$)



$$\Delta\rho_{(17)} \Delta E_{17} = -7.6, |v_{17}| = 0.11 \text{ (} p_{[TM]} \leftarrow \text{ligand } \sigma \text{)}$$

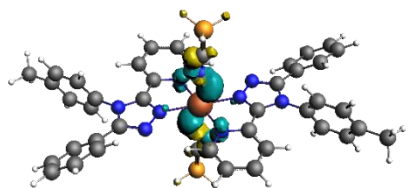


$$\Delta\rho_{(22)} \Delta E_{22} = -5.4, |v_{22}| = 0.09 \text{ (pol)}$$

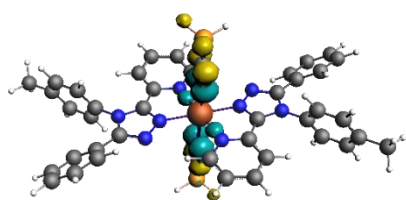


$$\Delta\rho_{(24)} \Delta E_{24} = -3.5, |v_{24}| = 0.09$$

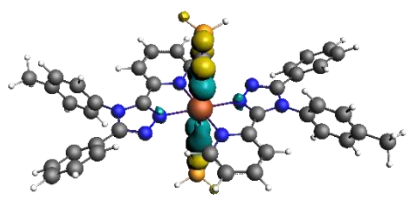
(d_{[TM]} \rightarrow \text{ligand } \pi)



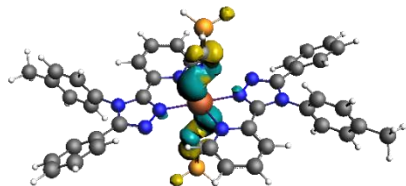
$$\Delta\rho_{(25)} \Delta E_{25} = -5.2, |v_{25}| = 0.09 \text{ (pol)}$$



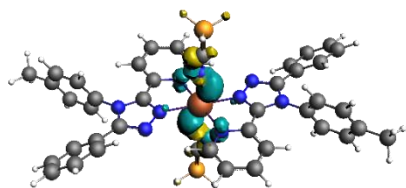
$$\Delta\rho_{(27)} \Delta E_{27} = -5.4, |v_{27}| = 0.09 \text{ (pol)}$$



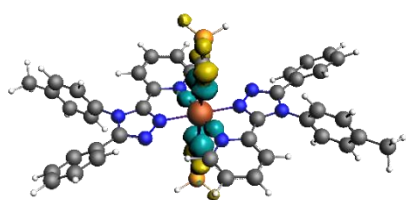
$$\Delta\rho_{(18)} \Delta E_{18} = -6.1, |v_{18}| = 0.11 \text{ (pol)}$$



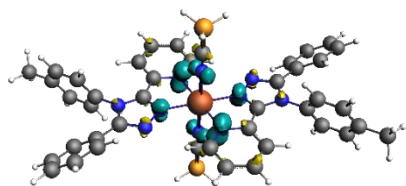
$$\Delta\rho_{(23)} \Delta E_{23} = -5.9, |v_{23}| = 0.09 \text{ (pol)}$$



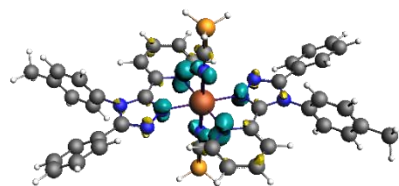
$$\Delta\rho_{(26)} \Delta E_{26} = -5.5, |v_{26}| = 0.09 \text{ (pol)}$$



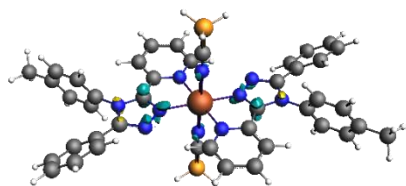
$$\Delta\rho_{(28)} \Delta E_{28} = -5.2, |v_{28}| = 0.09 \text{ (pol)}$$



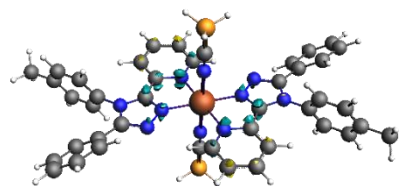
$$\Delta\rho_{(30)} \Delta E_{30} = -4.8, |v_{30}| = 0.08 \text{ (pol)}$$



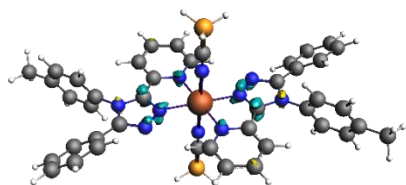
$$\Delta\rho_{(29)} \Delta E_{29} = -4.1, |v_{29}| = 0.08 \text{ (pol)}$$



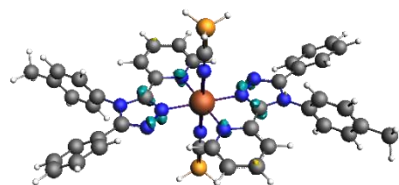
$$\Delta\rho_{(31)} \Delta E_{31} = -2.4, |v_{31}| = 0.6 \text{ (pol)}$$



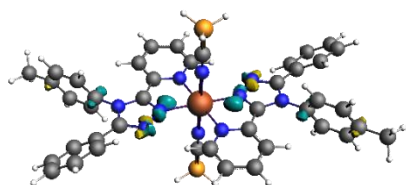
$$\Delta\rho_{(32)} \Delta E_{32} = -2.4, |v_{32}| = 0.06 \text{ (pol)}$$



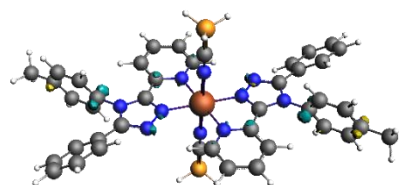
$$\Delta\rho_{(35)} \Delta E_{35} = -2.4, |v_{35}| = 0.06 \text{ (pol)}$$



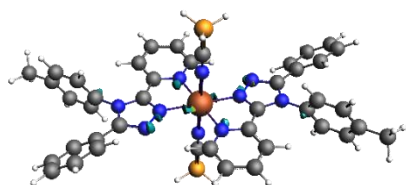
$$\Delta\rho_{(33)} \Delta E_{33} = -2.3, |v_{33}| = 0.06 \text{ (pol)}$$



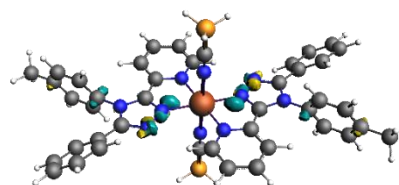
$$\Delta\rho_{(37)} \Delta E_{37} = -2.1, |v_{37}| = 0.05 \text{ (pol)}$$



$$\Delta\rho_{(34)} \Delta E_{34} = -1.6, |v_{34}| = 0.05 \text{ (pol)}$$



$$\Delta\rho_{(38)} \Delta E_{38} = -1.5, |v_{38}| = 0.05 \text{ (pol)}$$



$$\Delta\rho_{(36)} \Delta E_{36} = -2.0, |v_{36}| = 0.05 \text{ (pol)}$$

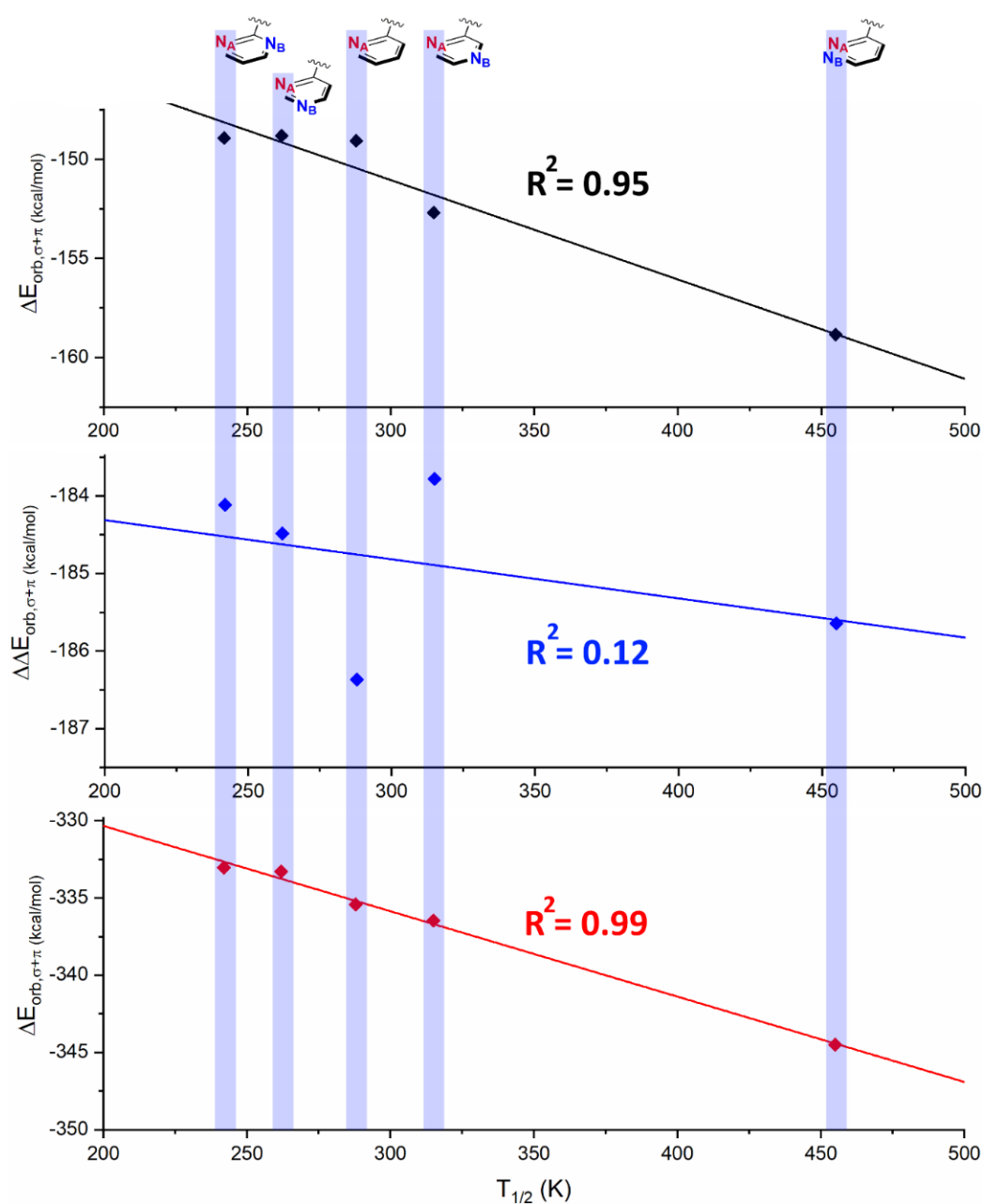


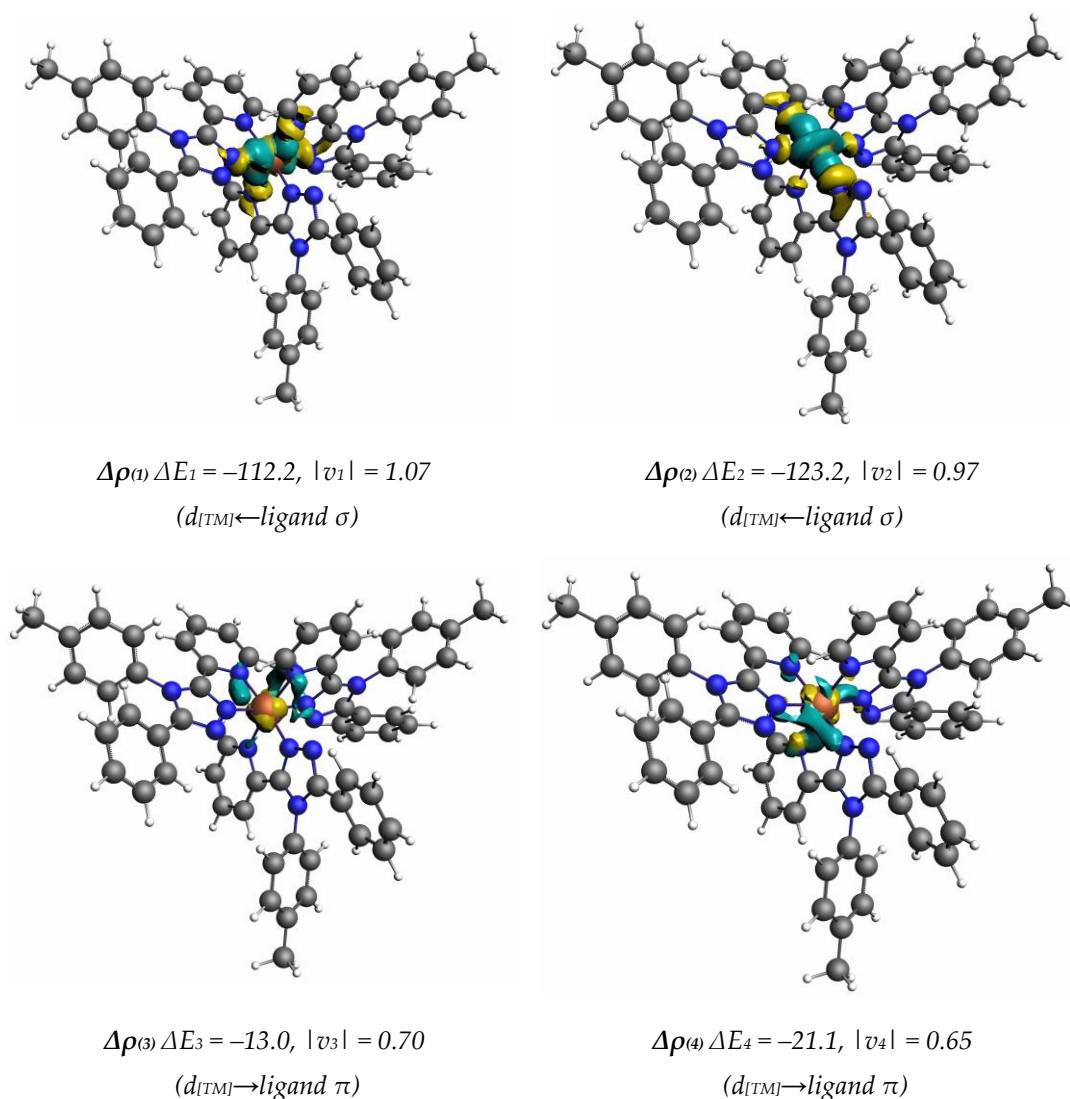
Figure A3.29. Comparison between correlation between $\Delta E_{orb,\sigma+\pi}$ terms and $T_{1/2}$ for the five $[Fe^{II}(Lazine)_2(NCBH_3)_2]$ complexes using fragmentation **5b**. LS state is reported in red ($R^2=0.99$), HS state is reported in black ($R^2=0.95$) and $\Delta \Delta E_{orb,\sigma+\pi}$ (HS-LS) term is reported in blue ($R^2=0.12$).

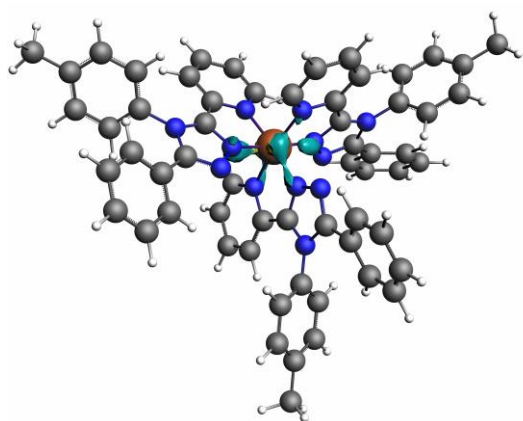
A3.3.6. Frag. 5b/5e - LS [Fe(L^{azine})₃]²⁺

Table A3.23. EDA-NOCV results (kcal/mol) reported for fragmentation 5b-5e for all the five LS [Fe(L^{azine})₃]²⁺ systems. First section (top) reports ΔE_{int} energy splitting 5e; second section (middle) reports ΔE_{orb} energy splitting; third section (bottom) reports all the nine orbital interaction due to M - L₆ interaction 5b.

	L ⁴ pyrimidine	L ² pyrimidine	L ¹ pyridine	L ¹ pyrazine	L ¹ pyridazine
ΔE_{int}	-279.67	-279.23	-296.52	-274.75	-306.31
ΔE_{Pauli}	652.76	653.73	659.72	657.48	667.52
ΔE_{elstat}	-402.13 (-43.1%)	-403.34 (-43.2%)	-421.13 (-44.0%)	-397.39 (-42.6%)	-425.32 (-43.7%)
ΔE_{orb}	-519.6 (-55.7%)	-518.99 (-55.6%)	-524.28 (-54.8%)	-524.06 (-56.2%)	-537.97 (-55.2%)
ΔE_{disp}	-10.7 (-1.2%)	-10.63 (-1.2%)	-10.82 (-1.2%)	-10.78 (-1.2%)	-10.54 (-1.1%)
$\Delta E_{orb,\sigma}$	-319.8	-317.5	-315.0	-316.9	-326.8
$\Delta E_{orb,\pi}$	-40.5	-43.5	-52.8	-51.6	-48.5
$\Delta E_{orb,\sigma+\pi}$	-360.3	-361.1	-367.8	-368.5	-375.4
$\Delta E_{orb,pol}$	-128.2	-128.4	-126.9	-125.9	-132.1
$\Delta E_{orb,rest}$	-37.0	-36.4	-36.6	-36.4	-37.7
$\Delta E_{orb,dz^2}$	-118.8	-115.6	-112.1	-112.1	-121.6
$\Delta E_{orb,dx^2-y^2}$	-125.5	-124.9	-123.1	-124.0	-128.3
$\Delta E_{orb,dzx}$	-11.0	-14.9	-13.0	-19.1	-12.1
$\Delta E_{orb,dzy}$	-13.3	-12.1	-21.0	-15.3	-18.4
$\Delta E_{orb,dxy}$	-16.0	-16.5	-18.7	-17.1	-17.9
$\Delta E_{orb,s}$	-25.1	-24.1	-24.2	-24.7	-23.7
$\Delta E_{orb,pz}$	-14.7	-16.02	-18.1	-19.5	-18.0
$\Delta E_{orb,px}$	-18.9	-18.2	-19.3	-19.1	-18.6
$\Delta E_{orb,py}$	-16.6	-18.4	-17.9	-17.1	-16.4

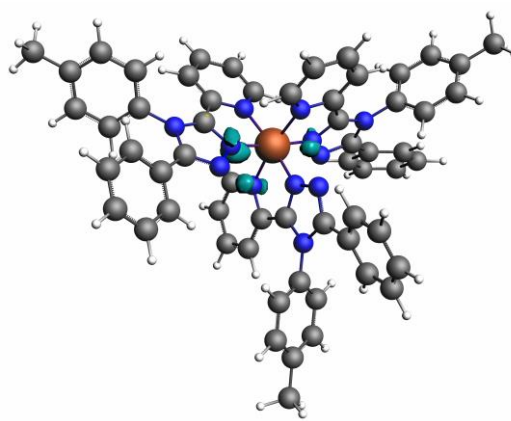
Figure A3.30. Plot of the deformation densities $\Delta\rho^{(i)}$ in fragmentation **5b** with corresponding energy contribution to the total orbital term ΔE (given in kcal/mol) of the $[TM]\leftarrow$ ligand σ -donation, the $[TM]\rightarrow$ ligand π -backdonation and polarisation in reference complex LS $[\text{Fe}(\text{Lpyridine})_3]^{2+}$. The direction of the charge flow is yellow \rightarrow turquoise. The eigenvalues $|v_i|$ indicate the relative size of the charge flow. Figures are reported using until $|v_i| = 0.1$ with cut-off on $\Delta\rho^{(i)}=0.003$. The choice of cut-off on deformation densities used to produce these images does not affect the results; as EDA-NOCV analysis are performed by applying default cut-off on NOCVs energies (0.5 kcal/mol) and individual SFO contribution (0.001).



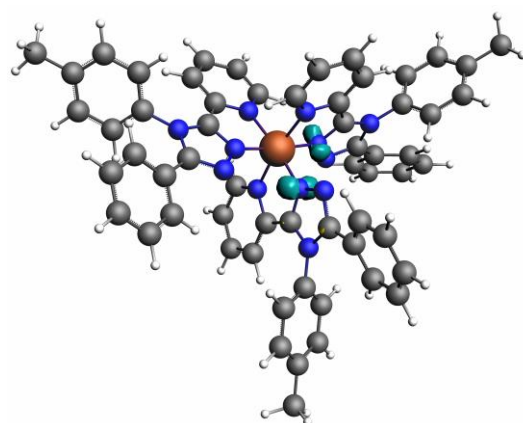


$$\Delta\rho^{(5)} \Delta E_5 = -18.7, |v_4| = 0.45$$

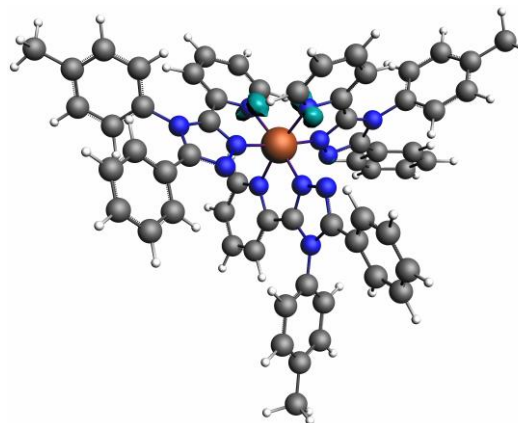
($d_{[TM]} \rightarrow \text{ligand } \pi$)



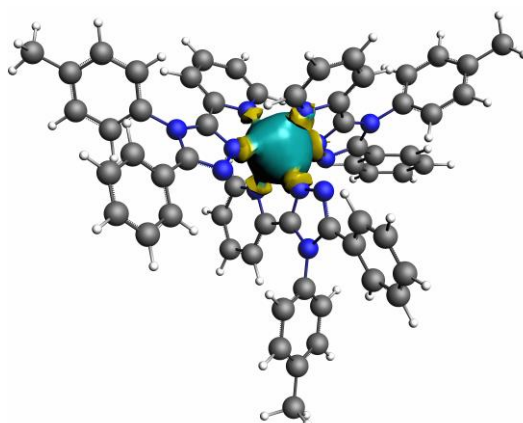
$$\Delta\rho^{(6)} \Delta E_6 = -19.5, |v_6| = 0.27 \text{ (pol)}$$



$$\Delta\rho^{(7)} \Delta E_7 = -17.5, |v_7| = 0.27 \text{ (pol)}$$

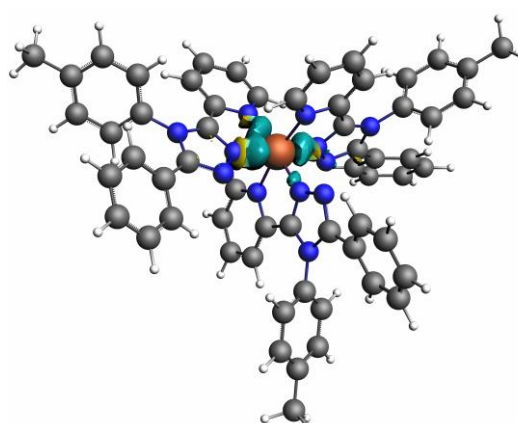


$$\Delta\rho^{(8)} \Delta E_8 = -17.8, |v_8| = 0.27 \text{ (pol)}$$



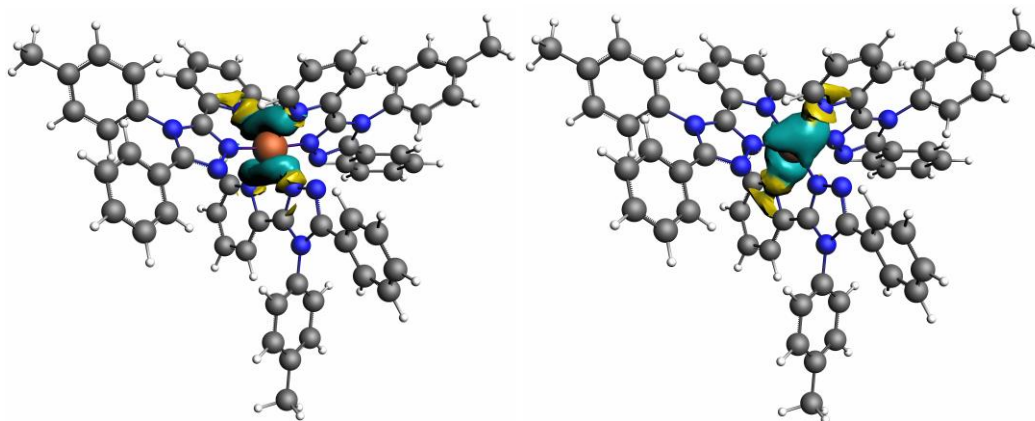
$$\Delta\rho^{(9)} \Delta E_9 = -24.3, |v_9| = 0.25$$

($s_{[TM]} \leftarrow \text{ligand } \sigma$)



$$\Delta\rho^{(10)} \Delta E_{10} = -18.2, |v_{10}| = 0.23$$

($p_{[TM]} \leftarrow \text{ligand } \sigma$)

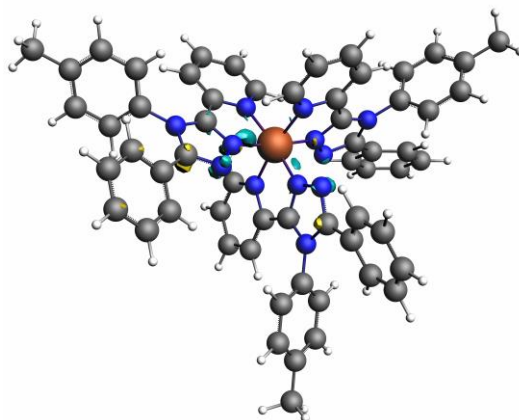


$$\Delta\rho_{(a1)} \Delta E_{11} = -19.3, |v_{11}| = 0.21$$

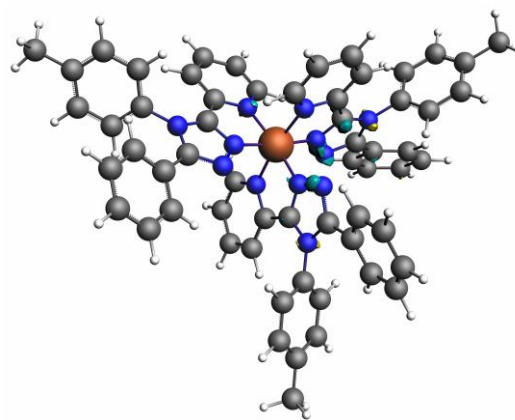
($p_{[TM]} \leftarrow \text{ligand } \sigma$)

$$\Delta\rho_{(a2)} \Delta E_{12} = -18.0, |v_{12}| = 0.21$$

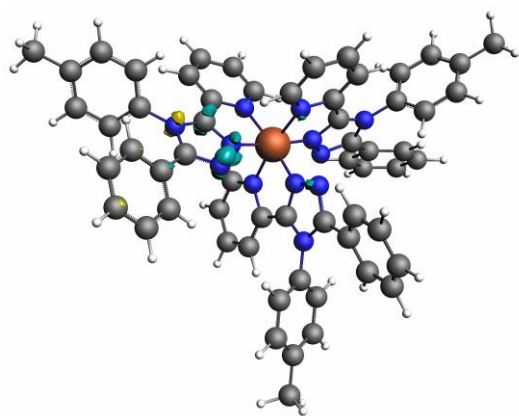
($p_{[TM]} \leftarrow \text{ligand } \sigma$)



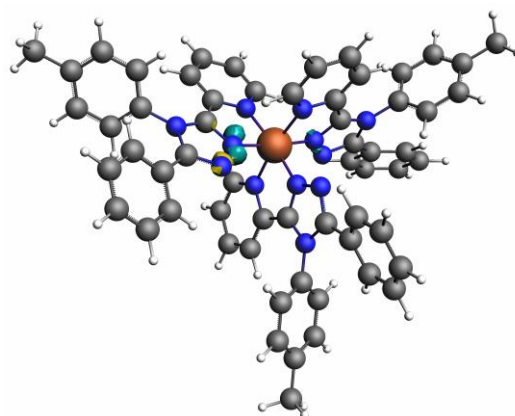
$$\Delta\rho_{(a3)} \Delta E_{13} = -10.9, |v_{13}| = 0.20 \text{ (pol)}$$



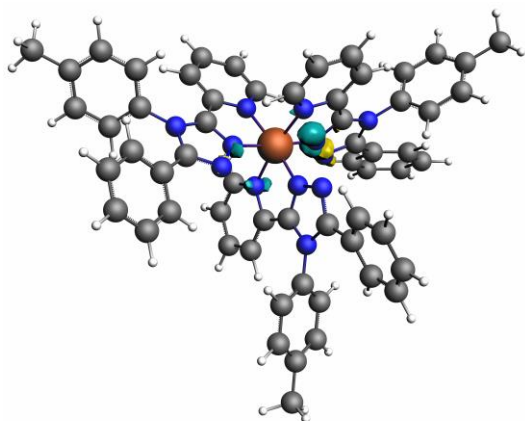
$$\Delta\rho_{(a4)} \Delta E_{14} = -6.85, |v_{14}| = 0.15 \text{ (pol)}$$



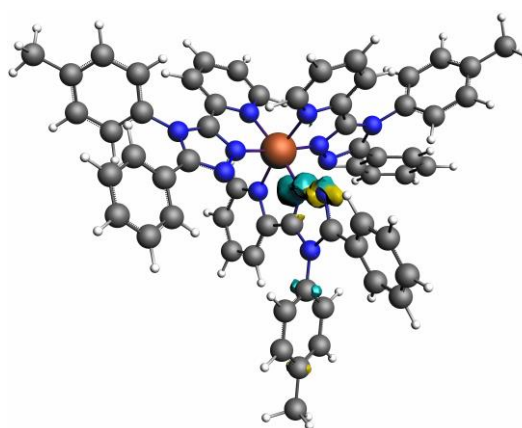
$$\Delta\rho_{(a5)} \Delta E_{15} = -6.4, |v_{15}| = 0.15 \text{ (pol)}$$



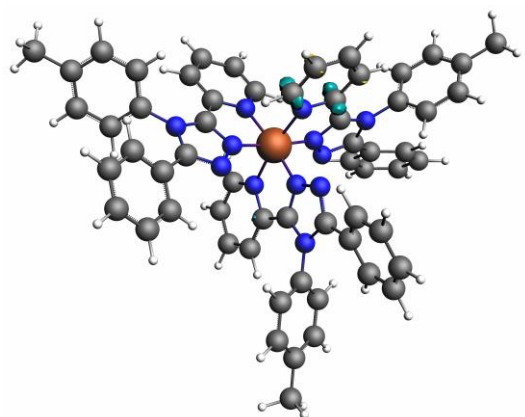
$$\Delta\rho_{(a6)} \Delta E_{16} = -6.3, |v_{16}| = 0.13 \text{ (pol)}$$



$$\Delta\rho_{(17)} \Delta E_{17} = -6.3, |v_{17}| = 0.12 \text{ (pol)}$$



$$\Delta\rho_{(18)} \Delta E_{18} = -6.0, |v_{18}| = 0.12 \text{ (pol)}$$



$$\Delta\rho_{(19)} \Delta E_{19} = -3.6, |v_{19}| = 0.10 \text{ (pol)}$$

A4 | Quantitative Assessment of the Energetic Contribution on the M-L Interaction in Fe(II) 2,6-Di(Pyrazol-1-yl) Pyridine Complexes

A4.1. Atomic Structure Results

The root-mean-square deviation of atomic positions (or simply root-mean-square deviation, *RMSD*) is the measure of the average distance between the atoms (usually the backbone atoms) of superimposed molecules. RMSD values are calculated using Equation A4.1 below.

$$RMSD = \sqrt{\frac{1}{n} \sum_{i=1}^n ((v_{ix} - w_{ix})^2 + (v_{iy} - w_{iy})^2 + (v_{iz} - w_{iz})^2)} \quad (A4.1)$$

Table A4.1. Calculated values of root mean square deviation (RMSD) for all sixteen of the $[\text{Fe}(\text{bpp}^{\text{X}})_2]^{2+}$ complexes (left column) relative to the unsubstituted complex, $[\text{Fe}(\text{bpp}^{\text{H}})_2]^{2+}$, used as a reference, are low so confirm that varying X does not cause any structural changes, so has no steric influence. Calculated values of RMSD are also provided (middle column) for all six of the $[\text{Fe}(\text{bpp}^{\text{X}})_2]^{2+}$ complexes for which the literature value of $T_{1/2}$ was measured in CH_3NO_2 , not in $(\text{CH}_3)_2\text{CO}$: for these the structure was optimised in both solvents, with the CPCM model, then the pair of structures compared to obtain the RMSDs shown in the middle column, which confirm that the structures are identical. Experimental $T_{1/2}$ for each $[\text{Fe}(\text{bpp}^{\text{X}})_2]^{2+}$ are reported in right column.

$[\text{Fe}(\text{bpp}^{\text{X}})_2]^{2+}$	RMSD (\AA) vs $[\text{Fe}(\text{bpp}^{\text{H}})_2]^{2+}$		$T_{1/2}(\text{K})$
	HS	LS	
X = NO ₂	0.052	0.0073	309 ²³
X = CO ₂ H	0.052	0.0052	281 ²³
X = Br	0.003	0.0048	234 ²³
X = I	0.004	0.0050	236 ²³
X = Cl	0.051	0.0050	226 ²³
X = H	-	-	248 ¹⁸⁹
X = SH	0.057	0.0083	246 ¹³⁴
X = F	0.004	0.0051	215 ²³
X = Me	0.043	0.0065	216 ²³
X = SMe	0.032	0.0079	194 ³⁵⁰
X = OMe	0.043	0.0083	158 ²³
X = OH	0.041	0.0081	164 ²³
X = NH ₂	0.039	0.0123	HS ²³
X = NMe ₂	0.029	0.0132	HS ²³
X = SOMe	0.035	0.0072	284 ³⁵⁰
X = SO ₂ Me	0.058	0.0082	294 ³⁵⁰

A1.1. AILFT Results

Table A4.2. Calculated Δ_o calculated of the sixteen LS $[\text{Fe}(\text{bpp}^{\text{X}})_2]^{2+}$ complex and the five LS $[\text{Fe}(\text{L}^{\text{azine}})_2(\text{NCBH}_3)_2]$ using Ab-initio Ligand Field Theory (AILFT)¹⁴⁵ as implemented in ORCA 4.1 computed at the NEVPT2/def2-SV(P)//BP86/def2-TZVPP level of theory, utilising auxiliary basis sets for the RI approximation. The active space for the underlying SA-CASSCF¹⁴⁴ calculation included all d orbitals and the six electrons of Fe(II) and considered all possible singlet, triplet and quintet configurations. * values estimated in Subsection 4.3.7.

$[\text{Fe}(\text{bpp}^{\text{X}})_2]^{2+}$	σ_p^+	$T_{1/2} / \text{K}$	$\Delta_o (\text{NEVPT2}) / \text{eV}$
X = NO₂	0.79	309 ²³	2.466
X = CO₂H	0.42	281 ²³	2.446
X = Br	0.15	234 ²³	2.413
X = I	0.14	236 ²³	2.414
X = Cl	0.11	226 ²³	2.411
X = H	0.00	248 ¹⁸⁹	2.428
X = SH	-0.03	246 ¹³⁴	2.381
X = F	-0.07	215 ²³	2.412
X = Me	-0.31	216 ²³	2.394
X = SMe	-0.60	194 ³⁵⁰	2.371
X = OMe	-0.78	158 ²³	2.364
X = OH	-0.92	164 ²³	2.371
X = NH₂	-1.30	HS ²³	2.324
X = NMe₂	-1.70	HS ²³	2.311
X = SMe	0.26*	284 ³⁵⁰	2.289
X = SO₂Me	0.60*	294 ³⁵⁰	2.311
$[\text{Fe}(\text{L}^{\text{4pym}})_2(\text{NCBH}_3)_2]$	-	232 ⁸³	2.138
$[\text{Fe}(\text{L}^{\text{2pym}})_2(\text{NCBH}_3)_2]$	-	262 ⁸³	2.342
$[\text{Fe}(\text{L}^{\text{pyt}})_2(\text{NCBH}_3)_2]$	-	288 ⁸³	2.300
$[\text{Fe}(\text{L}^{\text{pyrazt}})_2(\text{NCBH}_3)_2]$	-	315 ⁸³	2.362
$[\text{Fe}(\text{L}^{\text{pyrdt}})_2(\text{NCBH}_3)_2]$	-	455 ⁸³	2.745

A1.2. EDA-NOCV Results

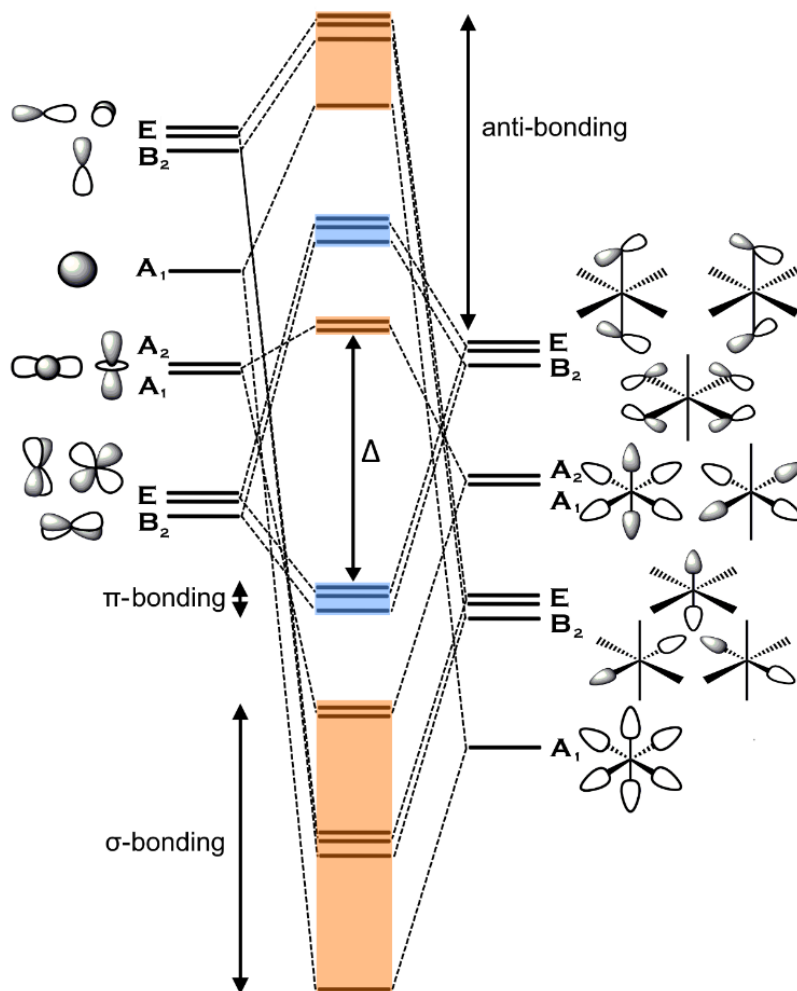
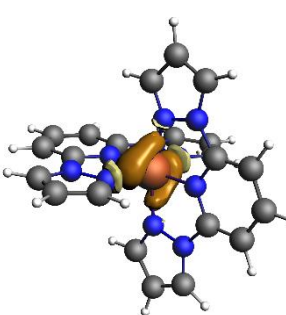
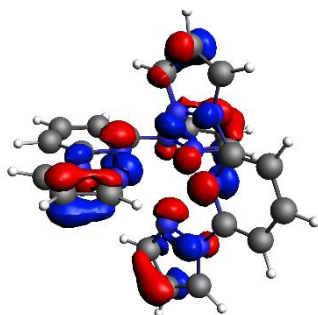
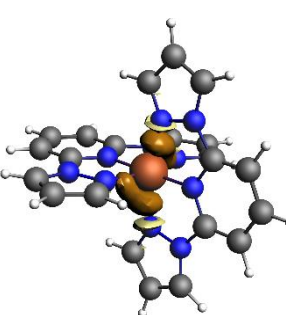
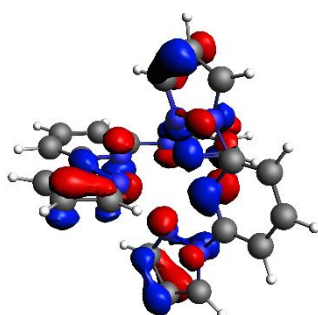
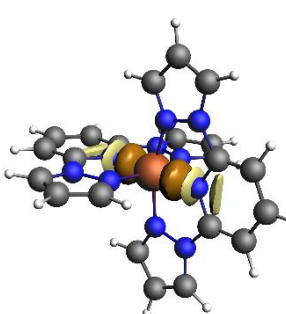
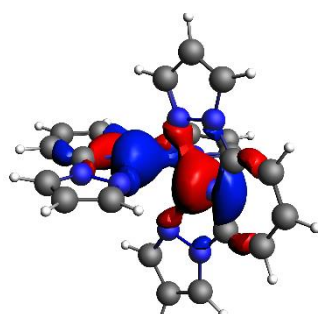
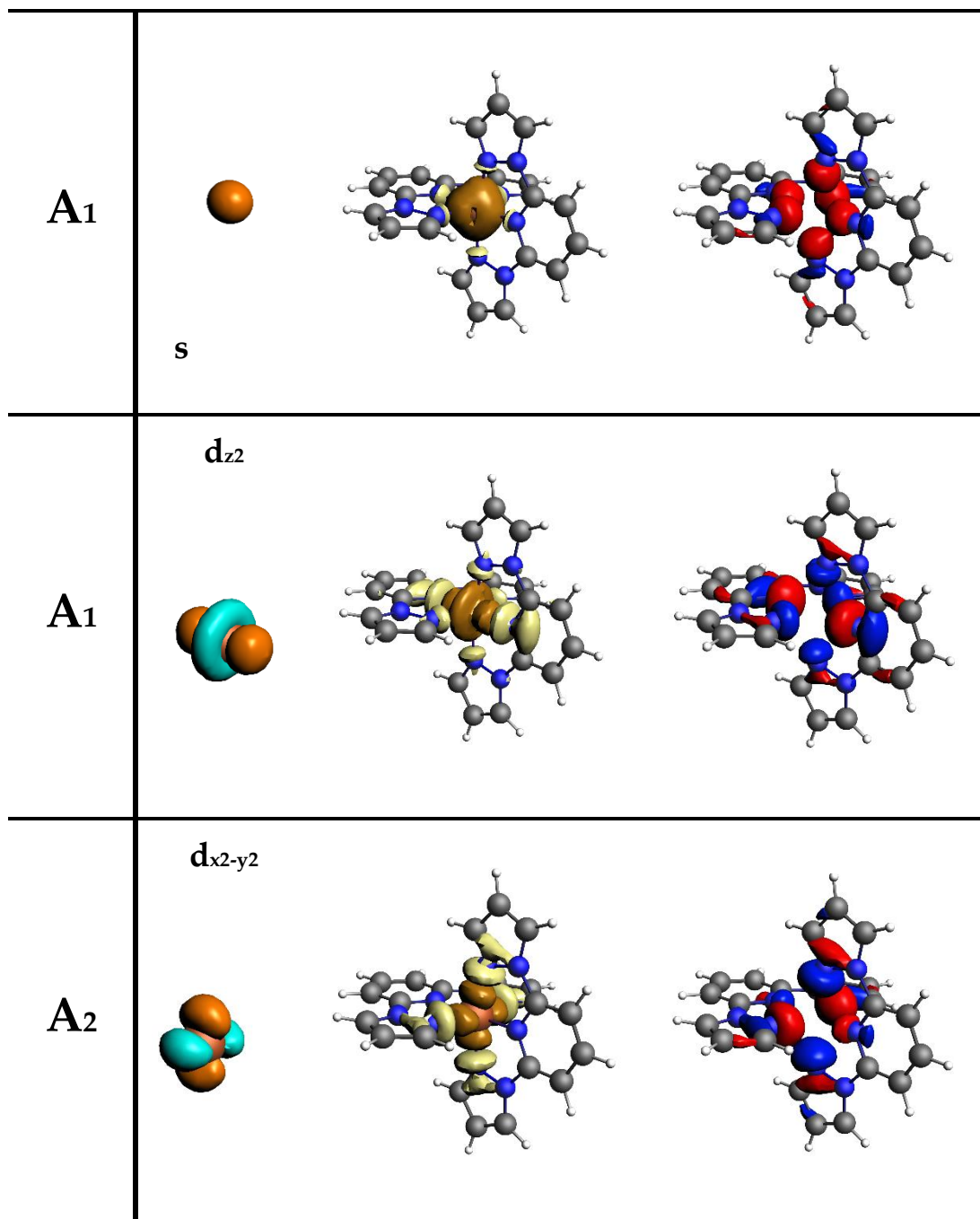
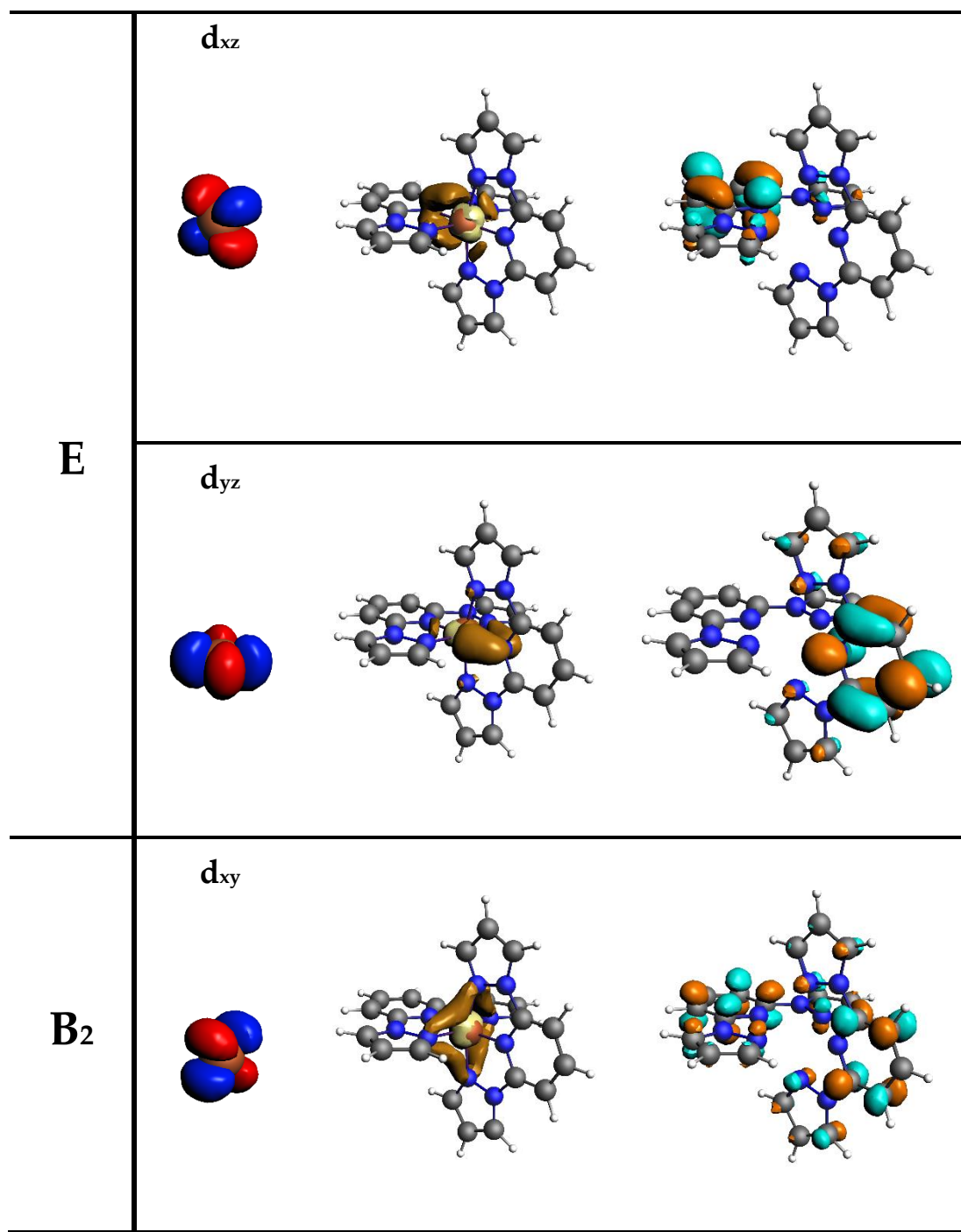


Figure A4.1. Classic qualitative representation of the ladder of MO energies (centre) for a distorted octahedral (D_{2d} symmetry) ML_6 complex (σ bonding MOs in blue; π bonding MOs in orange) which result from overlap of the valence AOs of M (left) with L_6 MOs of the same symmetry (right).

Table A4.3. Each column shows one of the Fe AOs (left column), the corresponding L_6 MOs (right column); unoccupied orbitals are reported in orange/light blue colours; occupied orbitals are reported in blue/red. Electron flow in EDA-NOCV analysis (middle column) goes from yellow \rightarrow turquoise (middle column).

<i>Irr.Repr.</i>	AOs (Fe)	EDA-NOCV (ML_6)	MOs (L_6)
E	p_x		
	p_y		
B₂	p_z		





A4.1.1. EDA: Fragmentation 5e

Table A4.4. EDA-NOCV results using fragmentation 5e for M^{n+} for the LS $[Fe(\text{bpp}^X)_2]^{2+}$ complexes: all energies are reported in kcal/mol. The total change in energy ΔE_{int} (left) is decomposed into several contributions, ΔE_{elstat} , ΔE_{Pauli} , ΔE_{orb} and ΔE_{disp} . Presented in order of decreasing Hammett parameter (value provided under the identify of X in the first column). * values estimated in Subsection 4.3.7.

X	σ_p^+	ΔE_{int}	ΔE_{int} splitting terms						
			ΔE_{Pauli}	ΔE_{elstat}	ΔE_{orb}	ΔE_{disp}			
NO ₂	+0.79	-205.65	679.18	-365.4	(41.30%)	-508.67	(57.49%)	-10.76	(1.22%)
CO ₂ H	+0.42	-223.72	678.69	-383.36	(41.81%)	-508.27	(56.98%)	-10.77	(1.21%)
Br	+0.15	-222.91	676.61	-383.11	(42.48%)	-505.64	(56.32%)	-10.76	(1.19%)
I	+0.14	-224.49	677.14	-382.46	(42.20%)	-508.4	(56.39%)	-10.77	(1.20%)
Cl	+0.11	-221.66	676.17	-383.07	(42.59%)	-504.01	(56.21%)	-10.75	(1.20%)
H	0.0	-229.07	676.79	-393.79	(42.42%)	-501.31	(56.39%)	-10.75	(1.19%)
SH	-0.03	-231.64	675.44	-390.73	(42.67%)	-505.58	(56.14%)	-10.77	(1.20%)
F	-0.07	-219.51	675.48	-385.00	(43.47%)	-499.26	(55.34%)	-10.73	(1.19%)
Me	-0.31	-235.6	675.89	-397.93	(43.08%)	-502.8	(55.74%)	-10.76	(1.19%)
SMe	-0.60	-239.55	675.26	-397.06	(43.02%)	-506.96	(55.78%)	-10.79	(1.20%)
OMe	-0.78	-238.92	674.59	-401.17	(43.40%)	-501.57	(55.42%)	-10.76	(1.18%)
OH	-0.92	-232.02	674.4	-396.16	(43.66%)	-499.51	(55.16%)	-10.75	(1.18%)
NH ₂	-1.30	-246.68	673.41	-409.42	(43.92%)	-499.91	(54.91%)	-10.76	(1.18%)
NMe ₂	-1.70	-255.27	673.26	-413.87	(43.71%)	-503.87	(55.11%)	-10.79	(1.19%)
SOMe	+0.26*	-224.39	676.78	-382.23	(44.50%)	-508.13	(54.33%)	-10.79	(1.17%)
SO ₂ Me	+0.60*	-215.35	677.74	-373.39	(44.57%)	-508.9	(54.27%)	-10.80	(1.16%)

Table A4.5. EDA-NOCV results using fragmentation **5e** for M^{n+} for the HS $[Fe(\mathbf{bpp}^X)_2]^{2+}$ complexes: all energies are reported in kcal/mol. The total change in energy ΔE_{int} (left) is decomposed into several contributions, ΔE_{elstat} , ΔE_{Pauli} , ΔE_{orb} and ΔE_{disp} . Presented in order of decreasing Hammett parameter (value provided under the identify of **X** in the first column). * values estimated in Subsection 4.3.7.

X	σ_p^+	ΔE_{int}	ΔE_{int} splitting terms					
			ΔE_{Pauli}	ΔE_{elstat}	ΔE_{orb}		ΔE_{disp}	
NO₂	+0.79	-71.6	554.5	-296.6 (47.37%)	-314.9	(50.29%)	-14.6	(2.33%)
CO₂H	+0.42	-89.0	553.0	-313.2 (48.78%)	-314.2	(48.40%)	-14.6	(2.28%)
Br	+0.15	-85.5	531.7	-301.1 (48.78%)	-301.8	(48.89%)	-14.4	(2.33%)
I	+0.14	-86.9	532.1	-300.5 (48.54%)	-304.1	(49.13%)	-14.4	(2.33%)
Cl	+0.11	-88.2	550.6	-312.4 (48.91%)	-311.8	(48.81%)	-14.6	(2.28%)
H	0.0	-89.9	531.7	-310.7 (49.98%)	-296.6	(47.72%)	-14.4	(2.31%)
SH	-0.03	-98.5	550.2	-320.1 (49.35%)	-314.0	(48.40%)	-14.6	(2.25%)
F	-0.07	-83.0	530.8	-302.9 (49.35%)	-296.5	(48.32%)	-14.3	(2.34%)
Me	-0.31	-104.4	530.9	-314.3 (49.46%)	-306.7	(48.27%)	-14.4	(2.27%)
SMe	-0.60	-101.5	550.1	-326.5 (50.10%)	-310.6	(47.66%)	-14.6	(2.24%)
OMe	-0.78	-104.0	547.1	-328.7 (50.49%)	-307.8	(47.28%)	-14.6	(2.23%)
OH	-0.92	-98.1	549.2	-325.0 (50.21%)	-307.7	(47.54%)	-14.5	(2.25%)
NH₂	-1.30	-113.0	548.8	-338.2 (51.10%)	-309.1	(46.70%)	-14.5	(2.20%)
NMe₂	-1.70	-120.1	530.3	-330.6 (50.83%)	-305.5	(46.96%)	-14.4	(2.21%)
SOMe	+0.26*	-90.1	530.6	-300.8 (48.46%)	-305.5	(49.22%)	-14.4	(2.32%)
SO₂Me	+0.60*	-81.0	551.7	-303.2 (47.93%)	-314.8	(49.75%)	-14.7	(2.32%)

A4.1.2. NOCV: Fragmentation 5b

Table A4.6. Results of ΔE_{orb} (kcal/mol) decomposition, calculated with BP86-D3BJ-TZ2P level of theory, focussing on two of the four components, $\Delta E_{orb,\sigma}$ and $\Delta E_{orb,\pi}$ (kcal/mol), which sum to $\Delta E_{orb,\sigma+\pi}$. Each of the three columns is ordered from the most negative to the least negative. Values reported are obtained using fragmentation **5b** for M^{n+} for the LS $[Fe(\mathbf{bpp}^X)_2]^{2+}$ complexes.

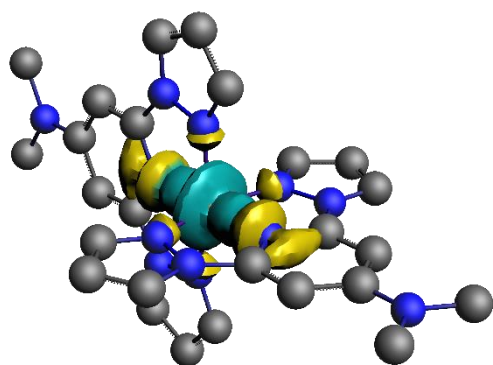
$\Delta E_{orb,\sigma+\pi}$		$\Delta E_{orb,\sigma}$		$\Delta E_{orb,\pi}$	
X	Kcal mol ⁻¹	X	Kcal mol ⁻¹	X	Kcal mol ⁻¹
NO ₂	-379.76	NO ₂	-331.89	NMe ₂	-52.55
CO ₂ H	-379.72	CO ₂ H	-331.13	SMe	-52.41
I	-378.94	SO ₂ Me	-330.32	SH	-51.04
SH	-378.65	H	-328.73	I	-50.41
SMe	-378.57	SOMe	-328.58	NH ₂	-50.17
SO ₂ Me	-378.56	I	-328.54	SOMe	-49.70
SOMe	-378.28	Br	-327.98	OMe	-49.69
Br	-377.61	Cl	-327.91	Br	-49.63
Cl	-376.99	Me	-327.76	Cl	-49.08
Me	-376.22	SH	-327.61	OH	-48.69
OMe	-376.16	F	-326.75	CO ₂ H	-48.59
H	-376.06	SMe	-326.16	F	-48.46
NMe ₂	-375.83	OH	-325.94	Me	-48.24
NH ₂	-374.84	NH ₂	-324.67	SO ₂ Me	-47.87
OH	-374.62	OMe	-326.47	NO ₂	-47.71
F	-374.46	NMe ₂	-323.28	H	-47.33

Table A4.7. Results of ΔE_{orb} (kcal/mol) decomposition, calculated with BP86-D3BJ-TZ2P level of theory, focussing on two of the four components, $\Delta E_{orb,\sigma}$ and $\Delta E_{orb,\pi}$ (kcal/mol), which sum to $\Delta E_{orb,\sigma+\pi}$. Each of the three columns is ordered from the most negative to the least negative. Values reported are obtained using fragmentation **5b** for M^{n+} for the HS [Fe(**bpp**^X)₂]²⁺ complexes.

$\Delta E_{orb,\sigma+\pi}$		$\Delta E_{orb,\sigma}$		$\Delta E_{orb,\pi}$	
X	Kcal mol ⁻¹	X	Kcal mol ⁻¹	X	Kcal mol ⁻¹
I	-214.25	NMe ₂	-175.12	NH ₂	-35.97
Br	-213.48	I	-172.45	NMe ₂	-35.89
F	-211.62	CO ₂ H	-172.19	H	-30.46
NMe ₂	-211.01	SO ₂ Me	-172.13	OMe	-30.36
H	-200.15	SH	-172.01	I	-21.07
NH ₂	-199.40	Me	-172.00	Br	-20.98
OMe	-199.17	Br	-171.83	F	-20.80
SH	-189.69	NO ₂	-170.88	SMe	-17.85
CO ₂ H	-188.74	Cl	-170.71	SH	-17.68
SMe	-188.47	F	-170.29	NO ₂	-16.87
SO ₂ Me	-188.32	OH	-170.00	Cl	-16.71
NO ₂	-187.75	H	-169.69	OH	-16.70
Cl	-187.42	SMe	-166.75	CO ₂ H	-16.55
OH	-186.70	SOMe	-166.00	Me	-16.47
Me	-184.60	OMe	-165.75	SOMe	-16.30
SOMe	-182.30	NH ₂	-164.52	SO ₂ Me	-16.19

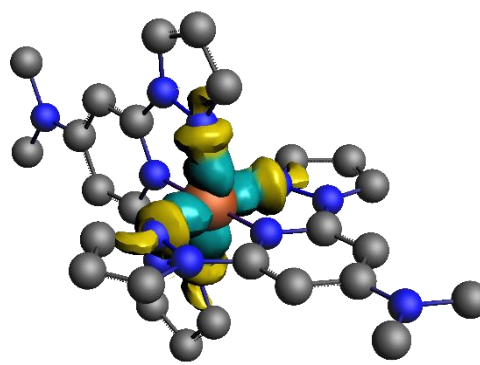
A4.1.3. NOCV Figures for LS $[\text{Fe}(\text{bpp}^{\text{X}})_2]^{2+}$

Figure A4.2. Plot of the deformation densities $\Delta\rho(i)$ with corresponding energy contribution to the total orbital term ΔE_i (given in kcal/mol) of the $\text{M} \leftarrow \text{L}_6$ σ -donation, the $\text{M} \rightarrow \text{L}_6$ π -backdonation and polarisation in complex LS $[\text{Fe}(\text{bpp}^{\text{NMe}_2})_2]^{2+}$ complexes. The direction of the charge flow is yellow \rightarrow turquoise. The eigenvalues $|v_i|$ indicate the relative size of the charge flow (reported values for $|v_i| > 0.1$; $\rho < 0.003$). The choice of cut-off on deformation densities used to produce these images does not affect the results; as EDA-NOCV analysis are performed by applying default cut-off on NOCVs energies (0.5 kcal/mol) and individual SFO contribution (0.001).



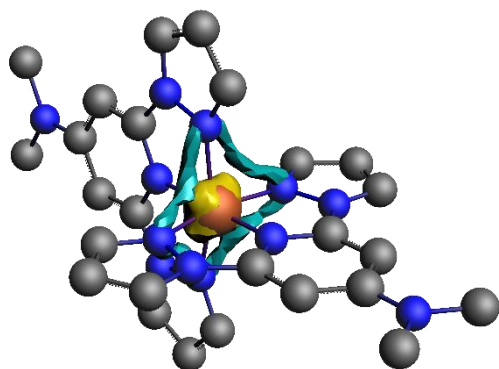
$$\Delta\rho_{(1)} \Delta E_1 = -127.4, |v_1| = 0.94$$

($\text{M}(\text{d}_{z^2}) \leftarrow \text{L}_6$ σ -donation)



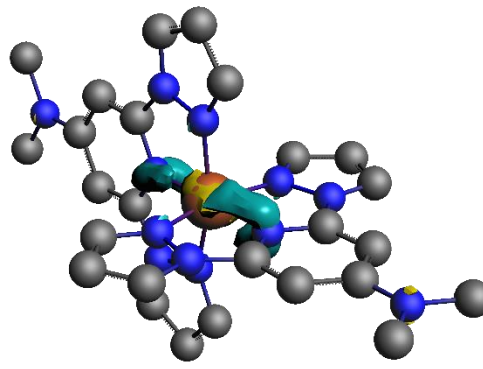
$$\Delta\rho_{(2)} \Delta E_2 = -113.2, |v_2| = 0.90$$

($\text{M}(\text{d}_{x^2-y^2}) \leftarrow \text{L}_6$ σ -donation)



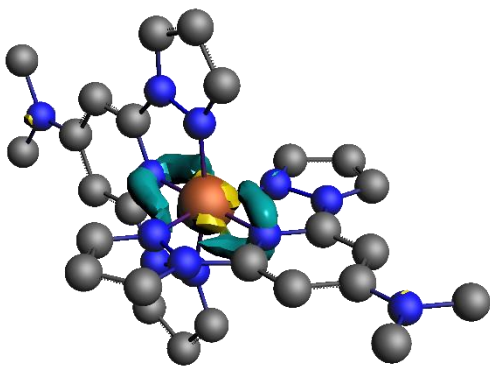
$$\Delta\rho_{(3)} \Delta E_3 = -9.4, |v_3| = 0.63$$

($\text{M}(\text{d}_{xy}) \rightarrow \text{L}_6$ π -backdonation)

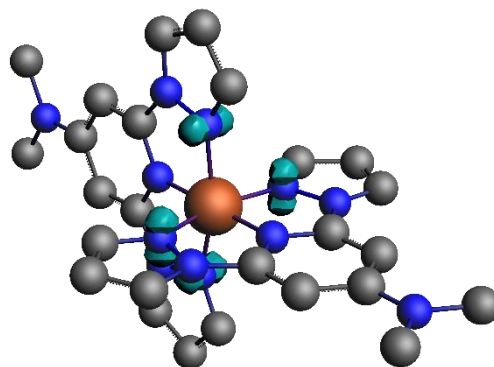


$$\Delta\rho_{(4)} \Delta E_4 = -21.6, |v_4| = 0.60$$

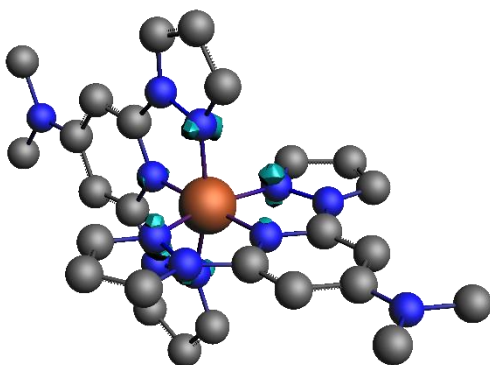
($\text{M}(\text{d}_{xz,yz}) \rightarrow \text{L}_6$ π -backdonation)



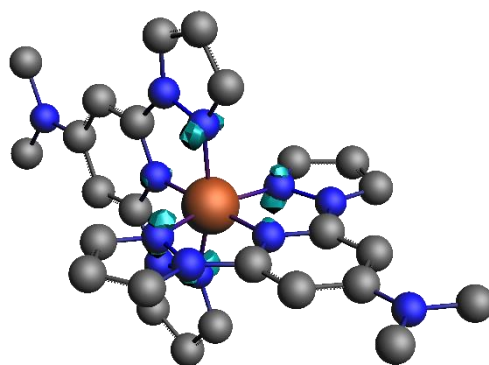
$\Delta\rho^{(5)} \Delta E_5 = -21.6, |v_5| = 0.60$
 ($M(d_{xz,yz}) \rightarrow L_6 \pi$ -backdonation)



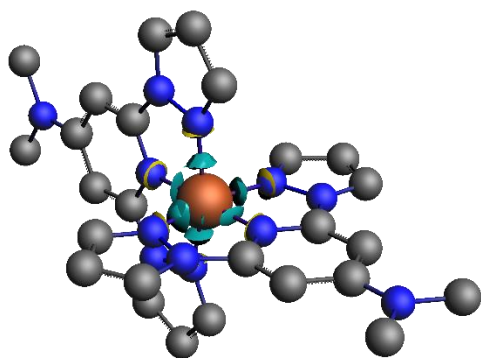
$\Delta\rho^{(6)} \Delta E_6 = -16.6, |v_6| = 0.25$ (pol)



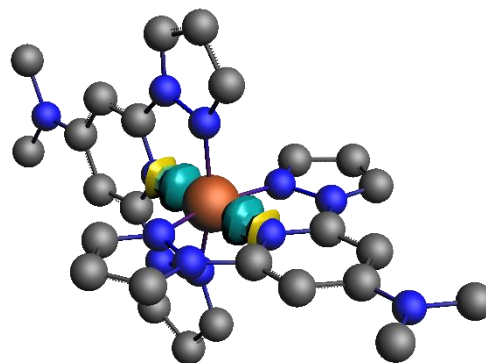
$\Delta\rho^{(7)} \Delta E_7 = -16.2, |v_7| = 0.24$ (pol)



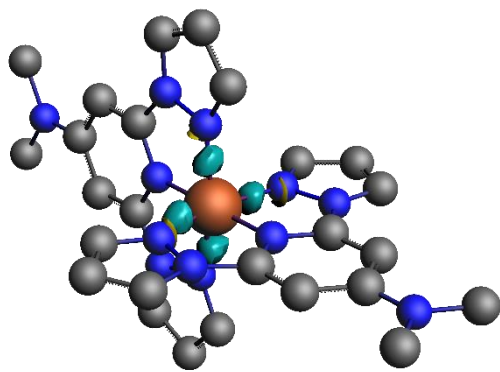
$\Delta\rho^{(8)} \Delta E_8 = -16.1, |v_8| = 0.24$ (pol)



$\Delta\rho^{(9)} \Delta E_9 = -24.2, |v_9| = 0.23$
 ($M(s) \leftarrow L_6 \sigma$ -donation)

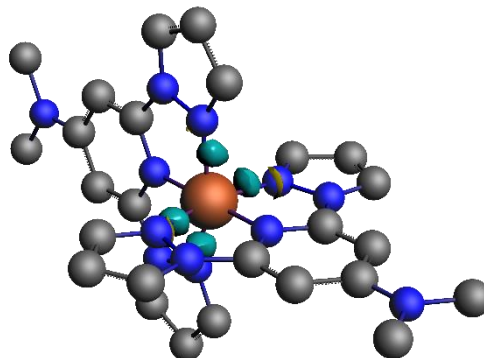


$\Delta\rho^{(10)} \Delta E_{10} = -21.3, |v_{10}| = 0.21$
 ($M(p_z) \leftarrow L_6 \sigma$ -donation)



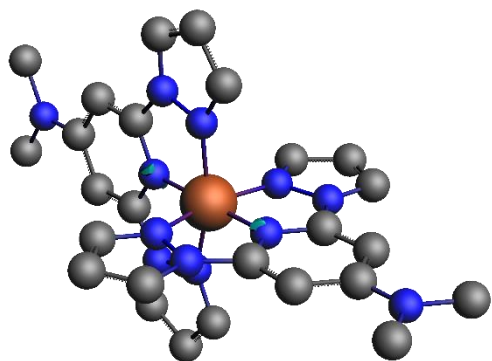
$$\Delta\rho_{(11)} \Delta E_{11} = -18.5, |v_{11}| = 0.20$$

$(M(p_{x,y}) \leftarrow L_6 \sigma\text{-donation})$

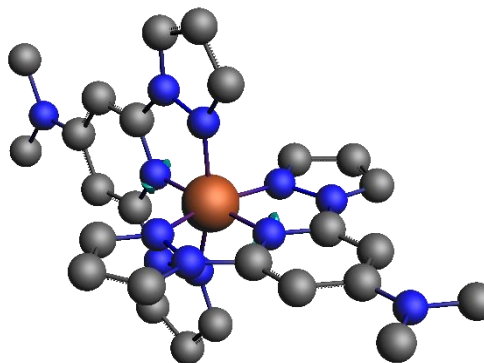


$$\Delta\rho_{(12)} \Delta E_{12} = -18.6, |v_{12}| = 0.20$$

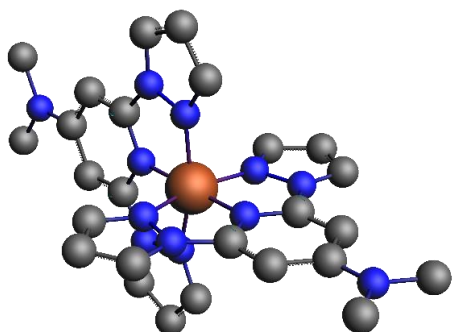
$(M(p_{x,y}) \leftarrow L_6 \sigma\text{-donation})$



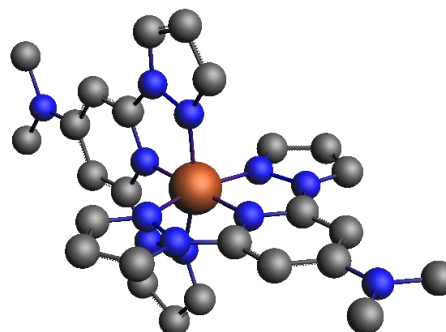
$$\Delta\rho_{(13)} \Delta E_{13} = -10.5, |v_{13}| = 0.18 \text{ (pol)}$$



$$\Delta\rho_{(14)} \Delta E_{14} = -10.5, |v_{14}| = 0.18 \text{ (pol)}$$

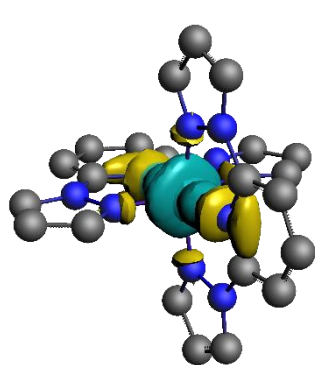


$$\Delta\rho_{(15)} \Delta E_{15} = -4.8, |v_{15}| = 0.13 \text{ (pol)}$$



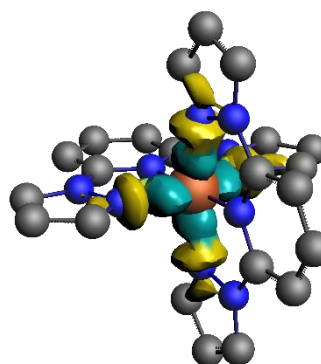
$$\Delta\rho_{(16)} \Delta E_{16} = -4.5, |v_{16}| = 0.12 \text{ (pol)}$$

Figure A4.3. Plot of the deformation densities $\Delta\rho(i)$ with corresponding energy contribution to the total orbital term ΔE_i (given in kcal/mol) of the $M \leftarrow L_6$ σ -donation, the $M \rightarrow L_6$ π -backdonation and polarisation in complex LS $[Fe(\mathbf{bpp}^H)_2]^{2+}$. The direction of the charge flow is yellow \rightarrow turquoise. The eigenvalues $|v_i|$ indicate the relative size of the charge flow (reported values for $|v_i| > 0.1$; $\rho < 0.003$). The choice of cut-off on deformation densities used to produce these images does not affect the results; as EDA-NOCV analysis are performed by applying default cut-off on NOCVs energies (0.5 kcal/mol) and individual SFO contribution (0.001).



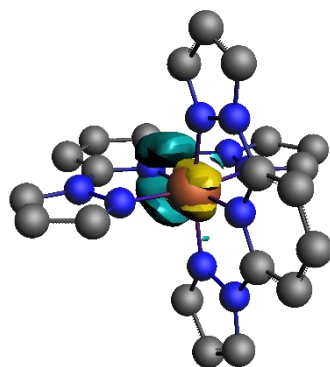
$$\Delta\rho^{(1)} \Delta E_1 = -129.0, |v_1| = 0.95$$

$(M(d_{z^2}) \leftarrow L_6 \sigma\text{-donation})$



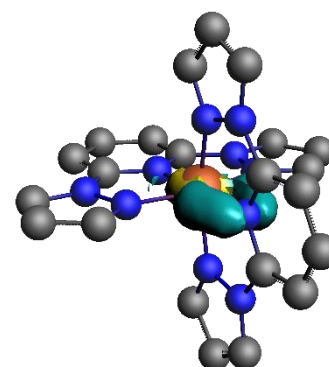
$$\Delta\rho^{(2)} \Delta E_2 = -115.8, |v_2| = 0.92$$

$(M(d_{x^2-y^2}) \leftarrow L_6 \sigma\text{-donation})$



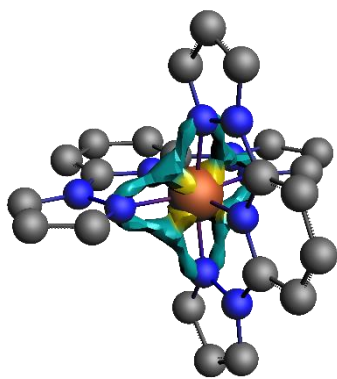
$$\Delta\rho^{(3)} \Delta E_3 = -17.9, |v_3| = 0.63$$

$(M(d_{xz,yz}) \rightarrow L_6 \pi\text{-backdonation})$



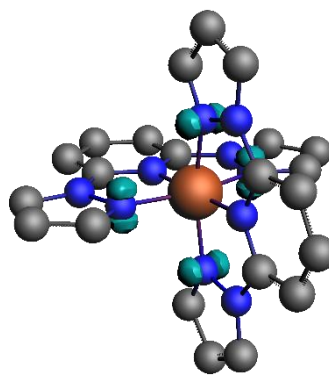
$$\Delta\rho^{(4)} \Delta E_4 = -18.0, |v_4| = 0.63$$

$(M(d_{xz,yz}) \rightarrow L_6 \pi\text{-backdonation})$

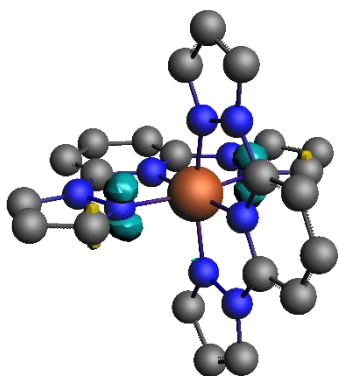


$$\Delta\rho^{(5)} \Delta E_5 = -11.5, |v_5| = 0.60$$

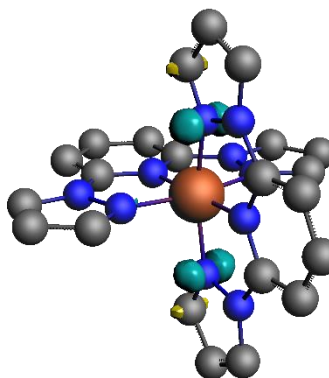
($M(d_{xy}) \rightarrow L_6 \pi$ -backdonation)



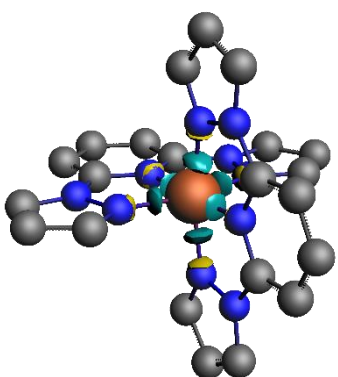
$$\Delta\rho^{(6)} \Delta E_6 = -17.1, |v_6| = 0.26 \text{ (pol)}$$



$$\Delta\rho^{(7)} \Delta E_7 = -16.8, |v_7| = 0.24 \text{ (pol)}$$

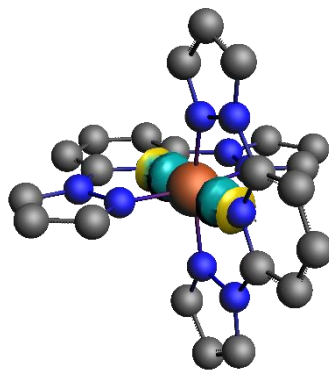


$$\Delta\rho^{(8)} \Delta E_8 = -16.8, |v_8| = 0.24 \text{ (pol)}$$



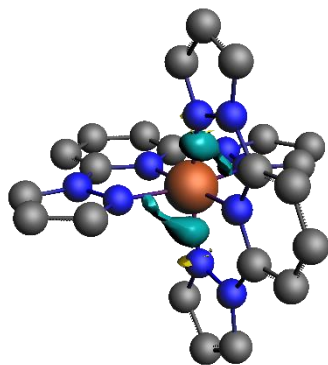
$$\Delta\rho^{(9)} \Delta E_9 = -24.4, |v_9| = 0.24$$

($M(s) \leftarrow L_6 \sigma$ -donation)



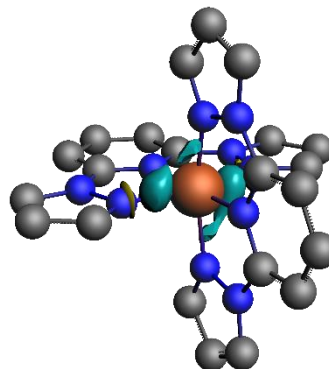
$$\Delta\rho^{(10)} \Delta E_{10} = -21.3, |v_{10}| = 0.21$$

($M(p_z) \leftarrow L_6 \sigma$ -donation)



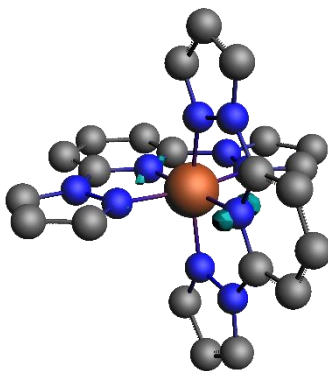
$$\Delta\rho_{(a1)} \Delta E_{11} = -19.2, |v_{11}| = 0.20$$

($M(p_{x,y}) \leftarrow L_6 \sigma$ -donation)

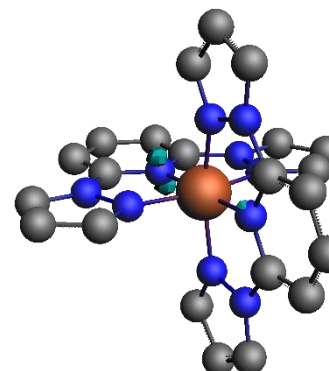


$$\Delta\rho_{(a2)} \Delta E_{12} = -19.2, |v_{12}| = 0.20$$

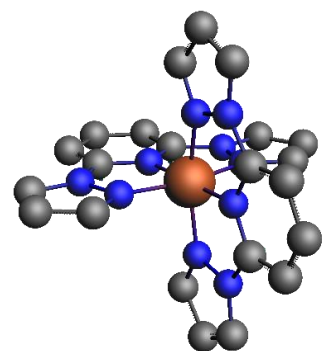
($M(p_{x,y}) \leftarrow L_6 \sigma$ -donation)



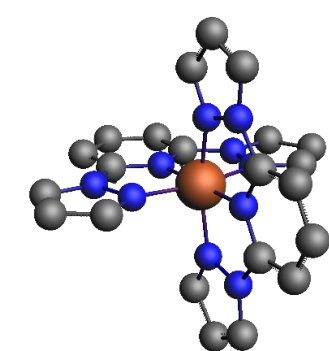
$$\Delta\rho_{(a3)} \Delta E_{13} = -8.7, |v_{13}| = 0.16 \text{ (pol)}$$



$$\Delta\rho_{(a4)} \Delta E_{14} = -8.7, |v_{14}| = 0.16 \text{ (pol)}$$

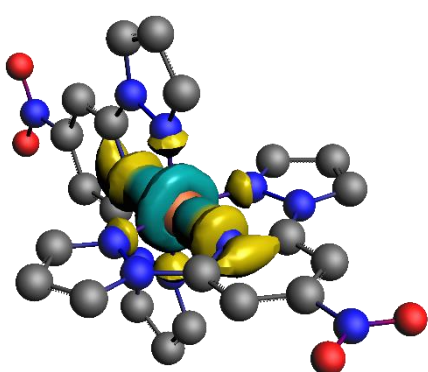


$$\Delta\rho_{(a5)} \Delta E_{15} = -5.0, |v_{15}| = 0.13 \text{ (pol)}$$

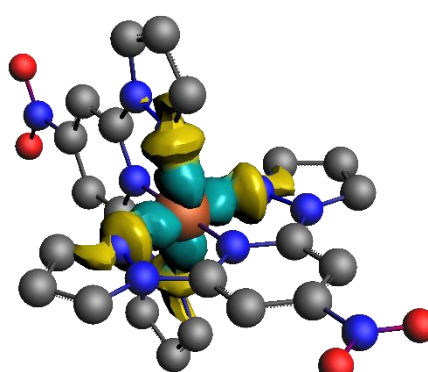


$$\Delta\rho_{(a6)} \Delta E_{16} = -4.7, |v_{16}| = 0.12 \text{ (pol)}$$

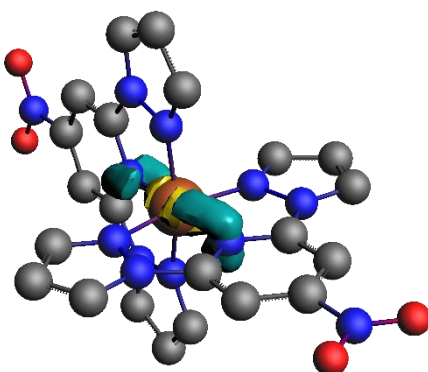
Figure A4.4. Plot of the deformation densities $\Delta\rho(i)$ with corresponding energy contribution to the total orbital term ΔE_i (given in kcal/mol) of the $M \leftarrow L_6$ σ -donation, the $M \rightarrow L_6$ π -backdonation and polarisation in complex LS $[\text{Fe}(\text{bpp}^{\text{NO}_2})_2]^{2+}$. The direction of the charge flow is yellow \rightarrow turquoise. The eigenvalues $|v_i|$ indicate the relative size of the charge flow (reported values for $|v_i| > 0.1$; $\rho < 0.003$). The choice of cut-off on deformation densities used to produce these images does not affect the results; as EDA-NOCV analysis are performed by applying default cut-off on NOCVs energies (0.5 kcal/mol) and individual SFO contribution (0.001).



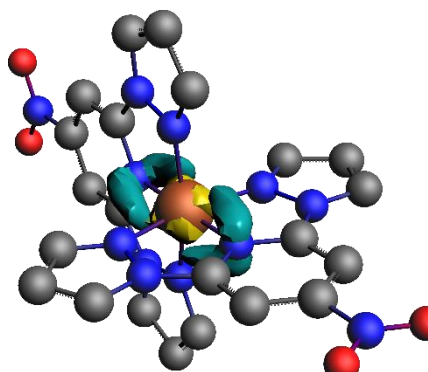
$\Delta\rho(1) \Delta E_1 = -130.6$, $|v_1| = 0.96$
($M(d_{z^2}) \leftarrow L_6$ σ -donation)



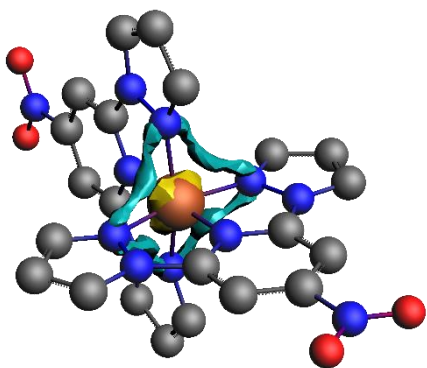
$\Delta\rho(2) \Delta E_2 = -116.8$, $|v_2| = 0.93$
($M(d_{x^2-y^2}) \leftarrow L_6$ σ -donation)



$\Delta\rho(3) \Delta E_3 = -17.7$, $|v_3| = 0.67$
($M(d_{xz,yz}) \rightarrow L_6$ π -backdonation)

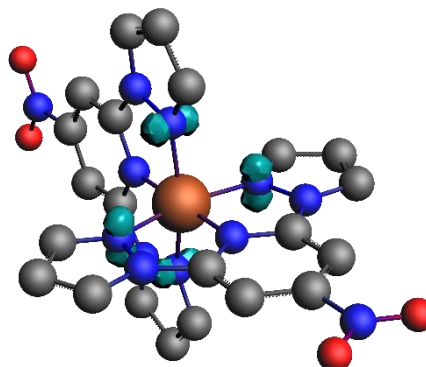


$\Delta\rho(4) \Delta E_4 = -17.8$, $|v_4| = 0.66$
($M(d_{xz,yz}) \rightarrow L_6$ π -backdonation)

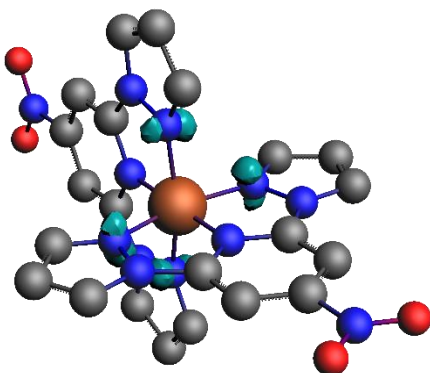


$$\Delta\rho^{(5)} \Delta E_5 = -12.4, |v_5| = 0.57$$

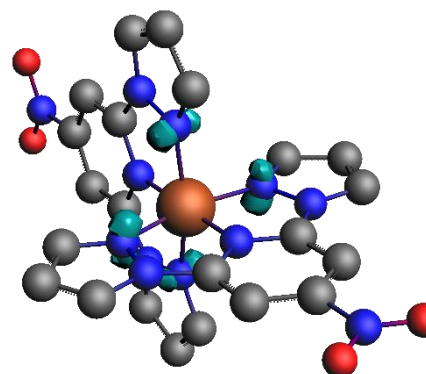
($M(d_{xy}) \rightarrow L_6 \pi$ -backdonation)



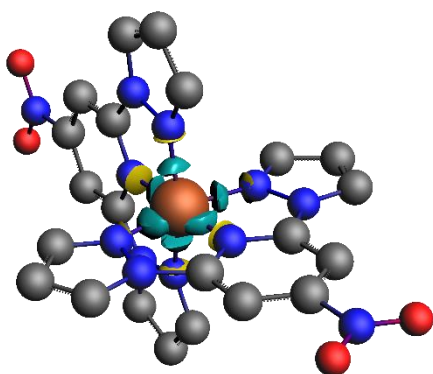
$$\Delta\rho^{(6)} \Delta E_6 = -17.1, |v_6| = 0.26 \text{ (pol)}$$



$$\Delta\rho^{(7)} \Delta E_7 = -17.5, |v_7| = 0.26 \text{ (pol)}$$

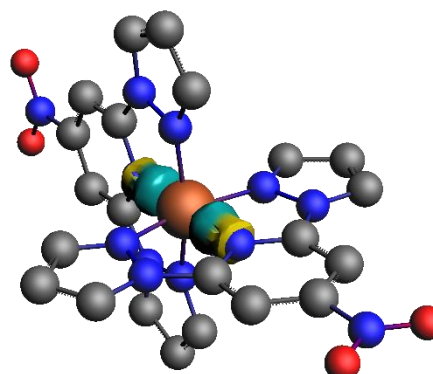


$$\Delta\rho^{(8)} \Delta E_8 = -17.5, |v_8| = 0.26 \text{ (pol)}$$



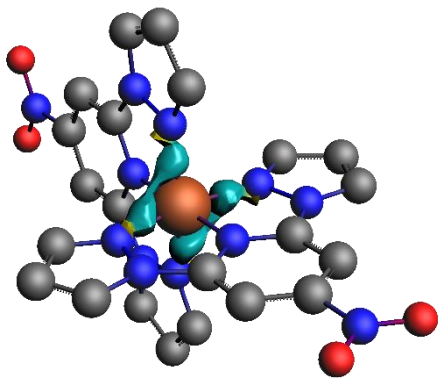
$$\Delta\rho^{(9)} \Delta E_9 = -24.4, |v_9| = 0.24$$

($M(s) \leftarrow L_6 \sigma$ -donation)



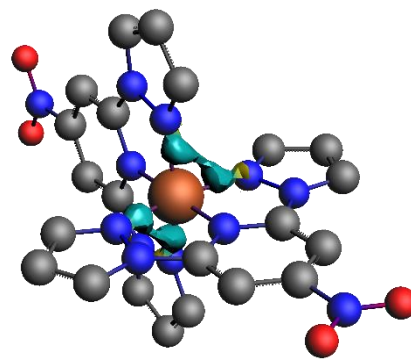
$$\Delta\rho^{(10)} \Delta E_{10} = -21.2, |v_{10}| = 0.21$$

($M(p_z) \leftarrow L_6 \sigma$ -donation)



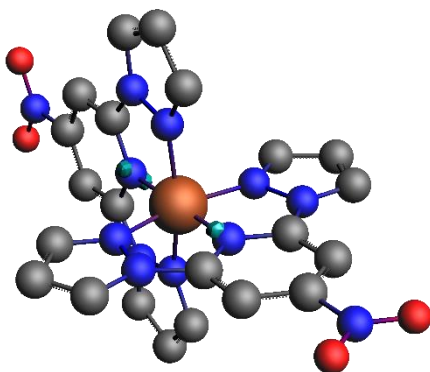
$$\Delta\rho_{(a1)} \Delta E_{11} = -19.5, |v_{11}| = 0.20$$

($M(p_{x,y}) \leftarrow L_6 \sigma$ -donation)

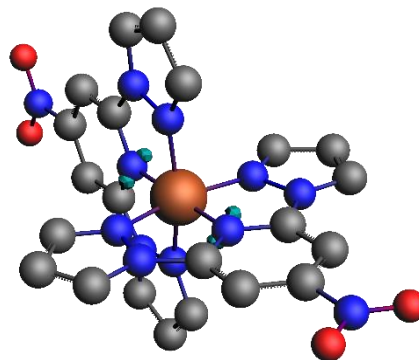


$$\Delta\rho_{(a2)} \Delta E_{12} = -19.5, |v_{12}| = 0.20$$

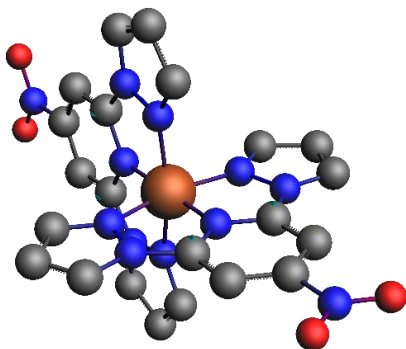
($M(p_{x,y}) \leftarrow L_6 \sigma$ -donation)



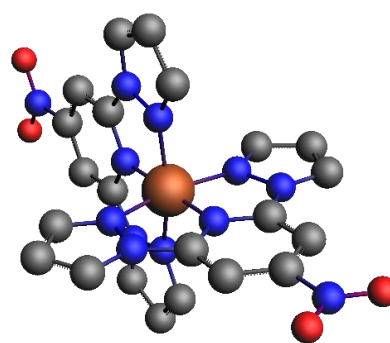
$$\Delta\rho_{(a3)} \Delta E_{13} = -8.8, |v_{13}| = 0.15 \text{ (pol)}$$



$$\Delta\rho_{(a4)} \Delta E_{14} = -8.8, |v_{14}| = 0.15 \text{ (pol)}$$



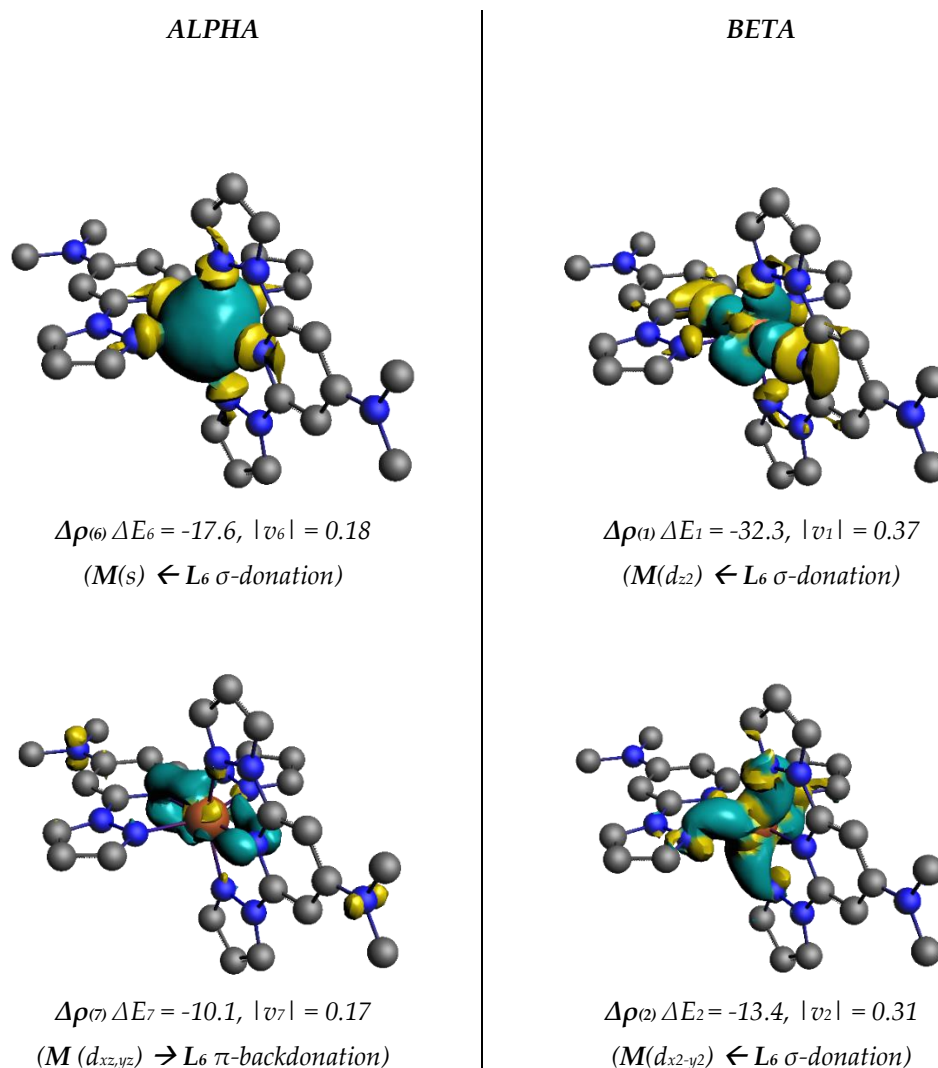
$$\Delta\rho_{(a5)} \Delta E_{15} = 5.2, |v_{15}| = 0.14 \text{ (pol)}$$

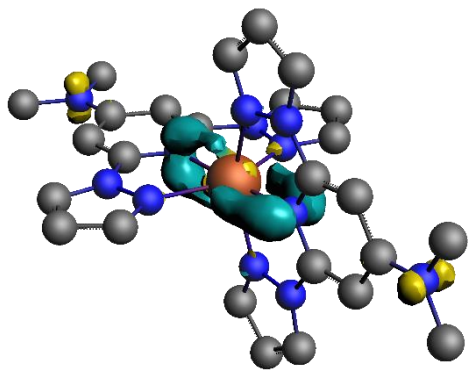


$$\Delta\rho_{(a6)} \Delta E_{16} = 5.0, |v_{16}| = 0.13 \text{ (pol)}$$

A4.1.4. NOCV Figures for $HS [Fe(bpp^X)_2]^{2+}$

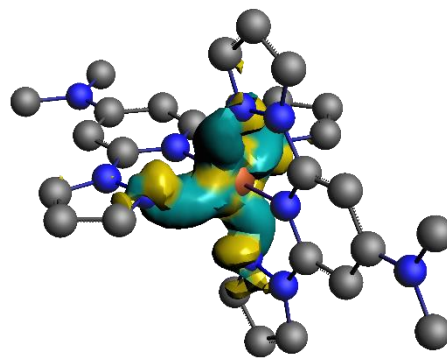
Figure A4.5. Plot of the deformation densities $\Delta\rho(i)$ with corresponding energy contribution to the total orbital term ΔE_i (given in kcal/mol) of the $M \leftarrow L_6$ σ -donation, the $M \rightarrow L_6$ π -backdonation and polarisation in complex $HS [Fe(bpp^{NMe_2})_2]^{2+}$ complexes. The direction of the charge flow is yellow \rightarrow turquoise. The eigenvalues $|v_i|$ indicate the relative size of the charge flow (reported values for $|v_i| > 0.05$; $\rho < 0.0003$). The choice of cut-off on deformation densities used to produce these images does not affect the results; as EDA-NOCV analysis are performed by applying default cut-off on NOCVs energies (0.5 kcal/mol) and individual SFO contribution (0.001).





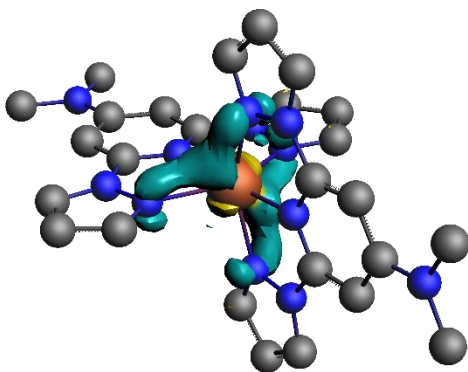
$$\Delta\rho^{(8)} \Delta E_8 = -9.5, |v_8| = 0.17$$

($M(d_{xy}) \rightarrow L_6 \pi$ -backdonation)



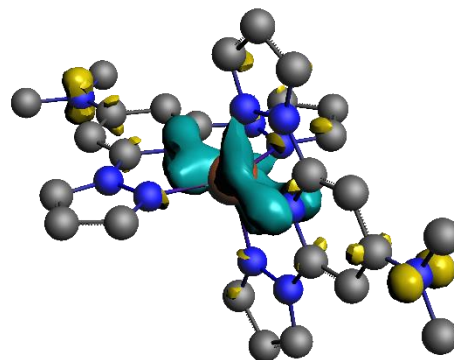
$$\Delta\rho^{(3)} \Delta E_3 = -14.5, |v_3| = 0.28$$

($M(d_{x^2-y^2}) \leftarrow L_6 \sigma$ -donation)

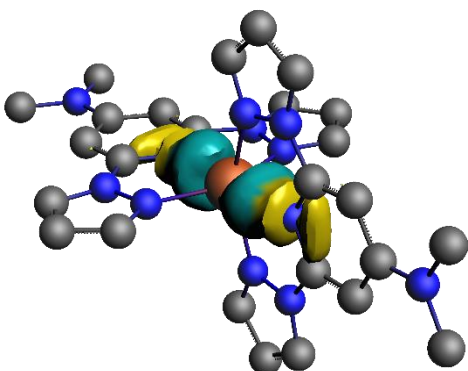


$$\Delta\rho^{(10)} \Delta E_{10} = -6.0, |v_{10}| = 0.15$$

($M(d_{xy}) \rightarrow L_6 \pi$ -backdonation)

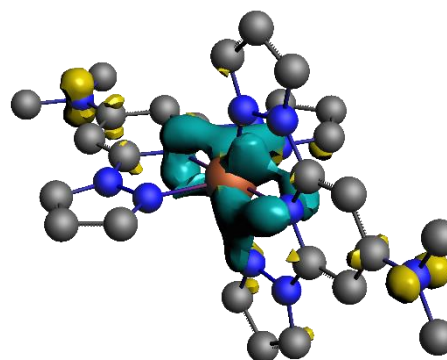


$$\Delta\rho^{(4)} \Delta E_4 = -16.7, |v_4| = 0.26 \text{ (pol)}$$

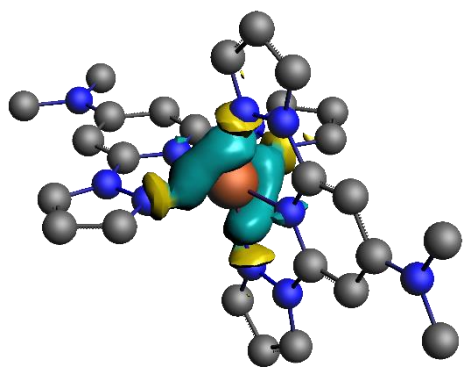


$$\Delta\rho^{(11)} \Delta E_{11} = -11.1, |v_{11}| = 0.13$$

($M(p_z) \leftarrow L_6 \sigma$ -donation)

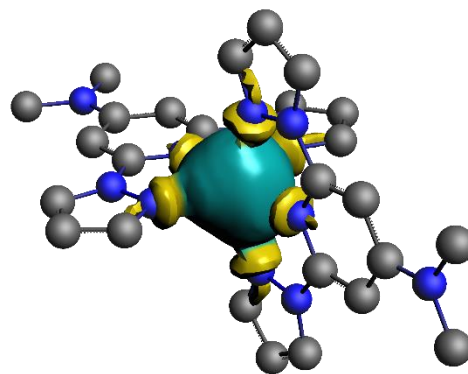


$$\Delta\rho^{(5)} \Delta E_5 = -16.3, |v_5| = 0.26 \text{ (pol)}$$



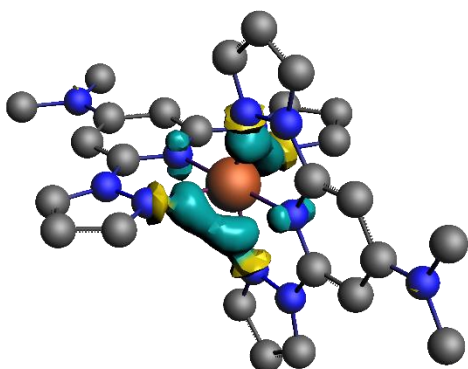
$$\Delta\rho_{(a5)} \Delta E_{15} = -8.3, |v_{15}| = 0.11$$

($M(p_{x,y}) \leftarrow L_6 \sigma$ -donation)



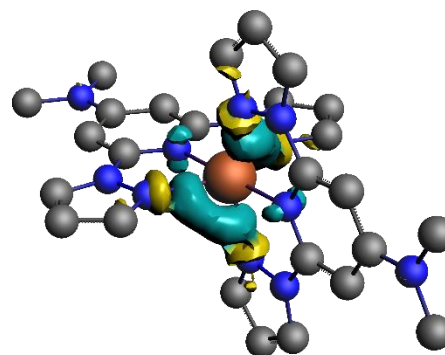
$$\Delta\rho_{(9)} \Delta E_9 = -13.5, |v_9| = 0.15$$

($M(s) \leftarrow L_6 \sigma$ -donation)



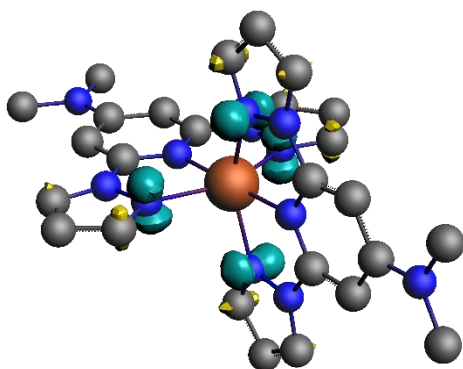
$$\Delta\rho_{(a6)} \Delta E_{16} = -7.8, |v_{16}| = 0.11$$

($M(p_{x,y}) \leftarrow L_6 \sigma$ -donation)

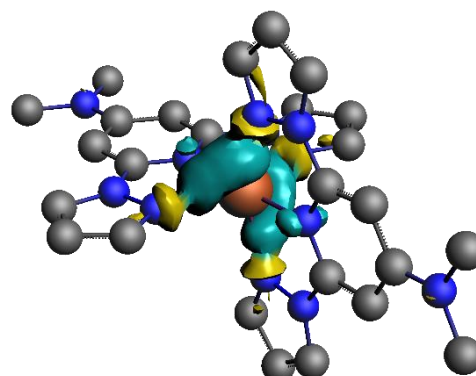


$$\Delta\rho_{(a2)} \Delta E_{12} = -9.5, |v_{12}| = 0.13$$

($M(p_{x,y}) \leftarrow L_6 \sigma$ -donation)

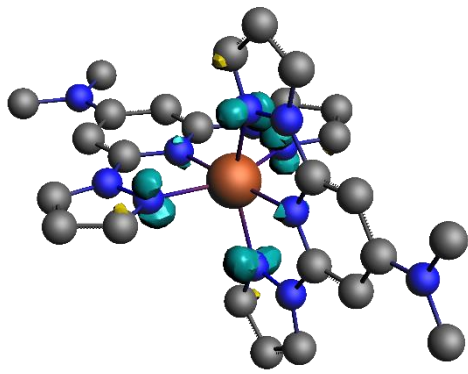


$$\Delta\rho_{(a7)} \Delta E_{17} = -5.4, |v_{17}| = 0.10 \text{ (pol)}$$

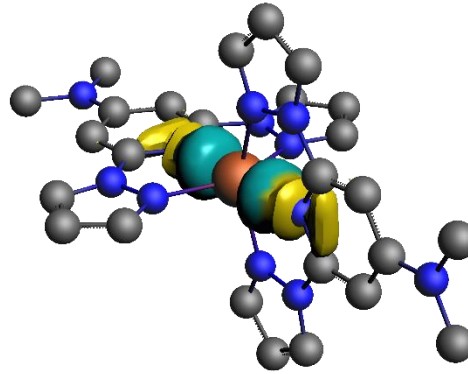


$$\Delta\rho_{(a3)} \Delta E_{13} = -9.0, |v_{13}| = 0.13$$

($M(p_{x,y}) \leftarrow L_6 \sigma$ -donation)

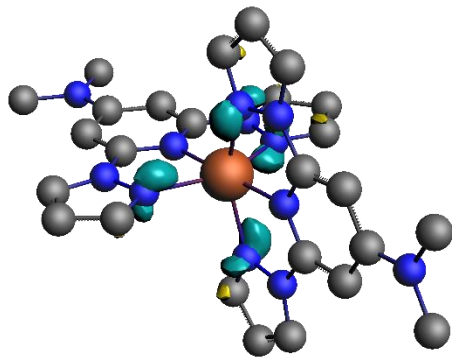


$$\Delta\rho_{(19)} \Delta E_{19} = -5.2, |v_{19}| = 0.09 \text{ (pol)}$$

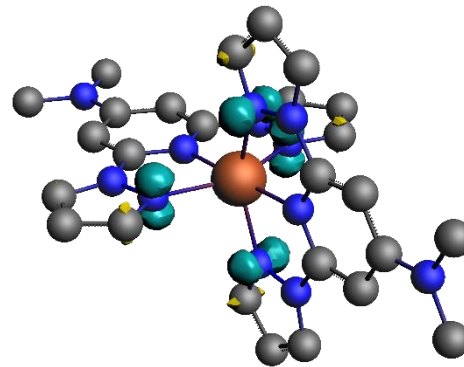


$$\Delta\rho_{(14)} \Delta E_{14} = -9.5, |v_{14}| = 0.11 \text{ (pol)}$$

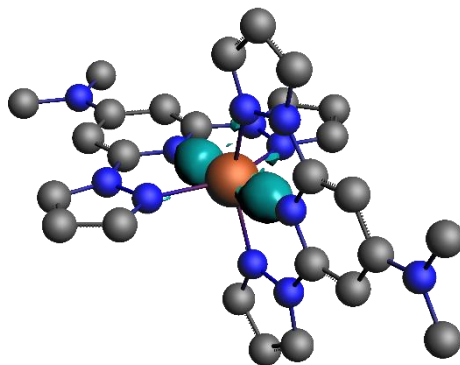
$(M(p_z) \leftarrow L_6 \sigma\text{-donation})$



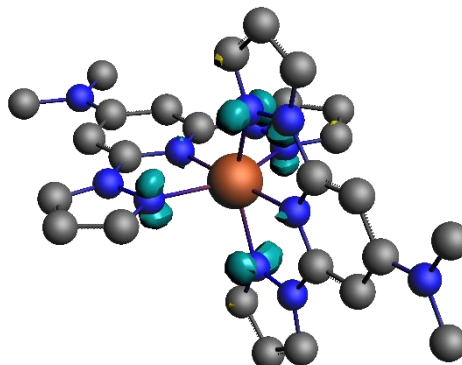
$$\Delta\rho_{(20)} \Delta E_{20} = -5.3, |v_{20}| = 0.09 \text{ (pol)}$$



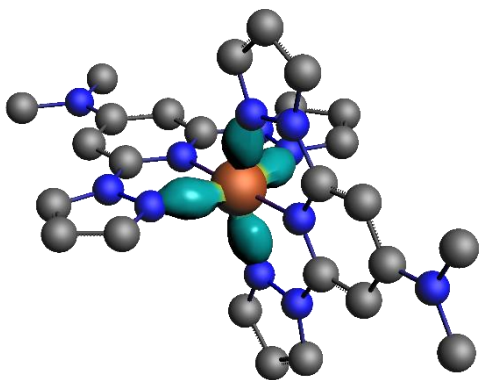
$$\Delta\rho_{(18)} \Delta E_{18} = -5.0, |v_{18}| = 0.09 \text{ (pol)}$$



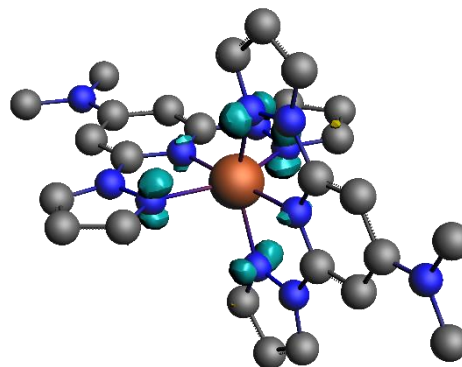
$$\Delta\rho_{(21)} \Delta E_{21} = -5.4, |v_{21}| = 0.09 \text{ (pol)}$$



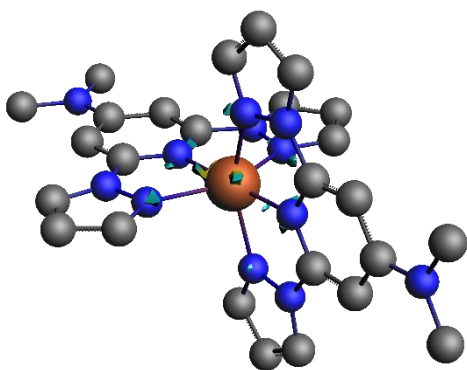
$$\Delta\rho_{(21)} \Delta E_{21} = -4.8, |v_{21}| = 0.09 \text{ (pol)}$$



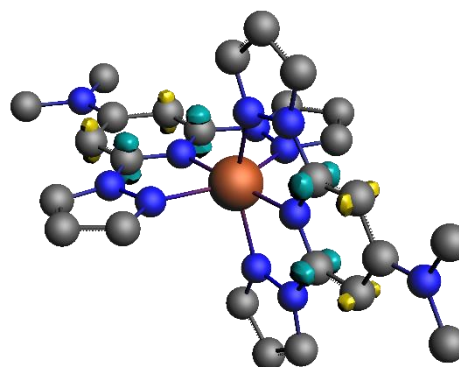
$$\Delta\rho_{(24)} \Delta E_{24} = -4.7, |v_{24}| = 0.07 \text{ (pol)}$$



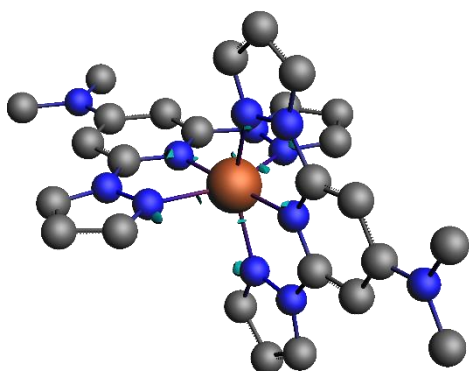
$$\Delta\rho_{(22)} \Delta E_{22} = -4.7, |v_{22}| = 0.09 \text{ (pol)}$$



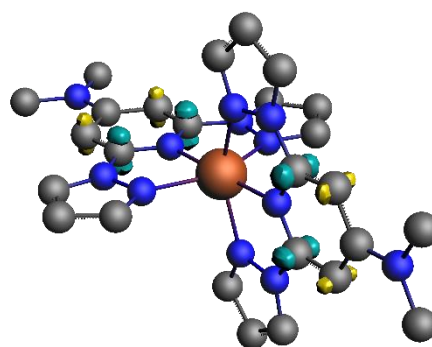
$$\Delta\rho_{(25)} \Delta E_{25} = -2.4, |v_{25}| = 0.07 \text{ (pol)}$$



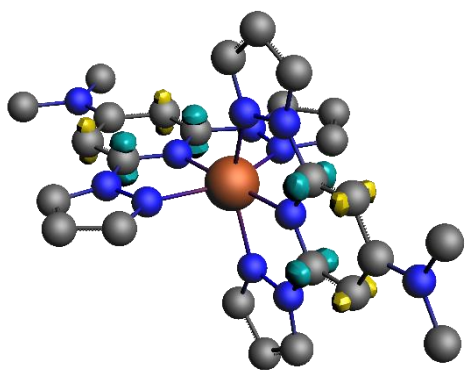
$$\Delta\rho_{(25)} \Delta E_{25} = -1.9, |v_{25}| = 0.05 \text{ (pol)}$$



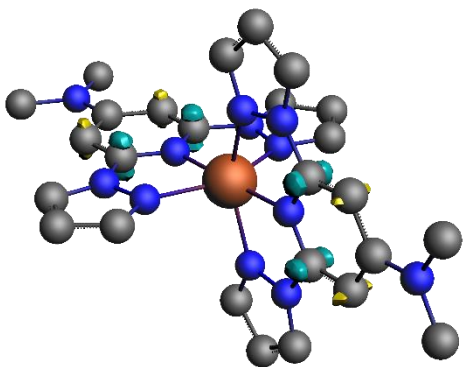
$$\Delta\rho_{(26)} \Delta E_{26} = -2.4, |v_{26}| = 0.067 \text{ (pol)}$$



$$\Delta\rho_{(28)} \Delta E_{27} = -1.8, |v_{27}| = 0.05 \text{ (pol)}$$

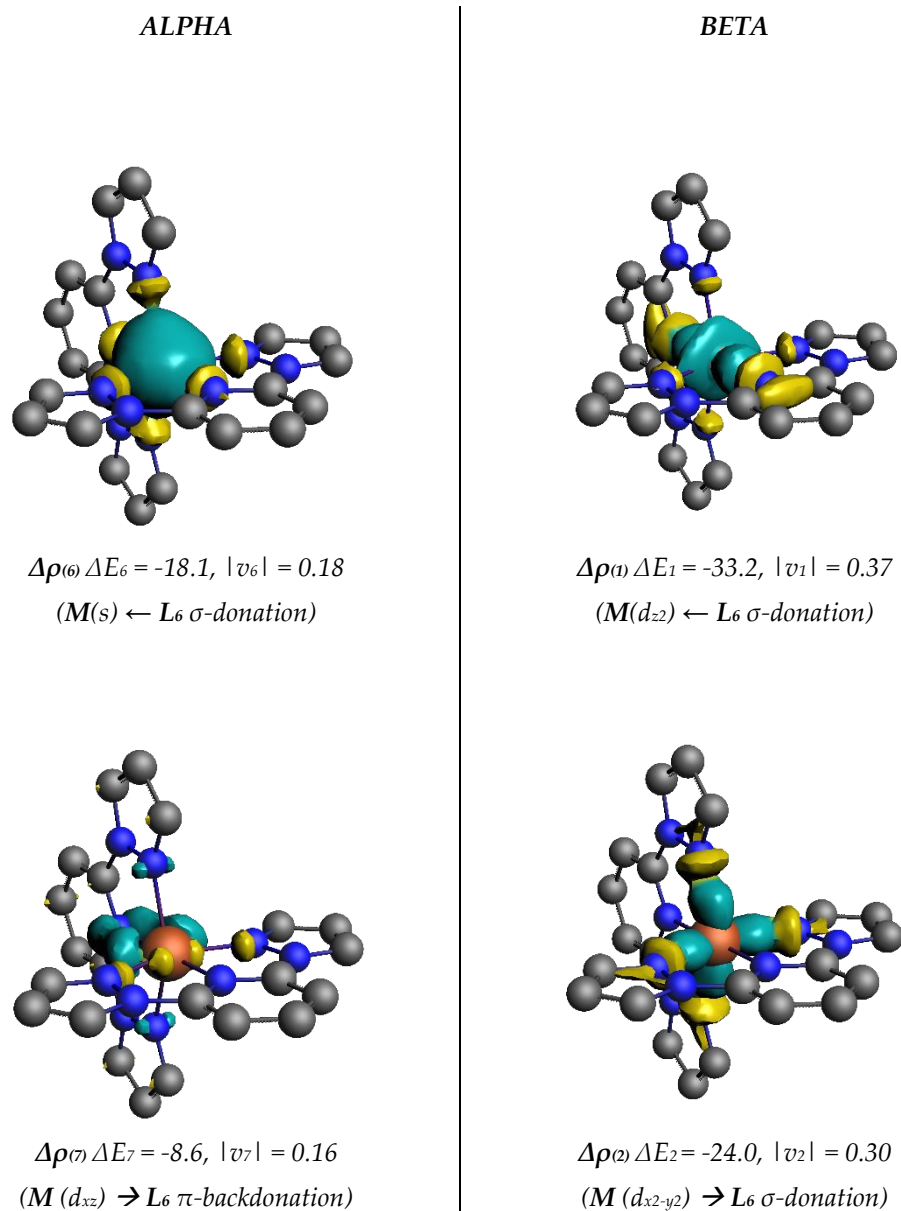


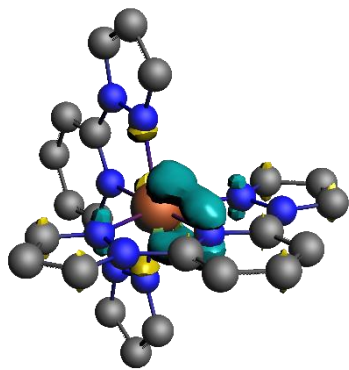
$$\Delta\rho_{(27)} \Delta E_{27} = -1.8, |v_{27}| = 0.06 \text{ (pol)}$$



$$\Delta\rho_{(29)} \Delta E_{29} = -1.8, |v_{29}| = 0.05 \text{ (pol)}$$

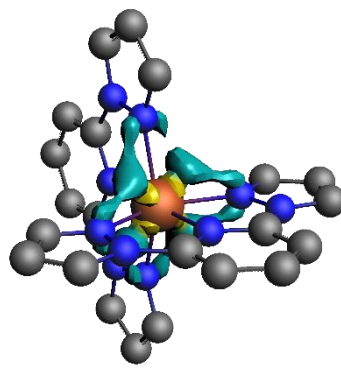
Figure A4.6. Plot of the deformation densities $\Delta\rho(i)$ with corresponding energy contribution to the total orbital term ΔE_i (given in kcal/mol) of the $M \leftarrow L_6$ σ -donation, the $M \rightarrow L_6$ π -backdonation and polarisation in complex HS $[\text{Fe}(\text{bpp}^{\text{H}})_2]^{2+}$. The direction of the charge flow is yellow \rightarrow turquoise. The eigenvalues $|v_i|$ indicate the relative size of the charge flow (reported values for $|v_i| > 0.05$; $\rho < 0.0003$). The choice of cut-off on deformation densities used to produce these images does not affect the results; as EDA-NOCV analysis are performed by applying default cut-off on NOCVs energies (0.5 kcal/mol) and individual SFO contribution (0.001).





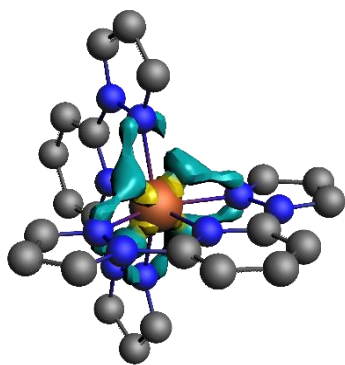
$$\Delta\rho^{(8)} \Delta E_8 = -8.5, |v_8| = 0.16$$

($M(d_{z^2}) \rightarrow L_6 \pi$ -backdonation)



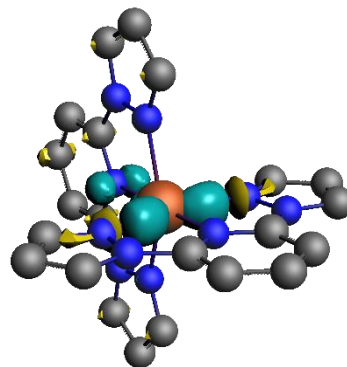
$$\Delta\rho^{(3)} \Delta E_3 = -3.5, |v_3| = 0.29$$

($M(d_{xy}) \rightarrow L_6 \pi$ -backdonation)



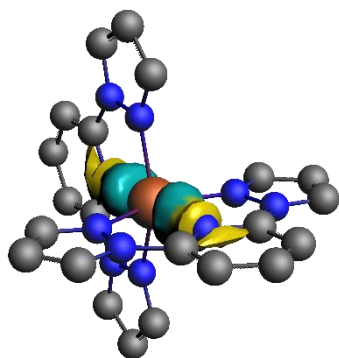
$$\Delta\rho^{(10)} \Delta E_{10} = -5.9, |v_{10}| = 0.15$$

($M(d_{xy}) \rightarrow L_6 \pi$ -backdonation)



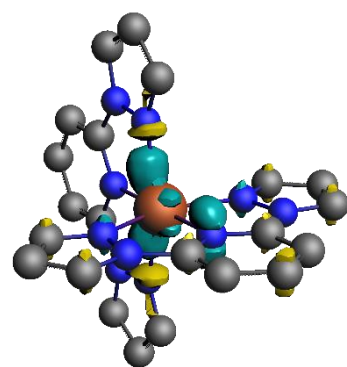
$$\Delta\rho^{(4)} \Delta E_4 = -14.0, |v_4| = 0.22$$

($M(d_{z^2}) \leftarrow L_6 \sigma$ -donation)



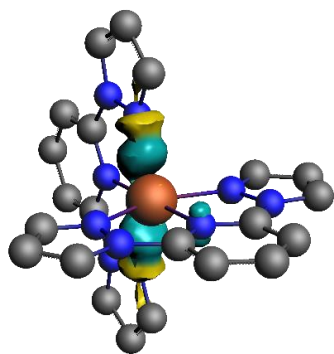
$$\Delta\rho^{(11)} \Delta E_{11} = -11.0, |v_{11}| = 0.13$$

($M(p_z) \leftarrow L_6 \sigma$ -donation)



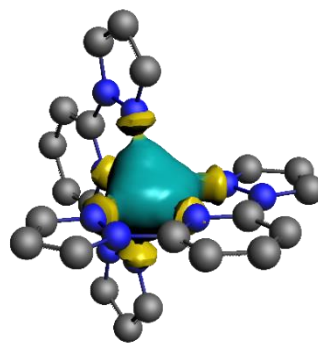
$$\Delta\rho^{(5)} \Delta E_5 = -13.3, |v_5| = 0.21$$

($M(d_{zx}) \leftarrow L_6 \sigma$ -donation)



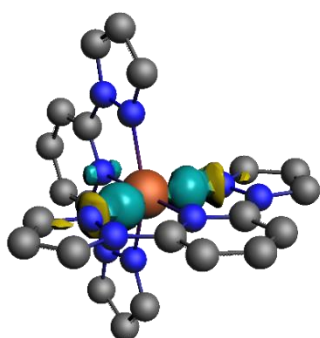
$$\Delta\rho_{(a5)} \Delta E_{15} = -7.9, |v_{15}| = 0.11$$

$(M(p_x) \leftarrow L_6 \sigma\text{-donation})$



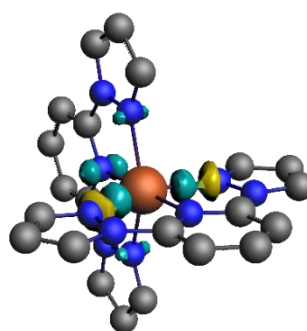
$$\Delta\rho_{(9)} \Delta E_9 = -13.8, |v_9| = 0.15$$

$(M(s) \leftarrow L_6 \sigma\text{-donation})$



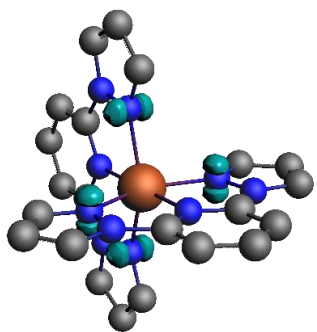
$$\Delta\rho_{(a6)} \Delta E_{16} = -7.9, |v_{16}| = 0.10$$

$(M(p_y) \leftarrow L_6 \sigma\text{-donation})$

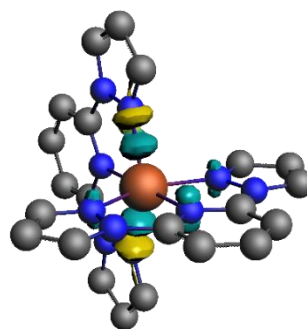


$$\Delta\rho_{(a2)} \Delta E_{12} = -8.6, |v_{12}| = 0.12$$

$(M(p_z) \leftarrow L_6 \sigma\text{-donation})$

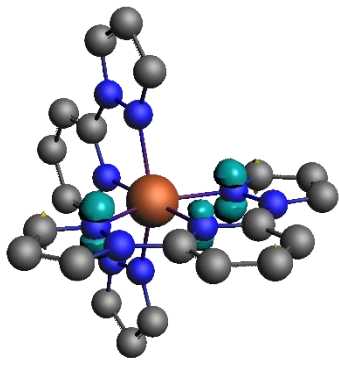


$$\Delta\rho_{(a7)} \Delta E_{17} = -5.6, |v_{17}| = 0.10 \text{ (pol)}$$

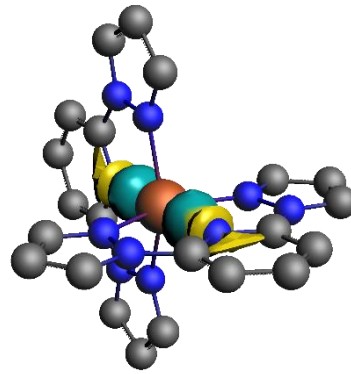


$$\Delta\rho_{(a3)} \Delta E_{13} = -8.7, |v_{13}| = 0.12 \text{ (pol)}$$

$(M(p_x) \leftarrow L_6 \sigma\text{-donation})$

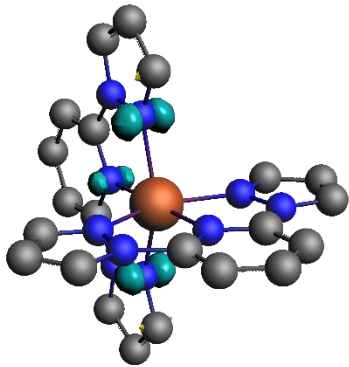


$$\Delta\rho_{(a9)} \Delta E_{19} = -5.0, |v_{19}| = 0.09 \text{ (pol)}$$

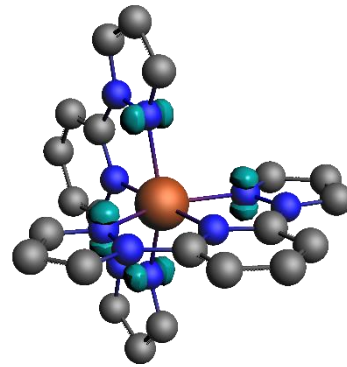


$$\Delta\rho_{(a4)} \Delta E_{14} = -9.4, |v_{14}| = 0.11$$

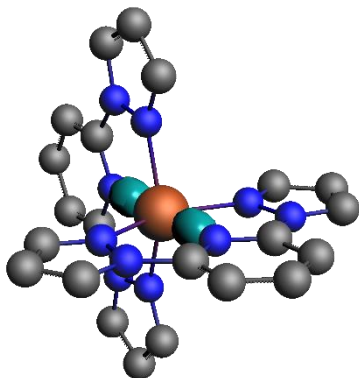
$(M(p_z) \leftarrow L_6 \sigma\text{-donation})$



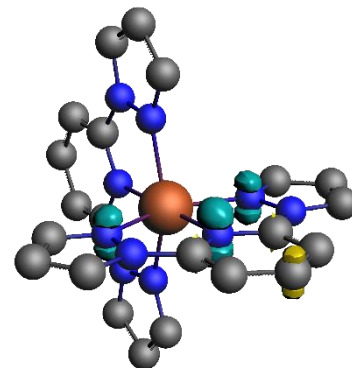
$$\Delta\rho_{(20)} \Delta E_{20} = -5.0, |v_{20}| = 0.09 \text{ (pol)}$$



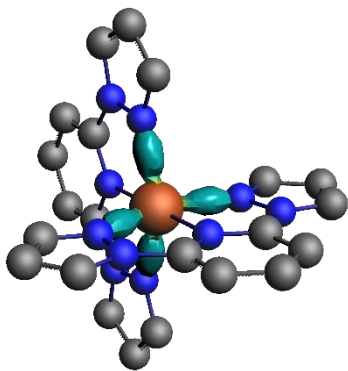
$$\Delta\rho_{(a8)} \Delta E_{18} = -5.3, |v_{18}| = 0.09 \text{ (pol)}$$



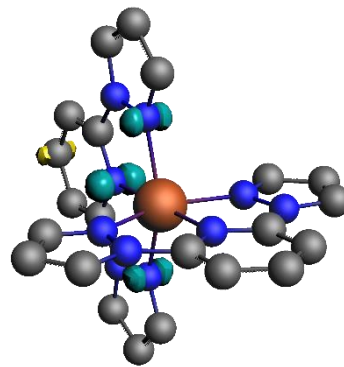
$$\Delta\rho_{(21)} \Delta E_{21} = -5.4, |v_{21}| = 0.08 \text{ (pol)}$$



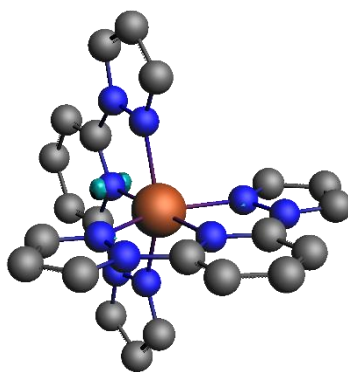
$$\Delta\rho_{(22)} \Delta E_{22} = -4.7, |v_{22}| = 0.09 \text{ (pol)}$$



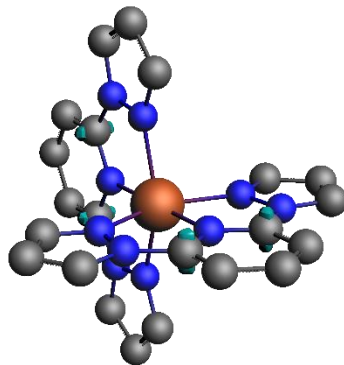
$$\Delta\rho_{(24)} \Delta E_{24} = -4.8, |v_{24}| = 0.08 \text{ (pol)}$$



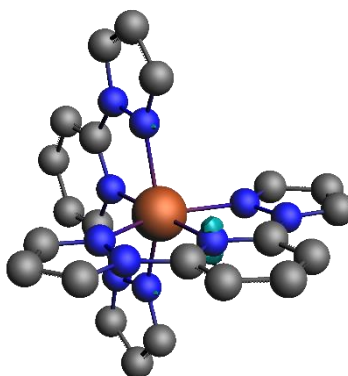
$$\Delta\rho_{(23)} \Delta E_{23} = -4.7, |v_{23}| = 0.08 \text{ (pol)}$$



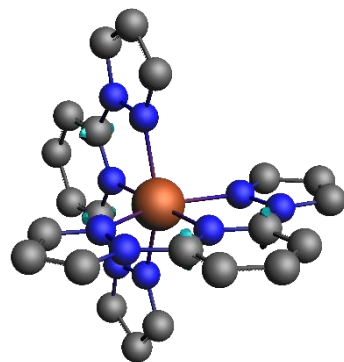
$$\Delta\rho_{(25)} \Delta E_{25} = -2.5, |v_{25}| = 0.06 \text{ (pol)}$$



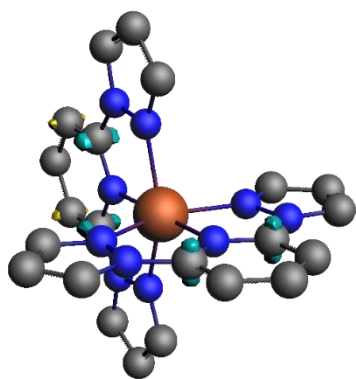
$$\Delta\rho_{(26)} \Delta E_{26} = -2.0, |v_{26}| = 0.06 \text{ (pol)}$$



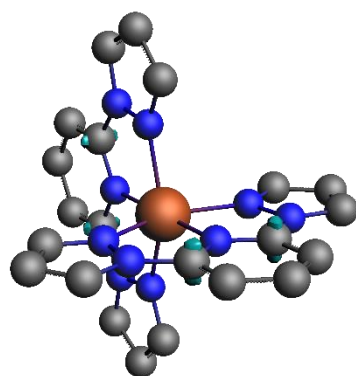
$$\Delta\rho_{(27)} \Delta E_{27} = -2.5, |v_{27}| = 0.06 \text{ (pol)}$$



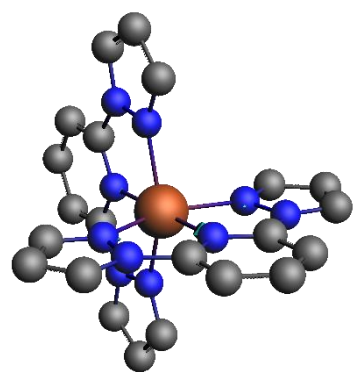
$$\Delta\rho_{(30)} \Delta E_{30} = -1.9, |v_{30}| = 0.06 \text{ (pol)}$$



$$\Delta\rho_{(28)} \Delta E_{28} = -2.0, |v_{28}| = 0.06 \text{ (pol)}$$

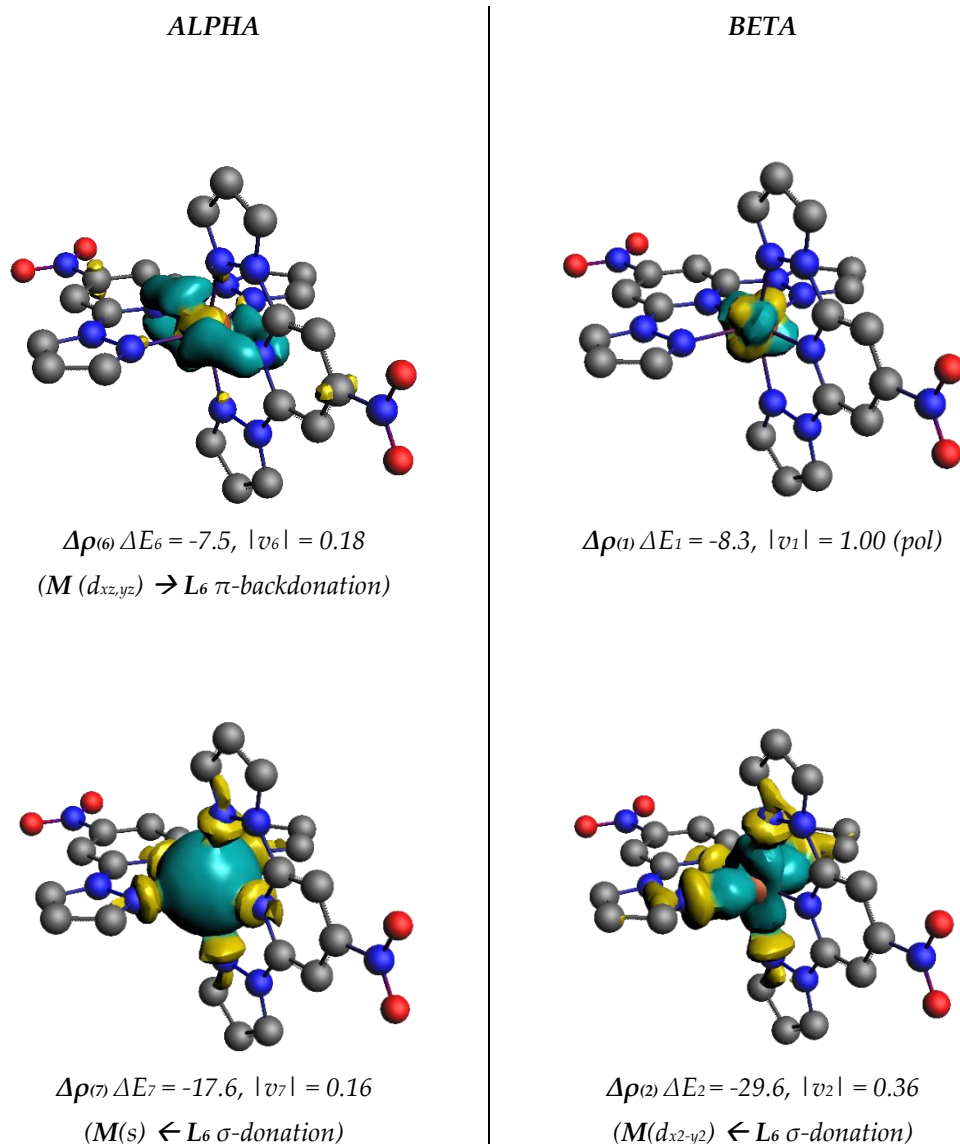


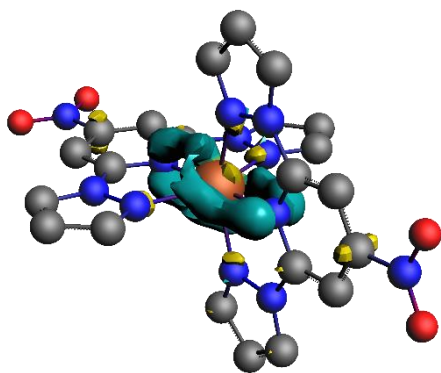
$$\Delta\rho_{(29)} \Delta E_{29} = -2.0, |v_{29}| = 0.06 \text{ (pol)}$$



$$\Delta\rho_{(31)} \Delta E_{31} = -1.9, |v_{31}| = 0.05 \text{ (pol)}$$

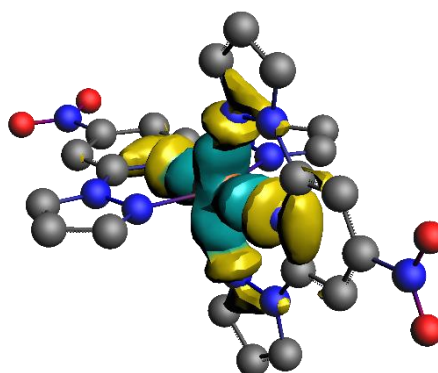
Figure A4.7. Plot of the deformation densities $\Delta\rho(i)$ with corresponding energy contribution to the total orbital term ΔE_i (given in kcal/mol) of the $M \leftarrow L_6$ σ -donation, the $M \rightarrow L_6$ π -backdonation and polarisation in complex HS $[Fe(\mathbf{bpp}^{\text{NO}_2})_2]^{2+}$. The direction of the charge flow is yellow \rightarrow turquoise. The eigenvalues $|v_i|$ indicate the relative size of the charge flow (reported values for $|v_i| > 0.05$; $\rho < 0.0003$). The choice of cut-off on deformation densities used to produce these images does not affect the results; as EDA-NOCV analysis are performed by applying default cut-off on NOCVs energies (0.5 kcal/mol) and individual SFO contribution (0.001).





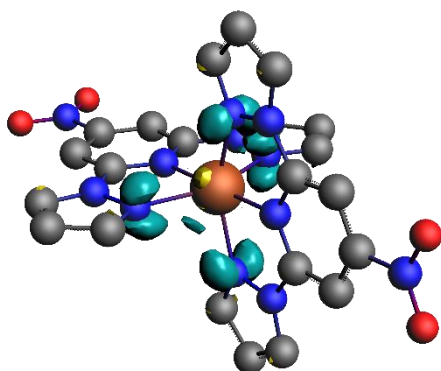
$$\Delta\rho^{(8)} \Delta E_8 = -9.0, |v_8| = 0.13$$

($M(d_{xz,yz}) \rightarrow L_6 \pi$ -backdonation)



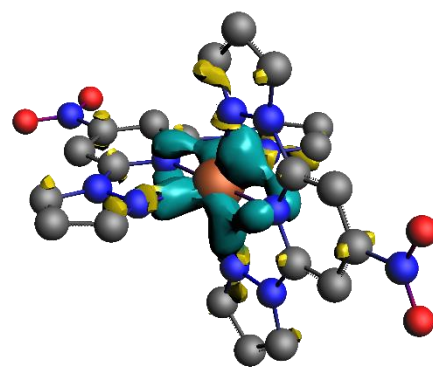
$$\Delta\rho^{(3)} \Delta E_3 = -33.3, |v_3| = 0.36$$

($M(d_{z^2}) \leftarrow L_6 \sigma$ -donation)

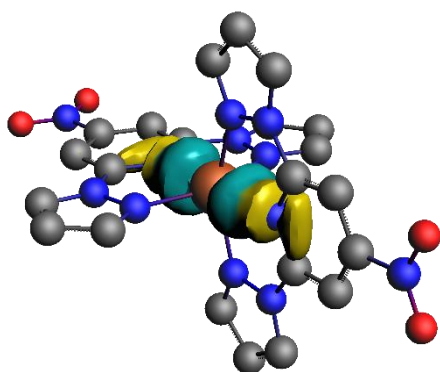


$$\Delta\rho^{(10)} \Delta E_{10} = -6.9, |v_{10}| = 0.15$$

($M(d_{xy}) \rightarrow L_6 \pi$ -backdonation)

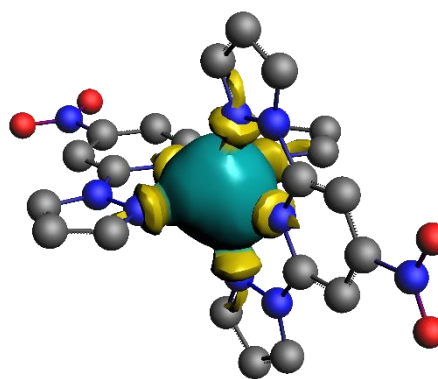


$$\Delta\rho^{(4)} \Delta E_4 = -14.8, |v_4| = 0.23 \text{ (pol)}$$



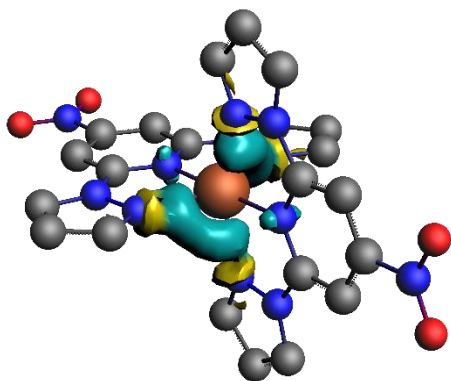
$$\Delta\rho^{(11)} \Delta E_{11} = -10.5, |v_{11}| = 0.12$$

($M(p_z) \leftarrow L_6 \sigma$ -donation)



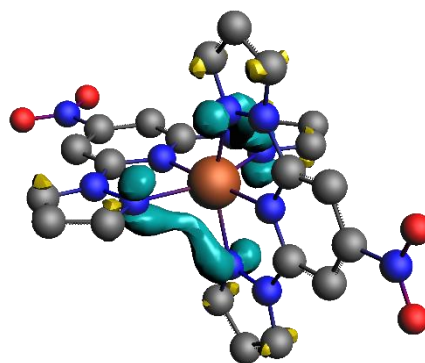
$$\Delta\rho^{(5)} \Delta E_5 = -13.6, |v_5| = 0.15$$

($M(s) \leftarrow L_6 \sigma$ -donation)

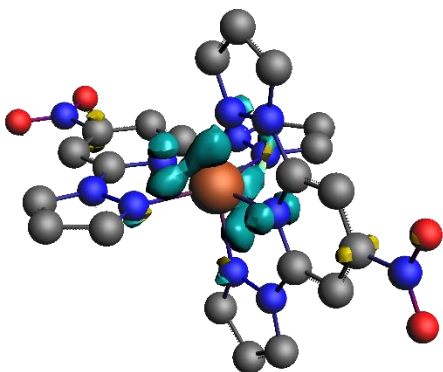


$$\Delta\rho_{(15)} \Delta E_{15} = -8.8, |v_{15}| = 0.12$$

$(M(p_{x,y}) \leftarrow L_6 \sigma\text{-donation})$

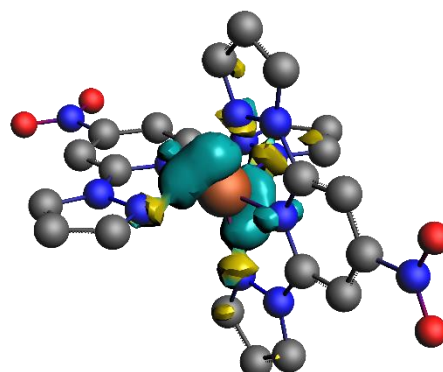


$$\Delta\rho_{(9)} \Delta E_9 = -8.3, |v_9| = 0.13 \text{ (pol)}$$



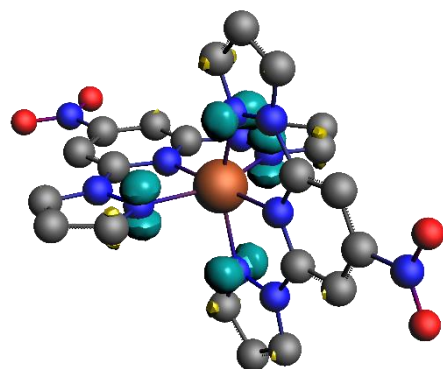
$$\Delta\rho_{(16)} \Delta E_{16} = -7.5, |v_{16}| = 0.11$$

$(M(p_{x,y}) \leftarrow L_6 \sigma\text{-donation})$

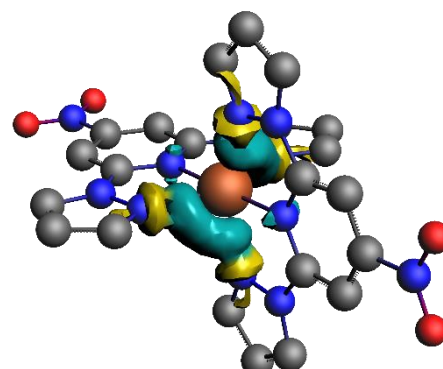


$$\Delta\rho_{(12)} \Delta E_{12} = -9.1, |v_{12}| = 0.13$$

$(M(p_{x,y}) \leftarrow L_6 \sigma\text{-donation})$

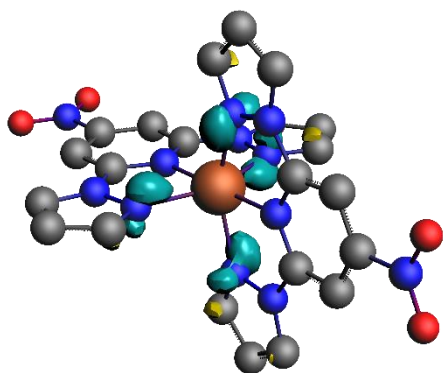


$$\Delta\rho_{(17)} \Delta E_{17} = -6.2, |v_{17}| = 0.11 \text{ (pol)}$$

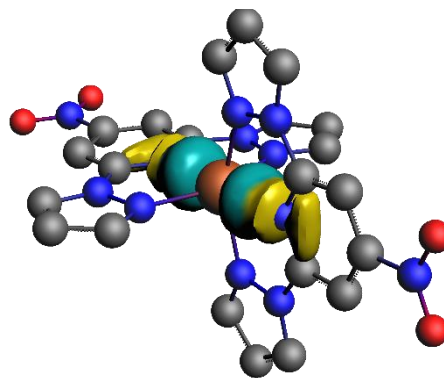


$$\Delta\rho_{(13)} \Delta E_{13} = -9.3, |v_{13}| = 0.12$$

$(M(p_{x,y}) \leftarrow L_6 \sigma\text{-donation})$

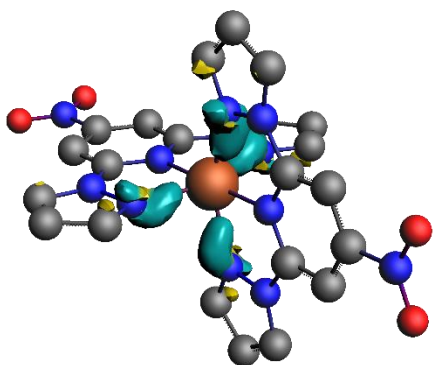


$$\Delta\rho_{(19)} \Delta E_{19} = -6.5, |v_{19}| = 0.11(\text{pol})$$

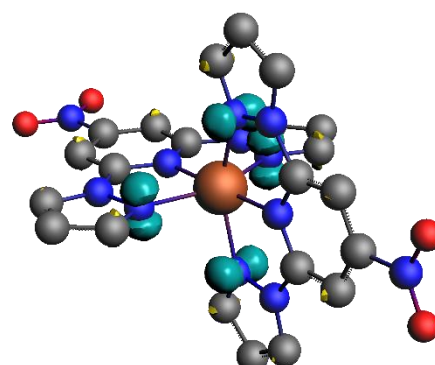


$$\Delta\rho_{(14)} \Delta E_{14} = -9.3, |v_{14}| = 0.11$$

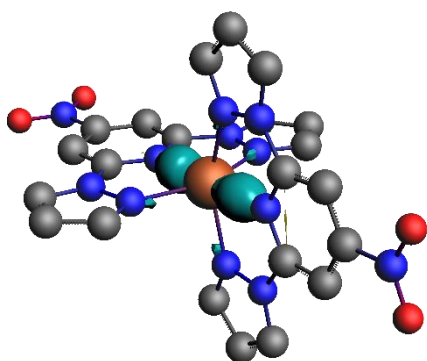
$(M(p_z) \leftarrow L_6 \sigma\text{-donation})$



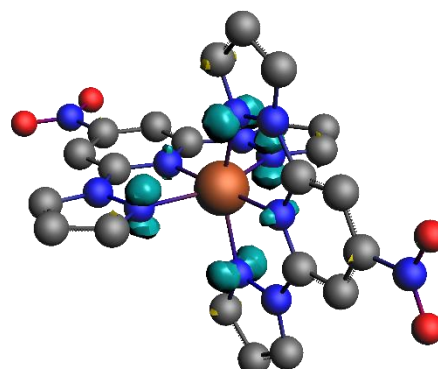
$$\Delta\rho_{(20)} \Delta E_{20} = -6.8, |v_{20}| = 0.09(\text{pol})$$



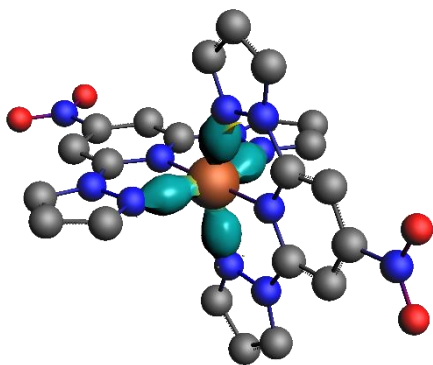
$$\Delta\rho_{(18)} \Delta E_{18} = -5.7, |v_{18}| = 0.11(\text{pol})$$



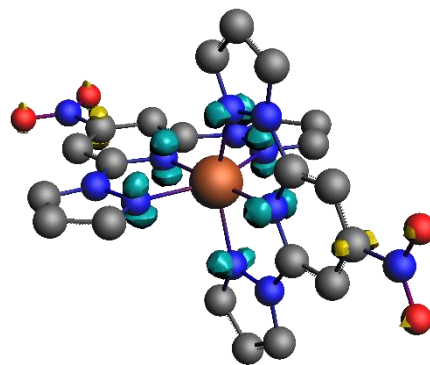
$$\Delta\rho_{(21)} \Delta E_{21} = -5.4, |v_{21}| = 0.08(\text{pol})$$



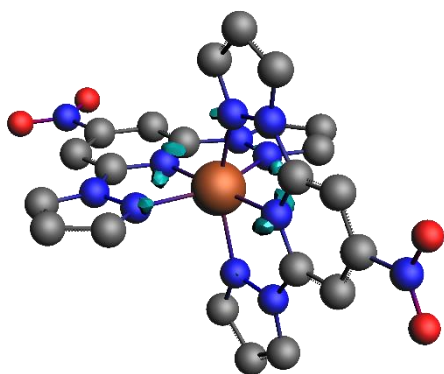
$$\Delta\rho_{(22)} \Delta E_{22} = -5.8, |v_{22}| = 0.10(\text{pol})$$



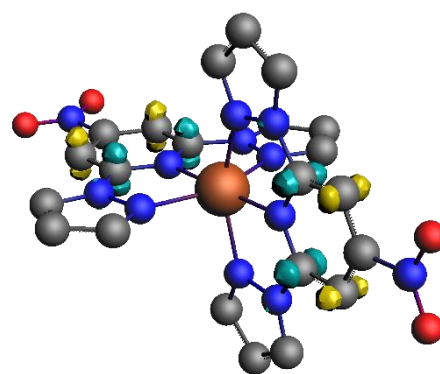
$$\Delta\rho_{(24)} \Delta E_{24} = -5.2, |v_{24}| = 0.07 \text{ (pol)}$$



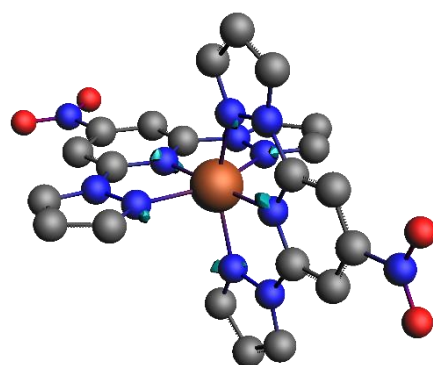
$$\Delta\rho_{(23)} \Delta E_{23} = -5.5, |v_{23}| = 0.10 \text{ (pol)}$$



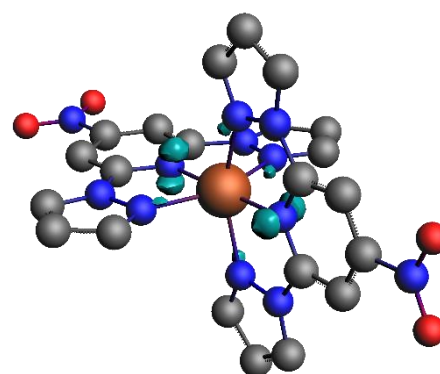
$$\Delta\rho_{(25)} \Delta E_{25} = -2.7, |v_{25}| = 0.07 \text{ (pol)}$$



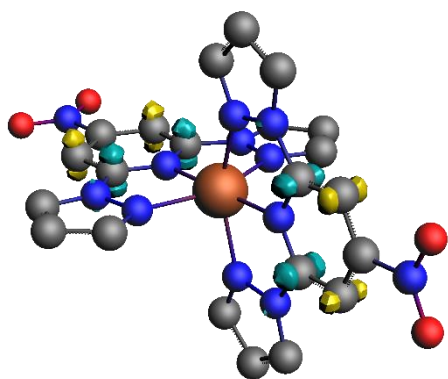
$$\Delta\rho_{(28)} \Delta E_{28} = -2.2, |v_{28}| = 0.07 \text{ (pol)}$$



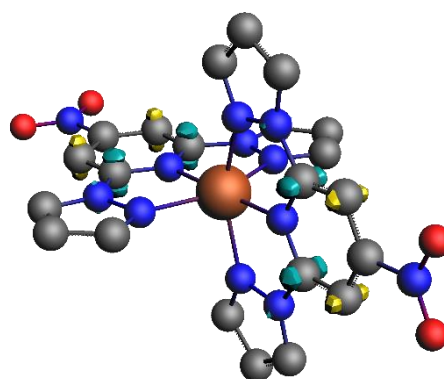
$$\Delta\rho_{(26)} \Delta E_{26} = -2.6, |v_{26}| = 0.07 \text{ (pol)}$$



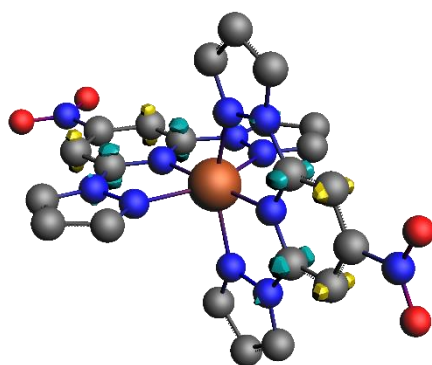
$$\Delta\rho_{(30)} \Delta E_{30} = -3.5, |v_{30}| = 0.06 \text{ (pol)}$$



$$\Delta\rho_{(27)} \Delta E_{27} = -2.1, |v_{27}| = 0.06 \text{ (pol)}$$



$$\Delta\rho_{(31)} \Delta E_{31} = -2.1, |v_{31}| = 0.06 \text{ (pol)}$$



$$\Delta\rho_{(29)} \Delta E_{29} = -2.0, |v_{29}| = 0.06 \text{ (pol)}$$

A4.2. Correlations of ΔE_i in LS $[\text{Fe}(\text{bpp}^X)_2]^{2+}$

A4.2.1. Transition Temperature $T_{1/2}$

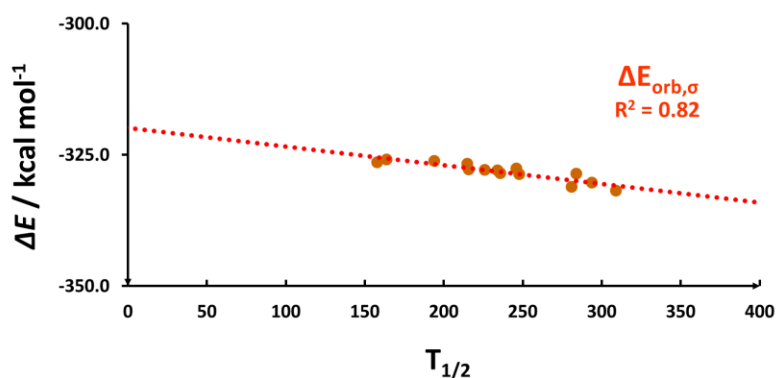


Figure A4.8. Strong correlation ($R^2 = 0.82$) of $\Delta E_{\text{orb},\sigma+\pi}$ with $T_{1/2}$ in the family of fourteen LS $[\text{Fe}(\text{bpp}^X)_2]^{2+}$ complexes ($X = \text{NH}_2, \text{NMe}_2$ are absent).

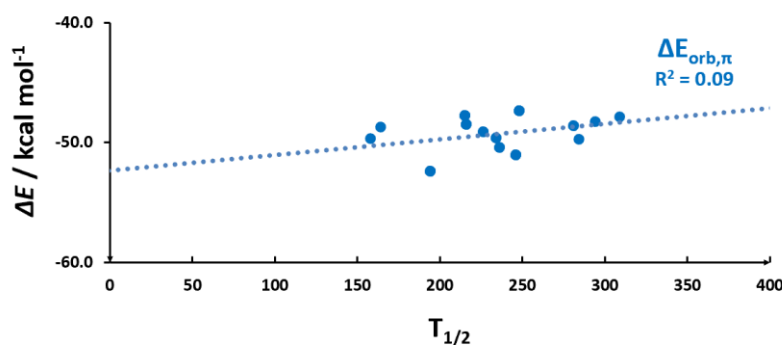


Figure A4.9. Absence of correlation ($R^2 = 0.09$) of $\Delta E_{\text{orb},\pi}$ with $T_{1/2}$ in the family of fourteen LS $[\text{Fe}(\text{bpp}^X)_2]^{2+}$ complexes ($X = \text{NH}_2, \text{NMe}_2$ are absent).

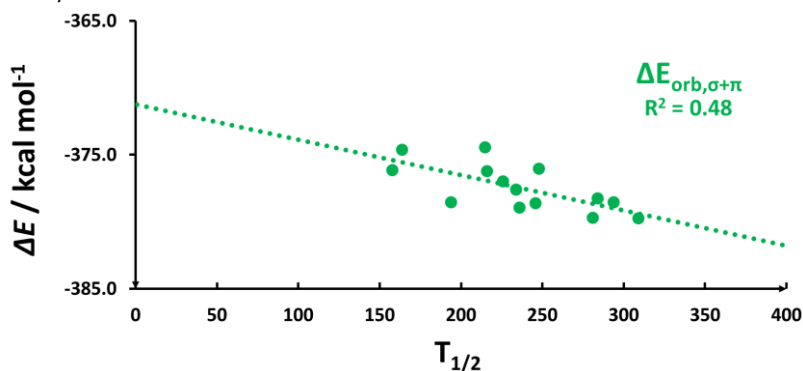


Figure A4.10. Weak correlation ($R^2 = 0.48$) of $\Delta E_{\text{orb},\sigma}$ with $T_{1/2}$ in the family of fourteen LS $[\text{Fe}(\text{bpp}^X)_2]^{2+}$ complexes ($X = \text{NH}_2, \text{NMe}_2$ are absent).

A4.2.2. $^{15}\text{N}_A$ NMR Chemical Shift (δN_A)

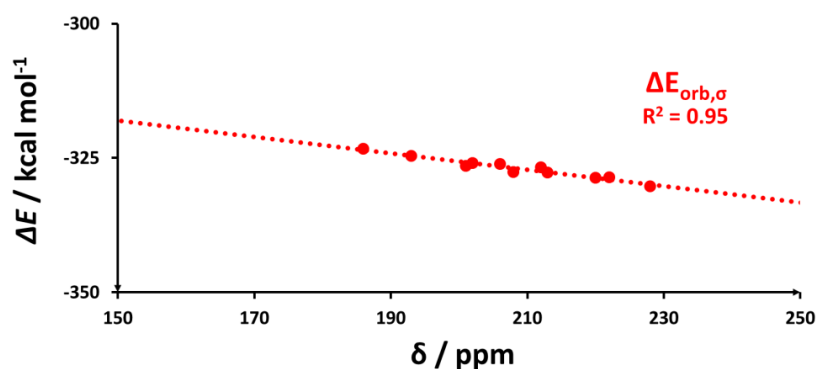


Figure A4.11. Strong correlation ($R^2 = 0.95$) of $\Delta E_{\text{orb},\sigma}$ with δN_A in the family of sixteen LS $[\text{Fe}(\text{bpp}^X)_2]^{2+}$ complexes.

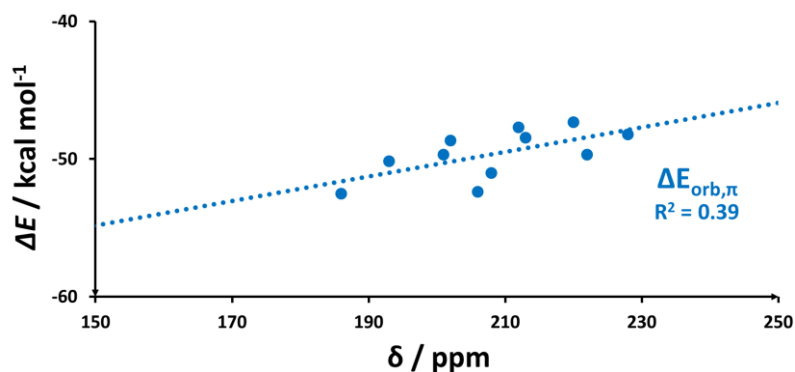


Figure A4.12. Weak correlation ($R^2 = 0.39$) of $\Delta E_{\text{orb},\pi}$ with δN_A in the family of sixteen LS $[\text{Fe}(\text{bpp}^X)_2]^{2+}$ complexes.

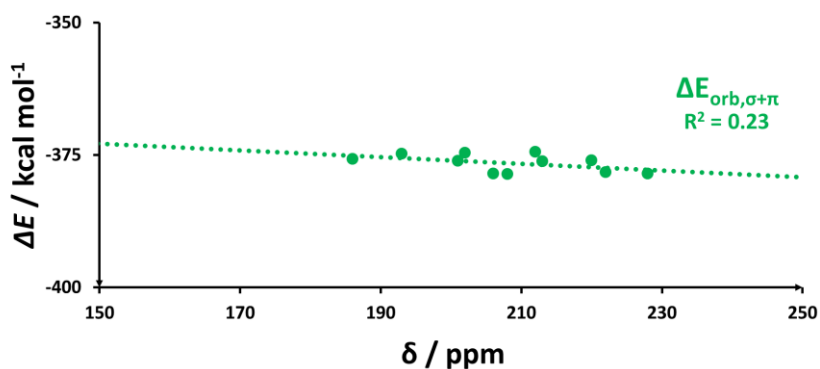


Figure A4.13. Weak correlation ($R^2 = 0.23$) of $\Delta E_{\text{orb},\sigma+\pi}$ with δN_A in the family of sixteen LS $[\text{Fe}(\text{bpp}^X)_2]^{2+}$ complexes.

A4.3. Correlations of ΔE_i in HS $[\text{Fe}(\text{bpp}^X)_2]^{2+}$

A4.3.1. Hammett Parameter $\sigma_p^+(X)$

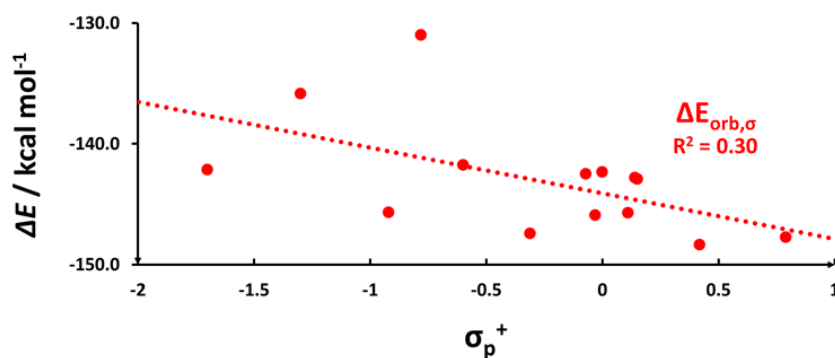


Figure A4.14. Absence of correlation ($R^2 = 0.30$) of $\Delta E_{\text{orb},\sigma}$ with the σ_p^+ Hammett parameter in the family of fourteen HS $[\text{Fe}(\text{bpp}^X)_2]^{2+}$ complexes ($X = \text{SOMe}, \text{SO}_2\text{Me}$ are absent).

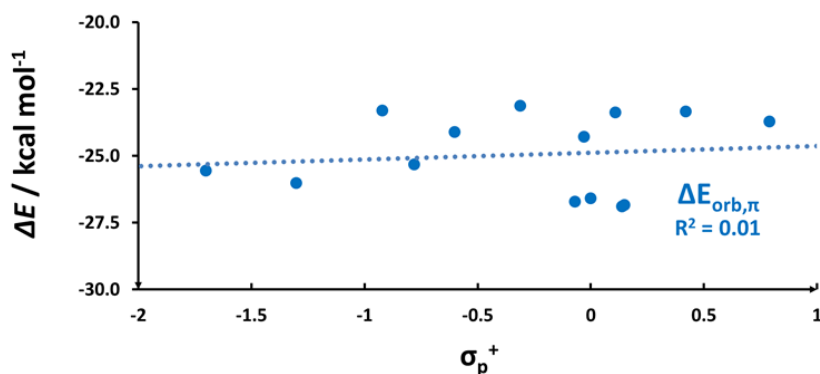


Figure A4.15. Absence of correlation ($R^2 = 0.01$) of $\Delta E_{\text{orb},\pi}$ with the σ_p^+ Hammett parameter in the family of fourteen $[\text{Fe}(\text{bpp}^X)_2]^{2+}$ complexes ($X = \text{SOMe}, \text{SO}_2\text{Me}$ are absent).

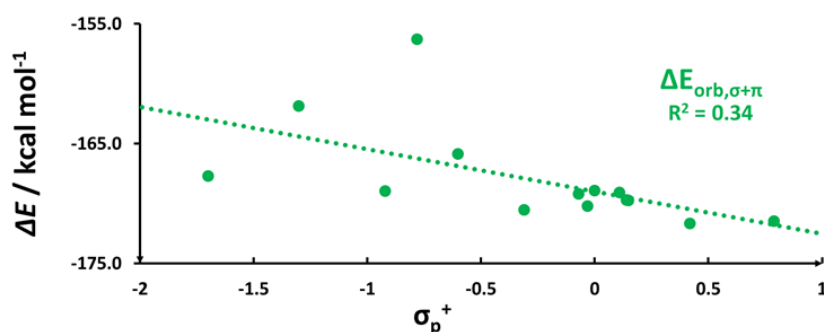


Figure A4.16. Weak correlation ($R^2 = 0.34$) of $\Delta E_{\text{orb},\sigma+\pi}$ with σ_p^+ Hammett parameter in the family of fourteen HS $[\text{Fe}(\text{bpp}^X)_2]^{2+}$ complexes ($X = \text{SOMe}, \text{SO}_2\text{Me}$ are absent).

A4.3.2. Transition Temperature $T_{1/2}$

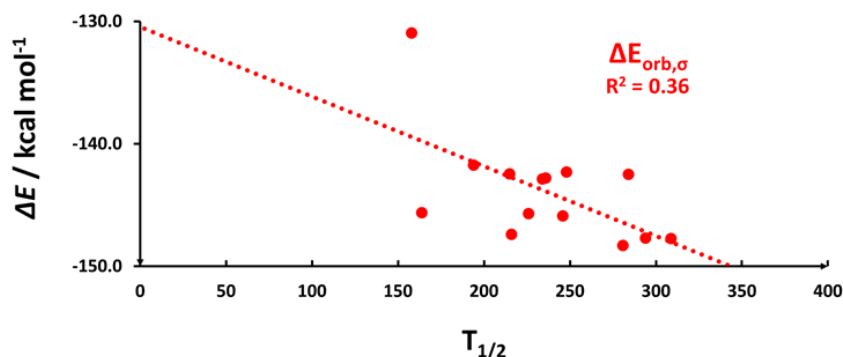


Figure A4.17. Absence of correlation ($R^2 = 0.36$) of $\Delta E_{orb,\sigma}$ with $T_{1/2}$ in the family of fourteen HS $[Fe(bpp^X)_2]^{2+}$ complexes ($X = NH_2, NMe_2$ are absent).

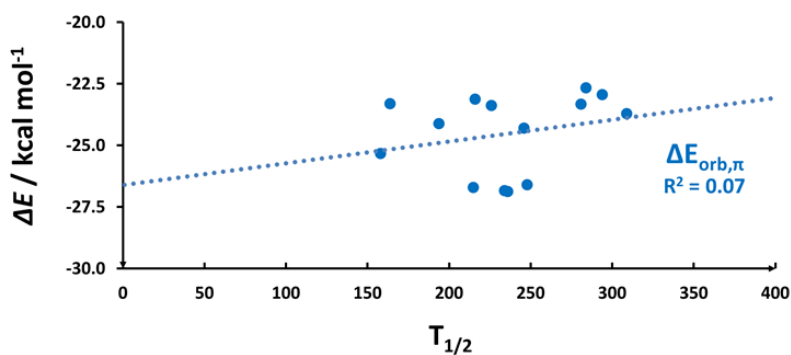


Figure A4.18. Weak correlation ($R^2 = 0.07$) of $\Delta E_{orb,\pi}$ with $T_{1/2}$ in the family of fourteen $[Fe(bpp^X)_2]^{2+}$ complexes ($X = NH_2, NMe_2$ are absent).

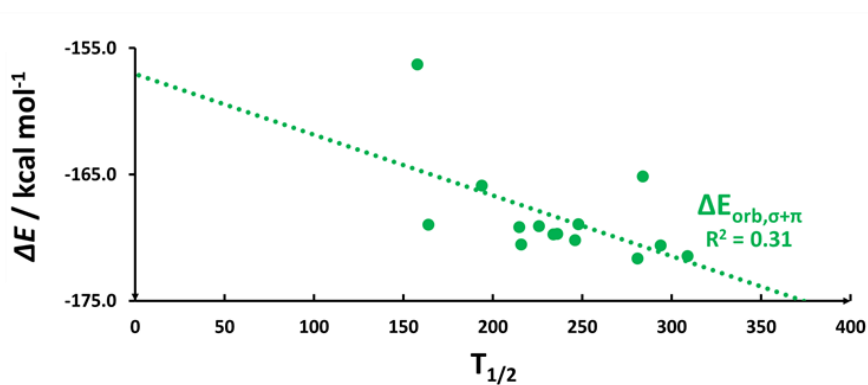


Figure A4.19. Weak correlation ($R^2 = 0.31$) of $\Delta E_{orb,\sigma+\pi}$ with $T_{1/2}$ in the family of fourteen HS $[Fe(bpp^X)_2]^{2+}$ complexes ($X = NH_2, NMe_2$ are absent).

A4.3.3. $^{15}\text{N}_A$ NMR Chemical Shift (δN_A)

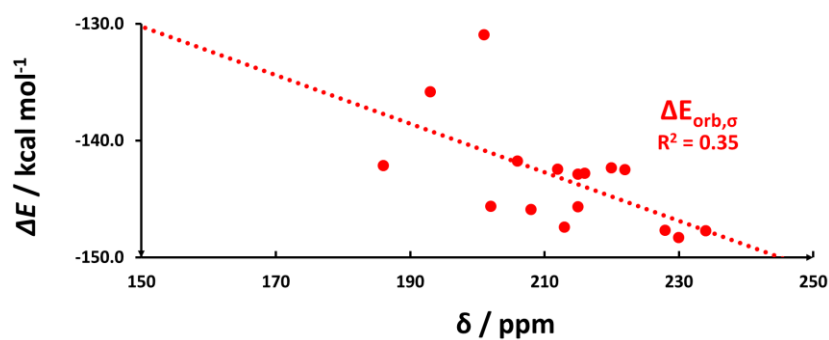


Figure A4.20. Absence of correlation ($R^2 = 0.35$) of $\Delta E_{orb,\sigma}$ with δN_A in the family of sixteen HS $[\text{Fe}(\text{bpp}^x)_2]^{2+}$ complexes.

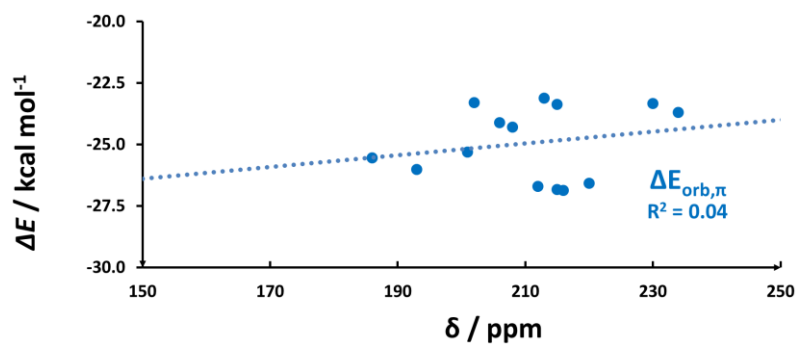


Figure A4.21. Weak correlation ($R^2 = 0.04$) of $\Delta E_{orb,\pi}$ with δN_A in the family of sixteen HS $[\text{Fe}(\text{bpp}^x)_2]^{2+}$ complexes.

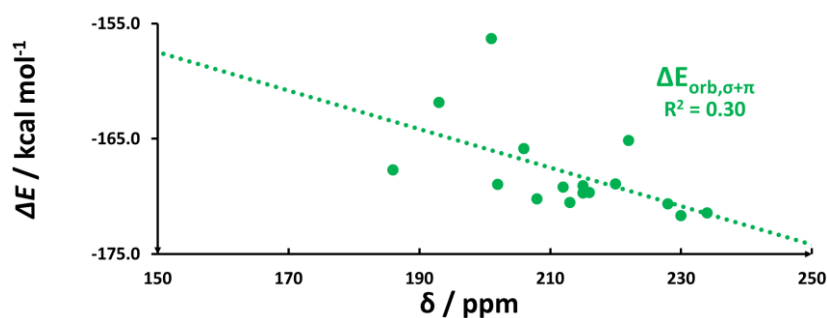


Figure A4.22. Weak correlation ($R^2 = 0.30$) of $\Delta E_{orb,\sigma+\pi}$ with δN_A in the family of sixteen HS $[\text{Fe}(\text{bpp}^x)_2]^{2+}$ complexes.

A4.4. Mulliken Population in the bpp^x Ligand

Table A4.8. Reported Mulliken analysis calculated with RI-BP86-D3(BJ)/def2-TZVPP+CPCM(acetone) level of theory²⁵⁹⁻²⁶⁷ for the coordinating nitrogen N of the sixteen bpp^x ligands. Firstly, the whole N population is reported; it follows the local population for each specific N(i) orbital ($i = s, p_{\perp}, p_{\pi}, p_{\sigma}$). The Mulliken populations are reported in number of electrons (e^-). * values estimated in Subsection 4.3.7.

X	σ_{p}^+	$\delta N / \text{ppm}$	$T_{1/2} / \text{K}$	N_{tot} / e^-	$N(s) / e^-$	$N(p_{\perp}) / e^-$	$N(p_{\pi}) / e^-$	$N(p_{\sigma}) / e^-$
NO₂	+0.79	234	309	6.295	3.650	1.443	0.967	1.170
CO₂H	+0.42	230	281	6.303	3.650	1.444	0.969	1.175
Br	+0.15	215	234	6.311	3.648	1.438	0.967	1.193
I	+0.14	216	236	6.312	3.649	1.438	0.966	1.194
Cl	+0.11	215	226	6.314	3.649	1.437	0.966	1.196
H	0.0	220	248	6.316	3.646	1.445	0.968	1.191
SH	-0.03	208	246	6.326	3.650	1.433	0.967	1.210
F	-0.07	212	215	6.321	3.651	1.436	0.965	1.204
Me	-0.31	213	216	6.323	3.648	1.438	0.969	1.201
SMe	-0.60	206	194	6.329	3.650	1.432	0.968	1.214
OMe	-0.78	201	158	6.334	3.651	1.429	0.966	1.222
OH	-0.92	202	164	6.334	3.651	1.430	0.966	1.222
NH₂	-1.30	193	HS	6.350	3.651	1.424	0.967	1.243
NMe₂	-1.70	186	HS	6.352	3.651	1.421	0.968	1.246
SOMe	+0.26*	222	284	6.310	3.648	1.441	0.967	1.188
SO₂Me	+0.60*	228	294	6.300	3.648	1.444	0.967	1.175

A4.5. Published Correlations

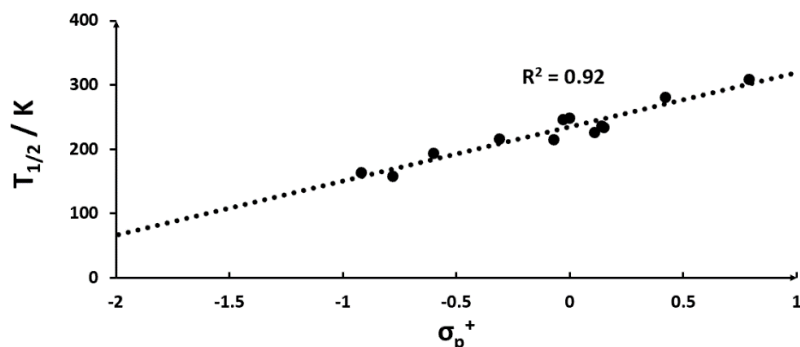


Figure A4.23. Correlation of $T_{1/2}$ with the σ_p^+ Hammett parameter ($R^2 = 0.92$) in the family of twelve $[\text{Fe}(\text{bpp}^X)_2]^{2+}$ complexes ($X = \text{SOMe}, \text{SO}_2\text{Me}, \text{NH}_2, \text{NMe}_2$ are absent), previously reported by Deeth, Halcrow et al.²³

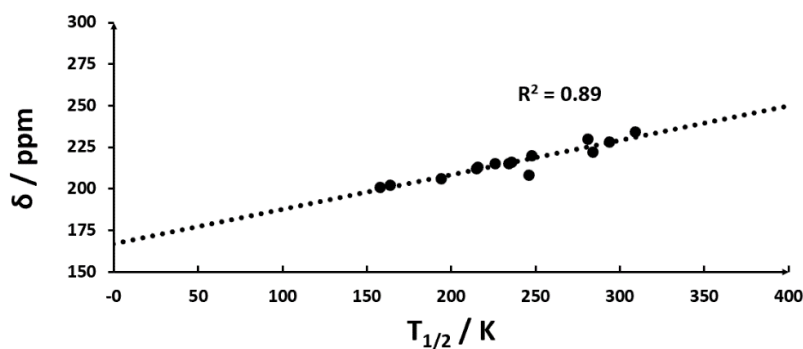


Figure A4.24. Correlation of $T_{1/2}$ with $\delta(\text{N}_A)$ ($R^2 = 0.89$) in the family of fourteen $[\text{Fe}(\text{bpp}^X)_2]^{2+}$ complexes ($X = \text{NH}_2, \text{NMe}_2$ are absent), previously reported by Brooker and et al.⁸³

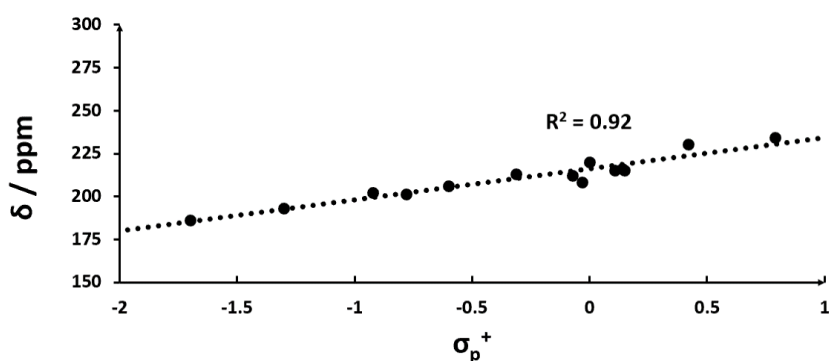


Figure A4.25. Correlation of $\delta(\text{N}_A)$ (the ^{15}N -NMR chemical shift) with the σ_p^+ Hammett parameter ($R^2 = 0.92$) in the family of fourteen $[\text{Fe}(\text{bpp}^X)_2]^{2+}$ complexes ($X = \text{SOMe}, \text{SO}_2\text{Me}$ are absent), previously reported in Chapter Two.

A5 | Accurate Prediction of Pressure and Temperature $T_{1/2}$ Variation in Solid State Spin Crossover by Ab Initio Methods: The $[\text{Co}^{\text{II}}(\text{dpzca})_2]$ Case

A5.1. Computational Protocol Validation

A5.1.1. U_{eff} Tuning in Geometry Optimisation Procedure

Calculated curves for geometry optimisation performed on crystalline $[\text{Co}(\text{dpzca})_2]$ at different values of $U_{\text{eff}}(\text{Co}(d))$ are reported in Figure A5.2. $U_{\text{eff}}(\text{Co}(d))$ range spreads from 3.0 eV (not reported in Figure A5.2 as $\Delta H_{\text{el,HS-LS}} < 0$ eV; detail in Table A5.1) to 1.5 eV. For $\Delta U_{\text{eff}}(\text{Co}(d)) = 1.5$ eV, $\Delta H_{\text{el,HS-LS}}$ change is about 3.0 eV; this is more than enough to change the magnetic response of $[\text{Co}(\text{dpzca})_2]$ from physically wrong (from $U_{\text{eff}} = 3.0$ eV, $\Delta H_{\text{el,HS-LS}} < 0$ eV), fully HS ($U_{\text{eff}} = 2.5$ eV), SCO-active ($U_{\text{eff}} = 2.375$ eV to $U_{\text{eff}} = 2.25$ eV), almost fully LS before 400K ($U_{\text{eff}} = 2.0$ eV) and, finally, fully LS ($U_{\text{eff}} = 1.5$ eV). Specifically, by decreasing U_{eff} magnitude of 0.125 eV (from $U_{\text{eff}} = 2.375$ eV to $U_{\text{eff}} = 2.25$ eV), the calculated $T_{1/2}$ rises of 200K (Table A5.1). The fragility of the SCO phenomenon should be extremely clear: even if the U_{eff} term can be used to fine-tune the $\Delta H_{\text{el,HS-LS}}$ gap, it is extremely complicated to get the exact value of experimental $T_{1/2}$; indeed, for small variation in U_{eff} magnitude, the SCO phenomenon shifts largely. Finally, the best value of U_{eff} to reproduce the experimental SCO transition of $[\text{Co}(\text{dpzca})_2]$ was set at 2.35 eV ($T_{1/2} = 175$ K, Table A5.1).

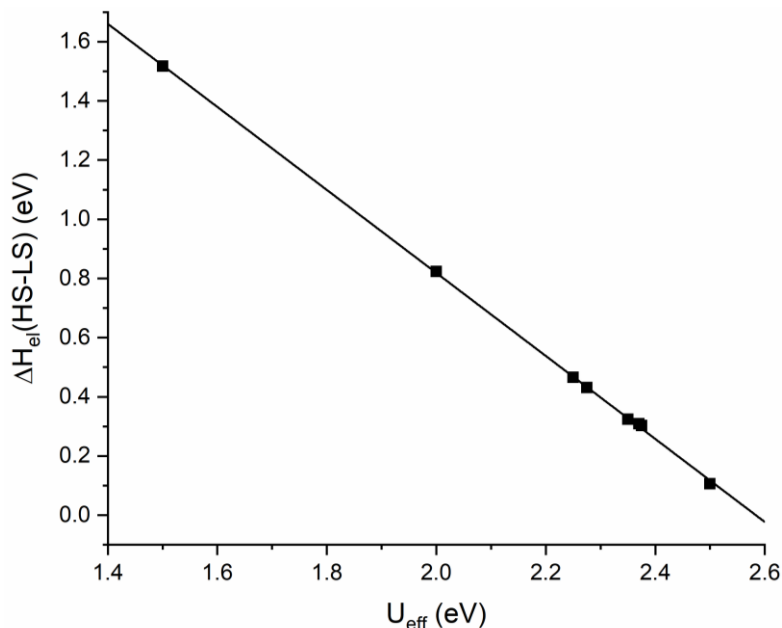


Figure A5.1. Correlation line established between the applied localising potential Hubbard U (U_{eff}) to the $\text{Co}(\text{II})$ d -orbitals. Reported line describes an extremely good correlation between the magnitude of the $\Delta H_{\text{el,HS-LS}}$ gap (eV) vs. the applied U_{eff} (eV).

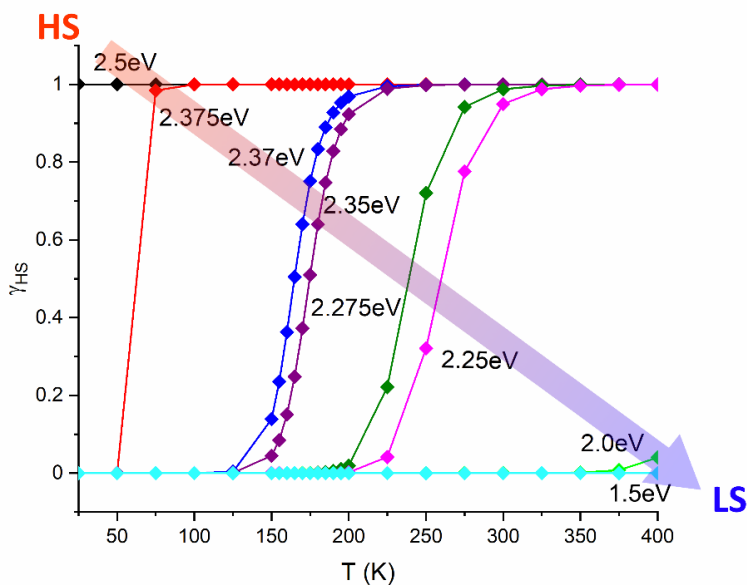


Figure A5.2. Reported results of the regular SCO transition of $\mathbf{1}_{\text{cry}}$ for different values of U_{eff} (from 2.5 eV to 1.5 eV). Normal modes were calculated from a first calculation on for $\mathbf{1}_{\text{cry,LS}}$ and $\mathbf{1}_{\text{cry,HS}}$ without applying any U_{eff} . Next, $\Delta H_{\text{el,HS-LS}}$ gap (eV) was obtained by proceed with a further step of cell optimisation by applying various U_{eff} terms at $\text{Co}(d)$ orbitals. Colour code: $U_{\text{eff}} = 2.5$ eV (black), $U_{\text{eff}} = 2.375$ eV (red), $U_{\text{eff}} = 2.37$ eV (blue), $U_{\text{eff}} = 2.35$ eV (purple), $U_{\text{eff}} = 2.275$ eV (olive), $U_{\text{eff}} = 2.25$ eV (magenta), $U_{\text{eff}} = 2.0$ eV (light green), $U_{\text{eff}} = 1.5$ eV (light blue).

Table A5.1. Results of calculated electronic Enthalpy (H) for $\mathbf{1}_{\text{cry,LS}}$ and $\mathbf{1}_{\text{cry,HS}}$ at different values of U_{eff} obtained in the protocol of geometry optimisation to the $\Delta H_{\text{el,HS-LS}}$ gap at the experimental $T_{1/2}$. In the last column on the right are reported theoretical values of $T_{1/2}$ at the different applied Hubbard potentials.

$U_{\text{eff}} / \text{eV}$	H_{HS} / H	H_{LS} / H	$H_{\text{HS-LS}} / H$	$\Delta H_{\text{HS-LS}} / \text{eV}$	$T_{1/2} (\text{K})$
3.0	-1718.070	-1718.010	-0.059	-1.625	HS
2.5	-1716.936	-1716.940	0.003	0.105	HS
2.375	-1716.938	-1716.949	0.011	0.302	$50 < T_{1/2} < 75$
2.37	-1716.938	-1716.949	0.011	0.308	165
2.35	-1716.938	-1716.950	0.012	0.324	175
2.275	-1716.939	-1716.955	0.015	0.430	$225 < T_{1/2} < 250$
2.25	-1716.939	-1716.957	0.017	0.465	$250 < T_{1/2} < 275$
2	-1716.944	-1716.974	0.030	0.823	$T_{1/2} > 400$
1.5	-1716.957	-1717.013	0.056	1.517	LS

A5.1.2. U_{eff} Tuning for Cell Parameters in Cell Optimisation Procedure

Table A5.2. Final cell parameters obtained in the protocol validation step of applying further U_{eff} for improving the emulation of $\mathbf{1}_{\text{cry,HS,1bar}}$.

LS	Cell Parameters						$U_{\text{eff}} / \text{eV}$				
	a / Å	b / Å	c / Å	$\alpha / ^\circ$	$\beta / ^\circ$	$\gamma / ^\circ$	Co(<i>d</i>)	N(<i>p</i>)	O(<i>p</i>)	C(<i>p</i>)	H(<i>s</i>)
EXP	8.668	27.656	8.514	90.00	91.52	90.00	-	-	-	-	-
	8.578	27.275	8.167	90.03	91.33	90.12	1.6	0	0	0	0
	8.577	27.276	8.168	90.03	91.38	90.10	1.75	0	0	0	0
	8.576	27.279	8.168	90.03	91.39	90.10	1.8	0	0	0	0
	8.575	27.286	8.169	90.05	91.42	90.12	1.875	0	0	0	0
	8.566	27.289	8.175	90.09	91.47	90.07	1.9	0	0	0	0
	8.575	27.237	8.186	90.00	91.48	90.23	1.65	1	0	0	0
	8.573	27.25	8.186	89.95	91.27	90.22	1.65	1.5	0	0	0
	8.569	27.238	8.197	89.96	91.19	90.23	1.65	2	0	0	0
	8.375	27.532	8.367	89.93	90.78	90.04	1.65	3	0	0	0
	8.566	27.243	8.200	89.97	91.15	90.25	1.65	2	0	0	0
	8.556	8.555	27.342	89.98	90.07	89.97	1.15	3	0	0	0
	8.375	27.532	8.367	89.94	90.77	90.04	1.65	3	0	0	0
	8.574	27.155	8.184	90.02	91.60	90.19	1.65	2	0	2	0
	8.38	27.561	8.386	89.96	90.76	89.92	2	3	0	2	0
	8.382	27.581	8.393	89.99	90.77	89.89	2	3	0	3	0

Table A5.3. Final cell parameters obtained in the protocol validation step of applying further U_{eff} for improving the emulation of $\mathbf{1}_{\text{cry},\text{LS},\text{1bar}}$.

HS	Cell Parameters						$U_{\text{eff}} / \text{eV}$				
	a / Å	b / Å	c / Å	$\alpha / ^\circ$	$\beta / ^\circ$	$\gamma / ^\circ$	Co(<i>d</i>)	N(<i>p</i>)	O(<i>p</i>)	C(<i>p</i>)	H(<i>s</i>)
EXP	8.795	8.795	27.918	90.00	90.00	90.00	-	-	-	-	-
	8.590	8.556	26.982	90.20	90.08	90.16	1.6	0	0	0	0
	8.586	8.553	29.963	90.19	90.07	90.15	1.75	0	0	0	0
	8.618	8.629	27.406	90.04	90.00	89.95	1.8	0	0	0	0
	8.656	8.665	27.536	90.03	90.00	89.97	1.875	0	0	0	0
	8.665	8.676	27.566	90.03	90.00	89.97	1.9	0	0	0	0
	8.590	8.569	26.991	90.24	90.19	90.10	1.65	1	0	0	0
	8.589	8.563	27.001	90.23	90.19	90.13	1.65	1.5	0	0	0
	8.567	8.567	27.046	90.18	90.38	89.99	1.65	2	0	0	0
	8.572	8.571	27.399	89.96	90.10	90.01	1.65	3	0	0	0
	8.584	8.561	26.967	90.24	90.19	90.11	1.65	2	0	2	0
	8.300	27.355	8.282	89.86	90.84	89.73	1.15	3	0	0	0
	8.586	8.585	27.369	89.98	90.05	90.01	2	3	0	2	0
	8.592	8.591	27.382	89.98	90.05	90.01	2	3	0	3	0
	8.615	8.610	27.086	89.99	90.01	90.02	2	3	3	3	1
	8.607	8.613	27.191	89.91	90.18	89.92	2	3	0	3	1

A5.1.3. $U_{\text{eff}}(\text{Co}(d))$ Tuning in Cell Optimisation Procedure

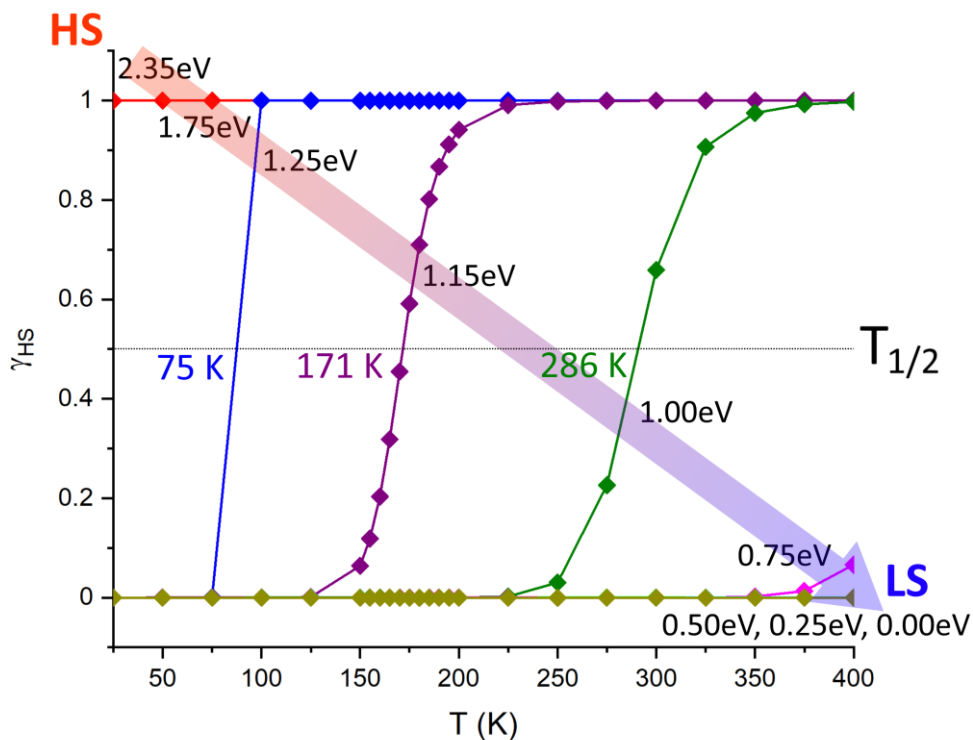


Figure A5.3. Calculated SCO transitions of 1_{cryst} for different values of $U_{\text{eff}}(\text{Co}(d))$ (from 2.35 eV to 0.00 eV). Normal modes were calculated from a first calculation on $1_{\text{cryst,LS}}$ and $1_{\text{cryst,HS}}$ without applying any $U_{\text{eff}}(\text{Co}(d))$ or $U_{\text{eff}}(\text{N}(p))$. Next, $\Delta H_{\text{el,HS-LS}}$ gap (eV) was obtained by proceeding with a further step of cell optimisation by applying various U_{eff} terms at Co(d) orbitals. Colour code: $U_{\text{eff}}(\text{Co}(d)) = 2.35$ eV (black), $U_{\text{eff}}(\text{Co}(d)) = 1.75$ eV (red), $U_{\text{eff}}(\text{Co}(d)) = 1.25$ eV (blue), $U_{\text{eff}}(\text{Co}(d)) = 1.15$ eV (purple), $U_{\text{eff}}(\text{Co}(d)) = 1.00$ eV (olive), $U_{\text{eff}}(\text{Co}(d)) = 0.75$ eV (magenta), $U_{\text{eff}}(\text{Co}(d)) = 0.50$ eV (light green), $U_{\text{eff}}(\text{Co}(d)) = 0.25$ eV (light blue) and $U_{\text{eff}}(\text{Co}(d)) = 0.0$ eV (green). The two highest values of $U_{\text{eff}}(\text{Co}(d))$ (2.35 and 1.75 eV) overlap as the complex is fully HS state; the three lowest values of $U_{\text{eff}}(\text{Co}(d))$ (0.50, 0.25, 0.00 eV) overlap as the complex is fully LS state.

Table A5.4. Results of calculated electronic Enthalpy (H) for $\mathbf{1}_{\text{cry,LS}}$ and $\mathbf{1}_{\text{cry,HS}}$ at different values of U_{eff} obtained in the protocol of cell optimisation to the $\Delta H_{\text{el,HS-LS}}$ gap at the experimental $T_{1/2}$. In the last column on the right are reported theoretical values of $T_{1/2}$ at the different applied Hubbard potentials.

$U_{\text{eff}} / \text{eV}$	H_{HS} / H	H_{LS} / H	$H_{\text{HS-LS}} / H$	$\Delta H_{\text{HS-LS}} / \text{eV}$	$T_{1/2} (\text{K})$
2.35	-1716.96	-1716.95	-0.013	-0.361	HS
1.75	-1713.68	-1713.66	-0.013	-0.348	HS
1.25	-1713.70	-1713.71	0.014	+0.373	$75 < T_{1/2} < 100$
1.15	-1713.70	-1713.71	0.012	+0.322	175
1.00	-1713.71	-1713.72	0.019	+0.526	$275 < T_{1/2} < 300$
0.75	-1713.72	-1713.75	0.030	+0.813	$T_{1/2} > 400$
0.50	-1713.72	-1713.77	0.044	+1.199	LS
0.25	-1713.73	-1713.79	0.058	+1.571	LS
0.00	-1713.75	-1713.81	0.069	+1.881	LS

Table A5.5. Error analysis of divergence between the calculated and the experimental unit cell parameters at the available pressures of 1 bar ($\mathbf{1}_{\text{cry,HS,1bar}}$ and $\mathbf{1}_{\text{cry,LS,1bar}}$) and 4300 bar ($\mathbf{1}_{\text{cry,LS,4300bar}}$). Note that each calculation is performed at the absolute temperature of 0 K. 1 bar = 10^4 Pa.

Cell Param.	$\mathbf{1}_{\text{cry,HS}}$		$\mathbf{1}_{\text{cry,LS}}$			
	1 bar		1 bar		4300 bar	
	Exp.	Calc.	%	Exp.	Calc.	%
$\mathbf{a} / \text{\AA}$	8.795	8.556	-2.7%	8.668	8.366	-3.5%
$\mathbf{b} / \text{\AA}$	8.795	8.555	-2.7%	27.656	27.536	-0.4%
$\mathbf{c} / \text{\AA}$	27.918	27.342	-2.1%	8.514	8.357	-1.8%
$\alpha / ^\circ$	90.00	89.979	-0.1%	90.00	89.971	-0.1%
$\beta / ^\circ$	90.00	90.065	+0.1%	91.52	90.925	-0.7%
$\gamma / ^\circ$	90.00	89.969	-0.1%	90.00	89.901	-0.1%
Av. Error	-	-	1.3%			1.1%

A5.2. Additional Structural Data

A5.2.1. Cell Parameters of 1_{cry} vs. Pressure and Measured $T_{1/2}$

$$RMSD = \sqrt{\frac{1}{n} \sum_{i=1}^n ((v_{ix} - w_{ix})^2 + (v_{iy} - w_{iy})^2 + (v_{iz} - w_{iz})^2)} \quad (\text{A5.1})$$

$$\zeta = \sum_{i=1}^6 |d_i - d_{\text{mean}}| \quad (\text{A5.2})$$

$$\Delta = \frac{1}{6} \sum_{i=1}^6 \left(\frac{|d_i - d_{\text{mean}}|}{d_{\text{mean}}} \right)^2 \quad (\text{A5.3})$$

$$\Sigma = \sum_{i=1}^{12} |90 - \phi_i| \quad (\text{A5.4})$$

$$\theta = \sum_{i=1}^{24} |90 - \theta_i| \quad (\text{A5.5})$$

$$\Omega = \sum_{i=1}^{24} |60 - \omega_i| \quad (\text{A5.6})$$

Table A5.6. Reported variation in the cell volume for on $\mathbf{1}_{\text{cry,LS}}$ and $\mathbf{1}_{\text{cry,HS}}$ at different pressures. Reference system is considered at the external pressure of 1 bar. Results are reported in \AA^3 .

p / bar	$HS / \text{\AA}^3$	$LS / \text{\AA}^3$	% HS	% LS
1	2001.27	1952.80	-	-
1800	1978.99	1906.64	-22.28 (-1.11%)	-46.16 (-2.36%)
2100	1974.65	1903.71	-26.62 (-1.33%)	-49.09 (-2.51%)
2500	1970.41	1899.97	-30.86 (-1.54%)	-52.83 (-1.54%)
2900	1960.62	1893.81	-40.65 (-2.03%)	-58.99 (-3.02%)
3900	1970.20	1862.75	-31.07 (-1.55%)	-90.05 (-4.61%)
4300	1965.55	1897.99	-35.72 (-1.78%)	-54.81 (-2.81%)

Table A5.7. Reported correlation factor in the analysis of the variation of the structural parameters of the unit cell for on $\mathbf{1}_{\text{cry,LS}}$ and $\mathbf{1}_{\text{cry,HS}}$ versus the seven different pressures (and related experimental $T_{1/2}$).

		$R^2 (\text{pressure})$	$R^2 (T_{1/2}(\text{exp.}))$
$\mathbf{1}_{\text{cry,LS}}$	$a / \text{\AA}$	0.47 (Fig. A5.3)	0.41 (Fig. A5.15)
	$b / \text{\AA}$	0.54 (Fig. A5.4)	0.64 (Fig. A5.16)
	$c / \text{\AA}$	0.63 (Fig. A5.5)	0.13 (Fig. A5.17)
	$\alpha / ^\circ$	0.74 (Fig. A5.6)	0.77 (Fig. A5.18)
	$\beta / ^\circ$	0.64 (Fig. A5.7)	0.70 (Fig. A5.19)
	$\gamma / ^\circ$	0.39 (Fig. A5.8)	0.36 (Fig. A5.20)
	$\mathbf{1}_{\text{cry,HS}}$	$a / \text{\AA}$	0.71 (Fig. A5.9)
$b / \text{\AA}$		0.59 (Fig. A5.10)	0.58 (Fig. A5.22)
$c / \text{\AA}$		0.93 (Fig. A5.11)	0.86 (Fig. A5.23)
$\alpha / ^\circ$		0.20 (Fig. A5.12)	0.23 (Fig. A5.24)
$\beta / ^\circ$		0.23 (Fig. A5.13)	0.25 (Fig. A5.25)
$\gamma / ^\circ$		0.20 (Fig. A5.14)	0.21 (Fig. A5.26)

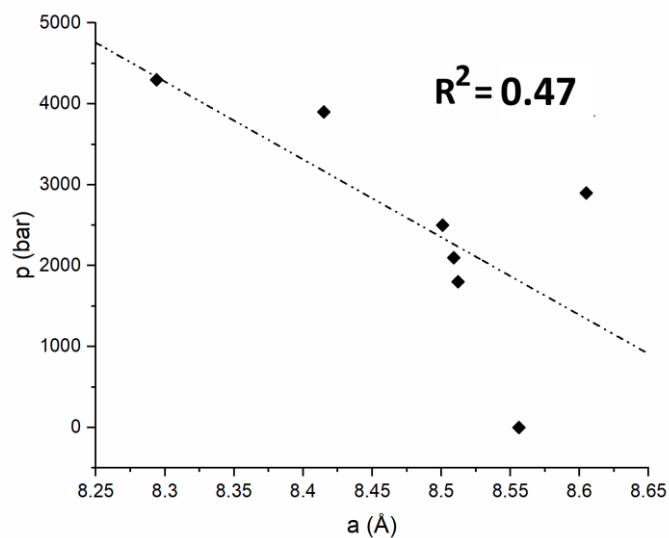


Figure A5.4. Reported correlation factor R^2 for the variation of the length of the a-axis of $1_{\text{cry},1\text{S}}$ at the pressure increase ($R^2 = 0.47$).

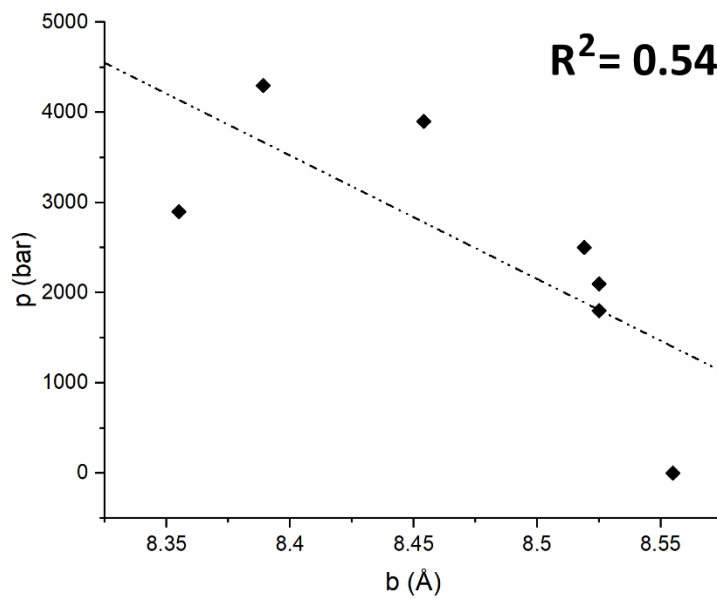


Figure A5.5. Reported correlation factor R^2 for the variation of the length of the b-axis of $1_{\text{cry},1\text{S}}$ at the pressure increase ($R^2 = 0.54$).

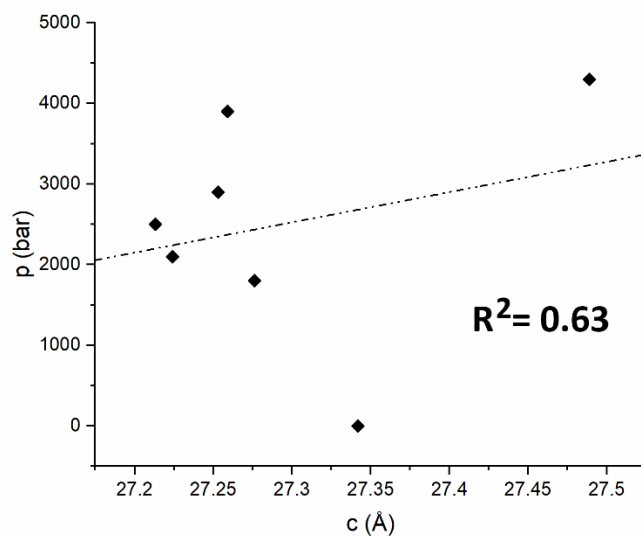


Figure A5.6. Reported correlation factor R^2 for the variation of the length of the c-axis of $1_{\text{cry,LS}}$ at the pressure increase ($R^2 = 0.63$).

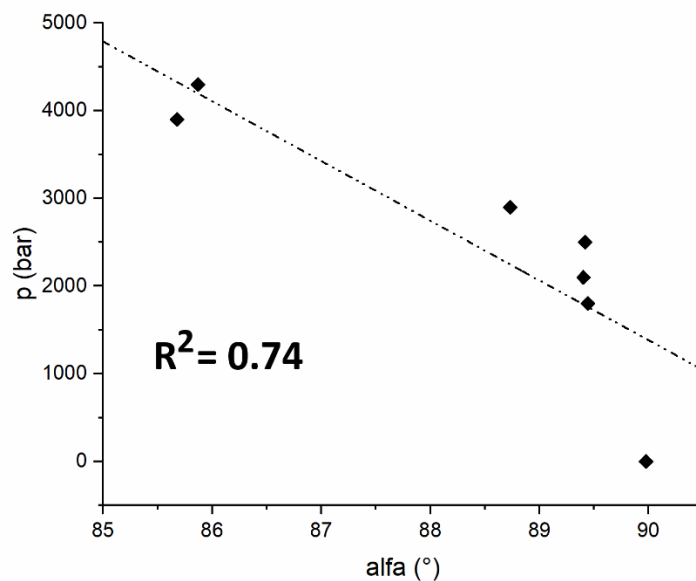


Figure A5.7. Reported correlation factor R^2 for the variation of the magnitude of the α angle of $1_{\text{cry,LS}}$ at the pressure increase ($R^2 = 0.74$).

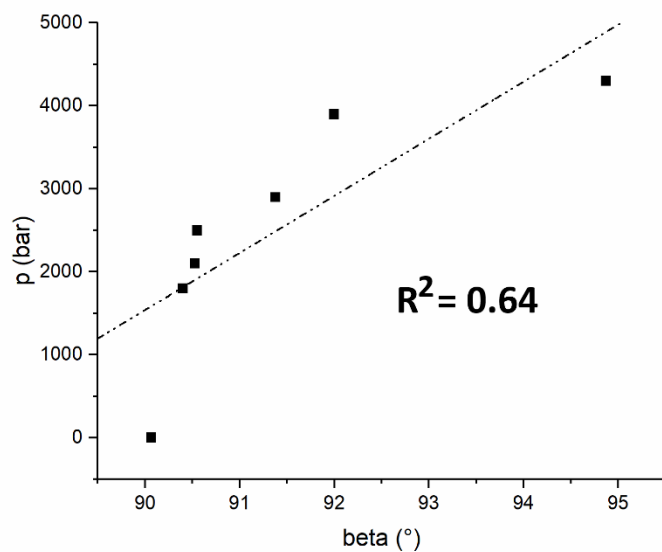


Figure A5.8. Reported correlation factor R^2 for the variation of the magnitude of the β angle of $\mathbf{1}_{\text{cry,LS}}$ at the pressure increase ($R^2 = 0.64$).

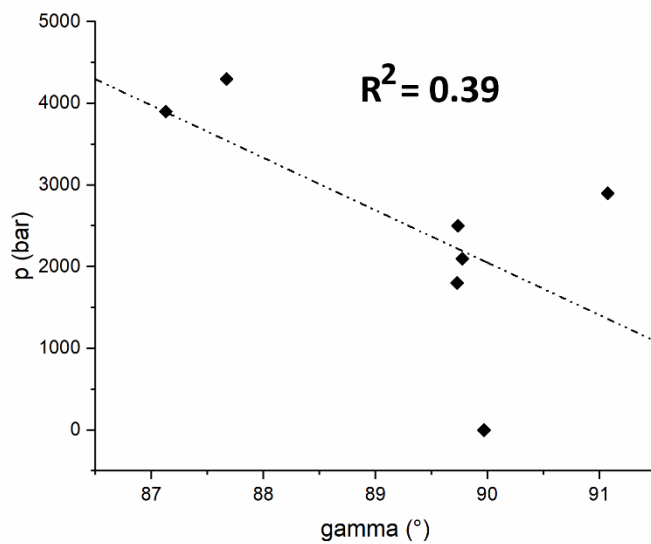


Figure A5.9. Reported correlation factor R^2 for of the variation of the magnitude of the γ angle of $\mathbf{1}_{\text{cry,LS}}$ at the pressure increase ($R^2 = 0.39$).

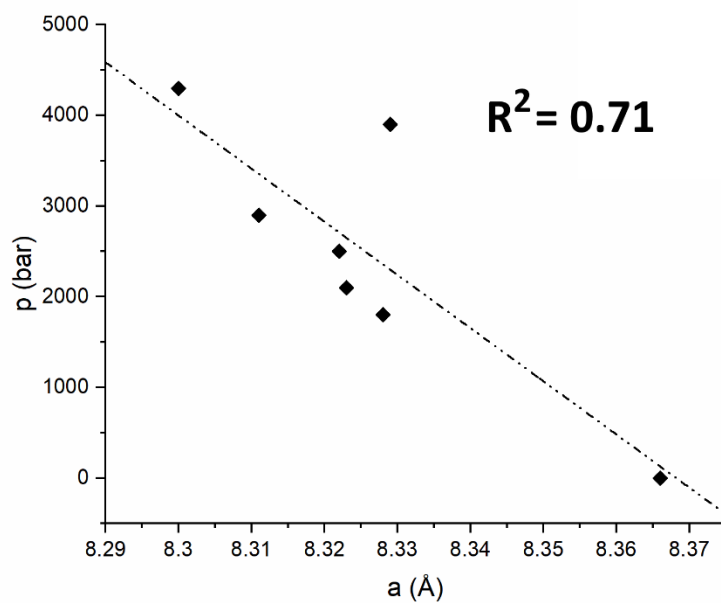


Figure A5.10. Reported correlation factor R^2 for the variation of the length of the a-axis of $\mathbf{1}_{\text{cry,HS}}$ at the pressure increase ($R^2 = 0.71$).

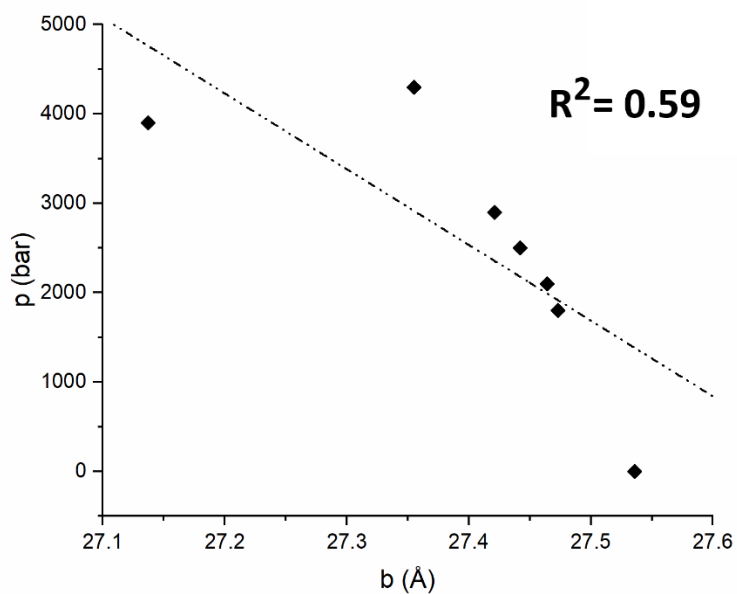


Figure A5.11. Reported correlation factor R^2 for the variation of the length of the b-axis of $\mathbf{1}_{\text{cry,HS}}$ at the pressure increase ($R^2 = 0.59$).

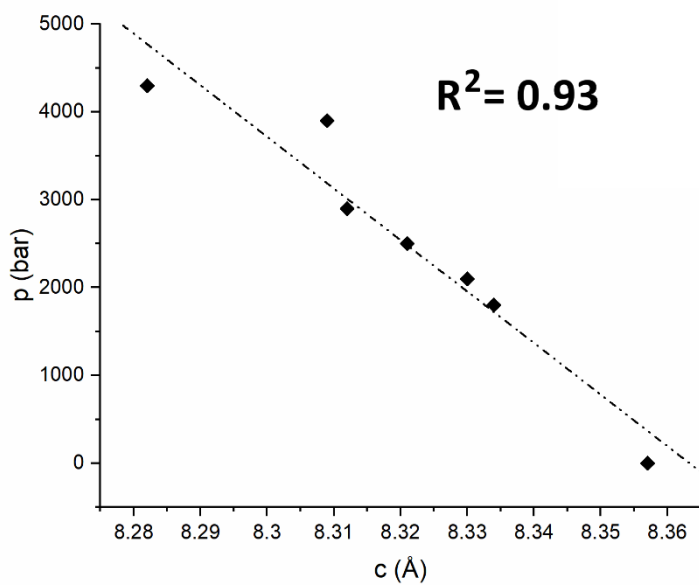


Figure A5.12. Reported correlation factor R^2 for the variation of the length of the c -axis of $\mathbf{1}_{\text{cry,HS}}$ at the pressure increase ($R^2 = 0.93$).

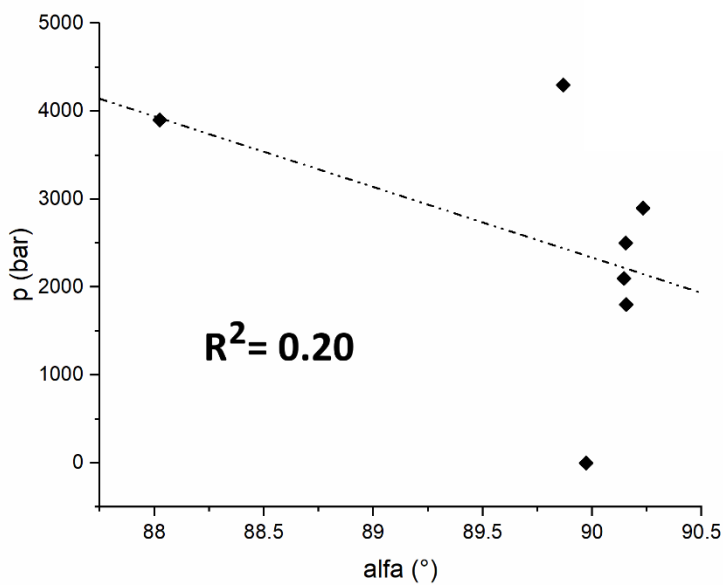


Figure A5.13. Reported correlation factor R^2 for the variation of the magnitude of the α angle of $\mathbf{1}_{\text{cry,HS}}$ at the pressure increase ($R^2 = 0.20$).

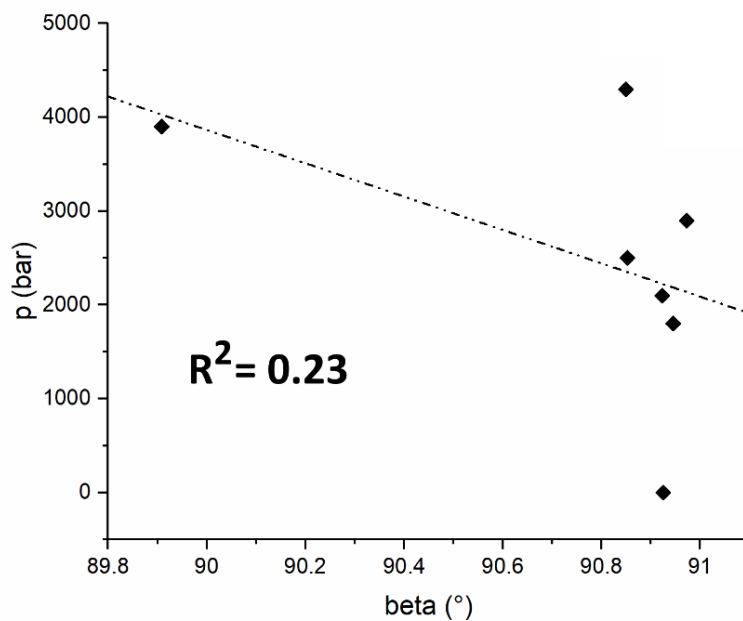


Figure A5.14. Reported correlation factor R^2 for the variation of the magnitude of the β angle of $\mathbf{1}_{\text{cry,HS}}$ at the pressure increase ($R^2 = 0.23$).

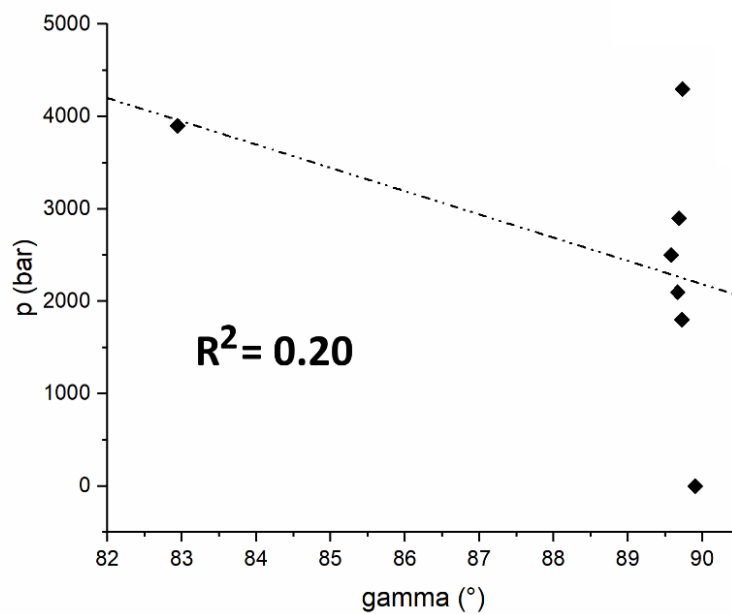


Figure A5.15. Reported correlation factor R^2 for the variation of the magnitude of the γ angle of $\mathbf{1}_{\text{cry,HS}}$ at the pressure increase ($R^2 = 0.20$).

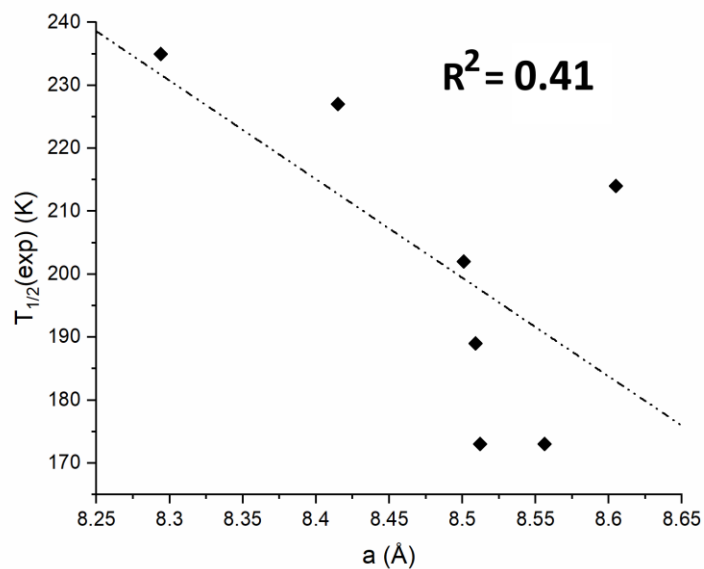


Figure A5.16. Reported correlation factor R^2 for the variation of the length of the a -axis of $\mathbf{1}_{\text{cry,LS}}$ at the increase of the measured $T_{1/2}$ ($R^2 = 0.41$).

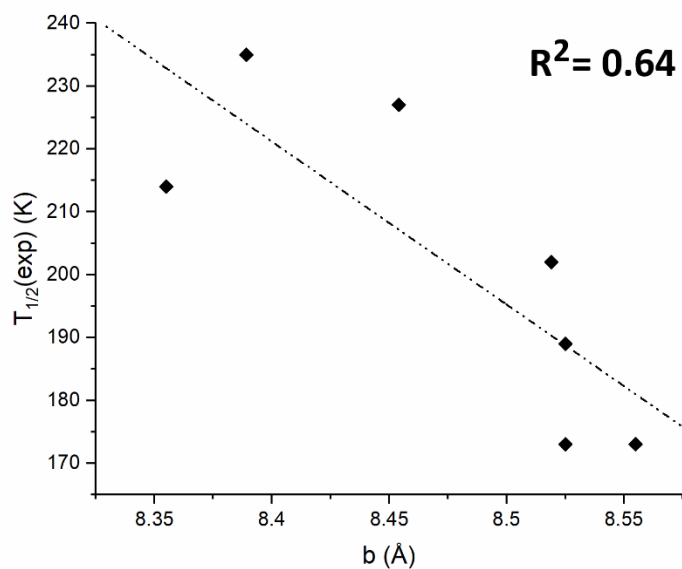


Figure A5.17. Reported correlation factor R^2 for the variation of the length of the b -axis of $\mathbf{1}_{\text{cry,LS}}$ at the increase of the measured $T_{1/2}$ ($R^2 = 0.64$).

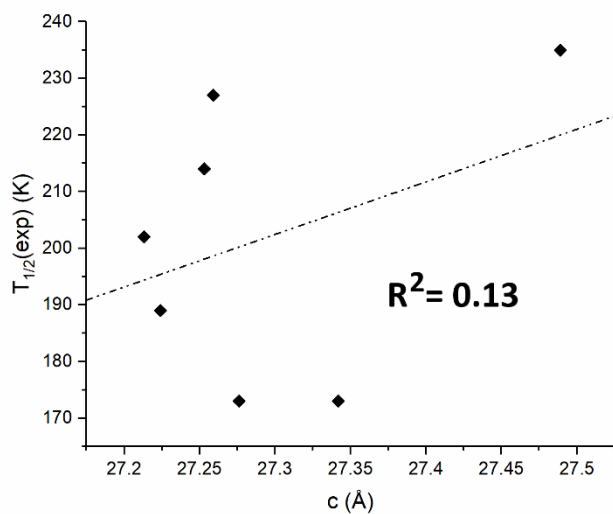


Figure A5.18. Reported correlation factor R^2 for the variation of the length of the c-axis of $1_{\text{cry,LS}}$ at the increase of the measured $T_{1/2}$ ($R^2 = 0.13$).

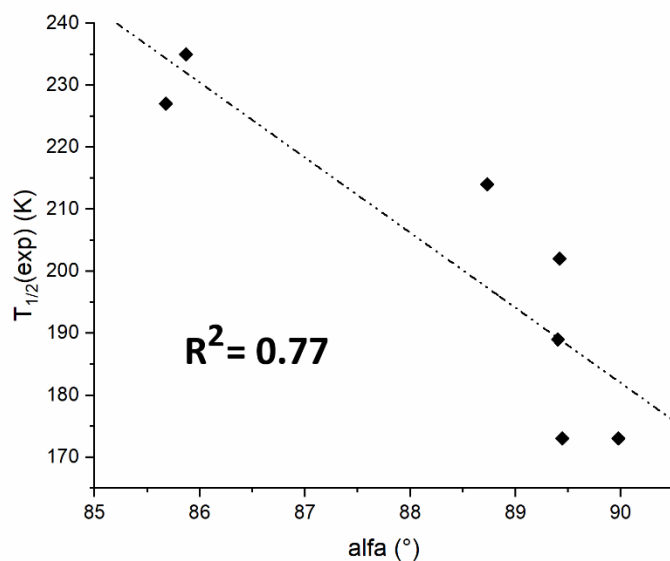


Figure A5.19. Reported correlation factor R^2 for the variation of the magnitude of the α angle of $1_{\text{cry,LS}}$ at the increase of the measured $T_{1/2}$ ($R^2 = 0.70$).

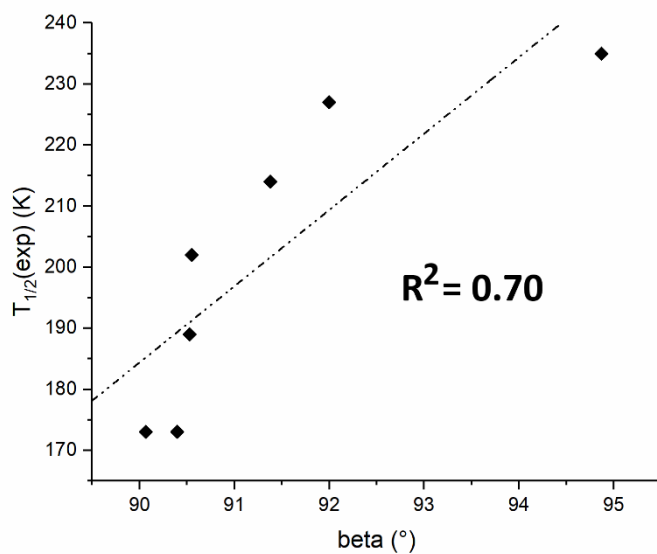


Figure A5.20. Reported correlation factor R^2 for the variation of the magnitude of the β angle of $\mathbf{1}_{\text{cry,LS}}$ at the increase of the measured $T_{1/2}$ ($R^2 = 0.70$).

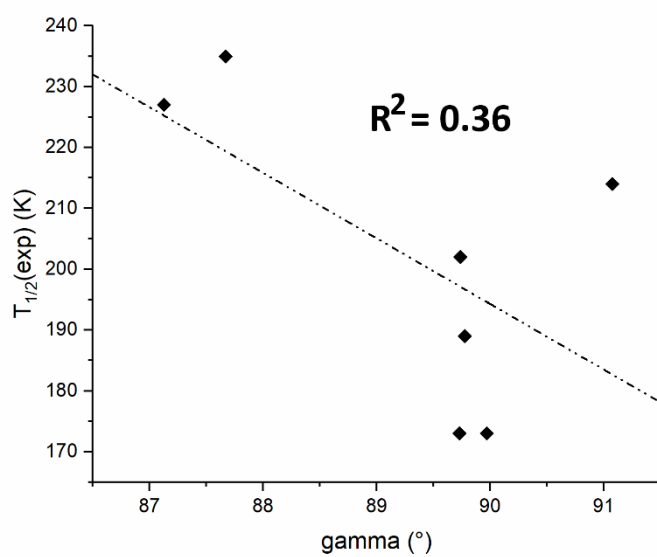


Figure A5.21. Reported correlation factor R^2 for the variation of the magnitude of the γ angle of $\mathbf{1}_{\text{cry,LS}}$ at the increase of the measured $T_{1/2}$ ($R^2 = 0.36$).

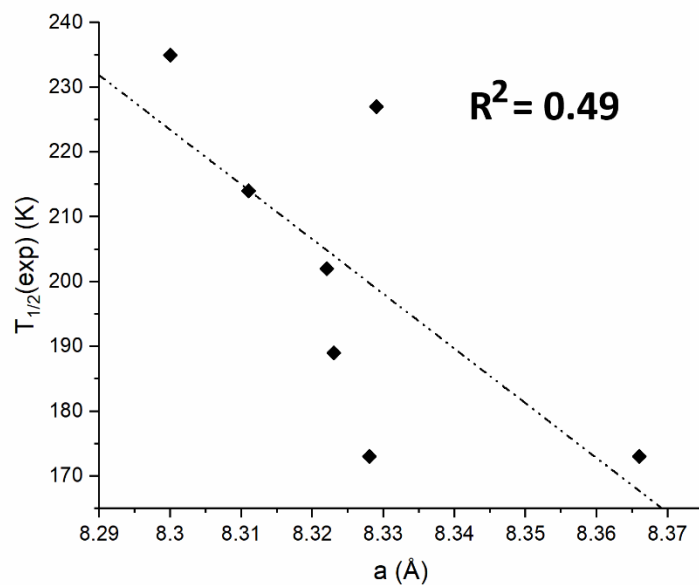


Figure A5.22. Reported correlation factor R^2 for the variation of the length of the a-axis of $\mathbf{1}_{\text{cry,HS}}$ at the increase of the measured $T_{1/2}$ ($R^2 = 0.49$).

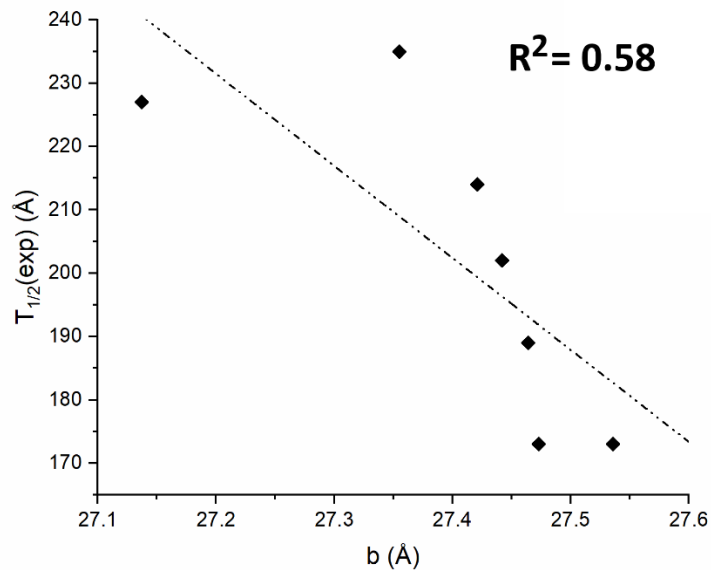


Figure A5.23. Reported correlation factor R^2 for the variation of the length of the b-axis of $\mathbf{1}_{\text{cry,HS}}$ at the increase of the measured $T_{1/2}$ ($R^2 = 0.58$).

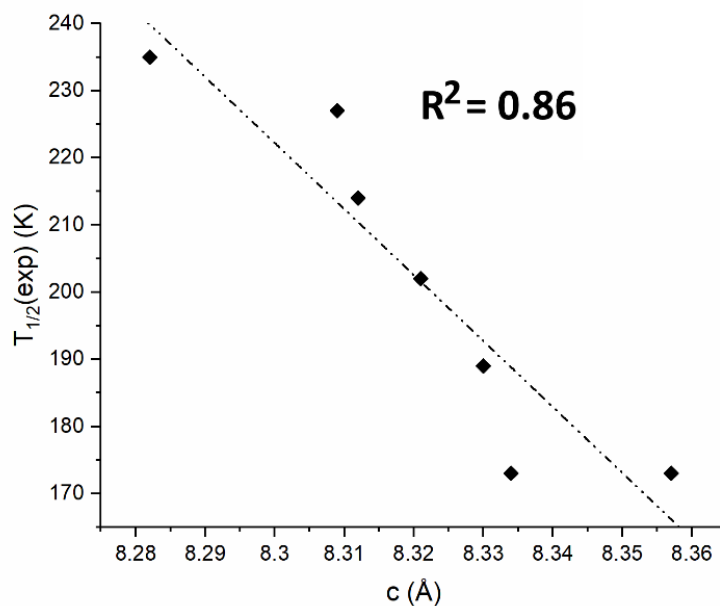


Figure A5.24. Reported correlation factor R^2 for the variation of the length of the c-axis of $\mathbf{1}_{\text{cry,HS}}$ at the increase of the measured $T_{1/2}$ ($R^2 = 0.86$).

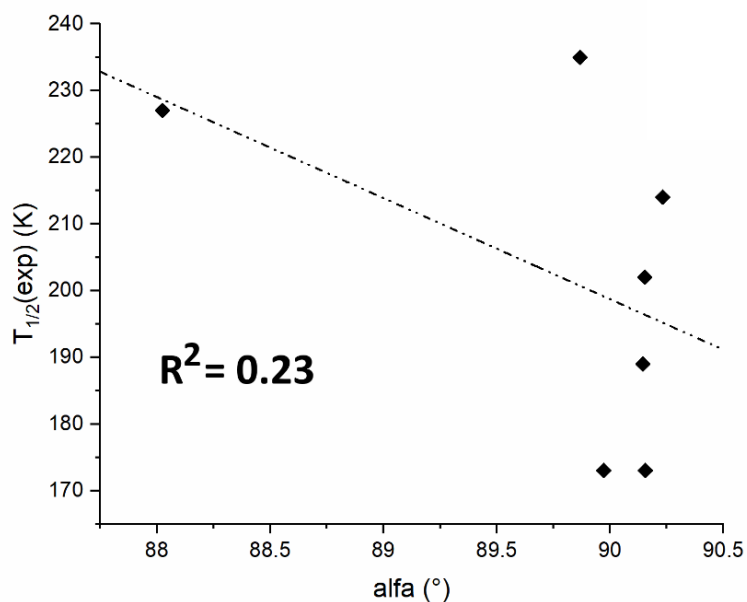


Figure A5.25. Reported correlation factor R^2 for the variation of the magnitude of the α angle of $\mathbf{1}_{\text{cry,HS}}$ at the increase of the measured $T_{1/2}$ ($R^2 = 0.23$).

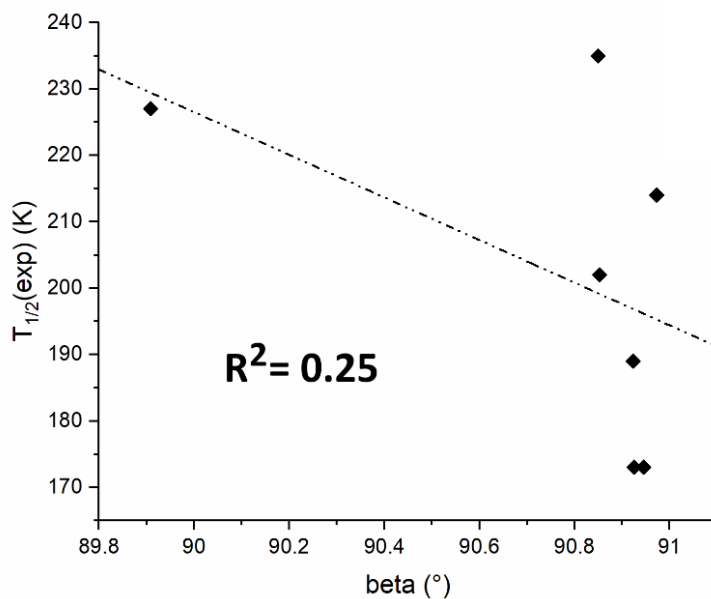


Figure A5.26. Reported correlation factor R^2 for the variation of the magnitude of the β angle of $\mathbf{1}_{\text{cry,HS}}$ at the increase of the measured $T_{1/2}$ ($R^2 = 0.25$).

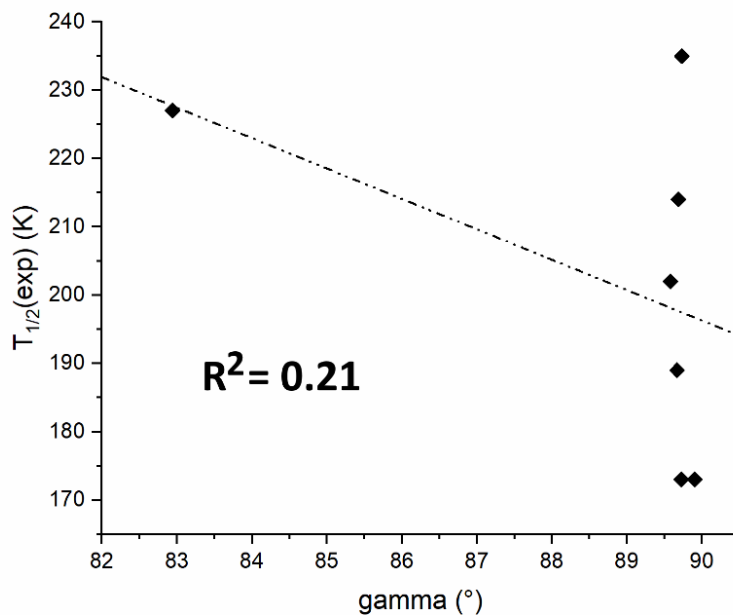


Figure A5.27. Reported correlation factor R^2 for the variation of the magnitude of the γ angle of $\mathbf{1}_{\text{cry,HS}}$ at the increase of the measured $T_{1/2}$ ($R^2 = 0.21$).

A5.2.1. Structural Distortion of 1_{cry} vs. Pressure

Table A5.8. Reported variation of structural parameters (internal to $[\text{Co}(\text{dpzca})_2]$: Co-N bond length and Σ octahedral distortion and external: Co-Co intermolecular distance) obtained after procedure of cell optimisation for $1_{\text{cry,LS}}$ at different pressures.

LS		Cell Parameters	
pressure	Co1-Co2 / Å	Co2-Co3 / Å	Co3-Co4 / Å
1	8.177	10.540	8.176
1800	8.171	10.500	8.161
2100	8.167	10.499	8.157
2500	8.161	10.498	8.152
2900	8.127	10.464	8.154
3900	8.123	10.455	8.133
4300	8.114	10.464	8.122

Table A5.9. Reported variation of structural parameters (internal to $[\text{Co}(\text{dpzca})_2]$: Co-N bond length and Σ octahedral distortion and external: Co-Co intermolecular distance) obtained after procedure of cell optimisation for $1_{\text{cry,HS}}$ at different pressures.

HS		Cell Parameters	
pressure	Co1-Co2 / Å	Co2-Co3 / Å	Co3-Co4 / Å
1	8.057	8.064	8.070
1800	8.013	8.072	8.062
2100	7.987	8.059	8.056
2500	7.991	8.061	8.066
2900	8.029	8.018	8.200
3900	8.028	8.007	8.199
4300	8.028	8.007	8.199

Table A5.10. Calculated structural distortion parameters for crystallographic and calculated structures (DFT) for 1_{cryst} at different pressures (1, 1800, 2100, 2500, 2900, 3900, 4300 bar), along with the experimental $T_{1/2}$ from ref¹⁹ and the calculated $T_{1/2}$. 1 bar = 10^5 Pa.

Pressure / bar		1	4300	1	1800	2100	2500	2900	3900	4300	R ² [pressure]	R ² [$T_{1/2}(\text{exp})$]
$T_{1/2}(\text{exp}) / \text{K}$		Exp.		173	173	189	202	214	218	235		
$T_{1/2}(\text{calc}) / \text{K}$		x-ray		171	164	190	173	LS	LS	-		
$1_{\text{cryst,LS}}$	RMSD / Å	-	-	-	0.03221	0.04415	0.05004	0.06016	0.06482	0.07082	0.92 (Fig. 5)	0.98 (Fig. 5)
	$\langle D \rangle / \text{Å}$	2.03444	2.0505	1.98033	1.97843	1.98299	1.97794	1.97733	1.97365	1.97700	0.43 (Fig. S28)	0.38 (Fig. S34)
	$\zeta / \text{Å}$	0.63404	0.4964	0.26140	0.25693	0.26407	0.25610	0.25331	0.23631	0.25671	0.34 (Fig. S29)	0.24 (Fig. S35)
	$\Delta(\text{geom.})$	0.00318	0.0020	0.00057	0.00054	0.00066	0.00054	0.00053	0.00049	0.00057	0.07 (Fig. S30)	0.09 (Fig. S36)
	$\Sigma / ^\circ$	76.0830	89.8708	69.3796	69.3845	70.5836	69.4735	69.5518	68.0682	69.199	0.17 (Fig. S31)	0.15 (Fig. S37)
	$\Theta / ^\circ$	271.161	306.325	230.475	230.731	235.439	231.269	231.510	221.259	231.135	0.13 (Fig. S32)	0.09 (Fig. S38)
	$\Omega / ^\circ$	127.36	143.16	126.84	119.64	130.00	126.68	126.80	117.28	127.00	0.06 (Fig. S33)	1.3E-8 (Fig. S39)
$1_{\text{cryst,HS}}$	RMSD / Å	-	-	-	0.04131	0.05112	0.05195	0.13196	0.25527	0.33967	0.95 (Fig. 5)	0.78 (Fig. 5)
	$\langle D \rangle / \text{Å}$	2.11373	-	2.08150	2.07902	2.07916	2.07866	2.07788	2.07954	2.07784	0.58 (Fig. S28)	0.45 (Fig. S34)
	$\zeta / \text{Å}$	0.25709	-	0.13399	0.13028	0.13310	0.13233	0.12746	0.13108	0.13081	0.26 (Fig. S29)	0.21 (Fig. S35)
	$\Delta(\text{geom.})$	0.00046	-	0.00021	0.00020	0.00021	0.00021	0.00021	0.00021	0.00020	0.01 (Fig. S30)	0.01 (Fig. S36)
	$\Sigma / ^\circ$	110.620	-	104.228	103.785	104.296	104.171	103.966	104.442	104.045	0.01 (Fig. S31)	0.03 (Fig. S37)
	$\Theta / ^\circ$	344.334	-	335.121	334.596	336.809	336.455	338.072	336.264	336.287	0.22 (Fig. S32)	0.36 (Fig. S38)
	$\Omega / ^\circ$	164.74	-	169.49	169.64	171.44	171.12	173.96	167.16	171.92	0.01 (Fig. S33)	0.07 (Fig. S39)
$1_{\text{cryst,LS-HS}}$	$\Delta\text{RMSD}/\text{Å}$	-	-	9.60	9.61	9.63	9.59	9.58	9.56	9.63	0.02 (Fig. 43)	0.02 (Fig. 44)
	$\Delta\Theta / ^\circ$	-	-	104.6461	103.8654	101.3695	105.1858	106.5625	115.0052	105.1516	0.60 (Fig. 45)	0.22 (Fig. 46)

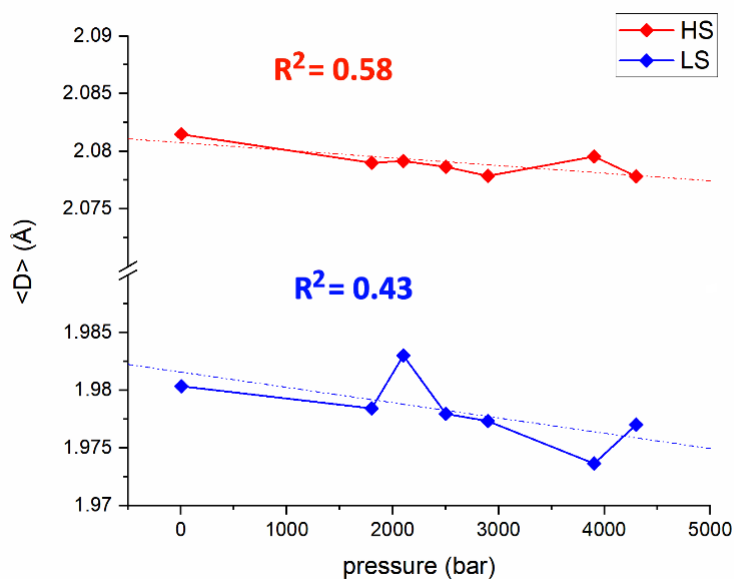


Figure A5.28. Reported effects of the pressure increase vs the average $\langle D_{\text{Co-N}} \rangle$ distance. Trend line reports the correlation factor for $1_{\text{cry,HS}}$ (red, $R^2 = 0.58$) and $1_{\text{cry,LS}}$ [Co(dpzca)₂] (blue, $R^2 = 0.43$).

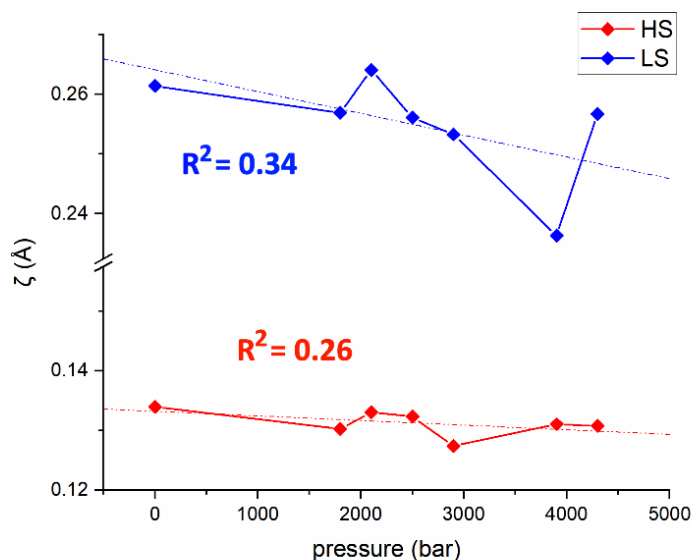


Figure A5.29. Reported effects of the pressure increase vs the sum of the Co-N bond differences from $\langle D_{\text{Co-N}} \rangle$, ζ . Trend line reports the correlation factor for $1_{\text{cry,HS}}$ (red, $R^2 = 0.26$) and $1_{\text{cry,LS}}$ (blue, $R^2 = 0.34$).

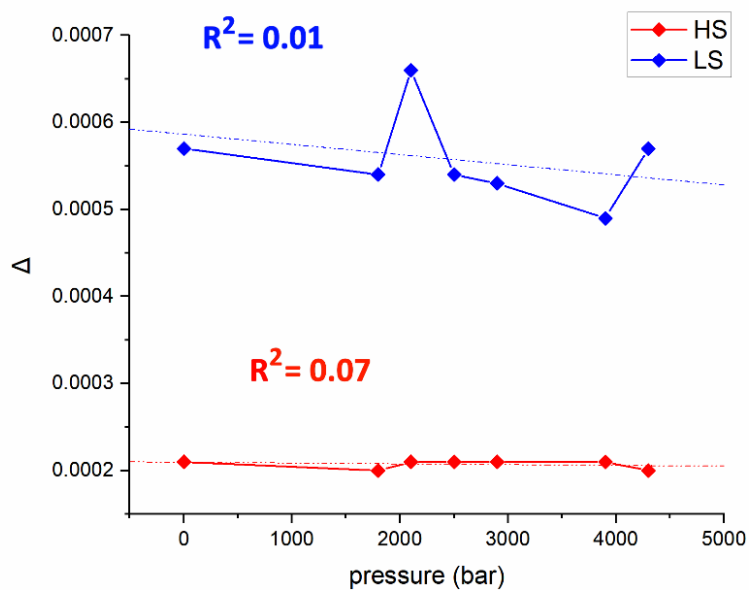


Figure A5.30. Reported effects of the pressure increase vs the averaged Co-N bond deviation from $\langle D_{\text{Co-N}} \rangle$, Δ . Trend line reports the correlation factor for $\mathbf{1}_{\text{cry,HS}}$ (red, $R^2 = 0.07$) and $\mathbf{1}_{\text{cry,LS}}$ (blue, $R^2 = 0.01$).

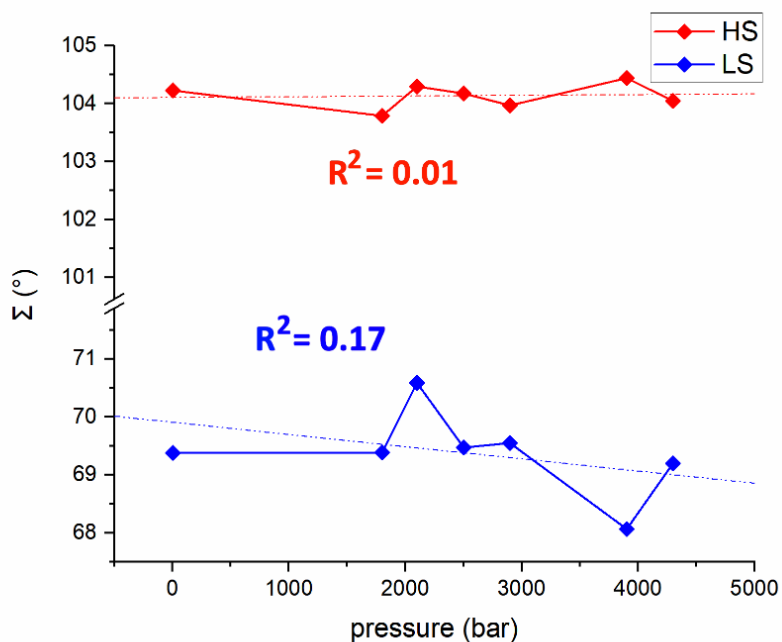


Figure A5.31. Reported effects of the pressure increase vs the octahedral distortion parameter Σ . Trend line reports the correlation factor for $\mathbf{1}_{\text{cry,HS}}$ (red, $R^2 = 0.01$) and $\mathbf{1}_{\text{cry,LS}}$ (blue, $R^2 = 0.17$).

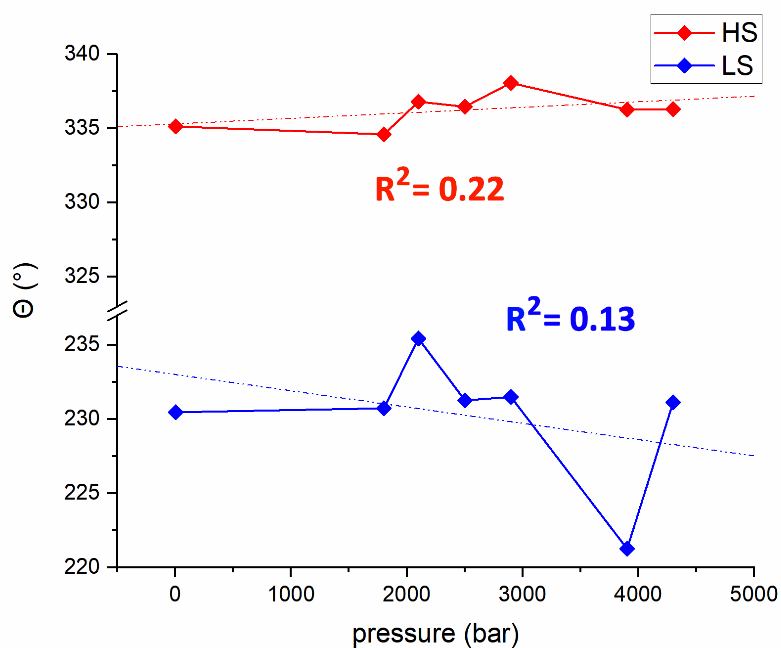


Figure A5.32. Reported effects of the pressure increase vs the trigonal torsion parameter Θ . Trend line reports the correlation factor for $\mathbf{1}_{\text{cry,HS}}$ (red, $R^2 = 0.22$) and $\mathbf{1}_{\text{cry,LS}}$ (blue, $R^2 = 0.13$).

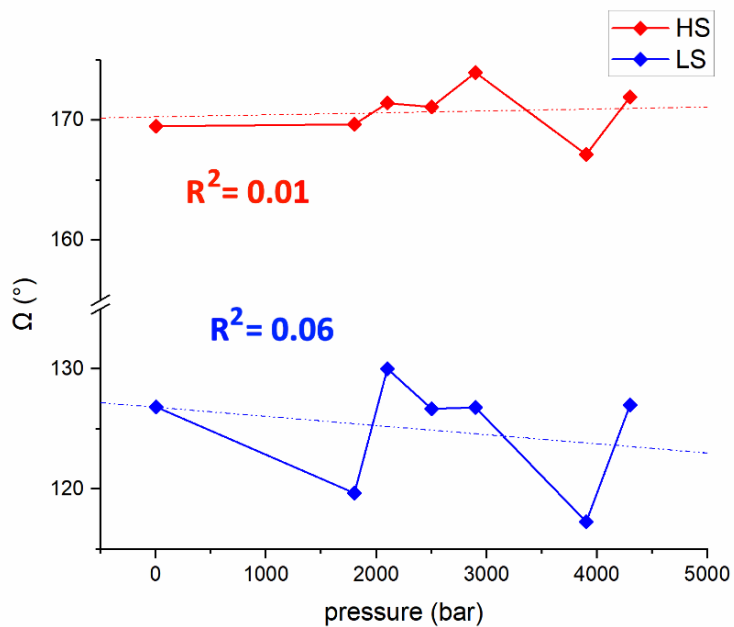


Figure A5.33. Reported effects of the pressure increase vs the distortion parameter Ω . Trend line reports the correlation factor for $\mathbf{1}_{\text{cry,HS}}$ (red, $R^2 = 0.01$) and $\mathbf{1}_{\text{cry,LS}}$ (blue, $R^2 = 0.06$).

A5.2.1. Structural Distortion of 1_{cry} vs. Measured $T_{1/2}$

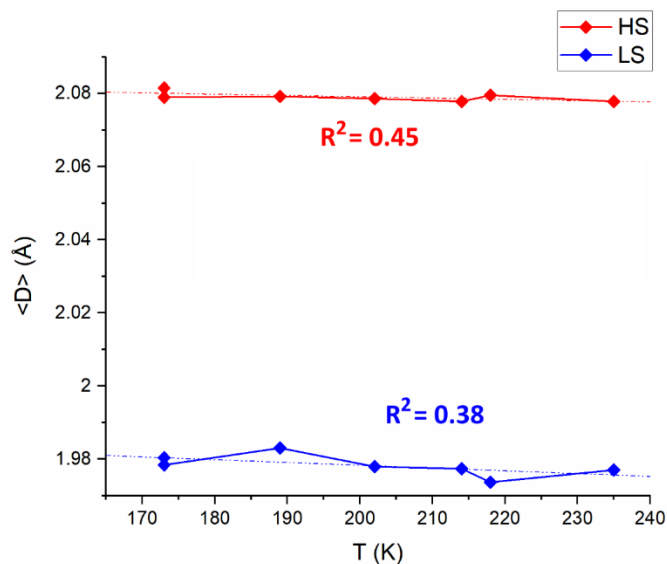


Figure A5.34. Reported effects of the measured $T_{1/2}$ values at pressure increase vs the vs the average $\langle D_{\text{Co-N}} \rangle$ distance. Trend line reports the correlation factor for $1_{\text{cry,HS}}$ (red, $R^2 = 0.45$) and $1_{\text{cry,LS}}$ (blue, $R^2 = 0.38$).

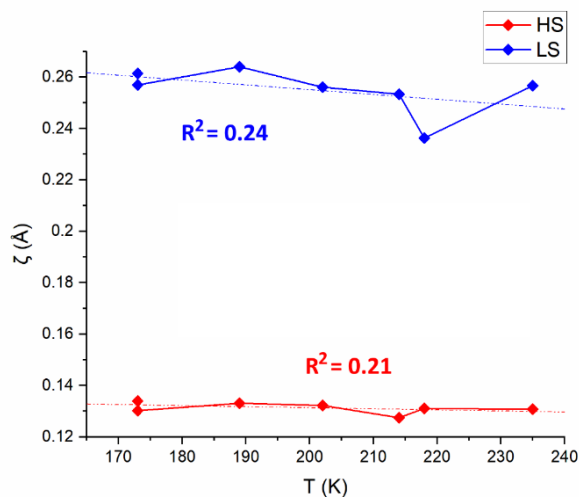


Figure A5.35. Reported effects of the measured $T_{1/2}$ values at pressure increase vs the sum of the Co-N bond differences from $\langle D_{\text{Co-N}} \rangle$, ζ . Trend line reports the correlation factor for $1_{\text{cry,HS}}$ (red, $R^2 = 0.21$) and $1_{\text{cry,LS}}$ (blue, $R^2 = 0.24$).

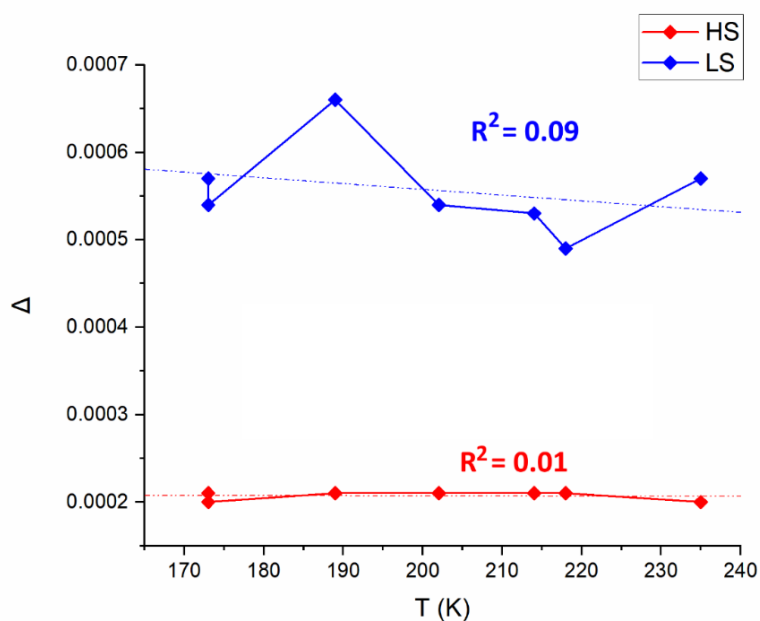


Figure A5.36. Reported effects of the measured $T_{1/2}$ values at pressure increase vs the averaged Co-N bond deviation from $\langle D_{\text{Co-N}} \rangle$, Δ . Trend line reports the correlation factor for $1_{\text{cry,HS}}$ (red, $R^2 = 0.01$) and $1_{\text{cry,LS}}$ (blue, $R^2 = 0.09$).

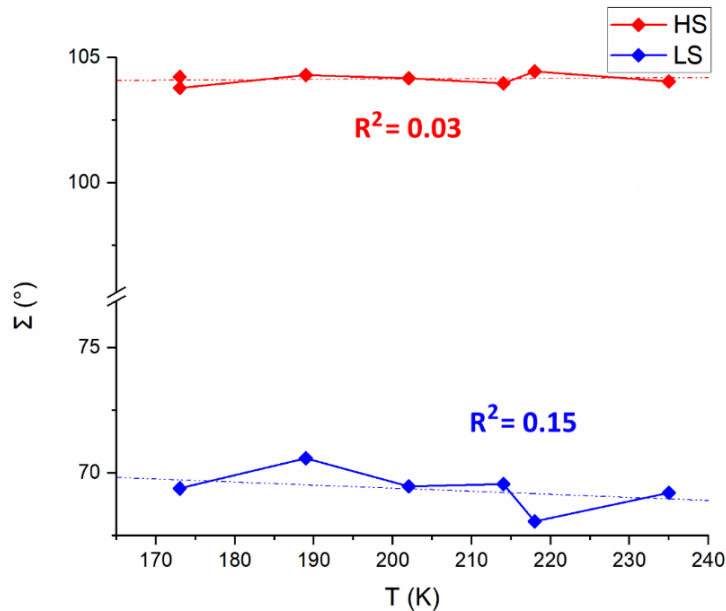


Figure A5.37. Reported effects of the measured $T_{1/2}$ values at pressure increase vs the octahedral distortion parameter Σ . Trend line reports the correlation factor for $1_{\text{cry,HS}}$ (red, $R^2 = 0.03$) and $1_{\text{cry,LS}}$ (blue, $R^2 = 0.15$).

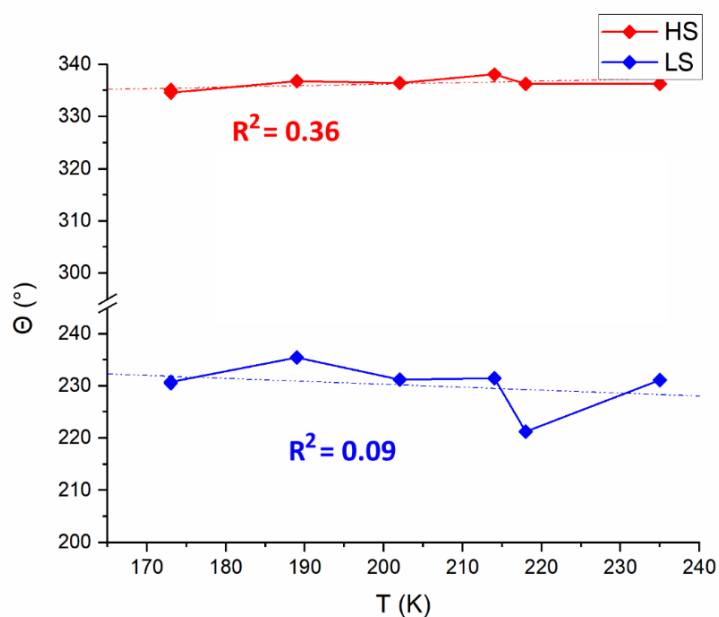


Figure A5.38. Reported effects of the measured $T_{1/2}$ values at pressure increase vs the trigonal torsion parameter Θ . Trend line reports the correlation factor for $1_{\text{cry,HS}}$ (red, $R^2 = 0.95$) and $1_{\text{cry,LS}}$ (blue, $R^2 = 0.92$).

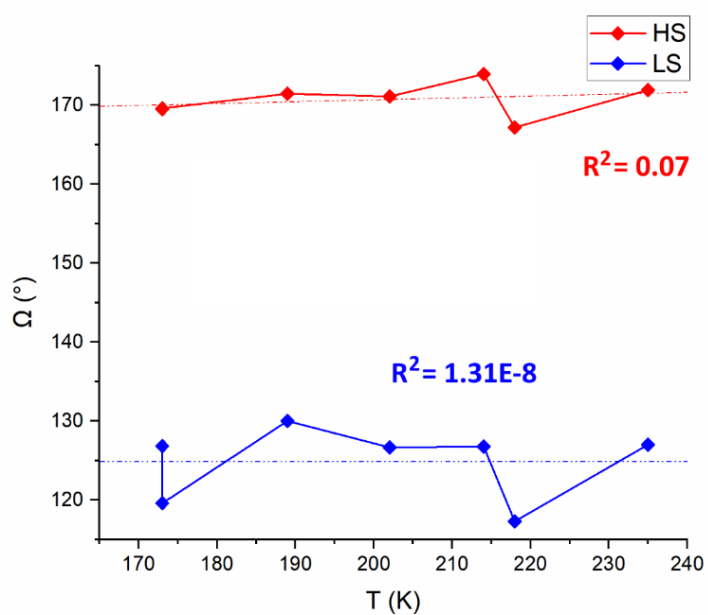


Figure A5.39. Reported effects of the $T_{1/2}$ values at pressure increase vs the distortion parameter Ω . Trend line reports the correlation factor for $1_{\text{cry,HS}}$ (red, $R^2 = 0.07$) and $1_{\text{cry,LS}}$ (blue, $R^2 = 1.13\text{E-}8$).

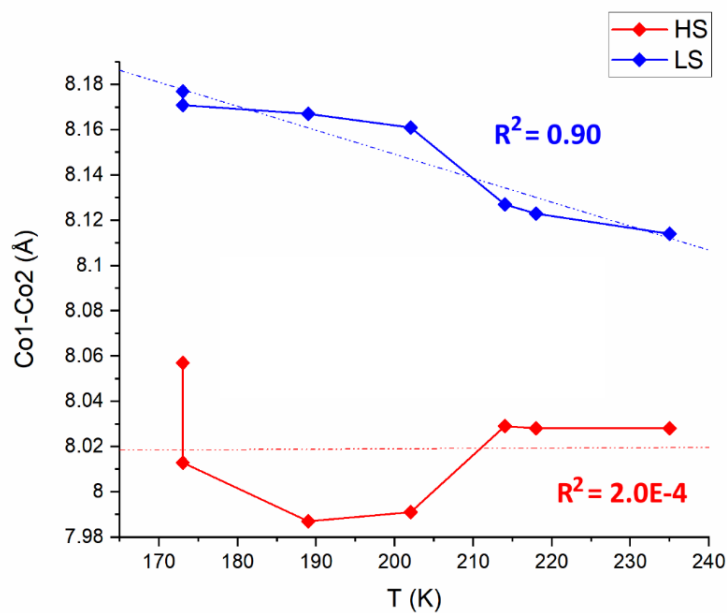


Figure A5.40. Reported effects of the measured $T_{1/2}$ values at pressure increase vs the intermolecular Co-Co ions distance ($d(\text{Co1-Co2})$). Trend line reports the correlation factor for $1_{\text{cry,HS}}$ (red, $R^2 = 2.0E-4$) and $1_{\text{cry,LS}}$ (blue, $R^2 = 0.90$).

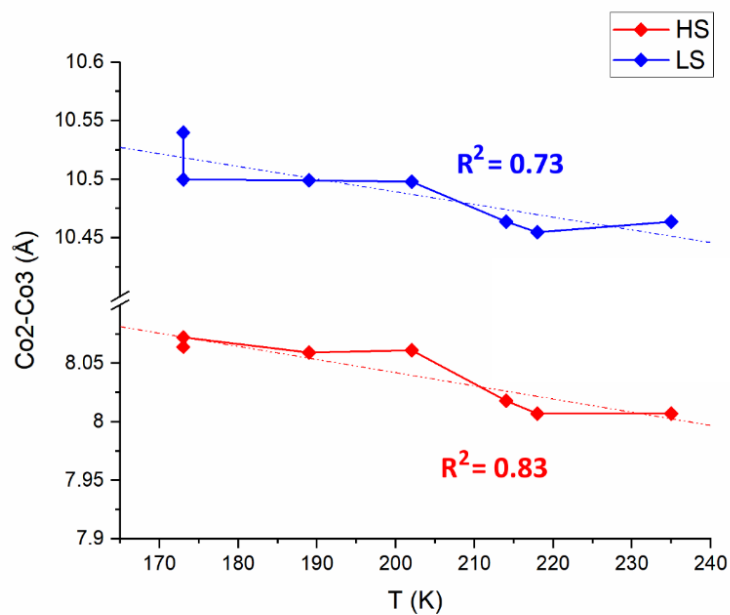


Figure A5.41. Reported effects of the measured $T_{1/2}$ values at pressure increase vs the intermolecular Co-Co ions distance ($d(\text{Co2-Co3})$). Trend line reports the correlation factor for $1_{\text{cry,HS}}$ (red, $R^2 = 0.83$) and $1_{\text{cry,LS}}$ (blue, $R^2 = 0.73$).

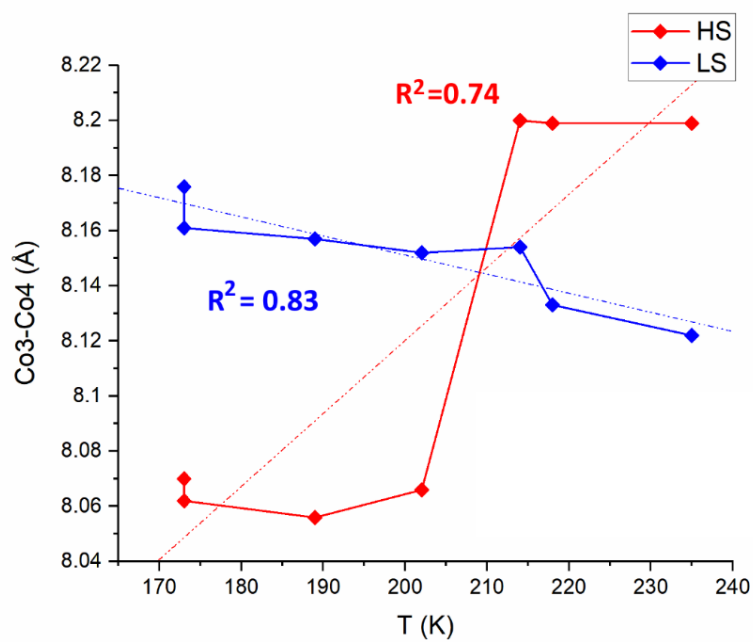


Figure A5.42. Reported effects of the measured $T_{1/2}$ values at pressure increase vs the intermolecular Co-Co ions distance ($d(\text{Co3-Co4})$). Trend line reports the correlation factor for $1_{\text{cry,HS}}$ (red, $R^2 = 0.74$) and $1_{\text{cry,LS}}$ (blue, $R^2 = 0.83$).

A5.2.1. Structural Distortions associated with Spin State Transition

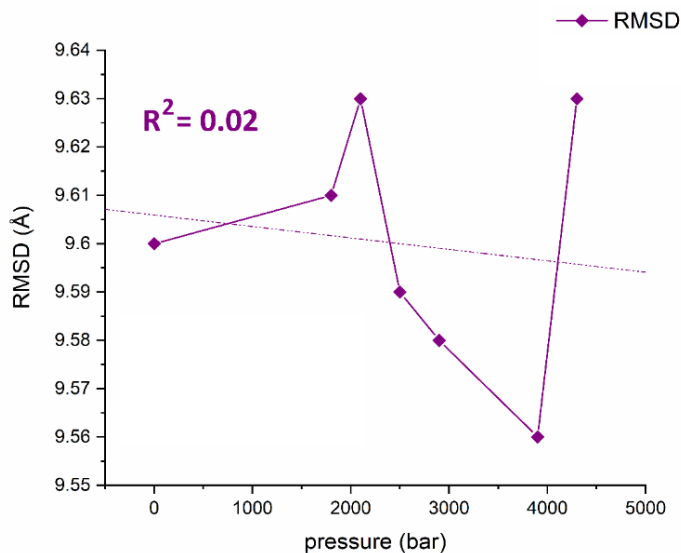


Figure A5.43. Reported effects of the pressure increase vs the ΔRMSD variation from $1_{\text{cry,LS}}$ to $1_{\text{cry,HS}}$. Trend line reports the $[p \text{ vs } \Delta\text{RMSD}]$ correlation factor (purple, $R^2 = 0.02$).

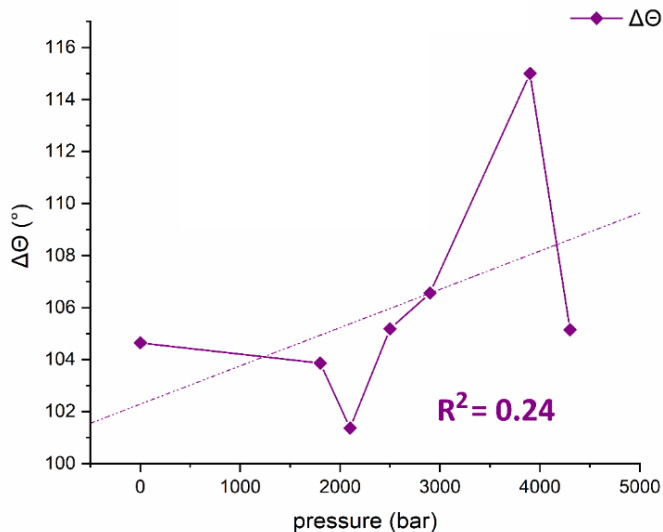


Figure A5.44. Reported effects of the pressure increase vs the variation of the trigonal torsion parameter $\Delta\Theta$ from $1_{\text{cry,LS}}$ to $1_{\text{cry,HS}}$. Trend line reports the $[p \text{ vs } \Delta\Theta]$ correlation factor (purple, $R^2 = 0.24$).

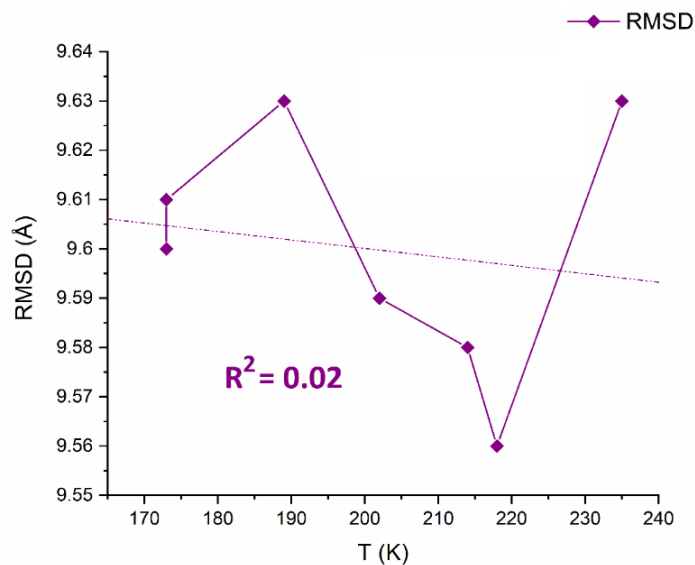


Figure A5.45. Reported effects of the measured $T_{1/2}$ at the pressure increase vs the ΔRMSD variation from $1_{\text{cry,LS}}$ to $1_{\text{cry,HS}}$. Trend line reports the $[T_{1/2}$ vs $\Delta\text{RMSD}]$ correlation factor (purple, $R^2 = 0.02$).

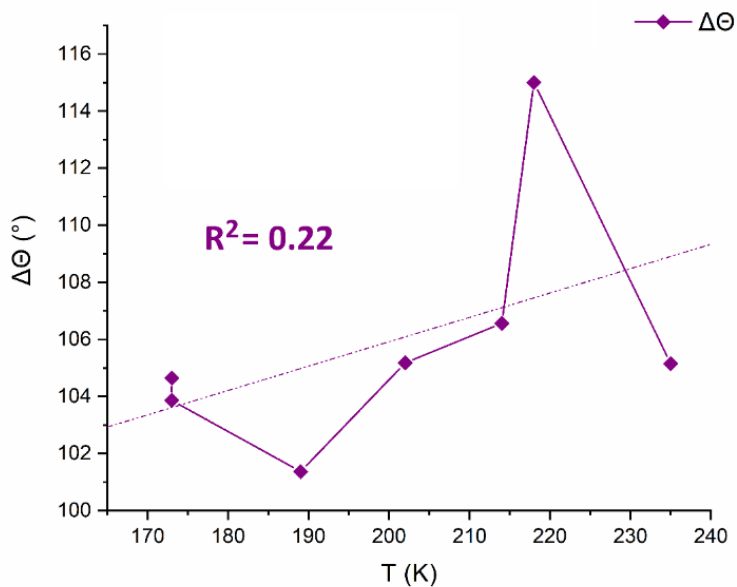


Figure A5.46. Reported effects of the measured $T_{1/2}$ at the pressure increase vs the variation of the trigonal torsion parameter $\Delta\Theta$ from $1_{\text{cry,LS}}$ to $1_{\text{cry,HS}}$. Trend line reports the $[T_{1/2}$ vs. $\Delta\Theta]$ correlation factor (purple, $R^2 = 0.22$).

A5.3. Additional Electronic Data

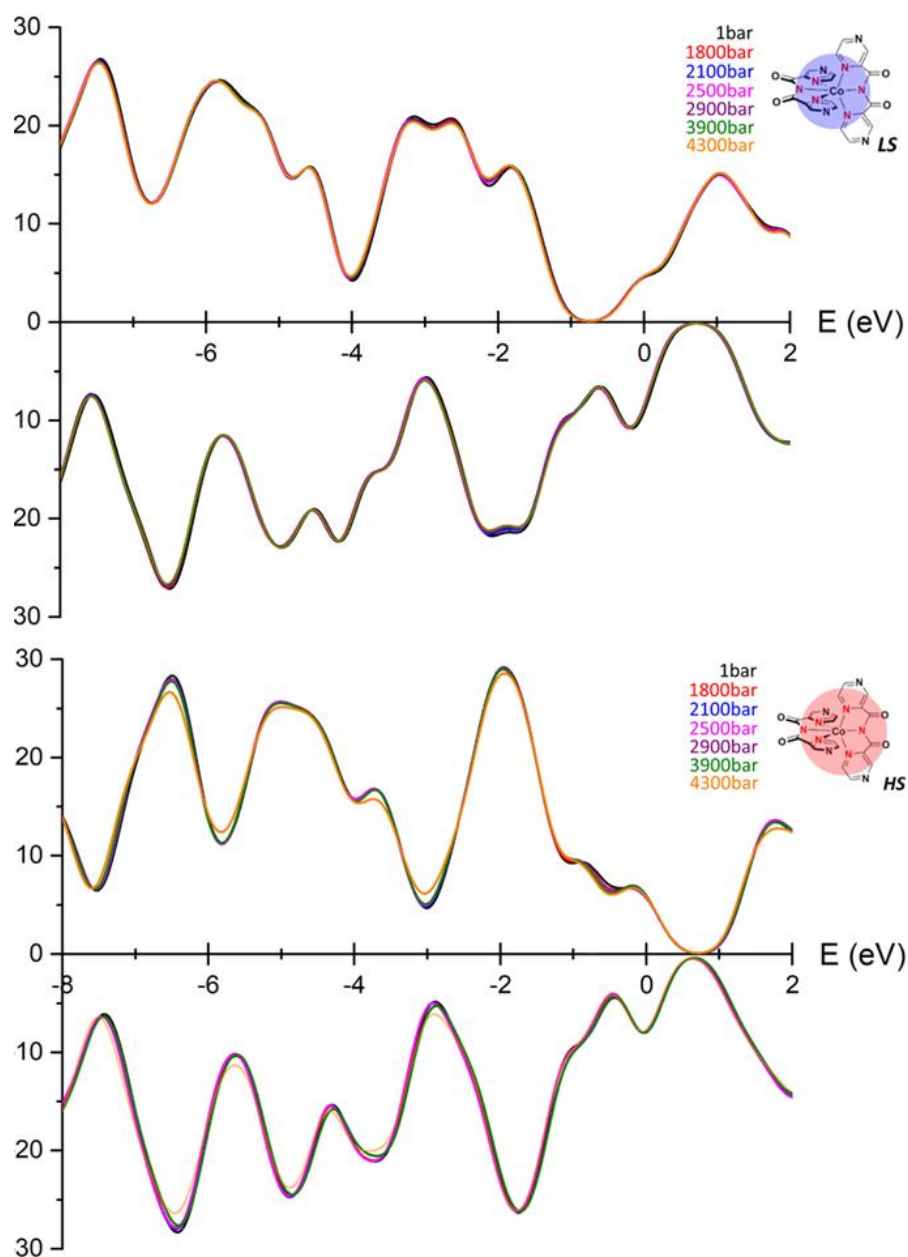


Figure A5.47. Calculated PDOS for $1_{\text{cryst,LS}}$ (top) and $1_{\text{cryst,HS}}$ (bottom) across the whole pressure range ($1 \text{ bar} < p < 4300 \text{ bar}$) in the energy range between -8 eV and $+2 \text{ eV}$. For each spin state are reported α - (+y axis) and β -orbitals (-y axis). Colour code: 1 bar (black), 1800 bar (red), 2100 bar (blue), 2500 bar (magenta), 2900 bar (purple), 3900 bar (olive), 4300 bar (orange). $1 \text{ bar} = 10^{-4} \text{ Pa}$.

Table A5.11. Reported correlation factor in the analysis of the variation of twelve characteristic peaks for TDOS and LDOS of $\mathbf{1}_{\text{cry,LS}}$ and to $\mathbf{1}_{\text{cry,HS}}$ versus the seven different pressures (and related experimental $T_{1/2}$).

p / bar			1	1800	2100	2500	2900	3900	4300	$R^2(p)$	R^2 ($T_{1/2}(\text{exp})$)
$T_{1/2}(\text{exp.}) / \text{K}$			173	173	189	202	214	227	235		
DOS	Figure	Energy / eV	Intensities								
1.LS_TDOS	7	-1.9	25.34	25.23	24.96	24.67	24.62	24.57	24.04	0.84 (Fig. S48)	0.92 (Fig. S60)
2.LS_TDOS	7	-2.6	42.13	41.54	41.45	41.38	41.34	41.12	40.92	0.97 (Fig. S49)	0.74 (Fig. S61)
3.LS_TDOS	7	-3.1	42.44	41.91	41.81	41.74	41.76	41.51	41.46	0.97 (Fig. S50)	0.74 (Fig. S62)
4.LS_PDOS(α)	S47	-2.1	13.89	14.21	14.31	14.32	14.53	14.55	14.65	0.97 (Fig. S51)	0.84 (Fig. S63)
5.LS_PDOS(α)	S47	-2.6	20.73	20.53	20.42	20.42	20.38	20.35	20.24	0.97 (Fig. S52)	0.81 (Fig. S64)
6.LS_PDOS(α)	S47	-3.2	20.93	20.67	20.67	20.61	20.63	20.46	20.41	0.97 (Fig. S53)	0.76 (Fig. S65)
7.LS_PDOS(β)	S47	-2.1	21.76	21.57	21.48	21.42	21.41	21.19	21.19	0.98 (Fig. S54)	0.89 (Fig. S66)
8.HS_TDOS	7	-0.5	11.27	10.73	10.52	10.44	10.63	10.65	10.15	0.75 (Fig. S55)	0.52 (Fig. S67)
9.HS_TDOS	7	-0.7	14.89	14.14	13.91	13.85	13.82	13.68	13.18	0.93 (Fig. S56)	0.73 (Fig. S68)
10.HS_TDOS	7	-1.9	54.78	54.66	54.63	54.58	54.45	54.45	54.21	0.86 (Fig. S57)	0.87 (Fig. S69)
11.HS_PDOS(α)	S47	-0.7	8.05	7.67	7.49	7.431	7.26	7.26	6.94	0.94 (Fig. S58)	0.84 (Fig. S70)
12.HS_PDOS(α)	S47	-2.0	29.17	29.10	29.07	29.04	28.97	28.97	28.56	0.64 (Fig. S59)	0.68 (Fig. S71)

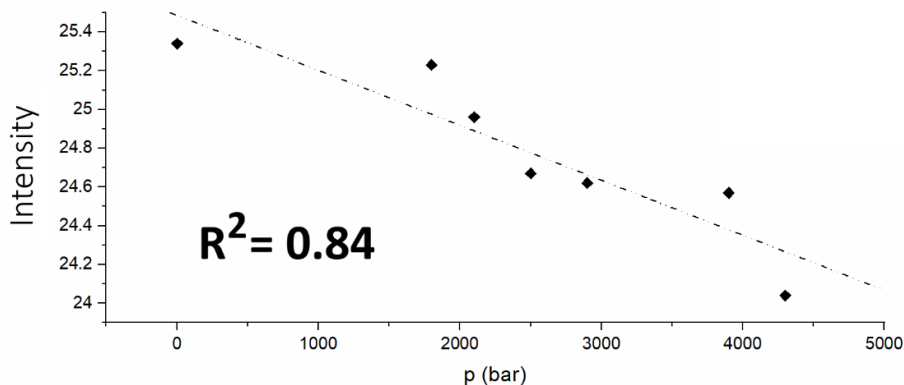


Figure A5.48. Reported Intensity of the band of $1_{\text{cry,LS}}$ at -1.9 eV (1.LS_TDOS, Table A5.11) vs the pressure increase. Trend line reports the [I vs. p] correlation factor ($R^2 = 0.84$).

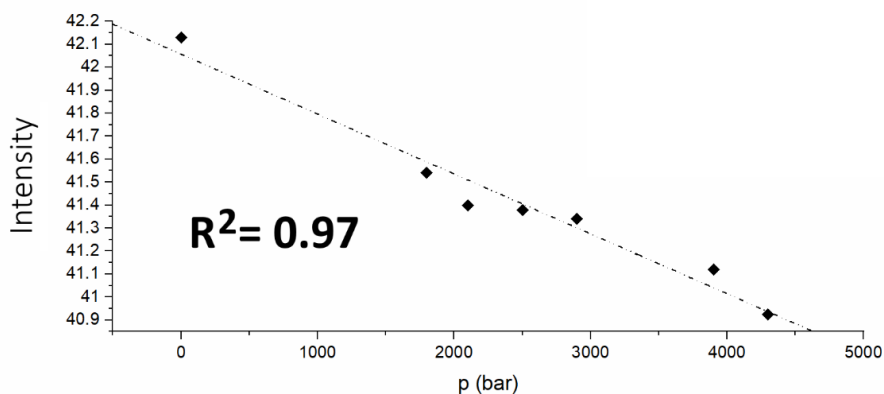


Figure A5.49. Reported Intensity of the band of $1_{\text{cry,LS}}$ at -2.6 eV (2.LS_TDOS, Table A5.11) vs the pressure increase. Trend line reports the [I vs. p] correlation factor ($R^2 = 0.97$).

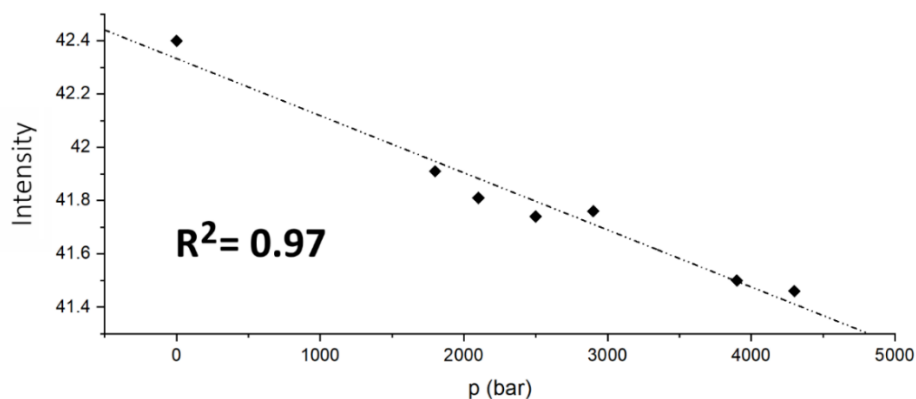


Figure A5.50. Reported Intensity of the band of $1_{\text{cry,LS}}$ at -3.1 eV (3.LS_TDOS, Table A5.11) vs the pressure increase. Trend line reports the [I vs. p] correlation factor ($R^2 = 0.97$).

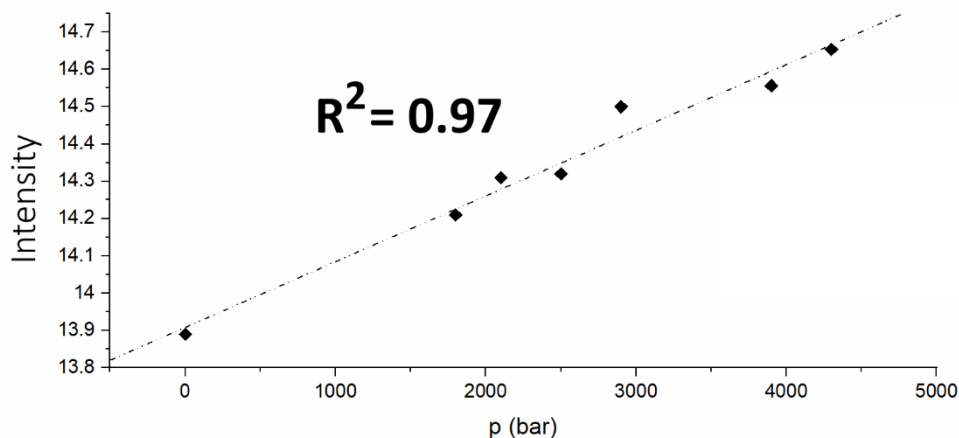


Figure A5.51. Reported Intensity of the band of $1_{\text{cry,LS}}$ at -2.1 eV ($4.\text{LS_PDOS}(\alpha)$, Table A5.11) vs the pressure increase. Trend line reports the $[I \text{ vs. } p]$ correlation factor ($R^2 = 0.97$).

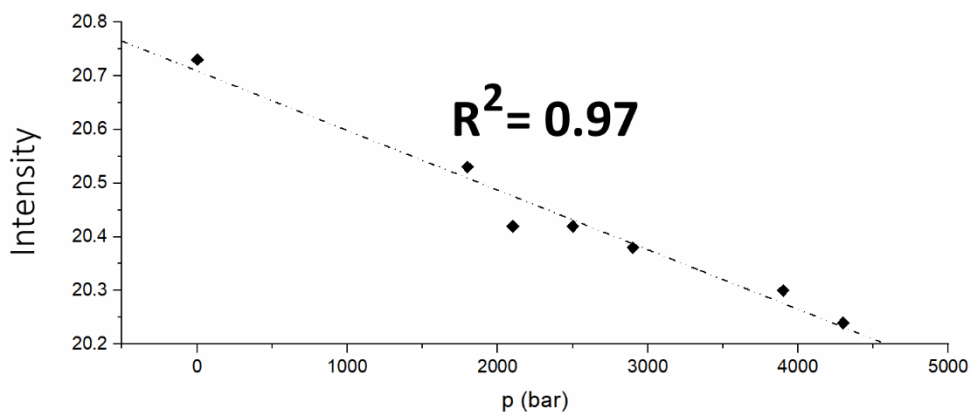


Figure A5.52. Reported Intensity of the band of $1_{\text{cry,LS}}$ at -2.6 eV ($5.\text{LS_PDOS}(\alpha)$, Table A5.11) vs the pressure increase. Trend line reports the $[I \text{ vs. } p]$ correlation factor ($R^2 = 0.97$).

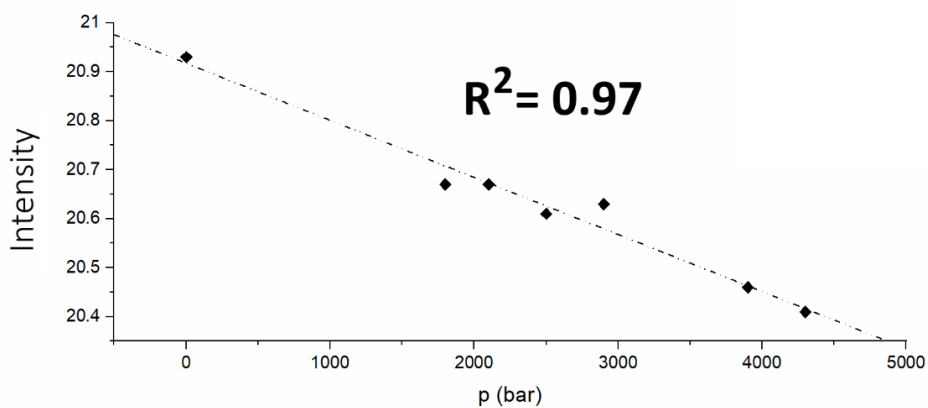


Figure A5.53. Reported Intensity of the band of $1_{\text{cry,LS}}$ at -3.2 eV ($6.\text{LS_PDOS}(\alpha)$, Table A5.11) vs the pressure increase. Trend line reports the $[I \text{ vs. } p]$ correlation factor ($R^2 = 0.97$).

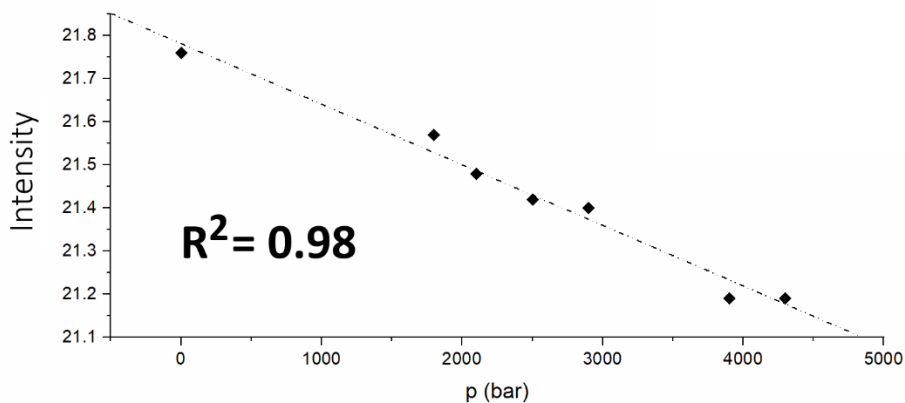


Figure A5.54. Reported Intensity of the band of $1_{\text{cry,LS}}$ at -2.1 eV (7.LS_PDOS(β), Table A5.11) vs the pressure increase. Trend line reports the [I vs. p] correlation factor ($R^2 = 0.98$).

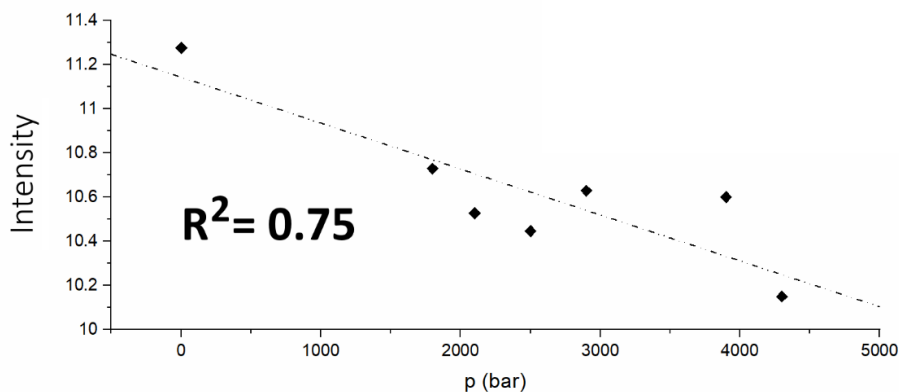


Figure A5.55. Reported Intensity of the band of $1_{\text{cry,HS}}$ at -0.5 eV (8.HS_TDOS, Table A5.11) vs the pressure increase. Trend line reports the [I vs. p] correlation factor ($R^2 = 0.75$).

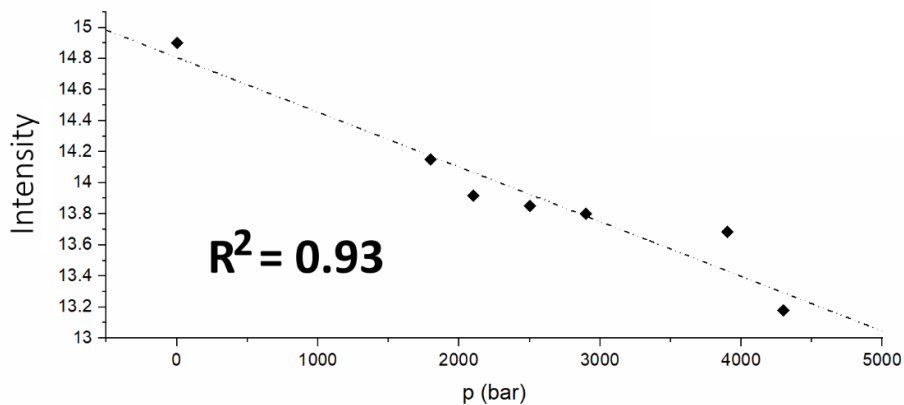


Figure A5.56. Reported Intensity of the band of $1_{\text{cry,HS}}$ at -0.7 eV (9.HS_TDOS, Table A5.11) vs the pressure increase. Trend line reports the [I vs. p] correlation factor ($R^2 = 0.93$).

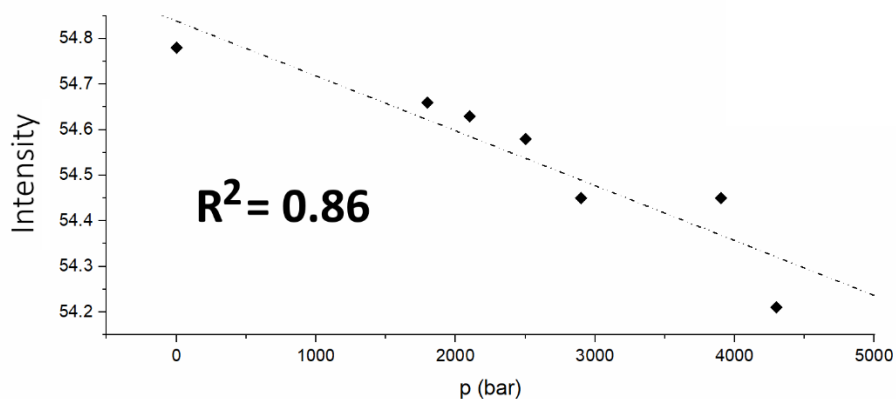


Figure A5.57. Reported Intensity of the band of $1_{\text{cry,HS}}$ at -1.9 eV (10.HS_TDOS, Table A5.11) vs the pressure increase. Trend line reports the [I vs. p] correlation factor ($R^2 = 0.86$).

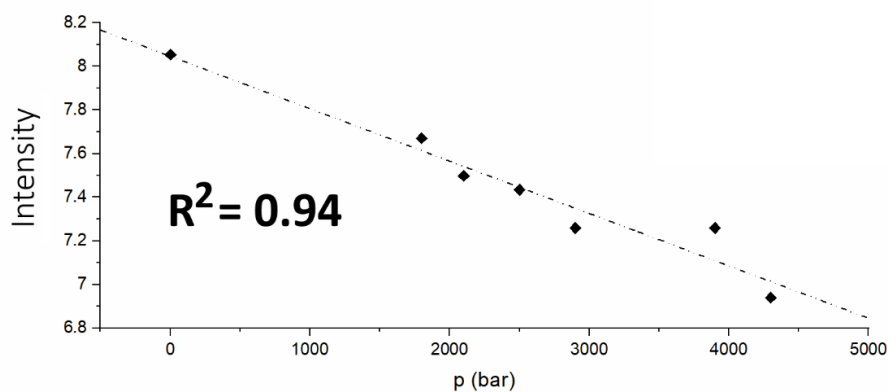


Figure A5.58. Reported Intensity of the band of $1_{\text{cry,HS}}$ at -0.7 eV (11.HS_PDOS(α), Table A5.11) vs the pressure increase. Trend line reports the [I vs. p] correlation factor ($R^2 = 0.94$).

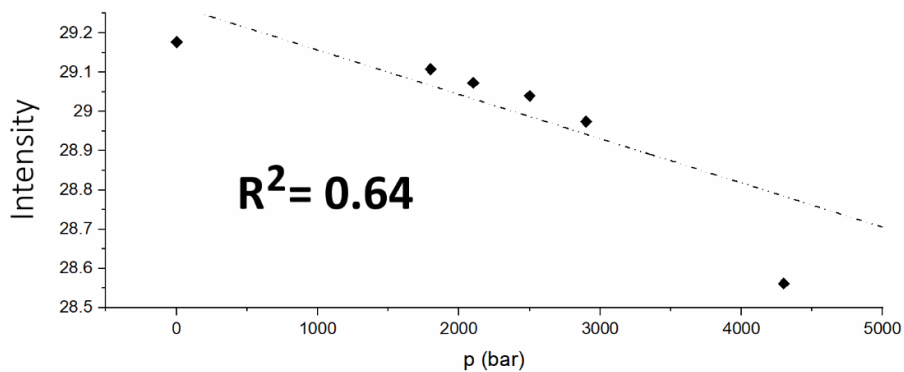


Figure A5.59. Reported Intensity of the band of $1_{\text{cry,HS}}$ at -2.0 eV (12.HS_PDOS(α), Table A5.11) vs the pressure increase. Trend line reports the [I vs. p] correlation factor ($R^2 = 0.64$).

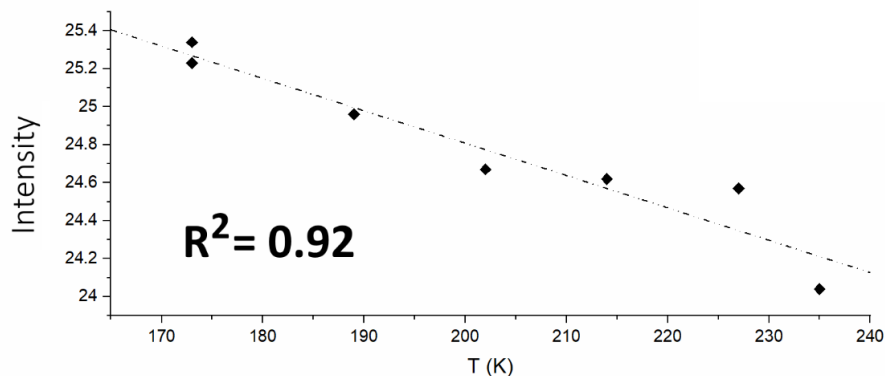


Figure A5.60. Reported Intensity of the band of $1_{\text{cry,LS}}$ at -1.9 eV (1.LS_TDOS, Table A5.11) vs the measured $T_{1/2}$. Trend line reports the [I vs. $T_{1/2}$] correlation factor ($R^2 = 0.92$).

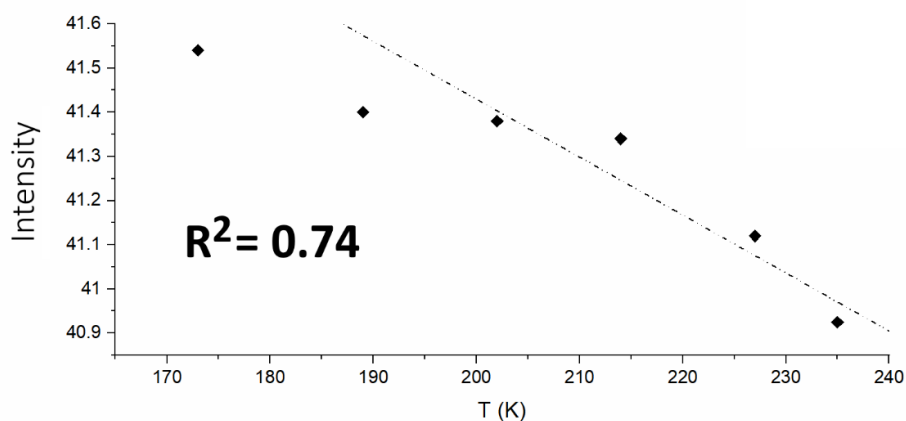


Figure A5.61. Reported Intensity of the band of $1_{\text{cry,LS}}$ at -2.6 eV (2.LS_TDOS, Table A5.11) vs the measured $T_{1/2}$. Trend line reports the [I vs. $T_{1/2}$] correlation factor ($R^2 = 0.74$).

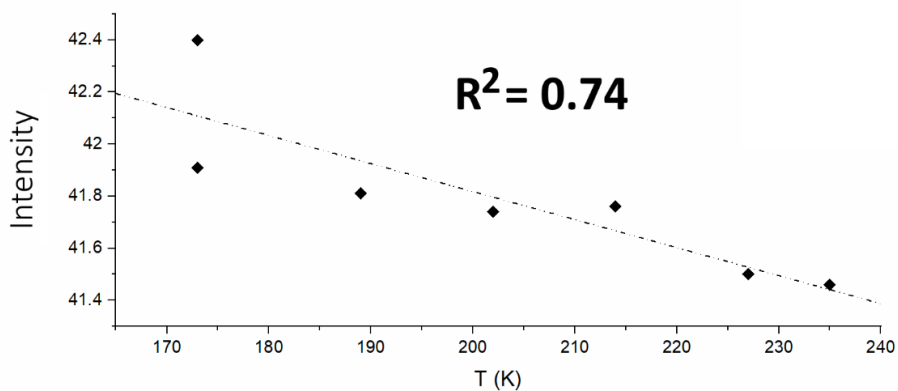


Figure A5.62. Reported Intensity of the band of $1_{\text{cry,LS}}$ at -3.1 eV (3.LS_TDOS, Table A5.11) vs the measured $T_{1/2}$. Trend line reports the [I vs. $T_{1/2}$] correlation factor ($R^2 = 0.74$).

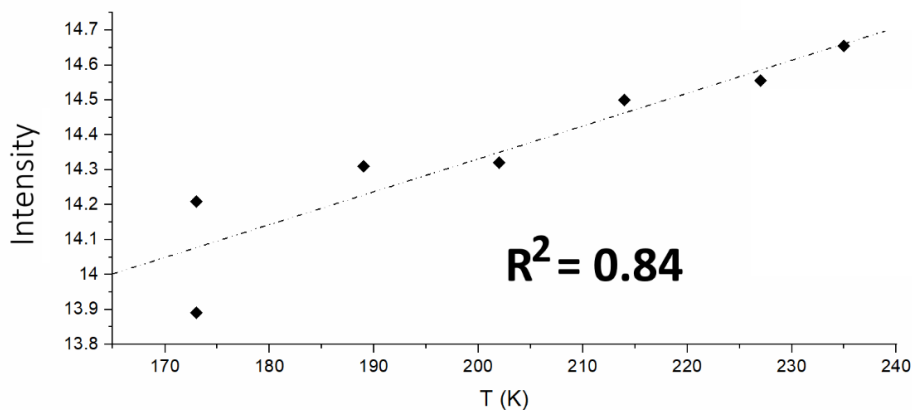


Figure A5.63. Reported Intensity of the band of $1_{\text{cry,LS}}$ at -2.1 eV ($4.\text{LS_PDOS}(\alpha)$, Table A5.11) vs the measured $T_{1/2}$. Trend line reports the $[I$ vs. $T_{1/2}]$ correlation factor ($R^2 = 0.84$)

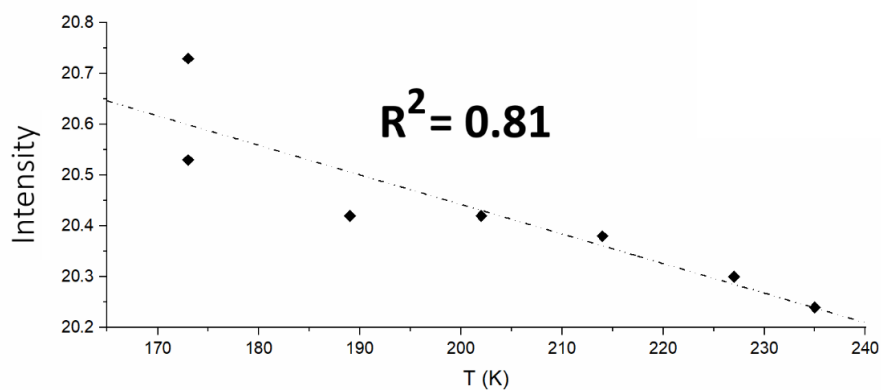


Figure A5.64. Reported Intensity of the band of $1_{\text{cry,LS}}$ at -2.6 eV ($5.\text{LS_PDOS}(\alpha)$, Table A5.11) vs the measured $T_{1/2}$. Trend line reports the $[I$ vs. $T_{1/2}]$ correlation factor ($R^2 = 0.81$).

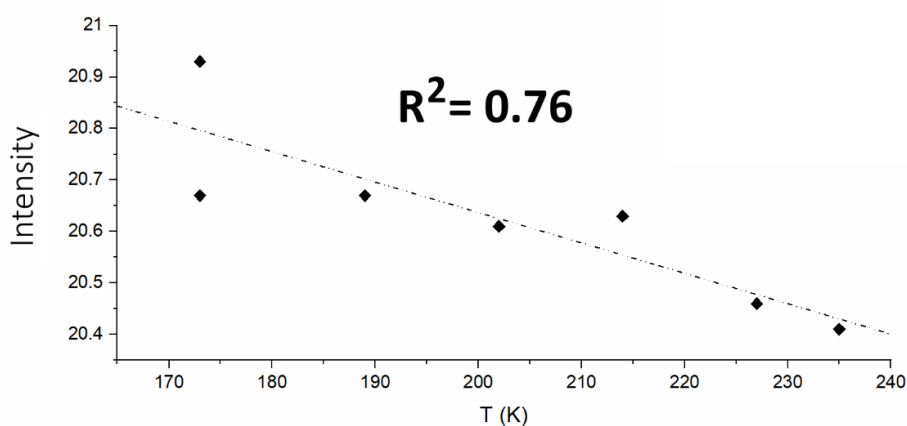


Figure A5.65. Reported Intensity of the band of $1_{\text{cry,LS}}$ at -3.2 eV ($6.\text{LS_PDOS}(\alpha)$, Table A5.11) vs the measured $T_{1/2}$. Trend line reports the $[I$ vs. $T_{1/2}]$ correlation factor ($R^2 = 0.76$).

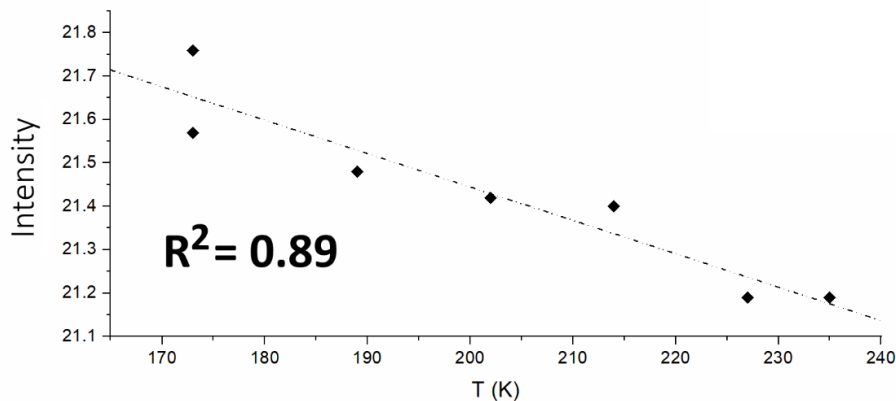


Figure A5.66. Reported Intensity of the band of $1_{\text{cry,LS}}$ at -2.1 eV (7.LS_PDOS(β), Table A5.11) vs the measured $T_{1/2}$. Trend line reports the [I vs. $T_{1/2}$] correlation factor ($R^2 = 0.89$).

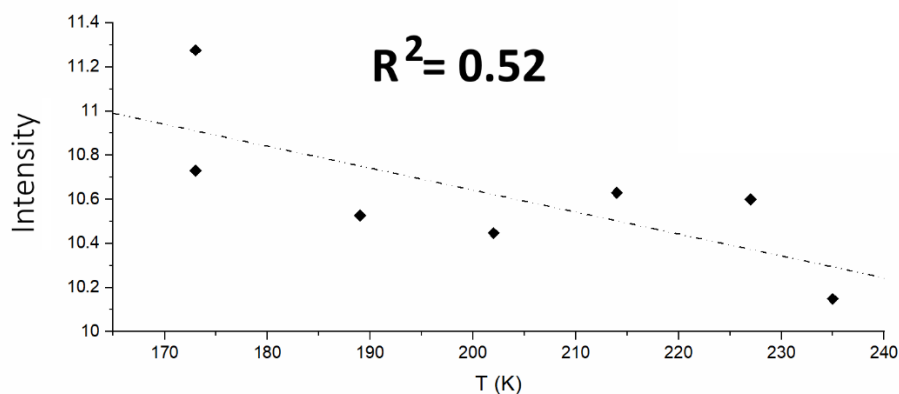


Figure A5.67. Reported Intensity of the band of $1_{\text{cry,HS}}$ at -0.5 eV (8.HS_TDOS, Table A5.11) vs the measured $T_{1/2}$. Trend line reports the [I vs. $T_{1/2}$] correlation factor ($R^2 = 0.52$).

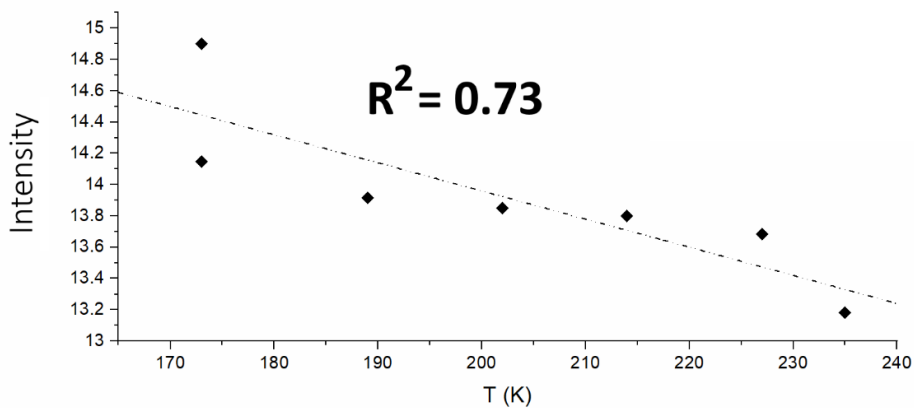


Figure A5.68. Reported Intensity of the band of $1_{\text{cry,HS}}$ at -0.7 eV (9.HS_TDOS, Table A5.11) vs the measured $T_{1/2}$. Trend line reports the [I vs. $T_{1/2}$] correlation factor ($R^2 = 0.73$).

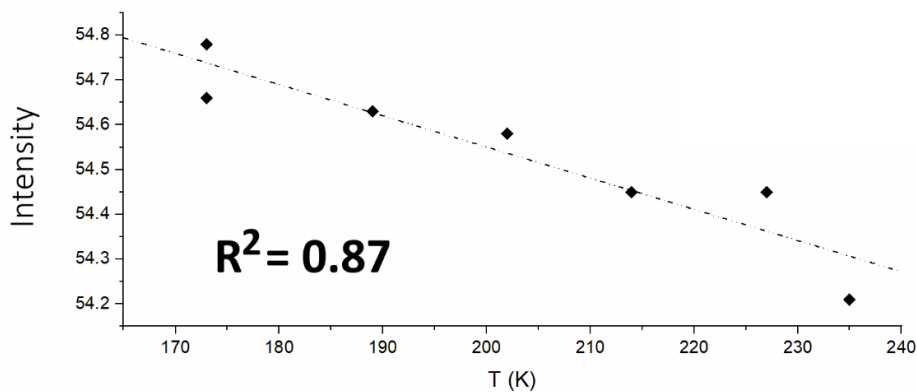


Figure A5.69. Reported Intensity of the band of $1_{\text{cry,HS}}$ at -1.9 eV (10.HS_TDOS, Table A5.11) vs the measured $T_{1/2}$. Trend line reports the [I vs. $T_{1/2}$] correlation factor ($R^2 = 0.87$).

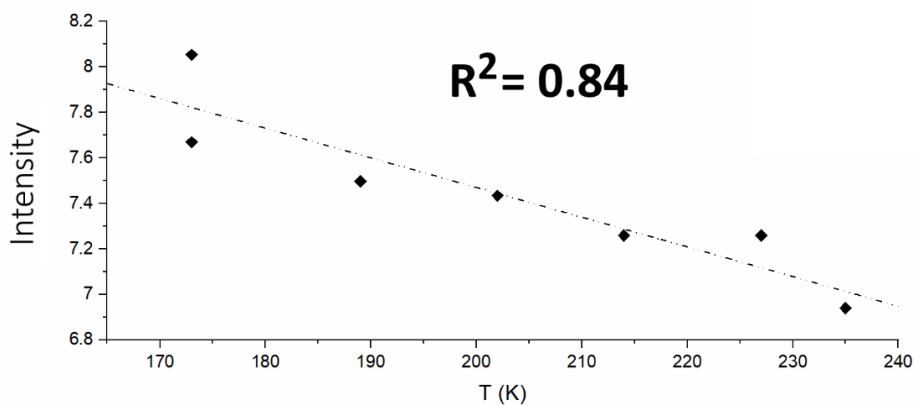


Figure A5.70. Reported Intensity of the band of $1_{\text{cry,HS}}$ at -0.7 eV (11.HS_PDOS(α), Table A5.11) vs the measured $T_{1/2}$. Trend line reports the [I vs. $T_{1/2}$] correlation factor ($R^2 = 0.84$).

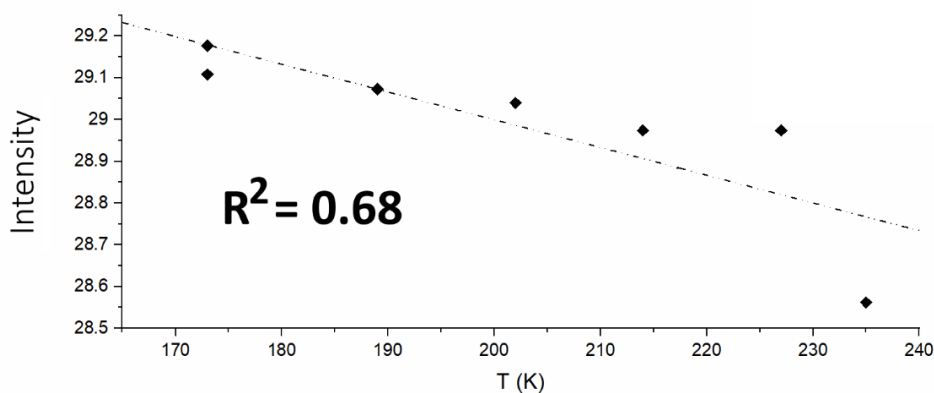


Figure A5.71. Reported Intensity of the band of $1_{\text{cry,HS}}$ at -2.0 eV (12.HS_PDOS(α), Table A5.11) vs the measured $T_{1/2}$. Trend line reports the [I vs. $T_{1/2}$] correlation factor ($R^2 = 0.68$).

A5.3.1. LDOS: Cobalt Atoms

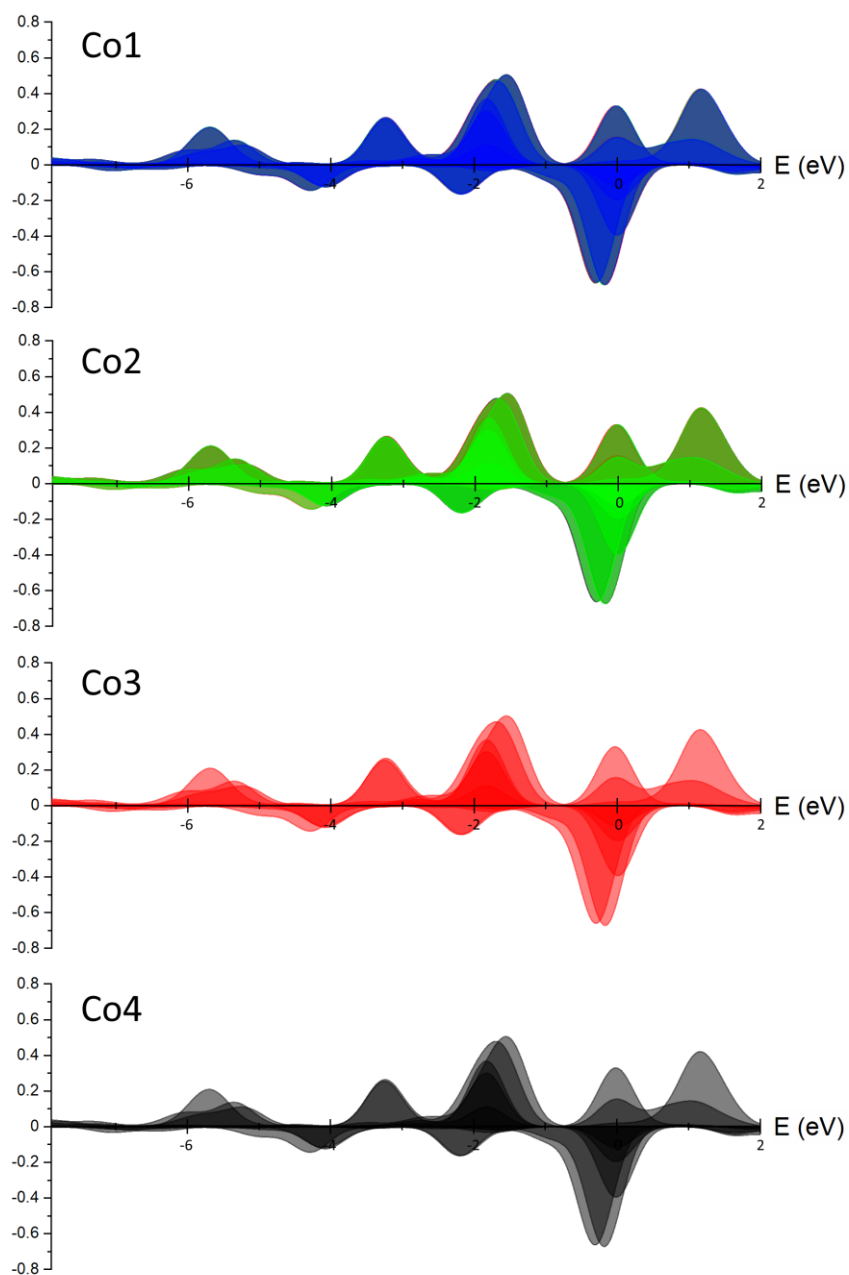


Figure A5.72. Reported LDOS of the four Co(II) ions for $1_{\text{ery,ts}}$ at the pressure of 1 bar in the energy range between -8 eV and +2 eV. For each spin state are reported α - (+y axis) and β -orbitals (-y axis). Colour code: first Co(II) (blue), second Co(II) ion (green), third Co(II) (red), fourth Co(II) (black).

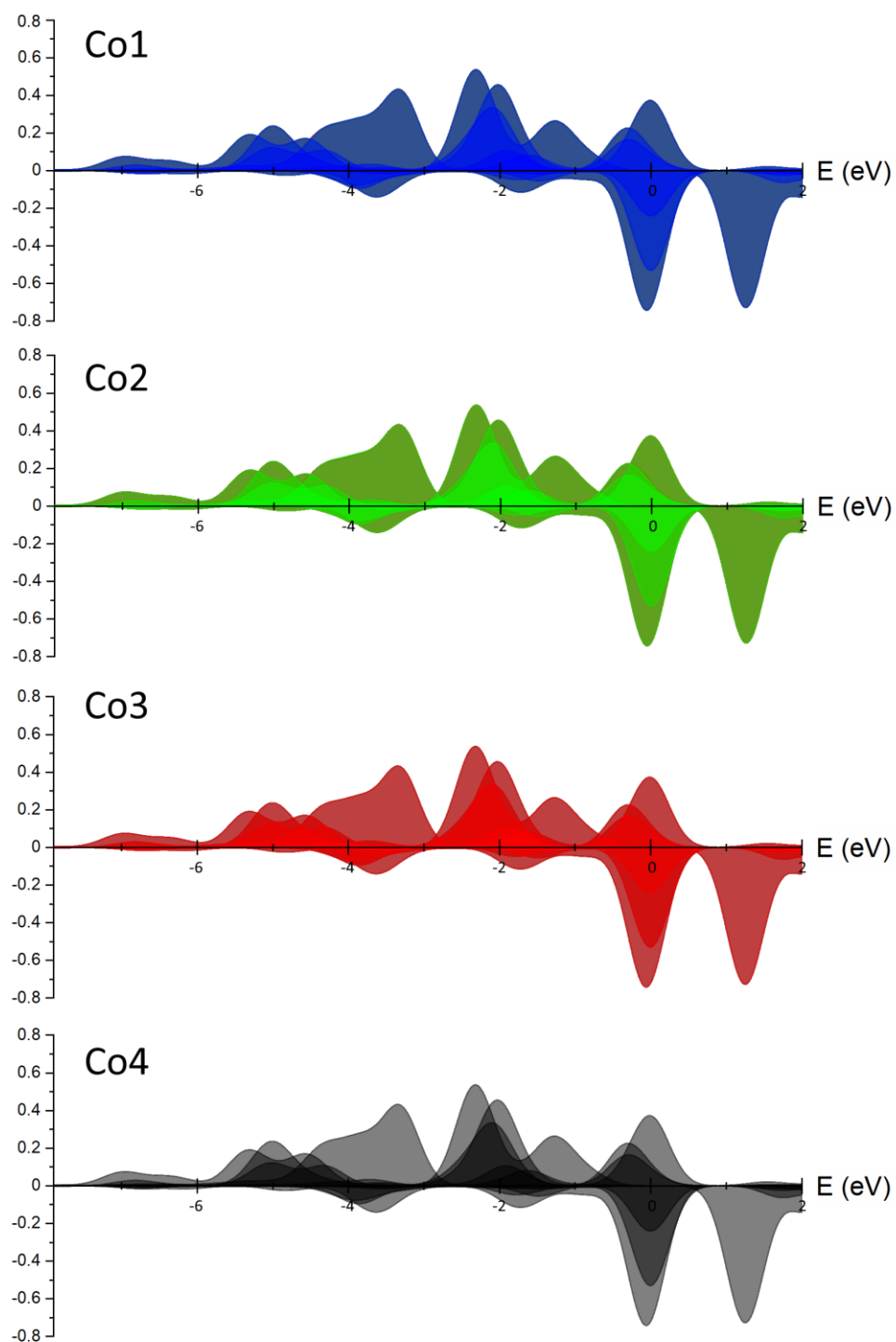


Figure A5.73. Reported LDOS of the four Co(II) ions for $1_{\text{cry,HS}}$ at the pressure of 1 bar in the energy range between -8 eV and +2 eV. For each spin state are reported α - (+y axis) and β -orbitals (-y axis). Colour code: first Co(II) (blue), second Co(II) ion (green), third Co(II) (red), fourth Co(II) (black).

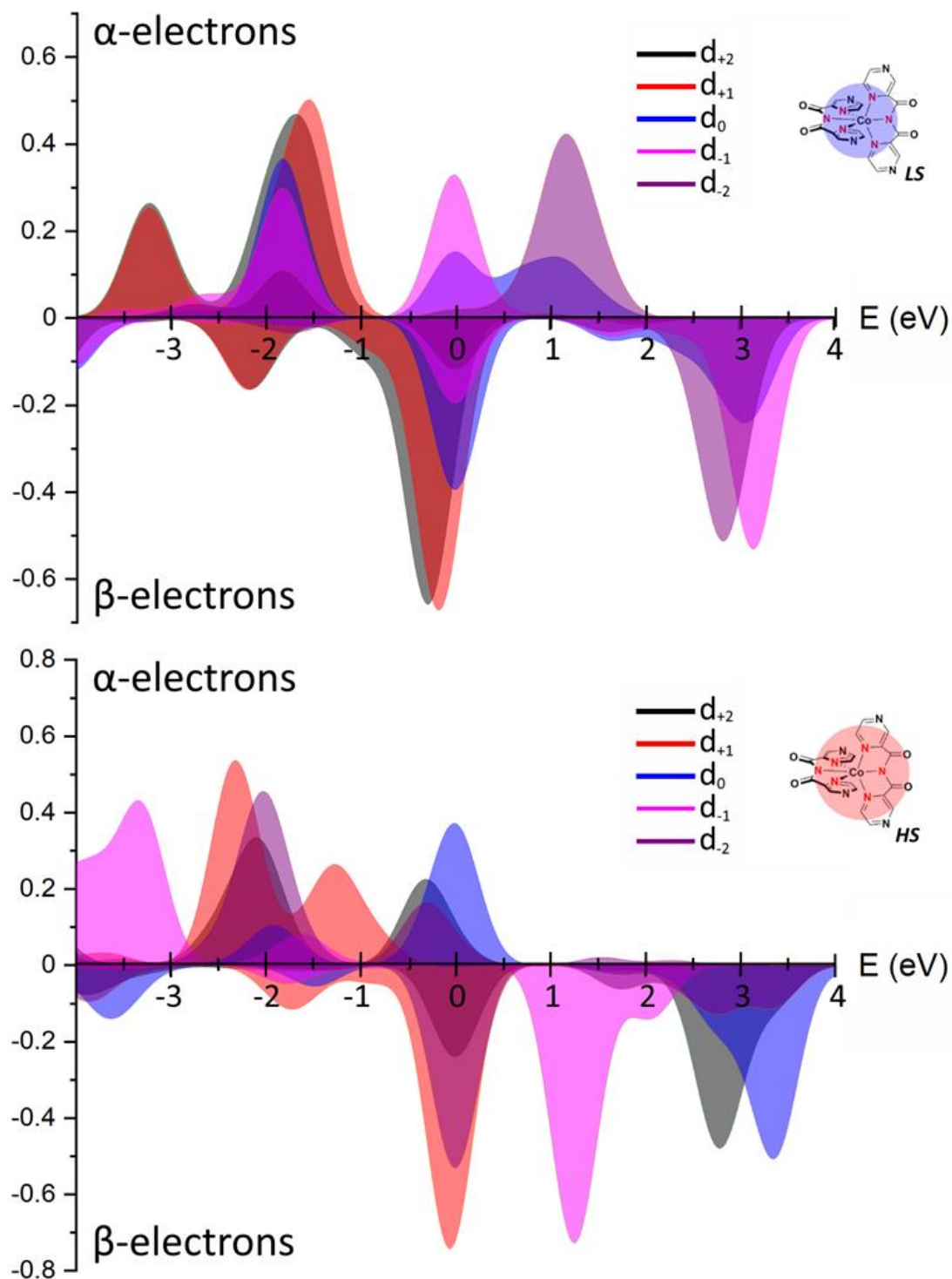


Figure A5.74. Calculated energy of the five d -orbitals represented by complex functions ($m_l = -2, -1, 0, +1, +2$) for $1_{\text{cry,LS}}$ (top) and to $1_{\text{cry,HS}}$ (bottom) in the energy range between -4 eV and $+4$ eV. For each spin state the α - (+y axis) and β - orbitals (-y axis) are reported. Colour code: d_{+2} (black), d_{+1} (red), d_0 (blue), d_{-1} (magenta), d_{-2} (purple).

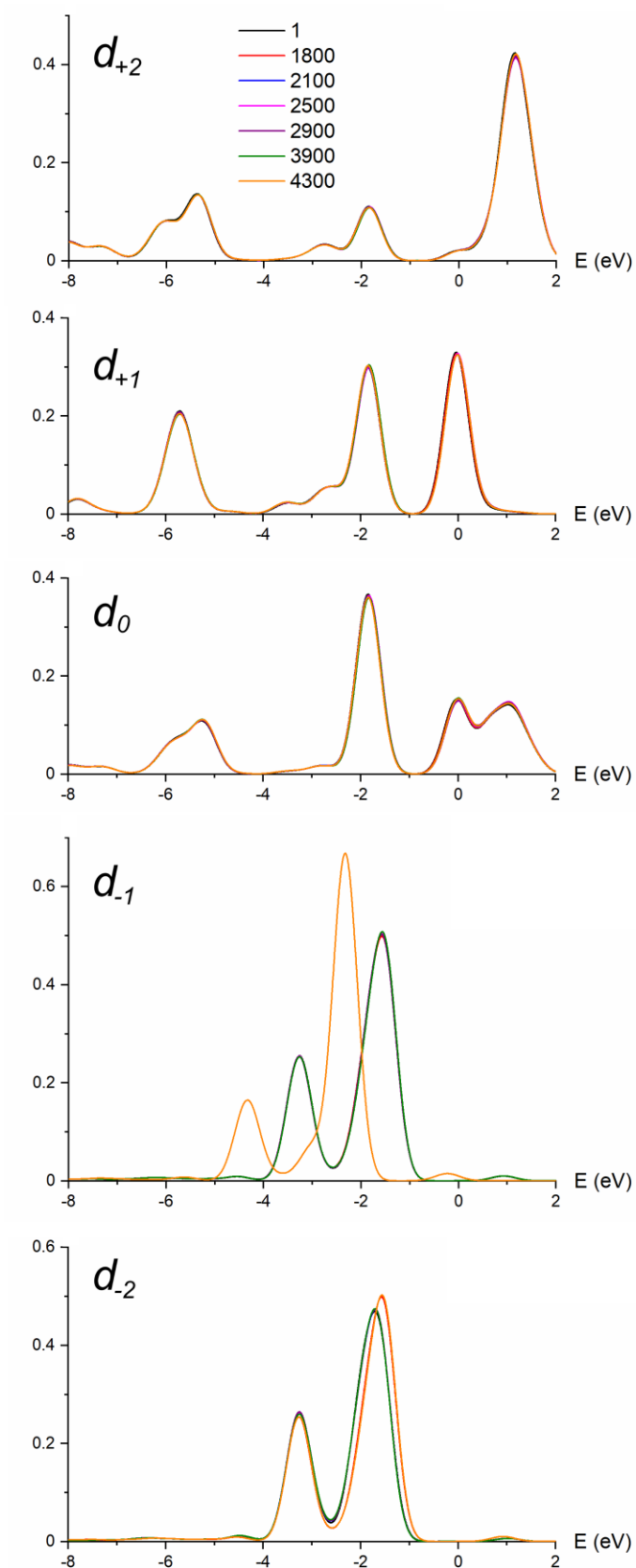


Figure A5.75. Reported LDOS of the alpha d-orbitals of the Co(II) ions of $1_{\text{cry,LS}}$ at the seven studied different pressures ($p = 1, 1800, 2100, 2500, 2900, 3900, 4300$ bar).

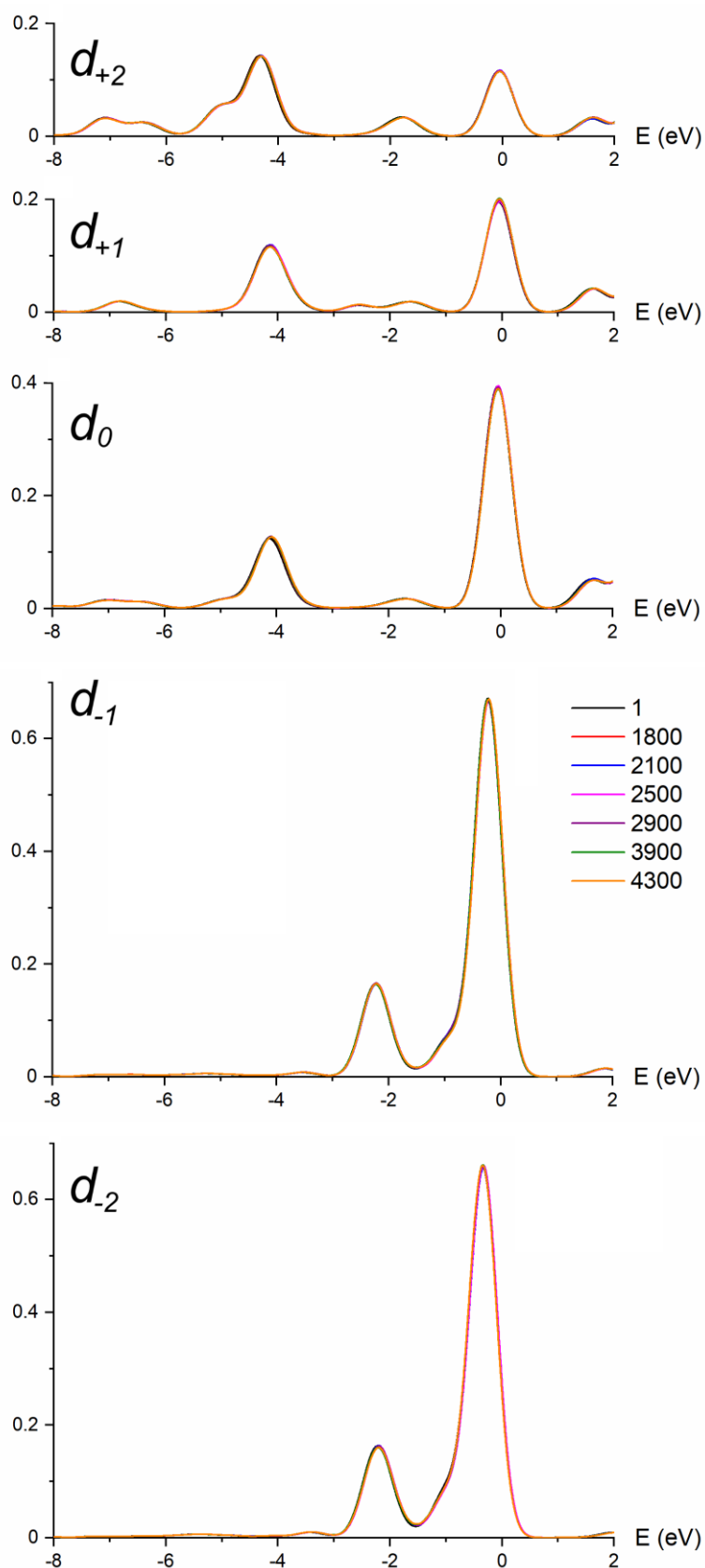


Figure A5.76. Reported LDOS of the beta d-orbitals of the Co(II) ions of 1_{crystal} at the seven studied different pressures ($p = 1, 1800, 2100, 2500, 2900, 3900, 4300$ bar).

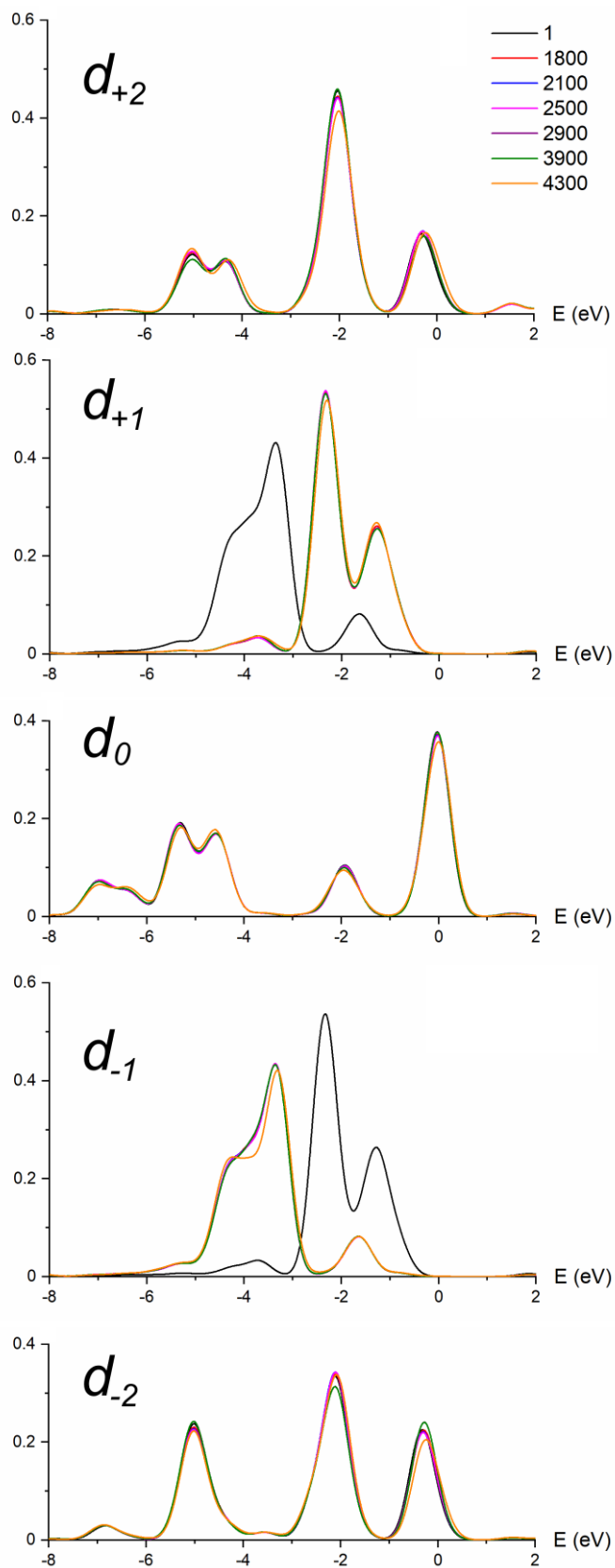


Figure A5.77. Reported LDOS of the alpha d-orbitals of the Co(II) ions of $1_{\text{cry,HS}}$ at the seven studied different pressures ($p = 1, 1800, 2100, 2500, 2900, 3900, 4300$ bar).

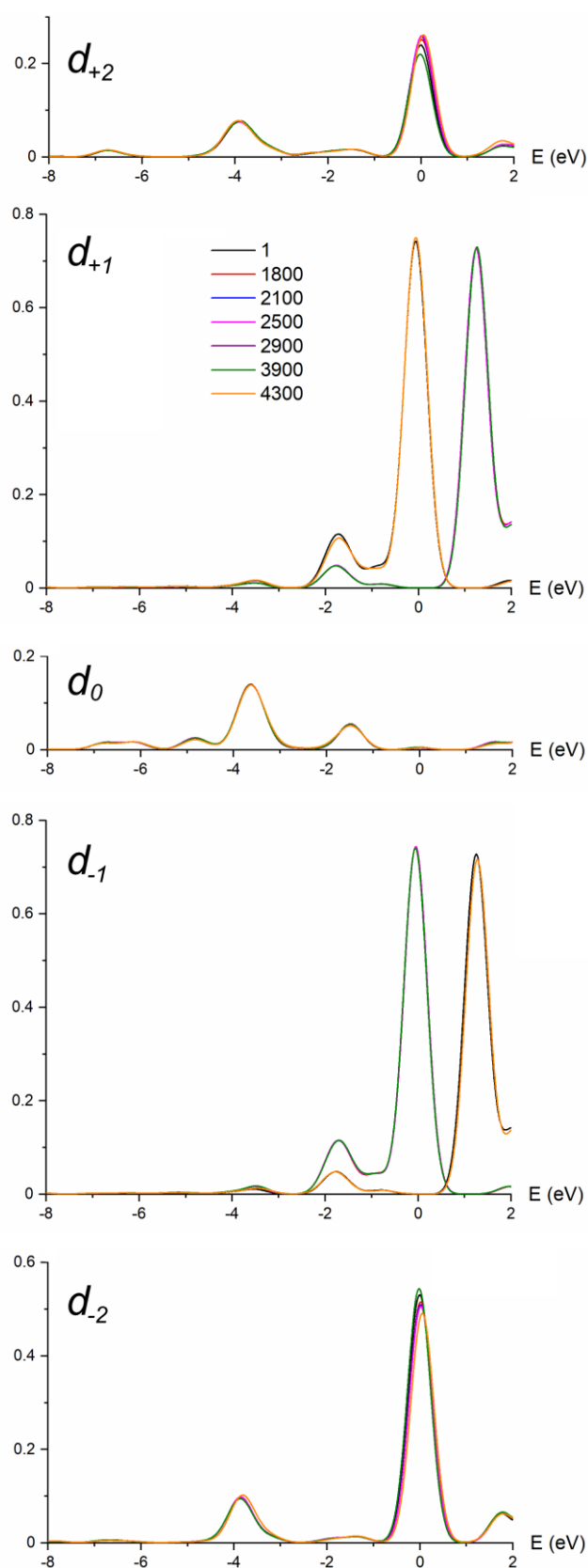


Figure A5.78. Reported LDOS of the beta d -orbitals of the $\text{Co}(\text{II})$ ions of $1_{\text{cry,HS}}$ at the seven studied different pressures ($p = 1, 1800, 2100, 2500, 2900, 3900, 4300$ bar).

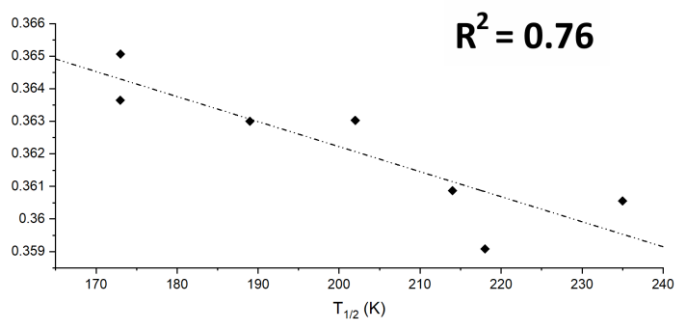


Figure A5.79. Reported Intensity of the band of $1_{\text{cry,LS}}$ at -1.85 eV of $\text{Co}(d_0)$ atomic orbitals vs the measured $T_{1/2}$. Trend line reports the [I vs. $T_{1/2}$] correlation factor ($R^2 = 0.76$).

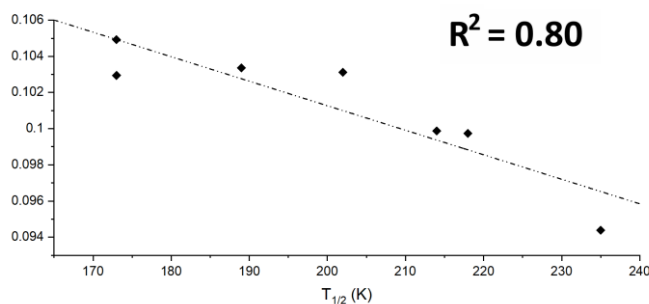


Figure A5.80. Reported Intensity of the band of $1_{\text{cry,HS}}$ at -1.93 eV of $\text{Co}(d_0)$ atomic orbitals vs the measured $T_{1/2}$. Trend line reports the [I vs. $T_{1/2}$] correlation factor ($R^2 = 0.80$).

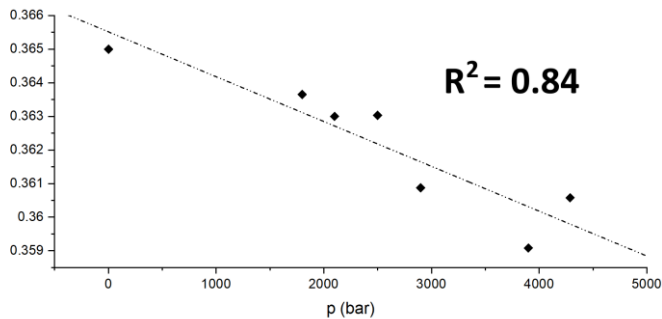


Figure A5.81. Reported Intensity of the band of $1_{\text{cry,LS}}$ at -1.85 eV of $\text{Co}(d_0)$ atomic orbitals vs the experimental pressures where the SCO phenomenon was monitored. Trend line reports the [I vs. p] correlation factor ($R^2 = 0.84$).

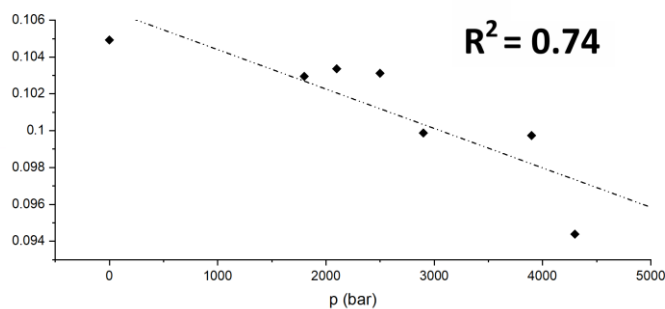


Figure A5.82. Reported Intensity of the band of $1_{\text{cry,HS}}$ at -1.93 eV of $\text{Co}(d_0)$ atomic orbitals vs the experimental pressures where the SCO phenomenon was monitored. Trend line reports the [I vs. p] correlation factor ($R^2 = 0.74$).

A5.3.2. LDOS: Nitrogen Atoms

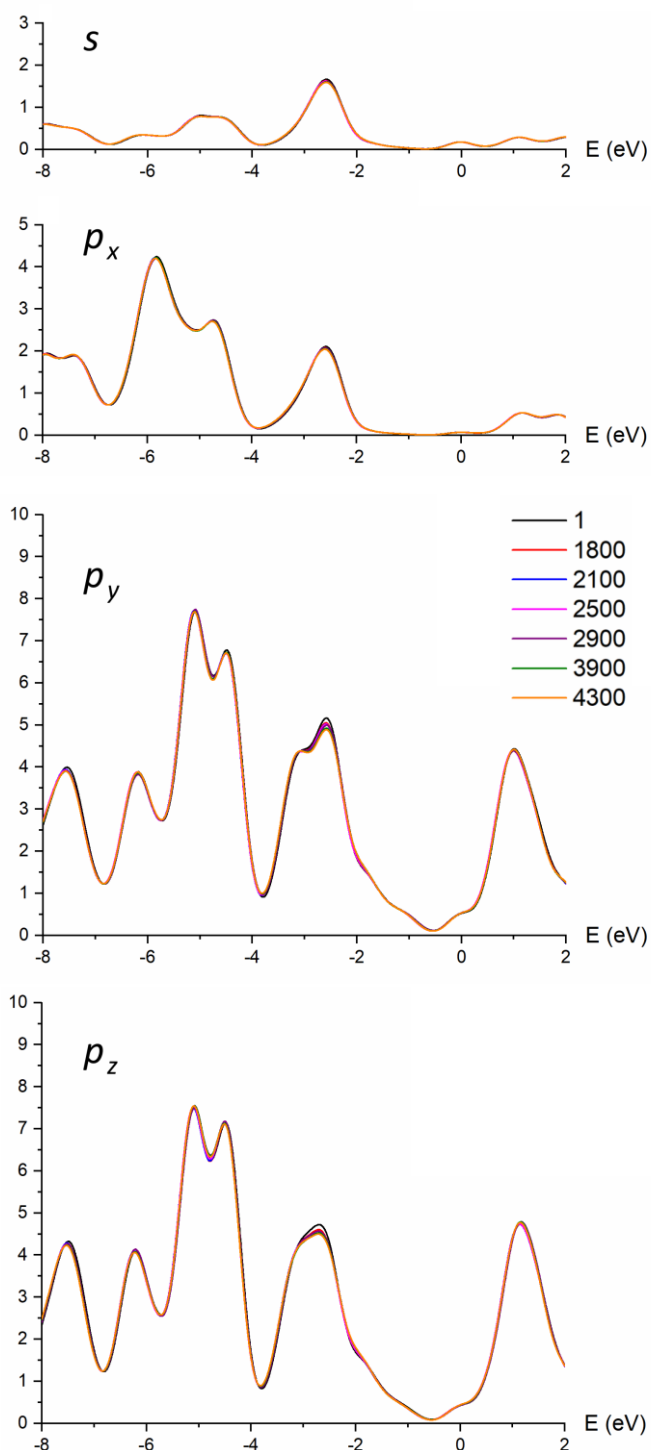


Figure A5.83. Reported LDOS of the orbitals of the N atoms of $\mathbf{1}_{\text{crystal}}$ at the seven studied different pressures ($p = 1, 1800, 2100, 2500, 2900, 3900, 4300$ bar).

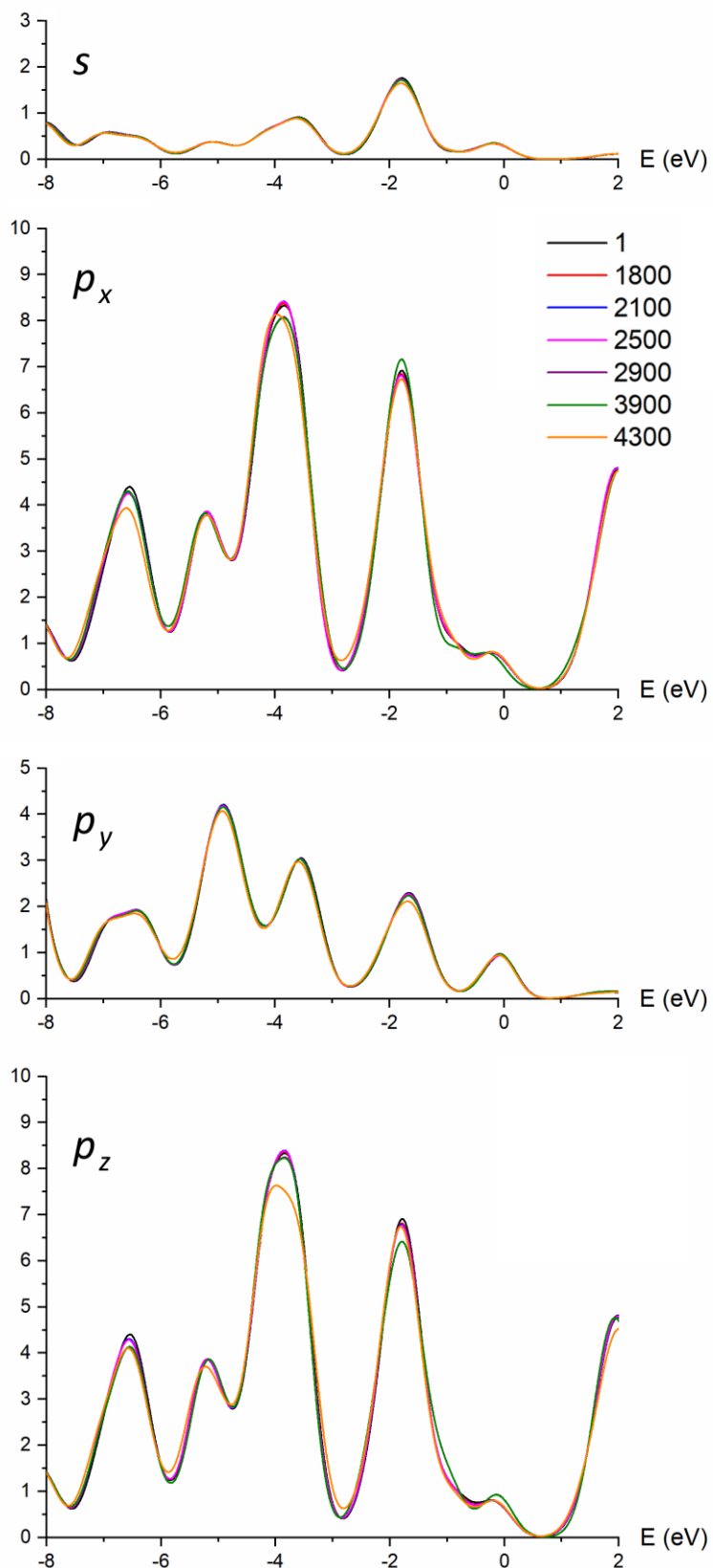


Figure A5.84. Reported LDOS of the orbitals of the N atoms of $\mathbf{1}_{\text{cry,HS}}$ at the seven studied different pressures ($p = 1, 1800, 2100, 2500, 2900, 3900, 4300$ bar).

A5.3.3. LDOS: Carbon Atoms

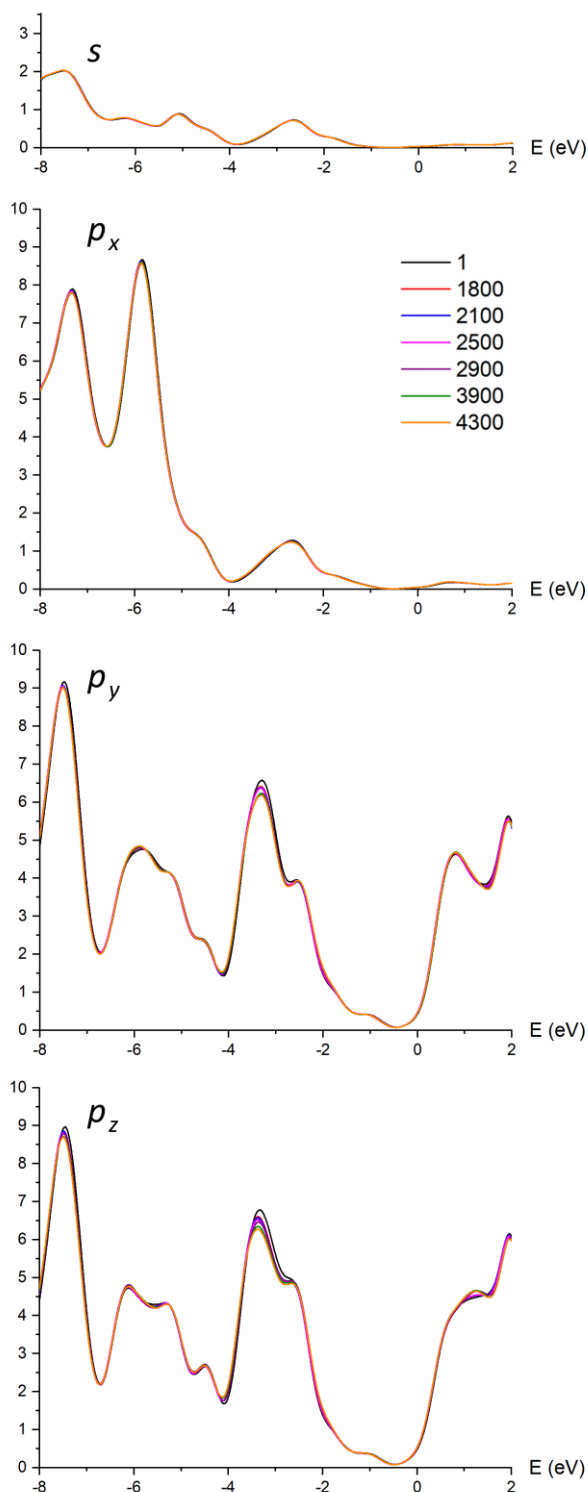


Figure A5.85. Reported LDOS of the orbitals of the C atoms of $1_{\text{cry,LS}}$ at the seven studied different pressures ($p = 1, 1800, 2100, 2500, 2900, 3900, 4300$ bar).

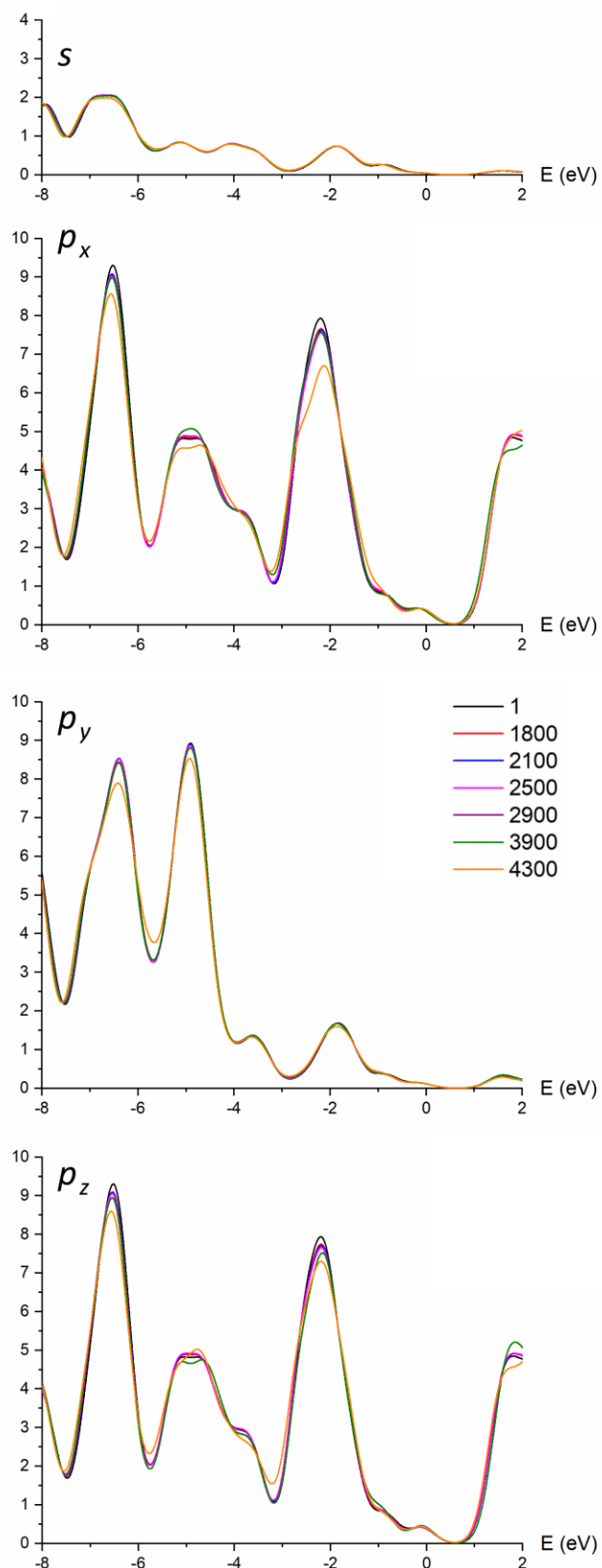


Figure A5.86. Reported LDOS of the orbitals of the C atoms of $1_{\text{cry,HS}}$ at the seven studied different pressures ($p = 1, 1800, 2100, 2500, 2900, 3900, 4300$ bar).

A5.4. Molecular Orbitals of $[\text{Co}(\text{dpzca})_2]$

Table A5.12. Reported metal-centred MOs contributing to the main peak at 1.9eV in $1_{\text{cry,LS}}$ and $1_{\text{cry,HS}}$ TDOS (Figure 5.7). Last three columns on the right reports the correlation factor of the MOs energies against all seven employed different pressures; six different pressures (excluding results for $p = 3900$ bar); and the seven different measured $T_{1/2}$.

p / bar		1	1800	2100	2500	2900	3900	4300	$R^2(p)$ (all pressures)	$R^2(p)$ ($p = 3900$ bar excluded)	$R^2(T_{1/2})$
$T_{1/2}(\text{exp.})$ / K		173	173	189	202	214	227	235			
$1_{\text{cry,LS}}$	277 β	-2.08711	-1.9946	-1.98643	-1.97011	-1.94562	-1.91296	-1.90208	0.99 (Fig. S89)	0.99 (Fig. S89)	0.79 (Fig. S107)
	278 β	-2.09528	-2.02181	-2.01364	-2.00004	-1.95378	-1.92929	-1.9184	0.98 (Fig. S90)	0.97 (Fig. S90)	0.85 (Fig. S108)
	279 β	-2.09528	-2.02997	-2.01909	-2.0082	-1.95922	-1.94017	-1.92929	0.97 (Fig. S91)	0.96 (Fig. S91)	0.86 (Fig. S109)
	280 β	-2.10072	-2.03813	-2.02725	-2.01909	-1.98915	-1.94017	-1.92929	0.98 (Fig. S92)	0.98 (Fig. S92)	0.85 (Fig. S110)
$1_{\text{cry,HS}}$	270 α	-2.65311	-2.57964	-2.56604	-2.54971	-2.49801	-2.49529	-2.33746	0.82 (Fig. S93)	0.89 (Fig. S93)	0.84 (Fig. S111)
	271 α	-2.64767	-2.5742	-2.56059	-2.54699	-2.49256	-2.48984	-2.31569	0.79 (Fig. S94)	0.88 (Fig. S94)	0.83 (Fig. S112)
	272 α	-2.64495	-2.5742	-2.55787	-2.54154	-2.46807	-2.46535	-2.31569	0.84 (Fig. S95)	0.89 (Fig. S95)	0.88 (Fig. S113)
	273 α	-2.6259	-2.54699	-2.53066	-2.54154	-2.46807	-2.46535	-2.25038	0.73 (Fig. S96)	0.83 (Fig. S96)	0.77 (Fig. S114)
	274 α	-2.61502	-2.54154	-2.52522	-2.51161	-2.45991	-2.45719	-2.23678	0.74 (Fig. S97)	0.84 (Fig. S97)	0.79 (Fig. S115)
	275 α	-2.61502	-2.53882	-2.52522	-2.50889	-2.45447	-2.45175	-2.22861	0.74 (Fig. S98)	0.84 (Fig. S98)	0.79 (Fig. S116)
	276 α	-2.61229	-2.53882	-2.5225	-2.50889	-2.42726	-2.42454	-2.22861	0.79 (Fig. S99)	0.85 (Fig. S99)	0.85 (Fig. S117)
	273 β	-2.24222	-2.16603	-2.1497	-2.13337	-2.098	-2.09256	-1.89391	0.75 (Fig. S100)	0.86 (Fig. S100)	0.79 (Fig. S118)
	274 β	-2.2395	-2.16331	-2.14698	-2.13337	-2.08439	-2.07895	-1.88847	0.78 (Fig. S101)	0.87 (Fig. S101)	0.81 (Fig. S119)
	275 β	-2.23406	-2.16059	-2.14426	-2.12793	-2.08167	-2.07895	-1.86942	0.75 (Fig. S102)	0.85 (Fig. S102)	0.80 (Fig. S120)
	276 β	-2.21773	-2.14426	-2.12521	-2.1116	-2.08167	-2.07895	-1.8667	0.72 (Fig. S103)	0.85 (Fig. S103)	0.76 (Fig. S121)
	277 β	-2.098	-2.01636	-1.99732	-1.98643	-1.92385	-1.92112	-1.73337	0.80 (Fig. S104)	0.88 (Fig. S104)	0.83 (Fig. S122)
	279 β	-2.08167	-2.00004	-1.98371	-1.96738	-1.91296	-1.90752	-1.72248	0.80 (Fig. S105)	0.88 (Fig. S105)	0.83 (Fig. S123)
	280 β	-2.07895	-1.99732	-1.98099	-1.96738	-1.91024	-1.9048	-1.70615	0.78 (Fig. S106)	0.87 (Fig. S106)	0.82 (Fig. S124)

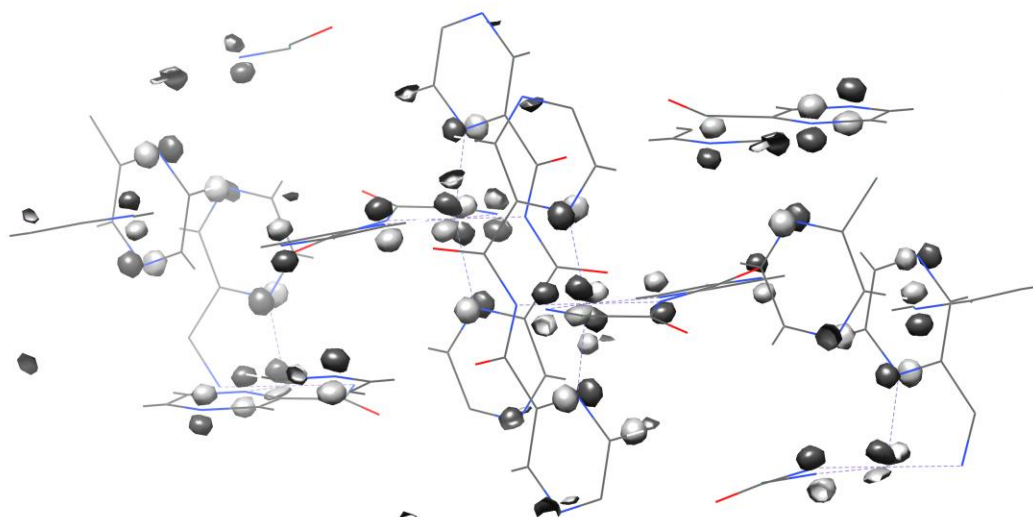


Figure A5.87. Plotted MOs 277α (t_{2g} shaped) for $1_{\text{cry,HS}}$ calculated at the pressure of 1bar (ρ cutoff = 0.04).

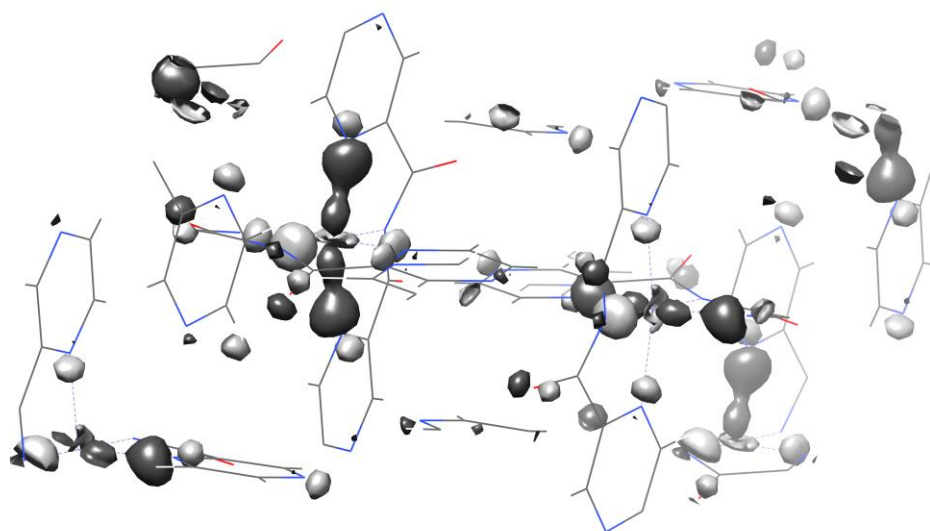


Figure A5.88. Plotted MOs 277β (e_g shaped) for $1_{\text{cry,HS}}$ calculated at the pressure of 1bar (ρ cutoff = 0.04).

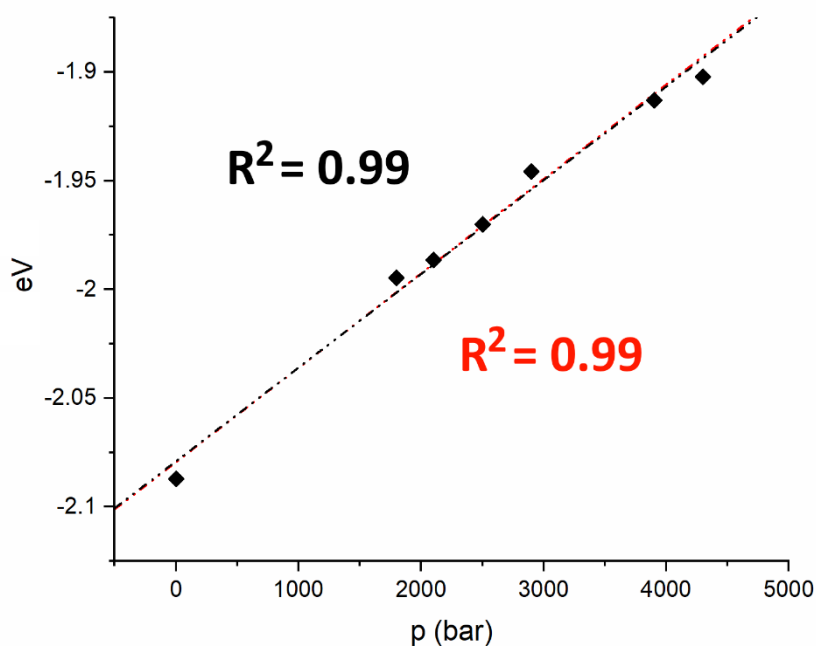


Figure A5.89. Reported trend for the variation of MO-277 β in $1_{\text{cry,LS}}$ at seven different pressures ($R^2 = 0.99$) and six different pressures (except $p = 3900$ bar, $R^2 = 0.99$).

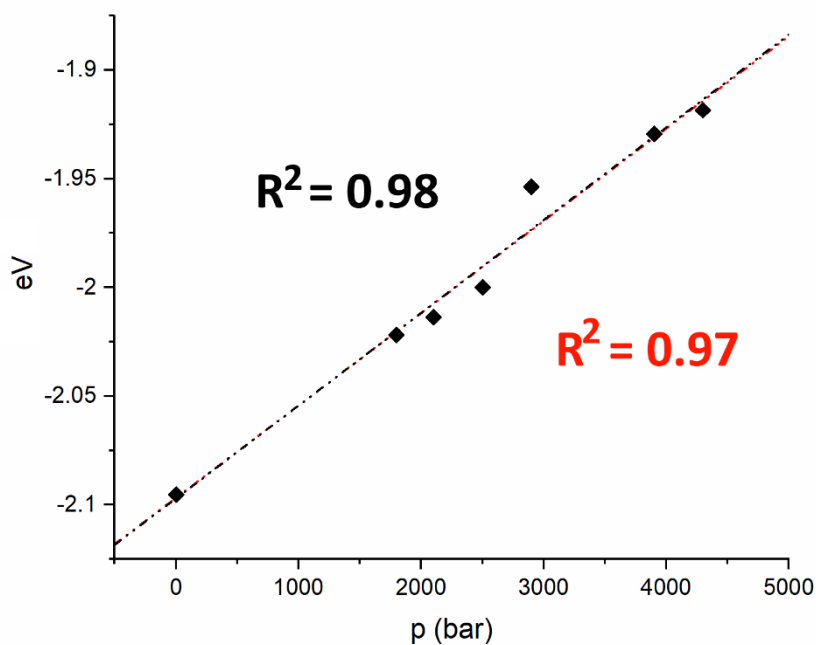


Figure A5.90. Reported trend for the variation of MO-278 β in $1_{\text{cry,LS}}$ at seven different pressures ($R^2 = 0.98$) and six different pressures (except $p = 3900$ bar, $R^2 = 0.97$).

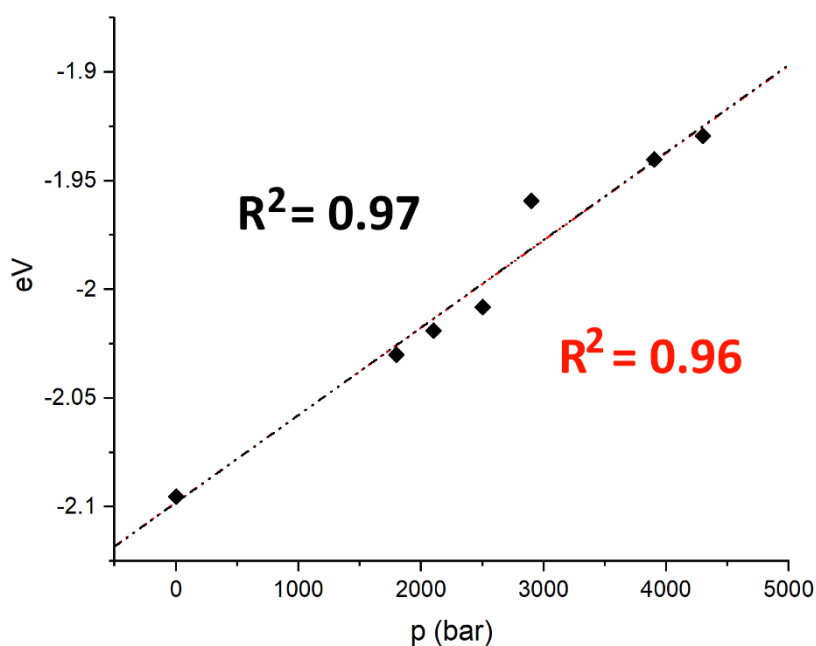


Figure A5.91. Reported trend for the variation of MO-279 β in $1_{\text{cry,LS}}$ at seven different pressures ($R^2 = 0.97$) and six different pressures (except $p = 3900$ bar, $R^2 = 0.96$).

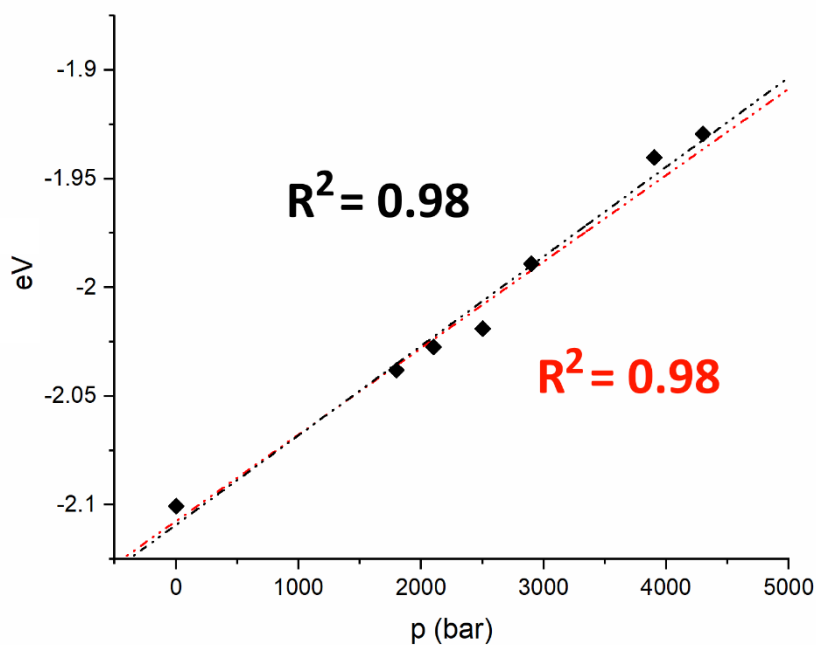


Figure A5.92. Reported trend for the variation of MO-280 β in $1_{\text{cry,LS}}$ at seven different pressures ($R^2 = 0.98$) and six different pressures (except $p = 3900$ bar, $R^2 = 0.98$).

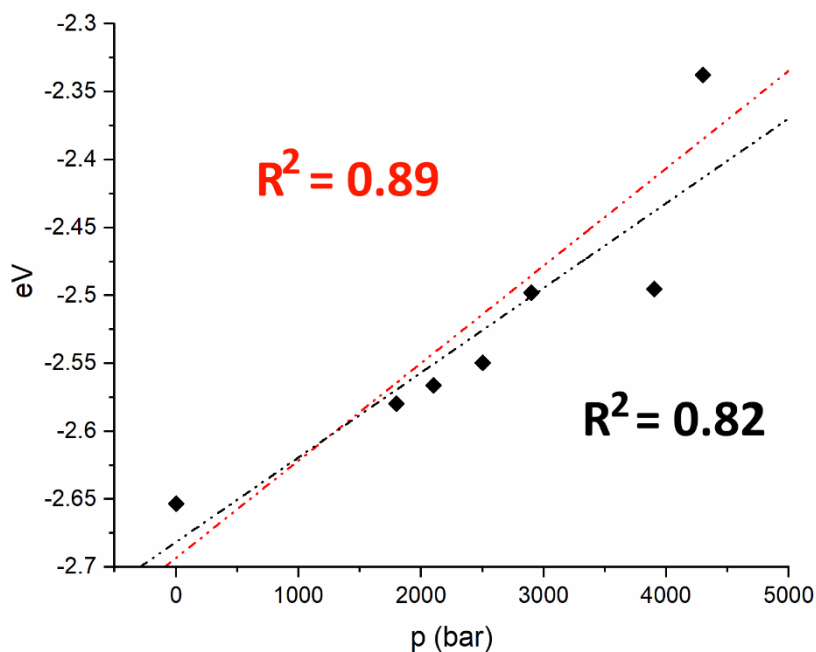


Figure A5.93. Reported trend for the variation of MO-270 α in $1_{\text{cry,HS}}$ at seven different pressures ($R^2 = 0.82$) and six different pressures (except $p = 3900$ bar, $R^2 = 0.89$).

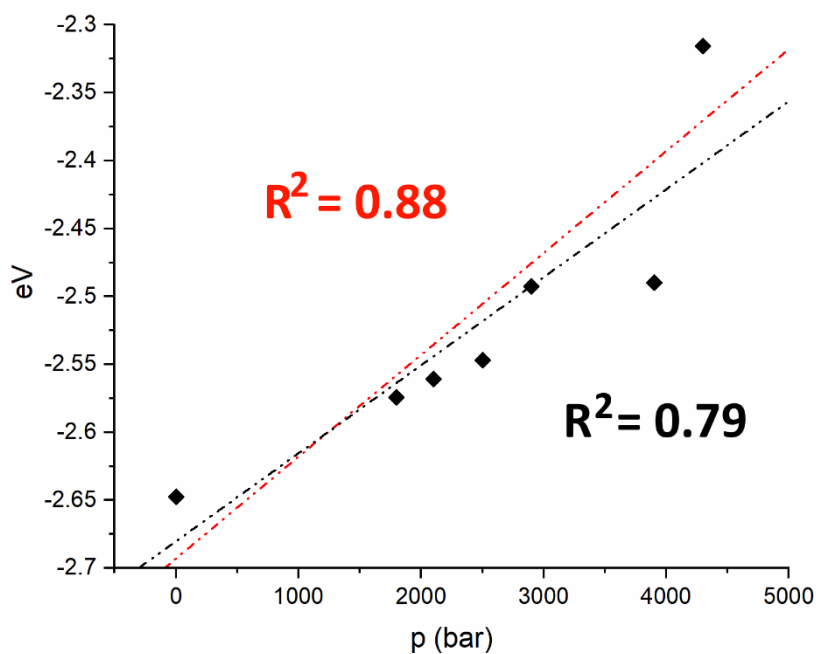


Figure A5.94. Reported trend for the variation of MO-271 α in $1_{\text{cry,HS}}$ at seven different pressures ($R^2 = 0.79$) and six different pressures (except $p = 3900$ bar, $R^2 = 0.88$).

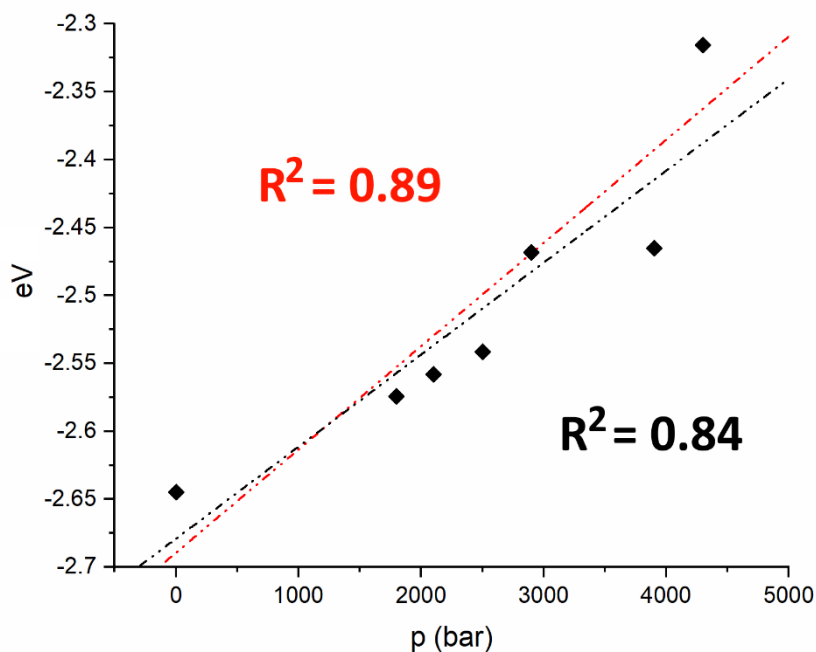


Figure A5.95. Reported trend for the variation of MO-272 α in $1_{\text{cry,HS}}$ at seven different pressures ($R^2 = 0.84$) and six different pressures (except $p = 3900$ bar, $R^2 = 0.89$).

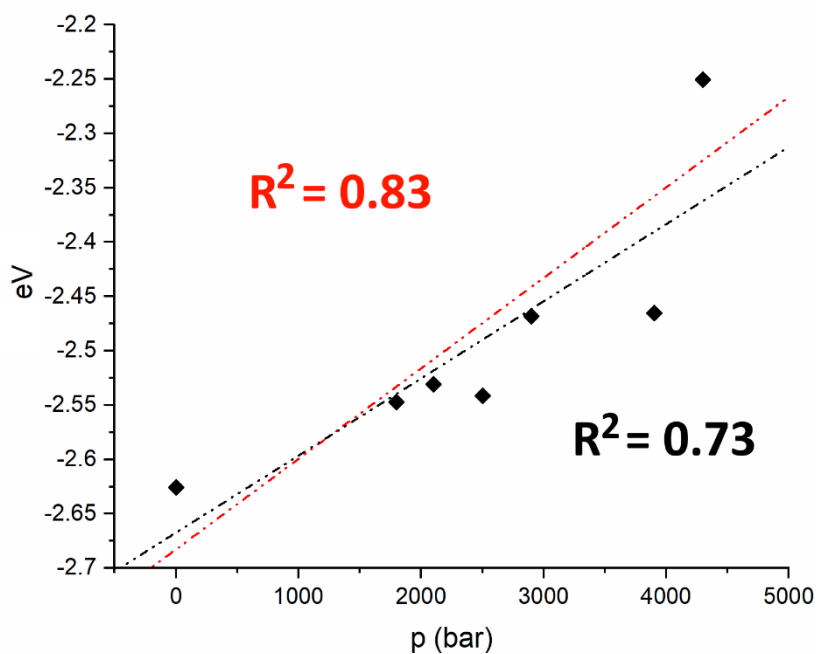


Figure A5.96. Reported trend for the variation of MO-273 α in $1_{\text{cry,HS}}$ at seven different pressures ($R^2 = 0.73$) and six different pressures (except $p = 3900$ bar, $R^2 = 0.83$).

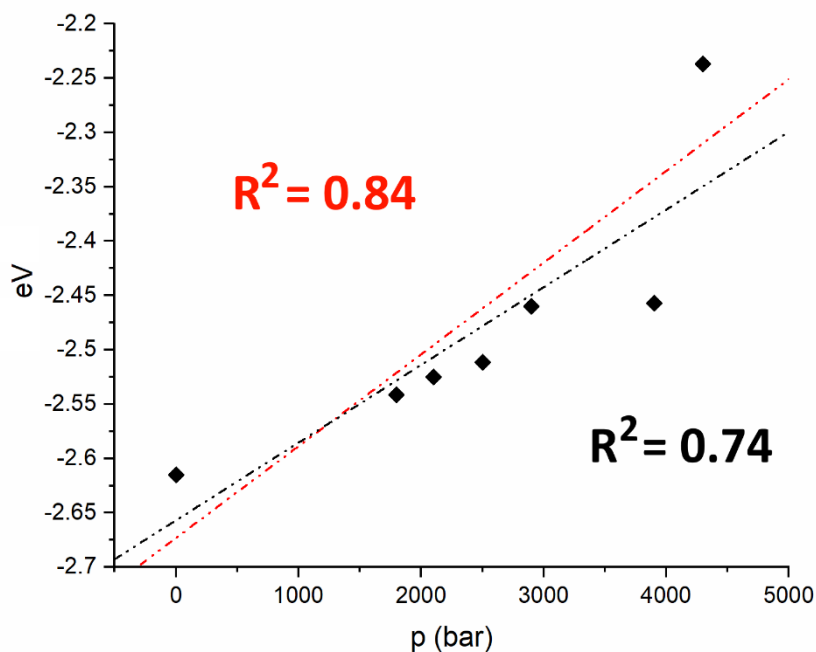


Figure A5.97. Reported trend for the variation of MO-274 α in $1_{\text{cry,HS}}$ at seven different pressures ($R^2 = 0.74$) and six different pressures (except $p = 3900$ bar, $R^2 = 0.84$).

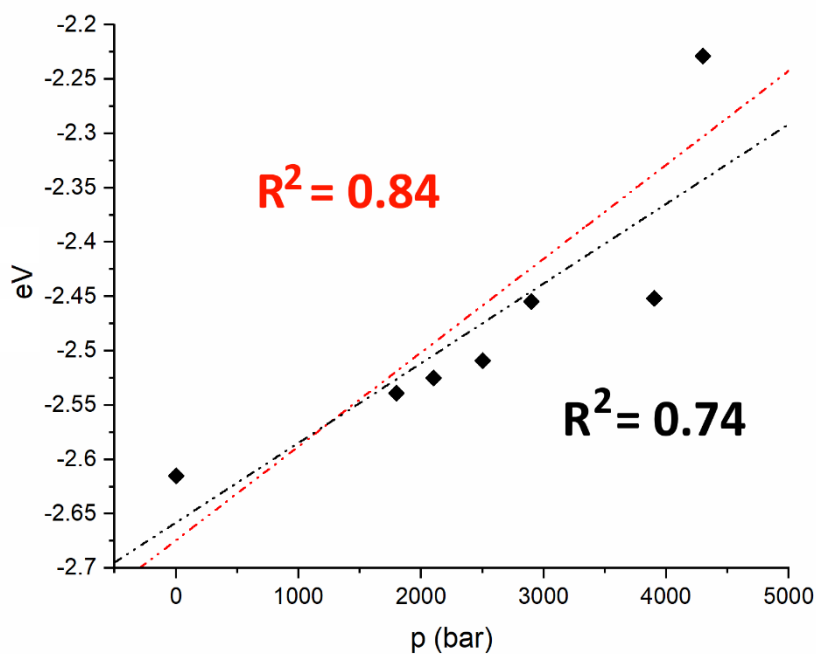


Figure A5.98. Reported trend for the variation of MO-275 α in $1_{\text{cry,HS}}$ at seven different pressures ($R^2 = 0.74$) and six different pressures (except $p = 3900$ bar, $R^2 = 0.84$).

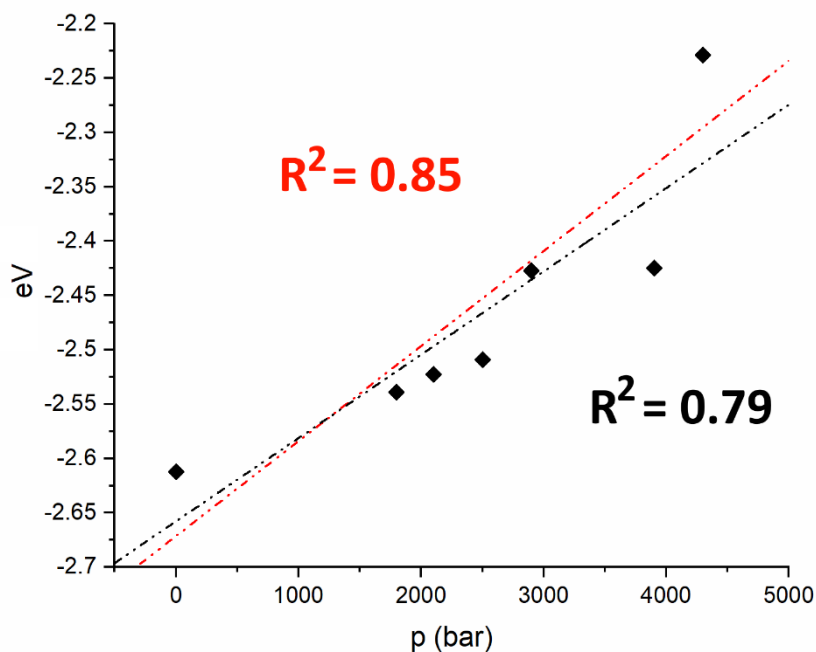


Figure A5.99. Reported trend for the variation of MO-276 α in $1_{\text{cry,HS}}$ at seven different pressures ($R^2 = 0.79$) and six different pressures (except $p = 3900$ bar, $R^2 = 0.85$).

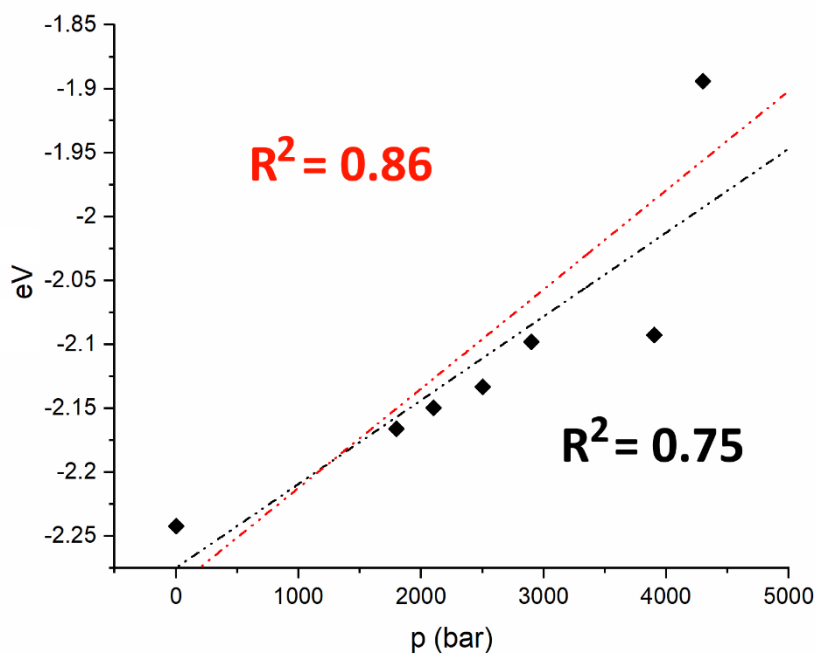


Figure A5.100. Reported trend for the variation of MO-273 β in $1_{\text{cry,HS}}$ at seven different pressures ($R^2 = 0.75$) and six different pressures (except $p = 3900$ bar, $R^2 = 0.86$).

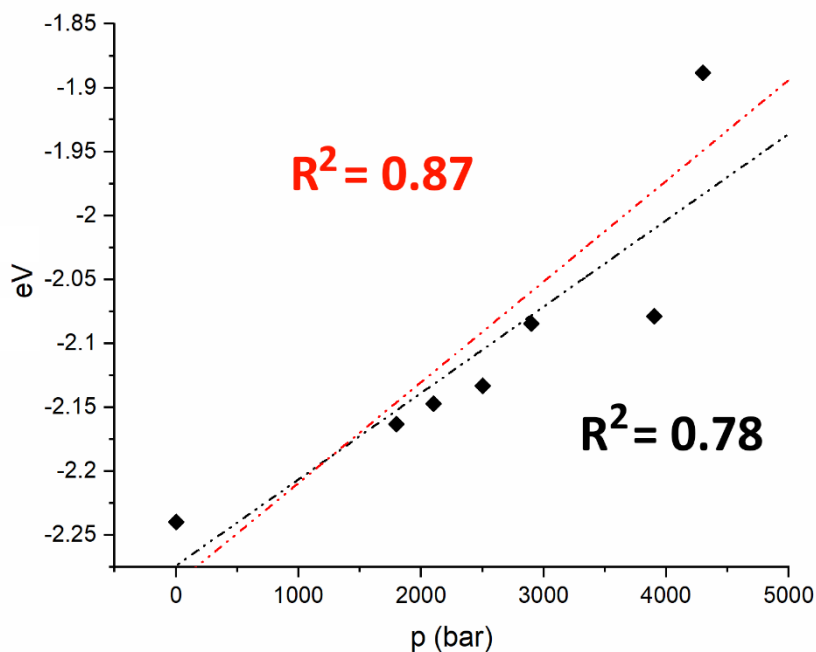


Figure A5.101. Reported trend for the variation of MO-274β in $1_{\text{cry,HS}}$ at seven different pressures ($R^2 = 0.78$) and six different pressures (except $p = 3900$ bar, $R^2 = 0.87$).

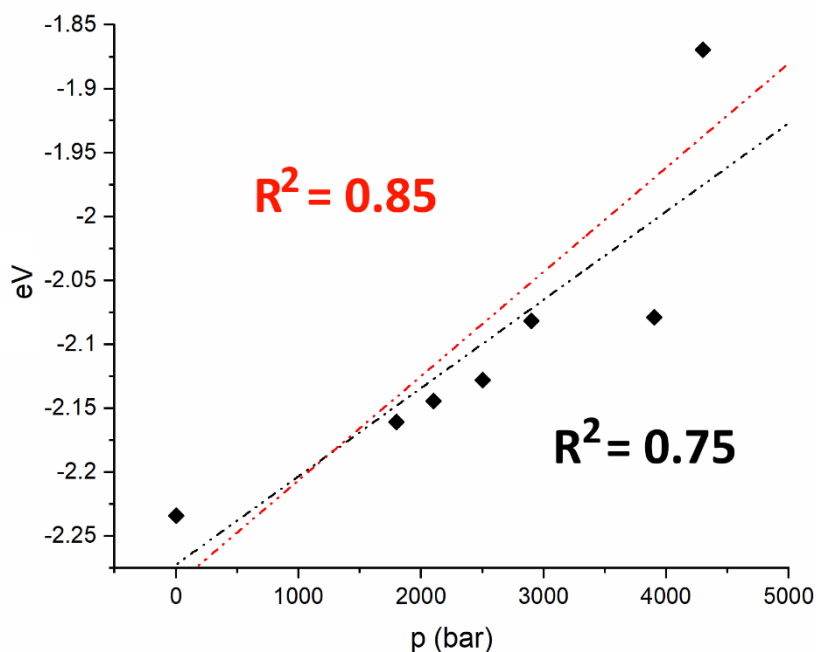


Figure A5.102. Reported trend for the variation of MO-275β in $1_{\text{cry,HS}}$ at seven different pressures ($R^2 = 0.75$) and six different pressures (except $p = 3900$ bar, $R^2 = 0.85$).

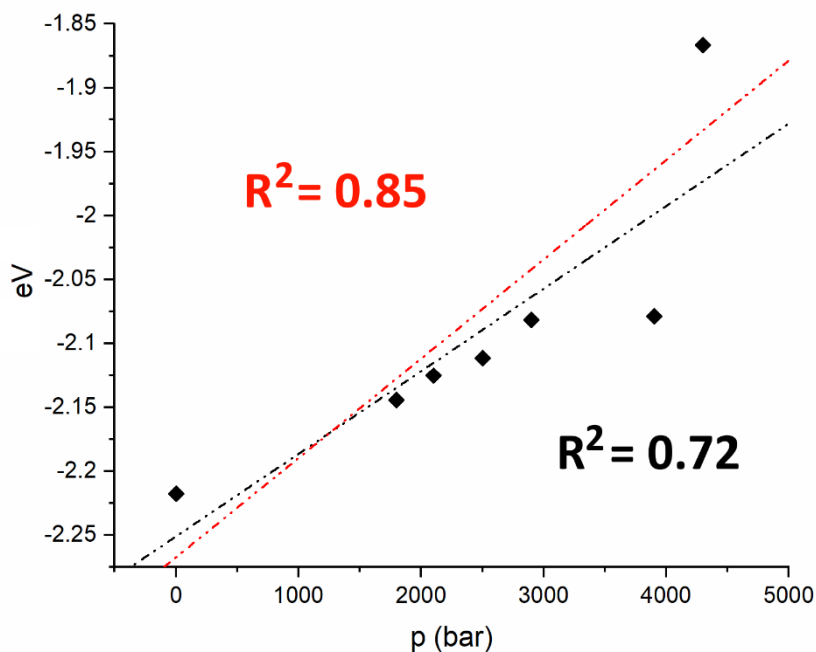


Figure A5.103. Reported trend for the variation of MO-276β in $1_{\text{cry,HS}}$ at seven different pressures ($R^2 = 0.72$) and six different pressures (except $p = 3900$ bar, $R^2 = 0.85$).

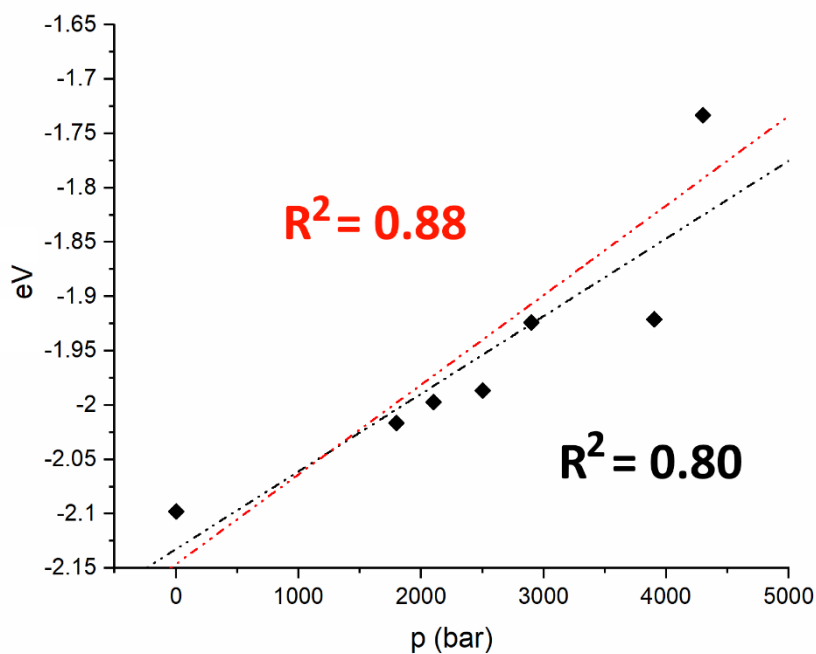


Figure A5.104. Reported trend for the variation of MO-277β in $1_{\text{cry,HS}}$ at seven different pressures ($R^2 = 0.80$) and six different pressures (except $p = 3900$ bar, $R^2 = 0.88$).

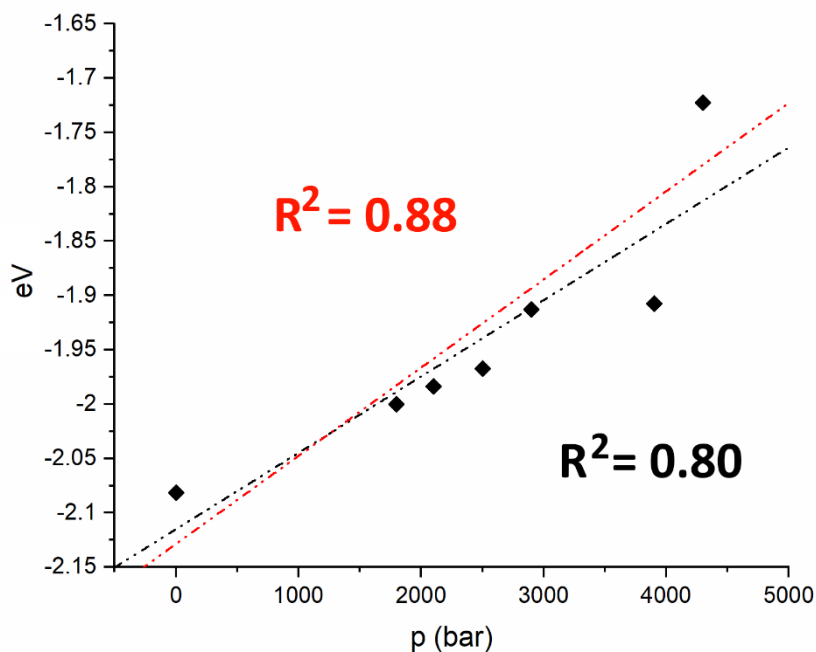


Figure A5.105. Reported trend for the variation of MO-279β in $1_{\text{cry,HS}}$ at seven different pressures ($R^2 = 0.80$) and six different pressures (except $p = 3900$ bar, $R^2 = 0.88$).

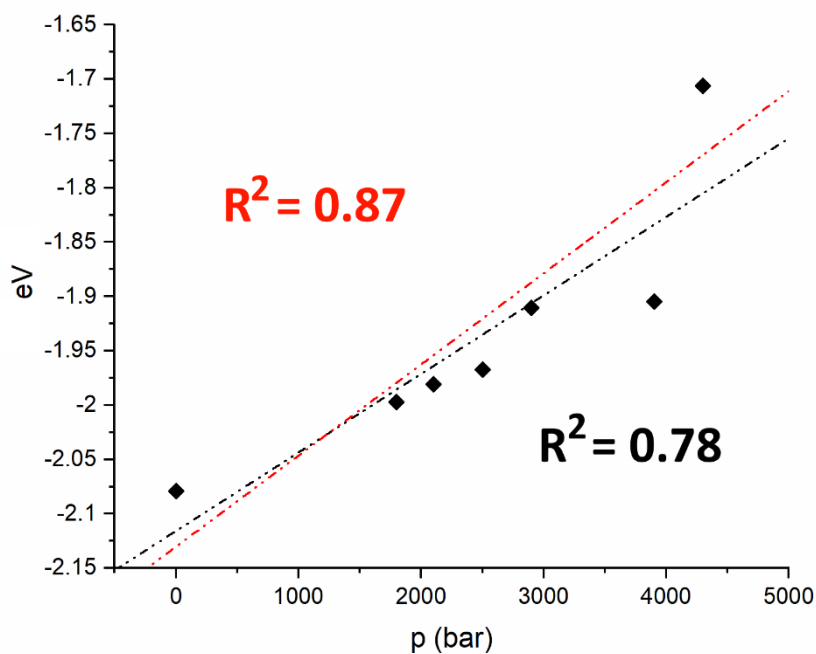


Figure A5.106. Reported trend for the variation of MO-280β in $1_{\text{cry,HS}}$ at seven different pressures ($R^2 = 0.78$) and six different pressures (except $p = 3900$ bar, $R^2 = 0.87$).

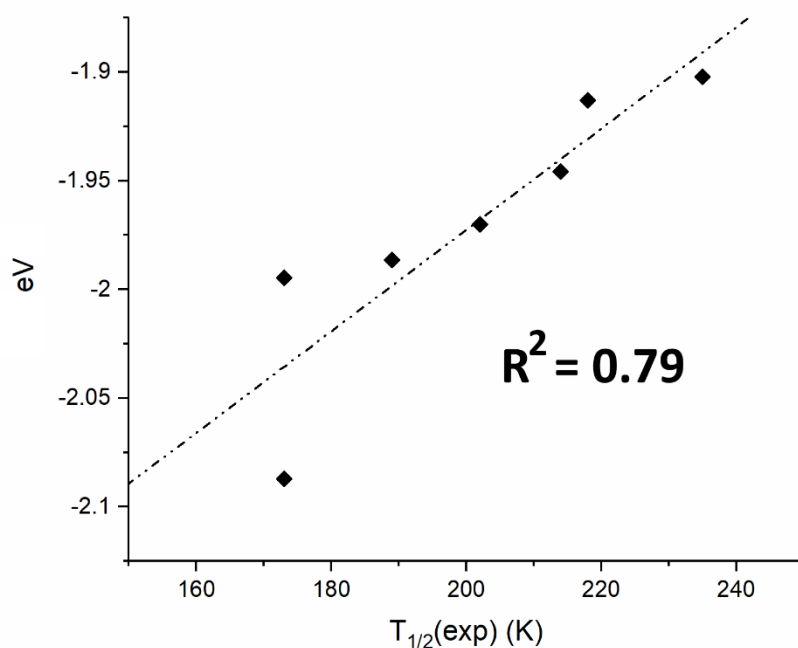


Figure A5.107. Reported trend for the variation of MO-277 β in $1_{\text{cry,LS}}$ versus the measured $T_{1/2}$ at seven different pressures ($R^2 = 0.79$).

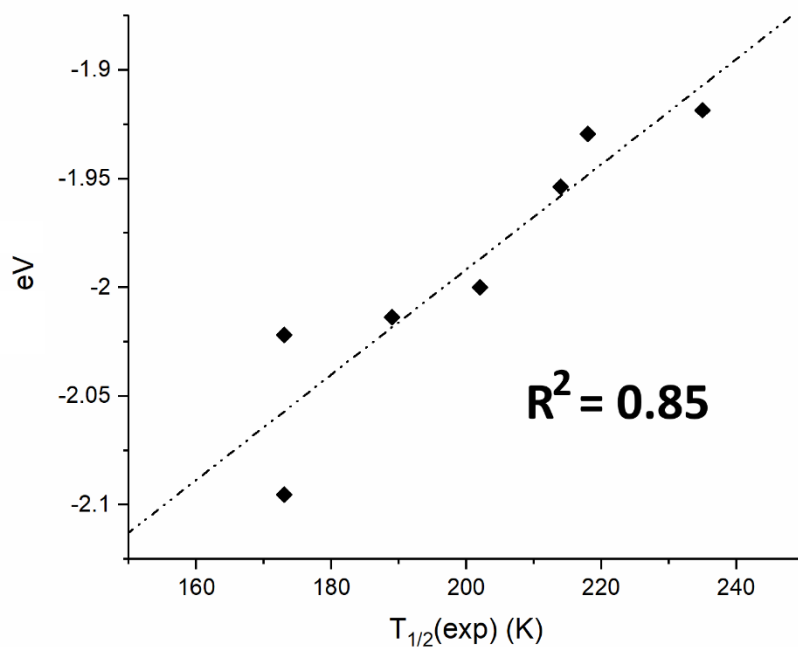


Figure A5.108. Reported trend for the variation of MO-278 β in $1_{\text{cry,LS}}$ versus the measured $T_{1/2}$ at seven different pressures ($R^2 = 0.85$).

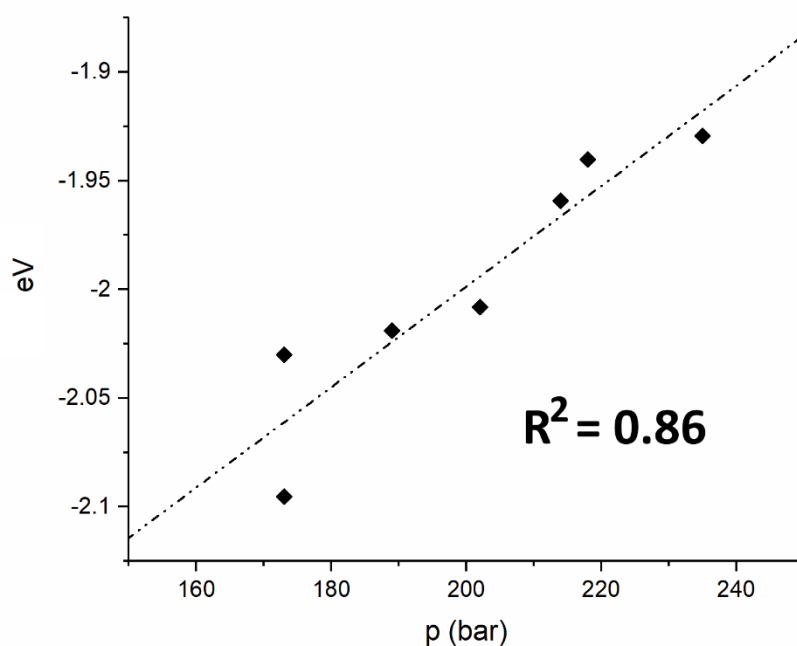


Figure A5.109. Reported trend for the variation of MO-279 β in $1_{\text{cry,LS}}$ versus the measured $T_{1/2}$ at seven different pressures ($R^2 = 0.86$).

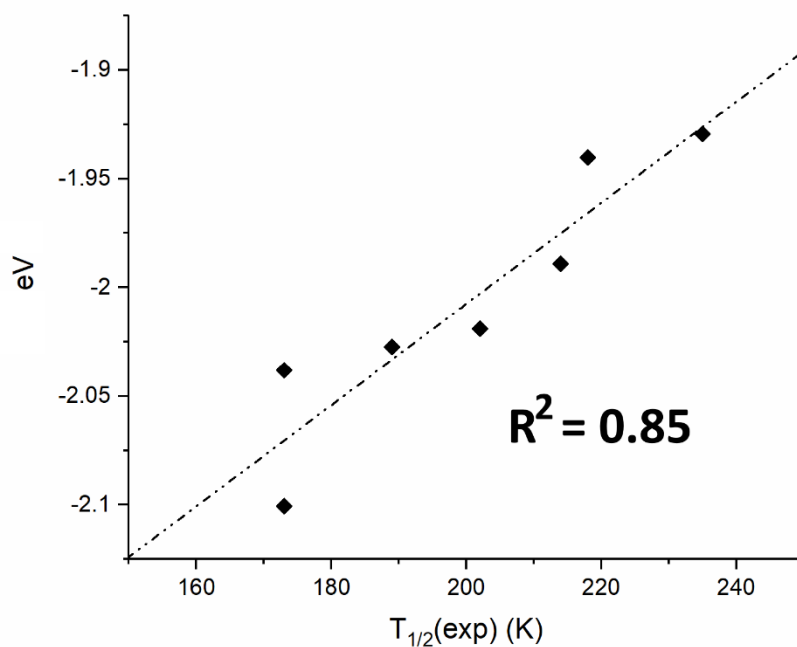


Figure A5.110. Reported trend for the variation of MO-280 β in $1_{\text{cry,LS}}$ versus the measured $T_{1/2}$ at seven different pressures ($R^2 = 0.85$).

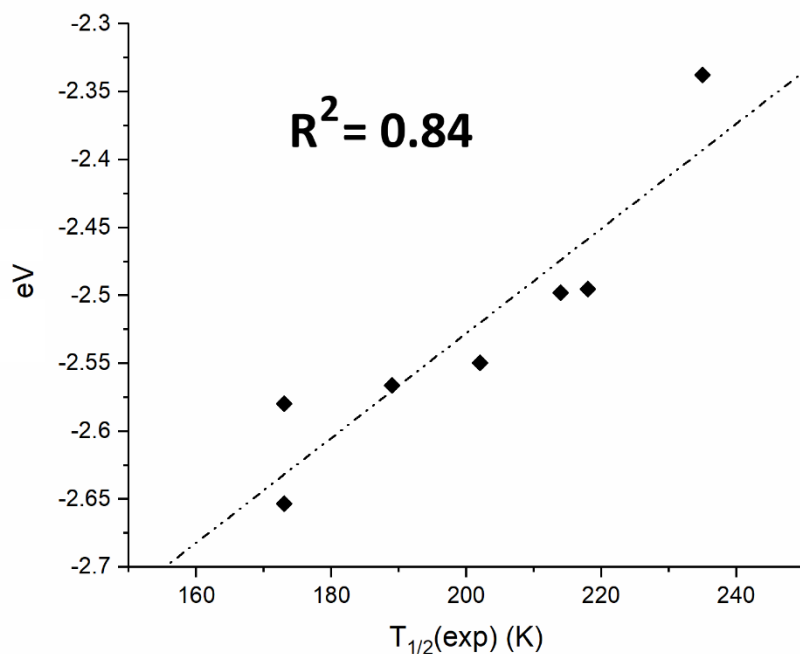


Figure A5.111. Reported trend for the variation of MO-270 α in $1_{\text{cry,HS}}$ versus the measured $T_{1/2}$ at seven different pressures ($R^2 = 0.84$).

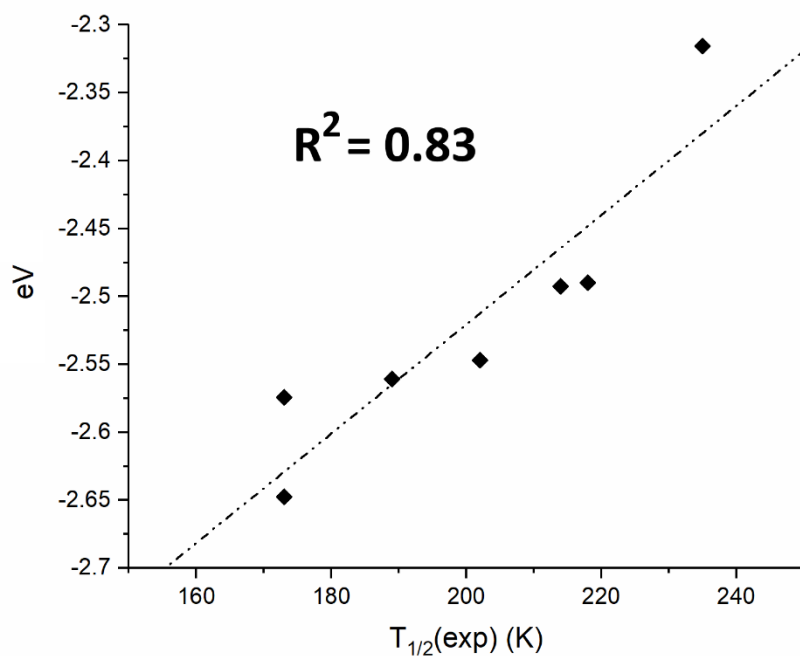


Figure A5.112. Reported trend for the variation of MO-271 α in $1_{\text{cry,HS}}$ versus the measured $T_{1/2}$ at seven different pressures ($R^2 = 0.83$).

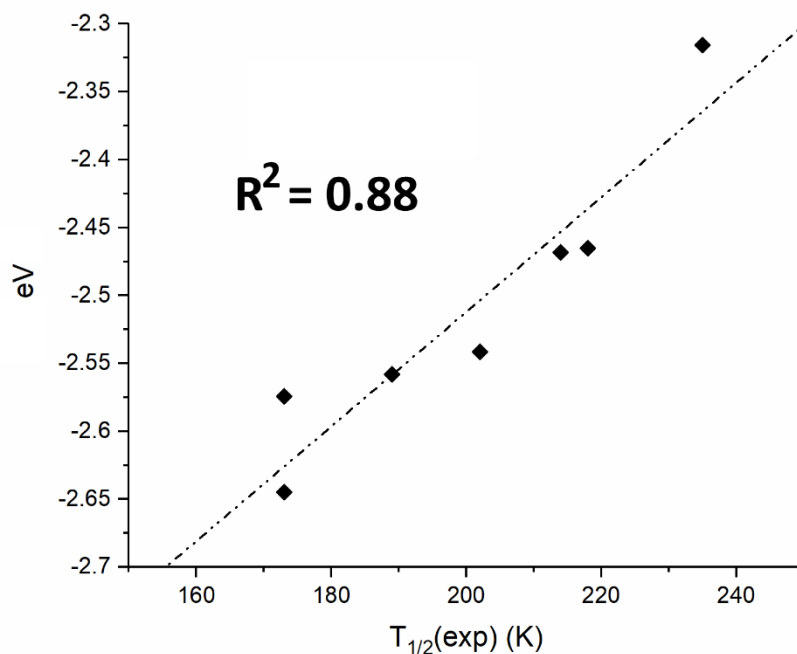


Figure A5.113. Reported trend for the variation of $\text{MO-272}\alpha$ in $1_{\text{cry,HS}}$ versus the measured $T_{1/2}$ at seven different pressures ($R^2 = 0.88$).

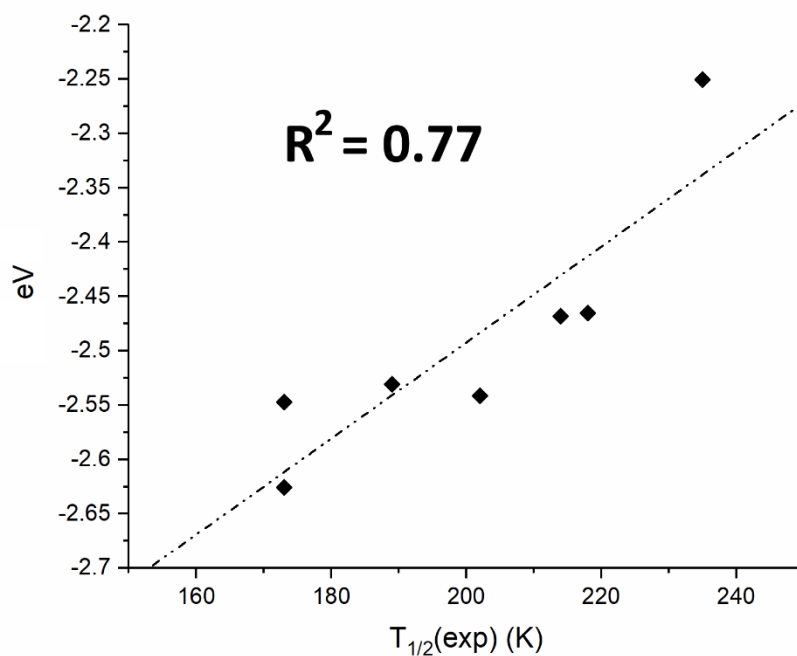


Figure A5.114. Reported trend for the variation of $\text{MO-273}\alpha$ in $1_{\text{cry,HS}}$ versus the measured $T_{1/2}$ at seven different pressures ($R^2 = 0.77$).

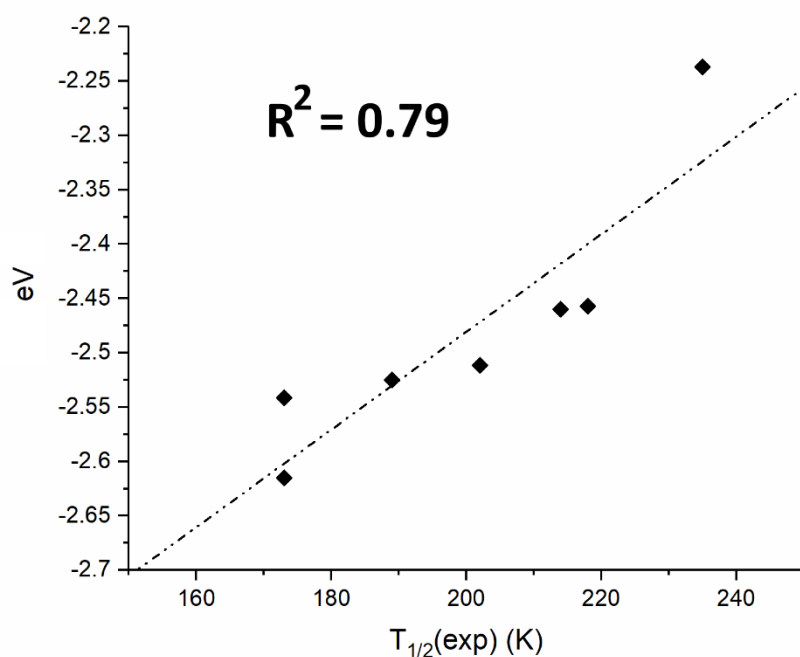


Figure A5.115. Reported trend for the variation of MO-274 α in $1_{\text{cry,HS}}$ versus the measured $T_{1/2}$ at seven different pressures ($R^2 = 0.79$).

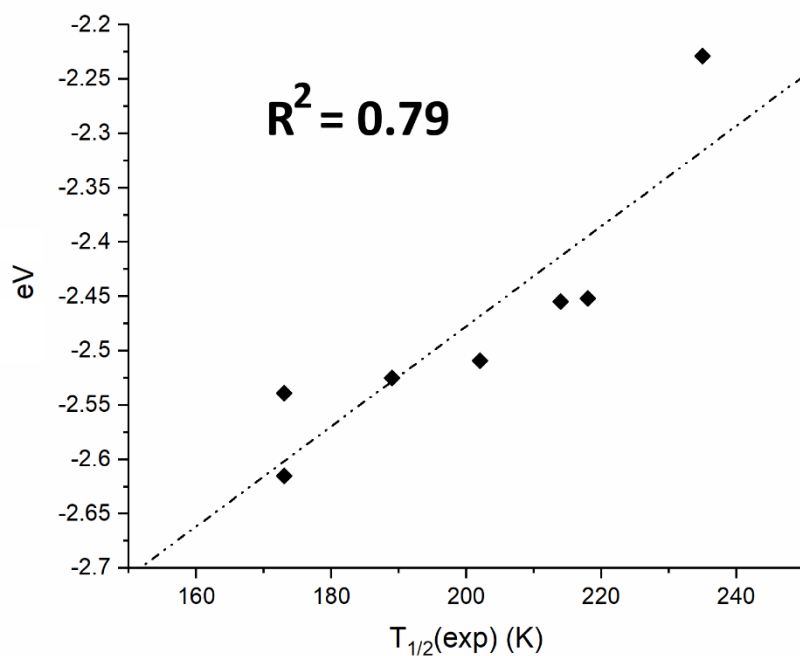


Figure A5.116. Reported trend for the variation of MO-275 α in $1_{\text{cry,HS}}$ versus the measured $T_{1/2}$ at seven different pressures ($R^2 = 0.79$).

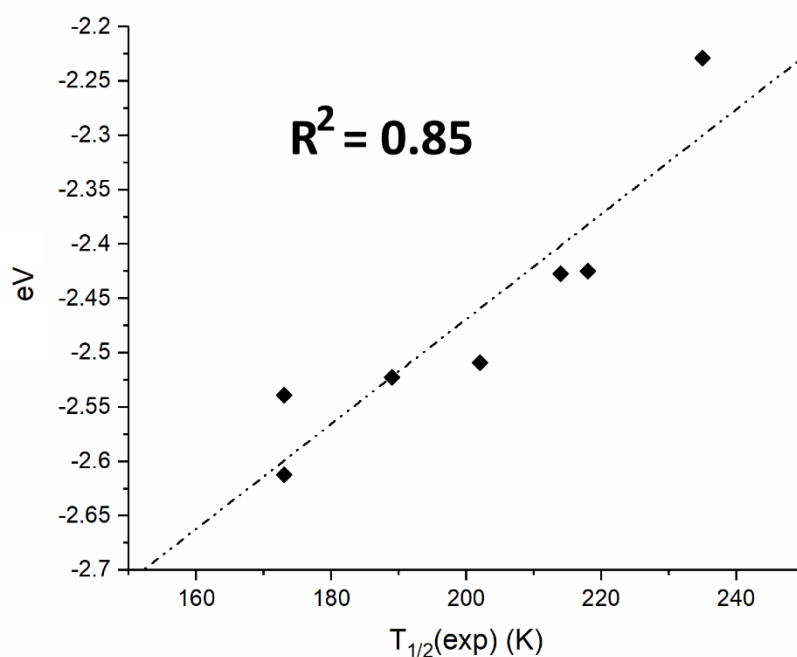


Figure A5.117. Reported trend for the variation of MO-276 α in $1_{\text{cry,HS}}$ versus the measured $T_{1/2}$ at seven different pressures ($R^2 = 0.85$).

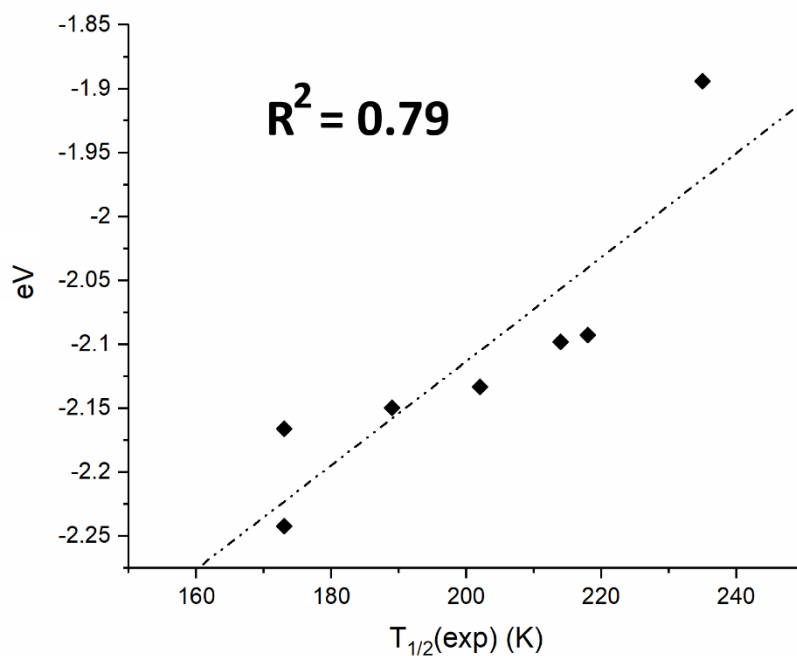


Figure A5.118. Reported trend for the variation of MO-273 β in $1_{\text{cry,HS}}$ versus the measured $T_{1/2}$ at seven different pressures ($R^2 = 0.79$).

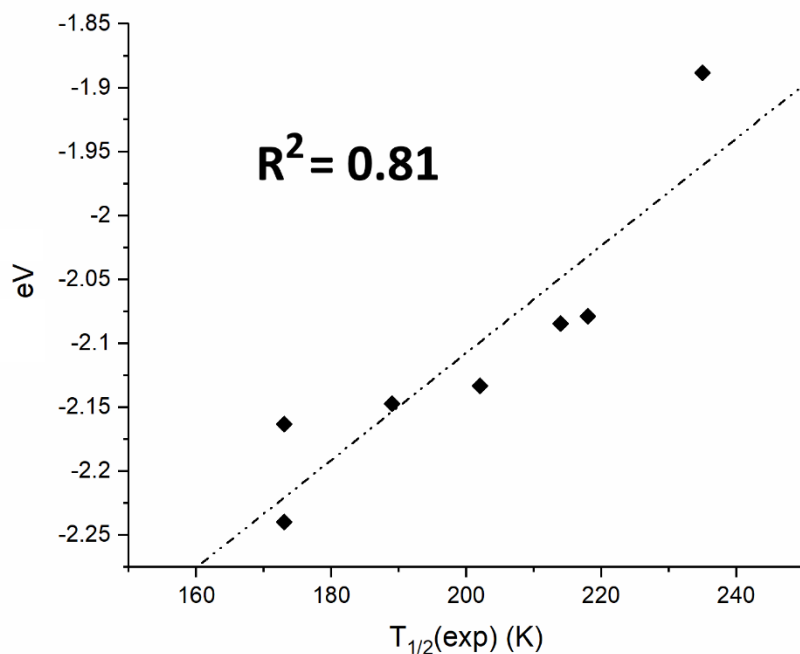


Figure A5.119. Reported trend for the variation of MO-274 β in $\mathbf{1}_{\text{cry,HS}}$ versus the measured $T_{1/2}$ at seven different pressures ($R^2 = 0.81$).

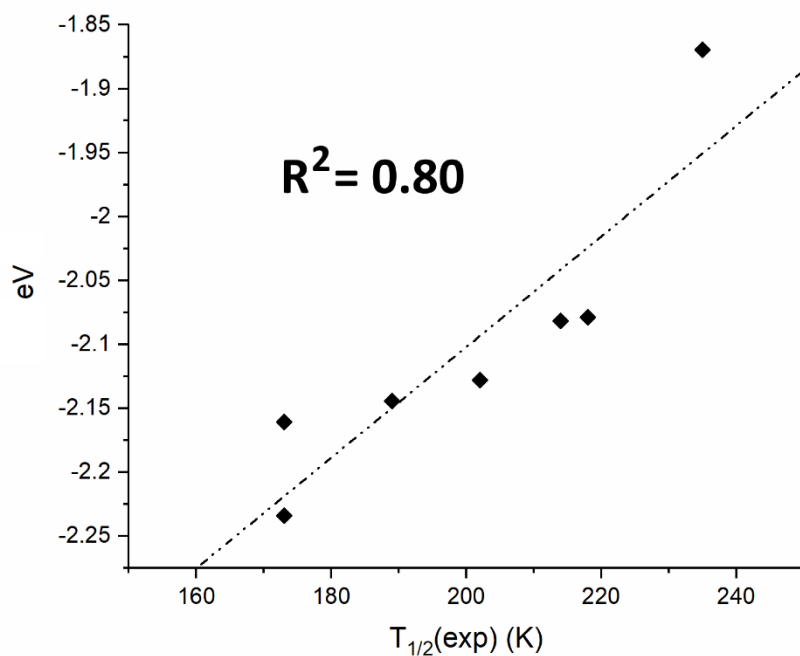


Figure A5.120. Reported trend for the variation of MO-275 β in $\mathbf{1}_{\text{cry,HS}}$ versus the measured $T_{1/2}$ at seven different pressures ($R^2 = 0.80$).

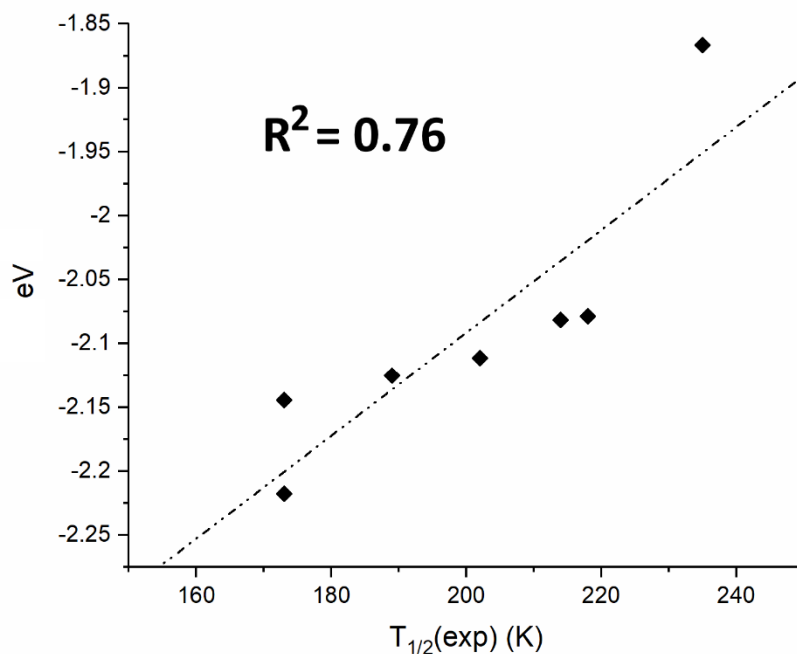


Figure A5.121. Reported trend for the variation of MO-276 β in $1_{\text{cry,HS}}$ versus the measured $T_{1/2}$ at seven different pressures ($R^2 = 0.76$).

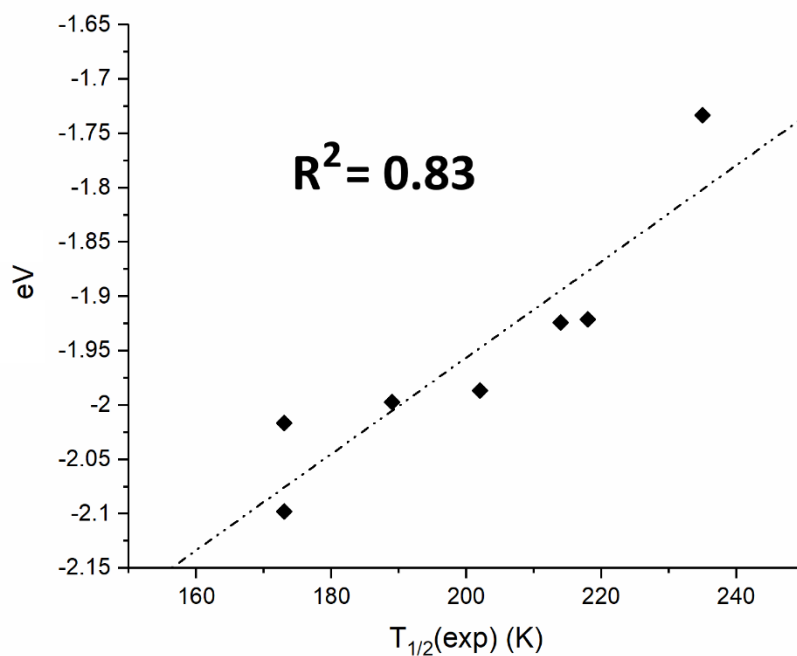


Figure A5.122. Reported trend for the variation of MO-277 β in $1_{\text{cry,HS}}$ versus the measured $T_{1/2}$ at seven different pressures ($R^2 = 0.83$).

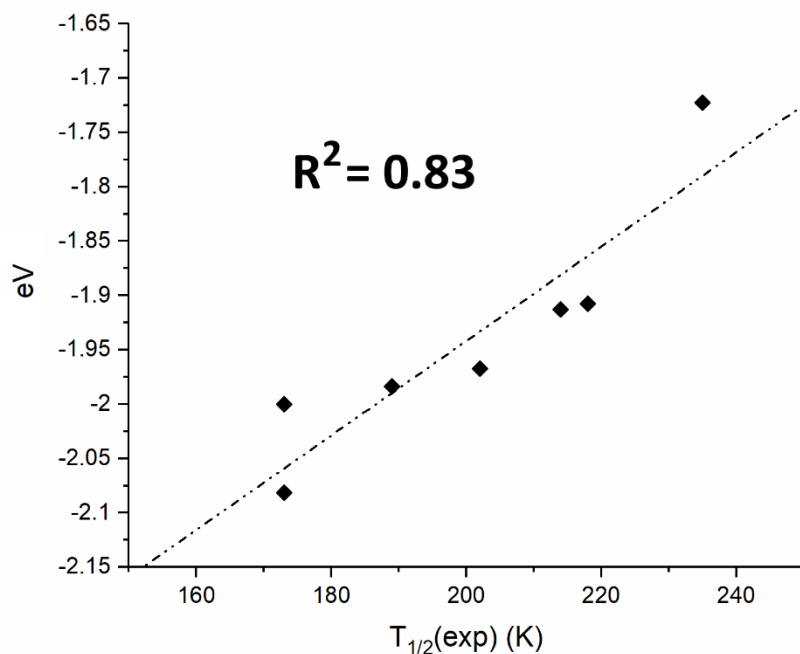


Figure A5.123. Reported trend for the variation of MO-279 β in $1_{\text{cry,HS}}$ versus the measured $T_{1/2}$ at seven different pressures ($R^2 = 0.83$).

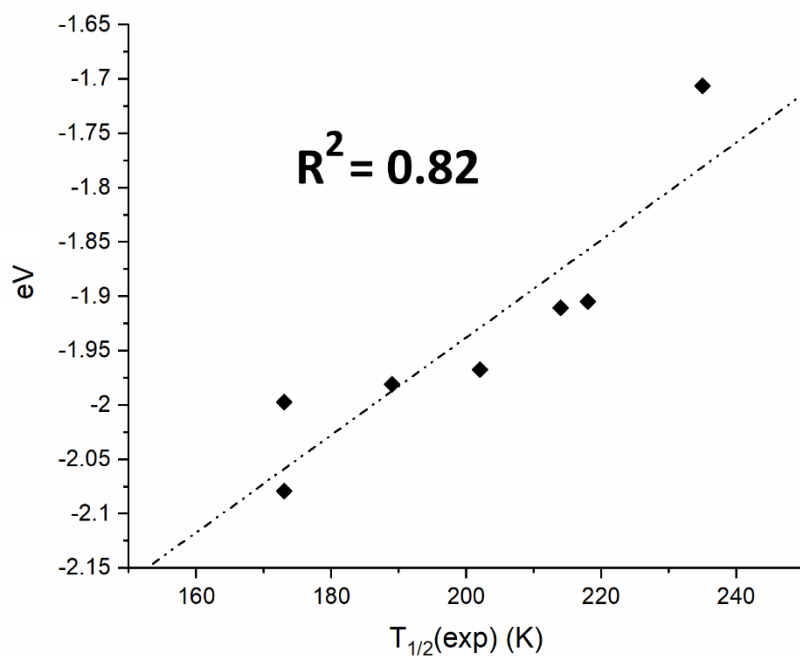


Figure A5.124. Reported trend for the variation of MO-280 β in $1_{\text{cry,HS}}$ versus the measured $T_{1/2}$ at seven different pressures ($R^2 = 0.82$).

Table A5.13. Calculated values of the frontier MOs (HOMO/LUMO) and the HOMO-LUMO gap ($\Delta(\text{MOs})$) for $\mathbf{1}_{\text{cry,LS}}$ and $\mathbf{1}_{\text{cry,HS}}$. Last two columns on the right reports the correlation factor for each of the three studied terms (HOMO, LUMO, HOMO-LUMO gap) for $\mathbf{1}_{\text{cry,LS}}$ and $\mathbf{1}_{\text{cry,HS}}$ against the seven pressures employed for this study and the relative experimental $T_{1/2}$ measured at that pressure conditions.

p / bar		1	1800	2100	2500	2900	3900	4300	$R^2(p)$	R^2
$T_{1/2}(\text{exp.}) / \text{K}$		173	173	189	202	214	227	235		$(T_{1/2}(\text{exp}))$
$\mathbf{1}_{\text{cry,LS}}$	HOMO	2.884681	2.971757	2.985363	2.999241	3.009037	3.056112	3.073147	0.99 (Fig. S125)	0.81 (Fig. S128)
	LUMO	3.330947	3.39816	3.409044	3.419929	3.446868	3.483059	3.495332	0.99 (Fig. S126)	0.87 (Fig. S129)
	$\Delta(\text{MOs})$	0.446267	0.426403	0.423681	0.420688	0.437831	0.426947	0.422185	0.40 (Fig. S127)	0.14 (Fig. S130)
$\mathbf{1}_{\text{cry,HS}}$	HOMO	1.683025	1.768741	1.783435	1.800578	1.845477	1.850919	2.057617	0.78 (Fig. S125)	0.74 (Fig. S128)
	LUMO	2.861823	2.932028	2.94645	2.960872	3.028629	3.032438	3.210836	0.80 (Fig. S126)	0.79 (Fig. S129)
	$\Delta(\text{MOs})$	1.178798	1.163287	1.163015	1.160566	1.183152	1.181519	1.153219	0.05 (Fig. S127)	0.01 (Fig. S130)

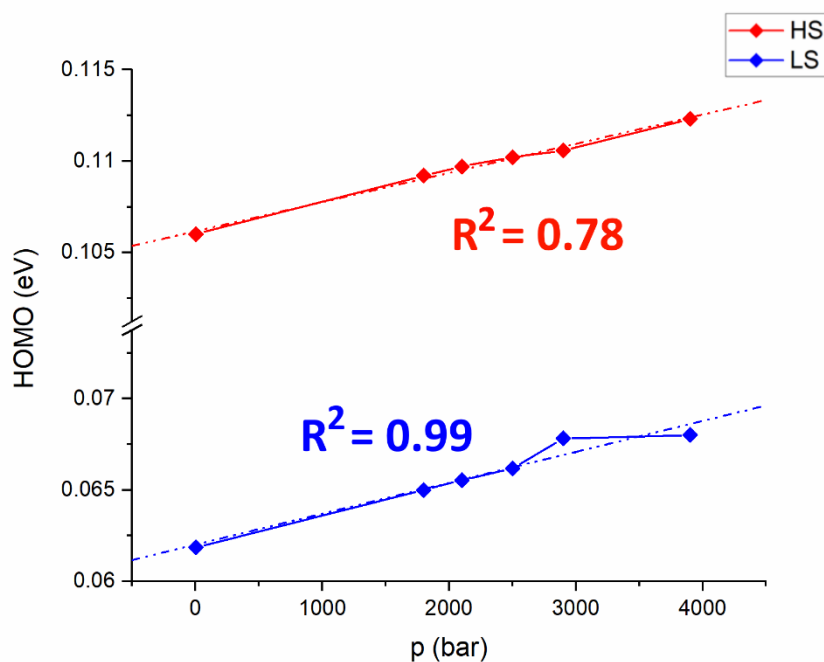


Figure A5.125. Reported trend for the variation of the HOMO energy levels at the pressure increase for $1_{\text{cry,HS}}$ ($R^2 = 0.78$) and $1_{\text{cry,LS}}$ ($R^2 = 0.99$).

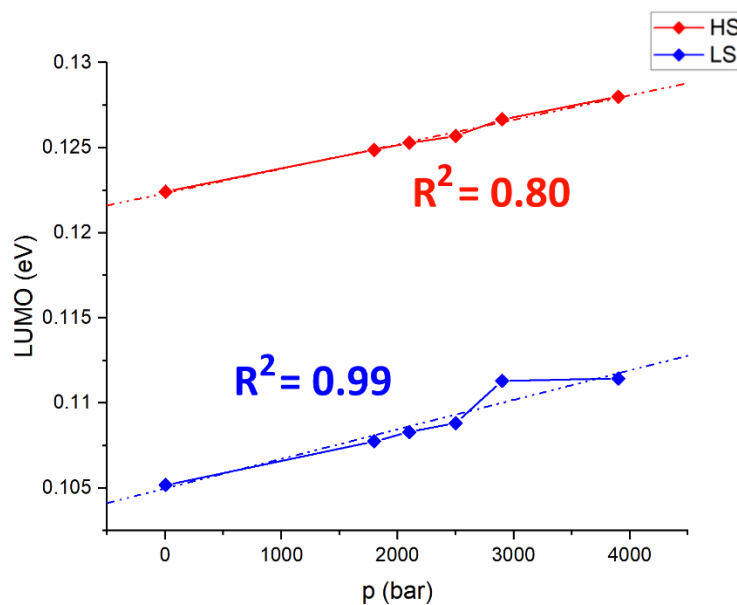


Figure A5.126. Reported trend for the variation of the HOMO energy levels at the pressure increase for $1_{\text{cry,HS}}$ ($R^2 = 0.80$) and $1_{\text{cry,LS}}$ ($R^2 = 0.99$).

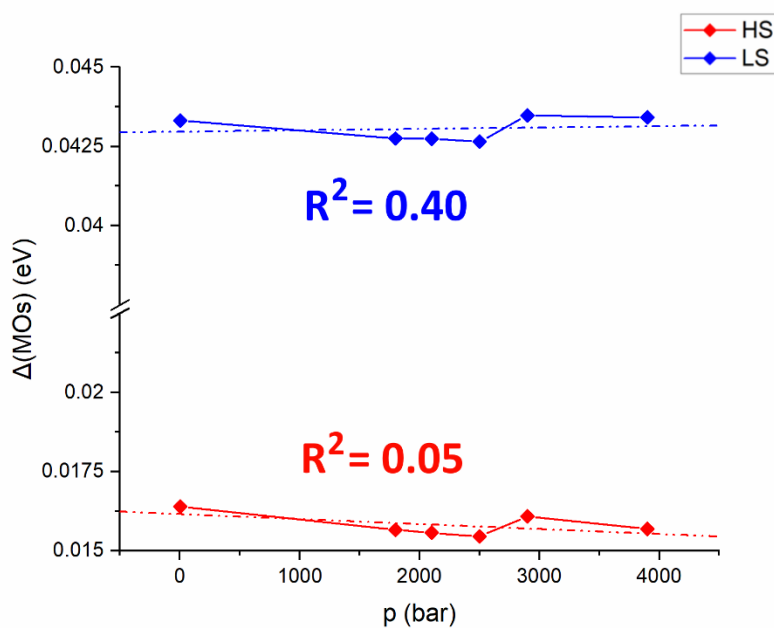


Figure A5.127. Reported trend for the variation of the HOMO-LUMO gap (ΔMOs) at the pressure increase for $1_{\text{cry,HS}}$ ($R^2 = 0.40$) and $1_{\text{cry,LS}}$ ($R^2 = 0.05$).

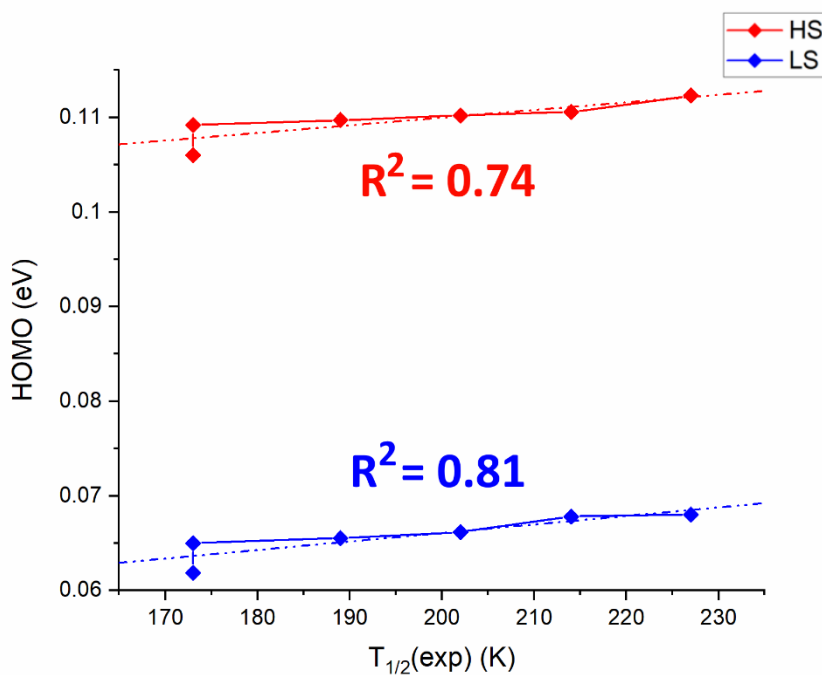


Figure A5.128. Reported trend for the variation of the HOMO energy levels of $1_{\text{cry,HS}}$ ($R^2 = 0.74$) and $1_{\text{cry,LS}}$ ($R^2 = 0.81$) at the measured $T_{1/2}$ at the pressure increase.

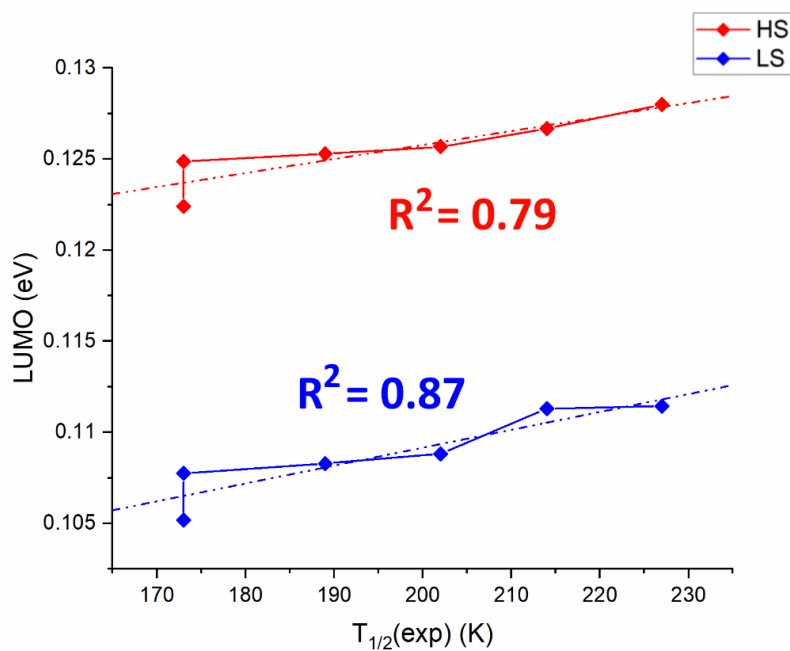


Figure A5.129. Reported trend for the variation of the LUMO energy levels of $1_{\text{cry,HS}}$ ($R^2 = 0.79$) and $1_{\text{cry,LS}}$ ($R^2 = 0.87$) at the measured $T_{1/2}$ at the pressure increase.

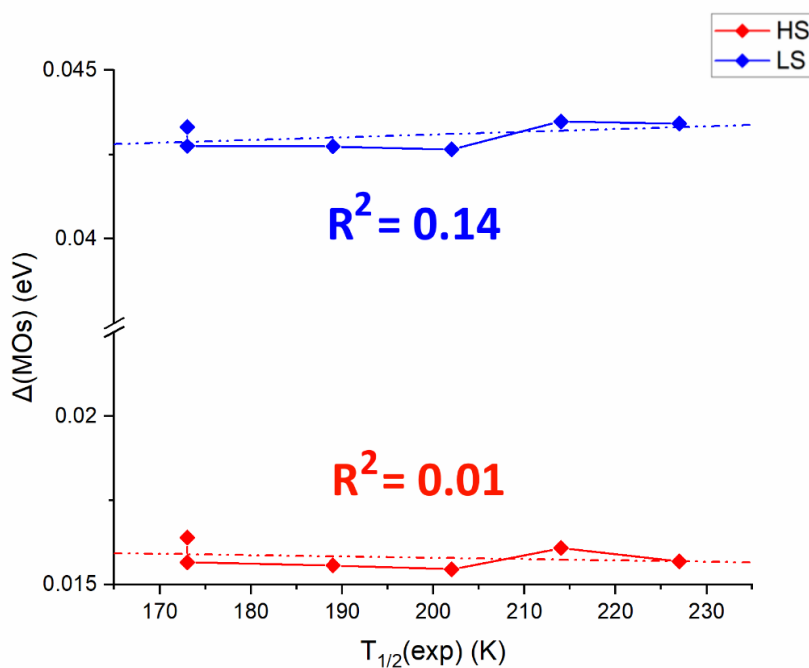


Figure A5.130. Reported trend for the variation of the HOMO-LUMO gap (ΔMOs) of $1_{\text{cry,HS}}$ ($R^2 = 0.14$) and $1_{\text{cry,LS}}$ ($R^2 = 0.01$) at the measured $T_{1/2}$ at the pressure increase.

A5.5. Additional Data for *Gradual* SCO Modelling

A5.5.1. CP2K 6.1 Calculated IR Spectra

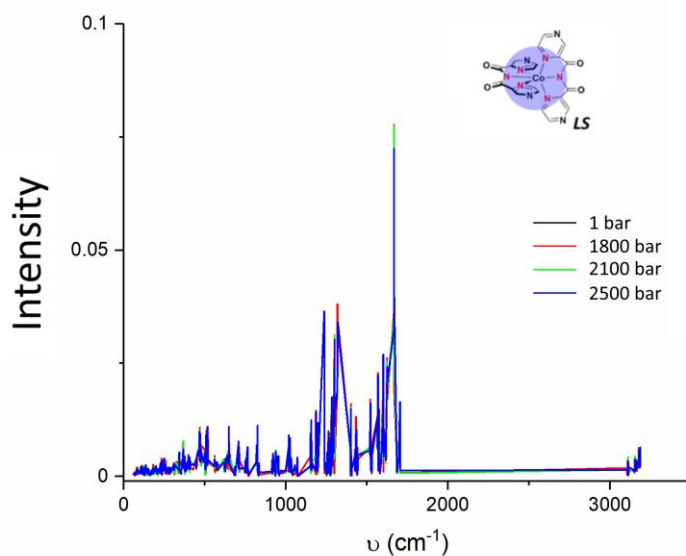


Figure 1e A5.131. Reported IR spectra calculated with CP2K6.1 code for $1_{\text{cry,LS}}$ at the four different pressures ($p = 1, 1800, 2100, 2500$ bar) where the SCO transition was modelled properly.

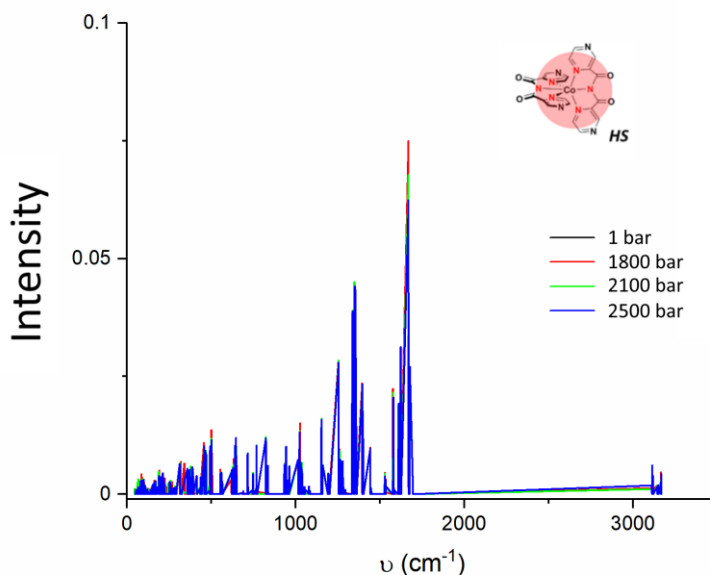


Figure A5.132. Reported IR spectra calculated with CP2K6.1 code for $1_{\text{cry,HS}}$ at three different pressures ($p = 1, 1800, 2100, 2500$ bar) where the SCO transition was modelled properly.

A5.5.1. IR/Raman Spectra ORCA4.1 Code

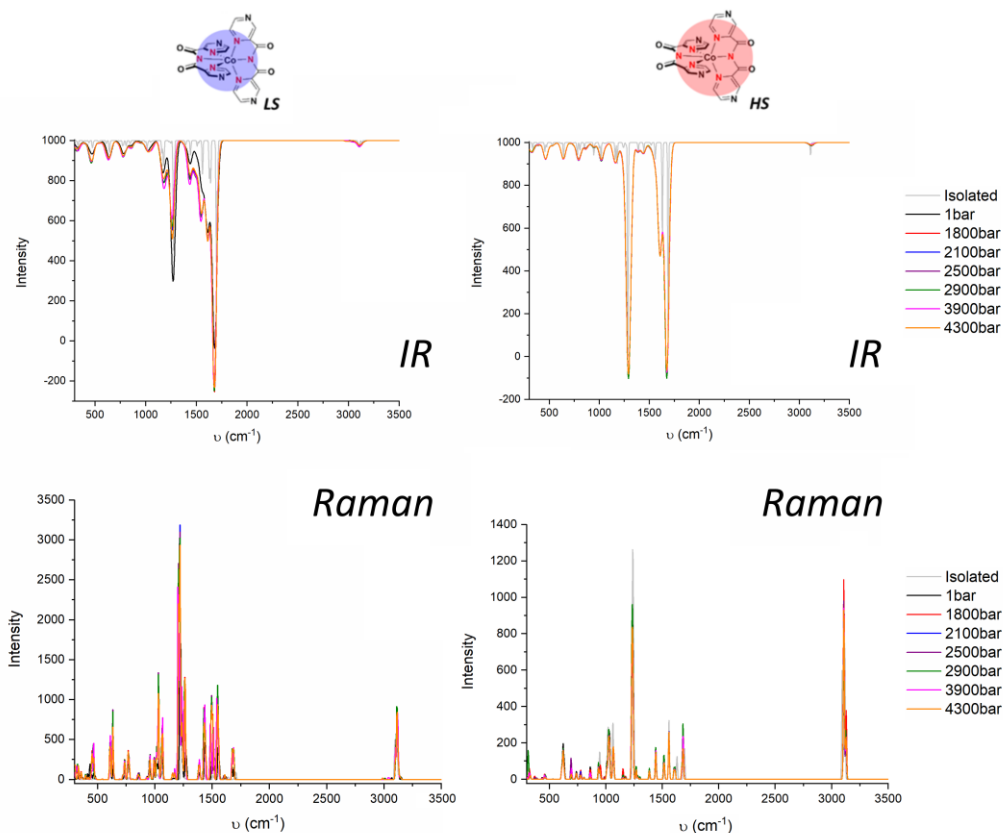


Figure A5.133. Calculated IR and Raman spectra for $1_{cf,LS}$ (left) and $1_{cf,HS}$ (right) obtained by extrapolation from the crystalline cell and re-optimised using ORCA4.1 code using RI-PBE-def2-TZVPP level of theory ($w = 10$).^{28,261-262}

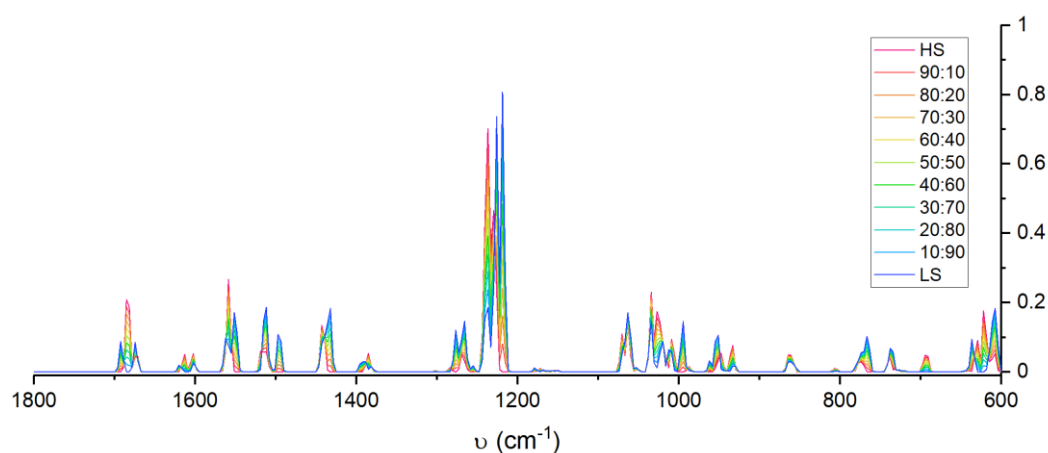


Figure A5.134. Variation of the calculated Raman Spectrum of 1_{cf} at $p = 1$ bar, from $1_{cf,LS}$ and $1_{cf,HS}$. Spectra were obtained using ORCA4.1 code: RI-PBE-def2-TZVPP level of theory ($w = 5$).^{28,261-262}

A5.5.2. Thermodynamic Terms

Table A5.14. Summary table of the thermodynamic contribution (H_{el}) for $1_{\text{cry,HS}}$ and $1_{\text{cry,LS}}$ at different pressure (from 1 bar to 2900 bar). Results are reported in eV.

H_{el} (eV)			
p / bar	HS	LS	Δ
1	-46632.1965	-46632.5185	0.3220
1800	-46632.1911	-46632.5068	0.3157
2100	-46632.1854	-46632.5027	0.3173
2500	-46632.1801	-46632.4962	0.3161
2900	-46631.4015	-46632.4855	1.0840
3900	-46631.3854	-46632.4632	1.0780
4300	-46630.8149	-46632.4516	1.6363

Table A5.15. Summary table of the thermodynamic contribution (S_{el}) for $1_{\text{cry,HS}}$ and $1_{\text{cry,LS}}$ at different pressure (from 1 bar to 2900 bar). Results are reported in eV.

S_{el} (eV)			
p / bar	HS	LS	Δ
1	0.000214	0.000134	0.00080
1800	0.000214	0.000134	0.00080
2100	0.000214	0.000134	0.00080
2500	0.000214	0.000134	0.00080
2900	0.000214	0.000134	0.00080
3900	0.000214	0.000134	0.00080

Table A5.16. Summary table of the thermodynamic contribution (H_{vib}) for $1_{\text{cry,LS}}$ at different pressure (from 1 bar to 2900 bar). Results are reported in eV.

p / bar	1	1800	2100	2500	2900	3900
T / K	$H_{\text{vib}} (\text{LS}) / \text{eV}$					
25	34.205	34.213	34.213	34.220	34.224	33.951
50	34.243	34.250	34.250	34.258	34.263	34.005
75	34.337	34.344	34.344	34.351	34.357	34.117
100	34.486	34.492	34.492	34.498	34.504	34.281
125	34.683	34.688	34.689	34.695	34.701	34.492
150	34.924	34.930	34.931	34.936	34.941	34.746
155	34.977	34.983	34.984	34.989	34.995	34.801
160	35.032	35.038	35.039	35.044	35.050	34.859
165	35.089	35.095	35.096	35.100	35.106	34.917
170	35.147	35.153	35.154	35.159	35.164	34.978
175	35.207	35.213	35.214	35.219	35.224	35.040
180	35.269	35.274	35.275	35.280	35.286	35.103
185	35.332	35.338	35.339	35.343	35.349	35.168
190	35.396	35.402	35.403	35.408	35.413	35.235
195	35.463	35.469	35.470	35.474	35.479	35.303
200	35.530	35.536	35.537	35.542	35.547	35.372
225	35.893	35.899	35.900	35.904	35.909	35.744
250	36.293	36.300	36.301	36.305	36.310	36.152
275	36.732	36.739	36.740	36.744	36.748	36.598
300	37.207	37.214	37.215	37.219	37.223	37.079
325	37.717	37.725	37.726	37.729	37.734	37.596
350	38.262	38.269	38.271	38.274	38.278	38.147
375	38.840	38.847	38.848	38.852	38.856	38.729
400	39.448	39.456	39.457	39.461	39.465	39.343

Table A5.17. Summary table of the thermodynamic contribution (H_{vib}) for $1_{\text{cry,HS}}$ at different pressure (from 1 bar to 2900 bar). Results are reported in eV.

p / bar	1	1800	2100	2500	2900	3900
T / K	$H_{\text{vib}} \text{ (HS)} / \text{eV}$					
25	34.046	34.059	34.068	34.064	34.124	34.218
50	34.098	34.112	34.119	34.116	34.174	34.258
75	34.215	34.227	34.232	34.230	34.284	34.356
100	34.385	34.397	34.401	34.399	34.448	34.510
125	34.602	34.613	34.616	34.615	34.660	34.713
150	34.861	34.871	34.874	34.873	34.915	34.960
155	34.918	34.927	34.930	34.930	34.970	35.015
160	34.976	34.985	34.988	34.988	35.028	35.071
165	35.036	35.045	35.048	35.047	35.087	35.129
170	35.097	35.106	35.109	35.108	35.147	35.188
175	35.159	35.168	35.171	35.171	35.209	35.249
180	35.223	35.232	35.235	35.235	35.272	35.311
185	35.289	35.298	35.301	35.300	35.337	35.375
190	35.356	35.365	35.368	35.367	35.404	35.441
195	35.425	35.433	35.436	35.436	35.472	35.508
200	35.495	35.503	35.506	35.506	35.542	35.576
225	35.868	35.876	35.879	35.879	35.912	35.942
250	36.277	36.285	36.288	36.288	36.319	36.346
275	36.722	36.730	36.733	36.733	36.762	36.787
300	37.203	37.211	37.214	37.214	37.241	37.264
325	37.718	37.726	37.729	37.730	37.755	37.775
350	38.267	38.275	38.278	38.278	38.303	38.321
375	38.848	38.856	38.858	38.859	38.882	38.899
400	39.459	39.467	39.470	39.470	39.493	39.508

Table A5.18. Summary table of the thermodynamic contribution (S_{vib}) for $1_{\text{cry,LS}}$ at different pressure (from 1 bar to 2900 bar). Results are reported in eV.

p / bar	1	1800	2100	2500	2900	3900
T / K	$S_{\text{vib}} \text{ (LS) / eV}$					
25	0.000	0.000	0.000	0.000	0.000	0.000
50	0.001	0.001	0.001	0.001	0.001	0.002
75	0.003	0.003	0.003	0.003	0.003	0.004
100	0.004	0.004	0.004	0.004	0.004	0.005
125	0.006	0.006	0.006	0.006	0.006	0.007
150	0.008	0.008	0.008	0.008	0.008	0.009
155	0.008	0.008	0.008	0.008	0.008	0.010
160	0.009	0.008	0.008	0.009	0.009	0.010
165	0.009	0.009	0.009	0.009	0.009	0.010
170	0.009	0.009	0.009	0.009	0.009	0.011
175	0.010	0.010	0.010	0.010	0.010	0.011
180	0.010	0.010	0.010	0.010	0.010	0.011
185	0.010	0.010	0.010	0.010	0.010	0.012
190	0.011	0.011	0.011	0.011	0.011	0.012
195	0.011	0.011	0.011	0.011	0.011	0.012
200	0.011	0.011	0.011	0.011	0.011	0.013
225	0.013	0.013	0.013	0.013	0.013	0.014
250	0.015	0.015	0.015	0.015	0.015	0.016
275	0.016	0.016	0.016	0.016	0.016	0.018
300	0.018	0.018	0.018	0.018	0.018	0.020
325	0.020	0.020	0.020	0.020	0.020	0.021
350	0.021	0.021	0.021	0.021	0.021	0.023
375	0.023	0.023	0.023	0.023	0.023	0.024
400	0.024	0.024	0.024	0.024	0.024	0.026

Table A5.19. Summary table of the thermodynamic contribution (S_{vib}) for $1_{\text{cry,HS}}$ at different pressure (from 1 bar to 2900 bar). Results are reported in eV.

p / bar	1	1800	2100	2500	2900	3900
T / K	$S_{\text{vib}} \text{ (HS)} / \text{eV}$					
25	0.000	0.000	0.000	0.000	0.000	0.000
50	0.002	0.002	0.002	0.002	0.002	0.001
75	0.003	0.004	0.003	0.003	0.003	0.003
100	0.005	0.005	0.005	0.005	0.005	0.005
125	0.007	0.007	0.007	0.007	0.007	0.006
150	0.009	0.009	0.009	0.009	0.009	0.008
155	0.010	0.010	0.009	0.010	0.009	0.008
160	0.010	0.010	0.010	0.010	0.010	0.009
165	0.010	0.010	0.010	0.010	0.010	0.009
170	0.011	0.011	0.011	0.011	0.010	0.010
175	0.011	0.011	0.011	0.011	0.011	0.010
180	0.011	0.011	0.011	0.011	0.011	0.010
185	0.012	0.012	0.012	0.012	0.011	0.011
190	0.012	0.012	0.012	0.012	0.012	0.011
195	0.013	0.013	0.012	0.012	0.012	0.011
200	0.013	0.013	0.013	0.013	0.013	0.012
225	0.015	0.015	0.014	0.015	0.014	0.013
250	0.016	0.016	0.016	0.016	0.016	0.015
275	0.018	0.018	0.018	0.018	0.018	0.017
300	0.020	0.020	0.020	0.020	0.019	0.018
325	0.021	0.021	0.021	0.021	0.021	0.020
350	0.023	0.023	0.023	0.023	0.023	0.022
375	0.025	0.025	0.024	0.025	0.024	0.023
400	0.026	0.026	0.026	0.026	0.026	0.025

References

1. Gütlich, P., Spin Crossover - Quo Vadis? *Eur. J. Inorg. Chem.* **2013**, 581-591.
2. Bousseksou, A.; Molnár, G.; Salmon, L.; Nicolazzi, W., Molecular spin crossover phenomenon: recent achievements and prospects. *Chem. Soc. Rev.* **2011**, *40*, 3313-3335.
3. Halcrow, M. A., *Spin-Crossover Materials: Properties and Applications*. 1st Ed. ed.; John Wiley & Sons, Ltd: Chichester, 2013.
4. Feltham, H. L. C.; Barltrop, A. S.; Brooker, S., Spin crossover in iron(II) complexes of 3,4,5-tri-substituted-1,2,4-triazole (Rdpt), 3,5-di-substituted-1,2,4-triazolate (dpt⁻), and related ligands. *Coord. Chem. Rev.* **2017**, *344*, 26–53.
5. Olguín, J.; Brooker, S., Spin crossover in discrete polynuclear complexes. In *Spin-Crossover Materials: Properties and Applications*, First Edition ed.; Halcrow, M. A., Ed. John Wiley & Sons, Ltd: **2013**; pp 77-120.
6. Cambi, L.; Cagnasso, A., *Ber. Deutsch. Chem. Ges.* **1931**, *64*, 167.
7. Brooker, S., Spin crossover with thermal hysteresis: practicalities and lessons learnt. *Chem. Soc. Rev.* **2015**, *44*, 2880-2892 and front cover feature.
8. Cambi, L.; Szego, L., *Ber. Dtsch. Chem. Ges.* **1931**, *64*, 2591.
9. Sundaresan, S.; Kühne, I. A.; Kelly, C. T.; Barker, A.; Salley, D.; Müller-Bunz, H.; Powell, A. K.; Morgan, G. G., Anion Influence on Spin State in Two Novel Fe(III) Compounds: [Fe(5F-sal2333)]X. *Crystals* **2018**, *9* (1), 19.
10. Arroyave, A.; Lennartson, A.; Dragulescu-Andrasi, A.; Pedersen, K. S.; Piligkos, S.; Stoian, S. A.; Greer, S. M.; Pak, C.; Hietsoi, O.; Phan, H.; Hill, S.; McKenzie, C. J.; Shatruk, M., Spin Crossover in Fe(II) Complexes with N₄S₂ Coordination. *Inorg. Chem.* **2016**, *55* (12), 5904-5913.
11. Chen, X.-Q.; Cai, Y.-D.; Jiang, W.; Peng, G.; Fang, J.-K.; Liu, J.-L.; Tong, M.-L.; Bao, X., A Multi-Stimuli-Responsive Fe(II) SCO Complex Based on an Acylhydrazone Ligand. *Inorg. Chem.* **2019**, *58* (2), 999-1002.
12. Chen, X.-Q.; Cai, Y.-D.; Ye, Y.-S.; Tong, M.-L.; Bao, X., Investigation of SCO property–structural relationships in a family of mononuclear Fe(II) complexes. *Inorg. Chem. Front.* **2019**, *6* (8), 2194-2199.
13. Cheng, X.; Yang, Q.; Gao, C.; Wang, B.-W.; Shiga, T.; Oshio, H.; Wang, Z.-M.; Gao, S., Thermal and light induced spin crossover behavior of a dinuclear Fe(II) compound. *Dalton Trans.* **2015**, *44* (25), 11282-11285.
14. Sim, P. G.; Sinn, E., First Manganese(III) Spin Crossover and First d⁴ Crossover. Comment on Cytochrome Oxidase. *J. Am. Chem. Soc.* **1981**, *103*, 241-243.
15. Morgan, G. G.; Murnaghan, K. D.; Müller-Bunz, H.; McKee, V.; Harding, C. J., A manganese(III) complex that exhibits spin crossover triggered by geometric tuning. *Angew. Chem. Int. Ed.* **2006**, *45*, 7192-7195.
16. Halepoto, D. M.; Holt, D. G. L.; Larkworthy, L. F.; Leigh, G. J.; Povey, D. C.; Smith, G. W., Spin Crossover in Chromium(ii) Complexes and the Crystal and Molecular Structure of the High Spin Form of Bis[1,2-bis(diethylphosphino)ethane]di-iodochromium(II). *Chem. Comm.* **1989**, (18), 1322-1323.

17. Ferraro, J. R.; Basile, L. J.; Sacconi, L., High Spin-Low Spin Crossover in Co(II) Complexes with Tris(2-diphenylphosphinoethyl)amine (NP₃) by Application of High External Pressures. *Inorg. Chim. Acta* **1979**, *35*, L317-L318.
18. McPherson, J. N.; Hogue, R. W.; Akogun, F. S.; Bondi, L.; Luis, E. T.; Price, J. R.; Garden, A. L.; Brooker, S.; Colbran, S. B., Predictable substituent control of Co^{III/II} redox potential and spin crossover in bis(dipyridylpyrrolide)cobalt complexes. *Inorg. Chem.* **2019**, *58*, 2218-2228.
19. Miller, R. G.; Narayanaswamy, S.; Clark, S. M.; Jameson, G. B.; Tallon, J. L.; Brooker, S., Pressure induced separation of phase-transition-triggered-abrupt vs gradual components of spin crossover. *Dalton Trans.* **2015**, *44*, 20843-20849 and front cover.
20. Bersuker, I. B., *Electronic structure and properties of transition metal compounds: introduction to the theory*. John Wiley & Sons: 2010.
21. Albright, T. A.; Burdett, J. K.; Whangbo, M.-H., *Orbital interactions in chemistry*. John Wiley & Sons: 2013.
22. Kimura, A.; Ishida, T., Spin-crossover temperature predictable from DFT calculation for iron(II) complexes with 4-substituted Pybox and related heteroaromatic ligands. *ACS Omega* **2018**, *3* (6), 6737-6747.
23. Kershaw Cook, L. J.; Kulmaczewski, R.; Mohammed, R.; Dudley, S.; Barrett, S. A.; Little, M. A.; Deeth, R. J.; Halcrow, M. A., A unified treatment of the relationship between ligand substituents and spin state in a family of iron(II) complexes. *Angew. Chem. Int. Ed.* **2016**, *55*, 4327-4331.
24. Prat, I.; Company, A.; Corona, T.; Parella, T.; Ribas, X.; Costas, M., Assessing the impact of electronic and steric tuning of the ligand in the spin state and catalytic oxidation ability of the Fe(II) (Pytacn) family of complexes. *Inorg. Chem.* **2013**, *52* (16), 9229-9244.
25. Ksenofontov, V.; Gaspar, A. B.; Gütllich, P., *Top. Curr. Chem.* **2004**, *235*, 23.
26. Gütllich, P.; Gaspar, A. B.; Garcia, Y., Spin state switching in iron coordination compounds. *Beilstein J. Org. Chem.* **2013**, *9*, 342-391.
27. Gütllich, P.; Hauser, A.; Spiering, H., Thermal and Optical Switching of Iron(II) Complexes. *Angew. Chem. Int. Ed. Engl.* **1994**, *33*, 2024-2054.
28. Bauer, W.; Pfaffeneder, T.; Achterhold, K.; Weber, B., Complete Two-Step Spin-Transition in a 1D Chain Iron(II) Complex with a 110-K Wide Intermediate Plateau. *Eur. J. Inorg. Chem.* **2011**, 3183-3192.
29. Feltham, H. L. C.; Johnson, C.; Elliot, A. B. S.; Gordon, K. C.; Albrecht, M.; Brooker, S., "Tail" tuning of spin crossover temperature by 100 K. *Inorg. Chem.* **2015**, *54*, 2902-2909.
30. Gütllich, P.; Goodwin, H. A., Spin crossover - an overall perspective. *Top. Curr. Chem.* **2004**, *233*, 1-47.
31. Tuchagues, J.-P.; Boussekou, A.; Molnár, G.; McGarvey, J. J.; Varret, F., The Role of Molecular Vibrations in the Spin Crossover Phenomenon. *Top. Curr. Chem.* **2004**, *234*, 85-103.
32. Gütllich, P.; Hauser, A., Excited Spin State Trapping (LIESST, NIESST). *Comprehensive Coordination Chemistry II* **2004**, *2*, 427-434.
33. Absmeier, A.; Bartel, M.; Carbonera, C.; Jameson, G. N. L.; Weinberger, P.; Caneschi, A.; Mereiter, K.; Létard, J.-F.; Linert, W., Both spacer length and parity influence the thermal and light-induced properties of iron(II) bis(tetrazole-1-yl)alkane coordination polymers. *Chem. Eur. J.* **2006**, *12*, 2235-2243.

34. Neville, S. M.; Halder, G. J.; Chapman, K. W.; Duriska, M. B.; Southon, P. D.; Cashion, J. D.; Letard, J.-F.; Moubaraki, B.; Murray, K. S.; Kepert, C. J., Single-Crystal to Single-Crystal Structure Transformations and Photomagnetism of a Porous Iron(II) Spin-Crossover Framework. *J. Am. Chem. Soc.* **2008**, *130* (9), 2869-2876.
35. Marino, A.; Chakraborty, P.; Servol, M.; Lorenc, M.; Collet, E.; Hauser, A., The Role of Ligand-Field States in the Ultrafast Photophysical Cycle of the Prototypical Iron(II) Spin-Crossover Compound [Fe(ptz)₆](BF₄)₂. *Angew. Chem. Int. Ed.* **2014**, *53* (15), 3863-3867.
36. Decurtins, S.; Gütllich, P.; Kohler, C. P.; Spiering, H.; Hauser, A., Light induced excited state spin state trapping in a transition metal complex: the hexa-1-propyltetrazole iron(II) tetrafluoroborate spin crossover system. *Chem. Phys. Lett.* **1984**, *105*, 1-4.
37. Absmeier, A.; Bartel, M.; Carbonera, C.; Jameson, G. N. L.; Werner, F.; Reissner, M.; Caneschi, A.; Létard, J.-F.; Linert, W., Mutual influence of spacer length and noncoordinating anions on thermal and light-induced spin-crossover properties of iron(II)-,bis(tetrazol-1-yl)alkane coordination polymers. *Eur. J. Inorg. Chem.* **2007**, 3047-3054.
38. Decurtins, S.; Gütllich, P.; Hasselbach, K. M.; Hauser, A.; Spierling, H., Light-induced excited-spin-state trapping in Iron(II) Spin-crossover Systems. Optical spectroscopic and magnetic susceptibility study. *Inorg. Chem.* **1985**, *24*, 2174-2178.
39. Real, J. A.; Gaspar, A. B.; Muñoz, M. C., Thermal, pressure and light switchable spin-crossover materials. *Dalton Trans.* **2005**, 2062-2079.
40. Molnár, G.; Niel, V.; Real, J.-A.; Dubrovinsky, L.; Bousseksou, A.; McGarvey, J. J., Raman Spectroscopic Study of Pressure Effects on the Spin-Crossover Coordination Polymers Fe(Pyrazine)[M(CN)₄]2H₂O (M = Ni, Pd, Pt). First Observation of a Piezo-Hysteresis Loop at Room Temperature. *J. Phys. Chem. B* **2003**, *107*, 3149-3155.
41. Garcia, Y.; Ksenofontov, V.; Gütllich, P., Spin Transition Molecular Materials: New Sensors. *Hyperfine Interact.* **2002**, *139-140* (1-4), 543-551.
42. Pressure Effect Studies on the Spin-Transition Behavior of a Dinuclear Iron(II) Compound. *Eur. J. Inorg. Chem.* **2013**, *2013* (5-6), 843.
43. Agustí, G.; Thompson, A. L.; Gaspar, A. B.; Muñoz, M. C.; Goeta, A. E.; Rodríguez-Velamazán, J. A.; Real, J. A., Thermal, pressure and light induced spin transition in the two-dimensional coordination polymer {Fe(pmd)₂[Cu(CN)₂]₂}. *Dalton Trans.* **2008**, 642-649.
44. Bhattacharjee, A.; Ksenofontov, V.; Goodwin, H. A.; Gütllich, P., Pressure-induced hysteresis in the high spin-low spin transition in bis(2,4-bis(pyridin-2-yl)thiazole) iron(II) tetrafluoroborate. *J. Phys. Condens. Matter* **2009**, *21* (2), 026011.
45. Halder, G. J.; Kepert, C. J.; Moubaraki, B.; Murray, K. S.; Cashion, J. D., Guest-dependent spin crossover in a nanoporous molecular framework material. *Science* **2002**, *298*, 1762-1765.
46. Shepherd, H. J.; Gural'skiy, I. A.; Quintero, C. M.; Tricard, S.; Salmon, L.; Molnár, G.; Bousseksou, A., Molecular actuators driven by cooperative spin-state switching. *Nat. Comm.* **2013**, *4*, 2607.
47. Quintero, C. M.; Félix, G.; Suleimanov, I.; Sánchez Costa, J.; Molnár, G.; Salmon, L.; Nicolazzi, W.; Bousseksou, A., Hybrid spin-crossover nanostructures. *Beilstein J. Nanotechnol.* **2014**, *5*, 2230-2239.
48. Halcrow, M. A., Trapping and manipulating excited spin states of transition metal compounds. *Chem. Soc. Rev.* **2008**, *37* (2), 278-289.

49. Ruiz, E., Charge transport properties of spin crossover systems. *Phys. Chem. Chem. Phys.* **2014**, *16*, 14-22.
50. Molnár, G.; Salmon, L.; Nicolazzi, W.; Terkib, F.; Bousseksou, A., Emerging properties and applications of spin crossover nanomaterials. *J. Mater. Chem. C* **2014**, *2*, 1360-1366.
51. Tissot, A., Photoswitchable spin crossover nanoparticles. *New J. Chem.* **2014**, *38* (5), 1840-1845.
52. Lacroix, P. G.; Malfant, I.; Real, J.-A.; Rodriguez, V., From Magnetic to Nonlinear Optical Switches in Spin-Crossover Complexes. *Eur. J. Inorg. Chem.* **2013**, *2013* (5-6), 615-627.
53. Bousseksou, A.; Salmon, L.; Molnar, G.; Cobo, S. Heat-sensitive spin-transition materials doped with one or more fluorescent agents for use as temperature sensor. WO2011058277A1, 2011.
54. Lavrenova, L. G.; Shakirova, O. G., Spin Crossover and Thermochromism of Iron(II) Coordination Compounds with 1,2,4-Triazoles and Tris(pyrazol-1-yl)methanes. *Eur. J. Inorg. Chem.* **2013**, 670-682.
55. Wei, R.-J.; Li, B.; Tao, J.; Huang, R.-B.; Zheng, L.-S.; Zheng, Z., Making spin-crossover crystals by successive polymorphic transformations. *Inorg. Chem.* **2011**, *50*, 1170-1172.
56. Nihei, M.; Yoshida, A.; Koizumi, S.; Oshio, H., Hetero-metal Mn-Cu and Mn-Ni clusters with tridentate Schiff-base ligands. *Polyhedron* **2007**, *26*, 1997-2007.
57. Li Zhang, G.-C. X., Hong-Bin Xu, Teng Zhang, Zhe-Ming Wang, Mei Yuana, Song Gao, Abrupt spin transition around room temperature and light induced properties in FeII complexes with N4O2 coordination sphere. *Chem. Commun.* **2010**, *46* (15), 2554-2556.
58. Kitchen, J. A.; Olgúin, J.; Kulmaczewski, R.; White, N. G.; Milway, V. A.; Jameson, G. N. L.; Tallon, J. L.; Brooker, S., Effect of N⁴-substituent choice on spin crossover in dinuclear iron(II) complexes of bis-terdentate 1,2,4-triazole-based ligands. *Inorg. Chem.* **2013**, *52*, 11185-11199.
59. Neville, S. M.; Leita, B., A.; Halder, G. J.; Kepert, C. J.; Moubaraki, B.; Letard, J.-F.; Murray, K. S., Understanding the Two-Step Spin-Transition Phenomenon in Iron(II) 1D Chain Materials. *Chem. Eur. J.* **2008**, *14*, 10123-10133.
60. Costa, J. S.; Rodríguez-Jiménez, S.; Craig, G. A.; Barth, B.; Beavers, C. M.; Teat, S. J.; Aromí, G., Three-way crystal-to-crystal reversible transformation and controlled spin switching by a nonporous molecular material. *J. Am. Chem. Soc.* **2014**, *136*, 3869-3874.
61. Hostettler, M.; Törnroos, K. W.; Chernyshov, D.; Vangdal, B.; Bürgi, H.-B., Challenges in Engineering Spin Crossover: Structures and Magnetic Properties of Six Alcohol Solvates of Iron(II) Tris(2-picolyamine) Dichloride. *Angew. Chem., Int. Ed.* **2004**, *40*, 4589.
62. Quesada, M.; de la Pena-O'Shea, V. A.; Aromi, G.; Geremia, S.; Massera, C.; Roubeau, O.; Gamez, P.; Reedijk, J., A molecule-based nanoporous material showing tuneable spin-crossover behavior near room temperature. *Adv. Mater.* **2007**, *19* (10), 1397-1402.
63. Miller, R. G.; Brooker, S., Reversible quantitative guest sensing via spin crossover of an iron(II) triazole. *Chem. Sci.* **2016**, *7*, 2501-2505 and front cover feature.
64. Rodríguez-Jiménez, S.; Feltham, H. L. C.; Brooker, S., Non-porous iron(II)-based sensor: crystallographic insights into a cycle of colorful guest-induced topotactic transformations. *Angew. Chem. Int. Ed.* **2016**, *55*, 15067-15071 and back cover.

65. Young, M. C.; Liew, E.; Hooley, R. J., Colorimetric barbiturate sensing with hybrid spin crossover assemblies. *Chem. Commun.* **2014**, 50 (39), 5043-5045.
66. Kahn, O., Molecules with short memories. *Chem. Br.* **1999**, 2, 24-27.
67. Kahn, O.; Martinez, C. J., Spin transition polymers: from molecular materials toward memory devices. *Science* **1998**, 279 (5347), 44-48.
68. Kahn, O.; Kröber, J.; Jay, C., Spin transition molecular materials for displays and data recording. *Adv. Mater.* **1992**, 4 (11), 718-728.
69. Boča, R.; Renz, F.; Boca, M.; Hartmut, F.; Haase, W.; Kickelbick, G.; Linert, W.; Vrbova-Schikora, M., Tuning the spin crossover above room temperature: iron(II) complexes of substituted and deprotonated 2,6-bis(benzimidazol-2-yl)pyridine. *Inorg. Chem. Commun.* **2005**, 8, 227-230.
70. Ikuta, Y.; Ooidemizu, M.; Yamahata, Y.; Yamada, M.; Osa, S.; Matsumoto, N.; Iijima, S.; Sunatsuki, Y.; Kojima, M.; Dahan, F.; Tuchagues, J.-P., A New Family of Spin Crossover Complexes with a Tripod Ligand Containing Three Imidazoles: Synthesis, Characterization, and Magnetic Properties of $[\text{Fe}(\text{II})\text{H}_3\text{LMe}](\text{NO}_3) \cdot 2.1.5\text{H}_2\text{O}$, $[\text{Fe}(\text{III})\text{LMe}] \cdot 3.5\text{H}_2\text{O}$, $[\text{Fe}(\text{II})\text{H}_3\text{LMe}][\text{Fe}(\text{II})\text{LMe}]\text{NO}_3$, and $[\text{Fe}(\text{II})\text{H}_3\text{LMe}][\text{Fe}(\text{III})\text{LMe}](\text{NO}_3)_2$ (H_3LMe = Tris[2-((2-methylimidazol-4-yl)methylidene)amino]ethyl)amine). *Inorg. Chem.* **2003**, 42, 7001-7017.
71. Gaspar, A. B.; Muñoz, M. C.; Moliner, N.; Ksenofontov, V.; Levchenko, G.; Gütlich, P.; Real, J. A., Polymorphism and Pressure Driven Thermal Spin Crossover Phenomenon in $[\text{Fe}(\text{abpt})_2(\text{NCX})_2]$ (X=S, and Se): Synthesis, Structure and Magnetic Properties. *Monatsh. Chem.* **2003**, 134, 285-294.
72. Hang, H.; Fei, B.; Chen, X. Q.; Tong, M. L.; Ksenofontov, V.; Gural'skiy, I. y. A.; Bao, X., Multiple spin phases in a switchable Fe(II) complex: polymorphism and symmetry breaking effects. *J. Mater. Chem. C* **2018**, 6 (13), 3352-3361.
73. Alhassanat, A.; Völker, L.; Gamer, C.; Rauguth, A.; Kredel, A.; Luo, C.; Radu, F.; Sapozhnik, A. A.; Mashoff, T.; Rentschler, E.; Elmers, H. J., Solvent-induced high-spin transition in double-decker 3d-4f metallacrowns. *Phys. Rev. B* **2019**, 99 (10), 104404.
74. Archer, R. J.; Scott, H. S.; Polson, M. I. J.; Mathonière, C.; Rouzières, M.; Clérac, R.; Kruger, P. E., Solvent Dependent Spin-Crossover and Photomagnetic Properties in an Imidazolylimine FeII Complex. *Chem. Asian J.* **2019**, 14 (13), 2225-2229.
75. Galet, A.; Gaspar, A. B.; Muñoz, M. C.; Real, J. A., Influence of the counterion and the solvent molecules in the spin crossover system $[\text{Co}(\text{4-terpyridone})_2]X_p \cdot n\text{H}_2\text{O}$. *Inorg. Chem.* **2006**, 45, 4413-4422.
76. Garcia, Y.; van Koningsbruggen, P. J.; Lapouyade, R.; Fournès, L.; Rabardel, L.; Kahn, O.; Ksenofontov, V.; Levchenko, G.; Gütlich, P., Influences of Temperature, Pressure, and Lattice Solvents on the Spin Transition Regime of the Polymeric Compound $[\text{Fe}(\text{hyetrz})_3]A_2 \cdot 3\text{H}_2\text{O}$ (hyetrz = 4-(2'-hydroxyethyl)-1,2,4-triazole and A- = 3-nitrophenylsulfonate). *Chem. Mater.* **1998**, 10, 2426-2433.
77. Johnson, C. J.; Morgan, G. G.; Albrecht, M., Predictable adjustment of spin crossover temperature in solutions of iron(III) complexes functionalized with alkyl-urea tails. *J. Mater. Chem. C* **2015**, 3 (30), 7883-7889.
78. Leita, B. A.; Neville, S. M.; Halder, G. J.; Moubaraki, B.; Kepert, C. J.; Létard, J.-F.; Murray, K. S., Anion-Solvent Dependence of Bistability in a Family of Meridional N-Donor-Ligand-Containing Iron(II) Spin Crossover Complexes. *Inorg. Chem.* **2007**, 46 (21), 8784-8795.

79. Lemerrier, G.; Bréfuel, N.; Shova, S.; Wolny, J. A.; Dahan, F.; Verelst, M.; Paulsen, H.; Trautwein, A.; Tuchagues, J. P., A Range of Spin-Crossover Temperature $T_{1/2} > 300$ K Results from Out-of-Sphere Anion Exchange in a Series of Ferrous Materials Based on the 4-(4-Imidazolylmethyl)-2-(2-imidazolylmethyl)imidazole (trim) Ligand, $[\text{Fe}(\text{trim})_2]\text{X}_2$ (X=F, Cl, Br, I): Comparison of Experimental Results with Those Derived from Density Functional Theory Calculations. *Chem. Eur. J.* **2006**, 7421-7432.
80. Ni, Z.; Shores, M. P., Magnetic observation of anion binding in iron coordination complexes: toward spin-switching chemosensors. *J. Am. Chem. Soc.* **2009**, 131, 32–33.
81. Sundaresan, S.; Kitchen, J. A.; Brooker, S., Hydrophobic tail length in spin crossover active iron(II) complexes predictably tunes $T_{1/2}$ in solution and enables surface immobilization. *Inorg. Chem. Front.* **2020**, 7, 2050–2059.
82. Martinho, P. N.; Ortin, Y.; Gildea, B.; Gandolfi, C.; McKerr, G.; O'Hagan, B.; Albrecht, M.; Morgan, G. G., Inducing hysteretic spin crossover in solution. *Dalton Trans.* **2012**, 41, 7461-7463.
83. Rodríguez-Jiménez, S.; Yang, M.; Stewart, I.; Garden, A. L.; Brooker, S., A simple method of predicting spin state in solution. *J. Am. Chem. Soc.* **2017**, 139 (50), 18392–18396.
84. Singh, S.; Brooker, S., Extension of azine-triazole synthesis to azole-triazoles reduces ligand field, leading to spin crossover in tris-L Fe(II). *Inorg. Chem.* **2020**, 59, 1265-1273.
85. Singh, S.; Brooker, S., Correlations between ligand field Δ_0 , spin crossover $T_{1/2}$ and redox potential E_{pa} in a family of five dinuclear helicates. *Chem. Sci.* **2021**, submitted.
86. Nowak, R.; Prasetyanto, E. A.; De Cola, L.; Bojer, B.; Siegel, R.; Senker, J.; Rossler, E.; Weber, B., Proton-driven coordination-induced spin state switch (PD-CISSS) of iron(II) complexes. *Chem. Comm.* **2017**, 53 (5), 971-974.
87. Strauß, B.; Gutmann, V.; Linert, W., Spin-crossover complexes in solution, II solvent effects on the high spin-low spin-equilibrium of $[\text{Fe}(\text{bzimpy})_2](\text{ClO}_4)_2$. *Monatsh. Chem.* **1993**, 124 (5), 515-522.
88. Rodríguez-Jiménez, S.; Barltrop, A. S.; White, N. G.; Feltham, H. L. C.; Brooker, S., Solvent polarity predictably tunes spin crossover $T_{1/2}$ in isomeric iron(II) pyrimidine triazoles. *Inorg. Chem.* **2018**, 57, 6266-6282.
89. Deeth, R. J.; Halcrow, M.; Kershaw Cook, L.; Raithby, P., Ab Initio Ligand Field Molecular Mechanics and the nature of metal-ligand π -bonding in Fe(II) 2,6-di(pyrazol-1-yl)pyridine spin crossover complexes. *Chem. Eur. J.* **2018**, 24, 5204–5212.
90. Banerjee, H.; Chakraborty, S.; Saha-Dasgupta, T., Design and Control of Cooperativity in Spin-Crossover in Metal–Organic Complexes: A Theoretical Overview. *Inorganics* **2017**, 5 (3), 47.
91. Bondi, L.; Garden, A. L.; Jerabek, P.; Totti, F.; Brooker, S., Quantitative and chemically intuitive evaluation of the nature of M-L bonds in paramagnetic compounds: application of EDA-NOCV theory to spin crossover complexes. *Chem. Eur. J.* **2020**, 26, 13677–13685.
92. Shores, M. P.; Klug, C. M.; Fiedler, S. R., Spin-state switching in solution. In *Spin-Crossover Materials: Properties and Applications*, John Wiley & Sons Ltd: Chichester, **2013**; pp 281-301.
93. Paulsen, H.; Duelund, L.; Winkler, H.; Toftlund, H.; Trautwein, A. X., Free Energy of Spin-Crossover Complexes Calculated with Density Functional Methods. *Inorg. Chem.* **2001**, 40, 2201-2203.

94. Hauser, A., Ligand Field Theoretical Considerations. *Top. Curr. Chem.* **2004**, *233*, 49.
95. Miller, R. G.; Narayanaswamy, S.; Tallon, J. L.; Brooker, S., Spin crossover with thermal hysteresis in cobalt(II) complexes and the importance of scan rate. *New J. Chem.* **2014**, *38*, 1932-1941.
96. Kulmaczewski, R.; Olguín, J.; Kitchen, J. A.; Feltham, H. L. C.; Jameson, G. N. L.; Tallon, J. L.; Brooker, S., Remarkable scan rate dependence for a highly constrained dinuclear iron(II) spin crossover complex with a record thermal hysteresis loop. *J. Am. Chem. Soc.* **2014**, *136*, 878–881.
97. Gütlich, P.; Goodwin, H. A., *Spin Crossover in Transition Metal Compounds I-III*. *Top. Curr. Chem.* Springer Berlin Heidelberg: 2004; Vol. 233-235.
98. Poneti, G.; Poggini, L.; Mannini, M.; Cortigiani, B.; Sorace, L.; Otero, E.; Sainctavit, P.; Magnani, A.; Sessoli, R.; Dei, A., Thermal and optical control of electronic states in a single layer of switchable paramagnetic molecules. *Chemical Science* **2015**, *6* (4), 2268-2274.
99. Warner, B.; Oberg, J. C.; Gill, T. G.; El Hallak, F.; Hirjibehedin, C. F.; Serri, M.; Heutz, S.; Arrio, M.-A.; Sainctavit, P.; Mannini, M.; Poneti, G.; Sessoli, R.; Rosa, P., Temperature- and Light-Induced Spin Crossover Observed by X-ray Spectroscopy on Isolated Fe(II) Complexes on Gold. *The Journal of Physical Chemistry Letters* **2013**, *4* (9), 1546-1552.
100. Mallah, T.; Cavallini, M., Surfaces, thin films and patterning of spin crossover compounds. *C. R. Chim.* **2018**, *21* (12), 1270-1286.
101. Roubeau, O.; Agricole, B.; Clérac, R.; Ravaine, S., Triazole-Based Magnetic Langmuir–Blodgett Films: Paramagnetic to Spin-Crossover Behavior. *J. Phys. Chem. B* **2004**, *108* (39), 15110-15116.
102. Hagiwara, H.; Matsumoto, N.; Iijima, S.; Kojima, M., Layered iron (II) spin crossover complex constructed by NH \cdots Br \cdots hydrogen bonds with 2 K wide thermal hysteresis, [Fe(II)H₃LMe] Br \cdot CF₃SO₃ (H₃LMe= tris [2-(((2-methylimidazol-4-yl) methylidene) amino) ethyl] amine). *Inorg. Chim. Acta* **2011**, *366* (1), 283-289.
103. Lazar, H. Z.; Forestier, T.; Barrett, S. A.; Kilner, C. A.; Létard, J.-F.; Halcrow, M. A., Thermal and light-induced spin-crossover in salts of the heptadentate complex [tris (4-{pyrazol-3-yl}-3-aza-3-butenyl) amine] iron (II). *Dalton Trans.* **2007**, (38), 4276-4285.
104. Cowan, M. G.; Olguín, J.; Narayanaswamy, S.; Tallon, J. L.; Brooker, S., Reversible switching of a cobalt complex by thermal, pressure and electrochemical stimuli: abrupt, complete, hysteretic spin crossover. *J. Am. Chem. Soc.* **2012**, *134*, 2892–2894 and front cover feature.
105. Rodríguez-Jiménez, S.; Brooker, S., Solid Versus Solution Spin Crossover and the Importance of Fe-N \equiv C(X) Angle. *Inorg. Chem.* **2017**, *56*, 13697-13708.
106. Alvarez, S., Relationships between temperature, magnetic moment, and continuous symmetry measures in spin crossover complexes. *J. Am. Chem. Soc.* **2003**, *125* (22), 6795-6802.
107. Holland, J. M.; McAllister, J. A.; Kilner, C. A.; Thornton-Pett, M.; Bridgeman, A. J.; Halcrow, M. A., Stereochemical Effects on the Spin-State Transition Shown by Salts of [FeL₂]²⁺ [L = 2,6-Di(pyrazol-1-yl)pyridine]. *Dalton Trans.* **2002**, 2002, 548.
108. Long, G. J.; Grandjean, D.; Reger, D. L., Spin crossover in pyrazolylborate and pyrazolylmethane complexes. *Top. Curr. Chem.* **2004**, *233*, 91-122.

109. Marchivie, M.; Guionneau, P.; Letard, J.-F.; Chasseau, D., Towards direct correlations between spin-crossover and structural features in iron(II) complexes. *Acta Cryst. B* **2003**, *59* (4), 479-486.
110. Renovitch, G. A.; Baker, W. A., Spin equilibrium in tris (2-aminomethylpyridine) iron (II) halides. *J. Am. Chem. Soc.* **1967**, *89* (24), 6377-6378.
111. Halcrow, M. A., Structure: function relationships in molecular spin-crossover complexes. *Chem. Soc. Rev.* **2011**, *40*, 4119-4142.
112. Barrett, S. A.; Kilner, C. A.; Halcrow, M. A., Spin-crossover in $[\text{Fe}(\text{3-bpp})_2][\text{BF}_4]_2$ in different solvents – A dramatic stabilisation of the low-spin state in water. *Dalton Trans.* **2011**, *40*, 12021-12024.
113. Lin, H.-J.; Siretanu, D.; Dickie, D. A.; Subedi, D.; Scepaniak, J. J.; Mitcov, D.; Clérac, R.; Smith, J. M., Steric and Electronic Control of the Spin State in Three-Fold Symmetric, Four-Coordinate Iron(II) Complexes. *J. Am. Chem. Soc.* **2014**, *136* (38), 13326-13332.
114. Ni, Z.; McDaniel, A. M.; Shores, M. P., Ambient temperature anion-dependent spin state switching observed in “mostly low spin” heteroleptic iron(II) diimine complexes. *Chem. Sci.* **2010**, *1*, 615-621.
115. Weber, B.; Walker, F. A., Solution NMR studies of iron(II) spin-crossover complexes. *Inorg. Chem.* **2007**, *46*, 6794-6803.
116. Piguet, C., Paramagnetic susceptibility by NMR: the 'solvent correction' removed for large paramagnetic molecules. *J. Chem. Ed.* **1997**, *74*, 815-816.
117. Gispert, J. R., *Coordination Chemistry*. Wiley-VCH: Weinheim, 2008; p 640.
118. Bain, G. A.; Berry, J. F., Diamagnetic Corrections and Pascal's Constants. *J. Chem. Educ.* **2008**.
119. Kahn, O., *Molecular Magnetism*. VCH Publishers Inc.: New York, 1993.
120. Valkai, S.; Liszi, J.; Szalai, I., Temperature dependence of the refractive index for three chloromethane liquids at 514.5 nm and 632.8 nm wavelengths. *J. Chem. Thermodyn.* **1998**, *30* (7), 825-832.
121. Palombo, F.; Paolantoni, M.; Sassi, P.; Morresi, A.; Giorgini, M. G., Molecular dynamics of liquid acetone determined by depolarized Rayleigh and low-frequency Raman scattering spectroscopy. *Phys. Chem. Chem. Phys.* **2011**, *13* (36), 16197-16207.
122. Evans, D. F.; James, T. A., Variable-temperature Magnetic-susceptibility Measurements of Spin Equilibria for Iron(III) Dithiocarbamates in Solution. *Dalton Trans.* **1979**, 723-726.
123. Rodríguez-Jiménez, S. Spin crossover by design. PhD thesis, University of Otago, New Zealand, **2017**.
124. Hammett, L. P., The effect of structure upon the reactions of organic compounds. Benzene derivatives. *J. Am. Chem. Soc.* **1937**, *59*, 96-103.
125. Hansch, C.; Leo, A.; Taft, R. W., A survey of Hammett substituent constants and resonance field parameters. *Chem. Rev.* **1991**, *91*, 165-195.
126. Phan, H.; Hrudka, J. J.; Igimbayeva, D.; Lawson Daku, L. M.; Shatruk, M., A simple approach for predicting the spin state of homoleptic Fe(II) tris-diimine complexes. *J. Am. Chem. Soc.* **2017**, *139*, 6437-6447.
127. Nakano, K.; Suemura, N.; Yoneda, K.; Kawata, S.; Kaizaki, S., Substituent effect of the coordinated pyridine in a series of pyrazolato bridged dinuclear diiron (II) complexes on the spin-crossover behavior. *Dalton Trans.* **2005**, (4), 740-743.
128. Létard, J.-F.; Carbonera, C.; Real, J. A.; Kawata, S.; Kaizaki, S., Photomagnetism of a Series of Dinuclear Iron(II) Complexes. *Chem. Eur. J.* **2009**, *15*, 4146-4155.

129. Phonsri, W.; Darveniza, L.; Batten, S.; Murray, K., Heteroleptic and Homoleptic Iron(III) Spin-Crossover Complexes; Effects of Ligand Substituents and Intermolecular Interactions between Co-Cation/Anion and the Complex. *Inorganics* **2017**, *5* (3), 51.
130. Park, J. G.; Jeon, I.-R.; Harris, T. D., Electronic Effects of Ligand Substitution on Spin Crossover in a Series of Diiminoquinonoid-Bridged Fe^{II} Complexes. *Inorg. Chem.* **2015**, *54* (1), 359-369.
131. Phonsri, W.; Macedo, D. S.; Vignesh, K. R.; Rajaraman, G.; Davies, C. G.; Jameson, G. N. L.; Moubaraki, B.; Ward, J. S.; Kruger, P. E.; Chastanet, G.; Murray, K. S., Halogen Substitution Effects on N₂O Schiff Base Ligands in Unprecedented Abrupt Fe(II) Spin Crossover Complexes. *Chem. Eur. J.* **2017**, *23* (29), 7052-7065.
132. Takahashi, K.; Hasegawa, Y.; Sakamoto, R.; Nishikawa, M.; Kume, S.; Nishibori, E.; Nishihara, H., Solid-state ligand-driven light-induced spin change at ambient temperatures in bis(dipyrazolylstyrylpyridine)iron(II) complexes. *Inorg. Chem.* **2012**, *51*, 5188-5198.
133. Nakano, K.; Suemura, N.; Yoneda, K.; Kawata, S.; Kaizaki, S., Substituent effect of the coordinated pyridine in a series of pyrazolato bridged dinuclear diiron(II) complexes on the spin-crossover behavior. *Dalton Trans.* **2005**, 740-743.
134. Kershaw Cook, L. J.; Kulmaczewski, R.; Barrett, S. A.; Halcrow, M. A., Iron(II) Complexes of 4-Sulfanyl-, 4-Sulfinyl- and 4-Sulfonyl-2,6-dipyrazolylpyridine Ligands. A Subtle Interplay Between Spin-Crossover and Crystallographic Phase Changes. *Inorg. Chem. Front.* **2015**, *2*, 662.
135. Kershaw Cook, L. J.; Fisher, J.; Harding, L. P.; Halcrow, M. A., An iron(II) spin-crossover metallacycle from a back-to-back bis-[dipyrazolylpyridine]. *Dalton Trans.* **2015**, *44* (20), 9417-9425.
136. Pritchard, R.; Kilner, C. A.; Barrett, S. A.; Halcrow, M. A., Two new 4',4''-disubstituted dipyrazolylpyridine derivatives, and the structures and spin states of their iron(II) complexes. *Inorg. Chim. Acta* **2009**, *362* (12), 4365-4371.
137. Pritchard, R.; Lazar, H.; Barrett, S. A.; Kilner, C. A.; Asthana, S.; Carbonera, C.; Letard, J.-F.; Halcrow, M. A., Thermal and light-induced spin-transitions in iron(II) complexes of 2,6-bis(4-halopyrazolyl)pyridines: the influence of polymorphism on a spin-crossover compound. *Dalton Trans.* **2009**, (33), 6656-6666.
138. Halcrow, M. A., Manipulating metal spin states for biomimetic, catalytic and molecular materials chemistry. *Dalton Trans.* **2020**, *49* (44), 15560-15567.
139. Kitchen, J. A.; Brooker, S., Spin crossover in iron(II) complexes of 3,5-di(2-pyridyl)-1,2,4-triazoles and 3,5-di(2-pyridyl)-1,2,4-triazolates. *Coord. Chem. Rev.* **2008**, *252*, 2072-2092.
140. Kitchen, J. A.; White, N. G.; Jameson, G. N. L.; Tallon, J. L.; Brooker, S., Effect of counter anion X on the spin crossover properties of a family of diiron(II) triazole complexes [Fe^{II}₂(PMAT)₂](X)₄. *Inorg. Chem.* **2011**, *50*, 4586-4597.
141. Kimura, A.; Ishida, T., Pybox-Iron(II) Spin-Crossover Complexes with Substituent Effects from the 4-Position of the Pyridine Ring (Pybox = 2,6-Bis(oxazolin-2-yl)pyridine). *Inorganics* **2017**, *5* (3), 52.
142. Kimura, A.; Ishida, T. In *Substituent effect in spin-crossover behavior of iron (II)-Ar-pybox complexes (Ar-pybox= 4-aryl-2, 6-bis (oxazolin-2-yl) pyridine)*, AIP Conference Proceedings, AIP Publishing LLC: 2018; p 020025.

143. Flöser, B. M.; Guo, Y.; Riplinger, C.; Tuczek, F.; Neese, F., Detailed Pair Natural Orbital-Based Coupled Cluster Studies of Spin Crossover Energetics. *J. Chem. Theory Comput.* **2020**, *16* (4), 2224-2235.
144. Malmqvist, P.-Å.; Roos, B. O., The CASSCF state interaction method. *Chem. Phys. Lett.* **1989**, *155* (2), 189-194.
145. Atanasov, M.; Ganyushin, D.; Sivalingam, K.; Neese, F., A modern first-principles view on ligand field theory through the eyes of correlated multireference wavefunctions. In *Molecular Electronic Structures of Transition Metal Complexes II*, Springer: 2011; pp 149-220.
146. Hysteresis, P. R. o. t. E. C. i. a. R. G. o., Magnetic bistability: From microscopic to macroscopic understandings of hysteretic behavior using *ab initio* calculations. *Phys. Rev. B* **2009**, *79*, 094428.
147. V., K. M. L. G. B. R., Primary Role of the Electrostatic Contributions in a Rational Growth of Hysteresis Loop in Spin-Crossover Fe(II) Complexes. *J. Am. Chem. Soc.* **2009**, *131*, 11498-11502.
148. Le Guennic, B.; Borshch, S.; Robert, V., Prussian Blue Analogue CsFe[Cr(CN)₆] as a Matrix for the Fe(II) Spin-Crossover. *Inorg. Chem.* **2007**, *46* (26), 11106-11111.
149. Angeli, C. In *Multireference perturbation theory: the n-electron valence state perturbation theory approach*, Recent Advances in Many Electron Theories, Raman Centre For Atomic, Molecular & Optical Science, Indian Association for the Cultivation of Science: 2010; pp 13-13.
150. Michelin, R. A.; Zanotto, L.; Braga, D.; Sabatino, P.; Angelici, R. J., Transition-Metal-Promoted Cyclization Reactions of Isocyanide Ligands. Synthesis of Cyclic An-electron valence state perturbation theory: A spinless formulation and an efficient implementation of the strongly contracted and of the partially contracted variantminooxycarbene Complexes of Platinum (II) and X-ray Structure of trans-[PPh₃]₂Pt[CN(C₆H₄-*p*-Me)CH₂CH₂O]Br]BF₄. *Inorg. Chem.* **1987**, *27* (1), 85-92.
151. Angeli, C.; Cimiraaglia, R.; Malrieu, J.-P., n-electron valence state perturbation theory: A spinless formulation and an efficient implementation of the strongly contracted and of the partially contracted variants. *J. Chem. Phys.* **2002**, *117* (20), 9138-9153.
152. Angeli, C.; Bories, B.; Cavallini, A.; Cimiraaglia, R., Third-order multireference perturbation theory: The n-electron valence state perturbation-theory approach. *J. Chem. Phys.* **2006**, *124* (5), 054108.
153. Rudavskiy, A.; Sousa, C.; de Graaf, C.; Havenith, R. W. A.; Broer, R., Computational approach to the study of thermal spin crossover phenomena. *J. Chem. Phys.* **2014**, *140*, 184318.
154. Sousa, C.; de Graaf, C.; Rudavskiy, A.; Broer, R., Theoretical Study of the Light-Induced Spin Crossover Mechanism in [Fe(mtz)₆]²⁺ and [Fe(phen)₃]²⁺. *J. Phys. Chem. A* **2017**, *121* (51), 9720-9727.
155. Domingo, A.; Àngels Carvajal, M.; De Graaf, C., Spin crossover in Fe (II) complexes: An *ab initio* study of ligand σ -donation. *Int. J. Quantum Chem.* **2010**, *110* (2), 331-337.
156. de Graaf, C.; Sousa, C., Study of the light-induced spin crossover process of the [Fe^{II}(bpy)₃]²⁺ complex. *Chem. Eur. J.* **2010**, *16* (15), 4550-4556.
157. Lang, L.; Atanasov, M.; Neese, F., Improvement of *Ab Initio* Ligand Field Theory by Means of Multistate Perturbation Theory. *J. Phys. Chem. A* **2020**, *124* (5), 1025-1037.
158. Grünsteudel, H.; Paulsen, H.; Meyer-Klaucke, W.; Winkler, H.; Trautwein, A.; Grünsteudel, H.; Baron, A.; Chumakov, A.; Rüffer, R.; Toftlund, H., Nuclear resonant

- scattering and molecular orbital calculations on an iron (II) spin-crossover complex. *Hyperfine interactions* **1998**, *113* (1-4), 311-317.
159. Ye, S.; Neese, F., Accurate modeling of spin-state energetics in spin-crossover systems with modern Density Functional Theory. *Inorg. Chem.* **2010**, *49*, 772-774.
160. Janet, J. P.; Chan, L.; Kulik, H. J., Accelerating Chemical Discovery with Machine Learning: Simulated Evolution of Spin Crossover Complexes with an Artificial Neural Network. *J. Phys. Chem. Lett.* **2018**, *9* (5), 1064-1071.
161. Reiher, M., Theoretical Study of the Fe(phen)₂(NCS)₂ Spin-Crossover Complex with Reparametrized Density Functionals. *Inorg. Chem.* **2002**, *41* (25), 6928-6935.
162. Jensen, K. P.; Cirera, J., Accurate Computed Enthalpies of Spin Crossover in Iron and Cobalt Complexes. *J. Phys. Chem. A* **2009**, *113* (37), 10033-10039.
163. Kepp, K. P., Theoretical Study of Spin Crossover in 30 Iron Complexes. *Inorg. Chem.* **2016**, *55* (6), 2717-2727.
164. Cirera, J.; Paesani, F., Theoretical prediction of spin-crossover temperatures in Ligand-Driven Light-Induced Spin Change systems. *Inorg. Chem.* **2012**, *51*, 8194-8201.
165. Isley Iii, W. C.; Zarra, S.; Carlson, R. K.; Bilbeisi, R. A.; Ronson, T. K.; Nitschke, J. R.; Gagliardi, L.; Cramer, C. J., Predicting paramagnetic ¹H NMR chemical shifts and state-energy separations in spin-crossover host-guest systems. *Phys. Chem. Chem. Phys.* **2014**, *16* (22), 10620-10628.
166. Vela, S.; Novoa, J. J.; Ribas-Arino, J., Insights into the Crystal-Packing Effects on the Spin Crossover of [Fe^{II}(1-bpp)₂]²⁺-Based Materials. *Phys. Chem. Chem. Phys.* **2014**, *16*, 27012.
167. Liechtenstein, A.; Anisimov, V. I.; Zaanen, J., Density-functional theory and strong interactions: Orbital ordering in Mott-Hubbard insulators. *Phys. Rev. B* **1995**, *52* (8), R5467.
168. Dudarev, S. L.; Botton, G. A.; Savrasov, S. Y.; Humphreys, C. J.; Sutton, A. P., Electron-energy-loss spectra and the structural stability of nickel oxide: An LSDA+U study. *Phys. Rev. B* **1998**, *57* (3), 1505-1509.
169. Lebegue, S.; Pillet, S.; Angyan, J. G., Modeling spin-crossover compounds by periodic DFT+U approach. *Physical Review B. Condensed Matter* **2008**, *78* (2), 024433.
170. Vela, S.; Fumanal, M.; Ribas-Arino, J.; Robert, V., Towards an accurate and computationally-efficient modelling of Fe (II)-based spin crossover materials. *Phys. Chem. Chem. Phys.* **2015**, *17* (25), 16306-16314.
171. Handley, C. M.; Deeth, R. J., A multi-objective approach to force field optimization: structures and spin state energetics of d⁶ Fe (II) complexes. *J. Chem. Theory Comput.* **2012**, *8* (1), 194-202.
172. Deeth, R. J.; Anastasi, A. E.; Wilcockson, M. J., An in silico design tool for Fe (II) spin crossover and light-induced excited spin state-trapped complexes. *J. Am. Chem. Soc.* **2010**, *132* (20), 6876-6877.
173. Cirera, J.; Babin, V.; Paesani, F., Theoretical modeling of spin crossover in metal-organic frameworks:[Fe(pz)₂Pt(CN)₄] as a case study. *Inorg. Chem.* **2014**, *53* (20), 11020-11028.
174. Taylor, M. G.; Yang, T.; Lin, S.; Nandy, A.; Janet, J. P.; Duan, C.; Kulik, H. J., Seeing Is Believing: Experimental Spin States from Machine Learning Model Structure Predictions. *J. Phys. Chem. A* **2020**, *124* (16), 3286-3299.
175. Ziegler, T.; Rauk, A., Carbon monoxide, carbon monosulfide, molecular nitrogen, phosphorus trifluoride, and methyl isocyanide as sigma donors and pi acceptors. A

- theoretical study by the Hartree-Fock-Slater transition-state method. *Inorg. Chem.* **1979**, *18* (7), 1755-1759.
176. Jerabek, P.; Roesky, H. W.; Bertrand, G.; Frenking, G., Coinage metals binding as main group elements: structure and bonding of the carbene complexes $[TM(cAAC)_2]$ and $[TM(cAAC)_2]^+$ (TM= Cu, Ag, Au). *J. Am. Chem. Soc.* **2014**, *136* (49), 17123-17135.
177. Jerabek, P.; Schwerdtfeger, P.; Frenking, G., Dative and electron-sharing bonding in transition metal compounds. *J. Comput. Chem.* **2019**, *40* (1), 247-264.
178. Mitoraj, M. P.; Parafiniuk, M.; Srebro, M.; Handzlik, M.; Buczek, A.; Michalak, A., Applications of the ETS-NOCV method in descriptions of chemical reactions. *J. Mol. Model.* **2011**, *17* (9), 2337.
179. Zhao, L.; Pan, S.; Holzmann, N.; Schwerdtfeger, P.; Frenking, G., Chemical bonding and bonding models of main-group compounds. *Chem. Rev.* **2019**, *119* (14), 8781-8845.
180. Munz, D., Pushing Electrons - Which Carbene Ligand for Which Application? *Organomet.* **2018**, *37* (3), 275-289.
181. Zhao, L.; von Hopffgarten, M.; Andrada, D. M.; Frenking, G., Energy decomposition analysis. *Wiley Interdiscip. Rev. Comput. Mol. Sci.*, e1345-n/a.
182. Mitoraj, M.; Michalak, A., Natural orbitals for chemical valence as descriptors of chemical bonding in transition metal complexes. *J. Molec. Modeling* **2007**, *13* (2), 347-355.
183. Lin, S.; Diercks, C. S.; Zhang, Y.-B.; Kornienko, N.; Nichols, E. M.; Zhao, Y.; Paris, A. R.; Kim, D.; Yang, P.; Yaghi, O. M., Covalent organic frameworks comprising cobalt porphyrins for catalytic CO₂ reduction in water. *Science* **2015**, *349* (6253), 1208-1213.
184. Frenking, G.; Shaik, S., *The Chemical Bond: Chemical Bonding Across the Periodic Table*. John Wiley & Sons: 2014; Vol. 2.
185. Ziegler, T.; Rauk, A., A theoretical study of the ethylene-metal bond in complexes between copper (1+), silver (1+), gold (1+), platinum (0) or platinum (2+) and ethylene, based on the Hartree-Fock-Slater transition-state method. *Inorg. Chem.* **1979**, *18* (6), 1558-1565.
186. Mitoraj, M.; Michalak, A., Applications of natural orbitals for chemical valence in a description of bonding in conjugated molecules. *J. Molec. Modeling* **2008**, *14* (8), 681-687.
187. Michalak, A.; Mitoraj, M.; Ziegler, T., Bond orbitals from chemical valence theory. *J. Phys. Chem. A* **2008**, *112* (9), 1933-1939.
188. Deegan, M. M.; Muldoon, J. A.; Hughes, R. P.; Glueck, D. S.; Rheingold, A. L., Synthesis and Structure of Metal Complexes of P-Stereogenic Chiral Phosphiranes: An EDA-NOCV Analysis of the Donor-Acceptor Properties of Phosphirane Ligands. *Organometallics* **2018**, *37* (9), 1473-1482.
189. **DUPLICATE!**; Holland, J. M.; McAllister, J. A.; Kilner, C. A.; Thornton-Pett, M.; Bridgeman, A. J.; Halcrow, M. A., Stereochemical effects on the spin-state transition shown by salts of $[FeL_2]^{2+}$ [L = 2,6-di(pyrazol-1-yl)pyridine]. *J. Chem. Soc., Dalton Trans.* **2002**, 548-554.
190. Takahashi, K.; Hasegawa, Y.; Sakamoto, R.; Nishikawa, M.; Kume, S.; Nishibori, E.; Nishihara, H., Solid-State Ligand-Driven Light-Induced Spin Change at Ambient Temperatures in Bis(dipyrazolylstyrylpyridine)iron(II) Complexes. *Inorg. Chem.* **2012**, *51*, 5188.

191. Kuo, L. C.; Makinen, M. W., Ground term splitting of high-spin cobalt (2+) ion as a probe of coordination structure. 2. The ligand environment of the active site metal ion of carboxypeptidase A in ester hydrolysis. *J. Am. Chem. Soc.* **1985**, *107* (18), 5255-5261.
192. Kepp, K. P., Consistent descriptions of metal–ligand bonds and spin-crossover in inorganic chemistry. *Coord. Chem. Rev.* **2013**, *257*, 196-209.
193. Dalle, K. E.; Warnan, J.; Leung, J. J.; Reuillard, B.; Karmel, I. S.; Reisner, E., Electro- and solar-driven fuel synthesis with first row transition metal complexes. *Chem. Rev.* **2019**, 2752-2875.
194. Maher, A. G.; Passard, G.; Dogutan, D. K.; Halbach, R. L.; Anderson, B. L.; Gagliardi, C. J.; Taniguchi, M.; Lindsey, J. S.; Nocera, D. G., Hydrogen evolution catalysis by a sparsely substituted cobalt chlorin. *ACS Catalysis* **2017**, *7* (5), 3597-3606.
195. Glaser, T.; Hoeke, V.; Gieb, K.; Schnack, J.; Schröder, C.; Müller, P., Quantum tunneling of the magnetization in $[\text{Mn}^{\text{III}}\text{M}]^{3+}$ (M=Cr^{III}, Mn^{III}) SMMs: Impact of molecular and crystal symmetry. *Coord. Chem. Rev.* **2015**, *289–290*, 261–278.
196. Dhers, S.; Feltham, H. L. C.; Brooker, S., A toolbox of building blocks, linkers and crystallisation methods used to generate Single-Chain Magnets. *Coord. Chem. Rev.* **2015**, *296*, 24–44.
197. Jaffé, H. H., A reexamination of the Hammett equation. *Chem. Rev.* **1953**, *53*, 191-260.
198. McDaniel, D. H.; Brown, H. C., An extended table of Hammett substituent constants based on the ionization of substituted benzoic acids. *J. Org. Chem.* **1958**, *23*, 420-427.
199. Krylov, A. I., The quantum chemistry of open-shell species. *Rev. Comp. Chem.* **2017**, *30*, 151-224.
200. Singh, S. K.; Eng, J.; Atanasov, M.; Neese, F., Covalency and chemical bonding in transition metal complexes: An ab initio based ligand field perspective. *Coord. Chem. Rev.* **2017**, *344*, 2-25.
201. Helmich-Paris, B., CASSCF linear response calculations for large open-shell molecules. *J. Comput. Chem.* **2019**, *150* (17), 174121.
202. Haasnoot, J. G., Mononuclear, oligonuclear and polynuclear metal coordination compounds with 1,2,4-triazole derivatives as ligands. *Coord. Chem. Rev.* **2000**, *200–202*, 131-185.
203. Kumar, K. S.; Ruben, M., Emerging trends in spin crossover (SCO) based functional materials and devices. *Coord. Chem. Rev.* **2017**, *346*, 176-205.
204. Hogue, R. W.; Singh, S.; Brooker, S., Spin crossover in discrete polynuclear iron(II) complexes. *Chem. Soc. Rev.* **2018**, *47*, 7303-7338 and inside front cover.
205. Kahn, O.; Codjovi, E., Iron(II)-1,2,4-triazole spin transition molecular materials. *Phil. Trans. R. Soc. Lond. A* **1996**, *354*, 359-379.
206. Milocco, F.; de Vries, F.; Bartels, I. M. A.; Havenith, R. W. A.; Cirera, J.; Demeshko, S.; Meyer, F.; Otten, E., Electronic Control of Spin-Crossover Properties in Four-Coordinate Bis(formazanate) Iron(II) Complexes. *J. Am. Chem. Soc.* **2020**.
207. Haasnoot, J. G., *1,2,4-Triazoles as ligands for iron(II) high spin-low spin crossovers*. Kluwer Academic Publishers: Dordrecht, **1996**; p 299-321.
208. Kitchen, J. A.; White, N. G.; Boyd, M.; Moubaraki, B.; Murray, K. S.; Boyd, P. D. W.; Brooker, S., Iron(II) tris-[N⁴-substituted-3,5-di(2-pyridyl)-1,2,4-triazole] complexes: structural, magnetic, NMR and density functional theory studies. *Inorg. Chem.* **2009**, *48*, 6670–6679.

209. Levitt, M., Relaxation. *Spin dynamics: John Wiley & Sons, Ltd* **2008**, 543-595.
210. Klingele, M. H.; Brooker, S., From *N*-substituted thioamides to symmetrical and unsymmetrical 3,4,5-trisubstituted 4*H*-1,2,4-triazoles: synthesis and characterisation of new chelating ligands. *Eur. J. Org. Chem.* **2004**, 3422-3434.
211. Singh, S.; Hogue, R. W.; Feltham, H. L. C.; Brooker, S., Dinuclear helicate and tetranuclear cage assembly using appropriately designed ditopic triazole-azine ligands. *Dalton Trans.* **2019**, 15435-15444.
212. Gardner, E. J.; Cobb, C. R.; Bertke, J. A.; Warren, T. H., Tris (pyrazolyl) borate Copper Hydroxide Complexes Featuring Tunable Intramolecular H-Bonding. *Inorg. Chem.* **2019**, *58* (16), 11248-11255.
213. Voronkov, A.; Holsworth, D. D.; Waaler, J.; Wilson, S. R.; Ekblad, B.; Perdreau-Dahl, H.; Dinh, H.; Drewes, G.; Hopf, C.; Morth, J. P., Structural basis and SAR for G007-LK, a lead stage 1, 2, 4-triazole based specific tankyrase 1/2 inhibitor. *J. Med. Chem.* **2013**, *56* (7), 3012-3023.
214. Hoveyda, H. R.; Fraser, G. L.; Roy, M.-O.; Dutheuil, G.; Batt, F.; El Bousmaqui, M.; Korac, J.; Lenoir, F.; Lapin, A.; Noel, S., Discovery and optimization of novel antagonists to the human neurokinin-3 receptor for the treatment of sex-hormone disorders (Part I). *Eur. J. Med. Chem.* **2015**, *58* (7), 3060-3082.
215. Figgis, B. N., *Ligand Field Theory and its Applications*. Wiley-VCH: **2000**.
216. Slichter, C. P.; Drickamer, H. G., Pressure-induced electronic changes in compounds of iron. *J. Chem. Phys.* **1972**, *56*, 2142-2160.
217. Hogue, R. W.; Feltham, H. L. C.; Miller, R. G.; Brooker, S., Spin crossover in dinuclear N₄S₂ iron(II) thioether-triazole complexes: access to [HS-HS], [HS-LS] and [LS-LS] states. *Inorg. Chem.* **2016**, *55*, 4152-4165.
218. Turner, J. W.; Schultz, F. A., Solution characterization of the iron(II) bis(1,4,7-triazacyclononane) spin-equilibrium reaction. *Inorg. Chem.* **2001**, *40*, 5296-5298.
219. Stoychev, G. L.; Auer, A. A.; Izsák, R.; Neese, F., Self-Consistent Field Calculation of Nuclear Magnetic Resonance Chemical Shielding Constants Using Gauge-Including Atomic Orbitals and Approximate Two-Electron Integrals. *J. Chem. Theory Comput.* **2018**, *14* (2), 619-637.
220. Stoychev, G. L.; Auer, A. A.; Neese, F., Efficient and Accurate Prediction of Nuclear Magnetic Resonance Shielding Tensors with Double-Hybrid Density Functional Theory. *J. Chem. Theory Comput.* **2018**, *14* (9), 4756-4771.
221. Tao, J.; Perdew, J. P.; Staroverov, V. N.; Scuseria, G. E., Climbing the density functional ladder: Nonempirical meta-generalized gradient approximation designed for molecules and solids. *Phys. Rev. Lett.* **2003**, *91* (14), 146401.
222. Kendall, R. A.; Dunning Jr, T. H.; Harrison, R. J., Electron affinities of the first-row atoms revisited. Systematic basis sets and wave functions. *J. Chem. Phys.* **1992**, *96* (9), 6796-6806.
223. Dalle, K. E.; Warnan, J.; Leung, J. J.; Reuillard, B.; Karmel, I. S.; Reisner, E., Electro- and solar-driven fuel synthesis with first row transition metal complexes. *Coord. Chem. Rev.* **2019**, 2752-2875.
224. Yarbrough, L. W.; Hall, M. B., Photoelectron spectra of substituted chromium, molybdenum, and tungsten pentacarbonyls. Relative pi-acceptor and sigma-donor properties of various phosphorus ligands. *Inorg. Chem.* **1978**, *17* (8), 2269-2275.
225. Zhou, G.; Ho, C. L.; Wong, W. Y.; Wang, Q.; Ma, D.; Wang, L.; Lin, Z.; Marder, T. B.; Beeby, A., Manipulating Charge-Transfer Character with Electron-Withdrawing Main-

- Group Moieties for the Color Tuning of Iridium Electrophosphors. *Adv. Funct. Mater.* **2008**, *18* (3), 499-511.
226. Constable, E. C.; Steel, P. J., N,N'-Chelating Biheteroaromatic Ligands; A Survey. *Coord. Chem. Rev.* **1989**, *93*, 205-223.
227. Wiberg, K. B.; Nakaji, D.; Breneman, C. M., Azines. A theoretical study of π -electron delocalization. *J. Am. Chem. Soc.* **1989**, *111*, 4178-4190.
228. Joule, J. A.; Mills, K.; Smith, G. F., *J. Heterocycl. Chem.* 3 ed.; Chapman & Hall, Padstow: 1995.
229. Frenking, G.; Zhao, L.; Zhou, M.; Pan, S.; Deng, G.; Lei, S.; Wang, G.; Jin, J., Filling a Gap: The Coordinatively Saturated Group 4 Carbonyl Complexes $\text{TM}(\text{CO})_8$ (TM= Zr, Hf) and Ti $(\text{CO})_7$. *Chem. Eur. J.* **2020**.
230. Lupinetti, A. J.; Jonas, V.; Thiel, W.; Strauss, S. H.; Frenking, G., Trends in Molecular Geometries and Bond Strengths of the Homoleptic d10 Metal Carbonyl Cations $[\text{M}(\text{CO})_n]^{x+}$ ($\text{M}^{x+} = \text{Cu}^+, \text{Ag}^+, \text{Au}^+, \text{Zn}^{2+}, \text{Cd}^{2+}, \text{Hg}^{2+}$; $n = 1-6$): A Theoretical Study. *Chem. Eur. J.* **1999**, *5* (9), 2573-2583.
231. Wang, Q.; Pan, S.; Lei, S.; Jin, J.; Deng, G.; Wang, G.; Zhao, L.; Zhou, M.; Frenking, G., Octa-coordinated alkaline earth metal–dinitrogen complexes $\text{M}(\text{N}_2)_8$ (M= Ca, Sr, Ba). *Nat. Commun.* **2019**, *10* (1), 1-8.
232. Kan, Y., The nature of metal–metal bond of the dimetalocene complexes $[\text{M}^2(\eta^5\text{-C}_5\text{R}_5)_2\text{A}]$ cobalt complex redox shuttle for dye-sensitized solar cells with high open-circuit potential (M= Zn, Cd, Hg; R= H, Me): An energy decomposition analysis. *J. Mol. Struct.* **2007**, *805* (1-3), 127-132.
233. Kneusels, N.-J. H.; Münzer, J. E.; Flosdorf, K.; Jiang, D.; Neumüller, B.; Zhao, L.; Eichhöfer, A.; Frenking, G.; Kuzu, I., Double donation in trigonal planar iron–carbodiphosphorane complexes – a concise study on their spectroscopic and electronic properties. *Dalton Trans.* **2020**, *49* (8), 2537-2546.
234. Jeremias, L. s.; Novotný, J.; Repisky, M.; Komorovsky, S.; Marek, R., Interplay of Through-Bond Hyperfine and Substituent Effects on the NMR Chemical Shifts in Ru (III) Complexes. *Inorg. Chem.* **2018**, *57* (15), 8748-8759.
235. von Hopffgarten, M.; Frenking, G., Energy decomposition analysis. *WIREs Comput. Mol. Sci.* **2012**, *2* (1), 43-62.
236. Lyubimova, O.; Sizova, O. V.; Loschen, C.; Frenking, G., The nature of the metal–nitric oxide bond in the $[\text{M}(\text{CN})_5(\text{NO})]_q$ (M= Cr, Mn, Fe, Ru, Os, and Co) and trans- $[\text{Ru}(\text{NH}_3)_4\text{L}(\text{NO})]_q$ (L= pyrazine, pyridine, N_2 , H_2O , Cl^- , CN^- , NO_2^-) complexes: A bond-energy decomposition analysis. *J. Mol. Struct.* **2008**, *865* (1-3), 28-35.
237. Suresh, C. H.; Frenking, G., Direct 1–3 Metal–Carbon Bonding and Planar Tetracoordinated Carbon in Group 6 Metallacyclobutadienes. *Organometallics* **2010**, *29* (21), 4766-4769.
238. Keypour, H.; Shooshtari, A.; Rezaeivala, M.; Bayat, M.; Rudbari, H. A., Synthesis and characterization of new Mn(II) and Cd(II) Schiff base complexes containing homopiperazine moiety: Spectral, X-ray crystal structural and theoretical studies. *Inorg. Chim. Acta* **2016**, *440*, 139-147.
239. Bayat, M.; Hatami, M., Nature of the metal–ligand bond in some $[(\text{CO})_4\text{M} \leftarrow \text{B}^{\text{II}}\text{M}(\text{R})]$ {M=Cr, Mo, W; R=H, F, Cl, Br} complexes: A theoretical study. *Polyhedron* **2016**, *110*, 46-54.
240. Pietrzyk, P.; Podolska, K.; Mazur, T.; Sojka, Z., Heterogeneous binding of dioxygen: EPR and DFT evidence for side-on nickel (II)–superoxo adduct with

- unprecedented magnetic structure hosted in MFI zeolite. *J. Am. Chem. Soc.* **2011**, *133* (49), 19931-19943.
241. Rabanal-León, W. A.; Murillo-López, J. A.; Arratia-Pérez, R., Insights into bonding interactions and excitation energies of 3d–4f mixed lanthanide transition metal macrocyclic complexes. *Phys. Chem. Chem. Phys.* **2016**, *18* (48), 33218-33225.
242. Chi, C.; Pan, S.; Jin, J.; Meng, L.; Luo, M.; Zhao, L.; Zhou, M.; Frenking, G., Octacarbonyl Ion Complexes of Actinides [An (CO)₈]^{+/-} (An= Th, U) and the Role of f Orbitals in Metal–Ligand Bonding. *Chem. Eur. J* **2019**, *25* (50), 11772-11784.
243. Jin, J.; Pan, S.; Jin, X.; Lei, S.; Zhao, L.; Frenking, G.; Zhou, M., Octacarbonyl Anion Complexes of the Late Lanthanides Ln (CO)₈–(Ln= Tm, Yb, Lu) and the 32-Electron Rule. *Chem. Eur. J* **2019**, *25* (13), 3229-3234.
244. Li, W.-L.; Zhang, Q.; Chen, M.; Hu, H.-S.; Li, J.; Zhou, M., Formation and Characterization of a BeOBeC Multiple Radical Featuring a Quartet Carbyne Moiety. *Angew. Chem. Int. Ed.* **2020**, *n/a* (n/a), Spin crossover-induced colossal positive and negative thermal expansion in a nanoporous coordination framework ma.
245. Yang, W.; Krantz, K. E.; Freeman, L. A.; Dickie, D. A.; Molino, A.; Frenking, G.; Pan, S.; Wilson, D. J. D.; Gilliard Jr., R. J., Persistent Borafluorene Radicals. *Angew. Chem. Int. Ed.* **2020**, *59* (10), 3850-3854.
246. Wu, X.; Zhao, L.; Jin, J.; Pan, S.; Li, W.; Jin, X.; Wang, G.; Zhou, M.; Frenking, G., Observation of alkaline earth complexes M(CO)₈ (M = Ca, Sr, or Ba) that mimic transition metals. *Science* **2018**, *361* (6405), 912-916.
247. Priya, A. M.; Lakshmipathi, S., Atmospheric fate of diketones and OH radical–kinetics, reaction force, ETS-NOCV analysis. *Mol. Phys.* **2017**, *115* (7), 839-859.
248. Stauch, T.; Chakraborty, R.; Head-Gordon, M., Quantum Chemical Modeling of Pressure-Induced Spin Crossover in Octahedral Metal-Ligand Complexes. *Chem. Phys. Chem.* **2019**, *20* (21), 2742-2747.
249. Sieber, R.; Decurtins, S.; Stoeckli-Evans, H.; Wilson, C.; Yufit, D.; Howard, J. A. K.; Capelli, S. C.; Hauser, A., A Thermal Spin Transition in [Co(bpy)₃][LiCr(ox)₃]. *Chem. Eur. J.* **2000**, *6*, 361-368.
250. Letard, J.-F., Photomagnetism of iron(II) spin crossover complexes - the T(LIESST) approach. *J. Mater. Chem.* **2006**, *16*, 2550-2559.
251. Oka, K.; Azuma, M.; Chen, W.-t.; Yusa, H.; Belik, A. A.; Takayama-Muromachi, E.; Mizumaki, M.; Ishimatsu, N.; Hiraoka, N.; Tsujimoto, M.; Tucker, M. G.; Attfield, J. P.; Shimakawa, Y., Pressure-induced spin-state transition in BiCoO₃. *J. Am. Chem. Soc.* **2010**, *132*, 9438-9443.
252. Murphy, M. J.; Zenere, K. A.; Ragon, F.; Southon, P. D.; Kepert, C. J.; Neville, S. M., Guest programmable multistep SCO in a porous 2-D Hofmann-type material. *J. Am. Chem. Soc.* **2017**, *139* (3), 1330-1335.
253. Chastanet, G.; Desplanches, C.; Baldé, C.; Rosa, P.; Marchivie, M.; Guionneau, P., A critical review of the T(LIESST) temperature in spin crossover materials – What it is and what it is not. *Chem. Sq.* **2018**, *2*, 2.
254. Rodríguez-Jiménez, S.; Bondi, L.; Yang, M.; Garden, A. L.; Brooker, S., Predictable electronic tuning by choice of azine substituent in five iron(II) triazoles: redox properties and DFT calculations. *Chem. Asian J.* **2019**, *14*, 1158–1166.
255. Baerends, E.; Branchadell, V.; Sodupe, M., Atomic reference energies for density functional calculations. *Chem. Phys. Lett.* **1997**, *265* (3-5), 481-489.

256. Loschen, C.; Frenking, G., Quantum chemical investigations and bonding analysis of iron complexes with mixed cyano and carbonyl ligands. *Inorg. Chem.* **2004**, *43* (2), 778-784.
257. Shannon, R. D., Revised effective ionic radii and systematic studies of interatomic distances in halides and chalcogenides. *Acta Cryst. A: crystal physics, diffraction, theoretical and general crystallography* **1976**, *32* (5), 751-767.
258. Neese, F., Software update: the ORCA program system, version 4.0. *WIREs Comput. Mol. Sci.* **2018**, *8* (1), e1327.
259. Grimme, S.; Ehrlich, S.; Goerigk, L., Effect of the damping function in dispersion corrected density functional theory. *J. Comput. Chem.* **2011**, *32* (7), 1456-1465.
260. Grimme, S.; Antony, J.; Ehrlich, S.; Krieg, H., A consistent and accurate ab initio parametrization of density functional dispersion correction (DFT-D) for the 94 elements H-Pu. *J. Chem. Phys.* **2010**, *132* (15), 154104.
261. Weigend, F.; Ahlrichs, R., Balanced basis sets of split valence, triple zeta valence and quadruple zeta valence quality for H to Rn: Design and assessment of accuracy. *Phys. Chem. Chem. Phys.* **2005**, *7* (18), 3297-3305.
262. Weigend, F., Accurate Coulomb-fitting basis sets for H to Rn. *Phys. Chem. Chem. Phys.* **2006**, *8* (9), 1057-1065.
263. Becke, A. D., Density-functional exchange-energy approximation with correct asymptotic behavior. *Phys. Rev. A* **1988**, *38* (6), 3098-3100.
264. Perdew, J. P.; Yue, W., Accurate and simple density functional for the electronic exchange energy: Generalized gradient approximation. *Phys. Rev. B* **1986**, *33* (12), 8800-8802.
265. Takano, Y.; Houk, K. N., Benchmarking the conductor-like polarizable continuum model (CPCM) for aqueous solvation free energies of neutral and ionic organic molecules. *J. Chem. Theory Comput.* **2005**, *1* (1), 70-77.
266. Vahtras, O.; Almlöf, J.; Feyereisen, M. W., Integral approximations for LCAO-SCF calculations. *Chem. Phys. Lett.* **1993**, *213* (5-6), 514-518.
267. Weigend, F.; Häser, M., RI-MP2: first derivatives and global consistency. *Theor. Chem. Acc.* **1997**, *97* (1-4), 331-340.
268. Van Lenthe, E.; Baerends, E. J., Optimized Slater-type basis sets for the elements 1-118. *J. Comput. Chem.* **2003**, *24* (9), 1142-1156.
269. Te Velde, G. t.; Bickelhaupt, F. M.; Baerends, E. J.; Fonseca Guerra, C.; van Gisbergen, S. J.; Snijders, J. G.; Ziegler, T., Chemistry with ADF. *J. Comput. Chem.* **2001**, *22* (9), 931-967.
270. Yum, J.-H.; Baranoff, E.; Kessler, F.; Moehl, T.; Ahmad, S.; Bessho, T.; Marchioro, A.; Ghadiri, E.; Moser, J.-E.; Yi, C.; Nazeeruddin, M. K.; Grätzel, M., A cobalt complex redox shuttle for dye-sensitized solar cells with high open-circuit potentials. *Nat. Comm.* **2012**, *3*, 631.
271. Hammett, L. P., Some relations between reaction rates and equilibrium constants. *Chem. Rev.* **1935**, *17*, 125-136.
272. Gerloch, M.; Woolley, R. G., The functional group in ligand-field studies: the empirical and theoretical status of the Angular Overlap Model. In *Prog. Inorg. Chem.*, 1984; pp 371-446.
273. Mitoraj, M.; Michalak, A., Donor-acceptor properties of ligands from the natural orbitals for chemical valence. *Organomet.* **2007**, *26* (26), 6576-6580.

274. Teng, Q.; Huynh, H. V., Determining the electron-donating properties of bidentate ligands by ^{13}C NMR spectroscopy. *Inorg. Chem.* **2014**, *53*, 10964-10973.
275. Ashley, D. C.; Jakubikova, E., Tuning the redox potentials and ligand field strength of Fe(II) polypyridines: the dual π -donor and π -acceptor character of bipyridine. *Inorg. Chem.* **2018**, *57*, 9907-9917.
276. Frenking, G., Understanding the nature of the bonding in transition metal complexes: from Dewar's molecular orbital model to an energy partitioning analysis of the metal–ligand bond. *J. Organomet. Chem.* **2001**, *635* (1-2), 9-23.
277. Hauser, A., Light-induced spin crossover and the high spin \rightarrow low-spin relaxation. *Top. Curr. Chem.* **2004**, *234*, 155-198.
278. Gaspar, A. B.; Seredyuk, M., Spin crossover in soft matter. *Coord. Chem. Rev.* **2014**, *268*, 41–58.
279. Murphy, M. J.; Zenere, K. A.; Ragon, F.; Southon, P. D.; Kepert, C. J.; Neville, S. M., Guest programmable multistep SCO in a porous 2-D Hofmann-type material. *Journal of the American Chemical Society* **2017**, *139* (3), 1330-1335.
280. Halcrow, M. A.; Capel Berdiell, I.; Pask, C. M.; Kulmaczewski, R., Relationship between the Molecular Structure and Switching Temperature in a Library of Spin-Crossover Molecular Materials. *Inorg. Chem.* **2019**, *58*, 9811-9821.
281. Cossi, M.; Rega, N.; Scalmani, G.; Barone, V., Energies, structures, and electronic properties of molecules in solution with the C-PCM solvation model. *J. Comput. Chem.* **2003**, *24* (6), 669-681.
282. Guo, Y.; Sivalingam, K.; Valeev, E. F.; Neese, F., SparseMaps—A systematic infrastructure for reduced-scaling electronic structure methods. III. Linear-scaling multireference domain-based pair natural orbital N-electron valence perturbation theory. *J. Chem. Phys.* **2016**, *144* (9), 094111.
283. Lefter, C.; Davesne, V.; Salmon, L.; Molnár, G.; Demont, P.; Rotaru, A.; Bousseksou, A., Charge transport and electrical properties of SCO materials: towards nanoelectronic and spintronic devices. *Magnetochemistry* **2016**, *2*, 18.
284. Moodera, J. S.; Koopmans, B.; Oppeneer, P. M., On the path toward organic spintronics. *MRS Bulletin* **2014**, *39* (7), 578-581.
285. Poggini, L.; Londi, G.; Milek, M.; Naim, A.; Lanzilotto, V.; Cortigiani, B.; Bondino, F.; Magnano, E.; Otero, E.; Sainctavit, P.; Arrio, M.-A.; Juhin, A.; Marchivie, M.; Khusniyarov, M. M.; Totti, F.; Rosa, P.; Mannini, M., Surface effects on a photochromic spin-crossover iron(II) molecular switch adsorbed on highly oriented pyrolytic graphite. *Nanoscale* **2019**, *11* (42), 20006-20014.
286. Poggini, L.; Milek, M.; Londi, G.; Naim, A.; Poneti, G.; Squillantini, L.; Magnani, A.; Totti, F.; Rosa, P.; Khusniyarov, M. M.; Mannini, M., Room temperature control of spin states in a thin film of a photochromic iron(ii) complex. *Mater. Horiz.* **2018**, *5* (3), 506-513.
287. Wang, J.-L.; Liu, Q.; Meng, Y.-S.; Liu, X.; Zheng, H.; Shi, Q.; Duan, C.-Y.; Liu, T., Fluorescence modulation via photoinduced spin crossover switched energy transfer from fluorophores to Fe II ions. *Chem. Sci.* **2018**, *9* (11), 2892-2897.
288. Nasser, J.; Boukheddaden, K.; Linares, J., Two-step spin conversion and other effects in the atom-phonon coupling model. *Eur. Phys. J. B* **2004**, *39* (2), 219-227.
289. Nasser, J.; Topçu, S.; Chassagne, L.; Wakim, M.; Bennali, B.; Linares, J.; Alayli, Y., Two-dimensional atom-phonon coupling model for spin conversion: role of metastable states. *Eur. Phys. J. B* **2011**, *83* (2), 115.

290. Enachescu, C.; Tanasa, R.; Stancu, A.; Codjovi, E.; Linares, J.; Varret, F., FORC method applied to the thermal hysteresis of spin transition solids: first approach of static and kinetic properties. *Phys. B* **2004**, *343*, 15-19.
291. Gudyma, I.; Maksymov, A.; Enachescu, C., Phase transition in spin-crossover compounds in the breathing crystal field model. *Phys. Rev. B* **2014**, *89* (22), 224412.
292. Spiering, H.; Meissner, E.; Köppen, H.; Müller, E.; Gütlich, P., The effect of the lattice expansion on high spin \rightleftharpoons low spin transitions. *Chem. Phys.* **1982**, *68* (1-2), 65-71.
293. Nishino, M.; Enachescu, C.; Miyashita, S.; Boukheddaden, K.; Varret, F., Intrinsic effects of the boundary condition on switching processes in effective long-range interactions originating from local structural change. *Phys. Rev. B* **2010**, *82* (2), 020409.
294. Nishino, M.; Boukheddaden, K.; Konishi, Y.; Miyashita, S., Simple two-dimensional model for the elastic origin of cooperativity among spin states of spin-crossover complexes. *Phys. Rev. Lett.* **2007**, *98* (24), 247203.
295. Römer, A.; Hasecke, L.; Blöchl, P.; Mata, R. A., A Review of Density Functional Models for the Description of Fe(II) Spin-Crossover Complexes. *Molecules* **2020**, *25* (21).
296. Sorai, M.; Seki, S., Phonon coupled cooperative low-spin 1A_1 high-spin 5T_2 transition in $[\text{Fe}(\text{phen})_2(\text{NCS})_2]$ and $[\text{Fe}(\text{phen})_2(\text{NCSe})_2]$ crystals. *J. Phys. Chem. Solids* **1974**, *35*, 555-570.
297. Ksenofontov, V.; Levchenko, G.; Spiering, H.; Gütlich, P.; Létard, J. F.; Bouhedja, Y.; Kahn, O., Spin crossover behavior under pressure of $\text{Fe}(\text{PM-L})_2(\text{NCS})_2$ compounds with substituted 2'-pyridylmethylene 4-anilino ligands. *Chem. Phys. Lett.* **1998**, *294* (6), 545-553.
298. Gaspar, A. B.; Ksenofontov, V.; Seredyuk, M.; Gütlich, P., Multifunctionality in spin crossover materials. *Coord. Chem. Rev.* **2005**, *249*, 2661-2676.
299. Kaiba, A.; Shepherd, H. J.; Fedouai, D.; Rosa, P.; Goeta, A. E.; Rebbani, N.; Létard, J. F.; Guionneau, P., Crystallographic elucidation of purely structural, thermal and light-induced spin transitions in an iron(II) binuclear complex. *Dalton Trans.* **2010**, *39*, 2910-2918.
300. Shepherd, H. J.; Rosa, P.; Vendier, L.; Casati, N.; Létard, J.-F.; Bousseksou, A.; Guionneau, P.; Molnár, G., High-pressure spin-crossover in a dinuclear Fe(II) complex. *Phys. Chem. Chem. Phys.* **2012**, *14*, 5265-5271.
301. Guionneau, P., Crystallography and spin-crossover. A view of breathing materials. *Dalton Trans.* **2014**, *43* (2), 382-393.
302. Collet, E.; Guionneau, P., Structural analysis of spin-crossover materials: From molecules to materials. *C. R. Chim.* **2018**, *21* (12), 1133-1151.
303. Ozarowski, A.; McGarvey, B. R.; Sarkar, A. B.; Drake, J. E., EPR study of manganese (II) in two crystalline forms of bis (2, 2'-bi-2-thiazoline) bis (thiocyanato) iron and the high-spin-low-spin transition that occurs in only one form. X-ray structure determination of both forms. *Inorg. Chem.* **1988**, *27* (4), 628-635.
304. Gentili, D.; Liscio, F.; Demitri, N.; Schaefer, B.; Borgatti, F.; Torelli, P.; Gobaut, B.; Panaccione, G.; Rossi, G.; Degli Esposti, A.; gazzano, m.; Milita, S.; Bergenti, I.; Ruani, G.; Salitros, I.; Ruben, M.; Cavallini, M., Surface induces different crystal structures in room temperature switchable spin crossover compound. *Dalton Trans.* **2015**, *45* (1), 134-143.
305. Aryasetiawan, F.; Karlsson, K.; Jepsen, O.; Schönberger, U., Calculations of Hubbard U from first-principles. *Phys. Rev. B* **2006**, *74* (12), 125106.

306. Bonadeo, H.; D'aleccio, E.; Halac, E.; Burgos, E., Lattice dynamics, thermodynamic functions, and phase transitions of p-dichloro-and 1, 2, 4, 5-tetrachlorobenzene. *J. Chem. Phys.* **1978**, *68* (10), 4714-4721.
307. McQuarrie, D., *Statistical Mechanics (University Science Books, CA, 2000)*. Sausalito, CA, 2000.
308. Ninova, S.; Lanzilotto, V.; Malavolti, L.; Rigamonti, L.; Cortigiani, B.; Mannini, M.; Totti, F.; Sessoli, R., Valence electronic structure of sublimated Fe₄ single-molecule magnets: an experimental and theoretical characterization. *J. Mater. Chem. C* **2014**, *2* (45), 9599-9608.
309. Kuehne, I. A.; Barker, A.; Zhang, F.; Stamenov, P.; O'Doherty, O.; Müller-Bunz, H.; Stein, M.; Rodriguez, B. J.; MORGAN, G. G., Modulation of Jahn-Teller Distortion and Electromechanical Response in a Mn³⁺ Spin Crossover Complex. *J. Phys. Condens. Matter* **2020**, *32* (40), 404002.
310. Gütlich, P.; Ksenofontov, V.; Gaspar, A. B., Pressure effect studies on spin crossover systems. *Coord. Chem. Rev.* **2005**, *249*, 1811–1829.
311. Hutter, J.; Iannuzzi, M.; Schiffmann, F.; VandeVondele, J., CP2K: atomistic simulations of condensed matter systems. *Wiley Interdiscip. Rev. Comput. Mol. Sci.* **2014**, *4* (1), 15-25.
312. Krack, M., Pseudopotentials for H to Kr optimized for gradient-corrected exchange-correlation functionals. *Theor. Chem. Acc.* **2005**, *114* (1-3), 145-152.
313. Hartwigsen, C.; Goedecker, S.; Hutter, J., Relativistic separable dual-space Gaussian pseudopotentials from H to Rn. *Phys. Rev. B* **1998**, *58* (7), 3641.
314. Goedecker, S.; Teter, M.; Hutter, J., Separable dual-space Gaussian pseudopotentials. *Phys. Rev. B* **1996**, *54* (3), 1703-1710.
315. Caldeweyher, E.; Bannwarth, C.; Grimme, S., Extension of the D3 dispersion coefficient model. *J. Chem. Phys.* **2017**, *147* (3), 034112.
316. Perdew, J. P.; Ruzsinszky, A.; Csonka, G. I.; Vydrov, O. A.; Scuseria, G. E.; Constantin, L. A.; Zhou, X.; Burke, K., Restoring the density-gradient expansion for exchange in solids and surfaces. *Phys. Rev. Lett.* **2008**, *100* (13), 136406.
317. Vydrov, O. A.; Van Voorhis, T., Nonlocal van der Waals density functional: The simpler the better. *J. Chem. Phys.* **2010**, *133* (24), 244103.
318. Sabatini, R.; Gorni, T.; de Gironcoli, S., Nonlocal van der Waals density functional made simple and efficient. *Phys. Rev. B* **2013**, *87* (4), 041108.
319. Perdew, J. P.; Yue, W., Accurate and simple density functional for the electronic exchange energy: Generalized gradient approximation. *Phys. Rev. B* **1986**, *33* (12), 8800-8802.
320. Neese, F., *Wiley Interdiscip. Rev. Comput. Mol. Sci.* **2012**, *2*, 73.
321. Buron-Le Cointe, M.; Hébert, J.; Baldé, C.; Moisan, N.; Toupet, L.; Guionneau, P.; Létard, J. F.; Freysz, E.; Cailleau, H.; Collet, E., Intermolecular Control of Thermoswitching and Photoswitching Phenomena in Two Spin-Crossover Polymorphs. *Phys. Rev. B: Condens. Matter Mater. Phys.* **2012**, *85*, 064114.
322. Lufaso, M. W.; Woodward, P. M., Jahn–Teller distortions, cation ordering and octahedral tilting in perovskites. *Acta Crystallogr. B Struct. Sci. Cryst.* **2004**, *60* (1), 10-20.
323. McCusker, J. K.; Rheingold, A. L.; Hendrickson, D. N., Variable-Temperature Studies of Laser-Initiated ⁵T₂ - ¹A₁ Intersystem Crossing in Spin-Crossover Complexes: Empirical Correlations between Activation Parameters and Ligand Structure in a Series of Polypyridyl Ferrous Complexes. *Inorg. Chem.* **1996**, *35*, 2100-2112.

324. Marchivie, M.; Guionneau, P.; Létard, J. F.; Chasseau, D., Photo-Induced Spin-Transition: the Role of the Iron(II) Environment Distortion. *Acta Crystallogr., Sect. B: Struct. Sci.* **2005**, *61*, 25.
325. Ketkaew, R.; Tantirungrotechai, Y.; Harding, P.; Chastanet, G.; Guionneau, P.; Marchivie, M.; Harding, D. J., OctaDist: A tool for calculating distortion parameters in spin crossover and coordination complexes. *Dalton Trans.* **2021**, *50*, 1086-1096.
326. Humphrey, W.; Dalke, A.; Schulten, K., VMD: visual molecular dynamics. *J. Mol. Graph.* **1996**, *14* (1), 33-38.
327. Krober, J.; Codjovi, E.; Kahn, O.; Groliere, F.; Jay, C., A spin transition system with a thermal hysteresis at room temperature. *J. Am. Chem. Soc.* **1993**, *115*, 9810-9811.
328. Meng, W.; Breiner, B.; Rissanen, K.; Thoburn, J. D.; Clegg, J. K.; Nitschke, J. R., A Self-Assembled M_8L_6 Cubic Cage that Selectively Encapsulates Large Aromatic Guests. *Angew. Chem. Int. Ed.* **2011**, *50* (15), 3479-3483.
329. Sheldrick, G. M., SADABS, An Empirical Absorption Correction Program For Area Detector Data; University of Göttingen: Germany. **1996**.
330. Saha, N. C.; Mandal, S.; Das, M.; Khatun, N.; Mitra, D.; Samanta, A.; Slawin, A. M. Z.; Butcher, R. J.; Saha, R., Synthesis, characterization, X-ray crystallography and antimicrobial activities of new Co(III) and Cu(II) complexes with a pyrazole based Schiff base ligand. *Polyhedron* **2014**, *68*, 122-130.
331. Palatinus, L.; Chapuis, G., SUPERFLIP. A computer program for the solution of crystal structures by charge flipping in arbitrary dimensions. *J. Appl. Crystallogr.* **2007**, *40* (4), 786-790.
332. Sheldrick, G. M., A short history of *SHELX*. *Acta Crystallogr., Sect. A: Found. Crystallogr.* **2008**, *A64*, 112-122.
333. Schrödinger, E., An undulatory theory of the mechanics of atoms and molecules. *Phys. Rev.* **1926**, *28* (6), 1049.
334. Born, M.; Oppenheimer, R., Zur quantentheorie der molekeln. *Ann. Phys.* **1927**, *389* (20), 457-484.
335. Löwdin, P.-O., Quantum Theory of Many-Particle Systems. III. Extension of the Hartree-Fock Scheme to Include Degenerate Systems and Correlation Effects. *Phys. Rev.* **1955**, *97* (6), 1509-1520.
336. McGuire, J., Electron Correlation Dynamics in Atomic Collisions Cambridge University Press. Cambridge: 1997.
337. Kohn, W.; Sham, L. J., Self-consistent equations including exchange and correlation effects. *Phys. Rev.* **1965**, *140* (4A), A1133.
338. Debye, P., Methods to determine the electrical and geometrical structure of molecules. *Nobel Lectures, Chemistry* **1922**, *1941*, 383-401.
339. Von Weizsäcker, C., CF Von Weizsäcker, *Z. Phys.* *96*, 431 (1935). *Z. Phys.* **1935**, *96*, 431.
340. Perdew, J. P.; Burke, K.; Ernzerhof, M., Generalized gradient approximation made simple. *Phys. Rev. Lett.* **1996**, *77* (18), 3865.
341. Burke, K.; Perdew, J. P.; Wang, Y., Derivation of a generalized gradient approximation: The PW91 density functional. In *Electronic Density Functional Theory*, Springer: 1998; pp 81-111.
342. Hammer, B.; Hansen, L. B.; Nørskov, J. K., Improved adsorption energetics within density-functional theory using revised Perdew-Burke-Ernzerhof functionals. *Phys. Rev. B* **1999**, *59* (11), 7413.

343. Becke, A. D., Becke's three parameter hybrid method using the LYP correlation functional. *J. Chem. Phys* **1993**, *98*, 5648-5652.
344. Lee, C.; Yang, W.; Parr, R., Density-functional exchange-energy approximation with correct asymptotic behaviour. *Phys. Rev. B* **1988**, *37*, 785-789.
345. Jeffrey, G. A.; Jeffrey, G. A., *An introduction to hydrogen bonding*. Oxford University Press New York: 1997; Vol. 32.
346. Desiraju, G. R.; Steiner, T., *The weak hydrogen bond in structural chemistry and biology*. Oxford University Press: Oxford, 1999.
347. Desiraju, G. R., C-H...O and other weak hydrogen bonds. From crystal engineering to virtual screening. *Chem. Comm.* **2005**, 2995-3001.
348. Evans, D. F., The determination of the paramagnetic susceptibility of substances in solution by nuclear magnetic resonance. *J. Chem. Soc.* **1959**, 2003-2005.
349. Brown, A. M., A step-by-step guide to non-linear regression analysis of experimental data using a Microsoft Excel spreadsheet. *Computer Methods and Programs in Biomedicine* **2001**, *65* (3), 191-200.
350. Galbraith, S. G.; Plieger, P. G.; Tasker, P. A., Cooperative sulfate binding by metal salt extractants containing 3-dialkylaminomethylsalicylaldimine units. *Chem. Commun.* **2002**, 2662-2663.

The End